

Design and Tooth Contact Analysis of Spiral Bevel Gear Pair Using Different Material by KISSsoft Software

Sunil Padole¹, Dr. Ravindra Pathak²

¹PhD Research Scholar, Mechanical Engineering Department, Medi-Caps University,
Indore

²Assoc. Professor, Mechanical Engineering Department, Medi-Caps University, Indore.

Abstract. In this paper Spiral Bevel Gear is design for the transmission of a real-gear vehicle drive. 3D Model has been done in PTC Creo software with number of teeth 11 and 54 and Normal module is 5 with Uniform Depth Klingelnberg System. Finite Element Analysis has been done in Ansys Workbench 14.0 of the drive with a certain load of 200Nm. Transmission Error and Contact Pattern obtained in KISSsoft Software at different material with applied standard torque 658.6Nm and Speed 1450RPM of Pinion with Klingelnberg System. The obtained results it indicates (stress, strain and transmission error and contact pattern) are compared with different material like (Steel, Cast Iron, Bronze and Dry Powered Metal) of Gear Pair. The material of SINT D39, Dry Powdered Metal is most suitable for the low level of noise during meshing.

Keywords: Tooth contact Analysis, Spiral bevel gear, Transmission error, Klingelnberg, Simulation

1. INTRODUCTION

Since it saves money before going through the manufacturing process, modelling is essential in industry. To verify that the model satisfies the design criteria, designers might simulate and compute, but Modeling is a delicate procedure because the model must be approximated to real-life running conditions while still delivering rapid and trustworthy results. When each tooth comes into touch with another, vibrations might occur. This relates to the design, production, and complexity of the generated gear. A designer must consider several factors when designing transmission or driveline gears. The most important are transmission error, bending stress, and surface stress. A tool called tooth contact analysis can calculate this outcome. In order to conduct theoretical assessments of contact characteristics and running quality, TCA (tooth contact analysis) was originally utilised in the early 1960s. Compared to finite element analysis, several technologies can now quickly complete this analysis and provide suitable findings. Experimentation can be done by trial and error, However, it is costly, time-consuming, and in some cases deadly. This enables the use of various gear calculation tools for virtual gear modelling and tooth contact investigation. Gear modeling utilizing various software will be covered in this study. The software's output will be displayed, and the results will be discussed and compared. Three different software will be used to model the investigated gear pair. PTC Creo is a solid modeling software, KISSsoft for tooth contact analysis comes next, Finally, there's ANSYS, which is a finite element software. The analysis will take into account three conditions. The first provides fundamental geometry with primary micro geometry modifications, the second is the misalignment and the third model incorporates the last micro geometry adjustment to compensate for misalignment

2. FIELD OF RESEARCH

When using tooth contact analysis to measure transmission noise and vibration, transmission error is a key topic. Theoretically, uniform angular motion should be transmitted by a pair of

meshing gears with perfectly involute tooth profiles. However, most gear systems are unable to convey a same angular motion. The discrepancy between the theoretical and actual angular velocity constitutes the transmission error of the pair in the mesh. It is regarded as the second-largest source of noise, after the result of tooth interaction, the angular speed fluctuation does not cause this. The vibrational bearing reactions caused by torsional acceleration excite the gearbox case, the noise is then propagated through the casing wall's pulsation.

Transmission error, according to Wright, can be defined as

$$TE = \theta_2 - \theta_1(Z_1/Z_2)$$

θ_1 = Pinion Rotation angle.

θ_2 = Gear Rotation angle.

Z_1 = Pinion of number of teeth.

Z_2 = Gear of number of teeth.

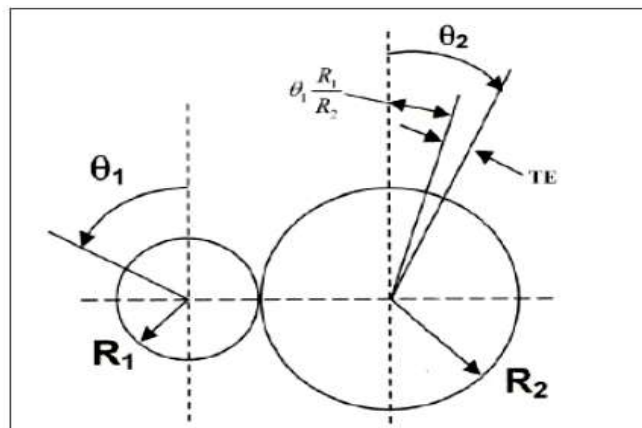


Figure 1. Transmission error definition

The units of measurement for transmission error include arcsec and μrad . The linear displacement can be translated to either μm or μin at the base radius or pitch radius.

Tharmakulasingam (2010) describes many types of transmission errors, including manufacturing transmission error, static transmission error, kinematic transmission error, and dynamic transmission error. This study is only concerned with a static transmission fault. Static transmission error (STE) is measured at low speeds to counteract the system's dynamic effect. This function of gear geometry is affected by mesh stiffness, manufacturing flaws, load, and mesh alignment, among other factors. In order to promote beneficial contact and lower transmission error, Kissling (2008) defines microgeometry modification in gears as the deliberate removal of material from the tooth profile and flank line. A poor macro geometry decision can never be made up for by an appropriate micro geometry adjustment at this point of gear construction. A single design, however, cannot be produced that satisfies every criteria, including those for loudness, scuffing, micro pitting, and service life. This kind of adjustment is done to take into account shaft misalignment brought on by the assembly as well as manufacturing tolerances. The profile, lead, and bias are three different alterations that can be present in the design. The first two types will be described here because they were used in the study, according to Zhao et al. (2018). The material is removed from the tip and root of the teeth in order to reduce excessive pressures in those areas. Relief may be linear or parabolic. It is essential to decide where the relief should start. The term "tip or root relief start diameter" refers to this dimension. Alternative terminology for profile crowning change is barrelling.

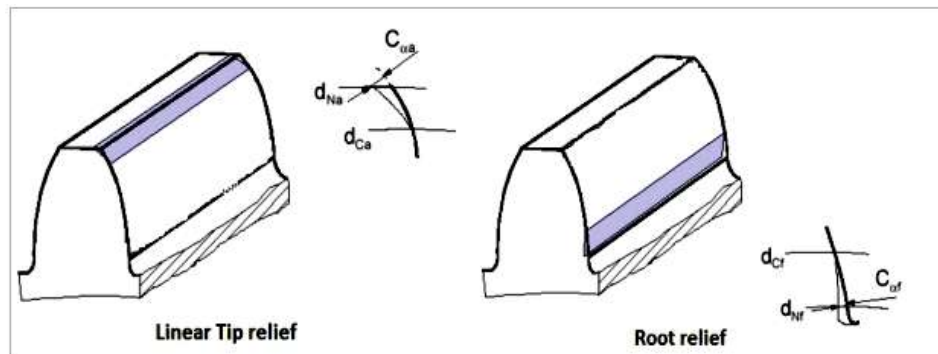


Figure 2. Linear tip and root relief

The material at the beginning and end of the active profile (Start at Profile) can be gradually removed (End at Profile). No material is removed from (Start at Profile) for the purpose of adjusting the slope of the profile, but the required amount is removed at the (End at Profile).

Advantage is it useful as a safety against overly close contact at the tooth's tip.

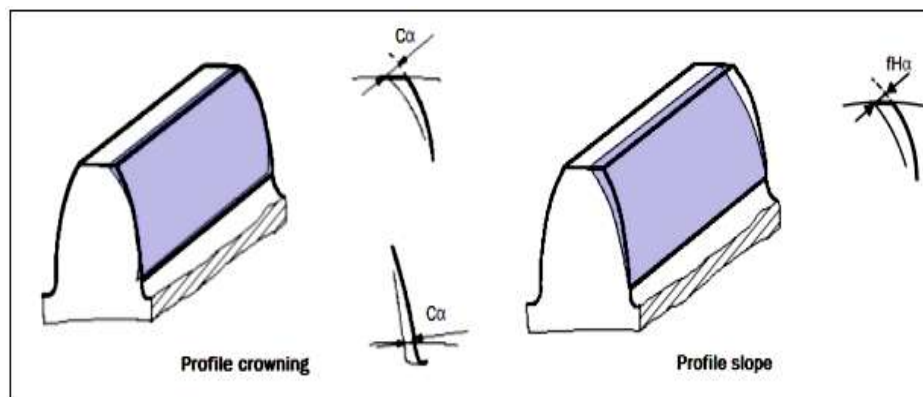


Figure 3. Profile crowning and profile slope modification

Material remove at both (tiff and root) of tooth in Profile crowning. Material remove at one end (tiff or root) of tooth in profile slope modification.

A lead modification is used to change the gear's axial direction. The surface of the tooth becomes considerably convex once the lead crown is applied.

Advantage is it serves as a safeguard against overly close contact at the tooth's tip. The lead slope is employed to remove a certain material from the face width's end while leaving the face width's beginning unaltered.

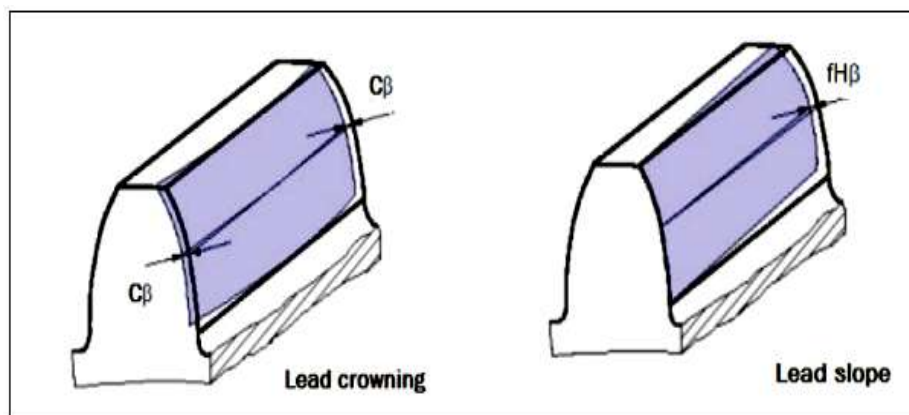


Figure 4. Lead crowning and Lead slope modification

Material remove at both end of face tooth in Lead crowning. Material remove at one end of face tooth in Lead slope modification.

Advantages are like micro geometry modifications are widely used by designers to remove corner contact, reduce transmission error, and improve gear tooth contact patterns.

3. PROBLEM IDENTIFICATION

The major goal of the research is to use appropriate optimization techniques to optimize the design of a differential gearbox while considering multiple objective functions and related restrictions..

The differential gearbox multi-objective design optimization presents numerous obstacles.

They are;

1. Using the proper optimization approach, locate the Pareto fronts.
2. The goal is to identify the global optimum value that provides the best solution to the problem.

The challenges of differential gearbox manufacturing optimization

3. Less weight of gears and hence cost saving.
4. Less volume and hence less space requirement.
5. High efficiency of transmission and hence better performance.
6. Reliable operation during service life.
7. Minimum peak-to-peak transmission error.

These difficulties are crucial in determining the differential gearbox's performance. The design of the gearbox must be optimized in the presence of numerous conflicting objectives that are exposed to several constraints in order to improve power transfer. The goal of the research presented here is to overcome the difficulties of multi-objective design optimization of a differential gearbox, which must be executed to meet certain requirements. Using a reliable model, it is desirable to identify the suitable simulation.

Problem Statement and Methodology

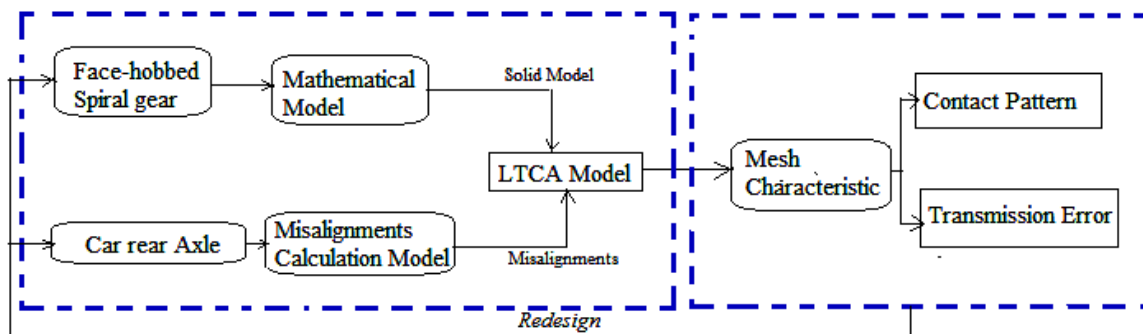


Figure 5. The Analysis Flow Chart

Based on the calculation of misalignments and the LTCA model. The approach for predicting mesh behaviours for face-hobbed Spiral Bevel gear while accounting for misalignments caused by system deformation is as follows. Initially, a manufacturing-based mathematic model of a face-hobbed spiral gear is established.

The misalignment calculation model is built around the entire back axle. The FEA model is then built using the result of the preceding sub-model. The mesh behaviour analysis can be performed using the LTCA model (different material).

The objectives for the proposed research work are as

1. To create the solid model of the Klingelnberg System's spiral bevel gear pair in PTC Creo.
2. To find out the Transmission error at under applying load Conditions in KISSsoft.
3. To obtained the Maximum Line Load in Dynamic Conditions.
4. To optimized the Material of gear pair for low noise Conditions.

5. To Computed the Stress, Strain and Displacement in Ansys Workbench.

Table1. Geometric data of the available model case. (Uniform Depth Klingenberg System)

		Pinion (A)	Gear (B)
Number of teeth	Z	11	54
Normal module	m	5	
Shaft angle	Σ	90°	
Mean Spiral Angle	β_m	30°	
Pressure Angle		20°	
Hand of Spiral		LH	RH
Facewidth (mm)	b	50	
Outer pitch diameter (mm)	da	73.489	360.763
Addendum(mm)	ha	7	3
Dedendum (mm)	df	4.25	8.25

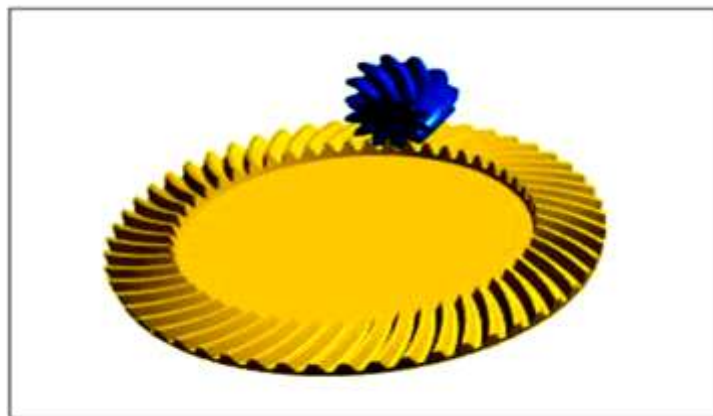


Figure 6. 3D Model of Spiral Bevel Gear (PTC Creo)

In the figure, the pinion has 11 teeth, the gear has 54 teeth, and there are 5 modules. Pressure angle is 20°, Spiral Angle is 35°, The tooth height is essentially constant and the tooth curve in the Klingelnberg System is involute.

Profile Modification

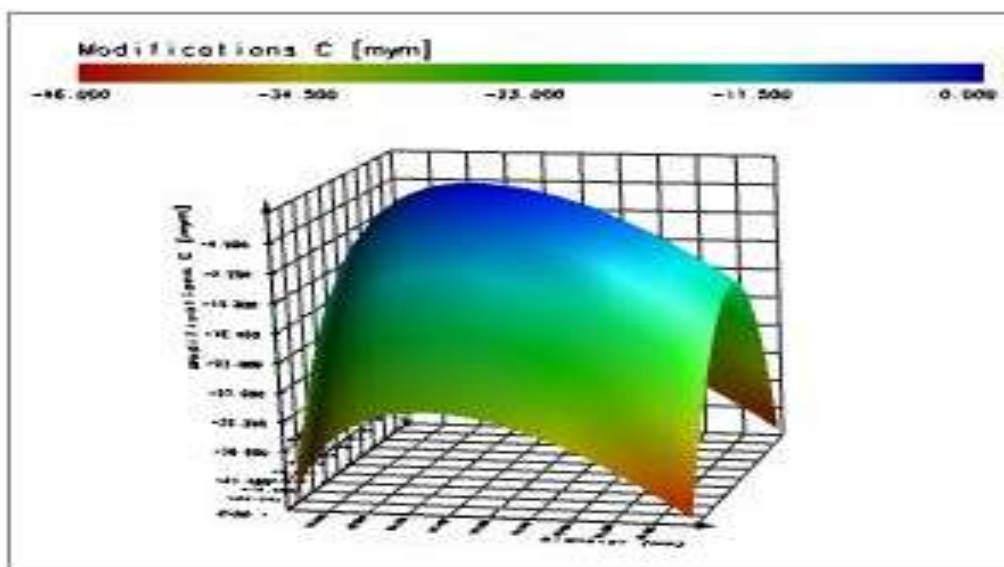


Figure 7. Gear of Profile crowning 15μm (KISSsoft)

In the diagram, there are 54 gear teeth, 5 gear modules, 15 μm of profile crowning gear, and 30 μm of crowning gear. The gear's outside pitch diameter is 360.763mm.

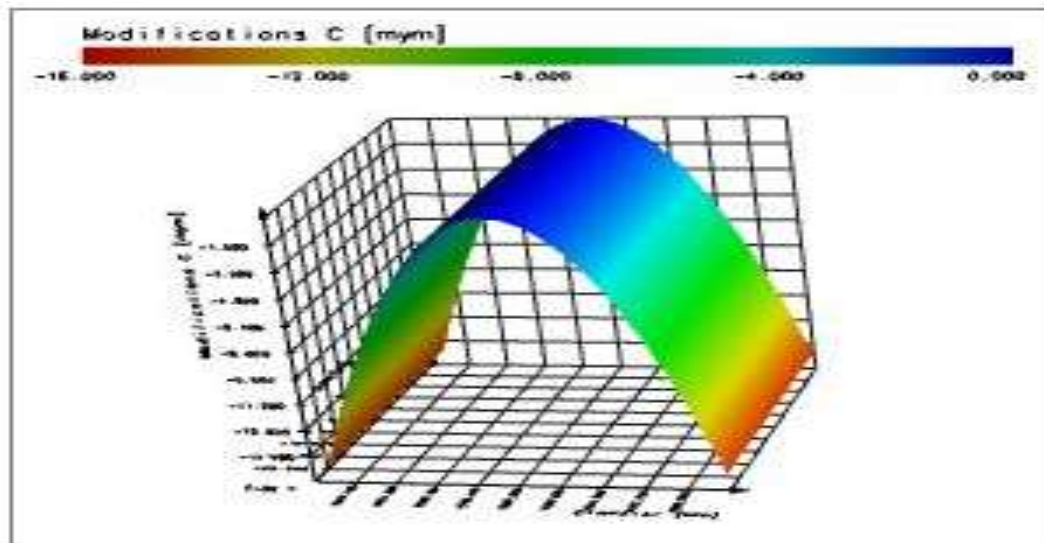


Figure 8. Pinion of Profile crowning 15 μm (KISSsoft)

The pinion in the figure has 11 teeth, a module of 5 teeth, and a profile-crowning pinion of 15 μm . The pinion's outside pitch diameter is 73.489mm.

Table 2: List of Material

S.N.	Material Type	Material	Power, Torque
1	Steel	18CrNiMo7-6 , Case Carburized Steel	Torque at Pinion, T1=658.6Nm Speed, N1=1450RPM and Power at 100Kw
2	Cast Iron flake Graphite	EN-GJL-200(GG 20)	
3	Bronze	ASTM B-148 Alloy954, Bronze Alloy	
4	Dry Powdered Metal	SINT D39, Dry Powdered Metal, unalloyed	

4. RESULTS AND DISCUSSIONS

Finite Element Analysis in Ansys Workbench 14.0

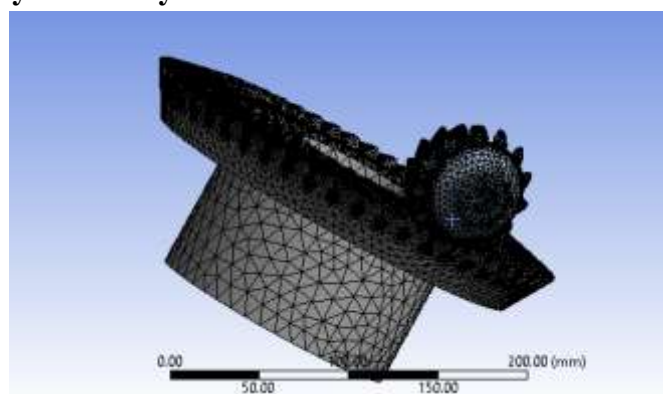


Figure 9. Mesh Model (Ansys Workbench 14.0)

Meshing the 3D model of Spiral Bevel Gear, Number of Element=& Number of Nodes =17516. Select, 9546 Material structural steel:

- E =200000 Mpa
- Poison ratio = 0.3
- Density= 7860 kg/cu. m
- Tensile Ultimate Strength= 460 Mpa

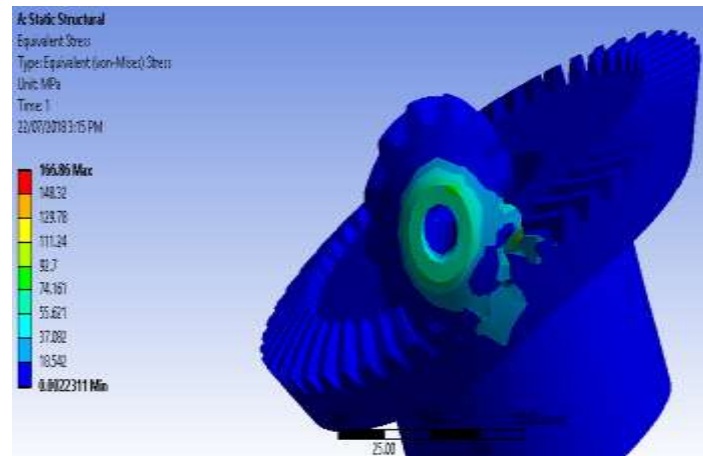


Figure 10. Equivalent (von-mises) Stress (Ansys Workbench 14.0)

After the applying the torque 200Nm, Max value of Stress is 167Mpa is obtained. The maximum stress is applied to the contact region of both gear.

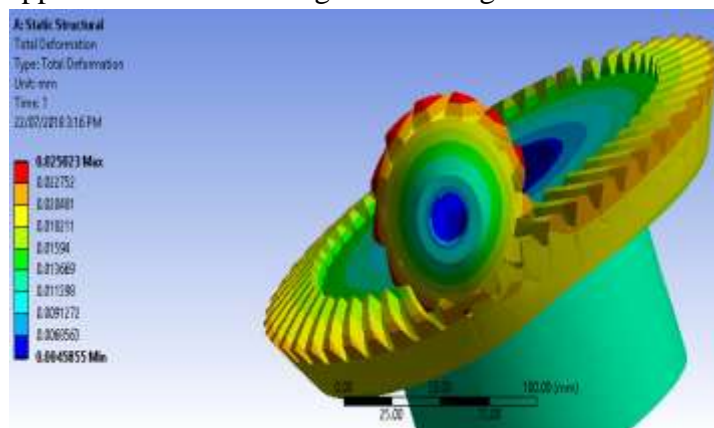


Figure 11. Total deformation (Ansys Workbench 14.0)

The maximum value of deformation is 0.026mm shown in the figure by red colour. The total deformation is the other side of the teeth because of the constraints.

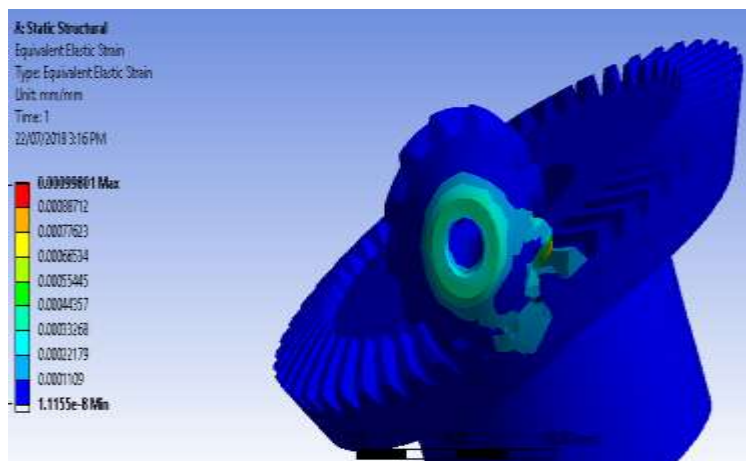


Figure 12. Equivalent Elastic Strain (Ansys Workbench 14.0)

The Max value of Equivalent Elastic Strain is 0.001 shown by red colour and Minimum Value is shown by blue colour.

Tooth Contact Analysis in KISSsoft Software

Applied Standard Torque at 658.6Nm, Speed 1450RPM and Power at 100Kw (Uniform Depth Klingelberg System)

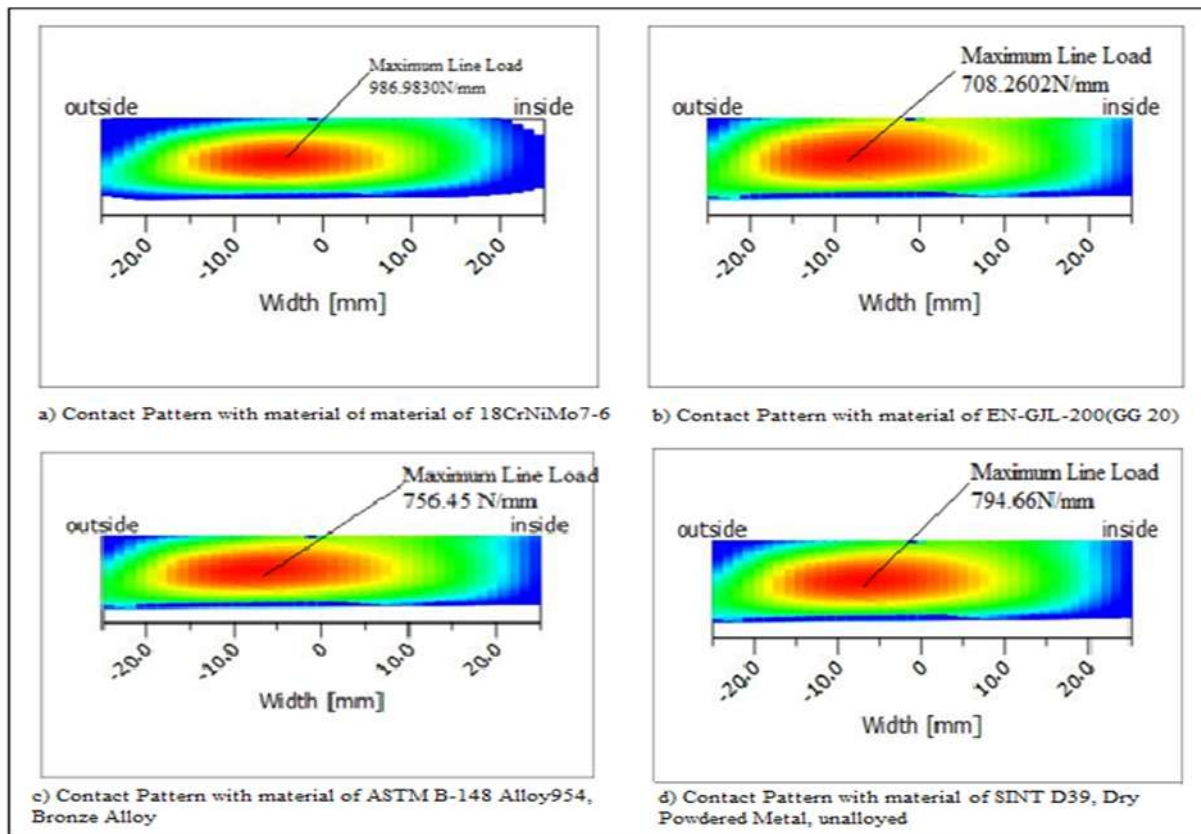


Figure 13. Simulation (KISSsoft) contact patterns in different materials

The figure has shown that the contact pattern on the flank of the gear at different materials. The Maximum Line Load is 986.98N/mm on the material of 18CrNiMo7-6, Case Carburized Steel.

Transmission Error using FEA (KISSsoft)

$$TE = \theta_2 - \theta_1 (Z_1/Z_2) \text{ in Degree}$$

θ_1 = Pinion rotation angle, in degrees

θ_2 = Gear rotation angle, in degrees

Z_1 denotes the number of teeth in a pinion.

Z_2 denotes the number of teeth in the gear.

Angle through which the gear turns = Length of an arc of contact x 360° / Circumference of gear

The angle through which the Gear turn = Length of Path of contact x 360° / (3.14 x Pitch circle diameter of Gear x $\cos 20^\circ$)

Length of Path of Contact (μm) = Angle through which the Gear turn x (3.14 x Pitch circle diameter of Gear x $\cos 20^\circ$) / 360

T.E. (μm) = T.E.(degree) x (3.14 x Pitch circle diameter of Gear x $\cos 20^\circ$) / 360

Peak to peak transmission error = Maximum T.E. – Minimum T.E.

The graph chart between transmission error and pinion rotational angle for various materials is shown in the figure. comparisons of simulation-based transmission faults at various pinion rotation angles. The simulated transmission error curve created using KISSsoft software is shown in the figure.

Figure 14a to 14d produces the peak to peak transmission error for different materials, i.e., steel, cast iron, bronze, and dry powdered metal. These graphs conclude that dry powdered metal, unalloyed, peak to peak transmission error comes at about 1.3562. 18CrNiMo7-6, Case Carburized Steel produced a maximum line load of 986.98N/mm.

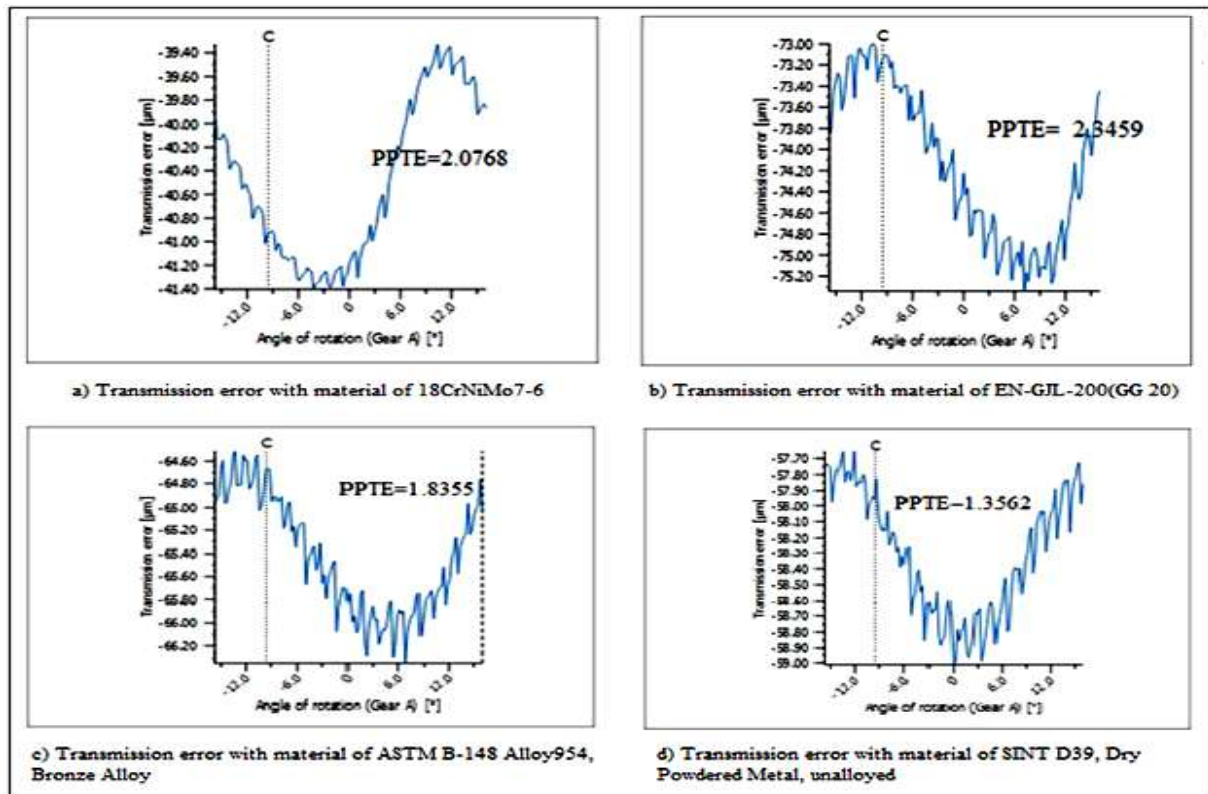


Figure 14. Simulation (KISSsoft) Transmission Error in different materials

5. CONCLUSION

3D Model of Spiral Bevel Gear has been done with PTC Creo software. Tooth contact analysis has been done with KISSsoft Software at torque at 658.6Nm, speed of 1450RPM, and power at 100Kw. After comparison of results and final conclusion with the material of SINT D39, Dry Powdered Metal is most suitable for the low level of noise during meshing. The Maximum Line Load is 986.98N/mm on the material of 18CrNiMo7-6, Case Carburized Steel. Finite Element Analysis has been done in Ansys Workbench 14.0 on spiral bevel gear the drive with a certain load of 200Nm with conclusion of maximum stress 167Mpa, displacement 0.026mm and strain is 0.001.

REFERENCES

- [1] Tharmakulasingham, R. (2010). Transmission error in spur gears: Static and dynamic finite-element modeling and design optimization (Doctoral dissertation, Brunel University School of Engineering and Design PhD Theses).
- [2] Kissling, U. (2008). Layout of the Gear Micro Geometry. KISSsoft AG.
- [3] Tharmakulasingham, R., Alfano, G., & Atherton, M. A. (2008). Reduction of gear pair transmission error with tooth profile modification.
- [4] Tuma, J. (2006). Dynamic transmission error measurements. *Engineering Mechanics*, 13(2), 101-106.
- [5] Vimercati, M. (2007). Mathematical model for tooth surfaces representation of face-hobbed hypoid gears and its application to contact analysis and stress calculation. *Mechanism and Machine Theory*, 42(6), 668-690.
- [6] Vimercati, M., & Piazza, A. (2005). Computerized design of face hobbed hypoid gears: tooth surfaces generation, contact analysis and stress calculation. AGMA.
- [7] Vogel, O., Griewank, A., & Bär, G. (2002). Direct gear tooth contact analysis for hypoid bevel gears. *Computer methods in applied mechanics and engineering*, 191(36), 3965-3982.
- [8] Keerthi, M., Sandya, K., & Srinivas, K. (2016). Static & dynamic analysis of spur gear using different materials. *International Research Journal of Engineering and Technology (IRJET)*, 3(01), 2395-0056.
- [9] Wang, Z. Y., Zhai, H. M., & Chen, H. (2013). On-machine measurement of tooth profile errors of spiral bevel gears and its simulation. In *Applied Mechanics and Materials* (Vol. 394, pp. 245-250). Trans Tech Publications Ltd.
- [10] Xuemei, C., Zongde, F., Hao, X., & Jinzhan, S. (2008). Design of pinion machine tool-settings for spiral

- bevel gears by controlling contact path and transmission errors. *Chinese Journal of Aeronautics*, 21(2), 179-186.
- [11] Yang, H., & Zhang, Y. (2010, March). Meshing Simulation and Experimental Analysis of Transmission Error for Modified Spiral Bevel Gear. In 2010 International Conference on Measuring Technology and Mechatronics Automation (Vol. 2, pp. 636-639). IEEE.
- [12] Yang, X., Song, C., Zhu, C., Liang, C., & Sun, R. (2019). Impacts of misalignments on mesh behaviors of face-hobbed hypoid gear considering system deformation. *IEEE Access*, 7, 79244-79253.
- [13] Yinong, L., Guiyan, L., & Ling, Z. (2010). Influence of asymmetric mesh stiffness on dynamics of spiral bevel gear transmission system. *Mathematical Problems in Engineering*, 2010.
- [14] Zhao, L., Du, M., & Yang, Y. (2018). Optimizing gear micro geometry for minimum transmission error when considering manufacturing deviation. *Int J Mater Mech Manuf*, 6(1), 74-77.
- [15] Vogel, O., Griewank, A., & Bär, G. (2002). Direct gear tooth contact analysis for hypoid bevel gears. *Computer methods in applied mechanics and engineering*, 191(36), 3965-3982.
- [16] Kong, X., Ding, H., Huang, R., & Tang, J. (2021). Adaptive data-driven modeling, prediction and optimal control for loaded transmission error of helicopter zero.
- [17] Fu, Y., Zhuo, Y., Zhou, X., Wan, B., Lv, H., & Wang, Z. (2020). Theoretical and experimental study on contact characteristics of spiral bevel gears under quasi-static and large loading conditions. *Applied Sciences*, 10(15), 5109.
- [18] Ding, H., Tang, J., Zhong, J., & Zhou, Z. (2016). A hybrid modification approach of machinetoool setting considering high tooth contact performance in spiral bevel and hypoid gears. *Journal of Manufacturing Systems*, 41, 228-238.
- [19] Guo, C. H., Yang, W. T., Liu, Z. F., & Zhang, Z. M. (2013). Tooth Contact Analysis and Transmission Error Optimization for Klingelnberg Spiral Bevel Gear. In *Applied Mechanics and Materials* (Vol. 310, pp. 323-327). Trans Tech Publications Ltd.
- [20] Cai, Y., Yao, L., Ding, J., Ouyang, S., & Zhang, J. (2019). Study on transmission error of double circular arc spiral bevel gears for nutation drive based on assembly errors and different loads. *Forschung im Ingenieurwesen*, 83(3), 481-490.
- [21] Simon, V. (2008). Influence of tooth errors and misalignments on tooth contact in spiral bevel gears. *Mechanism and Machine Theory*, 43(10), 1253-1267.

Delineation and analysis of non-inflated tyres with ansys

Shaik Chand MabhuSubhani, N.Hymavathi

Assistant professor, Dept. Of Mechanical Engineering, Eswar college of Engineering

Abstract: Non-inflated tires have wide application prospects due to their advantages of no run-flat, no need of air pressure maintenance, and low rolling resistance. In this project, the static and dynamic behaviours of NITs with different honeycomb spokes, Plate spokes and triangular spokes were investigated. Based on the static behaviour of three types of NITs with the same cell wall thickness of honeycomb or the same reference load carrying capacity, it is shown that the maximum stresses in spokes and tread of a NIT are much lower than that of traditional pneumatic tires, but its load carrying capacity is higher than the latter.

The design of three NIT's is designed in Catia V5 and analysis was done in ansys workbench 2019 R3. In comparison with the dynamic behaviour of three types of NITs designed with the same load carrying capacity, it is found that the stress level in spokes and tread under dynamic loading are higher than that under static loading. The rolling resistance of NITs with the smallest cell expanding angle is lowest, which is due to the lowest mass and smallest deformation of honeycomb spokes. Taking all these factors into account, it is suggested that an optimal NIT in applications is one with a small cell expanding angle and wall thickness.

Keywords non-pneumatic tire; honeycomb spokes; contact pressure; rolling resistance

1. INTRODUCTION

Since non-Inflated tires (NITs) were proposed, they have received increasing attention owing to their remarkable advantages such as no run-flat, no need of air pressure maintenance, and low rolling resistance, compared with traditional pneumatic tires. A typical NIT usually consists of a hub, a number of flexible spokes, a shear ring and a tread. Normally, tread is made of synthetic rubber, and shear ring is a composite structure composed of a shear band with two circumferential reinforcements (i.e., inner and outer rings). Flexible spokes are the most unique components in NITs and they are based on polyurethane materials. Uniform and flexible spokes that are designed to connect the composite shear ring and hub of NITs are mainly deformed by compression, tension, bending or buckling during rolling. Honeycombs possess high stiffness and strength in out-of-plane directions, and relatively lower mechanical resistance and higher resilience in in-plane directions. Therefore, the in-plane configuration of honeycombs is usually utilized in NITs. In addition, the cell structures of honeycombs are tenable to optimize in-plane properties, e.g. by changing the cell angle, wall thickness, and length to produce tailored stiffness and strength.

Recently, an attempt has been made to use honeycomb spokes in constructing NITs in trucks. There are also research works conducted to guide the structural design and optimization of NITs. For instance, developed finite element models of NITs with honeycomb structures as a shear band and investigated one-Dimensional contact pressure of tires. It was found that the auxetic hexagonal honeycomb shear band designed with a higher negative cell angle provided a lower contact pressure along the contact patch associated with in-plane shear flexible structures. Studied the static contact pressure of NITs with hexagonal-cell honeycomb spokes as a function of vertical loads. They discovered that the contact pressure of NITs was lower than that of traditional pneumatic tires due to a high lateral spoke stiffness of NITs. Here, it is worth noting that the load carrying capacity, defined as the displacement of a hub center under a vertical concentrated force, is one of the most important indicators of NITs. Compared two types of NITs with conventional and auxetic hexagonal honeycombs, and showed that, under the same load carrying capability, conventional hexagonal

honeycombs with a highly positive cell angle had low local stresses and mass.



Fig 1: non inflated tyres

In order to reduce the rolling resistance of a NIT, a hear band made of a porous and fiber-reinforced elastomeric was proposed, and numerical simulations were conducted to demonstrate the reduced energy loss by using hyper elastic and visco elastic material models. The influence of geometric and material parameters on overall performance of NITs has been also analyzed. To the best of our knowledge, however, there are few works about the dynamic behaviours of NITs with honeycomb spokes, especially on their rolling resistance.

A tire is most important part of any vehicle. Tire is a rubber member which provides cushioning effect as well as provides clearance to vehicle. The rubber member is mounted on wheel rim. In tube tire, tube is present inside the tire while in tubeless tire there is no tube. A tire is a ring shaped component that was mounted on a wheel's rim to transfer the vehicle's load from the axle.

Tire which is used in automobile, bicycle, motorcycle is pneumatically inflated structures which provide a good rolling, cushioning effect. Such tire is using numbers of year and they are developing. Some companies are trying to develop tire which are airless that means they are non pneumatic. Michelin and Bridgestone are the tire which are firstly design, they are non pneumatic. So begins an article discussing the development of air less tires, something that has become more prevalent in the past few years. Honeycomb tire are also a typr of non pneumatic tire

In this type of tire there is a special air retaining bead arrangement. These tires are directly mounted on the rim. In this tire the air is filled with the help of non returning valve which provide restriction to air to do not leave it from tube. The valve is mounted on rim. The bead is the air tight part which fit on the circumference of the wheel rim. It consists of bead cores made of number of strand of steel wire. Carcass is the main structural element that takes the load and consist of rubber bounded cords and beads

A tire is a product of complex engineered composites. It consists mainly of a reinforced rubber toroid mounted on a metallic rim. Their trapped inside creates an inflation pressure that is responsible for carrying the load, transmitting forces, absorbing shock, providing grip and resisting wear. In a tire, there are multitudes of components and rubber formulations. For reinforcement, tires also have several types of fabric and several kinds and sizes of steel. Some of the steel are twisted or braided into strong cables. On the external shell, the tread provides the required friction with the road surface and gives better traction. The purpose of the patterns on the tread is to facilitate the evacuation of water and optimize the wear rate. Compared to a rigid wheel, the conventional air-filled tire has Numerous advantages are good radial elasticity, better grip with the road, and a low mass.

2. LITERATURE REVIEW

Mohammad Fazelpour et al, [1] stayed considered about the evolution of meso-structures in the development of the shear band of non-pneumatic tyre and he concluded as follows below. To increase fuel efficiency in NASA manned exploration system. They replaced elastomeric material with shear of shear band with materials which can tolerate harsh temperatures and shear loads or to replace the materials with linear elastic low-hysteretic loss materials. Topologies were created such as honeycombs; new shapes like s-type meso-structures and the structural analysis were carried out of shear band of non-pneumatic tyre with meso-structure was investigated through shear flexure, shear strain, and contact pressure. At the end of research, they set up guidelines on custom-designing meso-structures for challenging applications such as non-pneumatic tyre and passive morphing airfoils

which will be addressed in future research.

A.M. Abdul-Yazid et al, [2] examined three dissimilar structures of the Tweel, resistant technologies, and NIT by seeking yielding spoke structures. He conducted the quasi-static, 2D analysis on contact pressure, vertical tire stiffness and stress which are affected by spoke structures and shear band by creating two NITs, a tire with a composite ring and another without composite ring. The results showed that shape and size of spokes has effect on tire behavior and the shear layer reduces the impact of the deformed spokes shape in contact pressure distribution.

Bert Bras et al, [3] discussed about the ecological effect of the Tweel tyre amid its lifecycle from assembling, through use and transfer. Since the Tweel tyre is as of now still in the examination stage and is most certainly not made and utilized on a vast scale, there are instabilities as for end-of-life situations and rolling resistance evaluates that will influence the LCA.

The pneumatic tire may have several disadvantages; catastrophic damage by flat while driving, requirement of maintenance of air pressure, and complicated manufacturing processes [1].

The non-uniform contact pressure distribution is also one of the disadvantages of pneumatic tire. The high contact stress peaks at the contact edges in the lateral direction due to the interaction of air pressure on the road surface causes a high contact pressure difference between the shoulder and the crown [2-5].

Traction, tire/pavement interaction noise, ride over road irregularities, passengers' comfort, vehicle handling and wear are worst affected by high contact pressure difference between the shoulder and the crown [1].

Therefore contact pressure distribution is an important issue on the tire design. Recently several tire engineers have attempted to develop non-pneumatic tires (NIT) by building polygon typed lattice spokes to replace air of the pneumatic tire [6-9].

Non pneumatic tire has several advantages; low rolling energy loss with a use of low visco elastic energy loss materials, low mass, and low contact pressure [9]. Considering the NIT structure, the spokes undergo the tension-compression cyclic loading while the tire rolls [10, 11].

Therefore, minimizing the local stress in the spokes is important for fatigue resistant design.

In this paper, we suggest lattice spokes of non-pneumatic tire which has honeycomb geometries. The honeycomb with two-dimensional cross section has a high out-of-plane stiffness [12, 13].

The in-plane properties of honeycomb with two-dimensional cross section are two to three orders of magnitude weaker than those of the out-of-plane loading [12]. Therefore, spokes of NITs which made of honeycomb with two-dimensional cross section have high lateral stiffness. In this paper, we suggest tree-dimensional hexagonal cellular spokes of NITs which has an out-of-plane stiffness under targeted load and a lower mass.

In this study, the NITs with two-dimensional hexagonal cellular spokes and tree-dimensional hexagonal cellular spokes are designed to have a load carrying capacity and their contact pressures are analyzed as a function of vertical loading. Due to the computational complexity of the hyperelastic material and large deformation induced geometric nonlinearity, a commercial FE code, ABAQUS, is used for numerical computation of contact pressure of NITs. This study investigates a contact pressure of NIT through comparison of FEA result between pneumatic and non-pneumatic tires with two-dimensional lattice spokes and tree-dimensional lattice spokes.

3. METHODOLOGY

Non inflated tires or flat-free tires are tires that are not supported by air pressure. They are used on some small vehicles such as riding lawn mowers and motorized golf carts. They are also used on heavy equipment such as backhoes, which are required to operate on sites such as building demolition, where risk of tire punctures is high. Tires composed of closed-cell polyurethane foam are also made for bicycles and wheelchairs. They are also commonly found on wheelbarrows which may be used for yard work or construction.

3.1 ADVANTAGES & DISADVANTAGES

The main advantage of airless tires is that they do not go flat. Other advantages are that airless tires need to be replaced less frequently, resulting in savings. Heavy equipment outfitted with airless tires will be able to carry more weight and engage in more rugged activities.

Airless tires generally have higher rolling resistance and provide somewhat less suspension than similarly shaped and sized pneumatic tires.



Fig2: Non inflated tires

3.2 BENEFITS OF AIRLESS TIRES FOR CARS

3.2.1 NO FLAT TIRES – EVER

With airless tires, you never have to worry about your tires leaking because--you knew this was coming--non-pneumatic tires have no air to leak. For most drivers, this feature will sound nothing short of revolutionary. When you run over a sharp object in the road, you won't have to worry about a flat tire because tires without air can't go flat. An end to the days of changing a tire on the highway shoulder would be welcome to drivers everywhere.

3.2.2 YOU WON'T NEED A SPARE TIRE

Since you won't be changing or repairing a flat, you don't need to carry a spare. Just like cars using run-flat tires, this feature could free up trunk space. No spare also means less weight and less weight means better fuel economy

3.2.3 VEHICLE-HEAVY INDUSTRIES CAN SAVE MONEY

Airless tires also may offer other specific advantages for trucks in industrial application. In the farming, mining, and construction industries, tire failure can cause a loss of productivity and efficiency. Tires that never leak or puncture would be a welcome advancement.

3.2.4 REDUCED CO2 EMISSIONS

About 90% of energy loss from tire rolling resistance comes from repeated changes in the shape of the tires as they roll. By simplifying the structure of the tire, Bridgestone was able to minimize the energy loss in these "air free concept tires." As a result, these tires have the same level of low rolling resistance as Bridgestone pneumatic fuel efficient Ecopia tires, contributing to reductions in CO2 emissions.

3.2.5 ECO-CONSCIOUS

The airless concept tire is one of the initiatives aimed toward Bridgestone's long-term vision of the use of sustainable materials. The materials used in the tire are recyclable, contributing to the efficient use of resources. No part of a non-pneumatic tire ever needs to go in the garbage, which goes hand-in-hand with Bridgestone's effort to create a "cradle-to-cradle" system in which all tires are first recycled and then factory-refashioned into new tires. Airless tires will be among the first for which this process is a reality.

3.3 THE FUTURE

Bridgestone is advancing development of the air-free concept tire are a more environmentally friendly product than existing tires and aims to bring about commercial use in a wide range of vehicles as soon as possible.

Bridgestone believes that through effective resource usage and efficient operations alongside CO2 emissions from improved fuel efficiency, as part of its aim to achieve a balance between its business and the environment, it can continue to offer attractive products to its consumers far into the future. Bridgestone will continue to implement multiple technological innovations to help bring about a more sustainable society.

4. MODELLING OF NON INFATED TYRES

Dassault systems have begun serving shipbuilders with CATIA V5 R8, which includes special
Dept. of Mech. Engg. PVPSIT

features useful to ship builders.

4.1 FEATURE BASED MODELLING -

A feature is defined as the smallest building block that can be modified individually. A model created in CATIA V5 is a combination of a number of individual features and each feature is related to other directly or indirectly. These features understand their limiting functions properly and therefore can be modified any time during the design process. If proper design intent is maintained while creating the model, then these features automatically adjust their value to any change in Assembly environment is used to provide mating to two or more part models to form complete assembly

4.2 DESIGN OF NON-INFLATED TIRES



Fig.3:Tire design in cad

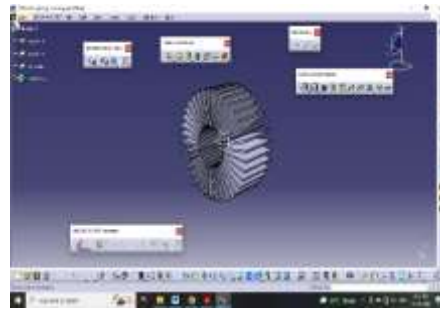


Fig.4: Rectangular airless non inflated tire

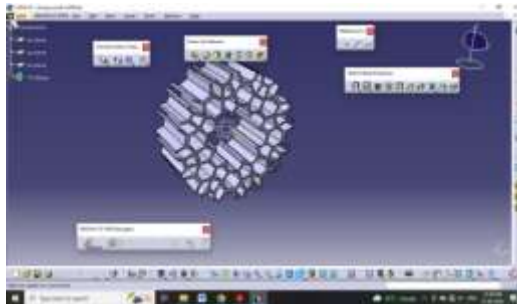


Fig 5:Honeycomb non inflated tire

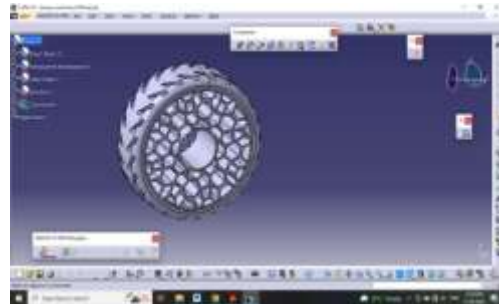


Fig.6: assembly of honeycomb tire

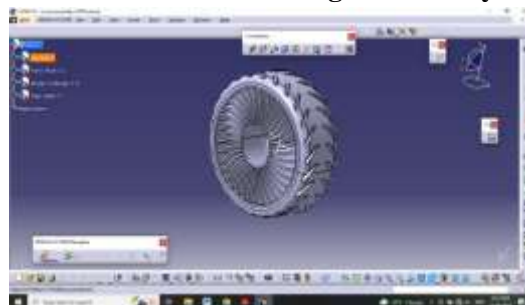


Fig.7: Design of curve model no inflated tire

5. ANALYSIS OF NON INFLATED TYRES USING ANSYS

5.1 RESULTS OF FINITE ELEMENT ANALYSIS

FEA has become a solution to the task of predicting failure due to unknown stresses by showing problem areas in a material and allowing designers to see all of the theoretical stresses within. This method of product design and testing is far superior to the manufacturing costs which would accrue if each sample was actually built and tested.

In practice, a finite element analysis usually consists of three principal steps:

Preprocessing: The user constructs a model of the part to be analyzed in which the geometry is divided into a number of discrete sub regions, or elements," connected at discrete points called nodes." Certain of these nodes will have fixed displacements, and others will have prescribed loads. These models can be extremely time consuming to prepare, and commercial codes vie with one another to have the most user-friendly graphical "preprocessor" to assist in this rather tedious chore. Some of these preprocessors can overlay a mesh on a preexisting CAD file, so that finite element analysis can be done conveniently as part of the computerized drafting-and-design process.

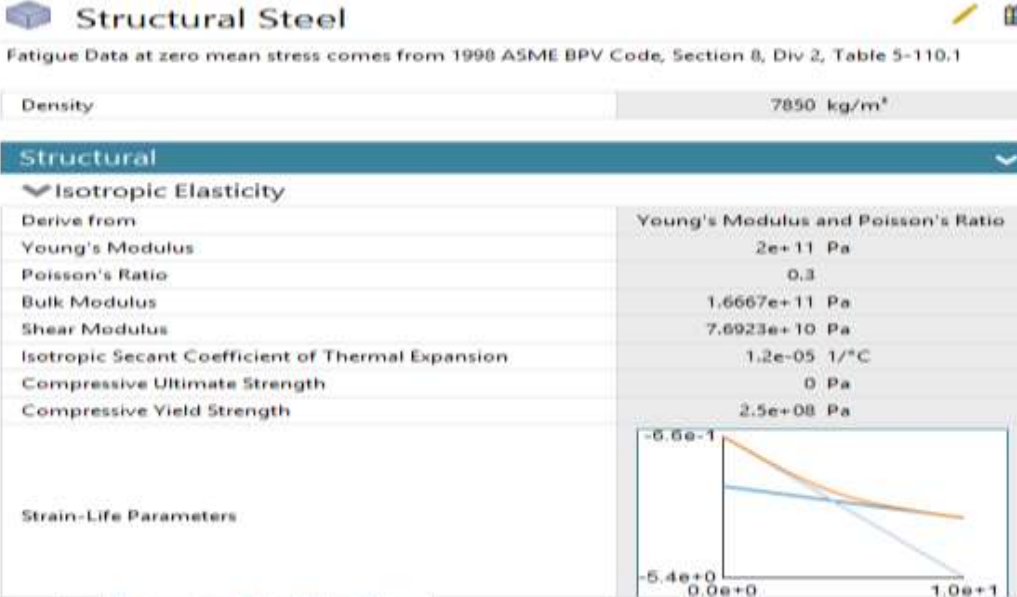
Analysis: The dataset prepared by the preprocessor is used as input to the finite element code itself, which constructs and solves a system of linear or nonlinear algebraic equations

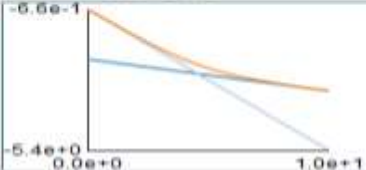
Post processing: In the earlier days of finite element analysis, the user would pore through reams of numbers generated by the code, listing displacements and stresses at discrete positions within the model. It is easy to miss important trends and hot spots this way, and modern codes use graphical displays to assist in visualizing the results. Typical postprocessor display overlays colored contours representing stress levels on the model, showing a full field picture similar to that of photo elastic or moiré experimental results.

5.2 RESULTS OF NON INFLATED TYRES

Materials: Structural steel

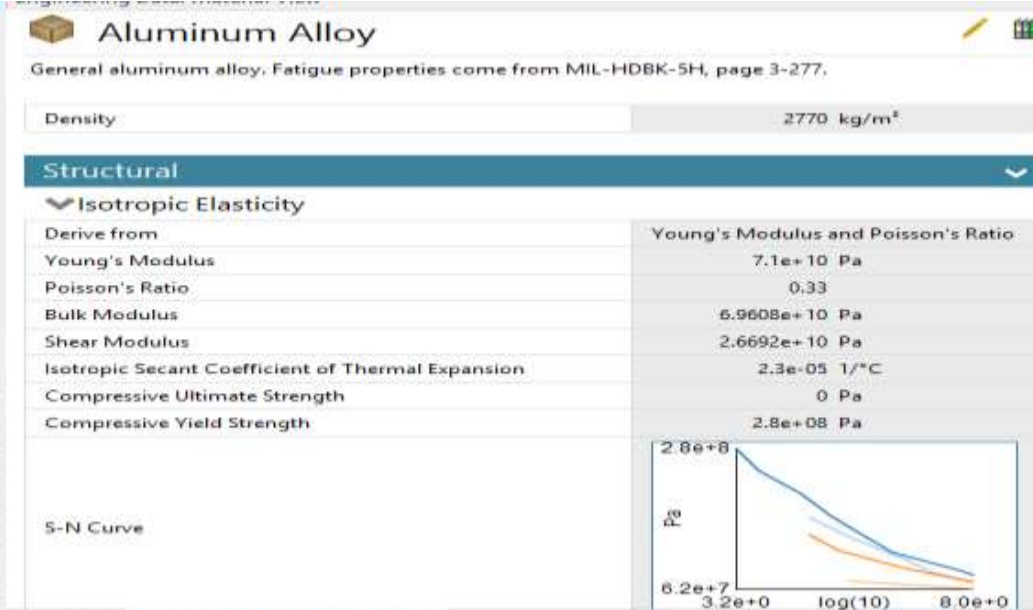
Table 1: properties of structural steel

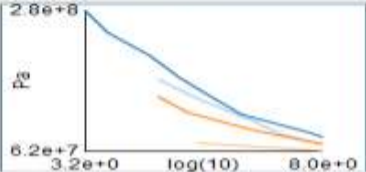


Structural Steel	
Fatigue Data at zero mean stress comes from 1998 ASME BPV Code, Section 8, Div 2, Table 5-110.1	
Density	7850 kg/m ³
Structural	
▼ Isotropic Elasticity	
Derive from	Young's Modulus and Poisson's Ratio
Young's Modulus	2e+11 Pa
Poisson's Ratio	0.3
Bulk Modulus	1.6667e+11 Pa
Shear Modulus	7.6923e+10 Pa
Isotropic Secant Coefficient of Thermal Expansion	1.2e-05 1/°C
Compressive Ultimate Strength	0 Pa
Compressive Yield Strength	2.5e+08 Pa
Strain-Life Parameters	

5.2.1 Materials: aluminum alloy

Table 2: aluminum alloy properties



Aluminum Alloy	
General aluminum alloy. Fatigue properties come from MIL-HDBK-5H, page 3-277.	
Density	2770 kg/m ³
Structural	
▼ Isotropic Elasticity	
Derive from	Young's Modulus and Poisson's Ratio
Young's Modulus	7.1e+10 Pa
Poisson's Ratio	0.33
Bulk Modulus	6.9608e+10 Pa
Shear Modulus	2.6692e+10 Pa
Isotropic Secant Coefficient of Thermal Expansion	2.3e-05 1/°C
Compressive Ultimate Strength	0 Pa
Compressive Yield Strength	2.8e+08 Pa
S-N Curve	

5.2.3 Polyurethane

Table 3 :polyurethene mechanical properties

polyurethane	
Density	1.25e-06 kg/mm ³
Structural	
▼ Isotropic Elasticity	
Derive from	Young's Modulus and Poisson's Ratio
Young's Modulus	6 MPa
Poisson's Ratio	0.4
Bulk Modulus	10 MPa
Shear Modulus	2.1429 MPa
Isotropic Secant Coefficient of Thermal Expansion	100 1/°C
Compressive Ultimate Strength	210 MPa
Compressive Yield Strength	131 MPa
Tensile Ultimate Strength	420 MPa
Tensile Yield Strength	300 MPa

5.3 : Results of honey comb tire

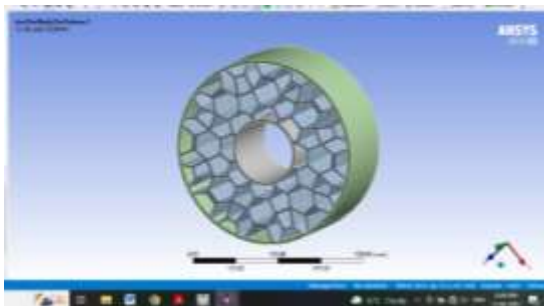


Fig.5.1 Imported file from catia



Fig.5.2 meshed file

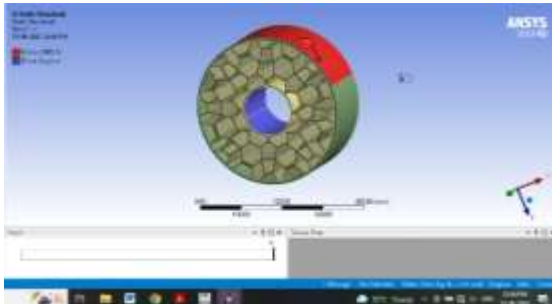


Fig.5.3 boundary conditions applied 3000N

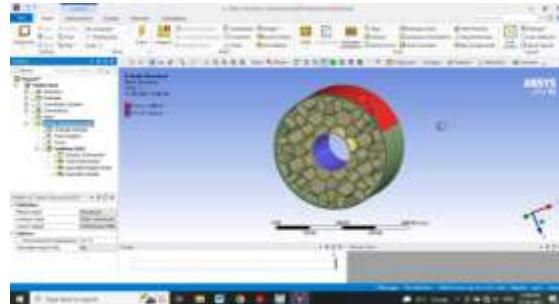


Fig.5.4: boundary conditions applied 3000N

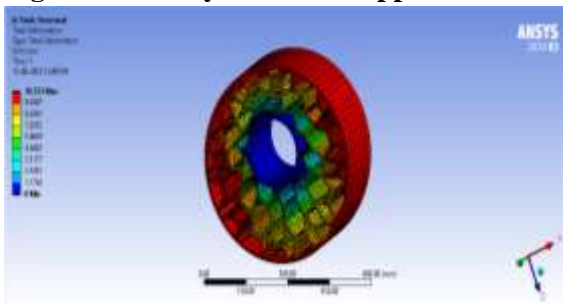


Fig.5.5: total deformation

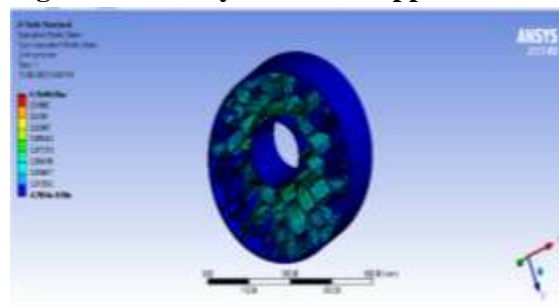


Fig.5.6: Equivalent elastic strain

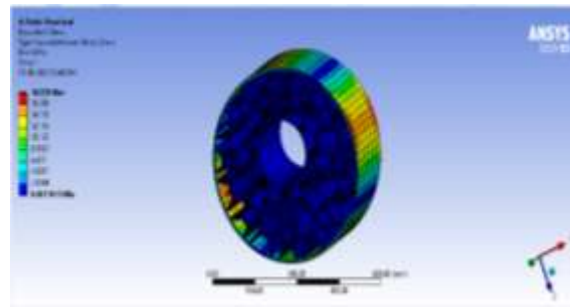


Fig.5.7: equivalent stress

Table 2: Results of honeycomb tire

Results	Minimum	Maximum	Units	Time (s)
Total Deformation	0.	10.553	mm	1.
Equivalent Elastic Strain	4.7894e-008	0.16496	mm/mm	1.
Equivalent Stress	1.1615e-003	18.229	MPa	1.

5.4 : Results of rectangular tire

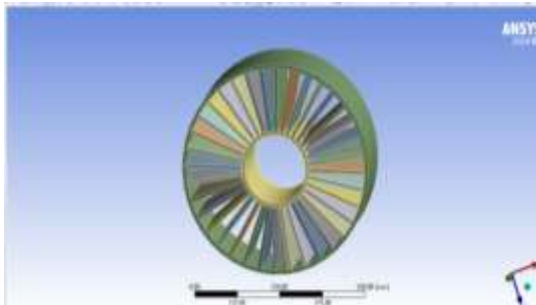


Fig.5.8: Imported file from catia

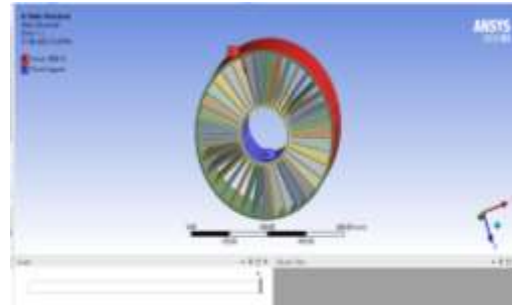


Fig.5.9: Boundary conditions

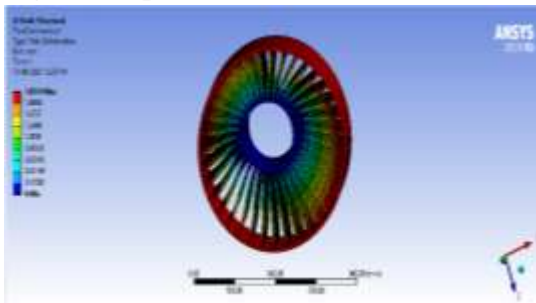


Fig.5.10 Total deformation

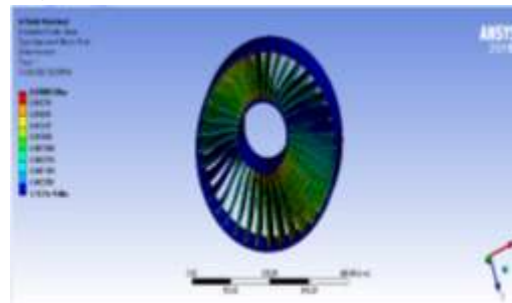


Fig.5.11 Equivalent elastic strain

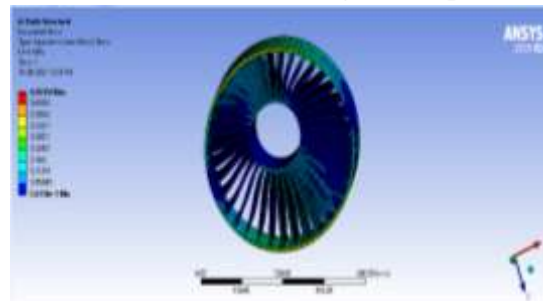


Fig.5.12 Equivalent stress

Table 3: Results of rectangular tire

● Result Summary

Results	Minimum	Maximum	Units	Time (s)
Total Deformation	0.	1.8974	mm	1.
Equivalent Elastic Strain	7.1371e-009	1.8893e-002	mm/mm	1.
Equivalent Stress	2.6558e-005	0.50454	MPa	1.

5.5: Results of curved tire

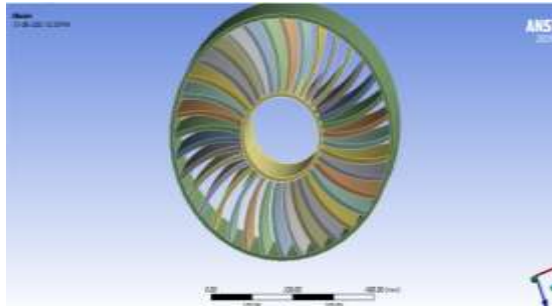


Fig.5.13: Imported file from catia

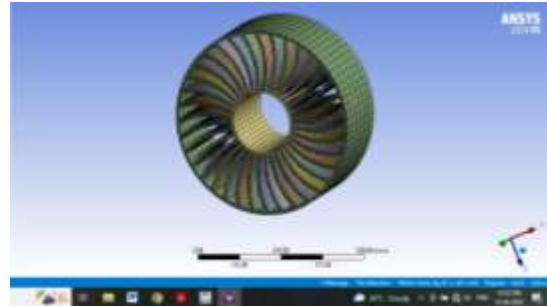


Fig.5.14: Boundary conditions

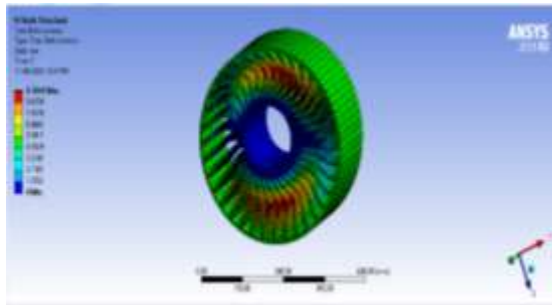


Fig.5.15: Total deformation

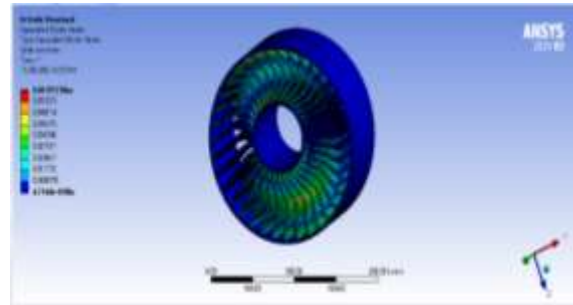


Fig.5.16: Equivalent elastic strain

Table 3: Results of curved no inflated tires

Result Summary

Results	Minimum	Maximum	Units	Time (s)
Total Deformation	0.	9.7041	mm	1.
Equivalent Elastic Strain	4.7144e-008	6.1912e-002	mm/mm	1.
Equivalent Stress	4.8552e-004	0.47566	MPa	1.

6. CONCLUSION

Modeling and analysis of the Non-Pneumatic Tire is done in CATIA and imported to Ansys (19.3) for processing work. An amount of load 3000N applied along the circumference of the tire, made up of hub ring with material Aluminum, spokes with material polyurethane, outer ring with material steel and shear band with material synthetic rubber.

- Four different spoke structures (Curved spoke, rectangular spoke, Honeycomb spoke) are designed using CATIA.
- Based on comparison of stress, strain, shear stress and total deformation when load of 3000N applied on all the structures, the highest values occurred in honey comb structure.
- Honey comb spoke structure is the best suitable design of spoke structure because of high stress, strain, shear stress and total deformation values.
- By manufacturing of honeycomb spoke structure, it is a good strength, fatigue life, reliability, reduces the overall weight and cost compared to the other two spoke structures.

References

1. Mohammad Fazelpoue "A comparison of design approaches to meso-structure development". ASME journal paper DETC 2013-12295, 2013, doi: 10.1115/ DETC 2013-12295.
2. A.M. Aboul-Yazid., "Effect of spokes structure on characteristics performance of non-Pneumatic tyres," ISSN: 2180-1606 Volume 11, pp. 2212-2223, January-June 2015.
3. Bert Bras., "Life-cycle environmental impact of Michelin tweel tyre for passenger vehicles" SAE International Journal 2011-01-0093, 2011, doi: 10.4271/2011-01-0093.
4. Gent, A.N, and Walter, J.D. 1985, The Pneumatic tire, National Highway Traffic Safety Administration Washington DC.
5. Gough V.E., (1958), "Tyre-To-Ground Contact Stress," Stress Analysis Group Conference on Contact Stress, vol.2, no. pp. 126-59,
6. Cho J.R., Kim K.W., Yoo W.S., and Hong S.I., (2004), "Mesh generation considering detailed tread blocks for reliable 3D tire analysis," Advances in engineering software, vol. 35, no. pp. 105-113,

Two-day International Conference on Recent Advances in Mechanical and Industrial Engineering – 2023
(ICRAMIE-2023)

7. Manuel J. Fabela-Gallegos, Ricardo Hernandez-Jimenez, Alberto Reyes-Vidales, (2007), "Effect of Load and Inflation Pressure on contact Force and Pressure Distribution for Two Types of Light Duty Truck Tires," *Society of Automotive Engineers Inc*, vol. 2146, no. pp.15-22.
8. X. Du, Y. Zhao, Q. Wang, and H. Fu, "Numerical analysis of the dynamic interaction between a non-pneumatic mechanical elastic wheel and soil containing an obstacle," *Proceedings of the Institution of Mechanical Engineers, Part D: Journal of Automobile Engineering*, vol. 231, no. 6. SAGE Publications Ltd, pp. 731–742, 2017. [2] A. Mohan, C. A. Johny, A. Tamilarasu, J. P. Bhasker, and K. Ravi, "Design and analysis of non-pneumatic tyre," in *IOP Conference Series: Materials Science and Engineering*, 2017, vol. 263, no. 6. [3] E. O. Bolarinwa and O. A. Olatunbosun, "Finite element simulation of the tyre burst test," *Proc. Inst. Mech. Eng. Part D J. Automob. Eng.*, vol. 218, no. 11, pp. 1251–1258, Nov. 2004. [4] W. Wang, S. Yan, and S. Zhao, "Experimental verification and finite element modeling of radial truck tire under static loading," *J. Reinf. Plast. Compos.*, vol. 32, no. 7, pp. 490–498, Apr. 2013. [5] F. Bruzelius, M. Hjort, and J. Svendenius, "Validation of a basic combined-slip tyre model for use in friction estimation applications," *Proc. Inst. Mech. Eng. Part D J. Automob. Eng.*, vol. 228, no. 13, pp. 1622–1629,
9. Mohsenimanesh A., Ward S.M., and Gilchrist M.D., (2009), "Stress analysis of a multi-laminated tractor tyre using non-linear 3D finite element analysis," *Materials and Design*, vol. 30, no. pp. 1124-1132, Alfredo, R. V., 1967, Airless Tire, U.S. Patent, US3,329,192,
10. Kubica, W. and Schmidt, O., 1979, Self-Supporting Motor Vehicle Tire, U.S. Patent, US 4,169,494,
11. Manesh, A., Terchea, M., Anderson, B., Meliska, B., Ceranski, F, Tension-Based Non-Pneumatic Tire, 2008, World Intellectual Property Organization, WO2008/118983 A1,
12. Rhyne, T. and Cron, S. M., 2006, "Development of a Non-Pneumatic Wheel," *Tire Science and Technology*, Vol. 34, pp.150- 169,
13. Rhyne, T.B., Cron, S.M., and Pompier, J.-P., 2006, Compliant Wheel, *U.S. Patent*, US 7,013,939 B2 Manesh, A., Terchea, M., Anderson, B., Meliska, B., Ceranski, F, Tension-Based Non-Pneumatic Tire, 2008, World Intellectual Property Organization, WO2008/118983 A1
14. Bitzer, T. (1997), Honeycomb Technology, Charpman & Hall, London, UK Ju J. and J.D. Summers,

Hygrothermal Impact on Mechanical Behavior of Carbon T300 and S Glass Hybrid Fiber-Reinforced Composites Under Various Staking Sequences

E.Kavitha ^a, K.Sivaji Babu ^b, M.R.S.Satyanarayana ^c

^{a,b} Mechanical Engineering Department, Prasad V.Potluri Siddhartha Institute of Technology,
Vijayawada - 520007, Andhra Pradesh, India

^c Mechanical Engineering Department, Gitam University, Visakhapatnam - 530045,
Andhra Pradesh India

*Corresponding author mail id: kavithavarikola@gmail.com

Coauthor¹ mail id: k_sivajibabu@yahoo.com

Coauthor² mail id: rssmunukurthi@yahoo.com

Abstract: Glass-carbon reinforced composites polymeric materials are one of the most effective hybrid composites for aviation and oceanic building components. Isolated glass and carbon fibers has recently been supplanted with hybrid FRP Composites in order to take full advantage of a hybridization effects. The new research looks at the effects of different fiber stacking sequences on the mechanical characteristics of carbon fiber (T300)/ S-glass composite laminates utilizing epoxy as the matrix material that have been made using hand lay-up technique. The impact of hybridization on six different Carbon (C) and Glass (G) stacking configurations (CGGC /CGCG /CCGG /GCCG /GCGC /GGCC) laminates at [0⁰/90⁰] orientations clearly show variation in tensile, flexural, and impact features. Tensile, flexural, and impact characteristics of the manufactured composite laminates were assessed under various acidic environments like HCl, H₂SO₄, NaCl and dry environments. From the experimental results, the tensile and flexural strength was diminished due to chemical degradation effect where as % of elongation at both tensile and flexural cases and impact strength of composite was enhanced. Scanning Electron microscopy has been used for microstructural characterization to verify the influence of chemical on bonding strength between fiber and matrix. From the examination it is evident that, under dry condition efficient load transformation has taken place as well neat fiber distribution to matrix. On the other hand, the fiber pulls out, matrix cracks, and voids were noticed due to chemical integration of fabricated laminates.

Keywords: Carbon; S-Glass; Epoxy; Hybrid; Mechanical Properties, Chemical absorption

1. INTRODUCTION

Since few decades, vast research is being conducted globally to manufacture the new hybrid materials which are most efficient in their thermal, physical, electrical and mechanical characteristics. In this context, FRPC (Fiber reinforced polymer composites) materials are highly eye-catching due to their widespread uses notably for structural, mechanical, air-craft and automotive components. As hybrid properties are highly enhanced in present day scientific discovery, it has become very essential to address the accurate production and application for the efficient usage. Fibers have such a special reinforcement that really is continuous in diameter from 120 to 7400 pins. When fibers are in bulk form, they will be remained perfectly flexible or linearly elastic but they become more stiffer and tougher structures. The most sufficient quantity are glass, carbon, and aramid (ballistic armor).
Dept. of Mech. Engg. PVPSIT 21

Evolving of whisker and fiber technologies is a continuous process [1]. The composite materials fabricated from these technologies are made of fibers like basalt, aramid, glass, carbon etc. along with the polymer matrix. Also, fibers including asbestos, wood and paper also used. Currently, phenol formaldehyde resin is utilized instead of epoxy, vinyl ester, or polyester thermoplastics plastics. The procedures utilized to make a polymer are additive polymerization and phase expansion polymerization. Post the bonding process of two or more homogenous materials but having variable properties for acquiring subsequent goods which have quality in material and better mechanical properties as well, the obtained result will be the plastic. Reinforced fiber plastic is one of the types of composite plastic which use fiber elements to increase the elasticity and strength of the materials. Matrix began off as a polymer compound having zero reinforcement. They have been reinforced with more stiff and strong reinforcing fibers or filaments, culminating in a harder but weaker material. The range of elasticity and strength which in a plastic that was fiber reinforced is limited by the mechanical behavior of both the matrix length and orientation of the fiber [2]. Matrix behavior is learned when Fiber reinforced polymer materials show some additional elasticity or strength in proportion with the elasticity and strength of matrix [3]. Fibers in thermoplastics can be organized into consistent specific design programs utilizing FRP. The resistance for the deformation of a polymer could be boosted by indicating the tougher fibers orientations. When compared to other composite materials and alloys with artificial fiber reinforcement are growing like much popular and significant in recent times and also have huge variety of applications because they acquire top quality mechanical characteristics, compact size, distinctive flexibility, resistance to corrosion, ease of processing, and more [4]. When contrasted to other synthetic fibers, Kevlar fibers (Poly aramid) do exhibit highly unique properties. Hence, it has also been identified as nylon, which is having additional benzene rings in the polymeric chains, resulting in greater rigidity [5]. As a consequence, it is rapidly used in advanced technology and sectors such as armour, firearms, chopper blades, pneumatic reinforcement, and sports equipment. It has a prolonged elongation and high strength and modulus as compared to other man-made fibers [6–8]. Epoxy resin has surpassed all other polymer matrixes as the majorly utilized polymer matrix in composites. In recent times, a wide range of research has been conducted to alter the characteristics of epoxy by including rubber [9, 10] or fillers [11, 12] in a thought of improving qualities of matrix dominated composite. This addition of rubber element increases toughness of epoxy's fracture while lowering its strength and modulus. The outcome suggests that adding of rubber element enhanced the toughness for fracture but reduces the strength and modulus, while introducing fillers enhanced the modulus and strength of epoxy while lowering the fracture toughness. Additionally, the heat distortion temperature of epoxy was boosted by fillers [13]. Micro and nano-scaled particles have lately been suggested as a filler material for epoxy in order to produce composites with improved properties and performance. When DMA is conducted right after the immersion of composites of composites in water at various temperatures, the outcomes like glass transition temperature and shear properties were proved to be sensitive to hygrothermal effects. Also, both the mechanical and thermal properties had been able to retained mostly only on the condition that moisture absorption had not exceeded the saturation point [13]. Also, when the composites had been undergone tests like XRD and SEM, the outcomes prove that spacing of interlayers in between clay platelets has been increased drastically which indicates the ability of intercalation of polymer between the clay layers [14]. For pure polyamide composite materials, the threshold of water concentration could be

observed at beyond points for which mechanical property values have reduced significantly [15]. Huge research is also being conducted using alternate metallic alloys like Titanium, Magnesium, Stainless steel etc. to know their mechanical stability and respective results have been analyzed including their modes of failure [16]. In the other trail of investigating the hygrothermal aging effect on both thermomechanical and static behavior for the composites of polyetherimide, the greater values of thermal expansion caused the mismatching problem in between PEI matrix and carbon fiber [17]. As for the case of composites of S2-glass/vinyl ester hygrothermal and thermal aging analysis, the resistance of indentation and strength of compression showed some increment in the stage of thermal exposure [18]. 3D printed reinforced glass fiber composites are also analyzed for the effects of aging. The results obtained proved that the change in mechanical properties which was induced due to hygrothermal aging had been influenced by the rivalry of various mechanisms [19]. The building materials which are bio-aggregate also when undergo tests of aging and the outcomes stressed the porosity impact on the complex structure of bio-concrete composite [20]. By the increment in uptake of water the hygrothermal aging effect is decreased, when the analysis is done using differential scanning calorimetry [21]. The results of experiments which conducted on glare and glass/epoxy laminates showed the autoclave pressure increases to some range of interfacial bonding of glare which have less voids, hence leads to increase for resistance to thermal and hygro aging [22]. After hygrothermal conditioning at elevated temperatures of FRPC's, it was observed that there is a reduction in values of strength properties [23].

From the literature survey it is noticed that alimited studies was noticed on this particular research work, this reason motivates to carry out current research workswwhich aims to investigate the impact of chemical environment on the mechanical behavior of carbon T300 and S glass fiber hybrid polymer in epoxy composites. The composite laminates were stacked with different sequences were chosen to explore the hygrothermal behavior laminates under various acidic solutions and validates to make use of marine application.

2. MATERIALS AND METHODOLOGY

2.1 Materials

The reinforcements, T-300 carbon fiber woven laminates, S-glass fiber woven laminates and epoxy resin as matrix materials were chosen in this investigation. The properties of these materials were represented in the Table 1. The epoxy resin and hardener were obtained from HUNTSMAN Corporation. In order to investigate the samples various acidic environments, the chemicals, HCl, H₂SO₄, and NaCl were chosen. Where, the HCl is obtained from industry and its concentration is about 99.00%. Similarly, NaCl with 99.00% concentration obtained from industry and H₂SO₄ with 99.00% concentration obtained from industry.

Table1: Properties of selected materials

Material	Type	Density (g/cm ³)	Diameter (μ m)	Tensile Strength (Mpa)	Elastic modulus (Gpa)
Carbon fiber	T-300	1.6	16-22	3400	240
Glass fiber	S-Glass	2.53	5-10	4600	89
Epoxy	LY556	1.15	-	58	-
Hardener	HY 951	0.97	-		

2.2 Sample Preparation

The hybrid laminates with different stacking configurations were fabricated through hand layup method due to its economical advantage. Initially, the surface preparation of the mold was carried out to make it tack free, where little or no moisture can be seen. The epoxy layer is applied first and a single carbon/ glass laminate in ($0^0/90^0$) was allowed to lay on. Upon laid layer, the matrix material was evenly spread through a hand roller and prepared surface for next consecutive layers and so on until the desired thickness was obtained for a single specimen. The distribution of matrix material upon laminates were carefully monitored to make sure, with less or no voids in samples. Similar, procedure was followed to prepare all the specimens with six different stacking configurations of carbon and glass unidirectional composite laminates shown in Figure 2. All the prepared specimens were allowed to cure under the room temperature of 30°C for 24 hours. The cured samples were then subjected to diamond disc cutting to obtained all samples in standard dimensions for tensile, flexural and impact tests.

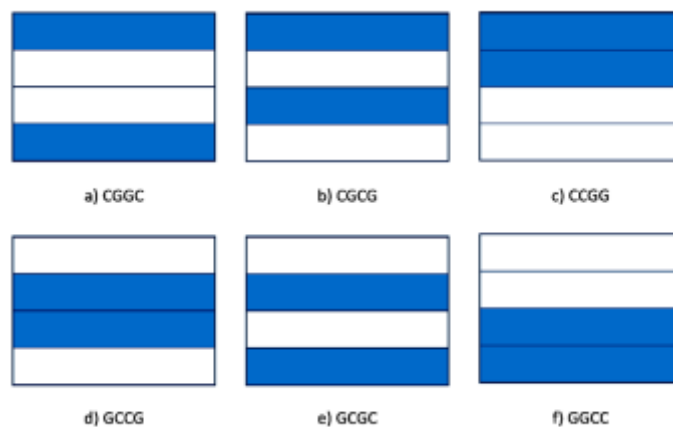


Figure 2: Stacking sequence of prepared Carbon (C)/ Glass(G) unidirectional composite laminates.

3. CHARACTERIZATION

3.1 Hygrothermal condition

Secondary processes were performed on the resulting composites in order to shape them into ASTM shapes acceptable for tensile, flexural, and impact tests. The composite samples were then placed in a hygrothermal environment. Initially, all of the samples were dried in an oven at $60-70^{\circ}\text{C}$ for 4 hours, until all of the moisture in the samples was evaporated. The samples were then weighed and the initial weight was recorded. The samples were now immersed in acidic environments such as HCl, H_2SO_4 , and NaCl for 24 hours to obtain saturation. Before weighing, specimens were removed from the acidic bath and allowed to dry at room temperature. Acidic absorption in the samples was determined by weighing the samples before and after immersion. Finally, the acidic treated samples were tested, and the results were compared to the properties of the non-acidic treated samples.

Amount of acid absorption is determined by $M = \frac{W_2 - W_1}{W_1} \times 100$

Where w_2 = weight of the sample after acid immersion and w_1 = initial weight of the sample.

3.2 Mechanical characterization

Tensile, flexural, and impact testing were performed on hybrid composites that were fabricated using a hand-layup procedure and then treated with chemicals to evaluate their mechanical properties. The results obtained from dry samples and chemically treated samples were compared.

3.2.1 Tensile test:

Tensile testing on Tensometer with 20KN load capacity were performed at room temperature (22-25°C). The fabricated composite samples were diamond cut according to the ASTM D638M89 standard, with dimensions of 165mm length, 19mm width, and 3mm thickness. The obtained samples were tensile tested on a gauge length of 57mm at a crosshead speed of 1mm/min. The test was ended when the strain rate of the samples reached 50%, and load-displacement and stress-strain curves were recorded. For accurate results, four sets of each sample were analyzed, and average values were recorded.

3.2.2 Flexural test:

The samples were subjected to three-point bending tests in accordance with ASTM D79M-86 standards. Secondary processes were performed on prepared composites with dimensions of 100mm length, 25mm width, and 3mm thickness to create test samples. Flexural tests were performed on three sets of each sample, and the average value was recorded. The test was carried out using a tensometer with a load capability of 20KN. The test was carried out with a constant cross-head speed of 1 mm/min and a span length of 40mm. When the load was reduced to 40%, the test was terminated. Because of chemical integration in the sample, fibres were split out and the matrix was shattered throughout the test.

3.2.3 Impact Properties

The samples were tested for impact according to the ASTM D256 standard, with dimensions of 63.5mm length, 12.7mm width, and 3mm thickness at room temperature of 22-25°C. Using a notch cutter, a V-notch with a depth of 2.5mm and a 45° angle was slotted on the sample. The samples were then placed on a computerized pendulum type izod/charpy impact testing machine with a hammer force of 22J energy purchased from International Equipments in Mumbai. Samples were put 2mm from the stoppers, and a hammer weighing 21.5kg was permitted to impact the center of the sample on the reverse side of the notch with an energy of 2.71J. The impact energy received by the samples prior to fracture was measured, and an average of four samples was collected for each set for accuracy. Later, the findings of hydrothermally treated samples and dry samples were compared.

4. RESULTS AND DISCUSSIONS

4.1 Hygrothermal Impact on Tensile Properties:

Experimental results shown tensile strength of non-aged specimens is greater than the aged specimens (Hygrothermally treated). From figure 3 it is observed that the CGCG composite has greater tensile strength in both dry and acidic conditions. The presence of acidity in between the layers of composite leads to decrement in their mechanical and physical characteristics. According to the results of the test, acid absorption causes a lack of interbonding forces between the fibers and the matrix, which leads to laminate inefficiency, leading composites to weaken and their properties to degrade. The load bearing capacity of the laminates is determined by the adhesive strength of the stacking sequences and matrix, which is influenced by two main impacts on aged samples: plasticization and temperature post-treating produced by hygrothermal behavior.

From different stacking samples dry CGCG sample shows higher tensile strength of 5700 N/mm² and for hygrothermal environment CGCG shows high tensile strength of 5300 N/mm² at HCl region, where as CGGC stacking sample shows low tensile property in both dry 3000N/mm² and aged condition 2700 N/mm² at NaCl region.

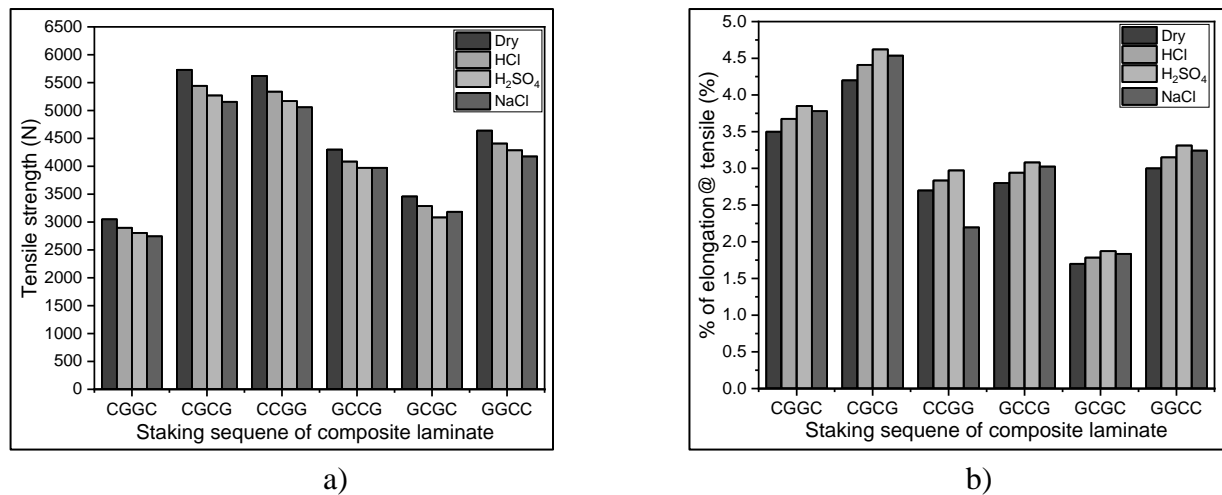


Figure 3: Comparison of specimens subjected to dry and acidic environment a) tensile strength b) elongation percentage

4.2 Hygrothermal Impact on Flexural Properties

Under three point bending test, aged samples exhibit a similar pattern of failure mechanisms through disbandment of mechanical characteristics. During the test, matrix cracks and fiber breakouts were detected due to weakened adhesive strength between laminates and the production of blow holes during sample fabrication, which generates voids and affects the elasticity modulus of the specimens. We observed that samples ruptured on the tension face during the test due to a lack of fracturing resistance, but the failure pattern also indicates that samples were converted into ductile materials by increasing elongation at break point. During the test, the samples initially entered an elastic zone with linear correspondence to the applied load, then into a plasticity region where deformation can be seen visually, and finally into a rupture region by delaminating the specimen internal layers and forming cracks by breaking the bond between matrix and fibers, ultimately leading to a decrease in mechanical properties and material failure.

Flexural strength of dry CCGG stacking composite is high with 8800 N/mm² and in hygrothermal condition flexural strength of same CCGG composite is high with 8300 N/mm² for NaCl region, according to the results. In the H₂SO₄ environment, flexural modulus was shown to be highly prevalent in GCCG composite for both dry and hygrothermal regions.

4.3 Hygrothermal Impact on Impact Properties

Carbon Glass Carbon Glass stacking composite (CGCG) displayed good impact resistance by absorbing more energy at old conditions in a NaCl environment, with a value of 0.52J. This sample has a higher impact strength than a dry sample, with 0.47J, due to its brittle nature. The test findings demonstrate that all of the composite samples exhibited low impact energy at dry circumstances due to the brittle nature of the fibers caused by non-treatment. The tests indicated that the orientation and order of the fibers in the matrix affect impact strength. The shear resistance of the covalent bonding between laminates transfers the impact load to polymeric chains all across stacked laminates, so the toughness of the samples treated hygrothermally is higher than the toughness of the samples evaluated in dry conditions. The impact resistance of CCGC composite differs little between dry and aged environments in this test due to de-cohesion and weak interbonding forces between fiber and matrix, resulting in material fracture and failure.

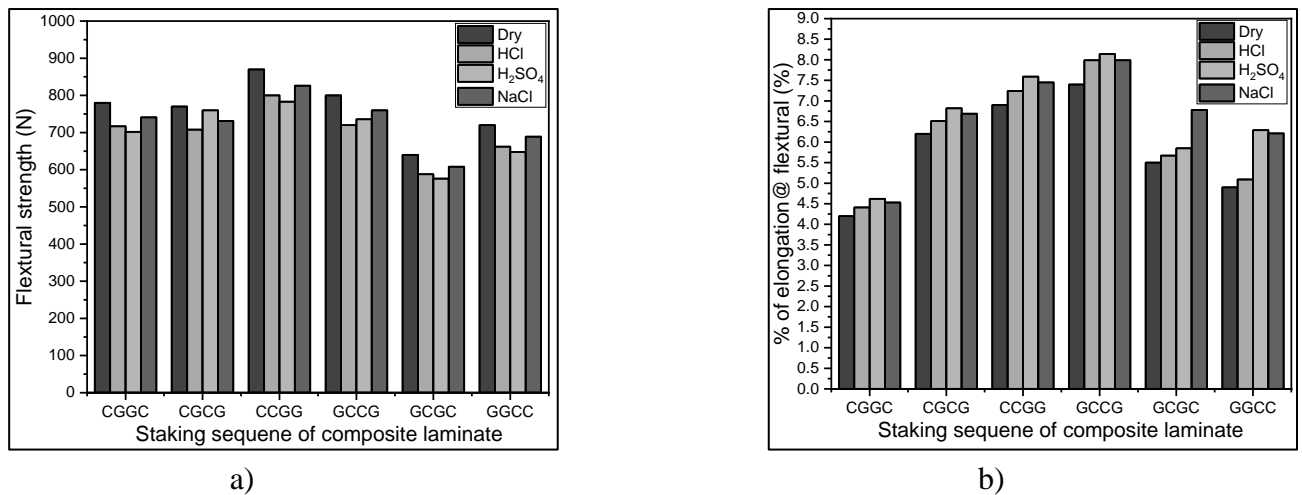


Figure 4: Comparison of specimens subjected to dry and acidic environment a) Flexural strength b) elongation percentage

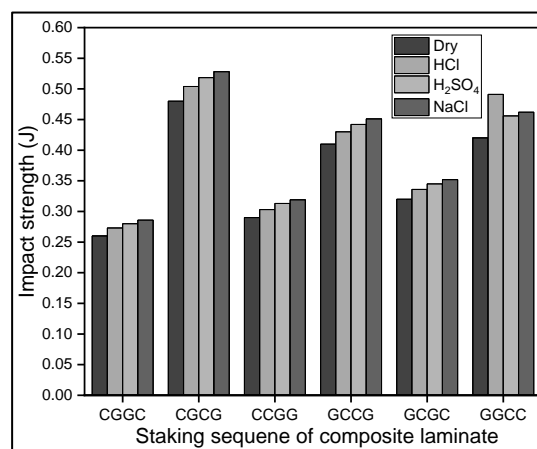


Figure 5: Impact strength of specimens subjected to dry and acidic environment

5. CONCLUSIONS

In this article, the effect of the hydrothermal impact on the mechanical properties of carbon/glass fiber laminates with different stacking configurations, fabricated through hand layup method were investigated. The samples fabricated were subjected to the various acidic (HCl, H₂SO₄, NaCl) and dry environments to compare their tensile, flexural and impact behaviors. From results, the following conclusions were drawn:

- The CGCG stacking configuration laminates exhibited higher tensile strength under acidic and dry conditions. Under acidic environments the samples subjected were degraded and their tensile strengths were decreased. Where, the NaCl exposed sample exhibited higher degradation behavior, followed by H₂SO₄ and HCl environments. However, the percentage of elongations were increased for the samples subjected to acidic environments, where HCl sample exhibited better elongation. The similar effect has been observed for all stacking configurations under tensile properties investigation.
- The CCGG laminates exhibited higher flexural strength under acidic and dry conditions compared to all laminates. Under acidic environments the samples subjected were degraded and their flexural strengths were decreased for almost all samples. The H₂SO₄ exposed sample exhibited higher degradation behavior, followed by HCl and NaCl environments.
- The GCCG laminates exhibited higher percentage of elongation under acidic and dry conditions during flexural properties investigation. The HCl exposed sample exhibited

higher degradation behavior, followed by H₂SO₄ and NaCl environments.

- From tensile and flexural tests, degradation of their strengths and increase in percentage of elongations was clearly evident and the influence of acidic environments on these properties for different stacking configurations was a considerable effect.
- The impact strengths were increased for all stacking configurations subjected to acidic environments compared dry. Where, NaCl exposed samples exhibited higher impact strengths, followed by H₂SO₄ and HCl and dry environments.

REFERENCES

1. Krishnudu, D. M., Sreeramulu, D., & Reddy, P. V. (2018, April). Optimization the mechanical properties of coir-luffa cylindrica filled hybrid composites by using Taguchi method. In *AIP Conference Proceedings* (Vol. 1952, No. 1, p. 020058). AIP Publishing.
2. Krishnudu, D. M., Sreeramulu, D., & Reddy, P. V. (2019). Synthesis and Characterization of Coir and Luffa Cylindrica filled with CaCo₃ hybrid composites. *International Journal of Integrated Engineering*, 11(1).
3. Badie, M. A., Mahdi, E., & Hamouda, A. M. S. (2011). An investigation into hybrid carbon/glass fiber reinforced epoxy composite automotive drive shaft. *Materials & Design*, 32(3), 1485-1500.
4. Barjasteh, E., & Nutt, S. R. (2012). Moisture absorption of unidirectional hybrid composites. *Composites Part A: Applied Science and Manufacturing*, 43(1), 158-164.
5. Xian, G., Li, H., & Su, X. (2012). Water absorption and hydrothermal ageing of ultraviolet cured glass- fiber reinforced acrylate composites. *Polymer Composites*, 33(7), 1120-1128.
6. Selzer, R., & Friedrich, K. (1997). Mechanical properties and failure behavior of carbon fibre-reinforced polymer composites under the influence of moisture. *Composites Part A: Applied Science and Manufacturing*, 28(6), 595-604.
7. Panthapulakkal, S., & Sain, M. (2007). Injection- molded short hemp fiber/glass fiber- reinforced polypropylene hybrid composites—Mechanical, water absorption and thermal properties. *Journal of Applied Polymer Science*, 103(4), 2432-2441.
8. Romanzini, D., Lavoratti, A., Ornaghi Jr, H. L., Amico, S. C., & Zattera, A. J. (2013). Influence of fiber content on the mechanical and dynamic mechanical properties of glass/ramie polymer composites. *Materials & Design*, 47, 9-15.
9. Ramesh, M., Palanikumar, K., & Reddy, K. H. (2013). Mechanical property evaluation of sisal-jute-glass fiber reinforced polyester composites. *Composites Part B: Engineering*, 48, 1-9.
10. Chen, D., Li, J., & Ren, J. (2011). Influence of fiber surface-treatment on interfacial property of poly (l-lactic acid)/ramie fabric biocomposites under UV-irradiation hydrothermal aging. *Materials Chemistry and Physics*, 126(3), 524-531.
11. Chunhong, W., Shengkai, L., & Zhanglong, Y. (2016). Mechanical, hydrothermal ageing and moisture absorption properties of bamboo fibers reinforced with polypropylene composites. *Journal of Reinforced Plastics and Composites*, 35(13), 1062-1074.
12. Wan, Y. Z., Wang, Y. L., Huang, Y., Luo, H. L., He, F., & Chen, G. C. (2006). Moisture absorption in a three-dimensional braided carbon/Kevlar/epoxy hybrid composite for orthopaedic usage and its influence on mechanical performance. *Composites Part A: Applied Science and Manufacturing*, 37(9), 1480-1484.
13. Tsai, Y.I., et al., Influence of hygrothermal environment on thermal and mechanical properties of carbon fiber/fiberglass hybrid composites. 2009. 69(3-4): p. 432-437.
14. Sharma, B., et al., Glass fiber reinforced polymer-clay nanocomposites: processing, structure and hygrothermal effects on mechanical properties. 2012. 4: p. 39-46.
15. Valentin, D., F. Paray, and B.J.J.o.m.s. Guetta, The hygrothermal behaviour of glass fibre reinforced Pa66 composites: a study of the effect of water absorption on their mechanical properties. 1987. 22(1): p. 46-56.
16. Chandrasekar, M., et al., An experimental review on the mechanical properties and hygrothermal behaviour of fibre metal laminates. 2017. 36(1): p. 72-82.
17. Arici, A.A.J.J.o.r.p. and composites, Effect of hygrothermal aging on polyetherimide composites. 2007. 26(18): p. 1937-1942.
18. Zhong, Y., J.J.J.o.r.p. Zhou, and composites, Study of thermal and hygrothermal behaviors of glass/vinyl ester composites. 1999. 18(17): p. 1619-1629.

Two-day International Conference on Recent Advances in Mechanical and Industrial Engineering – 2023
(ICRAMIE-2023)

19. Wang, K., et al., Hygrothermal aging effects on the mechanical properties of 3D printed composites with different stacking sequence of continuous glass fiber layers. 2021. 100: p. 107242.
20. Lagouin, M., et al., Influence of types of binder and plant aggregates on hygrothermal and mechanical properties of vegetal concretes. 2019. 222: p. 852-871.
21. Boubakri, A., et al., Investigations on hygrothermal aging of thermoplastic polyurethane material. 2009. 30(10): p. 3958-3965.
22. Park, S.Y., W.J. Choi, and H.S.J.C.S. Choi, The effects of void contents on the long-term hygrothermal behaviors of glass/epoxy and GLARE laminates. 2010. 92(1): p. 18-24.
23. Majerski, K., B. Surowska, and J.J.C.P.B.E. Bienias, The comparison of effects of hygrothermal conditioning on mechanical properties of fibre metal laminates and fibre reinforced polymers. 2018. 142: p. 108-116.

COLLABORATIVE LEARNING ROBOTS

Dr. P. Venu Madhav¹, U. Koteswara Rao², Yogitha. A³

Department of Electronics and Communication Engineering, Prasad V.Potluri Siddhartha

Institute of Technology, Vijayawada, Andhra Pradesh, India

venumadhav@pvpsiddhartha.ac.in

Abstract - Logistics is a global business in which multi-tasking and multiple sorting of packages or objects is critical to quickly determining their location before distribution. Part-time automated picking systems can address the challenge of acquiring personnel for operation and handling product ranges by creating a cooperative working environment between robots and humans. The paper proposes collaborative learning robots to enable a step-by-step transition from manual to highly automated picking processes.

Index Terms – collaborative, IGUS, robots, Industry 4.0, CPROG

I. INTRODUCTION

Under the new industrial paradigm known as "Industry 4.0," which requires robots to dynamically engage with other robots in a networked environment, robots face significant challenges. The primary goal of this paper is to provide a concise outline of how collective robots could be used to reduce human risk in Industry 4.0 production environments. Collaborative robot use undoubtedly has numerous advantages because these devices assist people with both physical and mental tasks, allowing for more efficient production processes. Machines make production systems more efficient.

Human-robot interaction, on the other hand, may pose certain problems if human factors concerns are not carefully considered throughout the process. Furthermore, The role that individuals have traditionally played in the manufacturing environment is rapidly changing. To adapt to these new systems, human employees will need to develop a set of abilities that have previously been overlooked.

Since the advent of the Fourth Industrial Revolution, collaborative robots have become increasingly important in the production and manufacturing industries. Collaborative robots outperform industrial robots in terms of productivity, flexibility, versatility, and safety. Collective robots are devised to perform tasks alongside human workers while sharing the same working space, allowing for greater mobility.

Collective robots improve production, manufacturing, and assembly tasks by reducing basic interaction with humans in a communal workspace. These robots are designed to be easily reprogrammed, with no programming experience. Collaborative robots offer promising methods for increasing productivity while lowering fabrication costs by combining human decision-making ability with robot repeatability and strength.

Path planning with lazy PRM, as proposed by R. Bohlin and L. E. Kavraki, [1] finds a suitable motion planner for two different scenes and three different queries. They suggested algorithms for sampling-based motion planning optimization.

Randomized Kinodynamic Planning, proposed by [2] LaValle, S.M., and Kuffner, J.J., introduces a randomized path planning technique to compute impact-free kinodynamic traces for high-degree-of-freedom challenges

P. Ferbach's [3] technique of progressive restraints for nonholonomic motion design presents a general method for nonholonomic motion design (NMD) that can solve difficulties for systems with high-dimensional structure spaces. The initial NMP problem is replaced by a sequence of progressively constrained ones that are solved sequentially and whose solution path unites towards the original problem's solution.

Frieder Loch, Gennadiy Koltun, Victoria Karaseva, Dorothea Pantforder, and Birgit Vogel-Heuser [4] used SysML models in their paper Prototype-based training of manual procedures in automatic production systems. The training system consists of an preliminary

virtual training system for assistance during procedures.

The proposal by [5] P. Poor, T. Broum, and J. Basl, Role of Collaborative Robots in Industry 4.0 with a Focus on Education in Industrial Engineering, ideally presents the first 3.0 industrial revolution, major inventions, and their impact on society and industrial growth. Then, Industry 4.0 is introduced, emphasis on the use of collaborative robots and their role underlined.

This paper examines the current significance of collaborative robots and speculates on their future potential.

The Robotic Arm:

A robotic arm is a particular kind of mechanical arm that can be programmed and performs tasks comparable to those of a human arm. It can be a standalone robot or a component of a more sophisticated robot. Such a manipulator has joints that allow for either translational (linear) displacement or rotational motion, similar to an articulated robot.

A kinematic chain may be thought of as being formed by the manipulator's linkages. The end effector, which is similar to the human hand, is the culmination of the manipulator's kinematic chain. However, the phrase "robotic hand" is frequently used as a synonym for the robotic arm.

Table 1 Robot Specifications

	5 axis small version	5 axis big version
Payload	0.5KG	2.5KG
Reach	600mm (450mm)	750mm (580mm)
JointVel	max 45-60°/sec	max 45-60°/sec



Figure 1 Robotic ARM

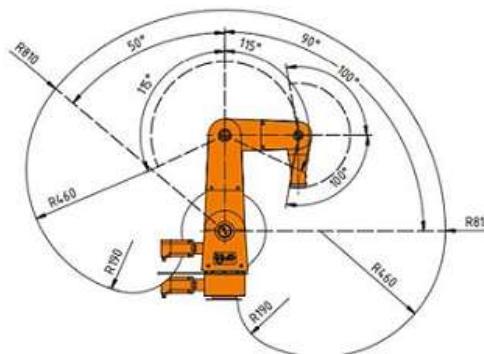


Figure 2 Arm Movement Zone

II. PERIPHERALS FOR COLLABORATION

DIGITAL INPUT/OUTPUT MODULE:

The DIO Module provides input and output channels, e.g., to operate a gripper valve. The outputs can switch up to 500 mA. The inputs use opto-couplers and are compatible with input Voltages between 12 and 24 V. If the current exceeds 500 mA, the solid-state relays can suffer damage. For safety reasons, the inputs and outputs of the DIO Module are electrically isolated. This means that the circuits of the inputs and outputs are not connected to the Dept. of Mech. Engg.

internal circuits of the controller.

It is, therefore, necessary to connect a supply voltage for the outputs and a ground line for the inputs. For this purpose, the 24 V available in the robot controller can be used, but also an external independent voltage source. In Software the inputs and outputs of the first DIO Module are numbered 21-27, the second DIO Module (if supplied) has numbers 31-37, and the third 41-47.

Digital Out connector A (D-out A): The output relays connect the pin of the power supply with the corresponding output pins.

Pin 1 (left): Input voltage (for all seven channels)

Pin 2: D-Out channel 1 (in software: Dout21)

Pin 3: D-Out channel 2 (in software: Dout22)

Pin 4: D-Out channel 3 (in software Dout23)

Digital Out connector B (D-out B): The D-out B pins are from left to right digital out channels 4-7.

Digital In connector A (D-in A): Pin 1 of D-In A is the corresponding GND pin for all input pins.

Pin 1 (left): Signal GND (for all seven channels)

Pin 2: D-In channel 1 (in software DIn21)

Pin 3: D-In channel 2 (in software DIn22)

Pin 4: D-In channel 3 (in software Din23)

Digital In connector B (D-in B): The D-in B pins are (from left to right) the Digital In channels 4-7.

III. CPRog CONTROL SOFTWARE

CPRog is a robot control and programming environment. The 3D user interface aids in quickly getting the robot up and running. Different kinematics and motor drivers can be controlled thanks to the modular structure. The CPRog programming environment allows for robot control and programming. You can work both online and offline, with or without the robot (with the robot switched off or not connected).

A. REFERENCING THE ROBOT

The position is kept in an EEPROM by the motor modules. However, when the motor power is turned off, the axes could move as a result of gravity or other forces. In this situation, the motor modules no longer inform the software of the proper position. Referencing must be done in order to synchronize the position of the software, stepper motor module, and robot axis.

Step-by-step guide to referencing:

- Start the robot controller and the CPRog Software.
- Press the buttons "Connect", "Reset" and "Activate".
- Click the "Reference" button in the button group "Physical
- Robot" in the "Motion" tab (or "Robot Reference" in the "File" tab) to open the referencing window.
- Click on the "Reference Axis" buttons to start referencing an axis. Multiple joints can perform referencing in parallel.
- You can also click on "Reference all", and then the axes will start referencing in an order defined in the project file.
- Once all movements have been executed and the robot is at rest again, click on "Reset" and "Activate". Now the robot is fully functional.

B. MOVING THE ROBOT

The robot can be moved manually (or "jogged") when no program is running. The following options are available for this purpose:

Software keys dragging joints in a 3D area

- Game pad
Software buttons allow the selection of the motion mode. Three modes are available:
- "Axis": Clicking on A1 to A6 moves the corresponding robot axis (if present). E1- E3 moves the external joints. This may be a linear or a rotational axis.
- "Base": (Cartesian mode) moves the robot in straight lines along the X, Y, and Z axes of the base coordinate system.
- "Tool": (Cartesian mode) moves the robot in X, Y, and Z of the current tool coordinate system.

C. DIGITAL INPUTS AND OUTPUTS

Under "Inputs/Outputs," you may check the status of the inputs and outputs. It is possible to manually activate or deactivate inputs and outputs:

- When no application is running, outputs can be manually configured.
- When there is no robot attached, inputs can only be changed in simulation. So even without hardware, you can test how programs respond to various inputs.

D. SOFTWARE INTERFACES

The robot controller provides various interfaces:

- PLC interface for control via the digital inputs and outputs. Especially for easy starting and stopping of programs via a PLC or push button.
- Mod-bus TCP interfaces for control via a PLC or PC.
- CRI Ethernet interface for control and configuration via a PLC or PC. This interface offers the widest range of functions, but requires individual implementation.
- ROS interface for operating the robot via the Robot Operating System.
- Interface for object detection cameras.
- Cloud interface for monitoring the robot state.

Proposed Collaborative Interface:

The blow code table displays the operating code used for collaborative picking from the partner robot. This code is used to select objects of various sizes and shapes and sort them into their proper positions. The program directs the movement of the arm's joints in various directions based on the requirements.

Co-bots are very useful in manufacturing industries where a large number of objects must be sorted and fixed together with a few lines of code modification based on changes in coordinate positions and object size (payload). It's hardware module includes internal storage and allows for multiple programs to be stored and used as needed.

IV. ESTABLISHING THE COLLABORATION

Collaboration between robots is defined as a type of coordinated activity in which two or more robots work together to complete a task or carry out the activities required to achieve a common goal. Typically, the process entails programming the robots so that the task is completed accurately.

It is critical for effective robot-robot collaboration that the robot understands and interprets several communication mechanisms similar to those used in human-human interaction. The robot must also communicate its own set of intentions and goals to the other in order to establish and maintain synchronization in order to coordinate its actions and achieve the desired output. Robots should be able to learn the required process in order to establish collaboration. The robots are interfaced with CPRog software to establish the collaboration.

The following section describes the proposed model in order to demonstrate the collaborative working mechanism that must be implemented in order for the IGUS robots to interact with one another.

Software Command interface programming:

The programming is based on the coordinate axis positions, and servo motor motion,

some variables and elements are required to access them.

Variables and Variable Access:

CPRog works with integer, float type and position variables, Cartesian and joint position.

User Variables:

“DefPosVariable” and “DefNumberVariable” are the user variables.

Element Access:

The subsequent elements of the variables can be retrieved with the “.” Operator:

- Position: x, y, z
- Rotation: A, B, C
- Joints: A1, A2, A3, A4, A5, A6

A. MOTION RELATED COMMANDS

Joint Motion

Leads to a target position in joint co-ordinates. The joint swiftness during the motion are constant. The resulting motion of the TCP is generally not a line, but a curve.

Table 2 Joint Motion

Nr	Cmd	X	Y	Z	A	B	C	E1	E2	E3	Vel	acc	smoo	cond	Desc
0	Joint	A1	A2	A3	A4	A5	A6	E1	E2	E3	10...	40%	50%	false	
		0	20	10	15	0	0	0	0	0					

A1 to A6: Joint values of the target in deg(°); E1 to E3: Joint values of the external joints; Vel: Velocity in percent; Acc: Acceleration in % ; Smooth: Utterance at the edge points; Condition: Abort state when true motion is aborted; Description: comment description

Linear Motion

A traditional linear motion for utterance of both position and orientation.

Table 3 Linear Motion

Nr	Cmd	X	Y	Z	A	B	C	E1	E2	E3	vel	acc	smo	con	desc
0	Linear	X	Y	Z	A	B	C	E1	E2	E3	10...	40%	50%	false	
		568.	1	230	177.	26.2	178.	1	2	3					
		8	5	1	9	1	4	0	0	0					

- X,Y,Z: Cartesian position of the target position(mm)
- A,B,C: Orientation of the target position in deg(°), encrypted in eular angles.
- E1 to E3: Joint values of the external joints
- Vel: Velocity in mm/s
- Acc: Acceleration in %
- Smooth: Interpolation at the edge places
- Condition: Abort condition
- Description: Free field

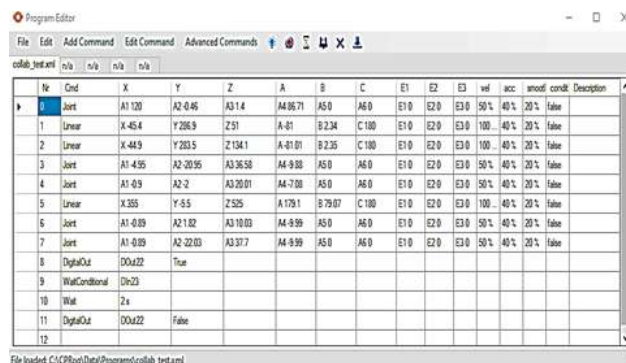


Figure 3 Sample Code

The step-by-step iterations and collaborative work of the IGUS robots are depicted in the figures below. The left arm is equipped with a self-contained vacuum compressor. It is

activated during component selection from a desired location, and the right-side robotic arm has a self-attached electromagnetic field generator end tool that is activated when robotic arm one receives the object. The operation was described in detail at each level in the steps below.



STEP-1



STEP-2



STEP-3



STEP-4



STEP-5



STEP-6

STEP 1: The robotic arm is in its starting position, ready to begin the iteration. The vacuum compressor located at the arm's mouth holds the selected object.

STEP-2: Based on the programme statements, the first arm now synchronises with the movement of the second arm.

STEP 3: The momentary objects must be correctly identified, and the positioning must be precisely at the centre of the receptor.

STEP 4: The robotic arm one sends a hand-shake signal to the arm 2 so that it can pick up the object before releasing it. A mutual exchange of the object is required. Once the object has been located, the vacuum gripping on the first robot must be released as soon as it is received by the second robot, which is equipped with an electromagnetic gripper.

STEP 5: After mutual exchange of the sensing hand shake signal to the robotic arm one, the object will be released.

STEP 6: At the receiving end, the object will be moved based on the coordinate positions defined in the programme.

Once the process of moving the object from one position to another has been completed, the same things can be repeated a greater number of times with fewer errors, providing greater accuracy in the placement of the object. This allows for quick sorting and placement of objects in the appropriate locations. Amazon now employs both object component sorters and goods sorters, both of which are costly. If developed at the subsystem level, this will be a cost-effective solution. Once the coordinate values for a task are fixed, we must reset the entire motion control logic to make the same robots work for a different task.

IV. DISCUSSION

In order to implement the collaborative robot mechanism, one must have sufficient space for the related equipment and trained personnel for its usage in terms of mechanical fixations and programming. Motor controllers and other accessories, if locally manufactured in house, then the development is feasible thereby reducing the cost. Complex programming is required for the robot to work in a multitasking environment and skilled programmers are

required for writing a complex code.

For example, if we join a third robot to the existing system, the coordinate positions have to be mapped individually with the help of a program with an understanding of the coordinate values. The transformation for the position of arm is to be done as shown in the figure:

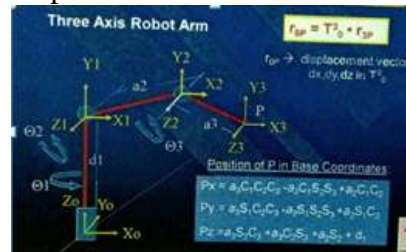


Figure 4 Position in base coordinates

One must have a clear understanding about multitasking and the corresponding delays or latencies in handling the tasks which needs to be addressed properly. The robot used in the present work is capable to pick up to 500gms of load. The end tool can be altered for different payloads from 5-10kg based on the availability in the market. The vacuum compressor that is attached is operating at 6 bars for a load up to 500gms. In complex programming or multitasking environment, the latency can be varied according to the requirement and initial operating conditions. The speed can also be varied as required, to reduce the latency.

V. CONCLUSION

Collaborative robots are opening up new possibilities for opportunities to automate an operation. They are a great approach to improve the areas where robots can assist and make our lives easier and our processes more efficient. a few successful co-bot applications can inspire fresh concepts for their application. A co-bot movement can even sync with the actions of humans working concurrently in a shared workspace. Additionally, co-bots are made to be simpler to programme than conventional robots.

REFERENCES

- [1] R. Bohlin and L. E. Kavraki, "Path planning using lazy PRM," Proceedings 2000 ICRA. Millennium Conference. IEEE International Conference on Robotics and Automation. Symposia Proceedings (Cat. No.00CH37065), 2000, pp.521-528vol.1, doi: 10.1109/ROBOT.2000.844107.
- [2] S.M.LaValle and J.J.Kuffner, "Randomized kinodynamic planning," Proceedings 1999 IEEE International Conference on Robotics and Automation (Cat. No.99CH36288C), 1999, pp.473-479vol.1, doi: 10.1109/ROBOT.1999.770022.
- [3] P. Ferbach, "A method of progressive constraints for nonholonomic motion planning," Proceedings of IEEE International Conference on Robotics and Automation, 1996, pp.2949-2955 vol.4. doi: 10.1109/ROBOT.1996.509160.
- [4] Frieder Loch, Gennadiy Koltun, Victoria Karaseva, Dorothea Pantförder, Birgit Vogel-Heuser, "Model-based training of manual procedures in automated production systems", 2018, Mechatronics, pp. 212-223, vol.55, doi:10.1016/j.mechatronics.2018.05.010.
- [5] P. Poór, T. Broum and J. Basl, "Role of Collaborative Robots in Industry 4.0 with Target on Education in Industrial Engineering," 2019 4th International Conference on Control, Robotics and Cybernetics (CRC), 2019, pp. 42-46, doi: 10.1109/CRC.2019.00018.

Finite Element Analysis of Bending and Buckling of Bimetallic Cantilever Beam and Column Subjected to Free End Concentrated Load

K. Durga Rao¹, S. Srinivasa Prasad² and M. Manzoor Hussain³

^{1*} Assistant Professor, Department of Mechanical Engineering, University College of Engineering, Adikavi Nannaya University, Rajahmundry - 533 296, India.

² Professors, Department of Mechanical Engineering, V R Siddhartha Engineering College, Vijayawada - 520007, India.

³ Professors, Department of Mechanical Engineering, JNTUH, Hyderabad - 500 085, India.

*Corresponding author e-mail: drdrk9@gmail.com

Abstract : The bi-metallic cantilever structural components are advantageously used where stiffness requirement is of great importance in the fields of automobile, aerospace, defence and power generation applications. The design of bi-metallic structural components is necessary due the stringent requirement of light weight and low margins of safety. The flexural behavior and flexural buckling behavior of bi-metallic cantilever beam and column with two segments of equal lengths, made up of two different materials, is investigated in this paper when bi-metallic structural components are subjected to free end concentrated load at three different temperatures. The material in the first segment from the clamped end to the $L/2$ is chosen to have a higher Young's modulus, when compared to the same for the remaining segment and area moment of inertia is constant for both segments. where L is the length of the structural component. Such two segmented bi-metallic structural components are used in many engineering structural applications, like bi-metallic engine valves, universal joints, gear hubs, diesel injectors, turbine blade assemblies, nuclear reactors, twisted drills etc. The specific material combinations Ti-Al, Invar-Al and Steel-Al are considered due to their light weight and good thermo mechanical properties.

It is essential to establish the design adequacy by evaluating the stiffness related behavior such as deflection, slope buckling load, mode-shapes through versatile finite element analysis. In addition, some of the properties are strong functions of temperature such as thermal conductivity, young's modulus, thermal expansion coefficient etc. Hence it is necessary to study the flexural behavior of bimetallic cantilever structural components at three different thermal environments namely cryogenic temperature, ambient temperature and elevated temperature. The temperatures-200°C, 20°C and 200°C are chosen for this study from cryogenic temperature zone, ambient temperature zone and elevated temperature zone respectively. In the present study the effect of important design parameters deflection, end slope, critical buckling load and mode-shapes of bi-metallic cantilever structural components made of Ti-Al, Invar-Al and Steel-Al at -200°C, 20°C and 200°C are studied by developing the simple finite element formulations and Matlab code. The present investigation reveals some interesting trends based on the numerical results obtained, hitherto not reported explicitly.

Keywords: Bending, flexural buckling, bimetallic cantilever beam, bimetallic cantilever column, critical buckling load parameters, mode-shapes, material nonlinearity, finite element method and Matlab code.

1. INTRODUCTION

Bending analysis of bimetallic cantilever beam subjected to free end concentrated load and buckling analysis of bimetallic cantilever column subjected to axial compressive concentrated load at free end has been studied at different temperatures using versatile Finite Element Method [1]. Such bimetallic structural components made up of different materials combinations are used in many fields of modern engineering such as automobile, aerospace and defense sector. Bimetallic engine valves, universal joints, gear hubs, diesel injectors, turbine blade assemblies, nuclear reactors, twisted drills etc., are a few applications of bimetallic structural components. The dual stepped or multiple stepped structural components with different flexural rigidities are used to obtain the optimum configuration with volume or mass as the objective function of the large scale structural systems with more number of degrees of freedom (dof). Such structural systems are the plane truss that contains two-dimensional beams, and also the structural members with the moderate dof, like beams, and columns [2 to 5]. In these studies the different behavioral constraints, considered are the deflection, buckling load, natural frequencies etc. computed by using the finite element method (FEM) based optimality criterion approach.

The bimetallic cantilever beam or bimetallic cantilever column is clamped at one end, for which the coordinate value $x = 0$ and is free at the other end the coordinate value $x = L$, where L is the length, and contains two segments of equal length $\frac{L}{2}$. The bimetallic structural cantilever component have two segments contain two different materials, for which the Young's modulus of the material in the first segment from $x = 0$ to $\frac{L}{2}$ is E_1 , and the same of the material in the second segment from $x = \frac{L}{2}$ to L is E_2 , as shown in Fig. 1(a). Though the area moment of inertia of the cross-section I for both the segments is taken as constant, but the flexural rigidities EI of the two segments will be different, as the materials of the two segments have different values of E_1 and E_2 . In the present investigation specific material combinations Ti-Al, Invar-Al and Steel-Al are considered due to their light weight and good thermo mechanical properties. But a parametric study of $n \left(= \frac{E_1}{E_2} \right)$ is carried out for different material combination and $n = 1$ represents the bimetallic cantilever beam or bimetallic cantilever column made of the same material. The values of E_1 and E_2 at three different temperatures environments namely Ambient Temperature 20°C , Cryogenic Temperature -200°C and Elevated Temperature 200°C are taken from the literature shown in table.1

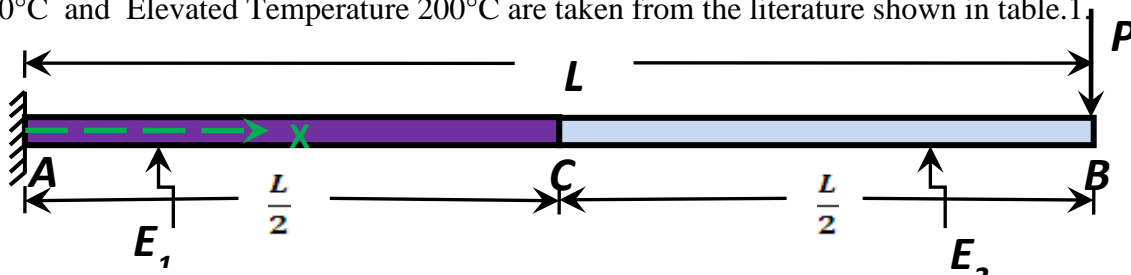


Fig 1 (a): A bimetallic cantilever beam subjected to concentrated lateral load at free

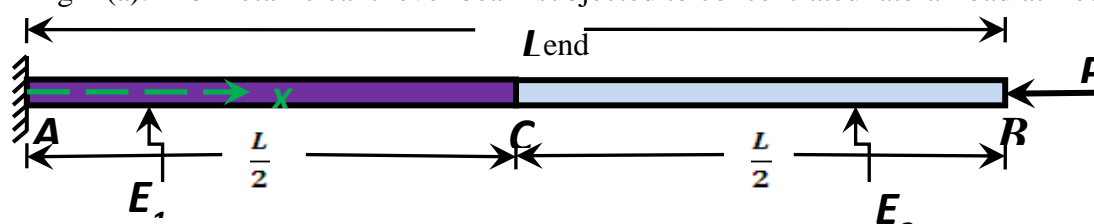


Fig 1 (b): A bimetallic cantilever column subjected to concentrated compressive load

Table.1: Young Modulus values(GPa) for different Materials at different temperatures			
Material	T=20°C	T= - 200°C	T=200°C
Titanium alloy (Ti)	106.87	--	96.52
Aluminum Alloy (Al)	71.62	80.34-77.64	59.98
Steel	198.8	214.4	182.71
Invar	150.8	140.5	--
Modular ratio (E₁/E₂) of different material combinations at different temperatures			
Steel-Al	2.775	2.669	3.046
Ti-Al	1.492	--	1.609
Invar-Al	2.106	1.749	--

This configuration of bimetallic cantilever beam increases the free end concentrated lateral load P to obtain the same deflection or slope parameters of the uniform cantilever beam. Similarly the flexural buckling load of bimetallic cantilever column will be increased from that of the uniform cantilever column, when this column is subjected to a free end axial compressive load P . In this study, the advantage of the use of two different materials in the two segments is brought out by defining the efficiency of bimetallic cantilever beam or bimetallic cantilever column. The efficiency of bimetallic cantilever column is defined as $\frac{P_n}{P_1}$, where P_n is the lateral concentrated load taken to produce the same lateral deflection at the free end, for a specific value of n , when the corresponding load is P_1 , for $n=1$, which represents the uniform cantilever beam. It is to be noted that the efficiency calculated for the free end slope parameter of bimetallic cantilever beam is different from that obtained for the free end lateral deflection. In a similar way the efficiency of bimetallic cantilever column is defined as $\frac{P_{bn}}{P_{b1}}$, where P_{bn} is the buckling load for the value of n other than 1 and P_{b1} is the same for $n = 1$.

The major aim of the present study is to evaluate the variation of the deflection and slope parameters of bimetallic cantilever beam along its length, and also to evaluate the flexural buckling load parameter and the corresponding mode shapes of deflection and slope along its length of bimetallic cantilever column for chosen material combination at different temperatures by through Matlab code. The other equally interesting aspect of the present investigation is to obtain the efficiency of bimetallic cantilever beam or bimetallic cantilever column in terms of the ratio of the increased the free end concentrated lateral load and the increased buckling load corresponding to the free end concentrated axial compressive load, for the different values of n at different temperatures with the same quantities of the uniform cantilever beam or column, with the value of $n = 1$.

Another important aspect to be considered in realizing bimetallic cantilever beam or bimetallic cantilever column, is the production technology, used in joining the two segments, made up of the two different materials at the midpoint ($x = \frac{L}{2}$). The joining of the two materials, with higher weld efficiency and without any unwanted effects like the heat affected zones, is a difficult task earlier. However, due to the development of the modern welding technologies [6, 7, 8], it is now possible to realize the perfect bimetallic cantilever beam or bimetallic cantilever column.

1. Deflection and slope of bimetallic cantilever beam

The geometry of bimetallic cantilever beam is shown in Fig. 1(a), in which the value of $E_1 > E_2$ or $\frac{E_1}{E_2} = n$. A special case of bimetallic cantilever beam is the uniform cantilever beam, for which the values of $E_1 = E_2 = E$, and the value of $n = 1$. The present investigation is mainly to obtain the variation of the lateral deflection w and the slope $w' \left(\frac{dw}{dx}\right)$ parameters, along the length $x = 0$ to L , when subjected to the concentrated lateral load P at the free end $x = L$, by using the FEM. Without going into the basic details of the very popular FEM [1], the equations of equilibrium of bimetallic cantilever beam is obtained, in the matrix form as

$$[K] \{W\} = \{F\} \quad (1)$$

In Eq. (1), $[K]$ is the global elastic stiffness matrix, which is obtained by assembling the N number of equal length beam element stiffness matrices $[k_e]$. The global solution vector $\{W\}$ is obtained by assembling the beam element solution vectors $\{w_e\}$, where the elements contain the values of the lateral deflection w and its first derivative w' , with respect to the axial coordinate x , at each node of bimetallic cantilever beam. The global load vector $\{F\}$ is obtained by assembling the element load vectors $\{f_e\}$. In the present investigation, the global load vector $\{F\}$ contains only the zero elements, as the distributed lateral loads are not present in bimetallic cantilever beam. However, the global load vector $\{F\}$, contains the lateral concentrated load P at the dof corresponding to the lateral deflection w at the free end.

The solution vector $\{W\}$ is obtained, from Eq. (1), after applying the essential boundary conditions of bimetallic cantilever beam, which is a standard procedure, as

$$\{W\} = [K]^{-1} \{F\} \quad (2)$$

The derivation of the element elastic stiffness matrix $[k_e]$ and the load vector $\{f_e\}$ of the beam element used for the flexural analysis of beams, as the FEM is well known, and these details are available in the Refs. [1,9]. It is mandatory to perform the convergence study, if the FEM is used in the analysis and in the present investigation also the convergence of the global displacement vector $\{W\}$ is studied systematically by idealizing the beam with the N number of equal length beam finite elements. It is to be noted that the value of N has to be even, so that the first segment (from $x = 0$ to $\frac{L}{2}$), with the value of E_1 , and the second segment (from $x = \frac{L}{2}$ to L), with the value of E_2 , are discretized by $\frac{N}{2}$ beam finite elements, in bimetallic cantilever beam. In the convergence study, the values of N are taken as 2, 4, 8 and 16, which is a standard procedure to study the convergence. The convergence study revealed an interesting phenomenon, perhaps not observed by others working on the finite element analysis (FEA) of the flexure of the uniform cantilever beam, with the constant value of E , from $x = 0$ to L , and also for bimetallic cantilever beam with the two values of E_1 and E_2 in the two segments.

2. Flexural buckling of bimetallic cantilever column

Flexural buckling of bimetallic cantilever column subjected to the axial compressive concentrated load P at the free end, as shown Fig. 1(b) is another practically interesting problem. The FEM is used to obtain the eigenvalues (buckling loads) and the corresponding eigenvectors (mode shapes), eigenvalues represents buckling loads and the corresponding eigenvectors represents mode shapes. Though the evaluation of the buckling load parameters

and the corresponding buckling mode shapes is straight forward for the uniform cantilever column with the constant E or $n = 1$ [10], but is relatively a difficult task involved to obtain the same, where the values of E_1 and E_2 are different in the two segments of bimetallic cantilever column.

The use of the FEM, to obtain the eigenvalues and eigenvectors requires not only the elastic stiffness matrix $[k_e]$ of the beam element, but also the geometric stiffness $[g_e]$ of the beam element. The bimetallic cantilever column is idealized with the N equal length beam finite elements, where N is even. The final matrix equilibrium equation governing the buckling of bimetallic cantilever column after applying the boundary conditions, is given by

$$[K] \{\delta\} - P_b[G]\{\delta\} = \{0\} \quad (3)$$

In Eq. (3), $[K]$ is the global elastic stiffness, $[G]$ is the global geometric stiffness matrices, P_b are the buckling loads and $\{\delta\}$ are the buckling mode shapes. Equation (3) represents the standard eigenvalue problem, the solution of which, gives as many eigenvalues and the eigenvectors, as the dof of the global matrix equilibrium equation. The eigenvalues and the eigenvectors can be obtained, by using the QR algorithm [11, 12] to evaluate the eigenvalues and eigenvectors. It is to be noted that the lowest eigenvalue (buckling load) and the corresponding normalized eigenvector (buckling mode shape) are of practical interest to the structural engineers. There are many ways of normalizing the eigenvector, and in the present investigation, the eigenvector is normalized by the free end lateral deflection of bimetallic cantilever column.

3. Numerical results and discussion

The numerical results, in the form of the free end of lateral deflection and slope parameters w_e and w'_e of the flexure of bimetallic cantilever beam, subjected to the concentrated lateral load P at the free end, as shown in Fig. 1(a), are obtained, by using the FEM in the present investigation. For bimetallic cantilever column shown in Fig. 1(b), the FEM is used to obtain the flexural buckling load parameter, subjected to the axial concentrated compressive load P at the free end. The details of the geometry, load and material properties of bimetallic cantilever beam or bimetallic cantilever column are shown in Fig. 1(a) and Fig. 1(b). Initially the deflection and slope analysis of bimetallic cantilever beam is presented and for a better appreciation of the flexural buckling of bimetallic cantilever column is presented. In the flexure of bimetallic cantilever beam, as FEM is used, it is essential to study the convergence of the numerical results, by varying the number of N equal length finite elements, which are used to discretize bimetallic cantilever beam. The numerical results obtained for the free end lateral deflection and slope parameters w_e and w'_e , from the convergence study, where the value of N varies from 4, 8 and 16, and for the different combination of materials at Ambient Temperature 20°C, Cryogenic Temperature -200°C and Elevated Temperature 200°C are presented in Table 2. It is very interesting to observe from Table 2 that the numerical values of w_e and w'_e are the same and independent of the number of finite elements N , with which bimetallic cantilever beam is discretized, for the values of n considered.

This unexpected phenomenon can be explained as the lateral deflection of the uniform cantilever beam, represented by $n = 1$, varies as a cubic polynomial with respect to the axial coordinate x of bimetallic cantilever beam. The elastic stiffness matrix of the beam element is also derived by using the cubic Hermite shape functions, which contains the term ξ^3 or lesser

powers of the element coordinate ξ . Hence, it is obvious that the deflection and slope parameters of the uniform cantilever column ($n = 1$) are the same, which is independent of N . However, for bimetallic cantilever beam the parameter n value is different for different combination of material, the convergence of the deflection and slope parameters is independent of N . This behavior of invariance of the parameters w_e and w'_e of bimetallic cantilever beam is unexpected, but based on the present numerical results, it can be inferred that for bimetallic cantilever beam also the deflection parameter varies as a cubic polynomial with respect to the axial coordinate x , along the length of bimetallic cantilever beam. As a further confirmation of these unexpected results for w_e and w'_e of bimetallic cantilever beam, obtained from FEM, the same values of w_e and w'_e are evaluated, by applying the Area-Moment method and double integration method [13], From these methods the values of the

TABLE-2: Convergence Study of Deflection and Slope Parameters of Flexure of Bimetallic Cantilever Beam subjected to Free end Concentrated Load P				
Material Combinations	Modular Ratio	No. of Elements N	At Ambient Temperature T = 20°C	
			α^*w	$\beta^{**}w'$
Uniform	1.0	4	0.3334	0.50
		8	0.3334	0.4999
		16	0.3334	0.4999
Steel-Al	2.7758	4	0.1467	0.2601
		8	0.1467	0.2600
		16	0.1467	0.2600
Invar-Al	2.1056	4	0.1802	0.3031
		8	0.1801	0.3030
		16	0.1801	0.3030
Ti-Al	1.4922	4	0.2371	0.3763
		8	0.2371	0.3763
		16	0.2371	0.3763
			At Cryogenic Temperature T = -200°C	
Steel-Al	2.6687	4	0.1510	0.2656
		8	0.1509	0.2655
		16	0.1509	0.2655
Invar-Al	1.7488	4	0.2084	0.3394
		8	0.2084	0.3394
		16	0.2084	0.3394
			At Elevated Temperature T = 200°C	
Steel-Al	3.0462	4	0.1375	0.2482
		8	0.1374	0.2481
		16	0.1374	0.2481

Ti-Al	1.6092	4	0.2229	0.3580
		8	0.2229	0.3580
		16	0.2229	0.3580

free end w_e and w'_e are obtained as $\frac{7+n}{24n}$ and $\frac{3+n}{8n}$. The values of the free end lateral deflection and slope parameters w_e and w'_e of bimetallic cantilever beam obtained for the different values of n at three different temperatures from the classical methods such as area-moment method, double integration method and the same obtained from FEM which are presented in Table 3.

Table-3: Free end Deflection and Slope Parameters of Bimetallic Cantilever Beam subjected to Free end Concentrated Load P – Comparison of Numerical Results of Finite Element Method-Area Moment Method – Double integration Method

Material Combinations	Modular Ratio	Finite Element Method		Area- Moment Method		Double Integration Method	
		At Ambient Temperature Environment T = 20 °C					
		α^*w	$\beta^{**}w'$	α^*w	$\beta^{**}w'$	α^*w	$\beta^{**}w'$
Uniform	1.0	0.3334	0.4999	0.3334	0.50	0.3334	0.50
Steel-Al	2.7758	0.1467	0.2600	0.1467	0.2600	0.1467	0.2600
Invar-Al	2.1056	0.1801	0.3030	0.1801	0.3030	0.1801	0.3030
Ti-Al	1.4922	0.2371	0.3763	0.2371	0.3763	0.2371	0.3763
At Cryogenic Temperature T = -200 °C							
Steel-Al	2.6687	0.1509	0.2655	0.1509	0.2655	0.1509	0.2655
Invar-Al	1.7488	0.2084	0.3394	0.2084	0.3394	0.2084	0.3394
At Elevated Temperature T = 200 °C							
Steel-Al	3.0462	0.1374	0.2481	0.1374	0.2481	0.1374	0.2481
Ti-Al	1.6092	0.2229	0.3580	0.2229	0.3580	0.2229	0.3580

The variation of the lateral deflection and slope parameters along the length of bimetallic cantilever beam at different temperatures are presented in Figs. 2, 3, 4 and Figs. 5, 6, 7 respectively. The number of finite elements N used to discretize the bimetallic cantilever beam do not effect these distributions as has been already discussed. It is worth noting here that the lateral deflection parameter is continuous and varies smoothly along the length of bimetallic cantilever beam. Whereas the variation of the slope parameter, which can be obtained by the differentiation of the lateral deflection parameter though continuous but shows an appreciable kink at the midpoint of bimetallic cantilever beam at $(x = \frac{L}{2})$, the discontinuity of E exists, when the value E_1 abruptly changes to E_2 . The continuity aspects are typical to FEA where the continuity of the quantities under investigation, which are the lateral deflection and slope parameters are continuous within the element. The requirement of

Dept. of Mech. Engg. PVPSIT 43

continuity between the two adjacent elements, which is satisfied through the assembly procedure, by using the requirement of continuity, where the dof consisting the lateral deflection and slope parameters at the common basic reason for the continuous variation of the lateral deflection and the slope parameters along the length of bimetallic cantilever beam. However, the kink existing in the continuously varying slope parameter, at the midpoint of bimetallic cantilever beam, suggests that the derivative of the slope with respect to x ($= \frac{d^2w}{dx^2}$) contributes to the internal moment term, which can be discontinuous, because of the sudden reduction of E from E_1 to E_2 . Thus, a kink in the slope parameters at $x = \frac{L}{2}$ is justified. Following a similar logical argument, no kink is observed in the length-wise variation of the lateral deflection parameter, as a kink makes its first derivative $\frac{dw}{dx}$ (slope parameter) discontinuous, which is not physically possible. As a consequence, the free end lateral concentrated load P acting on bimetallic cantilever beam increases to have the same free end lateral deflection (or slope) of the uniform cantilever beam with constant E_2 . The advantage of this configuration is the increase of the free end concentrated load P_n of bimetallic cantilever beam for different n values, when compared to the load P_1 , when $n = 1$. The increase in the load P is denoted here as the efficiency of bimetallic cantilever beam, and is defined as $\frac{P_n}{P_1}$. The numerical results of the efficiency of bimetallic cantilever beam are presented in Table 4.

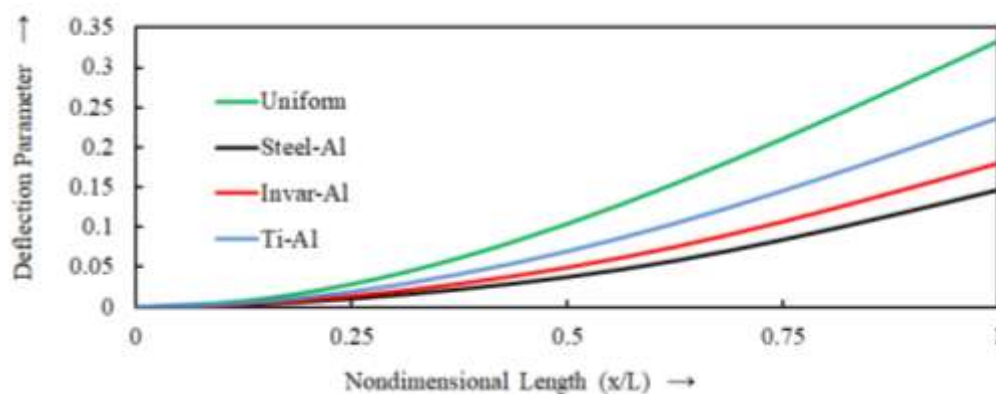


Fig 2: Variation of Deflection Parameter along the length of a bimetallic cantilever beam subjected to free end lateral concentrated load at ambient temperature $T=20^{\circ}\text{C}$

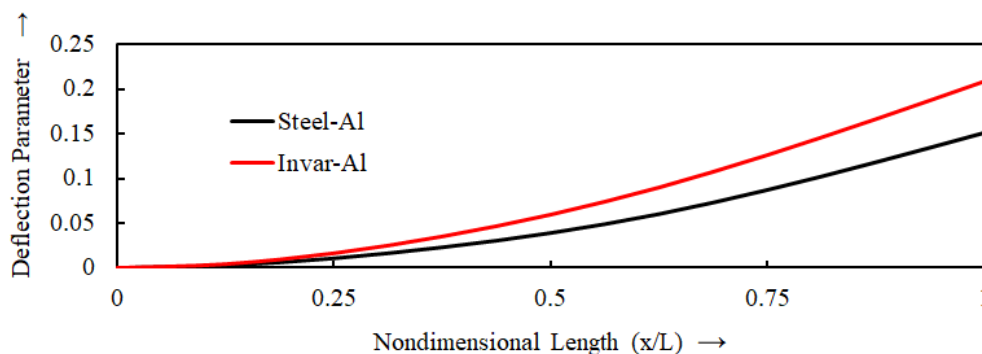


Fig 3: Variation of Deflection Parameter along the length of a bimetallic cantilever beam subjected to free end lateral concentrated load at cryogenic temperature $T= -200^{\circ}\text{C}$

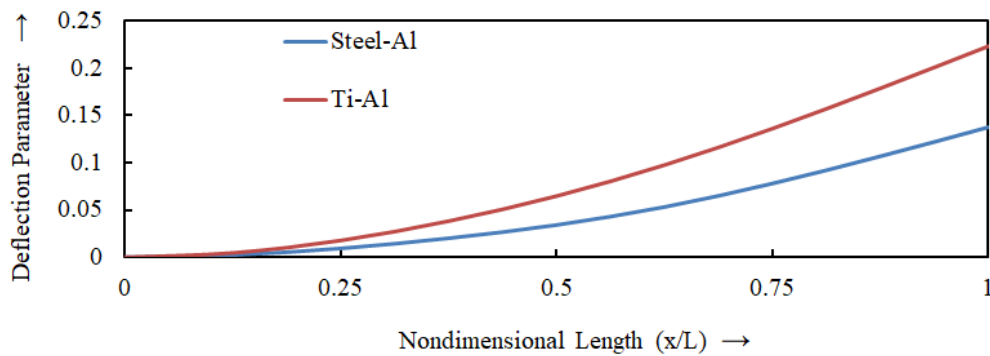


Fig 4: Variation of Deflection Parameter along the length of a bimetallic cantilever beam subjected to free end lateral concentrated load at elevated temperature T= 200°C

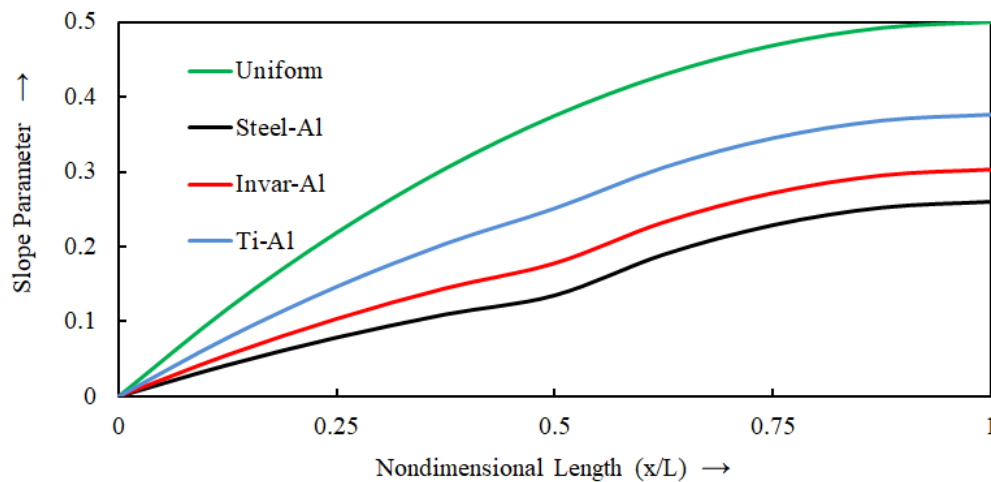


Fig 5: Variation of Slope Parameter along the length of a bimetallic cantilever beam subjected to free end lateral concentrated load at ambient temperature T= 20°C

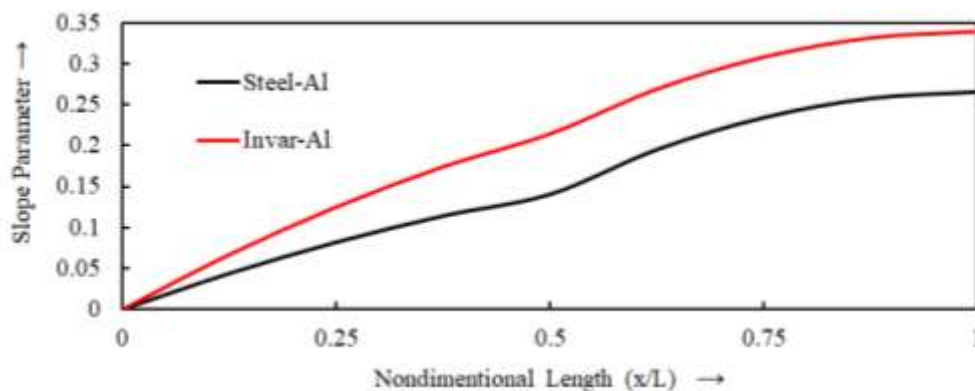


Fig 6: Variation of Slope Parameter along the length of a bimetallic cantilever beam subjected to free end lateral concentrated load at cryogenic temperature T= -200°C

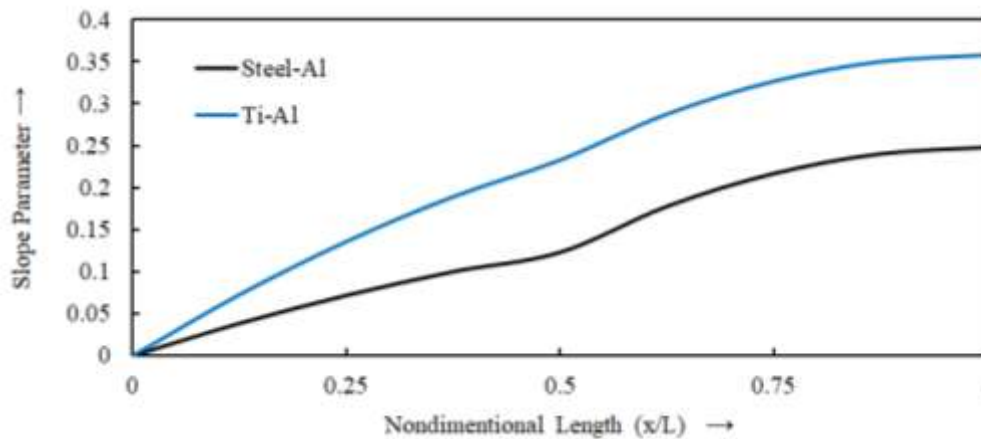


Fig 7: Variation of Slope Parameter along the length of a bimetallic cantilever beam subjected to free end lateral concentrated load at elevated temperature $T= 200^{\circ}\text{C}$

The numerical results for the flexural buckling of bimetallic cantilever column are discussed here, with respect to the buckling load parameters and the corresponding mode shapes, obtained by using the FEM for the different combinations of materials at Ambient Temperature 20°C , Cryogenic Temperature -200°C and Elevated Temperature 200°C . The lowest buckling load parameter, which is of practical interest, converged with the 8 equal length beam element discretization of bimetallic cantilever column, as shown in Table 5, for different material combinations considered at three different temperatures in this investigation. The corresponding buckling mode shapes, in terms of the variation of the lateral deflection and the slope parameters, which are normalized with respect to the free end lateral deflection and slope, are presented in Table. 6, with the main aim of demonstrating the effect of discontinuity of the Young's modulus at the midpoint of bimetallic cantilever column. The behavior of the normalized lateral deflection or the normalized slope parameters is similar to that of bimetallic cantilever beam shown in Fig. 8, 9 and 10. While the variation of the normalized lateral deflection parameter does not show any conspicuous behavior, the variation of the normalized slope parameter shows a clear kink at the midpoint of bimetallic cantilever column, where E is discontinuous. Finally, for the configuration of bimetallic cantilever column, the buckling load parameter increases with n other than 1 when compared to the value of $n = 1$, for which the buckling load parameter [10] is $\frac{\pi^2}{4}$ ($= 2.4674$). The efficiency of the buckling load parameter, obtained by using the two equal segments with E_1 and E_2 of bimetallic cantilever column is defined as $\frac{P_{bn}}{P_{b1}}$, where P_{bn} is the buckling load parameter when n is other than 1 and P_{b1} is the same for $n = 1$. The efficiency of the buckling load parameter for bimetallic cantilever column is presented in Table 7

Table-4: Values of $\frac{P_n}{P_1}$ of Bimetallic Cantilever Beam to obtain same free end deflection and slope parameters

Material Combinations	Modular Ratio	At Ambient Temperature $T = 20^{\circ}\text{C}$

		Deflection parameter^{\$}	$\left(\frac{P_n}{P_1}\right)^*$	Slope parameter[#]	$\left(\frac{P_n}{P_1}\right)^*$
Uniform	1.0	0.3334	1.0	0.4999	1.0
Steel-Al	2.7758	0.1467	2.2727	0.2600	1.9227
Invar-Al	2.1056	0.1801	1.8512	0.3030	1.6498
Ti-Al	1.4922	0.2371	1.4062	0.3763	1.3285
At Cryogenic Temperature T = -200 °C					
Steel-Al	2.6687	0.1509	1.5113	0.2655	1.8829
Invar-Al	1.7488	0.2084	2.5011	0.3394	1.4729
At Elevated Temperature T = 200 °C					
Steel-Al	3.0462	0.1374	1.5959	0.2481	2.0149
Ti-Al	1.6092	0.2229	2.7350	0.3580	1.3963

5. Conclusions

The flexural analysis of the bimetallic cantilever beam and the flexural buckling analysis of the bimetallic cantilever column which have two equal length $\left(\frac{L}{2}\right)$ segments, where L is the length of cantilever structural component at different temperatures is investigated in the present study. The first segment spans from $x = 0$ to $\frac{L}{2}$, with the Young's modulus E_1 and the second segment spans from $x = \left(\frac{L}{2}\right)$ to L , with the Young's modulus E_2 , where $E_1 > E_2$ or in terms of a parameter $n = \frac{E_1}{E_2}$, and a constant area and moment of inertia I of the cross-sections of both the segments is taken, in this study. Such configurations of bimetallic cantilever beam and bimetallic cantilever column are used to achieve the present day efficient and cost effective structural members that are used in the manufacturing sectors of automobile, aerospace, marine, nuclear, defense, and also in the consumer products sectors, like hand tools, domestic appliances, sports equipment etc. As a special case, if the Young's moduli $E_1 = E_2 = E$, or the value of the parameter $n = 1$, bimetallic cantilever beam or bimetallic cantilever column becomes a uniform cantilever beam or column. Based on the present investigation in this paper on the deflection, slope and flexural buckling analysis of bimetallic cantilever beam or bimetallic cantilever column, the important observations/conclusions are briefly summarized below.

- The flexural analysis of bimetallic cantilever beam shows that the numerical results in terms of the lateral deflection and slope parameters do not depend on the number of beam finite elements with which bimetallic cantilever beam is discretized. Though this behavior can be explained for the uniform beams ($n = 1$), as the variation of deflection along the length of the beam is cubic in x and the beam finite element is also derived by using the cubic Hermite

interpolation functions. However, this behavior is unexpected for bimetallic cantilever beam and perhaps hitherto not recognized by others.

- The same behavior of the independency of discretization of bimetallic cantilever beam with the number of beam elements is observed for the slope parameters also.
- The functions of the deflection and slope parameters, obtained from the FEA are continuous along the length of bimetallic cantilever beam. However, the function of the slope parameter shows a kink at the midpoint ($x = \frac{L}{2}$) of bimetallic cantilever beam, as at that point the E_1 of the first segment abruptly changes to E_2 (as a step) of the second segment. This behavior is due to the fact that at the midpoint of bimetallic cantilever beam, the bending moment obtained from the derivative of the function of the slope parameter with respect to the axial coordinate x is not continuous. A similar kink at the midpoint is not observed in the function for the lateral deflection parameter, as the function for the slope parameter, which is the derivative of the function for the deflection parameter with respect to x , becomes discontinuous at that point, which is physically not possible.
- Though the FEM gives reliable results, to cross-check this unexpected behavior, the free end lateral deflection and slope parameters are obtained from an altogether different Area-Moment method and Double Integration method. The results obtained by the Area-Moment method and Double Integration method exactly match with those obtained by using FEM, which clearly shows that the free end lateral deflection and slope parameters are accurate and no anomaly exists.
- The efficiency of the free end concentrated lateral load carrying capacity of bimetallic cantilever beam increases for *specific* material combinations Ti-Al, Invar-Al and Steel-Al at all three different temperature zones and for the same free end lateral deflection and slope parameters, when compared to the uniform cantilever beam represented by $n = 1$. It is to be noted that the efficiencies are different for the deflection and slope parameters.
- The flexural buckling loads of bimetallic cantilever column converged to the specified accuracy of four decimal digits, when the number beam elements used in FEA are eight.
- The mode shapes corresponding to the normalized lateral deflection and slope parameters are found to be continuous. However, the variation of the normalized mode shape corresponding to the variation of the slope parameter, shows a kink at the midpoint ($x = \frac{L}{2}$) of bimetallic cantilever column, which indicates that its derivative with respect to the axial coordinate x represents the bending moment that is not continuous at the midpoint, as anticipated, where the E_1 of the first segment changes abruptly as a step, to the E_2 of the second segment.
- The efficiency, in terms of the increasing flexural buckling load of bimetallic cantilever column for material combinations Ti-Al, Invar-Al and Steel-Al at all three different temperature zones, when compared to the same of the uniform cantilever column, for $n = 1$, is demonstrated in this investigation.

The present investigation of the bending and flexural buckling of bimetallic cantilever beam and bimetallic cantilever column revealed some unexpected interesting phenomena, hither to not mentioned explicitly by other researchers. A similar investigation on the bimetallic cantilever beams and bimetallic cantilever column with the other boundary conditions, and the other compound structural members like circular and rectangular plates, will be useful to the structural design engineers, to achieve cost effective designs.

Table:5 Convergence Study of P_b^* for Bimetallic Cantilever Column subjected to free end axial concentrated compressive load P			
Material Combinations	Modular Ratio	No. of Elements N	At Ambient Temperature $T = 20\text{ }^\circ\text{C}$
Uniform	1.0	4	2.4675
		8	2.4674
		16	2.4674
Steel-Al	2.7758	4	5.0491
		8	5.0487
		16	5.0487
Invar-Al	2.1056	4	4.2755
		8	4.2752
		16	4.2752
Ti-Al	1.4922	4	3.3702
		8	3.3701
		16	3.3701
			At Cryogenic Temperature $T = -200\text{ }^\circ\text{C}$
Steel-Al	2.6687	4	4.9381
		8	4.9377
		16	4.9377
Invar-Al	1.7488	4	3.7755
		8	3.7753
		16	3.7753
			At Elevated Temperature $T = 200\text{ }^\circ\text{C}$
Steel-Al	3.0462	4	5.3110
		8	5.3106
		16	5.3106
Ti-Al	1.6092	4	3.5601
		8	3.5599
		16	3.5599

Table:6 Buckling load parameter values of Bimetallic Cantilever Column subjected to free end Concentrated axial compressive load P		
At Ambient Temperature $T = 20\text{ }^\circ\text{C}$		
Material combinations	Galerkin FE Solution	Solution of differential equation (Timoshenko and Gere 1961)
Uniform	2.4674	2.4674
Steel-Al	5.0487	5.0487
Invar-Al	4.2752	4.2752

Ti-Al	3.3701	3.3701
At Cryogenic Temperature T = -200°C		
Steel-Al	4.9377	4.9377
Invar-Al	3.7753	3.7753
At Elevated Temperature T = 200°C		
Steel-Al	5.3106	5.3106
Ti-Al	3.5599	3.5599

Table:7 Values of Efficiency $\left(\frac{P_{bn}}{P_{b1}}\right)$ of Bimetallic Cantilever Column subjected to free end Concentrated axial compressive load P		
At Ambient Temperature T = 20 °C		
Material combinations	(P_{bn})	$\left(\frac{P_{bn}}{P_{b1}}\right)^{**}$
Uniform	2.4674	1.0
Steel-Al	5.0487	2.0461
Invar-Al	4.2752	1.7326
Ti-Al	3.3701	1.3658
At Cryogenic Temperature T = -200°C		
Steel-Al	4.9377	2.0011
Invar-Al	3.7753	1.5301
At Elevated Temperature T = 200°C		
Steel-Al	5.3106	2.1523
Ti-Al	3.5599	1.4427

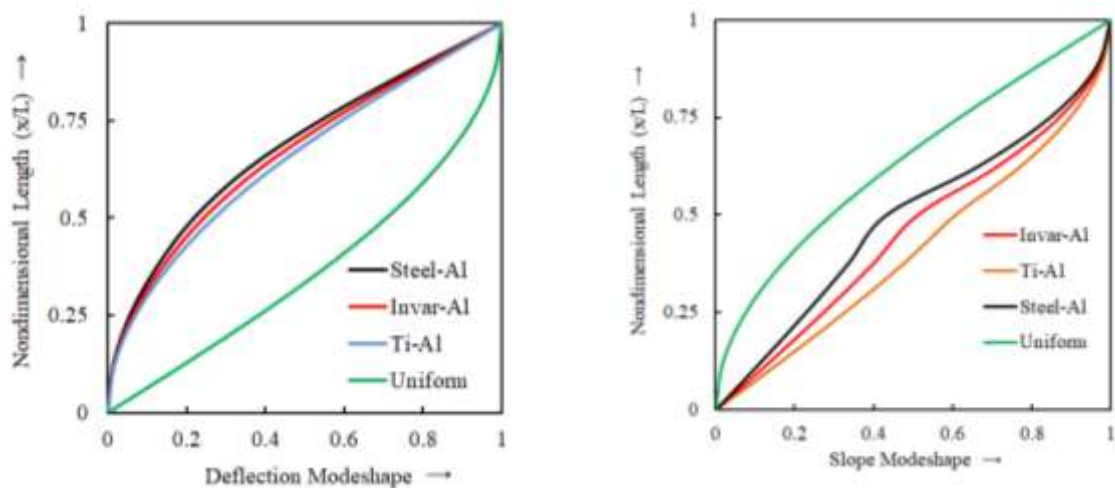


Fig 8: Variation of Deflection Modeshape and Slope Modeshape along the length of a bimetallic cantilever column subjected to free end concentrated compressive load at ambient temperature T= 20°C

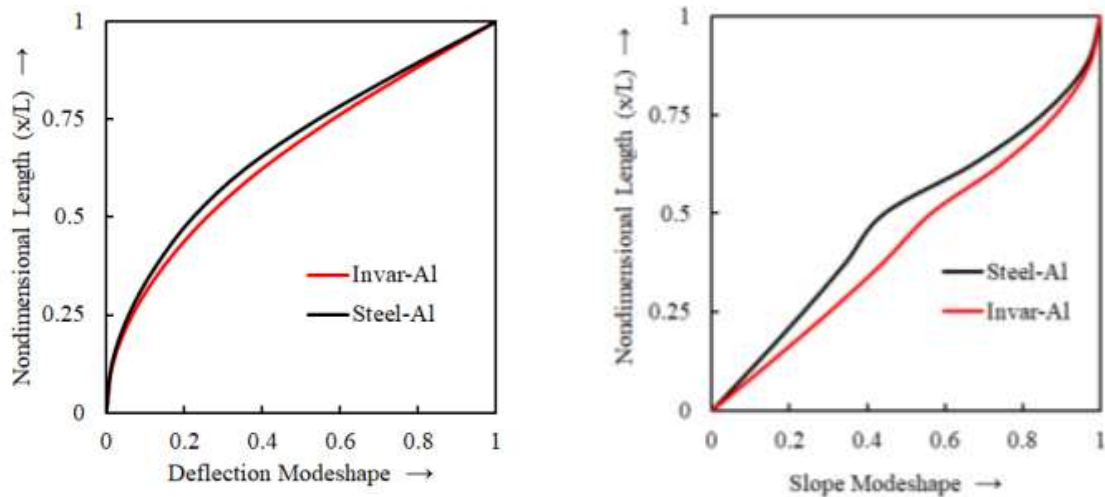


Fig 9: Variation of Deflection Modeshape and Slope Modeshape along the length of a bimetallic cantilever column subjected to free end concentrated compressive load at cryogenic temperature $T = -200^{\circ}\text{C}$

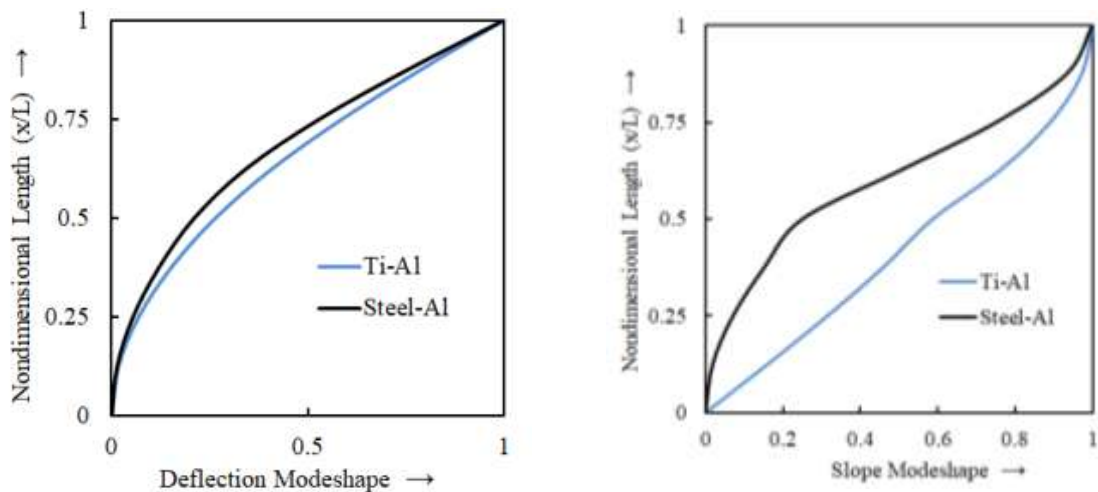


Fig 10: Variation of Deflection Modeshape and Slope Modeshape along the length of a bimetallic cantilever column subjected to free end concentrated compressive load at elevated temperature $T = -200^{\circ}\text{C}$

Acknowledgements

The authors would like to sincerely thank the Managements of their respective Institutions for the constant encouragements during the course of this work.

References

- [1] O. C. Zienkiewicz, "Finite Element Method in Engineering Science", McGraw-Hill, New York, 1971.
- [2] V. B. Venkayya, N. S. Khot and L. Berke, "Application of optimality criterion approaches to automated design of large practical structures", AGARD-CP-123 (1973) 3-1 - 3-19.
- [3] L. Berke and N. S. Khot, "Use of optimality criteria methods for large scale systems", AGARD-LS-70 (1974) 1-1 - 1-29.
- [4] N. S. Khot, V. B. Venkayya and L. Berke, "Optimum structural design with stability constraints", International Journal of Numerical methods in Engineering, 10 (1976) 1097-1114.
- [5] G. Venkateswara Rao and R. Narayanaswami, "Optimum design of cantilever columns in the post buckling region with constraint on axial load - An optimality criterion approach", Computers and Structures, 12 (1980) 843-848.
- [6] C. J. Dawes, "Micro-friction welding of aluminum studs mild steel plates", Metal Construction, 9 (1977) Dept. of Mech. Engg.

Two-day International Conference on Recent Advances in Mechanical and Industrial Engineering – 2023
(ICRAMIE-2023)

196-197.

- [7] M. Aritoshi, K. Okita, T. Enjo, K. Ikeuchi and F. Matsuda, "Friction welding of oxygen free copper to pure aluminum", Quarterly Journal of Japan Welding Society, 9 (1991) 467-474.
- [8] W. Lee, M. Schmuecker, U. A. Mercardo, G. Biallas and S. Jung, "Interfacial reaction in steel-aluminum joints made by friction stir welding", Scripta Materialia, 55 (2006) 355-358.
- [9] J. N. Reddy, "An Introduction to the Finite Element Method", McGraw-Hill, London, 2005.
- [10] S. P. Timoshenko and J.M. Gere, "Theory of Elastic Stability", McGraw-Hill, New York, 1961.
- [11] J. G. F. Francis, "The QR transformation, I", The Computer Journal, 4 (1961) 265-271.
- [12] J. G. F. Francis, "The QR transformation, II", The Computer Journal, 4 (1962) 332-345.
- [13] R. C. Hibbeler, "Structural Analysis", Upper Saddle River, NJ, Pearson, (2012), 316-325.

Buckling Behavior investigations on thin-walled rectangular open and extended closed-drop flange beams

Sarswati R Suryawanshi¹, Sudhir Sastry Y. B^{1*}, CH V K N S N Moorthy²

¹Department of Aerospace Engineering, JAIN (Deemed-to-be University), Kanakapura Road, Bengaluru-562112, Karnataka, India,

²Vasavi College of Engineering, Ibrahimbagh, Hyderabad, Telangana State, India

*Corresponding author: Sudhir Sastry, email: sudhirsastri@gmail.com.

Abstract: The study of thin-walled beams is very much required in the automobile and aerospace industry, in this paper it has been performed the lateral buckling analysis of cold-formed thin-walled beams subjected to pure bending moments by using the finite element analysis and the critical buckling loads are estimated. The estimated critical buckling stresses are compared with the analytical results and are observed to be in close agreement. The effect of the dimensions of the flanges, the thickness of the flanges and the length of the extended open flanges on the critical buckling stresses has been studied for several combinations of the geometry parameters of the beam. Among the three beams, for the given loading conditions, the critical buckling moments for the beam with the extended open flanges are found to be the maximum.

Keywords: Thin-walled Beams, cold-formed channels, FEM

Introduction

Thin-walled beams are preferably used in the aerospace industry and many other structural applications due to their better strength-to-weight ratio and easy manufacturing. They have a higher stiffness-to-weight ratio as compared to their counterpart hot-rolled thick steel products. Generally, cold-formed mild steel members have lower embodied carbon. Cold-formed beams are lighter in weight and they are easier to handle, transport and install. There is a need for more efficient cold-formed structural components for improved performance and minimize material use. Highly efficient cold formed thin walled beams will have increased environmental and economic benefits. Cold-formed structural components are generally fabricated by bending the metal in a press brake machine or a roll-forming process, using metal sheets. Therefore, these channels can be made in various different configurations as compared to hot-rolled steel elements.

The other advantages of using cold-formed structural members when compared with hot-rolled thick members are a higher stiffness-to-weight ratio, off-site manufacturing, and full recyclability. Cold-formed thin-walled beams can be reused without compromising the quality. They have smaller foundations, better durability and faster forming due to its malleability with lesser labour and easier fabrication. Cold-formed thin-walled structural members can be produced in larger volumes with minimal tools and machines. Such structural members are, however, likely to buckle locally in compression, bending or shear.

Literature Review

(Pignataro et al)[1] Performed post-buckling analysis of simply supported channels under uniform compression. The study is mainly focused on buckling modes interactions. Rehfeild [2] has found that a thin-walled composite c-channel has better buckling resistance which can be used over closed channels and Yu [5] has deduced increased strength of the C-section over the z-section using the FE model. Web width is also a determining factor when designing a

thin-walled beam. Ben Young [3] displayed thin-walled channel columns of different cross-sections to give optimum web width. B. W. Schafer, M. ASCE (Schafer and ASCE) [4] demonstrated design methods for local, distortional and Euler buckling modes in thin-walled cold-formed open sections. Schafer [6] developed a reliable Direct Strength Method for beams and columns. The Direct Strength Method by Schafer [6] employs gross cross-section properties. He states that for stability calculations the finite strip method or generalized beam theory, is the best choice [6]. The finite strip method is used by Mahendran [8], Ovesy [9] for the analysis of elastic and post-buckling behaviour of thin-walled beams respectively. Hancock and Rasmussen [7] compare all the test results of a research program which was performed on the interaction buckling behaviour of thin-walled beam columns over several years at the University of Sydney. Slender cross-section square hollow sections (SHS) and thin-walled I-sections experienced local buckling before overall buckling. Rondal [10] reviewed progress in the field of cold-formed steel members. Particularly emphasized progresses in the field of distortional buckling and in the recent development of new types of joints. Cold-formed lipped channel members' distortion buckling formulae were developed by Silvestre and Camotim [11] using GBT. Camotim and Basaglia[12] addressed the use of (GBT) to analyse the local and global buckling behaviour of hollow-flange lipped channel beams. The results are validated by comparing them with the values yielded by shell finite element analyses, performed in the commercial programs ABAQUS or ANSYS which are quite similar. Sastry [13] analyzed the post-buckling behaviour of stiffened composite panels using finite element methods. Al-Mosawi and Saka [14] demonstrated an optimized cross-section of thin-walled steel beams under different loading conditions where it is found that the lipped channel gives better results which are in line with Silvestre and camotim[11]. Magnucki K [15] has given optimal geometrical parameters under safe bending moments for open thin-walled beams with a flat web and circular flanges. Magnucki and Paczos[16] discussed shape optimization of cold-formed thin-walled channel beams with an open or closed profile of drop flanges. It is concluded that thin-walled channel beams with closed drop flanges are distinctly better than beams with open drop flanges or standard cold-formed channel beams Magnucki and Paczos[16] and Magnucka-Blandzi[17]. The numerical investigations clearly show that there is a need to search for new shapes of the cross-sections of cold-formed thin-walled beams in order to make them less prone to global and local buckling. Magnucka-Blandzi and Magnucki [17] reviewed selected problems of buckling behaviour of cold-formed thin-walled channel beams with open or closed flanges. The review includes simple analytical descriptions and calculations, numerical analyses, and laboratory tests of selected beams. Magnucka-Blandzi[18] presented analytical solutions for global and local buckling problems of thin-walled beams with double box flanges. He also concluded that double-box flanges are more buckling resistant than that of standard flanges. Szymczak and Kujawa[19] analyzed the initial post-buckling behaviour of a cold-formed channel member flange after its local buckling which is subjected to pure bending. The paper discusses the comparison of the proposed analytical solution with the finite element method (FEM) and finite strip method (FSM) results for validation. The buckling behaviour of double box flange thin-walled beams under pure bending is given by Magnucka-Blandzi [20]. The Finite strip method is used for numerical investigation and then results were compared with experimental investigation of buckling behaviour. They also stated that cold formed thin-walled beams with double box flanges are more buckling resistant than beams with riveted joints. Jin [21] developed a constrained shell Finite Element Method (cFEM) based on a force

approach for elastic buckling analysis of thin-walled members. The new cFEM can distinguish three fundamental deformation modes in buckling known as Global (G), Distortional (D), and Local (L). The development of a new constrained shell Finite Element Method (cFEM) enables the modal decomposition and identification in elastic buckling analysis of thin-walled members. Nguyen [22] discussed lateral buckling of functionally graded beams.

Thin walled open section beams are analysed with different types of material distributions using finite element methods. It also highlighted the load carrying capacity of thin walled functionally graded open channels. P. Paczos[23] investigated experimentally open channel beams with unconventional flanges under effect of pure bending. Sastry et al [24] performed buckling analysis of thin walled beams with different geometric parameters and various flange shapes subjected to pure bending where he concluded that rounded flange beams are buckling proof as compared to others. Jasion [25] investigated buckling behaviour of thin walled beams with different flange shapes using FEM. Modified flange may increase buckling and limit load of beams notably.

FE Analysis

Geometry

Beam mainly experiences bending moments and a little bit of twisting. The forces experienced by the beam are predominantly normal stress and very small shear stress. The stress distribution is non-uniform throughout the cross-section. Stress has the maximum value at the top and bottom of the beam and zero at the centroid. The conventional shape of the cross-section contains two flanges and a web connecting the flanges. As the flange is the most loaded part of the beam and also to increase the stiffness conventional cold-formed thin-walled open channels are amended with unconventional flange shapes. One such cross section with an unconventional flange is shown in Fig 1.

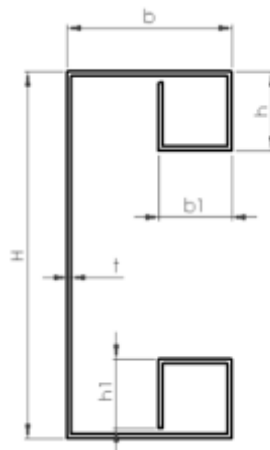


Fig.1

The geometry of the beam is made by drawing the cross section of the beam and extruding it to a length of 1000 mm. Different thickness of the beam are considered such as $t = 0.6, 1.1$ and 2 mm. Two different beams are considered one is an open channel and the other one is open channel with drop flange as shown in Fig 2. As the name suggests it is a thin walled beam, the beam is modelled using 3D shell elements for the thickness. Each thickness is analysed for different values of b_1, h and h_1 where b_1, h and h_1 are dimensions of the drop flange as shown in Fig 1.

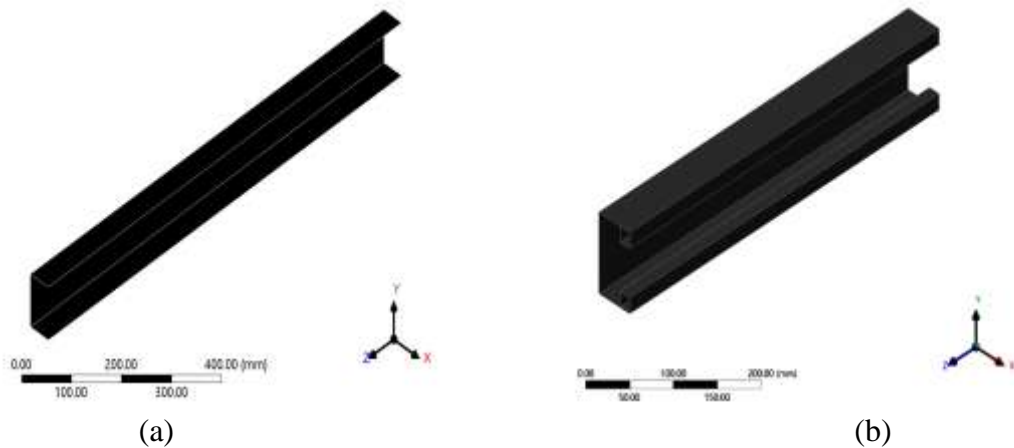


Fig. 2 (a) Open channel beam (b) Open channel beam with drop flange

Modelling

The element size is decided by convergence analysis. The beam is analysed using different element sizes. The number of elements changed from 12750 elements to 5511 elements. The results were approximately the same so the highest possible element size is considered for computation to reduce the computation time.

The modelled open channel and open channel with drop flange is illustrated in fig 3.

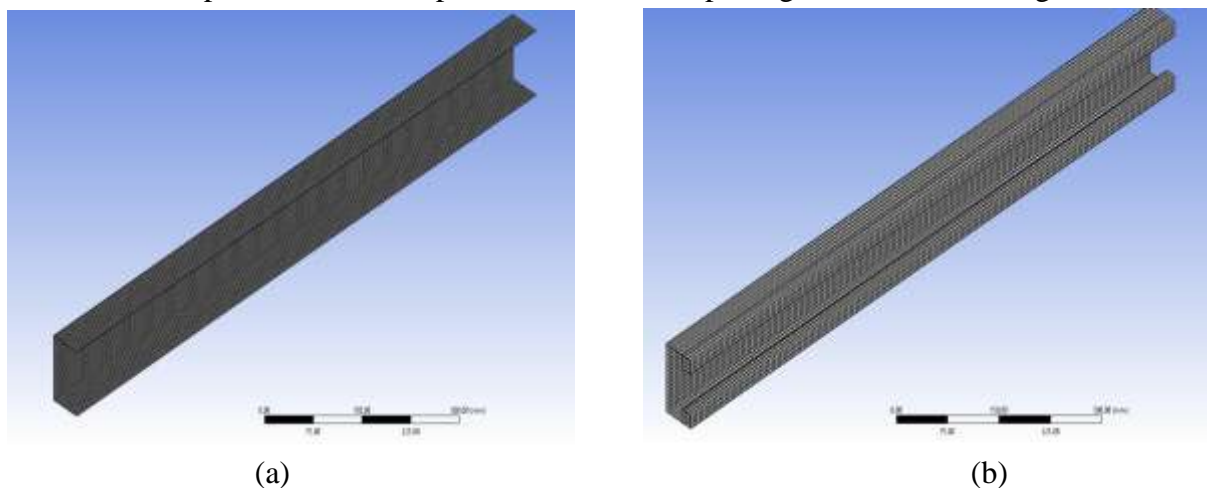


Fig 3 (a) Open channel mesh (b) Open channel with drop flange mesh

For FE analysis aluminium 6061 is considered. The material parameters are $\rho = 2710 \text{ kg/m}^3$, Young's modulus = 68000MPa, Poisson's ratio = 0.33.

Boundary conditions

Two types of analysis were conducted one static structural analysis and another is modal analysis.

For the modal analysis the beam is simply supported and analysed for 10 mode shapes.

For static structural analysis the beam is simply supported at the ends and the transverse force is applied on the upper surface.

The mathematical equations

The moment of inertia for the beam = I_w

The beam is divided into 5 sections.

$$I_w = I_{w1} + 2(I_{w2} + I_{w3} + I_{w4} + I_{w5}) \quad (1)$$

$$I_{w2} = I_{w2x} + A_{w2}y_2^2$$

$$I_{w3} = I_{w3x} + A_{w3}y_3^2$$

$$I_{w4} = I_{w4x} + A_{w4}y_4$$

$$I_{w5} = I_{w5x} + A_{w5}y_5$$

A_{w2}, A_{w3}, A_{w4} and A_{w5} are the area of section 2, section 3, section 4 and section 5 respectively.

y_2 = Distance of centroidal axis of section 2 from the centroid axis of the beam.

y_3 = Distance of centroidal axis of section 3 from the centroid axis of the beam.

y_4 = Distance of centroidal axis of section 4 from the centroid axis of the beam.

y_5 = Distance of centroidal axis of section 5 from the centroid axis of the beam.

R_A and R_B are the reaction forces on the beam. And w is applied load. L is the length of the beam. M is a moment acting at a point. Where A and B are the end points of the beam.

M at distance x from point A .

$$M = -R_A * x + w(x - L/2)$$

$$M = -w/2 * x + w(x - L/2)$$

$$EI_w d^2y/dx^2 = M$$

$$EI_w d^2y/dx^2 = -w/2 * x + w(x - L/2)$$

$$EI_w dy/dx = -w * x^2/4 + w(x - L/2)^2/2 + C_1$$

$$EI_w y = -w * x^3/12 + w(x - L/2)^3/6 + C_1x + C_2$$

$$EI_w y = -w * x^3/12 + w(x - L/2)^3/6 + 3wL^2/48 * x + C_2$$

$$y_{max} = (-w * L^3/96 + w(L/2 - L/2)^3/6 + 3wL^3/96) / (I_{w1} + 2(I_{w2} + I_{w3} + I_{w4} + I_{w5}))$$

I_w value can be calculated using the formula in equation (1), E is young's modulus (taken aluminium 6061 for the analysis which has $E=68$ GPa.)

RESULTS AND DISCUSSION

First of all, open channels with different thicknesses are analysed. Total deformation, Von mises stress and equivalent strain and mode shape of the open channel can be seen in fig.

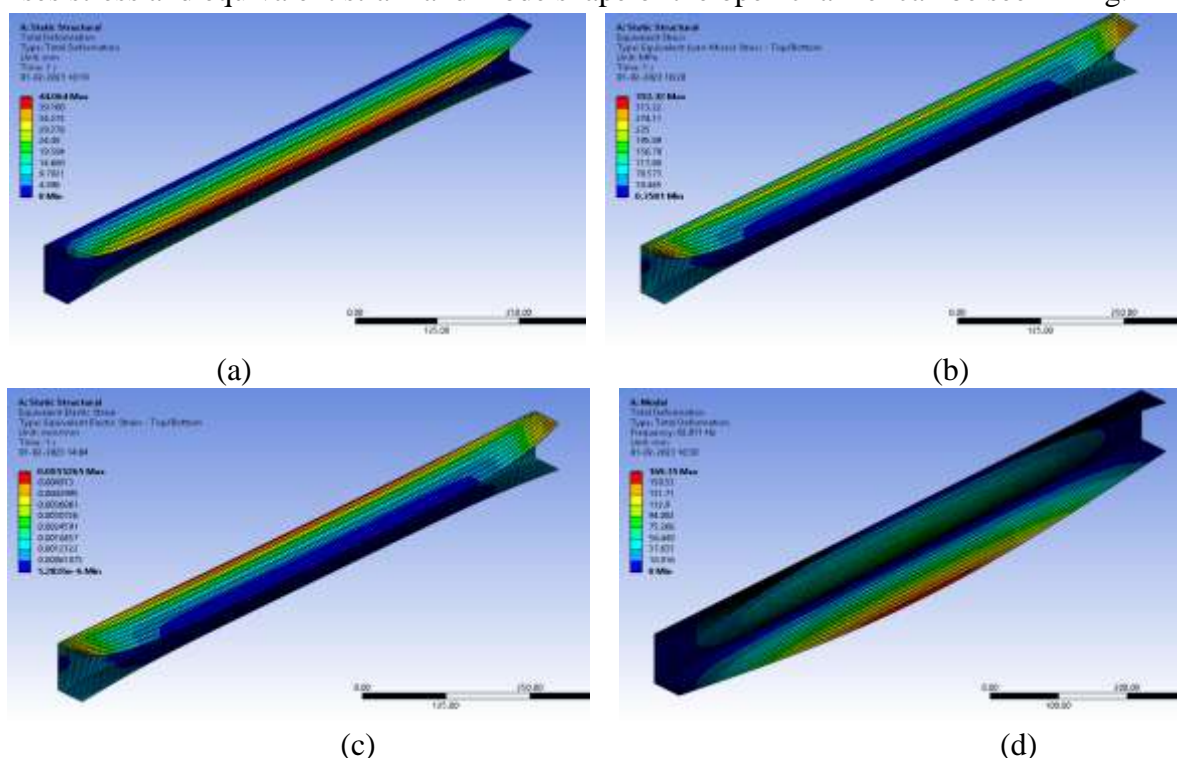


Fig 4. Open channel (a) Total deformation (b) Von mises stress (c) Equivalent strain (d) Mode shape

The total deformation, Von mises stress and equivalent strain for open channel with drop flange is as shown in fig.

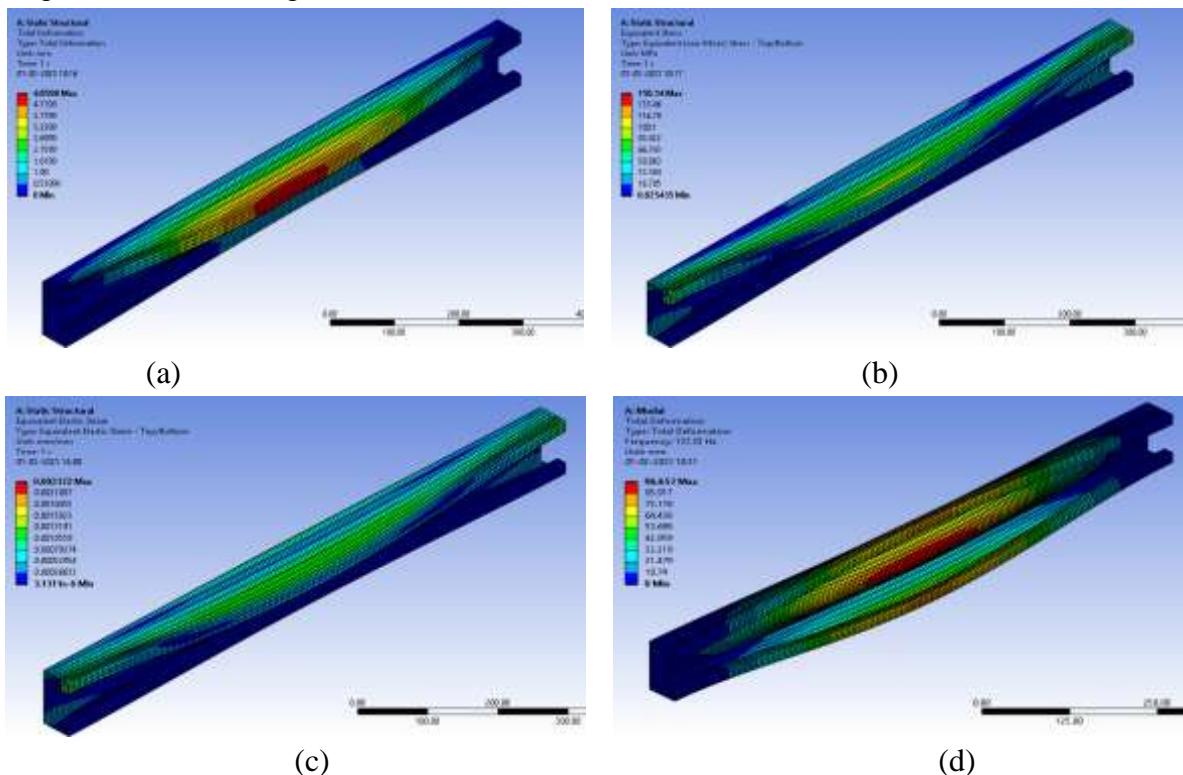


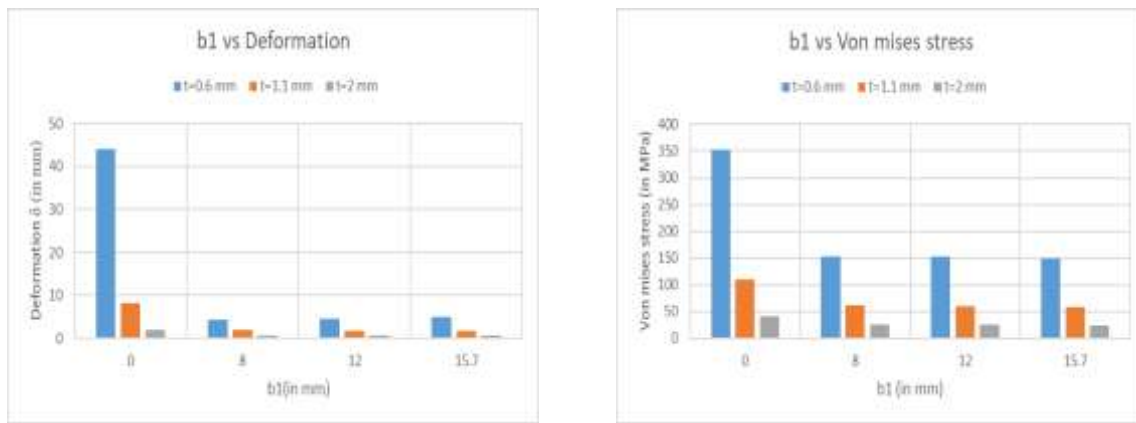
Fig 5. Open channel with drop flange (a) Total deformation (b) Von mises stress (c) Equivalent strain (d) Mode shape

Structural analysis

To understand the behaviour of the channel under load, different channels with unconventional flanges are analysed. Also the influence of thickness on the behaviour of the channel is examined using different thickness such as $t=0.6\text{mm}$, 1.1mm , 2mm . First open channel beam is compared with drop flange open channel beam to understand the effects of modification in the cross section of the beam. The comparison shows that stiffness of the beam increases with the application of drop flange. Then beams with drop flange having different values of b_1 (width of drop flange) are analysed to illustrate its effect on the stiffness of the channel. The graphs are plotted for b_1 vs deformation, b_1 vs Von mises stress, b_1 vs normal stress, b_1 vs shear stress, b_1 vs equivalent strain and b_1 vs deformation in Y direction. In the graph $b_1=0$ indicate open channel beam, and $b_1=8$ indicate open channel with a drop flange of width 8mm and so on and so forth.

The different colours of bars indicate different thickness of the beams.

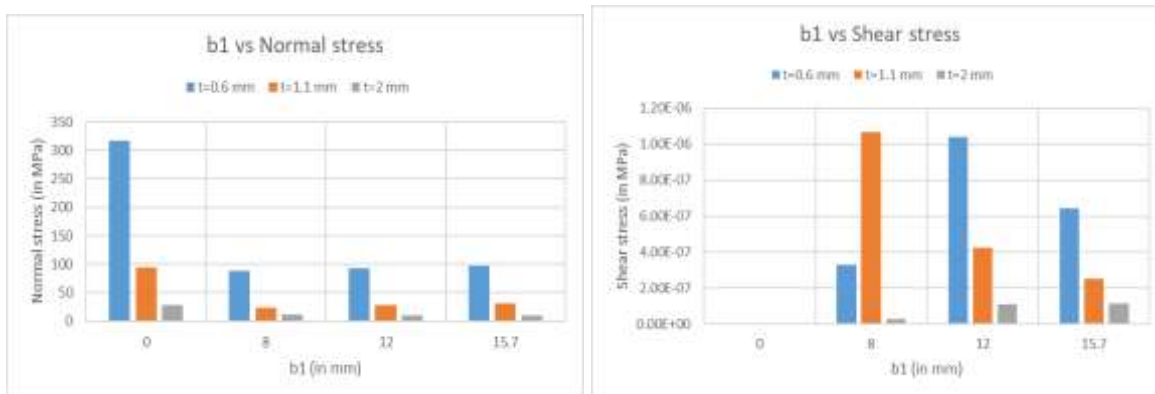
It can be seen from the above Fig 6(a) that deformation is drastically decreased when drop flange is added which means the stiffness of the beam increases with modification in the cross section of the beam. The reason behind it is that the moment of inertia is increased. More the moment of inertia, more the stiffness. Fig 6 (b) indicates the b_1 vs Von mises stress graph where it can be seen that the von mises stresses are decreasing with the application of drop flange in the open channel beam. So the load resisting capacity of the beam is increasing.



(a)

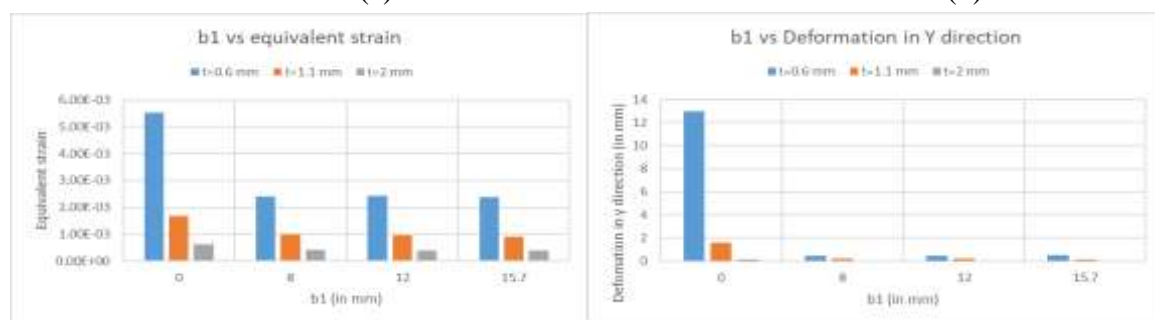
(b)

Under the transverse loading condition, the beam undergoes bending which induces normal and shear stresses. The normal stresses are more and shear stresses induced are very less which is nearly negligible. Fig 6 (c) and Fig 6(d) shows Normal stress and shear stress in the given beams with changing b1. It can be deduced that very small twisting occurs in the beam due to transverse loading.



(c)

(d)



(e)

(f)

Fig. 6 (a) b1 vs Deformation (b) b1 vs Von mises stress (c) b1 vs Normal stress (d) b1 vs Shear stress (e) b1 vs Equivalent strain (f) b1 vs Deformation in y direction.

Modal analysis

Modal analysis is carried out to find the natural frequencies and mode shapes of the beam in free vibration. Another reason to carry out the modal analysis is to find the effect of modification of cross section on the natural frequencies of the beam. The stiffness of the beam is proportional to the natural frequency of the beam so stiffness behaviour of the beam can be deduced using modal analysis.

Modal analysis of the open channel beam and open channel with drop flange is carried out with different b1 values. From Fig 7(a) it can be noticed that after the amendment of drop Dept. of Mech. Engg.

flange, the natural frequency of the beam is increased and so is the stiffness of the beam.

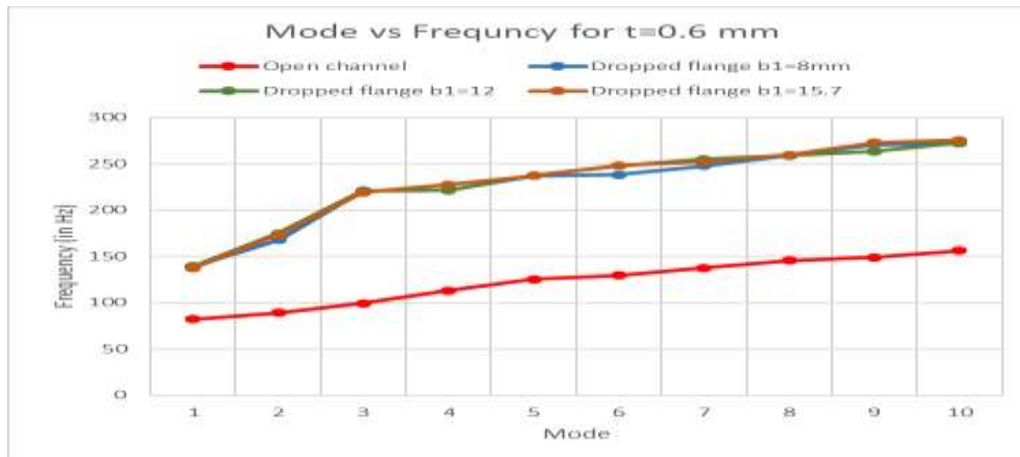


Fig 7(a) t=0.6

The analysis is carried out for different thickness values. From the Fig 7 (b) it can also be deduced that if drop flange is incorporated, natural frequencies of beam in different modes are increasing but the width of the flange is not a deciding factor. There is no uniform change in natural frequency with change in the width of drop flange i.e. b1.

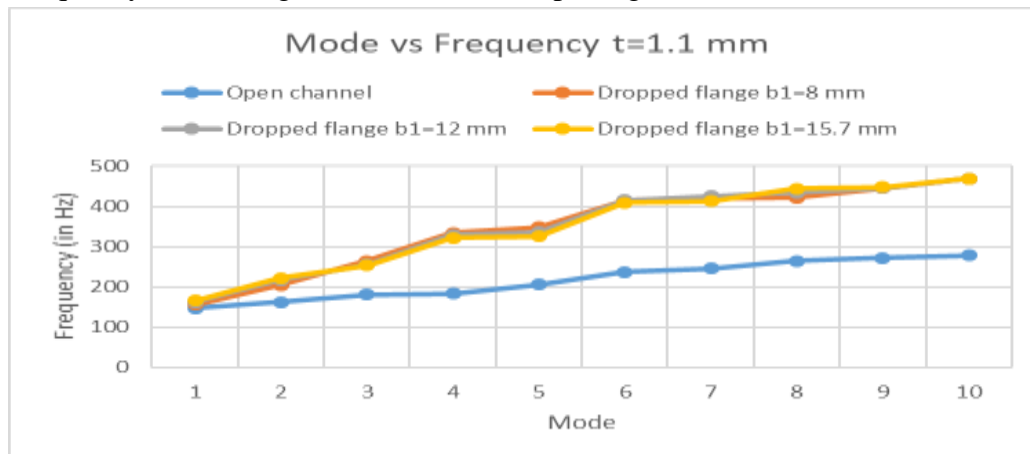


Fig 7 (b) t=1.1mm

The scale of Fig 7 (c) is different from the scale of Fig 7 (a) and Fig 7(b) which also indicate that the natural frequency of the beam with higher thickness is more. So the natural frequency increases with increase in thickness of the beam. With the thickness, stiffness of the beam increases which in turn results in an increase in the natural frequency of the beam.

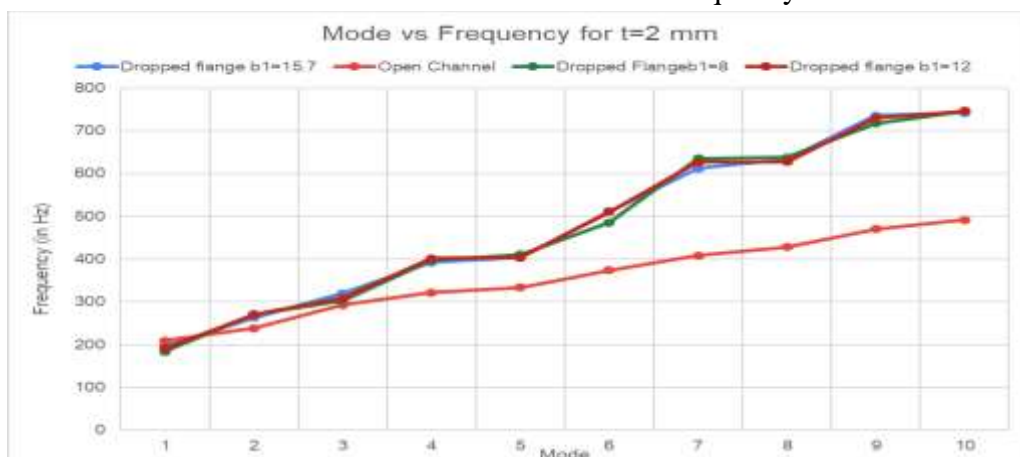


Fig 7(c) t=2mm

CONCLUSION

From the analysis of open channel beam and drop flange open channel beam. it is concluded that the modification in the cross section of the beam changes the behaviour of the beam. The stiffness of the drop flange open channel is more as compared to open channel beam. These beams have more buckling resistance when compared to standard channels. The modal analysis also shows that, the natural frequency of the beams are increased when amended with drop flange which also indicate that the stiffness is more decidedly more. Thickness is another contributing factor for the stiffness. If thickness is increased, stiffness increases but there are manufacturing limitations to increase the thickness so the modification of flange is a more feasible option. The values of b_1 also change the behavior of the beam. If b_1 is increased, the area moment of inertia of the drop flange increases, so does the stiffness but again the b_1 can be increased upto some limit. it should not increase the overall mass of the beam. Stiffness should increase without any increase in overall mass and also the manufacturing process should be easy enough hence the proposed design is best of all analysed designs.

REFERENCES

- [1] Pignataro, Marcello, et al. *On the Effect of the Local Overall Interaction on the Post buckling of Uniformly Compressed Channels*. Thin-Walled Structures 3, 1986.
- [2] Rehfield, Lawrence w., and Ulrich Mueller. *Design of thin-walled laminated composite beams to resist buckling*. American Institute of Aeronautics & Astronautics, 1999.
- [3] Young, Ben. *Bifurcation analysis of thin-walled plain channel compression members*. Finite Elements in Analysis and Design, 2004.
- [4] Schafer, B. W., and M. ASCE. *Local, Distortional, and Euler Buckling of Thin-Walled Columns*. JOURNAL OF STRUCTURAL ENGINEERING, 2002.
- [5] Yu, Cheng, and Benjamin W. Schafer. *Simulation of cold-formed steel beams in local and distortional buckling with applications to the direct strength method*. Journal of Constructional Steel Research, 2007.
- [6] Schafer, B. W. *Review: The Direct Strength Method of cold-formed steel member design*. Journal of Constructional Steel Research, 2008.
- [7] Hancock, G. J., and K. J. R Rasmussen. *Recent research on thin-walled beam-columns*. vol. 33, Thin-Walled Structures, 1998.
- [8] Mahendran, M., and N. W. Murray*. *Elastic Buckling Analysis of Ideal Thin-Walled Structures Under Combined Loading Using a Finite Strip Method*. Thin-Walled Structures, 1986.
- [9] Ovesy, H. R., et al. *Geometric non-linear analysis of channel sections under end shortening, using different versions of the finite strip method*. Computers and Structures, 2006.
- [10] Rondal, J. *Cold formed steel members and structures General Report*. Journal of Constructional Steel Research 55, 2000.
- [11] Silvestre, Nuno, and Dinar Camotim. *GBT-Based Distortional Buckling Formulae for Thin-Walled Channel Columns and Beams*. Sixteenth International Specialty Conference on Cold-Formed Steel Structures Orlando, Florida USA, 2002.
- [12] Camotim, Dinar, and Cilmar Basaglia. *Buckling analysis of thin-walled steel structures using generalized beam theory (GBT): state-of-the-art report*. Ernst & Sohn Verlag für Architektur und technische Wissenschaften GmbH & Co. KG, Berlin · Steel Construction, 2013.
- [13] Sastry, Sudhir, et al. *Buckling analysis of thin wall stiffened composite panels*.
- [14] Al-Mosawi, S., and M. P. Saka. *Optimum shape design of cold-formed thin-walled steel sections*. vol. 31, Advances in Engineering Software, 2000.
- [15] Magnucki, K. *Optimization of open cross section of the thin walled beam with flat web and circular flange*. vol. 40, Thin walled structures, 2002.
- [16] Magnucki, K., and P. Paczos. *Theoretical shape optimization of cold-formed thin-walled channel beams with drop flanges in pure bending*. vol. 65, Journal of Constructional Steel Research, 2009.
- [17] Magnucka-Blandzi, E., and K. Magnucki. *Buckling and optimal design of cold-formed thin-walled beams: Review of selected problems*. Thin-Walled Structures, 2011.
- [18] Magnucka-Blandzi, E. *Effective shaping of cold-formed thin-walled channel beams with double-box flanges in pure bending*. vol. 49, Thin walled structures, 2011.
- [19] Szymczak, Czesław, and Marcin Kujawa. *Buckling and initial post-local buckling behaviour of cold-formed channel member flange*. vol. 137, Thin-Walled Structures, 2019.
- [20] Magnucka-Blandzi, E., et al. *Buckling Study of Thin-walled Channel Beams with Double-box Flanges in Pure Bending*. An International Journal for Experimental Mechanics, 2011.

Two-day International Conference on Recent Advances in Mechanical and Industrial Engineering – 2023
(ICRAMIE-2023)

- [21] Jin, Sheng, et al. *Constrained shell finite element method for elastic buckling analysis of thin walled members*. Thin walled structure 145, 2019.
- [22] Nguyen, Tan-Tien, et al. *Lateral buckling analysis of thin-walled functionally graded open-section beams*. vol. volume 160, Composite structure, 2017.
- [23] P. Paczos, P. *Experimental investigation of C-beams with non-standard flanges*. vol. 93, Journal of construction steel research, 2014.
- [24] Sastry, Sudhir, et al. *Parametric studies on buckling of thin walled channel beams*. Computational Material Science, 2014.
- Jasion, Paweł, et al. *Buckling and post-buckling behaviour of selected cold-formed C-beams with atypical flanges*. vol. 244, Engineering structures, 2021.

MODELING AND STRESS ANALYSIS OF AEROSPACE BRACKET USING ABAQUS

Praveen Chapala^{1,*}, Shivanand Jha¹, V.J. Harry Asher¹, CH.B.V.S.S. Ram Raj¹, Ajay Sirra¹

¹NATIONAL INSTITUTE OF TECHNOLOGY ANDHRA PRADESH Near National Highway No.16, Kadakatla, Tadepalligudem – 534101 West Godavari District, Andhra Pradesh, India.

*Corresponding author email id: praveenchapala@gmail.com

Abstract: In Aerospace applications, every aspect of aircrafts is fixed by using tens of thousands of brackets to assemble the parts. Design of brackets in aerospace engines is a crucial part which needs to have inspection of numerous shapes and sizes. Main applications of these brackets are mounting bleed air ducting, starter air duct fuel lines and hydraulic lines engine core. These brackets are continuously subjected to constant and cyclic loading, which generates high amount of stress. So, the inspection is done manually which is time-taking and error-prone. To improve examination capability, many researchers have attempted to develop inspection techniques using certain software's. Abaqus is one of the software's, used for finite element analysis and computer aided engineering in the automotive, aerospace and industrial products. This software is used in research institutions in engineering because of the wide material modelling capability, and the editing capability. In Abaqus the users can construe their own materials as a result new materials could also be simulated. Abaqus also facilitates compilation of multiphysics capabilities like coupled acoustic-structural and structural-pore capabilities. So, it is convenient for production-level simulations.

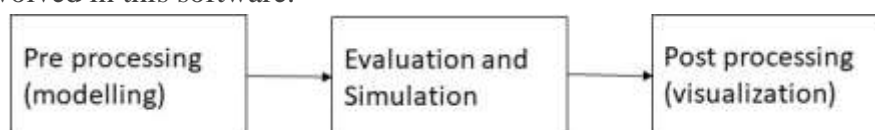
In this paper, a 3D prototype of the bracket used in aircraft engine component is created and the von-mises stress analysis is done. As this bracket under goes continuous load more stress is developed in it which may lead to failure of the material. Hence, the deformation and failure is examined using this ABAQUS software (early monitoring is possible). A 3D vision monitoring is also done by using Finite Element Analysis. The result is assuring for large-scale industrial application.

Key words: Abaqus, Aerospace bracket, Von mises stress, Deformation, stress concentration

1. Introduction:

Abaqus is a opted for software application [1-2] used for modelling [3] and analysis of mechanical components [4-5]. And one of the best suited software for finite elemental results [1-5]. The Abaqus uses programming languages like Java, Python for scripting and modifying. It is ideally suited for static, low speed dynamic and steady state transport applications. It enables analysis of a model in both time and frequency domain in one single simulation. It also delivers highly accurate stress analysis. Abaqus uses the neutral database files.

Sequence involved in this software:



The Abaqus follows the primary three steps in the designing and analysis of a model. The pre-processing or modelling includes creation of a input file for a finite-element analysis. The evaluation and simulation process includes applying the desired requirements like mechanical, thermal and electrical analysis. The post processing is a creation of output file from the

simulation [6].

Aerospace brackets, are the structural components that are used for attaching and supporting assemblies [7]. These brackets are found in large tens of thousands in aircrafts. These brackets are used for applications like fuselage airframe assembly, fuel tanks, landing gears, engine mounts, wings assembly, and electric wire installation brackets are meant for carrying loads, supports structures, bearing that supports the shafts. Most commonly L, T and Z shaped brackets are used. Mounting Brackets are used in various fields such as Aerospace Industries, applications etc [8].

In the present work we deal with the brackets used in the aerospace industries which are used to carry loads of pipelines, sliding rods, batteries, electronics goods etc. As minimum weight, sufficient strength, easy to manufacture to integrate the system are the critical factors in aerospace industries [9], we have considered working with Titanium Ti-6Al-4V (Grade 5), annealed. The titanium alloy consists of α and β phase. The α -phase is stable at low temperature and β at high temperature. Al stabilizes the α -phase and V stabilizes the β -phase. Al also reduces density and vanadium provides ductile β phase used for hot working. The detailed weight composition of the alloy is Aluminium of 6%, Vanadium of 4%, Iron of maximum (0.25%), Oxygen of up to (0.2%) and Titanium of major contribution of 90% [10-13].

Ti6Al4v provides high strength and toughness than steel and aluminium alloys and also has approximately same stiffness than pure titanium but have high strength.

	SS 316 L (annealed)	Ti6Al4V, wrought (annealed/aged)	Aluminium 6061 (tempered)
Density [kg/m ³]	8000	4420	2700
Young's modulus [GPa]	193	115	69
Tensile strength [MPa]	570	1030/1170	310

2. Deformation of aerospace bracket:

2.1 Working with the model:

On the basis of our objective of creating a model, applying the load, and analysing the model, three-dimensional finite element model of aerospace bracket is developed using Abaqus software. This bracket is used for holding sliding rods in aerospace frames and engine pipelines. The modelling steps are addressed as follows:

Firstly, an element type is defined as a solid extrude, in which a 2D shape is created and later protrude into 3D shape. Two hollow cylindrical pipes have been created for holding pipelines as shown in Fig. 1. The small hollow cylindrical pipe is placed at 56mm height from the surface with a diameter of 40mm and with an internal diameter of 18mm and the length of the cylindrical pipe is 30mm. The other hollow cylindrical pipe is placed at 118mm height from the bottom with a diameter of 55mm and with an internal diameter of 30mm and the length of this pipe is 36mm. The two pipes are connected to each other by a curvature with a radius of 25mm. One end of the cylinders is connected to the base and the arrangement of the two cylinders along their length are shown in the top view. In the top view, a rectangle of 140mmx85mm is observed which consists of two cylindrical holes for fixing the bracket. The two cylindrical holes have the diameter of 16mm and they are placed at a distance of 35mm and 105mm from the left respectively, and from the bottom both are placed at a height of 30mm as shown in Fig. 2. The width of the front view plate is 12mm and the width of the rectangular plate and its design used is shown in Fig. 3. From the side view, the clear arrangement of the hollow cylinders is observed and the height of the rectangular base is

18mm and it has a length of 85mm from which a 3mmx49mm part is removed.

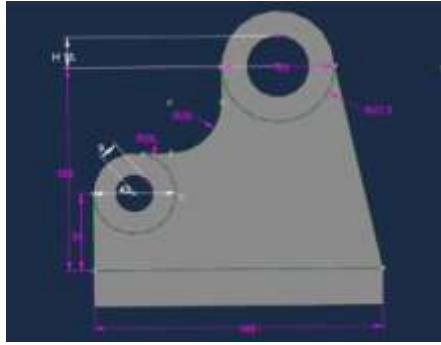


Fig .1. Front view

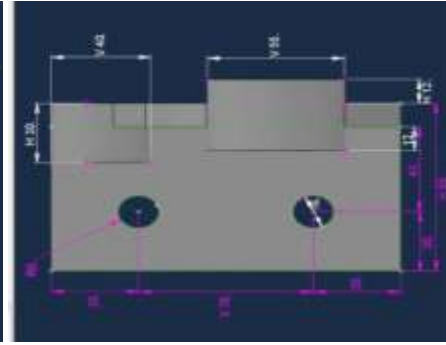


Fig.2. Top view

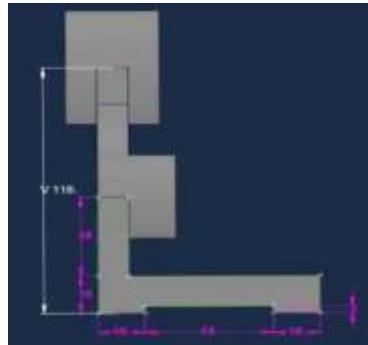


Fig.3. Side View

After the modelling of the bracket, the properties of Ti64 alloy is assigned to this model. The properties of this alloy are chosen based on ASM standards i.e., density (4.43g/cc), Young's modulus (113.8GPa) and Poisson's ratio (0.342). A section is created in the Abaqus software specifying the material with these properties and assigned to the model.

In order to assign coordinates for the model for positioning an 'instance' is created in the assembly module. A loading and output request step is created for the model. In the 'load' module, a boundary condition is considered for this bracket. The 16mm hollow cylinders are encastred. The other hollow cylinders of the bracket are holding sliding rods and pipelines a continuous and cyclic loads are acting on it. A pressure of 116GPa is applied on the surface of this hollow cylinders in two loading conditions as shown in the Fig.4.

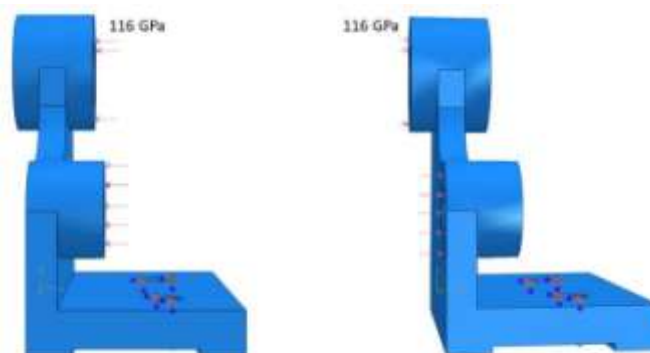


Fig.4. Boundary Conditions and Loading Conditions

Meshing is done to the model; it contains nodes and elements. Meshing involves defining nodes and connecting them to form elements. Seeds of size 30mm with curvature of 0.5mm (number of elements per circle:2) is considered and these nodes are connected to form tetrahedral shaped elements [4] as shown in Fig.5. For this finite element model a 'job' is created for visualizing and analysing the final result in graphics and graphical formats [11].

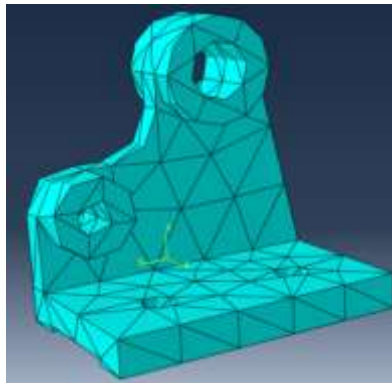


Fig.5. Mesh applied to the model

3. Results and discussion:

The different colours in the plot shows the affected area due to the application of load, the intensity of the stress field is observed in the bracket. Red coloured region shows the more stress concentration and as the stress concentration decreases the colour changes from yellow to green and green to blue. Even the blue coloured regions also show some deformation. The plate of the bracket used for boundary condition acts as more stress concentrated region because the movement of this plate is restricted in all the directions resulting in the degree of freedom as zero with respect to the force applied on this bracket. While the other part of the bracket that is experiencing the force results in rotatory motion around the edge that connects the two parts of the bracket. As it is able to rotate in one dimension it is having a degree of freedom as one. The plate of bracket used for holding pipelines is not symmetrical and because of this asymmetry the stress distribution in the bracket is varied. Since the bracket holds the sliding rods and avionics it experiences both the forward and backward application of loads by considering as two separate conditions i.e., the bracket experiencing the load in the front side towards it at the holding region of pipes as shown in Fig.6, and the other condition is the bracket experiencing the load in the back side towards the bracket at the holding region of the pipes as shown in the Fig.7, material deformation can be analysed. Analysing the results helps us to monitor and decide the ability of the material to withstand the load.

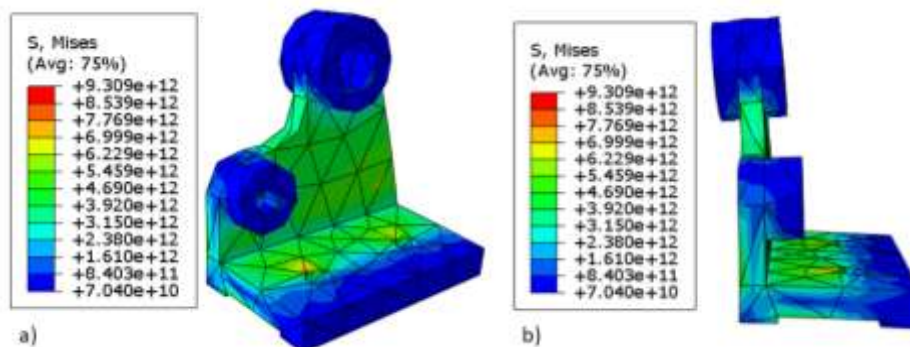


Fig. 6. Load applied on the front side, a) front view, b) side view

When the load is applied it acts as a torque resulting in the material to bend and the dislocation movement from the load applied region to the constrained region results in bending of the material. The deformation of the material starts with the movement of dislocations. At the boundary condition region, where it is constrained with riveting, high stress concentration is present which is surrounded by high strain energy. The bent region in the L shaped bracket also acts as a constrain with some stress concentration. During deformation, when the dislocations move towards these regions, the dislocations are locked

(immobile) because of strain field interactions between the dislocations and constrained region. This results in pile up of dislocations and the dislocation density in the bracket also increases. This is observed clearly by the colour variation in Fig. 6 and Fig.7.

In Fig.6, the load applied lead the bracket to open in obtuse angle. As the distance from loading region (cylindrical hole with small diameter) to the constrained region is less, high stress is accumulated at constrained region (riveted region) because of pile up of dislocations which is observed in red colour. The distance from the cylindrical hole (large diameter) i.e., from the load applied region to the constraint region is high. As the bracket is L shaped, the bent region will also act as obstacle for the movement of dislocations. At this region also pile up of dislocations takes place but the dislocation density is less compared to the constrained region. Hence the stress concentration region is observed in yellow colour. The decrease in stress concentration or the distribution of stress is observed in the other regions of bracket and it is indicated in green and blue colour.

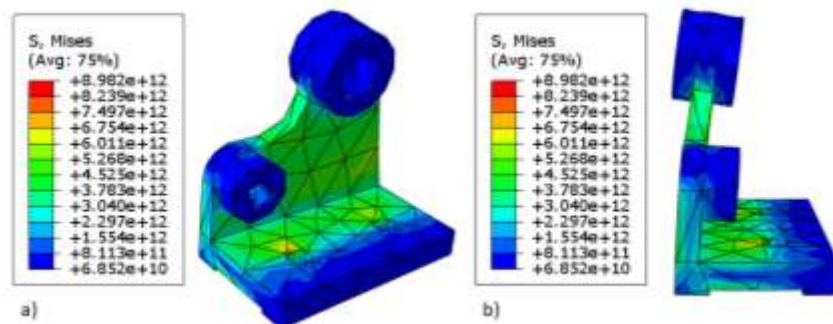


Fig. 7. Load applied on the back side, a) Front view, b) side view

In Fig.7, the load applied is on back of the bracket which tends the bracket to close into the acute angle. Here the force is acting as torque resulting in internal anti parallel torque generation, in order to maintain stability. The stress concentration observed and the dislocation interaction with the constrained region (riveted) is similar with respect to Fig. 6 which is shown in red colour. But the bracket is observed to be closing towards the base plate which generate compressive forces leading to pile up of dislocation at that region and stress concentration is observed in yellow colour. The decrease in stress concentration or the distribution of stress is observed in the other regions of bracket and it is indicated in green and blue colour.

The addition of Aluminium plays an important role in increasing the strength of the alloy by stabilizing and strengthening the α phase and also forms strong precipitates with titanium which act as obstacles for the movement of dislocations. High plastic deformation region is maintained by the addition of Vanadium which results in delay of crack propagation before failure. The two conditions stating that the pile up of dislocations is the cause of the stress concentration, if the load is further increased the dislocations having higher energy move easily towards the defect region and until the UTS point the material with stands the load. If the load exceeds the critical load, crack initiates at the high stress concentration region leading to failure of the bracket.

4. Conclusion:

- Ti64 alloy is used for modelling and analysis of aerospace bracket using ABAQUS software.

- Tensile stresses are developed in the bracket when load is applied on the front side and compressive forces are generated at the bent region on the application of load on back side of the bracket.
- High stress accumulation is observed at the riveted region in both loading conditions. From the simulation data, high amount of stress accumulation is observed in the bracket when load is applied on the front side.

References:

- [1] Fan Jiang Peng, Li Bolin, Zhang Yan, Finite Element Analysis of Crankshaft using Abaqus, 978-0-7695-4455-7/11 \$26.00 © 2011 IEEE DOI 10.1109/ICDMA.2011.137.
- [2] Shilpi Ghosh, Ankesh Yadav, Snigdha Sharma, Dr. Shabana Urooj, Vikas Singh Bhadoria, Computational Analysis of Composite Layered Structure Using ABAQUS Software for Engineering Applications, 2016 1st International Conference on Innovation and Challenges in Cyber Security (ICICCS 2016), 978-1-4799-8433-6/15/\$31.00©2015IEEE.
- [3]V. Kvočák , M. Tomko and V. Kožlejová, Modelling of Encased Steel Beamsin Abaqus Program,INES 2013 IEEE 17th International Conference on Intelligent Engineering Systems June 19-21, 2013, Costa Rica978-1-4799-0830-1/13/\$31.00 ©2013 IEEE.
- [4]T. Tejaswini , Dr.M.V.Rama Raju, Analysis of RCC Beams using ABAQUS,International Journal of Innovations in Engineering and Technology (IJET),Volume 5 Issue 3 June 2015,ISSN: 2319 – 1058.
- [5] Zhou Kaihong, Li Yunpeng, Wang Congyi,Li Cheng, Non-circular gear modal analysis based on ABAQUS, 2015 8th International Conference on Intelligent Computation Technology and Automation, 978-1-4673-7644-0/15 \$31.00 © 2015 IEEE, DOI 10.1109/ICICTA.2015.147.
- [6]Weisberg David. "22"The engineering design revolution.
- [7] Kalyan Kumar, P.S. Srinivas and Srinivasa Rao, Modeling and Stress Analysis of Aerospace Bracket Using ANSYS And FRANC3D, International Journal of Engineering Research & Technology (IJERT) Vol. 1 Issue 8, October - 2012 ISSN: 2278-0181.
- [8] Honnorat, Yves. "Issues and breakthrough in manufacture of turbo engine titanium parts." *Materials Science and Engineering*, A213, 1996: 115-123.
- [9]AdikiSivaiahInfotech Enterprises Limited, Bangalore – India, Innovative Bracket Design Concepts for the Installation of Aircraft Systems *J. Aerospace. Technol. Manager.*, São José dos Campos, Vol.4, No 3, pp. 289-295, Jul.-Sep., 2012 doi.10.5028jatm.2012.04030912.
- [10] *Materials Properties Handbook: Titanium Alloys*, R. Boyer, G. Welsch, and E. W. Collings, eds. ASM International, Materials Park, OH, 1994.
- [11] Abaqus/CAE User's Manual version 6.14.
- [12]Xiaoixn Ye, Zion T.H. Tse and Guoyi Tang, mechanical properties and tensile fracture of Ti-6Al-4V alloy strip under electro pulsing-induced phase change. 15 December 2014.
- [13]Lewis, A.C., Qidwai, S.M., Rowenhorst, D.J., and Geltmacher, A.B.: Correlation between crystallographic orientation and mechanical response in a three-dimensional beta-Ti microstructure. *J. Mater. Res.* 26, 957.

Design of Iot Based System for Ensuring Reliable Functioning of Solar Powered Unmanned Aircrafts

I Manoj kumar¹, V L Krishnan², V Sravani³, G Pavan Kumar⁴
K Kiran Kumar⁵

^{1,3,4,5}Department of Mechanical Engineering, Prasad V. Potluri Siddhartha Institute of Technology,
Kanuru, Vijayawada

²Department of Mechanical Engineering Velagapudi Ramakrishna Siddhartha Engineering College,
Kanuru, Vijayawada

Abstract: PV based solar Power systems are nowadays being widely used in domestic and commercial installations for fulfilling the in-house power requirement, auxiliary power requirement in buses, trains and can be extended to solar powered UAVs (Unmanned Aerial Vehicles). However, Solar Powered UAVs can be rendered useless in the event of rapid and drastic decline of performance level in terms of power back up to the UAVs. The probable reason for such a decline may be failure of an individual solar cell of the panel, accumulation of dust and/ or shading of the solar panel etc. The present work aims at developing an IOT based system for energy monitoring in a solar powered UAV. It is expected that through the real time monitoring, data pertaining to relevant performance variables of the solar power back-up system can be acquired in advance.

INTRODUCTION

Power generation and consumption capacity is a major indicator of the development stage of countries across the world. Hence worldwide attention is oriented towards discovering and harnessing renewable energy source to produce green energy for meeting the energy requirement. Among the various renewable sources, solar photovoltaic technique is gaining popularity due to huge availability, reduced cost, easy installation, and maintenance. Hence real-time solar monitoring system is essential for ensuring optimum performance of the PV based solar power plants. Currently, Internet of Things (IoT) is an evolving technology that makes things smarter and user-friendly when connected through the communication protocol and cloud platform in monitoring solar power plants functioning [1]. In recent years, several research works have been carried out with reference to IOT application for PV panel performance monitoring. A PV monitoring system is developed based on wired and wireless networks to transmit the parameters to a remote coordinator that offers a web-based application for remote access [2]. Research endeavour to monitor solar power plant operations using IOT and Machine learning techniques is however limited to the static installations on commercial building rooftops and solar farms.

The importance of similar systems for tracking performance of PV based solar power systems on various applications likes transport modes viz. Bus, Trains, Drones etc. cannot be undermined. However, monitoring and diagnosis system developed for these fixed installations do not offer a turnkey type solution and hence need to be customized keeping in view the constraints involved in the mobile power support system [3]. Next chapter presents a literature review carried out to identify the design considerations involved in the design and

development of monitoring and diagnosis systems for the PV based solar system performance in unmanned aerial vehicles or popularly referred as drones.

LITERATURE REVIEW

The literature review performed to identify the considerations involved in the design and development of monitoring and diagnosis systems for the PV based solar system performance.

Energy Monitoring System

Solar monitoring systems operate through the solar system's inverter(s). Companies often offer solar inverters that come with a proprietary monitoring software setup [4]. As the solar inverter converts DC current into AC current for use in a home, information about power levels and production is collected and sent to the cloud-based monitoring systems and their companion apps [5]. As a result, if the personal internet connection is lost, one may still be able to access the solar monitoring system. Systems with power optimizers don't rely on a wireless connection to transmit data, so monitoring continues during internet outages. Depending on the interface that has been set up, one can access the monitoring data even when the internet is down. However, this isn't the case for micro inverter monitoring systems. They rely on a Wi-Fi connection to monitor each panel individually, in real time [6] [7]. This means that when the internet goes down, the monitoring capabilities also suffer. Monitoring software often can help detect problems and defects with panels, and recommend repairs to your setup [8]. One can often track historical data from the system. For example, monitoring systems offer data on historical weather-based performance, so anybody can know how the weather has impacted solar production in the past, and what one can expect in the future [9]. An effective monitoring system for a PV array must address several aspects such as, the placement and accuracy of sensors, communication systems that can transfer the database, algorithms to manage and process the collected data and user interfaces to visualize the state of the PV arrays. These measurements can then be transmitted to a central server and integrated into an automated monitoring system.[10].

IoT in solar Energy Monitoring System

Energy monitoring systems are the most significant demands to decrease the energy expenditure from the businesses. Smart energy monitoring system technique tracks the usage of energy of different regions of the plant throughout round-the-clock. The energy Monitoring System is accomplished through the use of Energy meters, along with data loggers. Data loggers are utilized to get these data from Energy meters via communication interface protocol [11]. The Smart Monitoring Devices can interface with IoT networked imaging sensors to predict shading. The development of customized prediction algorithms for cloud movement and panel shading represents a significant advancement over previous efforts and can enable new strategies for power grid control, array topology reconfiguration, and control of inverter transients [12]. The new SMDs will enable us to develop and embed machine learning methods that employ recently developed divergence measures which will reduce uncertainty in fault detection. Moreover, new imaging techniques can allow improved shading prediction [13].

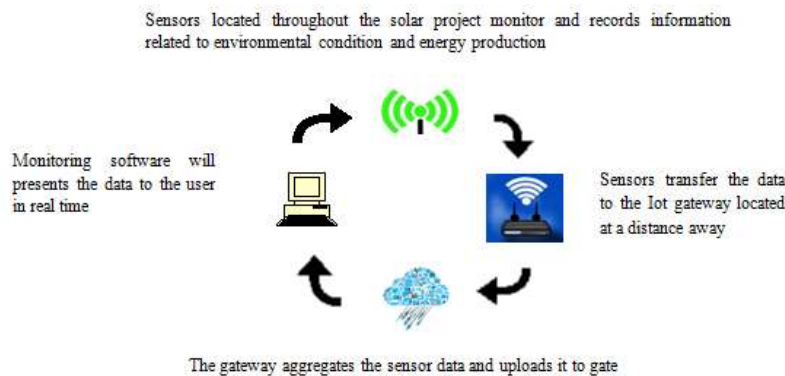


Fig.2.1: Applications of IoT Enabled Solar Power Monitoring

Multifaceted benefits leading to improvements in productivity and profitability can be achieved by tracking and analysis, early malfunction detection, predictive maintenance, operational intelligence, system portfolio, and increased life efficiency.

Conclusion of Literature Review

Hence, Photovoltaic based solar power systems with lithium ion batteries as storage medium have emerged as a popular choice for driving Direct Current (DC) based applications. Due to the potential risk of solar cell fault, shading etc. there exists a risk of underutilisation of the PV based solar power system. Hence monitoring the solar power system is indispensable for realising optimum performance.

Project Objectives

Based on the literature review, the project objectives are specified as below.

- i) Design a customized IOT based system for monitoring and diagnosing the PV based solar power system mounted on an Unmanned Aerial Vehicle. It is to be noted that the PV based solar power system is being used to provide power back up to a UAV.
- (ii) The device should yield data pertaining to Solar Power system performance to a ground control station so that any degradation in system performance can be identified at the earliest and a corrective action can be taken.

In essence, the project objective is to design an IOT based system for ensuring reliable performance of a solar powered Unmanned Aerial Vehicle.

METHODOLOGY

The project is envisaged to be carried out in following phases:

- A. Modelling and Simulation for the system identification purpose.
- B. Building the prototype of IOT based device for monitoring solar power system performance.
- C. Validating efficacy of the device for monitoring system performance.

BUILDING IOT BASED DEVICE FOR MONITORING SOLAR POWER SYSTEM PERFORMANCE

In order to build a physical prototype for monitoring the solar power system performance, parameters related to critical components need to be identified. For the purpose, modelling and simulation of solar power system dynamics has been carried out through for modelling and Simulation of the solar power system dynamics, MATLAB/ SIMULINK have been used.

Simulation of Solar panel in Simulink: A model of PV panel based power system using MATLAB/ SIMULINK has been built. The model has been built with an objective to initially investigate solar power system performance at multiple temperatures and at different

irradiance values. The model has been built using multiple blocks for representing real-time monitoring of solar power system performance [14].

The model has been further simulated for obtaining Current (i), Voltage (V) and power (P) obtained from the solar panel, and maximum power point related condition at various operating temperature and irradiance value combinations [15] [16].

SIMULATION

Simulation of Performance without MPPT charge controller Implementation The figures below depict the simulation of solar powered IoT device which take irradiance as input and gives temperature, voltage and current as outputs without MPPT and with MPPT.

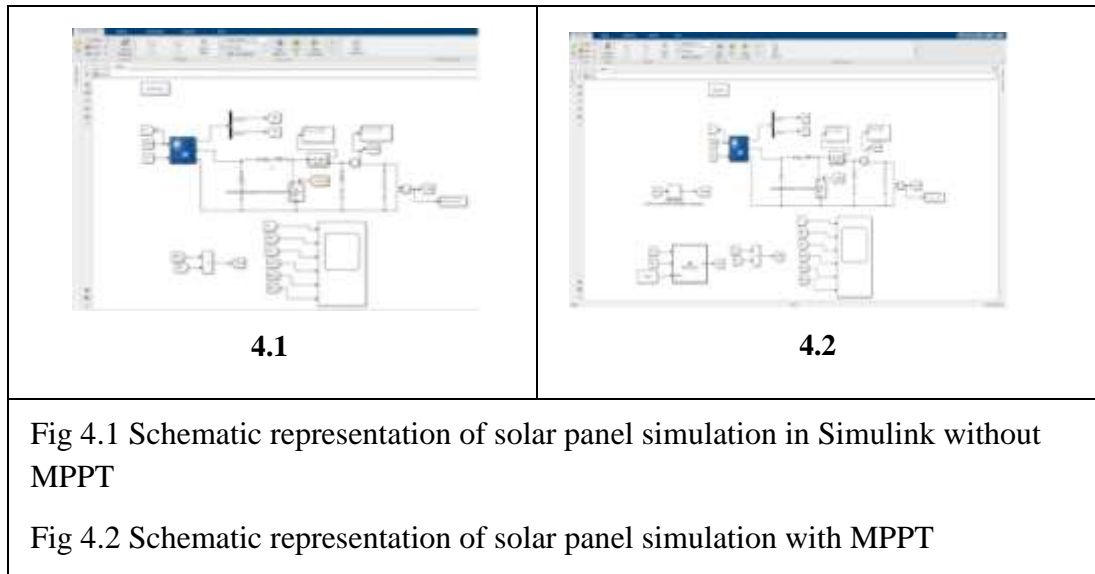


Fig 4.1 Schematic representation of solar panel simulation in Simulink without MPPT

Fig 4.2 Schematic representation of solar panel simulation with MPPT

RESULTS

Simulation results without and with Maximum power point tracking

CASE 1: At Constant temperature (25degrees) and at different ranges of irradiance the solar panel is simulated and corresponding voltage and current values are taken.

CASE 2: At constant Irradiances (1000) and at different range of temperatures the solar panel is simulated and corresponding voltage and current values are taken.

Table 4.1 Results at Constant Temperature without MPPT and with MPPT

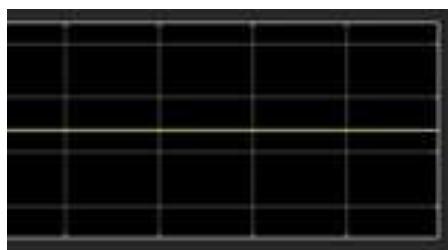
Temperature (°C)	Irradiance (W/m ²)	Voltage (volts)	Current (Amps)	Power (watts)
25	800	30.17	5.028	151.695
25	900	30.79	5.132	158.014
25	1000	31.24	5.207	162.667
25	1100	31.59	5.265	166.321
25	1200	31.87	5.311	169.262

Temperature (°C)	Irradiance (W/m ²)	Voltage (volts)	Current (Amps)	Power (watts)
25	1000	31.24	5.207	162.667
30	1000	30.68	5.113	156.867
35	1000	30.11	5.018	151.092
40	1000	29.54	4.924	145.455
45	1000	28.97	4.828	139.867

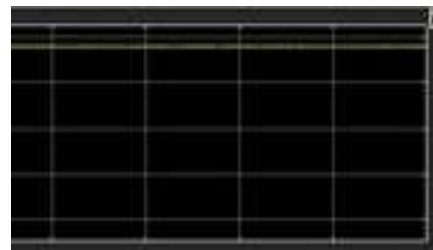
Temperature (°C)	Irradiance (W/m ²)	Voltage (Volts)	Current (Amp)	Power (Watts)
25	800	31.39	5.232	164.232
25	900	33.21	5.535	183.817
25	1000	34.9	5.816	202.978
25	1100	36.49	6.081	221.895
25	1200	37.97	6.328	240.276

Temperature (°C)	Irradiance (W/m ²)	Voltage (Volts)	Current (Amps)	Power (Watts)
25	1000	34.9	5.816	202.97
30	1000	34.53	5.755	198.72
35	1000	34.12	5.687	194.04
40	1000	33.76	5.627	189.96
45	1000	33.37	5.561	1185.57

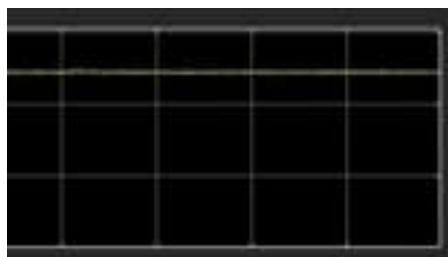
Note: The Temperature coefficient makes a note that in a percentage per degree Celsius, how much power a solar panel will lose when the temperature increases by 1 degree over 25 degree Centigrade [17].



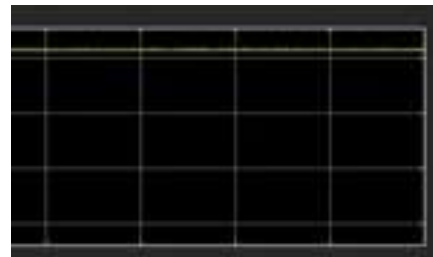
(a)



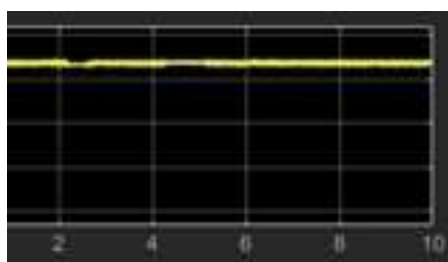
(b)



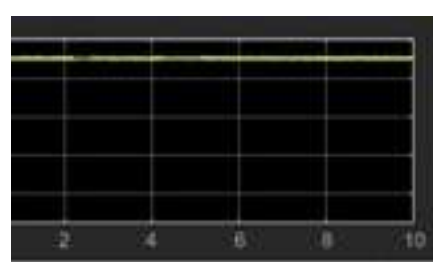
(c)



(d)



(e)



(f)

Fig 4.3 (a) Irradiance value at 1250W/m² (b) Ambient temperature (c) PV Panel output Current (d) PV Panel Output Voltage (e) Output Current from MPPT Controller (f) Power Output from MPPT Controller

Experimental Investigation of Solar Power System Monitoring

In the previous observation we have simulated the solar power monitoring of a solar panel with and without Maximum Power Point Tracking (MPPT) system using MATLAB/SIMULINK software. In this experimental investigation pertaining to influence of shading and dusting on the solar panel performance has been carried out through experimental testbed in the form of a solar powered quadcopter has been developed to do so.

Description of PV based Solar Power System enabled with IoT device The experimental setup consists of Electro–Mechanical components are used in this device we can measure the voltage, light intensity (irradiance), current, temperature using multiple sensors obtained from the solar panel and also current is calibrated.

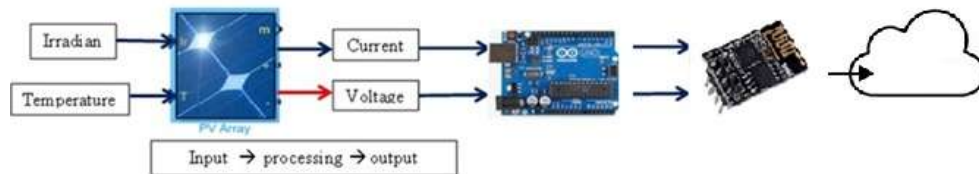


Fig. Block diagram representation of Solar Power System with IOT device

ThingSpeak Channel: ThingSpeak is an IoT analytics platform service that allows aggregating, visualizing, and analysing live data streams in the cloud. Data can be sent to ThingSpeak from devices, create instant visualization of live data, and send alerts.



Fig. Thingspeak Channel (Courtesy: <https://thingspeak.com/>)

Description of Quadcopter:

For performing experiment, a Solar Powered Quadrotor has been built for being used as test-bed for investigating the efficacy of the IOT system implementation. The quadrotor has been built for the purpose of inspecting large solar power generation farms and such captive power plants. Hence the built size has been kept small. Weight of the Quadrotor is limited to 3 Kg and its footprint area is less than 0.25 sq. m.

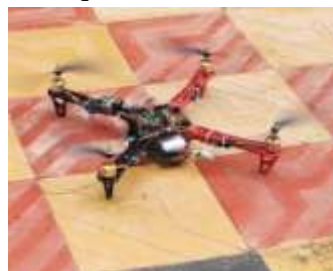


Figure. Quadrotor Prototype

Endurance of the solar panel is the attainable flight duration per recharge of the power source. Power source used here is a 3-cell battery pack. The nominal operating voltage of the pack is 11.1 volts or 3.7V per cell.

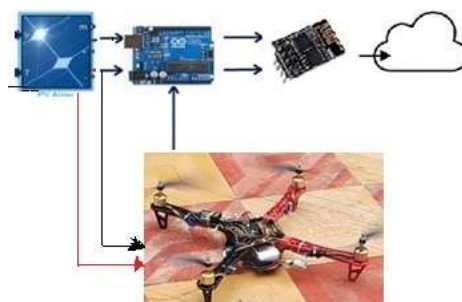


Figure: Schematic of Solar Powered Quadcopter Enabled with Internet of Things

The solar panel along with all the sensors have been mounted on the unmanned aerial vehicle. The voltage, current, temperature and light intensity are sensed by the respective sensors. The sensory data is acquired by Arduino UNO microcontroller board. The data is processed according to a program to record the appropriate values of all the above-mentioned performance characteristics. The code used for the purpose is presented in the appendix II.



Fig. Sensory Data Transmitted to ThingSpeak

The processed data is communicated to “Thingspeak” through the ESP8266 Wi-F module. ThingSpeak is an open-source online portal where we receive the recorded sensory data and can also have its graphical visualisation. The recorded data can be downloaded in the form of comma separated values (.CSV format) file. In order to test the influence of integrating the solar power system on the endurance of the quadcopter, endurance tests were performed. Solar insolation rate and ambient temperature was recorded prior to the endurance tests for the Solar Powered Quadrotor. During the tests, Solar Insolation rate varied within $650\text{--}700\text{W/m}^2$ and temperature was around 32°C . The average endurance time has increased from 8 to 10 minutes.

Experiments for Validating Efficacy of the IOT Device

In this experiment we have taken the whole experimental setup and left it ideal for 10 minutes and corresponding current, voltage, light intensity and temperature are taken.



Fig. 5.13: General condition of Solar Power system Monitoring

To investigate the effect of shading, multiple situations have been considered. The solar panel has been covered in three different ways i.e., 33.33%, 66.66%, 99.99% and corresponding results from the ThingSpeak are taken.

i) Solar panel covered 33.33%:

The solar panel that have been taken have 36 cells out of 36 cells 12 cells are covered completely and remaining cells in the PV array are subjected to irradiance and temperature, and allowed to set for 5 min and the values are extracted from the Thingspeak cloud web.

ii) Solar power covered 66.66%:

In this situation the solar panel is covered 66.66% by covering an area of 24 cells of the solar panel, remaining 12 cells are subjected to irradiance at room temperature, the results thus obtained are stored in Thingspeak cloud web.

iii) Solar Panel Covered Completely:

In this condition the solar panel is completely, all the cells in the PV array are covered and left it for 5 min to get isolated and then the values corresponding to this condition are saved in the Thingspeak cloud web.



Fig. 5.14: Shading Effect Investigation: 33% Covered Solar Panel

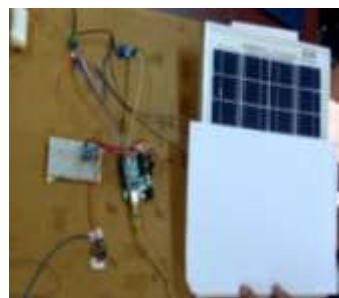


Fig. 5.15: Shading Effect Investigation: 66% Covered Solar Panel

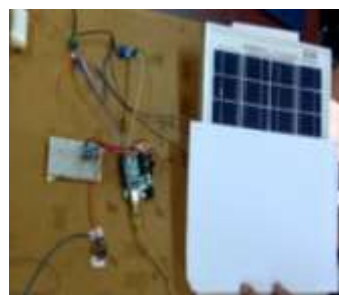
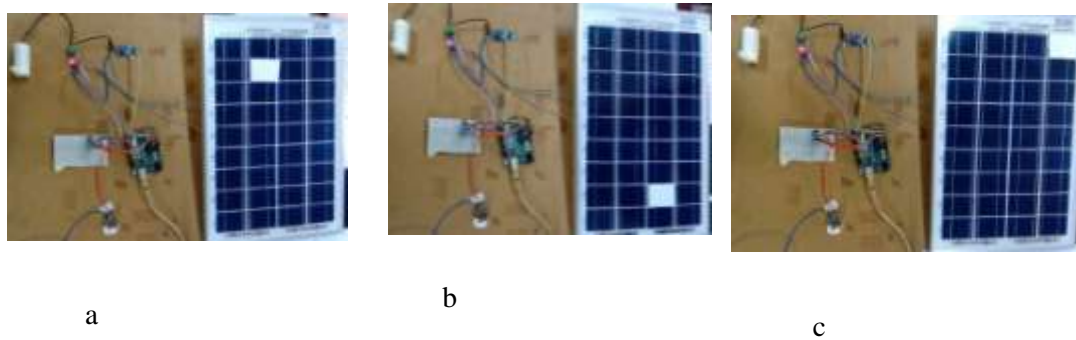


Fig. 5.16: Shading Effect Investigation: 100% Covered Solar Panel

Solar Cell Fault Simulation:

In this type of experimentation cells are identified by assigning names to it, here we have taken rows with digits from (1-9) and columns are assigned with alphabets from (A-D) such that cells can be defined as A1- A4, B1- B4, C1- C4, D1-D4. Now we have covered any one of the cells in the panel and values are taken from the Thingspeak web. We have covered A4, B8, C2, and D9 at different times and values for 5 min time limit are taken and corresponding current, temperature, voltage and light intensity are calculated.



Solar Cell fault Investigation (a) B-8 cell (b) C-2 cell (c) D-9 cell

Experimental Results and Discussion

The presents the plots based on data recorded in Thingspeak channel and the .csv file thus generated. The results plotted are pertaining to the shading effect on the solar power system performance. It can be noted that the Voltage output decreases from 12 V to 4V corresponding to the 33.3% shading effect. It further drops down to Zero Volts under the 66.6% shading effect.

The result presented in figure indicates that the solar power system performance undergoes exponential decline due to shading effect. Hence, whenever there is a trend of sharp decline in the voltage output it may be interpreted as due to the shading effect and hence the fail-safe mode be triggered for avoiding failure of the overall solar powered quadrotor. Thus, it ensures the reliable operation of the overall system.

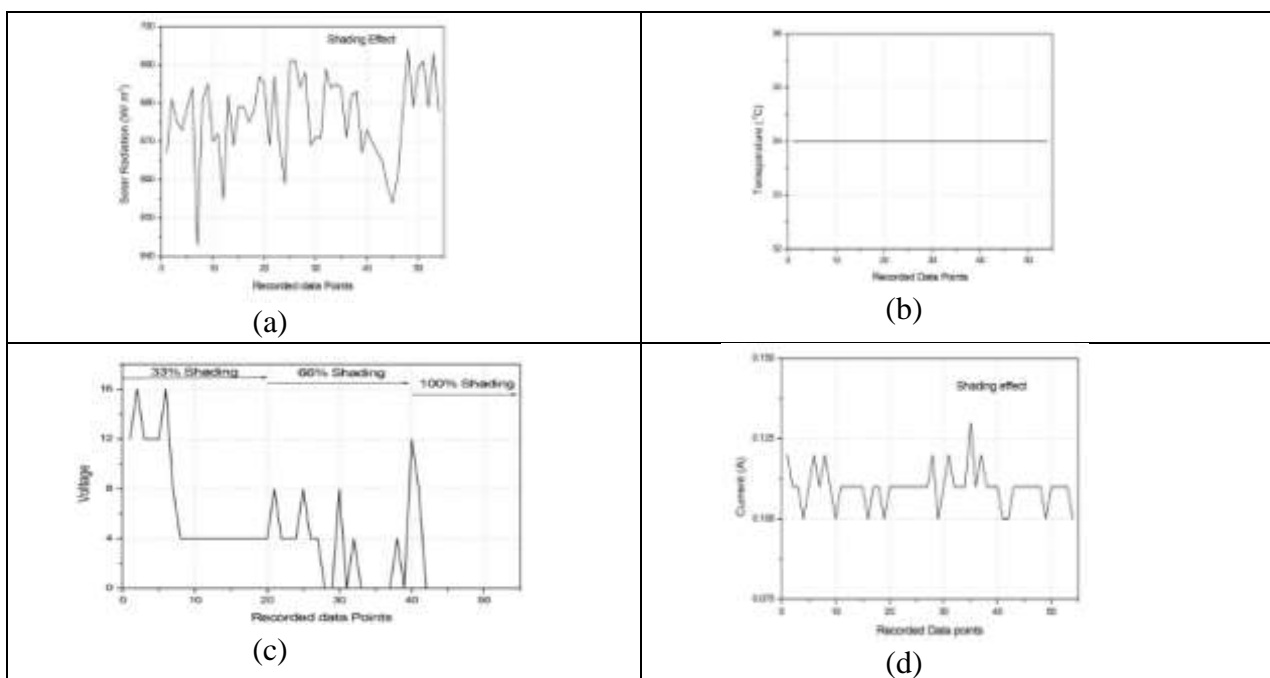


Fig. 5.18: Experimental Results from Thingspeak Channel corresponding to Shading of PV panel (a) Solar Radiation (b) Temperature (c) Voltage (d) Current

Figure 5.13 presents the plots pertaining to the Cell fault effect on the solar power system performance. Figure represents a continuum of observation for four different cell faults simulated. The cells A-4, B-8, C-2, and D-9 have been considered to fail (one at a time only). For each cell fault simulation, sensory data pertaining to solar radiation, ambient temperature, voltage and current data has been recorded for 5 minutes. Thingspeak channel is

updated every 15 seconds based on the prevalent internet protocol used for online communication. Hence every 20 recorded data points as shown on the x-axis corresponds to a single cell fault. Hence the entire X-axis scale comprising of 85 recorded data points corresponding to the cell faults in the order A4, B8, C2, and D9 (though one at a time only!). It can be noted from fig. 5.13 (C) that the voltage generated is around 8V. The voltage output can be considered to drop from the nominal solar panel output voltage of 12 Volts to 8 V as a result of cell fault simulation. Fig. 5.13 (d) indicates that the current drawn is almost constant varying slightly between narrow ranges of 0.10 to 0.125 Amperes. Fig. 5.13 (a) and (b) respectively presents the solar radiation value and ambient temperature values over the period.

It can be noted that sharp decrease in the voltage generated due to cell fault is quite alarming. It droops down from 12V to 8V. Literature suggests that a single cell fault initiation, if overlooked may cause colossal damage to the functioning of the entire solar panel. Hence the sharp decline in the voltage output needs to be taken care of by calling back the Quadcopter by triggering the Fail-Safe mode. Then the repair or replacement of the solar panel can be addressed.

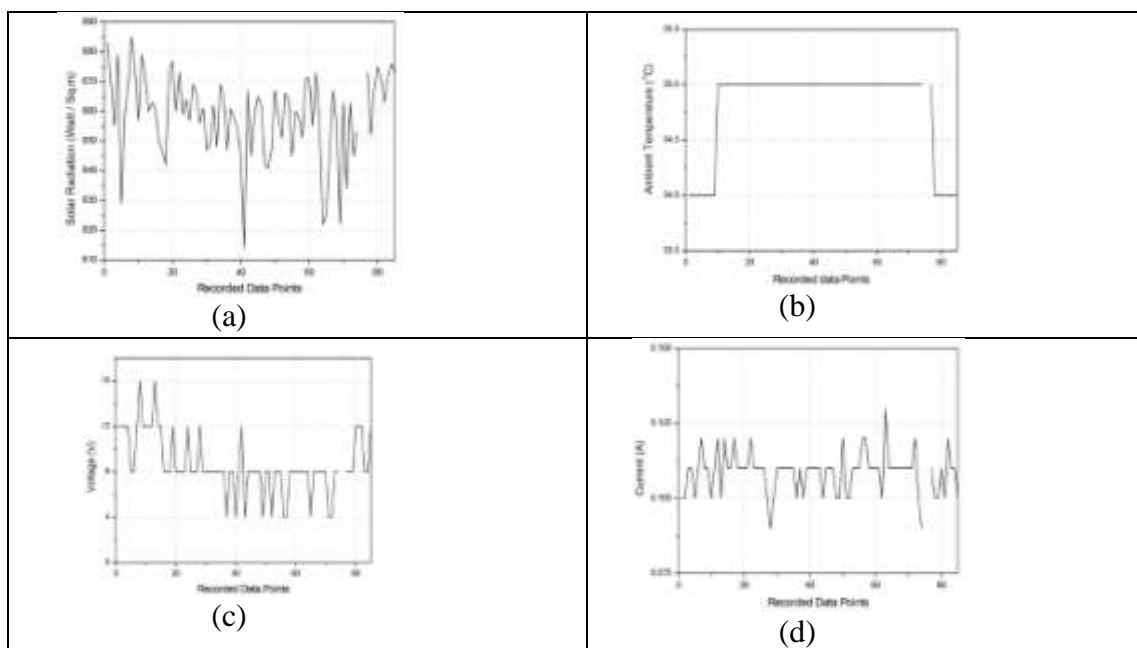


Fig. 5.19: Experimental Results from Thingspeak Channel corresponding to Cell Fault Simulation (a) Solar Radiation (b) Temperature (c) Voltage (d) Current

CONCLUSION

The work presented in this report describes the development of a solar powered quadcopter enabled with IOT technology. An IOT system based on Arduino Uno, ESP8266 and ThingSpeak (an Open source IOT platform) has been used for sensory data acquisition and communication to the ThingSpeak portal. Thingspeak offers for recording and visualizing the solar powered quadcopter system performance data remotely. In the context of the problem, the data generated by a flying quadcopter can be observed at the ground control station and timely control/ corrective action can be initiated to ensure reliable (safe) operation of the quadcopter. Based on the data observed through Thingspeak portal, a fail-safe mode can be triggered remotely causing the quadcopter to return to the ground control station safely.

Advanced algorithms can be also implemented to ensure automatic retreat of the quadcopter to ground control station.

REFERENCES

1. R. Nagalakshmi, B. Kishore Babu, D. Prashanth, "Design and Development of a Remote Monitoring and Maintenance of Solar Plant Supervisory System", *International Journal Of Engineering And Computer Science*, Vol.3, pp.9382-9385, 2014.
2. P. Papageorgas, D. Piromalis, K. Antonakoglou, G. Vokas, D. Tseles and K. G. Arvanitis, "Smart Solar Panels: In-situ Monitoring of Photovoltaic Panels based on Wired and Wireless Sensor Networks", *International Conference on Advancements in Renewable Energy and Clean Environment*, Vol.36, pp.535-545, 2013.
3. Spanias A.S., "Solar energy management as an Internet of Things (IoT) Application", 8th *International Conference on Information, Intelligence, Systems and Applications*, IISA 2017, pp.1-4, January 2018.
4. Chaoyen Wu, "How to Derive the Maximum Benefit From Solar Energy by Using IIoT-Enabled Energy Storage Systems", Moxa, White Paper, October 2017.
5. Hossein Motlagh, N.; Mohammadrezaei, M.; Hunt, J.; Zakeri, B., "Internet of Things (IoT) and the Energy Sector", *Energies*, 13, 494, January 2020.
6. S. Daliento, A. Chouder, P. Guerriero, A. Massi Pavan, A. Mellit, R. Moeini and P. Tricoli, "Monitoring, Diagnosis, and Power Forecasting for Photovoltaic Fields: A Review", *Hindawi International Journal of Photoenergy*, 2017.
7. Tao Hong, Pierre Pinson, Shu Fan, Hamidreza Zareipour, Alberto Troccoli, and Rob J. Hyndman, "Probabilistic energy forecasting: Global energy forecasting competition 2014 and beyond", *International Journal of Forecasting*, 32 (3), pp.896 – 913, 2016.
8. S. Adhya, D. Saha, A. Das, J. Jana and H. Saha, "An IoT based Smart Solar Photovoltaic Remote Monitoring and Control Unit," 2nd *International Conference on Control, Instrumentation, Energy & Communication (CIEC)*, Kolkata, pp. 432-436, 2016.
9. Mohd Nafis Akram, "Modeling and Fault Detection in DC Side of Photovoltaic Arrays", M Tech Thesis, B.S. American International University-Bangladesh, 2008.
10. V. Kavitha and V. Malathi, "A Smart Solar PV Monitoring System using IOT", SRAIC-2019, pp. 01-33, 2019
11. MohdIrwanYusoff, Universiti Malaysia Perlis, Investigation of the Effect Temperature on Photovoltaic (PV) Panel OutputPerformance, Article in International Journal on Advanced Science Engineering and Information Technology October 2016.
12. Vimala Devi K. Rajendran, VIT University| VIT · School of Computing Science and Engineering (SCSE), M.E, Ph.D, Solar Energy Monitoring System by IOT, Int. Jnl. Of Advanced Networking & Applications (IJANA).
13. Isha M. Shirbhate, Sunita S. Barve School of Computer Engineering & Technology, MIT Academy of Engineering, India, Solar panel monitoring and energy prediction for smart solar system, International Journal of Advances in Applied Sciences (IJAAS) Vol. 8, No. 2, June 2019,
14. Chandini Sharma, Quantum University, Solar Panel Mathematical Modelling Using Simulink. Article -2014.,
15. Roshen Tariq Ahmed Hamdi, University of Technology / Baghdad / IRAQ, Solar cell system simulation using Matlab-Simulink., Article in Kurdistan Journal of Applied Reserch. June 2017.
16. Md.W.Shah, Robert L.Biate, Design and simulation of solar pv model using Simulink and MATLAB., international journal of Scientific and Engineering research, Volume 7, Issue 3, March 2016.
17. MohdIrwanYusoff, Universiti Malaysia Perlis, Investigation of the Effect Temperature on Photovoltaic (PV) Panel OutputPerformance, Article in International Journal on Advanced Science Engineerin.g and Information Technology October 2016.

Comment on extrusion-based 3D printing of porcelain ceramics with diverse infill patterns and infill percentages

Palivela Bhargav Chandan¹, Aye Aye Thet², Mamilla Ravi Sankar^{1*}

¹Department of Mechanical Engineering, Indian Institute of Technology Tirupati,
Andhra Pradesh, 517619, India

²Department of Mechanical Engineering, Technological University Lashio,
Northern Shan, 6301, Myanmar

Abstract: The ceramic block was printed with eight infill patterns (rectilinear, line, concentric, honeycomb, 3D honeycomb, Hilbert curve, Archimedean chords, and octagram spiral) by varying the infill percent. The infill percentages are 5%, 10%, 15%, 20%, 25%, 30%, 40%, 50%, 60%, 70%, 80%, 90%, and 100%. The area of the block is 60mm × 60mm square in shape, and the thickness depends on the layer height and the number of layers. The printing time and material consumption changed according to the infill pattern, the infill percent, and the layer height of the part. The density, weight, structural, and other properties depend on the effect of the infill pattern and infill percentage. The extrusion flow depends on the pressure in the nozzle and the slurry viscosity.

1. Introduction

3D printing, also referred to as additive manufacturing, is a computer-aided design prototype of the required model to deposit layer by layer of materials using various techniques. This manufacturing aspect provides distinct advantages compared to the standard manufacturing processes by eradicating the need for model-dependent jigs and fixtures for every precise model design, offering multiple custom designs within a single parallel build, and efficiently utilizing materials, thereby lowering the scrap [1],[2]. Recent advancements in the additive manufacturing sector include multi-material and multi-color manufacturing, allowing variable properties and aesthetics across the model and printing complex structures [3]. The progress in the additive manufacturing process provides new insights into the distinct capabilities of the technologies besides the opportunities to improve the manufacturing of the products widely [2]. There are three classes of complexity involved. They are shape, material, and hierarchy. Shape complexity affects the ability to build any form that can be geometrically customized [4]. Material complexity involves the ability to have conventional processes manufacture a complex material.

The hierarchical complexity demands manufacturing parts with features of ranging scales. For instance, microstructure through a geometric mesostructure [2]. This work uses infill patterns (line, rectilinear, honeycomb, concentric, 3D honeycomb, Archimedean chord, Hilbert curve, Octa gram spiral) with infill percentages ranging from 5 % to 100 % are 3D printed by extrusion-based 3D printing technology. The porcelain ceramic is a model archetype or framework. Also, the literature underlining the importance of various infill patterns and infill percentages in different ceramic 3D printing processes is discussed.

The rectilinear geometry with an orientation of 45° has shown enhanced mechanical

*Corresponding author. Tel.: +91-877-250-3410

E-mail address: evmrs@iittp.ac.in

response with high strength. Also, at the solid loading of 70 wt.% and 67.5 wt.%, the 45° rectilinear pattern showed enhanced compression strength of 8 mol% dense yttria-stabilized zirconia parts [5]. The change in the infill orientation could also lead to defects and porosity in the printed samples [6]. Characterizing yttria-stabilized zirconia, 3D-printed features for prostheses revealed relatively low porosity, low roughness, and enhanced compressive strength [7]. Catalytic experiments and finite element modeling performed for alumina ceramic inks displayed that additively manufactured features with 40% infill density and rectilinear infill pattern favored catalytic activity [8]. The combination of engineered macro porosity and internal nano porosity derived from 3D printed yttria partially stabilized zirconia rectilinear pattern makes the ceramic features ideal for demanding gas flow in a corrosive or high-temperature application [9]. In a study on additive manufacturing of alumina ceramics and the characterization of sintered parts, a rectilinear filling pattern with a filling angle of 90° is observed to be beneficial among all the designs [10]. 3D printing of partially stabilized tetragonal zirconia with eight molar percent of yttria solid oxide fuel cell electrolytes revealed that the rectilinear pattern yielded the best outcomes for the cylindrical geometry than the concentric ones [11]. Extrusion and sintering of binder-coated zirconia with a rectilinear infill pattern revealed that the low layer thickness enhanced the mechanical properties [12]. In extrusion-based 3D printing of alumina and zirconia models, the external contour profile that is accountable for the surface quality of the models is discarded, and a rectilinear infill pattern with a fill angle of 45° is considered. The part orientation of the zirconia and alumina samples with vertical direction showed significantly enhanced Vickers hardness than the horizontal orientation as the load bearing or the resistance against micro-scale penetration; that is, the hardness is higher in specimens that are vertically oriented [13]. 3D printing using non-cylindrical nozzles added a new degree of freedom. It allowed obtaining surfaces with more specific surface area and even introducing concave surfaces in the architecture printed.

Due to the rectilinear pattern used and the nature of the direct ink writing process, even a non-cylindrical nozzle resulted in an interlinked pore network. Most pores were open besides trace amounts (less than 0.2 %) of closed porosity due to air bubbles [14]. 3D printed hydroxyapatite scaffolds with the rectilinear arrangement of pores and with a thermoplastic binder polyvinyl alcohol were found not to affect the adhesion and cell colonization. Still, elevated temperatures during scaffold sintering are better for colonizing cells. Scaffolds sintered at low temperatures inhibited cell proliferation [15].

A report on the impact and role of 3D printing in casting recommends line infill patterns in parting lines [16]. The line pattern is also used for filling the space between the tool path lines, which are closer [17]. Similarly, the line pattern can also be used in printed circuit boards. The printability of the zirconia coated with binder was assessed by printing a line pattern under several process parameters' combinations like extrusion flow rate and printing speed [12]. Lauder et al. reported that surface integrity and microstructures are improved by optimization of process parameters like line spacing, droplet spacing, layer spacing, and placement [18]. The Low-Temperature Co-fired Ceramic (LTCC) slurry filled a layer-by-layer pattern following the moving extruder's path. The deposited line of the slurry could bond with the adjacent bar, forming a relatively flat upper surface. However, for the side walls, no such fusion behavior was found. The previously deposited layer is solidified when the new layers are printed, retaining layer lines on the side walls [19]. On the other hand, while printing the delicate patterns, the flow of the paste can be reduced slightly, thereby making the patterns of the line clear [20]. Increasing the overlap between the 0-45-90-

135 orientation lines lowered local stress, whereas the double-layered configurations are mechanically weaker [21]. The width of the line is directly proportional to the extrusion flow in a user interactive fabricating framework. The modelling is made using sweeping lines as the design tool for clay 3D printing [22].

A concentric infill pattern is akin to the onion consisting of concentric layers around the center from the center to the exterior. 3D printing of nanocomposites containing polypropylene and different kaolinite contents with concentric infill patterns showed lower mechanical properties. This is out of its giant cavity formation between the layers in the structure [23]. In a concentric fill pattern, the alignment of the deposits in the loading direction yielded desirable flexural tensile and tensile properties [24]. A concentric infill pattern with 100 % density has displayed enhanced recovery time [25]. Due to the lack of pattern connectivity, in the case of a concentric pattern, there is a lowered stress transfer observed [26].

The concentric multi-layered structure is an essential feature in bone osteons, also seen in tree annular rings, sea sponges, and bamboo [27]. 3D printing uses a novel in-line mixing system to design functionally graded composites: boron carbide at the bottom and silicon carbide at the top as a gradient [28]. The concentric patterns in 3D printing for hip and knee replacements using carbon fiber composite akin to bone ceramics revealed that the more concentric fiber fill is added per layer, the stronger the part [29]. The scaffolds containing alternating layers deposited in concentric fill patterns made using polylactic acid and carbohydrate particles formed integrity surfaces [30]. The mechanical properties are varied by changing the interaction between the polylactic acid and carbohydrate particles [31]. A concentric fill pattern was found to be a stable geometry mechanically when stressed by a fatigue load frame in the case of piezoelectric films for pressure sensor applications [32]. 3D-printed alumina concentric filling patterns exhibit a minimal effect on the mechanical properties and density of the additive manufactured parts [10]. Attaining isotropic behaviors while depositing concentric patterns is challenging [33]. Bone healing with concentric rings guided new bone formation between the struts [34]. The electric field circular component as concentric curves led to a strong magnetic field in dielectric anisotropic composite 3D printed with meta-material characteristics [35]. Implants 3D printed for bone tuberculosis treatment with powder containing poly (DL-lactic acid) in multilayer concentric cylinder shape. Each layer was loaded with the antibiotics rifampicin or isoniazid [36]. The effect of continuous concentric Kevlar fiber rings on the elastic characteristics of polyamide composites revealed that an increase in the number of Kevlar fiber rings enhanced the composites' mechanical properties [37]. Laminated 3D printed composites with isotropic infill patterns had improved tensile performance compared to the concentric infill pattern [38]. 3D printing of nanoporous ceramics using a 406 μm nozzle in the concentric circle line spacing with a cylinder height of 10 in the wagon wheel structure revealed the smallest feature size printed was 250 μm [9]. The assessment of bending characteristics of additive manufactured coconut wood poly lactic acid showed that the enhanced bending properties are attained by 75 % infill concentric pattern [39]. Examination of thermal characteristics of tube-in-tube porous alumina ceramics for recovering the heat from the thermochemical solar reactor led to enhanced heat transfer coefficient [40]. Flexible bio-ceramic-dependent scaffolds with concentric microstructures are successfully manufactured by combining additive manufacturing and two-dimensional bio-ceramics [41]. Additive manufacturing of calcium phosphate scaffolds revealed that the bone was distributed homogeneously over the complete implant in the calcium-deficient

hydroxyapatite foams. Also, no considerable differences among the five concentric volumes of interest are observed [42].

In the four-dimensional printing of energy harvesting devices and pressure sensors, the concentric fill pattern was set up to maximize tensile strength for dynamic load frame testing [43].

A filling pattern of hierarchical models like 3D honeycomb and honeycomb is applied for low-weight designs. 3D printed honeycomb infill patterned scaffold with poly lactic acid altered with hydroxyapatite and chitosan revealed enhanced proliferation and attachment of human osteosarcoma cells *in vitro* [44]. Self-propagation of photopolymerization is restricted to the models with linear characteristics, which protrude from the exposed surface like honeycombs [45]. As per the few reports, the mechanical stability of the additive manufactured parts is attributed to the honeycomb structure [46],[47]. Additive manufactured alumina honeycomb-shaped structures displayed a reduction in density and increased compressive strength with the introduction of nanoparticles [48]. Comparatively, it is also suggested that for the more efficient designs of lattice structures like honeycombs, a significant enhancement in the compressive strength properties can be achieved [49]. The sandwich panel's bending performance relies heavily on the geometric configuration. A ceramic sandwich reinforced with the honeycomb core exhibited enhanced mechanical characteristics in simulation [50]. Direct foam writing of hexagonal closed-cell porous struts revealed exceptional specific stiffness, a major step for the scalable formation of porous materials like tissue scaffolds and lightweight structures [51]. The largest honeycomb fill factor in 3D printing of transformer core gave the greatest printed core performance [52]. Hierarchical re-entrant honeycomb manufactured by 3D printing technique enhanced specific initial-buckling strength, specific stiffness, specific energy absorption capacity, and structural stability [53]. Improving rheology, homogeneity of ceramic suspension, and optimized sintering, a honeycomb structure can be made with no cracking and high specific strength besides better dimensional stability [54]. The potential of additive manufacturing in the monolith design with a sophisticated honeycomb structure for catalytic end applications is unveiled [55]. A study on the compression evolution of prismatic metal-ceramic composite disclosed that the ceramic particles are apprehended between the honeycomb-like metallic phase that maintained the potential for carrying the load even after the ceramic phase had attained the failure stress value [56]. 3d printing of ultra-high temperature porous multi-scale zirconium diboride honeycomb infilled ceramics revealed a high strength ratio to density in a 4-point bending test [57]. Honeycomb infill cordierite samples with perpendicular and regular vertical channels were fabricated, and the samples sintered were almost intact without many observable visible cracks, and the shape retained undistorted [58].

Copper or active ceria phase loaded on traditional and enhanced monoliths of honeycomb are used for the acceleration of oxidation of carbon monoxide in excess oxygen. They are also used to accelerate carbon monoxide in hydrogen-rich mixture. These are the reactions corresponding to the response of environmental protection's actual relevance, and perfect utilization of energy in the fuel cells, respectively [59]. 4D printing of honeycomb elastomer-extracted ceramics led to structural applications of high-temperature microelectromechanical systems, electronic devices, aerospace propulsion components, space exploration, and autonomous morphing structures [60]. Additive manufactured structures with honeycomb infill patterns in the longitudinal direction exhibited the most effective strength ratio to mass and were mainly used for low-weight applications. A 100% dense honeycomb pattern

indicates high strength and is nominated for application with no restrictions on weight [61]. 3D-printed silicon nitride ceramics with honeycomb patterns exhibited high compressive strength as high as 1.1GPa [62]. The 3D-printed inner honeycomb pattern can exceptionally resist mechanical loads [63]. Hexagonal honeycomb structures displayed enhanced specific strength under high compression force [54]. Inkjet 3D printing of honeycomb infill antenna provides 15 % higher efficiency than a similarly manufactured solid substrate antenna. The 3D-printed antenna showed less weight, low dielectric constant value, and significant dielectric loss, which are advantageous [64]. In the combination of the 3D printing process of pattern making and investment casting, the honeycomb patterns manufactured from aluminum alloys exhibited good strength, high stiffness, excellent surface accuracy, and dimension [65]. By bridging silicon carbide chemical vapor infiltration and 3D printing, 3D porous lattices with remarkable mechanical characteristics are fabricated [66]. Multi-material 3D printed carbonyl iron powder/barium titanate composites with honeycomb structural absorber exhibited enhanced microwave absorption of electromagnetic waves [67]. 3D printing of polymer-extracted honeycomb ceramics, namely polylactic acid lattices dip-coated with two preceramic polymers. Dip-coated polymers are then converted into silicon carbide nitride and silicon carbide ceramics. 3D printed stable silicon-based 3D non-oxide ceramic materials displayed retention of highly porous honeycomb structure after pyrolysis [68]. 3D printing of oblique honeycomb alumina silicon carbide whisker structure provides a practical and novel avenue for the fabrication of structural composites with higher and broader microwave absorption performance [69]. Barium titanate-dependent piezoelectric composite ceramics with honeycomb infill structure design, which are 3D printed, are more effective than those produced by traditional dicing-filling [70].

Samples 3D printed with a raster angle of 90° in a Hilbert curve infill pattern showed a better outcome than the 0° value. These outcomes indicate that the research should be done along the lines of ignored parameters which may yield more precise results than earlier [71]. A high temperature is maintained when the raster is deposited at fewer distances in the Hilbert curve, resulting in better fusion and bonding between the adjacent raster [72]. The lower number of voids in the Hilbert pattern indicates better mechanical properties. However, in the designs with low infill density, the Hilbert pattern presented lower tensile and flexural strength [72]. Structural quality and textural quality of the mashed potatoes with Hilbert curve infill pattern and various infill percentages reveal that, although a direct relationship has been followed between infill percentage, gumminess, hardness, and Young's modulus of the additive manufactured samples, no comparable akin outcomes have been found for the infill pattern [73]. The Hilbert curve infill algorithm proposed by Butz has become a most popular infill techniques in the additive manufacturing are out of its scope in reducing deformation of the material and ensuring better mechanical properties of the model [74]. The Hilbert curve pattern showed the enhanced compressive strength of 121.35 MPa of neat poly lactic acid printed at 60 mm/s, 210°C , 0.2 mm layer thickness with three shells and infill, 60°C bed temperature [75]. For improving the printing time and path planning for a feasible infill of 3D objects by lowering sharp angles that have continuity in the path, the Hilbert pattern is preferred over the other designs [76]. Few defects were also observed in the Hilbert curve infill pattern. The printing time of Hilbert curve patterns is found to increase compared to the other designs [77]. The amount of material required and time are affected by the type of infill pattern chosen [78]. The texture strength is high in the case of the Hilbert infill pattern. The modification in the strength of the texture was determined via the alterations in the internal

Dept. of Mech. Engg. PVPSIT 84

structure of the hard food material, using 3D printing, which showed diverse categories of modifications compared with the soft traditional food materials [79]. The surface smoothness of the models considerably enhanced the Hilbert curve pattern. However, the outcomes proved that surface roughness and Young's modulus of the printed parts varied directly proportional to the infill density in the Hilbert pattern [80]. Griffiths proposed a tool path strategy for machining curved surfaces based on the Hilbert curve [81]. A study is also presented based on the Hilbert curve for fused filament fabrication [82]. In the printing of solid infill patterns using the Hilbert pattern, it is observed from the outcomes the best mechanical properties besides high build duration and high material consumption [83].

There are no observable changes to the external structure or texture with the Archimedean chord infill pattern for an Osteo Ink [84].

The Archimedean chord infill pattern has a near diamond-like pore shape with curved edges recommended for tissue engineering applications [85]. In 3D printing of gelatine methacrylate/silica bioactive nanocomposite bio-ink for osteogenic differentiation of the stem cell, the Archimedean chord fill pattern with layer height as constant yielded the best outcomes [86]. In 3D printing of Archimedean chords complex geometries with hydrogel-based printing ink, the error percentage in the y and z directions is found to be in the order of 0.1% and 2%, respectively [87]. In an attempt to evaluate the effect of heating on tensile behavior and dimensional stability of additive-manufactured reinforced carbon fiber composites, the rectilinear pattern gave 33% higher strength than the Archimedean chord infill pattern [88].

Open designs like octa gram spiral would favor the spreading of the liquid electrolyte, unlike the closed patterns discussed earlier for fluid electrolyte uptake in the 3D printed electrolyte battery systems [89]. It is well known that the compressive strength varies in direct proportion to the infill density. The compressive strength reported for fused deposition additive manufacturing poly lactic acid materials with octa gram spiral infill pattern is 70.07 MPa [80]. The flexural strength and modulus are found to vary in direct proportion with the infill density in the case of the sole octa-gram spiral infill pattern and are reported to be lowest for the octa-gram spiral infill pattern in point of comparison with other designs [39]. The octagram spiral pattern has the weakest young's modulus, with 0.1482GPa with 3D printed copper composition. Ultimate tensile strength, young's modulus, and flexural strength is found to be lowered with an increase in the copper content. The flexural modulus increased with the copper content [90].

2. Materials and methods

2.1. Materials

The ceramic material composition includes 75 grams of porcelain, 1.5 grams of polymer, and 29 grams of water. The total weight of the slurry is 105.5 grams.

2.2. Slurry preparation

All the ingredients are mixed to obtain a slurry optimized to extrude the part. Sometimes the stirring is laborious before completely dissolving in water due to the stickiness of a slurry. Little alcohol is added and stirred until it dissolves completely to get a suitable slurry. This is very important to optimize the slurry composition to obtain high density, low shrinkage, and sufficient strength to produce a product. If water is added in excess amounts, the slurry becomes softer, and the expansion rate is high, which can cause more deformation and change the line thickness. Moreover, the slurry can leak above the piston in the nozzle

during the extrusion. This effect can cause a flow due to pressure leakage.

In contrast, the flow problem is found when the slurry is stickier. Therefore, the slurry condition is critical for printing the part with desired properties, structure, etc.

2.3. 3D printing

Nowadays, ceramic 3D printing technology is widely used in various fields to produce products, mainly in medicine, to replace ceramic human body parts. Moreover, ceramic 3D printing technology has reduced the waste of materials and labor. It can reduce the cost and time to produce a part. 3D printing technology can create complex shapes and more precise details. The model is printed on the platform using the layer-by-layer deposition method in this study. The position of the nozzle movement is in the X-Y plane, and the platform is moved along the Z direction. The nozzle is moved by rectilinear motion and driven by a screw gear. The nozzle has approached the build platform with a 45 ° diagonal path to print the part. The motion speed of the nozzle is 30mm/s for the unloading operation, and the nozzle diameter is 1.2mm, which is the same dimension as the extruder width. The actual printing speed is only 5mm/s. All the layer's height is 0.6mm, and the infill density varies according to the part's infill percentage. The platform is dived along the Z axis after the printing of each layer. When the whole piece is complete to print, the extruder or nozzle automatically returns to the home position.

2.4. Experimental procedure

After the preparation of suitable slurry, it is loaded into the syringe. The syringe is then set up in the assigned location of the printer to print the part. The desired program is chosen according to the structure of the part. Before printing the part, the flow condition must be tested to avoid bubbles and intermittent flow during the printing of the part. And then, the distance has to be adjusted in the z-direction between the nozzle and the platform, as this distance affects the material's expansion and flow. If the platform and nozzle are very close, the material is more expanded, making the line thicker. In addition, the skirt structure is also printed before printing the actual part to detect and adjust the adhesion and cohesion of the flow. The gap between the skirt and the object is 5mm, and the layer height is 0.6 mm. The number of loops is two loops, and the number of layers is one layer for the skirt. The skirt layer height is equal to the actual part layer height. The actual part is printed according to its infill percentage and pattern. Therefore, the number of lines, the printing time, and material utilization are varied according to their infill pattern and share.

3. Results and discussion

3.1. Rectilinear infill pattern

In this infill pattern, the infill density and properties of the part differ according to the infill percentage. Figure 1 shows the relationship between the printing time and the infill percentage of the rectilinear pattern. The corresponding infill percentages for the rectilinear pattern are shown in Figure 2. Moreover, the detailed data of printing conditions and parameters for this pattern are described in table 1. In 5% infill density, the part is lightweight. The density and mechanical properties are also weak because the space is ample in part. For 10% infill, the number of lines is increased. So, the vacuum is also less inside the part. Moreover, the density and other mechanical properties are also increased. But, the printing time and own weight are more. At the 15% of the infill, the amount of space is less in part. Therefore the weight, density, and printing time increase. However, the mechanical properties are better than the previous infill percentage (5% and 10%). For the 20% infill, the number of

lines increases, so the line gap is less and close to each other. The printing time and own weight are higher. But it has better mechanical properties and density.

Table 1. *The printing time and printing parameters of the rectilinear infill pattern*

Rectilinear			
Infill (Percentage)	Printing time (minutes)	Number of lines	Height of the printed part (mm)
5	21	451	60×60×5
10	12.57	325	60×60×2
15	13.95	343	60×60×2
20	15.23	367	60×60×2
25	16.525	385	60×60×2
30	18	409	60×60×2
40	20.57	451	60×60×2
50	23.22	493	60×60×2
60	25.8	535	60×60×2
70	28.38	577	60×60×2
80	31.02	613	60×60×2
90	33.62	655	60×60×2
100	36.2	703	60×60×2

The 25% infill density slightly increases the number of lines and the printing time. The vacuum, in part, is decreased. Although the weight is heavier, the density is improved. This improves the mechanical properties of the part. In the 30% infill pattern, the material consumption is slightly more, and the gap between the lines is less. This infill percentage is suitable for lightweight and to get some mechanical properties of the part. Increasing the infill percentage to 40%, the number of lines and usage of the material is significantly high. Moreover, the structure is more compact and denser because the space area is less in part. The line spacing is much less, and material and printing time consumption is a little high in the 50% infill density. So, the density and the mechanical properties also increase. This infill percentage has medium weight and medium properties of the part. In 60% infill for this infill pattern, the vacuum is minimal in the part that almost lacks vacuum. This is due to the number of lines increasing, corresponding to the infill percentage. Moreover, for the 70% infill, there is no space between lines corresponding to the increase in the infill rate; the number of lines also increases. Therefore, the gap becomes tiny. And then, the material is separated when it touches the bed.

Due to these effects, the part does not have the space. The part significantly becomes a solid type for 80%. There is no space in part. This can get dense and withstand the force and any other effect. But the weight is heavier, and material consumption and printing time are also higher. In 90% infill, the part is denser and has more robust mechanical properties. The number of infill lines is increasing, and the cost is higher because time and material consumption are high. Whereas for the full percent (100%) infill, the part has become entirely solid, so the density and weight of the part are increased. Moreover, the number of lines, utilization of materials, and production time are the highest than any other infill percentage.

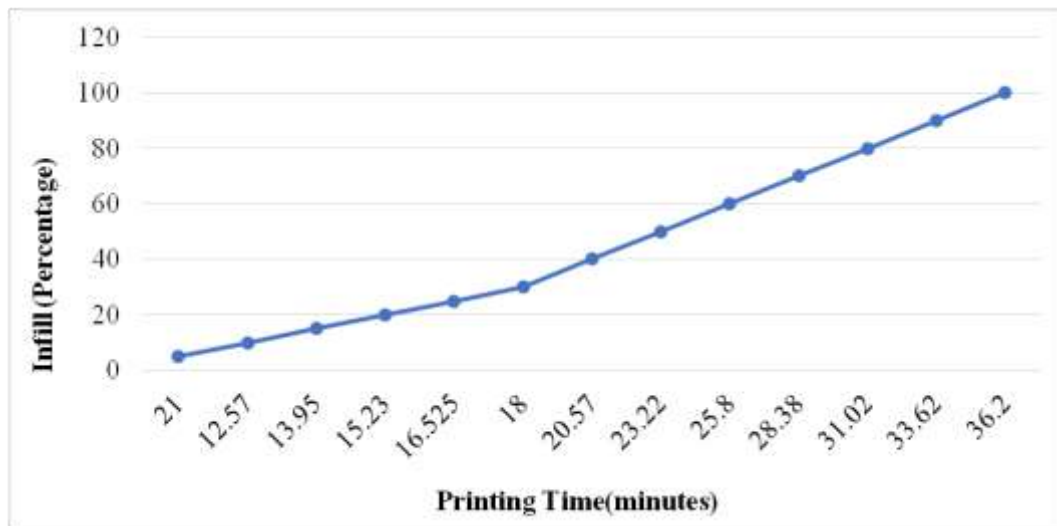


Figure 1. The relation of the infill percentage and printing time for the rectilinear infill pattern.

In conclusion, the thickness of the lines is decided by the gap between the bed and the nozzle. As the expansion rate of the material depends on this gap, the thickness of the line varies according to the material's expansion. If the distance is very close, the expansion rate is high, and the line is thicker. Moreover, this expansion rate of the material also depends on the slurry.

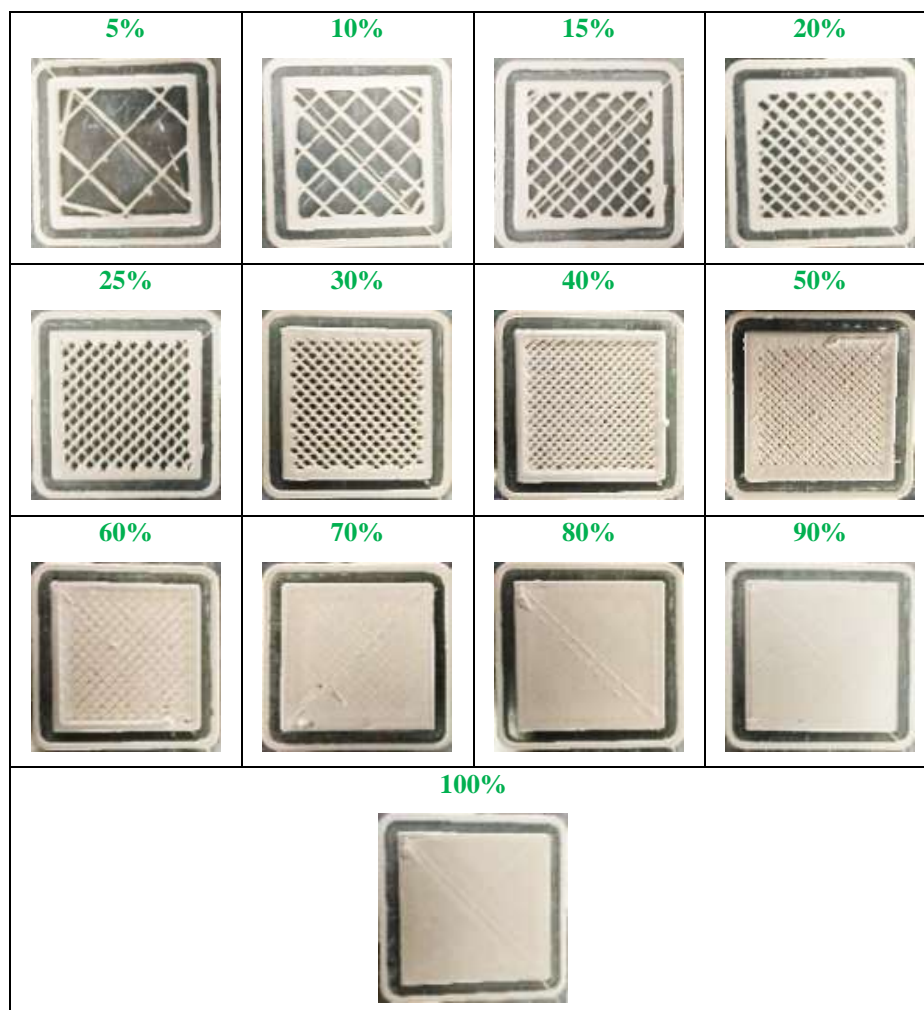


Figure 2. The infill design and infill percentages of the rectilinear infill pattern.

3.2. Line infill pattern

The detailed data of the printed part for the line infill pattern is presented in table 2. Figure 3 describes the relationship between the printing time and infill density. The various infill densities are shown in figure 4. For a 5% infill percentage, there is very little material consumption and printing time. There are so many spaces in part. It is lightweight and has less density, so the withstand force is also less. The increase in the infill percentage to 10, the number of lines, the printing time, and material usage are also high. As a result, the density and weight of the part also increase. The other mechanical properties are more robust because the amount of space is decreased. In the 15% infill, the number of lines is about 343, and the production time is 14.25 minutes. The weight is not heavy, and the gap of lines in the part becomes less. Therefore, the amount of resistance force and density is slightly higher.

At the 20% infill density, the number of lines is higher by 24 lines than the 15% infill percentage. Compared to the less infill percentage part, the space in part is less; heavier weight and compact density can be obtained in this part. The amount of material consumption, printing time, and the number of lines increase in the 25% infill. Therefore, density, weight, and other mechanical properties are also increased. Increasing the infill percentage to 30%, the number of lines and the production time also increased. Moreover, the spacing between lines is decreased, so the vacuum in part is reduced. This increases the density and weight of the product, and then the other properties (such as stress, strain, deformation, etc.) of the part are also improved. For 40% infill, the number of lines slightly increases, so the amount of material consumption is more. Therefore, the time takes a little longer to complete the part, but the density of the part becomes high. The space area inside of the part is less. Moreover, the weight of the part is increased as well. On the other hand, the mechanical properties of the part are improved. The gap between lines is minimal in 50% of the infill pattern. The printing time and the number of lines are increased. The weight is heavier, but the density of the part is better. Moreover, the amount of material usage is increased, and the part's mechanical properties are advanced. For 60% infill density, the space in part is slightly decreased because the infill percentage is higher. Therefore, the material requirement and the time to print the part are higher. The part's weight, density, and other properties (mechanical properties) are improved.

Table 2. *The printing time and printing parameters of the line infill pattern*

Line			
Infill (Percentage)	Printing time (minutes)	Number of lines	Height of the printed part (mm)
5	11.02	301	60×60×2
10	12.97	325	60×60×2
15	14.35	343	60×60×2
20	15.77	367	60×60×2
25	17.05	385	60×60×2
30	18.33	409	60×60×2
40	20.87	451	60×60×2
50	23.43	493	60×60×2
60	26.02	535	60×60×2
70	28.27	577	60×60×2
80	31.12	613	60×60×2

90

33.67

655

60×60×2

In the 70% infill design, the part is an almost solid state, and the gap is scarce in part. So, the weight, material usage, density, and resistance to load are increased. The number of lines, materials, and time consumed to print the part becomes growth for 80% infill density. There is no space in part due to the effect of material expansion and the increase in the infill percentage. Therefore, the part is quite a solid type in this infill percentage pattern. Consequently, some mechanical properties such as; weight, density, hardness, strength, etc., are improved.

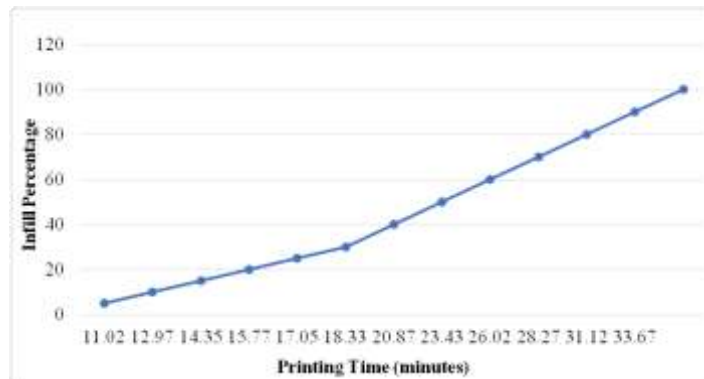
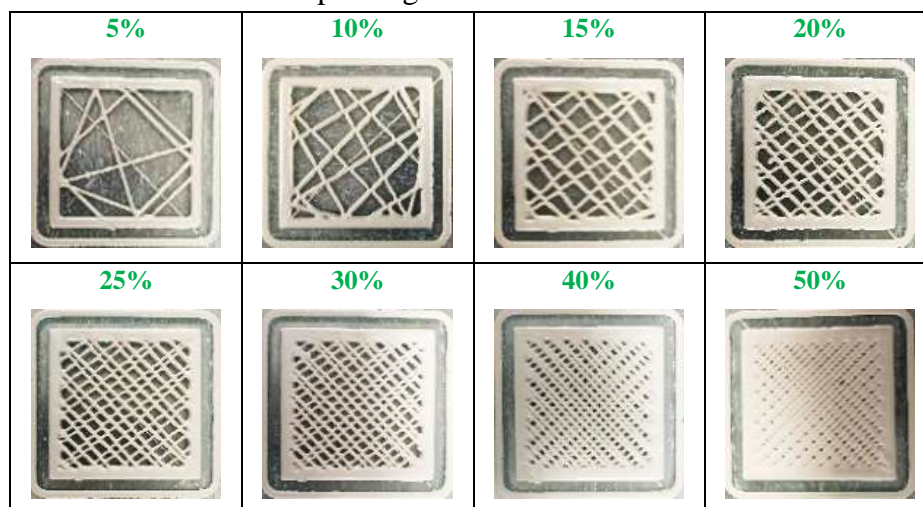


Figure 3. The relation of the infill percentage and printing time for the line infill pattern.

For 90% of infill for this pattern, the vacuum, in part, is less and becomes a robust solid state. The infill pattern type is not found. The weight is heavy, and the density is higher. Moreover, the mechanical properties are advanced. In addition, the time to print, the amount of used material, and the number of lines are high to print the part. There is no space in the part to print a 100% infill percentage. Therefore, no printing is possible for a 100% infill pattern. In summary, the number of lines, printing time, and other characteristics of the part are different according to the infill density.

3.3. Concentric infill pattern

The details of the printing time and parameters of the concentric infill pattern are shown in table 3. Moreover, the relationship between the printing time and infill density for this pattern is shown in figure 5. Figure 6 shows the individual infill percentages of this pattern. In this type of infill pattern, the shape of the part is like a shell or sleeve type for the amount of 5% infill. The number of lines and the printing time is more than the rectilinear and line patterns.



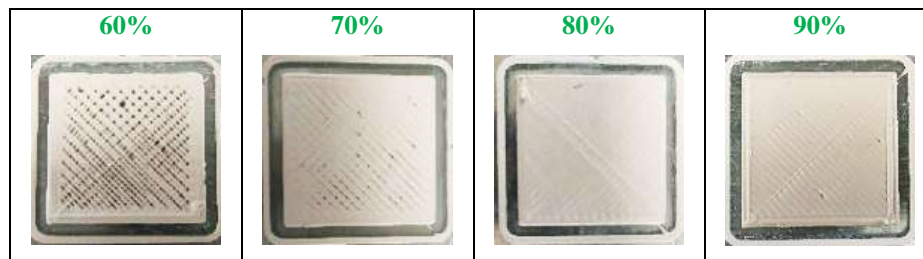


Figure 4. *The infill design and infill percentages of the line infill pattern.*

Moreover, the material used is also higher than in the previous patterns. But strength, strain, the resistance of force, etc., are less than the above infill pattern types. The space, in part, is vast. Although the amount of infill percentage is increased to 10%, the infill line in the part is separate. Therefore, the part's density and other mechanical properties are not improved because of the lack of supporting force in each part. The 15% infill density is less space in the part because the number of pattern lines is increased, corresponding to the infill percentage. However, this pattern type is a sleeve shape, so the infill lines are separated into individual profiles. In addition, the part is not united because the infill lines are not connected with each other. Therefore, each infill line's density, weight, and other mechanical properties are also different. Increasing the percentage of the infill by 20%, the number of pattern lines is more. The printing time and the amount of material required are more. The gap in the line is becoming closer. However, there is just a sleeve shape, and they are not in contact with each other, so the infill line is individual. These results can reduce the specific density, weight, and resistance force. Moreover, these cannot be used as a whole part. It is suitable for users to prefer the dimensional of individual infill lines. The 25% amount of infill percentage is only slightly different from the 20% infill pattern. There is less space between lines because the number of lines is improved. But the infill line in the part does not support each other. Therefore, the weight, density, and other mechanical properties are assigned by individual parts corresponding to the infill line and their dimension. For 30% infill density, the number of lines and the printing time also increased.

However, the printing lines are individual in part, and there is no link to each other printing line. So, the resistance force, the density of the part, and the weight are separate for each print line. In 40% infill, the number of lines, the amount of material usage, and the production time are increased, corresponding to the amount of infill percent. But there is still space in part. There is no improvement in the part's specific density, weight, and other mechanical properties because the printing lines are individual conditions. For the 50% infill percentage, the line spacing is significantly less and close to each other. They did not wholly bind, except the outermost printing line is combined. So the printing lines are still separated. Therefore, there is no whole part printed. Consequently, the mechanical properties, weight, and density are also individual, corresponding to the individual printed lines. In 60% infill density, the flow is less due to the reduced pressure effect. Therefore, the thickness of the printing line is small, and the lines are not binding. But almost all the printing lines bind each other as the infill percentage increases, and the material is diffused when touching the bed. After that, the part becomes a unit product. But the density and other mechanical properties of force resistance are weak. For the infill percentage of 70%, the printing lines are binding to each other except for the lines with less material which is the effect of the low pressure as the printing infill percentage is higher and the gap between the infill line is reduced.

Table 3. *The printing time and printing parameters of the concentric infill pattern*

Concentric			
Infill (Percentage)	Printing time (minutes)	Number of lines	Height of the printed part (mm)
5	11.68	316	60×60×2
10	12.93	334	60×60×2
15	14.17	352	60×60×2
20	15.4	370	60×60×2
25	16.63	388	60×60×2
30	17.97	424	60×60×2
40	20.52	460	60×60×2
50	23.03	496	60×60×2
60	25.63	550	60×60×2
70	28.17	586	60×60×2
80	30.75	583	60×60×2
90	33.3	613	60×60×2
100	35.4	643	60×60×2

It is due to the spread of the material when it comes into contact with the platform. In addition, the inside of the innermost layer is like a hollow, which is very small. But the product is as like a part. At the same time, the structural properties of the part are poor. For 80% infill, according to the high infill percentage, the consumption of material and printing time is also high. Moreover, the number of lines is increased, and the space in part is absent. Sometimes, the flow is a shortage due to the slurry and pressure effect. However, all the printing lines combine because the space between each line is minimal, and the material expands the line. In the 90% infill percentage, the binding of the line is significant, and the part becomes solid type. Therefore, the weight and density can be expressed for the whole part. After that, the resistance force and other mechanical properties are stronger due to like the solid type. In the 100% infill density, the part becomes a clear solid type, and the binding capacity of the printing line is improved. There is no gap in the part between the infill lines. Therefore, the part is dense, and the weight of the part is increased. This fact increases the mechanical properties of the part. The printing time and the amount of material required are also growing because the number of lines is increasing.

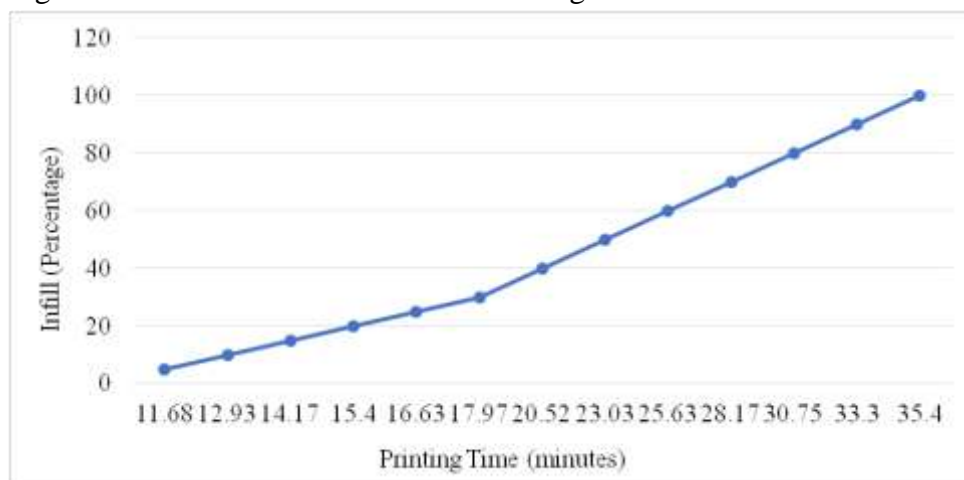


Figure 5. *The relation between the infill percentage and printing time for the concentric infill pattern.*

3.4. Honeycomb infill pattern

The printing time and parameters of the honeycomb infill pattern corresponding to their infill percentage are presented in table 4. Figure 7 shows the relation between the infill percentage and printing time for the honeycomb, and figure 8 describes each infill density for the honeycomb infill pattern.

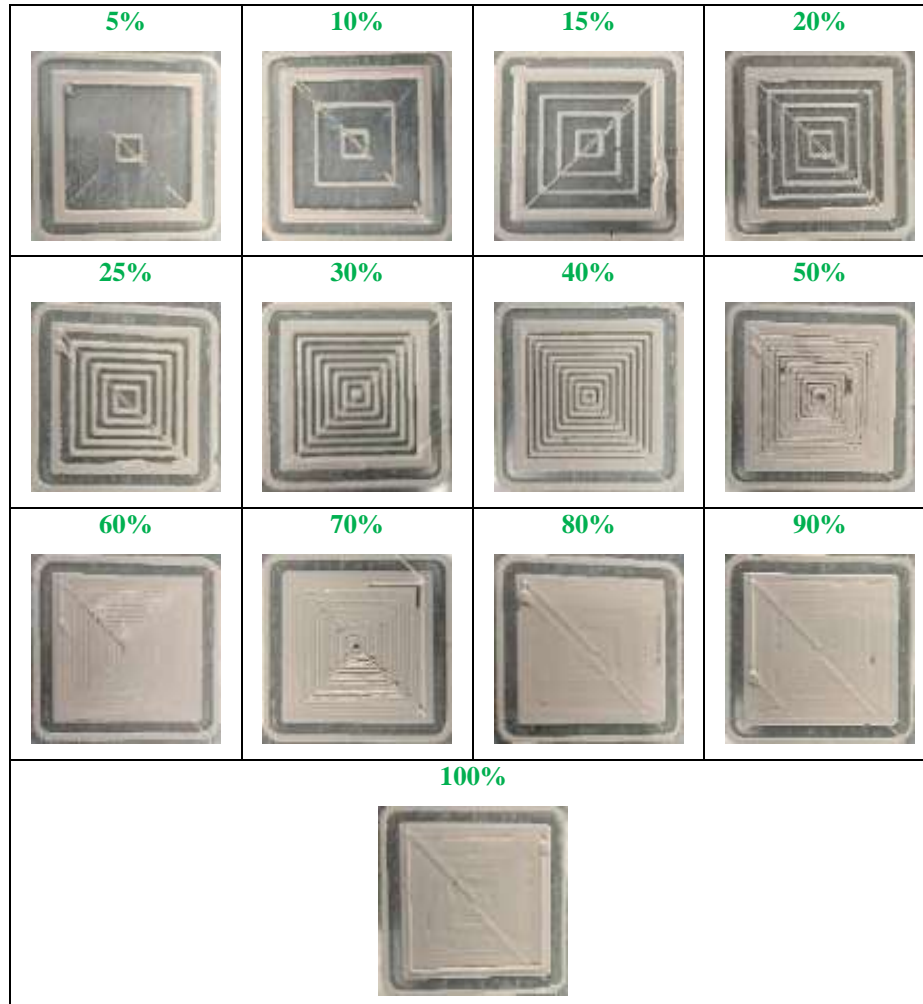


Figure 6. *The infill design and infill percentages of the concentric pattern.*

The observations of the experiment about the honeycomb infill pattern are detailed as per the infill percentage. In this 5% infill pattern, the printing time was decreased because it reduced the layer's height. But the number of lines and material consumption is slightly higher than other patterns of 5% infill. The vacuum is large, the part being the less infill percentage. For the 10% infill pattern, the layer height has been reduced to 1.2mm, so the time is less to print the part. However, the material requirement is more to print this pattern as the number of pattern designs increases. Therefore, the vacuum is small in part. Moreover, this pattern design supports each other lines by contacting each point. This results in increases in weight, density, and other mechanical properties. The pattern design is more and more to accommodate the 15% infill percentage. In addition, the pattern design is neater, and the amount of gap is low in the part. Therefore, the printing line and time are higher to produce the part. The part is stronger due to the reaction force to each other of the infill pattern. The amount of density, the resistance forces, and other properties of the part improve. In this 20% of infill percentage, the printing line is more than 121 lines than the 15% infill, but the printing time is increased slightly. The clearance, in part, is small, and the material utilization is so high.

In contrast, the part's mass and natural properties rise. For 25% infill density, reducing the layer height to one-half, the time also declines to print the part. As a result, the number of lines is directly proportional to the layer's size. However, the percentage of infill and the occupied area of the pattern in part is higher. Therefore, the gap area between the pattern is less, and the other mechanical features are robust. Moreover, the pattern design is neater and pretty. At the 30% infill, although the layer height is the same as the 25% infill, due to the increase in the ability of infill percentage to 30%, the number of lines and the production time are slightly high. The number of pattern designs is also increasing, so the space area in part is low. Consequently, the ability of the part, such as weight, density, stress, strain, etc., becomes improved. For the 40% infill, the number of lines and the printing time is higher than 30% infill. Once, the flow is occurring shortage, but this cause is very short and affects only one pattern design. Therefore, there is no effect on the other properties of the part. The internal space area of the pattern is very narrow due to increasing the infill percentage. In 50% infill, the flow rate is not constant as the pressure in the nozzle is low because the amount of material in the nozzle is decreased. So this can cause an interruption of flow during the printing of the part. According to the part's structure, the part's mass and other characteristics are better, and the clearance volume in the part is low in quantity. But the number of lines, the material usage, and the printing time are relatively high.

Table 4. *The printing time and printing parameters of the honeycomb infill pattern*

Honeycomb			
Infill (Percentage)	Printing time (minutes)	Number of lines	Height of the printed part (mm)
5	8.55	302	60×60×1.2
10	9.78	369	60×60×1.2
15	10.97	458	60×60×1.2
20	11.88	579	60×60×1.2
25	7.55	468	60×60×0.6
30	8.00	554	60×60×0.6
40	9.00	777	60×60×0.6
50	9.83	1040	60×60×0.6
60	10.67	1359	60×60×0.6
70	11.45	1746	60×60×0.6
80	12.17	2187	60×60×0.6
90	12.83	2661	60×60×0.6

The number of lines in this 60% infill percentage is significantly increased, and the time required to print the part is slightly more than 50% infill. The amount of material expended is high, and the space area, in part, is minimal due to the expansion of the material. Therefore, the pattern design of the part is not explicit. But the weight, density, and other mechanical properties are increased. In this 70% infill pattern, the number of lines is increased by about 387 lines than 60% infill. However, the time increment is only 0.78 minutes. Therefore, the time increment is less compared with the increment of lines. The flow problem occurred during printing because the amount of material in the syringe was less, and the pressure in the syringe was low. Except for this flow interrupt area, other areas in part have no space. But this space is tiny. This lack of space is caused by a higher amount of infill percentage and the expansion of the material. The shape of the product is as like a solid part. The number of

lines for this 80% infill structure is higher than 70 percent. There is no space in part, and the capacity of binding between the lines is perfect. The surface of the part is as like a plane surface, and it is not obviously found in the shape of the honeycomb pattern. The pattern is only like a waveform. A small cavity is located on the surface because of the bubble flow of the material. However, it is very tiny. The print structure is heavy and dense. Therefore, the material's strength and other structural properties are so high. In the 90% infill part, the piece is entire of a solid structure form. There is no clearance in the component. The number of lines, printing time, and material consumption are too high. But if the incremental rate expresses the time, it is less than the previous infill percentages. The part becomes heavyweight, and density also rises. Whereas the resistance force and mechanical characteristics of the part are more potent.

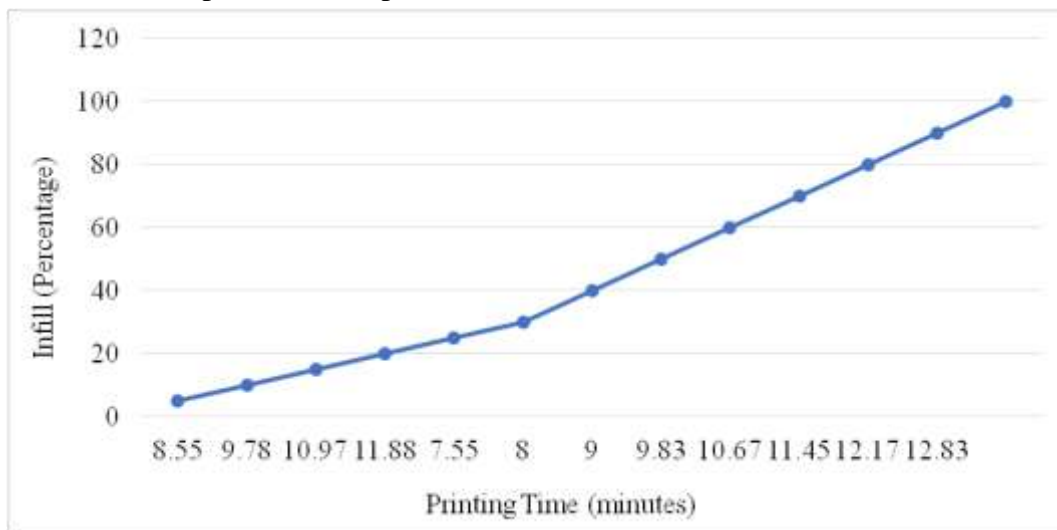
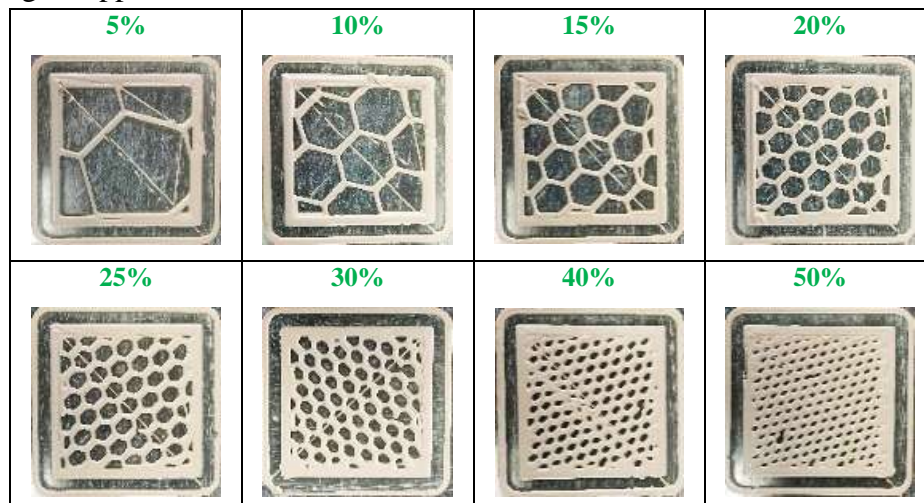


Figure 7. The relation of the infill percentage and printing time for the honeycomb infill pattern.

For a 100% infill pattern, it is impossible to print the total percentage because there is no space in the part. The part is thicker if the print is for the 100% infill pattern. Therefore, the part increases in weight, and the cost increases to print. But, other abilities and attributes of the part are not significantly different from the 90% infill structure. In summary, this infill pattern is more potent than any other infill pattern because this pattern type is like a network with a stronger support form to each other.



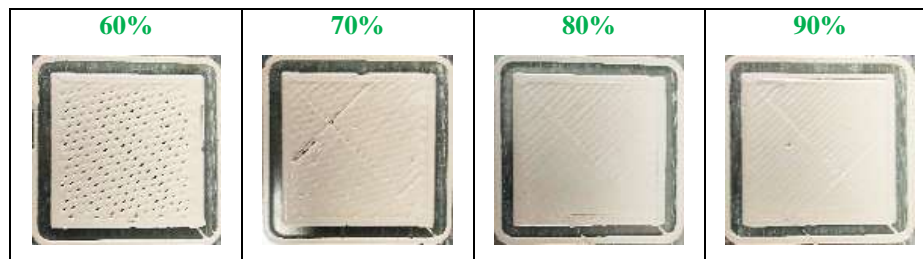


Figure 8. The infill design and infill percentages of the honeycomb infill pattern.

3.5. 3D Honeycomb infill pattern

The printing time and parameters of the 3D honeycomb infill pattern are shown in table 5. The relationship between the printing time and infill percentage is shown in figure 9 and figure 10 shows the infill density of patterns from 5% to 90%. In the 5% infill percentage for this pattern, the layer height is 0.6mm, and the number of lines is 253. The printing time is 5.05 minutes, and the amount of material used is more than any other infill pattern. The vacuum, in part, is wide. The part is lightweight, and the density is poor. The part's strength is weak due to the effect of the vacuum. The height of the layer is not changed for 10% infill density. But the infill percentage increases, so the number of lines and the printing time increase. Therefore, the demand for materials and pattern design is increasing. The space between lines is narrow, and the weight of the component increases. For the 15% infill, the number of lines is more than 74 lines compared with the 10% infill, and the time required to print the part is over 0.69 minutes than the 10% infill structure.

The gap between the infill lines is reduced in the part, and the part's weight is slightly increased. The pattern design is neat and pretty. In the 20% infill pattern, the total number of lines is 455 lines, and there are 86 more lines than in the 15% infill pattern. But the time requirement is only 0.36 minutes than the 15% infill part. The material consumption is slightly rising, and the space area in part becomes less. The weight, density, and other structural attributes are increased. For 20% infill density in this type of pattern, the printing time is more, 0.54 minutes than 15%, and the number of lines is 118 lines increasing over the previous infill percent (15%). The material consumption rate is slightly high, and the gap space between the pattern line is more contract. Therefore, the clearance volume in part is reduced. Consequently, the part's mass, density, and strength are somewhat improved. For the 30% infill percentage, although the number of lines is extra by 124 lines than 25% infill, the time taken is increased to only 0.33 minutes to print the part. This printing time increment is less amount compared with the increment of lines. The utilization of material is also increasing. Therefore, the vacuum area is less in part, and the other structural properties (such as; stress, strain, density, etc.) grow. The whole printing time of the part is almost 9 minutes, and the number of lines is 1053 lines for 40% infill type. The material consumption is high, and the weight and density of the part are increased. The space area in part is small, and the mechanical properties of the component are advanced.

Table 5. The printing time and printing parameters of the 3D honeycomb infill pattern

3D Honeycomb

Infill (Percentage)	Printing time (minutes)	Number of lines	Height of the printed part (mm)
5	5.05	253	60×60×0.6
10	5.58	295	60×60×0.6
15	6.27	369	60×60×0.6

20	6.63	455	60×60×0.6
25	7.17	573	60×60×0.6
30	7.5	697	60×60×0.6
40	8.33	1053	60×60×0.6
50	9.17	1510	60×60×0.6
60	9.73	1975	60×60×0.6
70	10.72	2645	60×60×0.6
80	12.00	3474	60×60×0.6
90	12.98	4195	60×60×0.6

In this 50% infill percent, the flow problem was found at almost finishing the printing part. Because the amount of material in the pump is less and the pressure is low. Therefore, the flow rate of material is significantly less. As a result, the printing line is very thin, and the pattern quality of the part is not the same as any other pattern in part. So, the part is not good looking, and different mechanical abilities cannot get the perfect condition. For the 60% infill density, the number of lines is higher than 465 lines than 50% infill, and the incrementation in production time is 0.566 minutes. The line gap is very narrow, and the lines are in close contact. There is no original pattern, and it is like a straight line. The amount of material usage is rising, and the part becomes heavier. But the other characteristics of the part are improved. In the 70% infill percent, there are more than 670 printing lines than in the 60% infill pattern, and the total manufacturing time for the whole part is 10.72 minutes. There is no space in part because of the growing number of lines and expansion of the material. The density and the resistance properties of the part are better. In the 80% infill for this design, corresponding to the higher infill percentage, the number of printing lines also increased. There are 3474 lines, and the printing time is 12 minutes to print the part. Except for a small hole found near the side due to the bubble effect of the material and the remaining area of the part is perfect. The part is completed with the solid type, and the surface is like a plane.

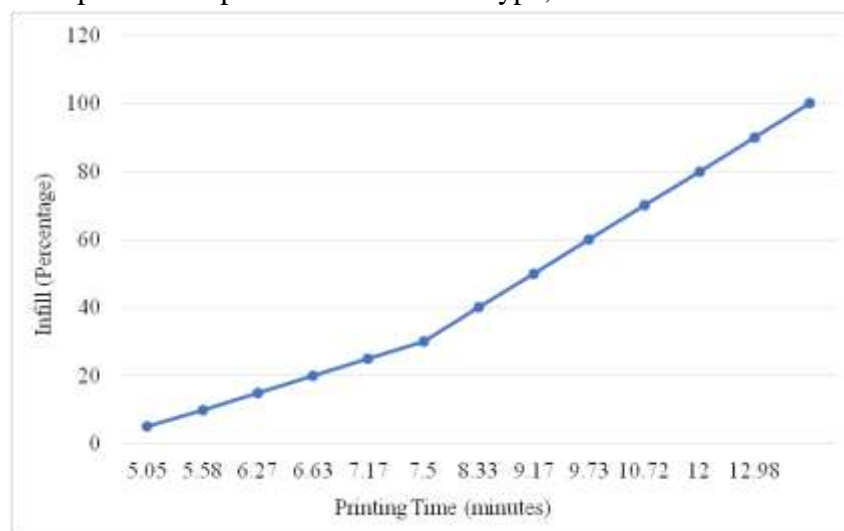


Figure 9. The relation of the infill percentage and printing time for the 3D honeycomb infill pattern.

The weight, density, and mechanical features are more advanced. The amount of material consumption in the 90% infill percentage is significantly high, and the printing lines are 4195. The manufacturing time is nearly 13 minutes long. The part is heavier and more compact. But the last line is thin because the material flow rate is less due to pressure and reduces the amount of material in the extruder. The part possessed properties corresponding to the amount

of material in part. This 100% infill percent is unachievable because there is no area to print in part. Moreover, there are no apparent changes in the shape and properties of the part compared with 90% infill. To sum up, in this infill pattern type, the material utilization is more than in the honeycomb infill pattern. But the printing time is less than the honeycomb type. Moreover, although the pattern shape is like a honeycomb, the structure is different, and this type of structure is like a pillar type. Therefore, this is not strong as the like honeycomb.

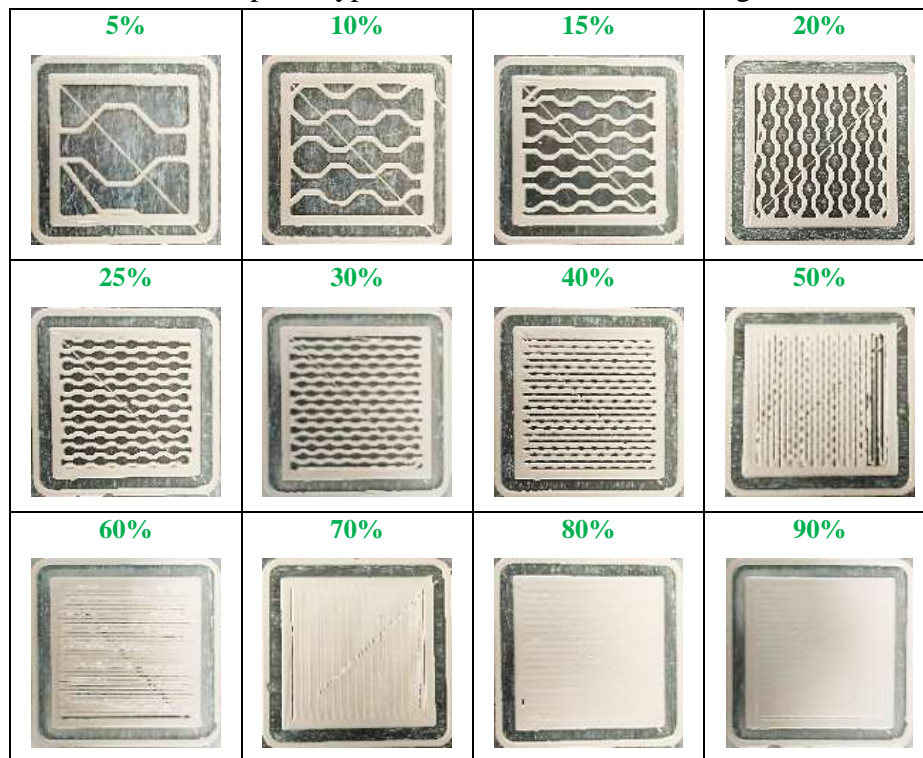


Figure 10. *The infill design and infill percentages of the 3D honeycomb infill pattern.*

3.6. Hilbert curve infill pattern

The data for the Hilbert curve infill pattern, infill density, and their related parameters are described in Table 6. Moreover, the relation between the printing time and individual infill percentage is shown in figure 11. The variation in the infill density is shown in figure 12. In general, this 5% infill pattern is less material requirement and lead time reduced to print the part compared with other infill designs. The layer's height is 0.6 mm, and the length and width of the part are equal to 60 mm. The number of infill lines is 247, and the printing time is 4.9 minutes. The pattern design is an open one-end, and the space area is partly enlarged. Therefore, the withstand force of the part is weak and lightweight. For 10% infill, according to the experiment data, the number of lines is higher by 27 lines than 5% infill. The total printing time is 5.367 (nearly 5.5) minutes. The vacuum portion in the part is high, so the part's density is inferior. The strength and other properties of the part are also poor. In this 15% infill percentage, the total number of lines is 318, and the manufacturing lead time is nearly six minutes. But the clearance volume is not significantly reduced, and the part's characteristics also have no changes compared with the 10% infill. For this pattern's 20% infill density, the amount of infill and the printing time is slightly increased. The pattern's infill percentage is higher, but the vacancy area of the part left is high. Therefore, the part's structural properties are only slightly improved than the previous infill percentage. In this 25% infill percentage, the total number of lines is 400, and the production time is 6.68 minutes. The amount of material utilization is increased, and the space area in part is less. The weight of the part is a little rising, but the density of the part is poor. Moreover, the part's

strength is weak because this pattern design cannot be supported for more robust support at the center of the part. For the 30% infill percentage, the production time and the number of infill lines are increased. The mass is increased corresponding to the amount of material used, but the structural characteristics and properties are not significantly improved.

Table 6. *The printing time and printing parameters of the Hilbert curve infill pattern*

Hilbert Curve

Infill (Percentage)	Printing time (minutes)	Number of lines	Height of the printed part (mm)
5	4.9	247	60×60×0.6
10	5.37	274	60×60×0.6
15	5.83	318	60×60×0.6
20	6.25	345	60×60×0.6
25	6.68	400	60×60×0.6
30	7.002	471	60×60×0.6
40	8.00	615	60×60×0.6
50	8.87	812	60×60×0.6
60	9.72	1042	60×60×0.6
70	10.55	1307	60×60×0.6
80	11.45	1610	60×60×0.6
90	12.28	1956	60×60×0.6
100	13.17	2316	60×60×0.6

The clearance volume is reduced due to the effect of the material's infill percent and expansion properties. In the 40% infill density, the number of lines is 144 lines, more than 30% infill, and the total printing time is 8 minutes. Sometimes, the flow rate is not constant due to the effect of pressure inside the pump. Therefore, the thickness of the lines is not equal. The gap space between the lines is narrow. And the shape of the pattern design is not precise in some portions of the part because some lines are in contact with each other due to the flow's effect and the material's expansion when the material is in touch with the platform's bed. For 50% infill, the flow is intermittent, but this cause is significantly less, and all the line thicknesses are nearly the same. Therefore, the pattern design is neat, and the space in part is considerably less. Moreover, the material consumption is slightly increased, and the part's mass is high. The density and other mechanical attributes are also increased. To print for 60% infill density, the total number of infill lines is 1042, and the time taken is about 10 minutes. The line spacing limit is minimal, and the vacuum is also less. Moreover, in some areas of the part is no space because lines are bound with each other. The material consumption is slightly high, and the properties and characteristics of the part are improved. The material consumption and printing time are increased, for 70% infill percentage. The clearance in part is less, and most lines are binding. The part is heavyweight and denser.

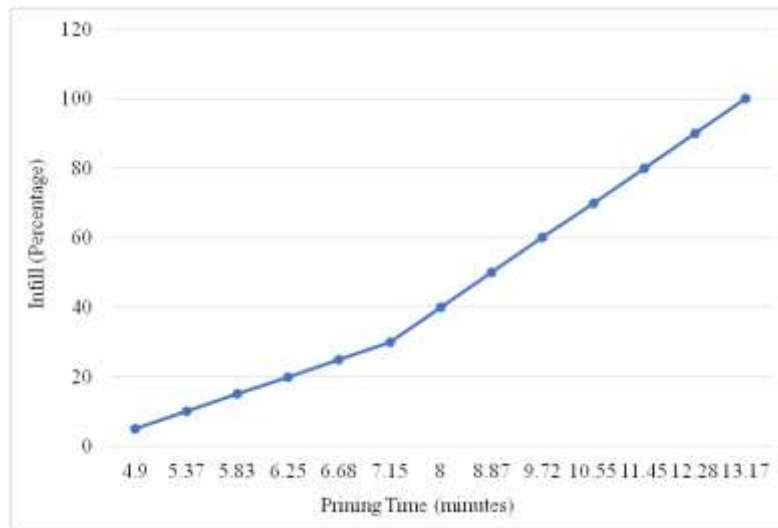
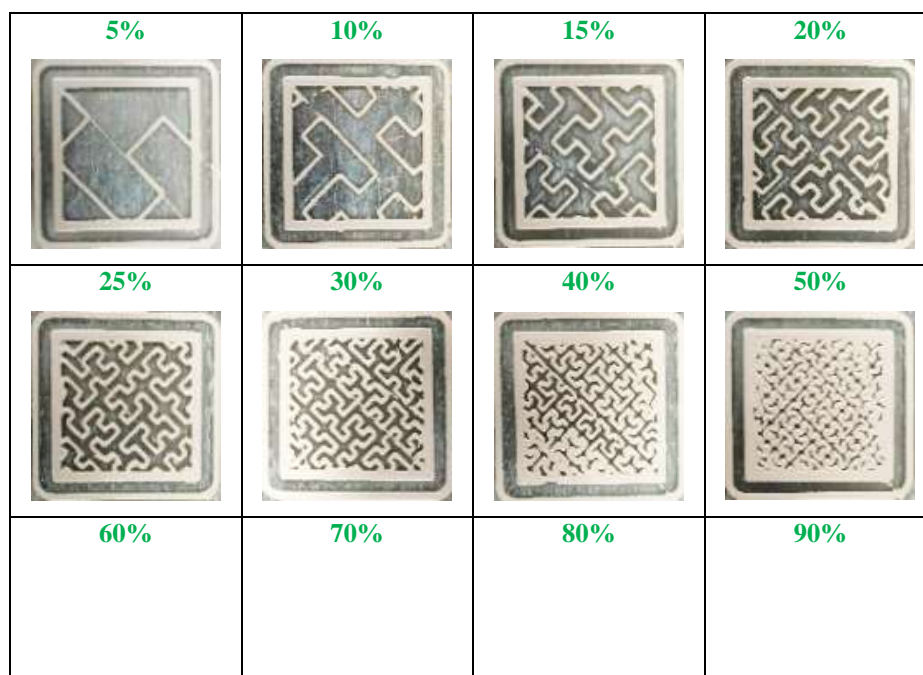


Figure 11. The relation of the infill percentage and printing time for the Hilbert curve infill pattern.

Therefore, this part is slightly strong to withstand the force acting upon it. In 80% infill percent, some area of the part is fully binding and have no gap between lines. But some areas have minimal vacancy areas left. The most binding area is the side of the part. Because of the expansion of the material and the number of lines increased, the gap space is very few in part. Consequently, the mass and weight of the part are also high, and the mechanical attributes of the part are better than the previous infill percentage. For the 90% infill percentage, the total number of infill lines is 1956, and all the lines are bound due to the properties of material expansion. But some areas of the part lack material because of the flow problem. The flow is a shortage due to the loss of material and low pressure in the pump. Therefore, the part is not in a fully solid state. But the weight and mass are rising correspondingly to high material consumption. However, the strength characteristics of the part are weak according to the flowing material shortage. In this 100% infill percentage, the utilization of material and production time are high. However, the properties of the part are not improved. There are many vacant areas in the part because the effect of the pressure in the nozzle is an extrusion problem.



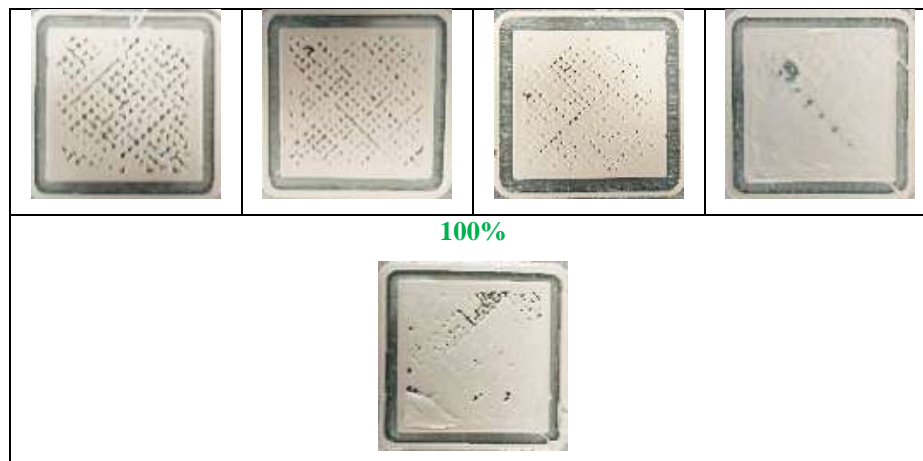


Figure 12. The infill design and infill percentages of the Hilbert Curve infill pattern.

Exactly, this infill percentage is poor than the 90% infill for the structural and other mechanical properties except for the weight.

3.7. Archimedean chords infill pattern

The details of the infill percentage and related parameters are expressed in Table 7. The overview of the infill percentage with the printing time is presented in figure 13, and figure 14 shows the infill percentage variation of the Archimedean chords infill pattern. This 5% infill percentage of this pattern has less material usage and time taken to print the part compared with the previous pattern. Moreover, the vacuum area in part is enlarged. For 10% infill density, the printing time and the number of lines also increase. The space area in part is reduced. But the density and the strength of the part are not significantly improved. In the 15% infill percentage, the distance between the lines is narrow because the number of lines is also increasing. Therefore, the clearance volume in part is reduced, and the material used is a little more. The strength and weight of the part also rise. For the 20% infill, there is more the number of lines to correspond with the infill percentage. The flow condition is no problem, and the gap area is small between the lines in the part. But the density and other properties are not improving compared with the previous (15%) infill percent.

Table 7. The printing time and printing parameters of the Archimedean chords infill pattern

Archimedean Chords			
Infill (Percentage)	Printing time (minutes)	Number of lines	Height of the printed part (mm)
5	4.78	247	60×60×0.6
10	5.03	266	60×60×0.6
15	5.77	303	60×60×0.6
20	6.22	351	60×60×0.6
25	6.65	411	60×60×0.6
30	7.00	481	60×60×0.6
40	7.95	663	60×60×0.6
50	8.8	887	60×60×0.6
60	9.67	1157	60×60×0.6
70	10.53	1479	60×60×0.6
80	11.38	1839	60×60×0.6
90	12.23	2239	60×60×0.6
100	13.1	2694	60×60×0.6

For the 25% infill percentage of this pattern, the flow is intermittent due to the vacuum in the syringe. But there is not an occurrence in a long time. Increasing the infill percentage, the space area of the part is less. The weight and density are more and more. Other structural characteristics are also rising. This pattern has no flow problem for the 30% infill, but the material is accumulated at some of the starting points due to the soft slurry. Moreover, the pattern design is like the same circle and has no precise shape of the chord design. The material utilization and printing time are rising. The space area in part is less and mechanical attributes are also increased. The thickness of some lines is thin due to the less flow of material in the 40% infill. Moreover, the contact point of each other of the lines is thicker than any other line of the part because of the expansion of the material. The vacancy of the part is small, and the mass and strength of the part are better than the previous infill percent. For a 50% infill percentage, the flow shortage often occurred, but its time was only a moment. Therefore, except the thickness of the lines is a little thin, it cannot affect the pattern design of the part. For the 60% infill, the material flow rate is difficult to control for getting a constant flow due to the material leakage above the piston. Its effect can cause intermittent flow and less flow rate during printing. Due to this effect, some printing lines are very thin, and some are the same as the dots. Consequently, the density and other mechanical properties are weak compared with the infill percentage.

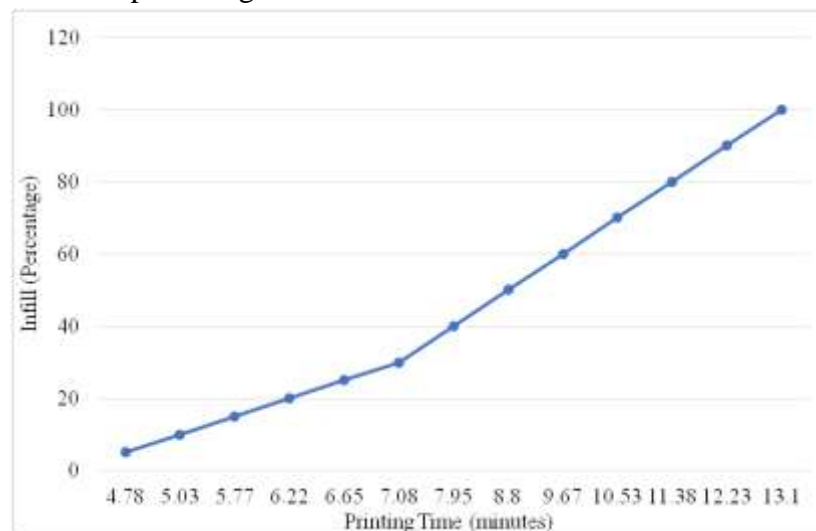


Figure 13. *The relation of the infill percentage and printing time for the Archimedean chords infill pattern.*

For 70% of infill in this type of pattern, all the infill lines are bound, so there is no space in part. Therefore, the part is as like a solid state. However, the unsteady flow finds small holes in the part's surface. The material consumption is high. The density, weight, and structural properties also improved. For the 80% infill percentage, sometimes the flow is a shortage, but this portion is tiny and is like a crack in part. Another area is full of material, and there is no space in part. The mass and density are improved. The strength of the part is also advanced. In this pattern's 90% infill density, the amount of material consumption is high, and there is no vacancy in part because of the increase in the infill percentage. Moreover, the materials expand when it is touching the building platform. The part is in a fully solid state and has more weight. Other mechanical properties are significantly improved. For this 100% infill percentage, the number of lines is increased. But the flow is intermittent due to the less pressure in the nozzle. Therefore, in part are found many small vacuums. Its effect can cause poor density, mechanical and other properties.

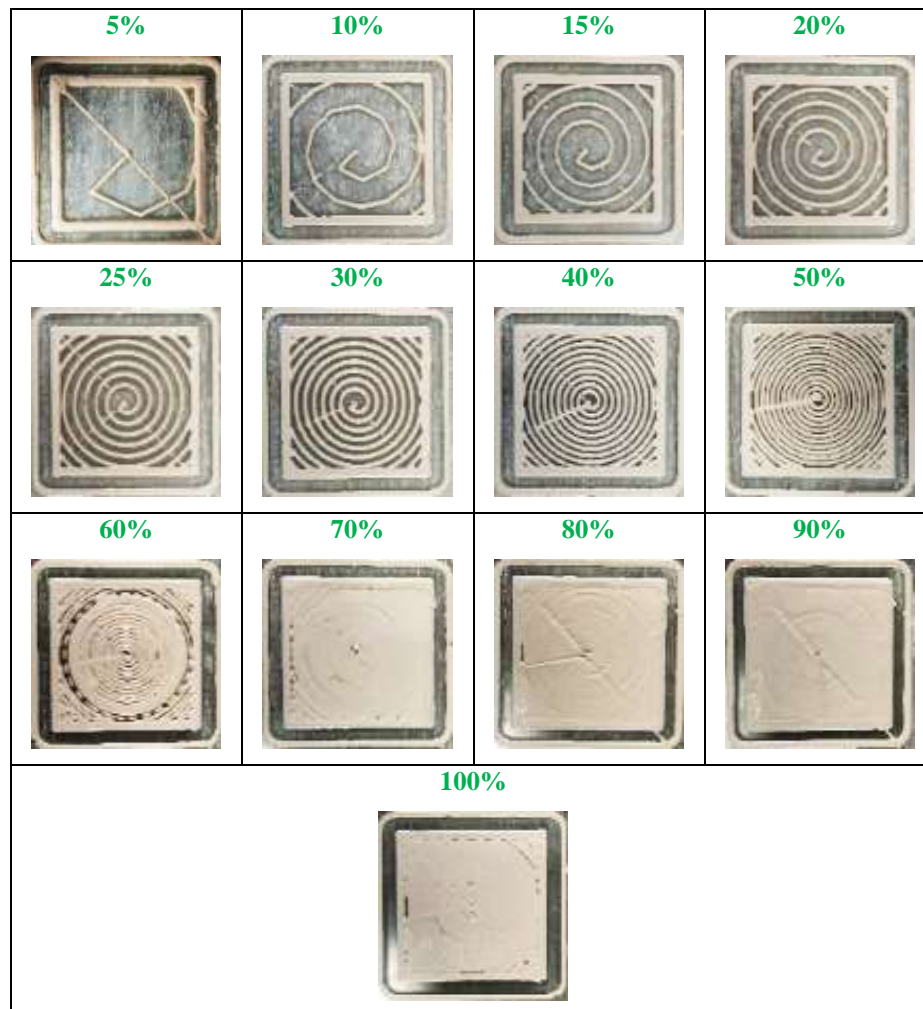


Figure 14. The infill design and infill percentages of the Archimedean chords infill pattern.

3.8. Octagram spiral infill pattern

The relation between the printing time and infill percentage is shown in figure 15 and infill pattern and their percentage are shown in figure 16. Table 8 expresses the individual infill percent and related parameters of Octagram spiral infill pattern. According to the figure, for the 5% infill pattern and percentage, the occupancy of the part is enlarged, and the shape of the part is rectangular. Therefore, the density and weight are less. The resistance and structural attributes are also weak. For this pattern's 10% infill density, the flow has no problem, and the pattern design is neat. The vacuum area is reduced compared with the 5% infill pattern. Therefore, the weight and other properties are a little increased. In the 15% infill, according to the increase in the infill percentage, the infill lines are more and more. Therefore, the gap space area in part is less. The flow is discontinuous only while printing the skirt, but there is no flow problem while printing the actual part. The material usage and printing time are little rises. However, the mechanical properties of the part are not significantly changed. The shortage of the flow occurred two times in the 20% infill density. But the duration time of shortage is considerably less. Therefore, the area of the lack of material is minimal. The line spacing becomes narrow because the infill percentage is increased. The attributes of the part properties are a little improved.

Table 8. The printing time and printing parameters of the Octagram Spiral infill pattern

Octagram Spiral			
Infill	Printing time	Number of lines	Height of the printed part

(Percentage)	(minutes)		(mm)
5	4.73	250	60×60×0.6
10	5.27	282	60×60×0.6
15	5.63	284	60×60×0.6
20	6.02	314	60×60×0.6
25	6.48	348	60×60×0.6
30	6.82	362	60×60×0.6
40	7.6	395	60×60×0.6
50	8.42	459	60×60×0.6
60	9.2	467	60×60×0.6
70	9.97	507	60×60×0.6
80	10.75	537	60×60×0.6
90	11.53	587	60×60×0.6
100	12.3	624	60×60×0.6

For the 25% infill percentage, one time, the flow occurred discontinuously during the printing of the borderline. However, there is no problem with the flow while printing the part. The pattern design is neater, and the vacuum area in part is less. The weight and material consumption are increased. The structural characteristics are also advanced. The flow condition is perfect for this pattern's 30% infill density, and the printing time is more. The demand for material is increasing due to the more significant number of lines. The part's mass is increased, and the vacancy area in part is less. For the 40% infill, according to the increase in the percent of infill, the number of infill lines and the lead time to print the part is high. Sometimes, flowing off the slurry is intermittent, but this time is short, and the area of material shortage is minimal. In this 50% infill pattern, the number of infill lines increased by 64 lines, more than 40% infill. Therefore, the amount of vacuum in part is less. Moreover, some lines are binding in the part because the space is less between the lines, and the material is expanded. So, the density of the part is improved. The weight and other mechanical properties are also increased. For the 60% infill, due to the decreasing material in the syringe, the pressure is also decreased. Therefore, the flow occurs intermittently flow. Some infill lines combine because of the expansion properties of the material and the less space between lines. Especially in the corner of the part are more binding the lines due to the pattern design. For this 70% infill percent, the material shortage occurred due to the low pressure in the nozzle during the extrusion.

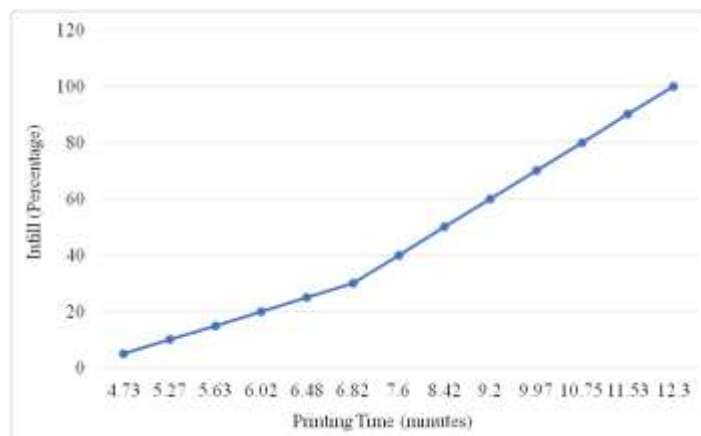


Figure 15. The relation of the infill percentage and printing time for the Octagram spiral infill pattern.

However, this effect is insignificant because the infill line spacing is narrow and the expansion of the material. The number of lines and the printing time is increased. But, the part's characteristics are only slightly changed compared with the 60% infill part. In this pattern for 80% infill, the hole is found in some areas of the part due to the intermitted flow of material. The space area, in part, is not significantly reduced more than the previous infill percentage. The density and other structural properties are only slightly increased. For this pattern's 90% infill density, there is no space area in the part, and the whole part is filled with the material. The part is solid, and the surface is like a plane. But some places have thin cavities due to the effect of air bubbles during the extrusion process. The density of the part is high, and other mechanical properties are also improved. For the 100% infill percentage, the material consumption and the printing time of the part become rise. Therefore, the weight and density of the part are slightly increased. However, other properties and characteristics of the part are not significantly changed compared with the 90% infill. In summary, most 100% infill patterns are the same as a solid type and not a transparent form of pattern design. Moreover, the part's properties are not clearly different from the 90% infill.

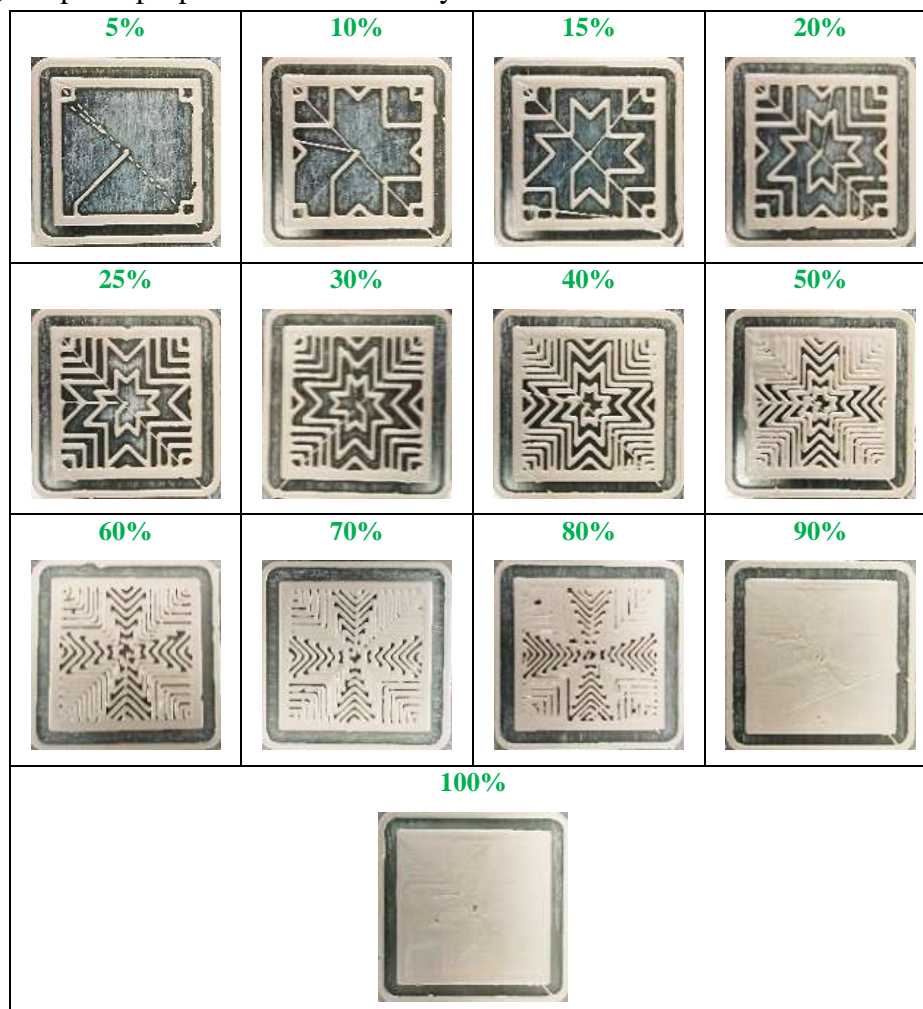


Figure 16. The infill design and infill percentages of the Octagram spiral infill pattern.

The graph (figure 17) describes the relationship between the printing time and infill percentage. Generally, the printing time is extended when the infill percentage is significant. The highest time is about 35 minutes in a rectilinear infill pattern for 100% infill, and the lowest time is 4.73 minutes for an octagram spiral with 5% infill. For 5% infill, the rectilinear is the highest time consumption, about 36.2 minutes. The line is 11.02 minutes, and the concentric is 11.68 minutes. The honeycomb and the 3D honeycomb are 8.55 and 5.05

minutes, respectively. The printing time of the Hilbert curve is about 5 minutes, and the archimedean chord is over 13 minutes.

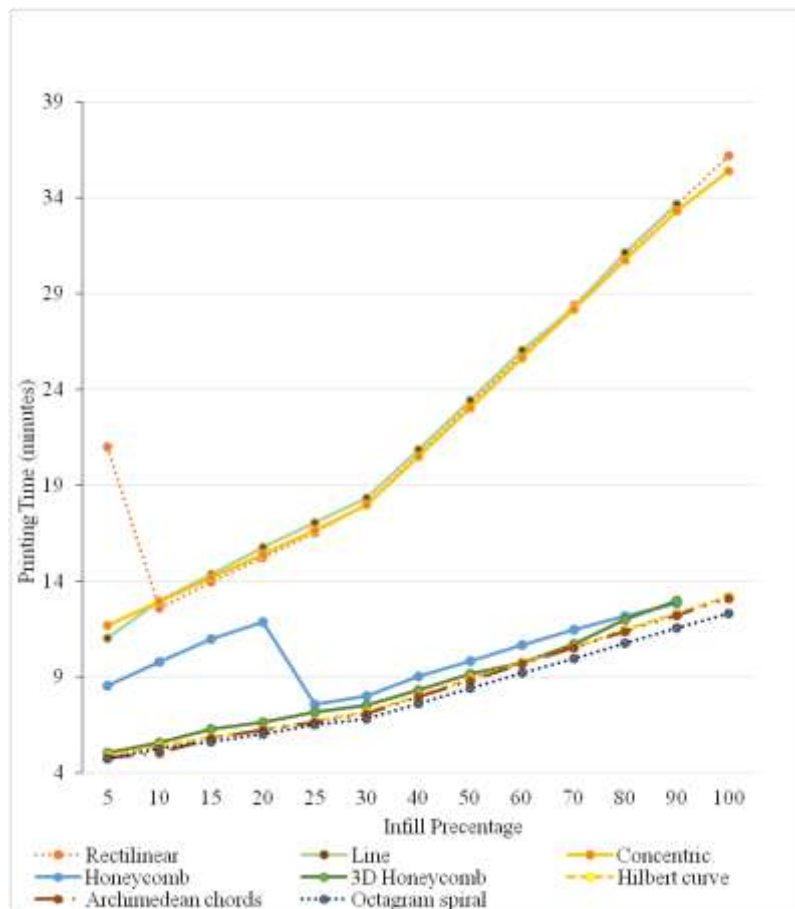


Figure 17. The relation of the infill percentage and printing time for all patterns.

From 10% to 100% infill, the printing times are nearly the same to produce the part for the line, the rectilinear, and the concentric. Moreover, the time consumption of the Hilbert curve and Archimedean chords are mostly the same for all infill percentages. For all infill percentages, the printing time of the octagram spiral is the lowest compared with the other infill pattern. In summary, the printing time differs depending on the infill pattern and density.

4. Conclusion

To sum up, the line, rectilinear and concentric lines have higher printing times than other infill patterns. The reason is that the printing part's thickness for these infill patterns is more than different infill patterns. The parameter of the part for these infill patterns is $60 \times 60 \times 2$. The number of lines in rectilinear and line infill patterns is the same for all infill percentages, but the printing time is different. The rectilinear pattern has more printing time than the line pattern, about 3 minutes for each infill percentage. However, the number of printing lines is the same for both rectilinear and line patterns. But the amount of space is not the same in part, because of the expansion rate and due to the pattern design. Therefore, the line pattern has no space to produce 100% infill density. The concentric infill pattern has more infill lines than the line and rectilinear pattern, but the number of infills decreases from 80% infill density. However, the printing time is less than the line infill pattern except for 5% infill density. The parameter of the honeycomb, 3D honeycomb, Hilbert curve, Archimedean chords, and octagram pattern are $60 \times 60 \times 0.6$. Although the number of infill lines of the honeycomb infill pattern is less than that of the 3D honeycomb infill pattern, the printing time is higher than that of the 3D honeycomb. The honeycomb and 3D honeycomb patterns are

impossible to print for 100% infill density because there is no space for both patterns to produce full density. The number of lines and time consumption of the Hilbert curve pattern is less than the 3D honeycomb. The printing time of the Archimedean chords is less than the Hilbert curve. But the amount of material utilization is higher than the Hilbert curve. The material consumption and the printing time of the octagram spiral pattern are less than the others infill pattern. In summary, the 3D honeycomb has the highest printing time and the number of lines. Therefore, material consumption is also high. The octagram spiral pattern is the lowest time and material consumption rate. According to the data, the printing time and the material consumption differ depending on the infill pattern, infill percentage, and printing parameter. Moreover, the number of printing lines varies according to the part's infill percent and infill pattern. In addition, the thickness of the line and the expansion rate depends on the gap between the nozzle and the build platform. It also depends on the slurry condition.

5. Future Prospects

The main contributions of this experiment are the pattern design and infill percentage. The printing time and the number of infill lines differ depending on the infill pattern design and ratio. Moreover, the part's properties also rely on the infill pattern design and infill percentage. Therefore, the next set of experiments would depend on more analysis of printing time, material consumption, and their properties corresponding to their infill percentage according to the infill pattern design.

Acknowledgment

The authors are grateful to the Department of Science and Technology (DST)-Innovation of Science Pursuit for Inspire Research (INSPIRE) for fellowship support (IF190716).

References

- [1] N. Guo and M. C. Leu, "Additive manufacturing: technology, applications and research needs," *Front. Mech. Eng.*, vol. 8, no. 3, pp. 215–243, 2013, doi: 10.1007/s11465-013-0248-8.
- [2] B. C. Palivela, S. D. Bandari, and R. S. Mamilla, "Extrusion-based 3D printing of bioactive glass scaffolds-process parameters and mechanical properties: A review," *Bioprinting*, vol. 27, p. e00219, 2022, doi: 10.1016/j.bprint.2022.e00219.
- [3] C. Hicks *et al.*, "Molecular Analysis of Central Nervous System Disease Spectrum in Childhood Acute Lymphoblastic Leukemia," *Clin. Med. Insights Oncol.*, vol. 10, p. CMO-S18180, 2016, doi: 10.4137/CMO.S18180.
- [4] B. C. Palivela, A. Manoj, K. K. Gajrani, S. Dhaka, and M. R. Sankar, "Sustainability Issues in Advanced Machining Processes," *Adv. Mach. Sci. CRC Press*, pp. 425–468, 2022, doi: 10.1201/9780429160011-15.
- [5] J. Zhang *et al.*, "Robocasting of dense 8Y zirconia parts: rheology, printing, and mechanical properties," *J. Eur. Ceram. Soc.*, 2022, doi: 10.1016/j.jeurceramsoc.2022.11.042.
- [6] S. Cano *et al.*, "Influence of the infill orientation on the properties of zirconia parts produced by fused filament fabrication," *Materials (Basel)*, vol. 13, no. 14, p. 3158, 2020, doi: 10.3390/ma13143158.
- [7] I. Buj-corral, D. Vidal, A. Tejo-otero, A. Padilla, E. Xuriguera, and F. Fenollosa-art, "Characterization of 3D Printed Ytria-Stabilized Zirconia Parts for Use in Prostheses," *Nanomaterials*, vol. 11, no. 11, p. 2942, 2021, doi: 10.3390/nano11112942.
- [8] F. Alvarez *et al.*, "Optimization of the sintering thermal treatment and the ceramic ink used in direct ink writing of α -Al₂O₃: Characterization and catalytic application," *J. Eur. Ceram. Soc.*, vol. 42, no. 6, pp. 2921–2930, 2022, doi: 10.1016/j.jeurceramsoc.2022.01.032.
- [9] A. L. Troksa *et al.*, "3D-printed nanoporous ceramics: Tunable feedstock for direct ink write and projection microstereolithography," *Mater. Des.*, vol. 198, p. 109337, 2021, doi: 10.1016/j.matdes.2020.109337.
- [10] S. Mamatha, P. Biswas, P. Ramavath, D. Das, and R. Johnson, "Effect of parameters on 3D printing of alumina ceramics and evaluation of properties of sintered parts," *J. Asian Ceram. Soc.*, no. May, 2021,

- doi: 10.1080/21870764.2021.1920159.
- [11] P. Claude, "3D-printing of 8Y-TZP solid oxide fuel cell electrolytes," *Master's thesis, Univ. Politècnica Catalunya*, 2019, [Online]. Available: <http://hdl.handle.net/2117/172010>.
- [12] R. Huang *et al.*, "Material extrusion and sintering of binder-coated zirconia: Comprehensive characterizations," *Addit. Manuf.*, vol. 45, p. 102073, 2021, doi: 10.1016/j.addma.2021.102073.
- [13] K. Rane, M. A. Farid, W. Hassan, and M. Strano, "Effect of printing parameters on mechanical properties of extrusion-based additively manufactured ceramic parts," *Ceram. Int.*, vol. 47, no. 9, pp. 12189–12198, 2021, doi: 10.1016/j.ceramint.2021.01.066.
- [14] Y. Raymond, E. Thorel, M. Liversain, A. Riveiro, J. Pou, and M. P. Ginebra, "3D printing non-cylindrical strands: Morphological and structural implications," *Addit. Manuf.*, vol. 46, p. 102129, 2021, doi: 10.1016/j.addma.2021.102129.
- [15] A. Thurzo *et al.*, "Fabrication and In Vitro Characterization of Novel Hydroxyapatite Scaffolds 3D Printed Using Polyvinyl Alcohol as a Thermoplastic Binder," *Int. J. Mol. Sci.*, vol. 23, no. 23, p. 14870, 2022, doi: 10.3390/ijms232314870.
- [16] J. Wu Kang and Q. Xian Ma, "The role and impact of 3D printing technologies in casting," *China Foundry*, vol. 14, no. 3, pp. 157–168, 2017, doi: 10.1007/s41230-017-6109-z.
- [17] J. A. Lewis, J. E. Smay, J. Stuecker, and J. Cesarano, "Direct ink writing of three-dimensional ceramic structures," *J. Am. Ceram. Soc.*, vol. 89, no. 12, pp. 3599–3609, 2006, doi: 10.1111/j.1551-2916.2006.01382.x.
- [18] A. Lauder, M. J. Cima, E. Sachs, and T. Fan, "Three dimensional printing: surface finish and microstructure of rapid prototyped components," *MRS Online Proc. Libr.*, p. 249, 1991, doi: 10.1557/PROC-249-331.
- [19] P. Wang, J. Li, G. Wang, L. He, Y. Yu, and B. Xu, "Multimaterial Additive Manufacturing of LTCC Matrix and Silver Conductors for 3D Ceramic Electronics," *Adv. Mater. Technol.*, p. 2101462, 2022, doi: 10.1002/admt.202101462.
- [20] M. Wang, X. Zhao, and D. Sun, "Application of Digital 3D Printing Technology in Ceramic Art Creation," *Sci. Program.*, 2022, doi: 10.1155/2022/6152558.
- [21] L. Moroni, J. R. De Wijn, and C. A. Van Blitterswijk, "3D fiber-deposited scaffolds for tissue engineering: influence of pores geometry and architecture on dynamic mechanical properties," *Biomaterials*, vol. 27, no. 7, pp. 974–985, 2006, doi: 10.1016/j.biomaterials.2005.07.023.
- [22] F. Zhong, W. Liu, Y. Zhou, X. Yan, Y. Wan, and L. Lu, "Ceramic 3D printed sweeping surfaces," *Comput. Graph.*, vol. 90, pp. 108–115, 2020, doi: 10.1016/j.cag.2020.05.007.
- [23] K. T. Chaka, L. Fambri, and N. Govindan, "Kaolinite/Polypropylene Nanocomposites. Part 3: 3D Printing," *Int. Res. J. Eng. Technol.*, vol. 4, pp. 132–147, 2017.
- [24] D. Zhao and W. Guo, "Shape and Performance Controlled Advanced Design for Additive Manufacturing: A Review of Slicing and Path Planning," *J. Manuf. Sci. Eng.*, vol. 142, no. 1, p. 010801, 2020, doi: 10.1115/1.4045055.
- [25] M. S. Cadete, T. E. Gomes, I. Gonçalves, and V. Neto, "Controlling Morphing Behavior in 4D Printing: A Review About Microstructure and Macrostructure Changes in Polylactic Acid," *3D Print. Addit. Manuf.*, 2022, doi: 10.1089/3dp.2022.0088.
- [26] S. Guessasma and S. Belhabib, "Infill Strategy in 3D Printed PLA Carbon Composites: Effect on Tensile Performance," *Polymers (Basel)*, vol. 14, no. 19, p. 4221, 2022, doi: 10.3390/polym14194221.
- [27] Z. Jia, Y. Yu, and L. Wang, "Learning from nature: Use material architecture to break the performance tradeoffs," *Mater. Des.*, vol. 168, p. 107650, 2019, doi: 10.1016/j.matdes.2019.107650.
- [28] J. Pelz, N. Ku, and M. Meyers, "Additive Manufacturing Utilizing a Novel In-Line Mixing System for Design of Functionally Graded Ceramic Composites," *CCDC Army Res. Lab.*, 2019.
- [29] B. Milne, X. Yuan, A. Kvalsvig, and P. Cao, "3D printed carbon fibre composite knee and hip replacements," *24th Int. Conf. Mechatronics Mach. Vis. Pract.*, pp. 1–6, 2017, doi: 10.1109/M2VIP.2017.8211518.
- [30] V. Raeisdasteh Hokmabad, S. Davaran, A. Ramazani, and R. Salehi, "Design and fabrication of porous biodegradable scaffolds: a strategy for tissue engineering," *J. Biomater. Sci. Polym. Ed.*, vol. 28, no. 16, pp. 1797–1825, 2017, doi: 10.1080/09205063.2017.1354674.
- [31] B. I. Oladapo, S. A. Zahedi, and A. O. M. Adeoye, "3D printing of bone scaffolds with hybrid biomaterials," *Compos. Part B Eng.*, vol. 158, pp. 428–436, 2019, doi: 10.1016/j.compositesb.2018.09.065.

- [32] H. Kim, F. Torres, Y. Wu, D. Villagran, Y. Lin, and T.-L. Tseng, "Integrated 3D printing and corona poling process of PVDF piezoelectric films for pressure sensor application," *Smart Mater. Struct.*, vol. 26, no. 8, p. 085027, 2017, doi: 10.1088/1361-665x/aa738e.
- [33] A. Bedel, Y. Coudert-Osmont, J. Martínez, R. I. Nishat, S. Whitesides, and S. Lefebvre, "Closed space-filling curves with controlled orientation for 3D printing," *Comput. Graph. Forum*, vol. 41, no. 2, pp. 473–492, 2022, doi: 10.1111/cgf.14488.
- [34] C. D. Lopez *et al.*, "Three dimensionally printed bioactive ceramic scaffold osseointegration across critical-sized mandibular defects," *J. Surg. Res.*, vol. 223, pp. 115–122, 2018, doi: 10.1016/j.jss.2017.10.027.
- [35] D. V. Isakov, Q. Lei, F. Castles, C. J. Stevens, C. R. M. Grovenor, and P. S. Grant, "3D printed anisotropic dielectric composite with meta-material features," *Mater. Des.*, vol. 93, pp. 423–430, 2016, doi: 10.1016/j.matdes.2015.12.176.
- [36] W. Wu, Q. Zheng, X. Guo, J. Sun, and Y. Liu, "A programmed release multi-drug implant fabricated by three-dimensional printing technology for bone tuberculosis therapy," *Biomed. Mater.*, vol. 4, no. 6, p. 065005, 2009, doi: 10.1088/1748-6041/4/6/065005.
- [37] G. W. Melenka, B. K. O. Cheung, J. S. Schofield, M. R. Dawson, and J. P. Carey, "Evaluation and prediction of the tensile properties of continuous fiber-reinforced 3D printed structures," *Compos. Struct.*, vol. 153, pp. 866–875, 2016, doi: 10.1016/j.compstruct.2016.07.018.
- [38] A. N. Dickson, J. N. Barry, K. A. McDonnell, and D. P. Dowling, "Fabrication of continuous carbon, glass and Kevlar fibre reinforced polymer composites using additive manufacturing," *Addit. Manuf.*, vol. 16, pp. 146–152, 2017, doi: 10.1016/j.addma.2017.06.004.
- [39] S. Kesavarma, C. K. Kong, M. Samykano, K. Kadirgama, and A. K. Pandey, "Bending properties of 3D printed coconut wood-PLA composite," *IOP Conf. Ser. Mater. Sci. Eng.*, vol. 736, no. 5, p. 052031, 2020, doi: 10.1088/1757-899X/736/5/052031.
- [40] A. Banerjee, R. B. Chandran, and J. H. Davidson, "Experimental investigation of a reticulated porous alumina heat exchanger for high temperature gas heat recovery," *Appl. Therm. Eng.*, vol. 75, pp. 889–895, 2015, doi: 10.1016/j.applthermaleng.2014.10.033.
- [41] Z. Yang *et al.*, "3D printing of sponge spicules-inspired flexible bioceramic-based scaffolds," *Biofabrication*, vol. 14, no. 3, p. 035009, 2022, doi: 10.1088/1758-5090/ac66ff.
- [42] A. Barba *et al.*, "Osteoinduction by Foamed and 3D-Printed Calcium Phosphate Scaffolds: Effect of Nanostructure and Pore Architecture," *ACS Appl. Mater. Interfaces*, vol. 9, no. 48, pp. 41722–41736, 2017, doi: 10.1021/acsami.7b14175.
- [43] T. L. B. Tseng, A. Akundi, and H. Kim, "4-D printing of pressure sensors and energy harvesting devices for engineering education," *ASEE Annu. Conf. Expo. Conf. Proc.*, 2018, doi: 10.18260/1-2--29654.
- [44] M. Anwaar, O. Can, I. Sevgili, E. Yilgor, I. Halil, and I. Yilgor, "3D printed poly (lactic acid) scaffolds modified with chitosan and hydroxyapatite for bone repair applications," *Mater. Today Commun.*, vol. 25, p. 101515, 2020, doi: 10.1016/j.mtcomm.2020.101515.
- [45] M. Mahmoudi *et al.*, "Three-Dimensional Printing of Ceramics through 'Carving' a Gel and 'Filling in' the Precursor Polymer," *ACS Appl. Mater. Interfaces*, vol. 12, no. 28, pp. 31984–31991, 2020, doi: 10.1021/acsami.0c08260.
- [46] L. J. Gibson, "The hierarchical structure and mechanics of plant materials," *JR Soc Interface*, vol. 9, pp. 2749–2766, 2012, doi: 10.1098/rsif.2012.0341.
- [47] L. J. Gibson, "Cellular Solids," *Mrs Bull.*, vol. 28, no. 4, pp. 270–274, 2003, doi: 10.1557/mrs2003.79.
- [48] M. Weiß, P. Sälzler, N. Willenbacher, and E. Koos, "3D-Printed lightweight ceramics using capillary suspensions with incorporated nanoparticles," *J. Eur. Ceram. Soc.*, vol. 40, no. 8, pp. 3140–3147, 2020, doi: 10.1016/j.jeurceramsoc.2020.02.055.
- [49] J. Bauer, S. Hengsbach, I. Tesari, R. Schwaiger, and O. Kraft, "High-strength cellular ceramic composites with 3D microarchitecture," *Proc. Natl. Acad. Sci.*, vol. 111, no. 7, pp. 2453–2458, 2014, doi: 10.1073/pnas.1315147111.
- [50] Z. Wang, Z. Li, and W. Xiong, "Numerical study on three-point bending behavior of honeycomb sandwich with ceramic tile," *Compos. Part B*, vol. 167, pp. 63–70, 2019, doi: 10.1016/j.compositesb.2018.11.108.
- [51] J. T. Muth, P. G. Dixon, L. Woish, L. J. Gibson, and J. A. Lewis, "Architected cellular ceramics with tailored stiffness via direct foam writing," *Proc. Natl. Acad. Sci.*, vol. 114, no. 8, pp. 1832–1837, 2017, doi: 10.1073/pnas.1616769114.

- [52] L. M. Bollig *et al.*, "3D Printed Magnetic Polymer Composite Transformers," *J. Magn. Magn. Mater.*, vol. 442, pp. 97–101, 2017, doi: 10.1016/j.jmmm.2017.06.070.
- [53] C. Zhan, M. Li, R. McCoy, L. Zhao, and W. Lu, "3D printed hierarchical re-entrant honeycombs: Enhanced mechanical properties and the underlying deformation mechanisms," *Compos. Struct.*, vol. 290, p. 115550, 2022, doi: 10.1016/j.compstruct.2022.115550.
- [54] J. Maurath and N. Willenbacher, "3D printing of open-porous cellular ceramics with high specific strength," *J. Eur. Ceram. Soc.*, vol. 37, no. 15, pp. 4833–4842, 2017, doi: 10.1016/j.jeurceramsoc.2017.06.001.
- [55] C. Y. Chaparro-garnica, E. Bailón-garcía, D. Lozano-castelló, and A. Bueno-lópez, "Design and fabrication of integral carbon monoliths combining 3D printing and sol-gel polymerization: effects of the channel morphology on the CO-PROX reaction," *Catal. Sci. Technol.*, vol. 11, no. 19, pp. 6490–6497, 2021, doi: 10.1039/d1cy01104a.
- [56] S. M. Khan, Z. Deng, T. Yang, and L. Li, "Bio- Inspired Ceramic-Metal Composites Using Ceramic 3D Printing and Centrifugal Infiltration," *Adv. Eng. Mater.*, vol. 24, no. 4, p. 2101009, 2022, doi: 10.1002/adem.202101009.
- [57] M. L. Sesso, S. Slater, J. Thornton, and G. V. Franks, "Direct ink writing of hierarchical porous ultra- high temperature ceramics (ZrB₂)," *J. Am. Ceram. Soc.*, vol. 104, no. 10, pp. 4977–4990, 2021, doi: 10.1111/jace.17911.
- [58] Z. Chen *et al.*, "Mechanical properties and microstructures of 3D printed bulk cordierite parts," *Ceram. Int.*, vol. 45, no. 15, pp. 19257–19267, 2019, doi: 10.1016/j.ceramint.2019.06.174.
- [59] A. Davó-quiñonero, D. Sorolla-rosario, E. Bailón-garcía, and D. Lozano-castelló, "Improved asymmetrical honeycomb monolith catalyst prepared using a 3D printed template," *J. Hazard. Mater.*, vol. 368, pp. 638–643, 2019, doi: 10.1016/j.jhazmat.2019.01.092.
- [60] G. Liu, Y. Zhao, G. Wu, and J. Lu, "Origami and 4D printing of elastomer-derived ceramic structures," *Sci. Adv.*, vol. 4, no. 8, p. eaat0641, 2018, doi: 10.1126/sciadv.aat0641.
- [61] H. Ji, X. Zhang, X. Huang, L. Zheng, X. Ye, and Y. Li, "Effect of extrusion on viscoelastic slurry 3D print quality: numerical analysis and experiment validation," *SN Appl. Sci.*, vol. 1, no. 9, pp. 1–11, 2019, doi: 10.1007/s42452-019-1097-9.
- [62] Z. Huang *et al.*, "Stereolithography 3D printing of Si₃N₄ cellular ceramics with ultrahigh strength by using highly viscous paste," *Ceram. Int.*, 2022, doi: 10.1016/j.ceramint.2022.10.137.
- [63] A. Mansour *et al.*, "Evaluating the 3D Printing Capabilities," *Proc. Int. Conf. Ind. Eng. Oper. Manag. 10th Annu. Int. IEOM Conf. Dubai, UAE*, pp. 10–12, 2020.
- [64] G. Mckerricher, D. Titterington, and A. Shamim, "A fully inkjet-printed 3-D honeycomb-inspired patch antenna," *IEEE Antennas Wirel. Propag. Lett.*, vol. 15, pp. 544–547, 2015, doi: 10.1109/LAWP.2015.2457492.
- [65] K. Naplocha, A. Dmitruk, P. Mayer, and J. W. Kaczmar, "Design of Honeycomb Structures Produced by Investment Casting," *Arch. Foundry Eng.*, vol. 19, no. 4, pp. 76–80, 2019, doi: 10.24425/afe.2019.129633.
- [66] H. Mei, Y. Tan, W. Huang, P. Chang, Y. Fan, and L. Cheng, "Structure design influencing the mechanical performance of 3D printing porous ceramics," *Ceram. Int.*, vol. 47, no. 6, pp. 8389–8397, 2021, doi: 10.1016/j.ceramint.2020.11.203.
- [67] P. Gong, Y. Li, C. Xin, Q. Chen, L. Hao, and Q. Sun, "Multimaterial 3D-printing barium titanate / carbonyl iron composites with bilayer-gradient honeycomb structure for adjustable broadband microwave absorption," *Ceram. Int.*, vol. 48, no. 7, pp. 9873–9881, 2022, doi: 10.1016/j.ceramint.2021.12.190.
- [68] G. El Chawich *et al.*, "Design and Manufacturing of Si-Based Non-Oxide Cellular Ceramic Structures through Indirect 3D Printing," *Materials (Basel)*, vol. 15, no. 2, p. 471, 2022, doi: 10.3390/ma15020471.
- [69] H. Mei, X. Zhao, S. Zhou, D. Han, S. Xiao, and L. Cheng, "3D-printed oblique honeycomb Al₂O₃/SiCw structure for electromagnetic wave absorption," *Chem. Eng. J.*, vol. 372, pp. 940–945, 2019, doi: 10.1016/j.cej.2019.05.011.
- [70] Y. Zeng, L. Jiang, Y. Sun, Y. Yang, Y. Quan, and S. Wei, "3D-Printing Piezoelectric Composite with Honeycomb Structure for Ultrasonic Devices," *Micromachines*, vol. 11, no. 8, p. 713, 2020, doi: 10.3390/mi11080713.
- [71] H. K. Dave, N. H. Patadiya, and A. R. Prajapati, "Effect of infill pattern and infill density at varying part

- orientation on tensile properties of fused deposition modeling-printed poly-lactic acid part," *Proc. Inst. Mech. Eng. Part C J. Mech. Eng. Sci.*, vol. 235, no. 10, pp. 1811–1827, 2021, doi: 10.1177/0954406219856383.
- [72] B. Akhouni and A. H. Behraves, "Effect of filling pattern on the tensile and flexural mechanical properties of FDM 3D printed products," *Exp. Mech.*, vol. 59, no. 6, pp. 883–897, 2019, doi: 10.1007/s11340-018-00467-y.
- [73] Z. Liu, B. Bhandari, S. Prakash, and M. Zhang, "Creation of internal structure of mashed potato construct by 3D printing and its textural properties," *Food Res. Int.*, vol. 111, pp. 534–543, 2018, doi: 10.1016/j.foodres.2018.05.075.
- [74] A. R. Butz, "Alternative algorithm for Hilbert's space-filling curve," *IEEE Trans. Comput.*, vol. 100, no. 4, pp. 424–426, 1971, doi: 10.1109/T-C.1971.223258.
- [75] P. Yadav and A. Sahai, "Strength and Surface Characteristics of FDM-Based 3D Printed PLA Parts for Multiple Infill Design Patterns," *J. Inst. Eng. Ser. C*, vol. 102, no. 1, pp. 197–207, 2021, doi: 10.1007/s40032-020-00625-z.
- [76] A. Papacharalampopoulos, H. Bikas, and P. Stavropoulos, "Path planning for the infill of 3D printed parts utilizing Hilbert curves," *Procedia Manuf.*, vol. 21, pp. 757–764, 2018, doi: 10.1016/j.promfg.2018.02.181.
- [77] G. Domínguez-Rodríguez, J. J. Ku-Herrera, and A. Hernández-Pérez, "An assessment of the effect of printing orientation, density, and filler pattern on the compressive performance of 3D printed ABS structures by fuse deposition," *Int. J. Adv. Manuf. Technol.*, vol. 95, no. 5, pp. 1685–1695, 2018, doi: 10.1007/s00170-017-1314-x.
- [78] R. Palaniappan, *Life cycle analysis and wear and fatigue behavior of polymeric biomaterials*. Woodhead Publishing, 2018.
- [79] G. Kim, S. Boo, J. Lim, J. Chung, and M. Park, "Texture Modification of 3D-Printed Maltitol Candy by Changing Internal Design," *Appl. Sci.*, vol. 12, no. 9, p. 4189, 2022, doi: 10.3390/app12094189.
- [80] A. Qavi, M. Reyaz, and U. Rahim, "A review on effect of process parameters on FDM-based 3D printed PLA materials," *Int. Res. J. Mod. Eng. Technol. Sci.*, vol. 4, no. 6, pp. 3088–3100, 2022.
- [81] J. G. Griffiths, "Toolpath based on Hilbert's curve," *Comput. Des.*, vol. 26, no. 11, pp. 839–844, 1994, doi: 10.1016/0010-4485(94)90098-1.
- [82] S. Shaikh, N. Kumar, and P. K. Jain, *Hilbert Curve Based Toolpath for FDM Process*. New Delhi: Springer, 2016.
- [83] M. A. Pop, T. Bedo, V. Geam, I. Radomir, S. M. Zaharia, and L. A. Chicos, "Influence of Internal Innovative Architecture on the Mechanical Properties of 3D Polymer Printed Parts," *Polymers (Basel)*, vol. 12, no. 5, p. 1129, 2020, doi: 10.3390/polym12051129.
- [84] D. Rogozea, "Design, 3D Bioprinting, and Testing of Otic Prosthesis," 2018.
- [85] P. Ravi, "Towards the fabrication of bioresorbable constructs with customized properties using additive manufacturing," *PhD Diss.*, 2017, [Online]. Available: <http://hdl.handle.net/10106/27151>.
- [86] M. T. Tavares, V. M. Gaspar, M. V. Monteiro, and J. P. S. Farinha, "GelMA/bioactive silica nanocomposite bioinks for stem cell osteogenic differentiation," *Biofabrication*, vol. 13, no. 3, p. 035012, 2021, doi: 10.1088/1758-5090/abdc86.
- [87] A. Dine, E. Bentley, L. A. Poulmarck, D. Dini, A. E. Forte, and Z. Tan, "A dual nozzle 3D printing system for super soft composite hydrogels," *HardwareX*, vol. 9, p. e00176, 2021, doi: 10.1016/j.ohx.2021.e00176.
- [88] A. Nassar, M. Younis, M. Elzareef, and E. Nassar, "Effects of Heat-Treatment on Tensile Behavior and Dimension Stability of 3D Printed Carbon Fiber Reinforced Composites," *Polymers (Basel)*, vol. 13, no. 24, p. 4305, 2021, doi: 10.3390/polym13244305.
- [89] A. Maurel *et al.*, "Three-dimensional printing of a LiFePO₄/graphite battery cell via fused deposition modeling," *Sci. Rep.*, vol. 9, no. 1, pp. 1–14, 2019, doi: 10.1038/s41598-019-54518-y.
- [90] A. Kottasamy, M. Samykano, K. Kadirgama, and M. Rahman, "Experimental investigation and prediction model for mechanical properties of copper-reinforced polylactic acid composites (Cu-PLA) using FDM-based 3D printing technique," *Int. J. Adv. Manuf. Technol.*, vol. 119, no. 7, pp. 5211–5232, 2022, doi: 10.1007/s00170-021-08289-4.

Microhardness and wear rate analysis on laser cladded composites of AZ91D alloy with SiC by grey technique

L. Karthick¹, Ganesh Babu Loganathan², Irfan Nazir wani³, B. Somasundaram⁴,
Sumanth Ratna. Kandavalli⁵, P. Chithambaranathan⁶

¹Department of Mechanical Engineering, Hindusthan College of Engineering and Technology,
Coimbatore 641032, India.

²Department of Mechatronics Engineering, Faculty of Engineering, Tishk International
University, Erbil, Kurdistan Region, Iraq

³Department of Aerospace Engineering, Nims school of Mechanical and Aerospace
Engineering, NIET Nims University, Jaipur, Rajasthan – 303121.

⁴School of Mechanical engineering, REVA University

⁵Department of Mechanical Engineering, Tandon School of Engineering, New York
University, Brooklyn, 6 Metro Tech Center, NY, 11201, United States of America.

⁶Department of Mechanical Engineering, Rajalakshmi Engineering College, Thandalam,
Chennai – 602105

*Corresponding Author: L.Karthick

*Email: bemechkarthick@gmail.com

Abstract: Owing to increments in heavy vehicles for transporting the materials and reducing the vehicle weight, magnesium alloys play the mandatory role in various fabricating industries. The Mg alloy alone is not satisfied their necessities without adding the strengthening particles, therefore this investigation stated the silicon carbide (SiC) was the reinforcing into AZ91D Mg alloy to compose the coating metal matrix composites through the laser cladding process. This method is unique when appropriated processing parameters is chosen and compared to laser melting process; laser cladding is the significant one. The laser cladding processing parameters are scanning speed (3 to 5 m/s), SiC proportions (10 to 30%) and laser output power (0.6 to 0.8 kW), respectively. Then the composed coating AZ91D Mg alloy with SiC specimen is accounted for experimentation of microhardness and wear rates. The microhardness and wear rates are improved at increasing of weight percentage from 20 to 30%, maximum of scanning speed at 5 m/s and 0.7 kW of laser output power parameters. The grey relational multi task optimization method was utilized to recognize the single responses from various laser cladding processing parameters. Finally the SEM with worn surfaces was taken on the optimal specimen composite.

Keywords: SiC, laser, AZ91D, Hardness, SEM

1. Introduction

In aerospace and automotive industries, the magnesium alloys are much influenced as a capable material due to less weight with maximum strength, lower density and more strength to weight ratio. The magnesium alloys normally had a lesser corrosion, weaker hardness and low in wear resistances when appropriated process does not meet with magnesium materials [1-5]. But the laser surface method is most appropriated technique to improve their properties which is related to surface enhancement exclusive modifying the bulk material properties and this technique is recently developed in many fabricating sectors. The metal substrate is

iridescences with maximum sources of laser beam while in processing, from their surfaces it was melts into some numerous micrometers depth and then suddenly solidification is achieved in the molten pool. Finally the grain refinement is attained in the selected substrates and secondary phases are restructured [6-8].

The laser cladding process is influenced with ceramic based strengthening particles or metallic powders are illuminated through the laser beam to compose the additional thickness layer on the substrates which consists of hard ceramics reinforcements improves the substrate surfaces with superior characteristics like corrosion, hardness and wear resistances. These laser processes are extensively utilized and are confirmed to improve the surface characteristics of magnesium based alloys [9-12]. Laser cladding process is an alternative technique to the conventional methods like cold spray and electroplating process but especially in magnesium alloys, this treatment improves the surface properties when compared to convention methods. The laser melting process on the magnesium alloy with sequence of CO₂ laser wave causes the fine grain structure and improved intermetallic phases. Similarly, the corrosion resistance and hardness properties are improved by the laser melting process [13-15].

In some studies, the corrosion resistances are enhanced by the influence of laser with 500 Hz with magnesium alloy. The refinement of microstructure is attained owing to manipulated galvanic corrosion among the secondary phases and matrix which happened by laser treatment. Similarly diminishes the proportions of secondary phase's also significant reason for improving the properties [16-18]. Subsequently, the acceleration and laser power manipulated the structure of grains in the molten pool. During the process of corrosion behavior by salt based solution, the development of better grains and improved deposition of calcium phosphates were reason for superior properties [19-20].

Some researchers carried out the laser cladding process on magnesium alloys with various composite reinforcement, ceramic materials and metal. They found that the processed magnesium alloys enhances the mechanical properties with superior corrosion rated when contrasted to the laser melting process. Based on the environments of fabricated components were utilized, the appropriate processing condition will be used. Therefore, the aluminium is commonly used in various applications but in the process of cladding this alloy is broadly spread. This alloy much similar to magnesium alloy and it enhances the fine bonding strength along with substrate of magnesium [21].

Compared to various ceramic particulates, the silicon based materials are extensively used owing to maximum wear resistances, hardness strength and thermal steadiness in different process and this material is the most significant strengthening materials while in laser cladding process, this combination of aluminium and silicon carbide composes the metal matrix composites which is more preferable to improve the coating strength and mechanical characteristics. During the process of laser cladding on the material of aluminium and silicon carbide coating on the magnesium alloy, the silicon and titanium combinations were developed to improve the hardness strength due to the added proportion of silicon. Similarly, some researchers studied that the addition of silicon carbide particles on the aluminium alloy during the laser cladding the tribological behaviors were improved. At the same time some researchers, the maximum proportions of silicon carbide with more than 25% proportions on the magnesium alloy during the coating through the laser cladding hardness and wear rates are improved [22].

The zirconium and titanium based ceramic particles on the magnesium alloy through the coating of laser cladding the corrosion and tribological performances were enhanced. The aluminium silicon alloy on the magnesium based substrate, the mechanical properties were enhanced with maximum of scanning speed due to the attained intermetallic regions are a major impact to improve the thickness. Subsequently, the scanning speed was established at certain time during the coating process, the hardness strength is similarly diminished. This results solidification was not properly attained owing to volume fraction; shapes of the particles, dispersed secondary phases are the secondary reason for decreasing the mechanical performances. Based on above the ample reviews, the combinations of aluminium and silicon particles as significant aspects to carrying the mechanical properties due to the silicon was presented with cladded form layer at maximum temperature. Due to that maximum temperature, silicon was occurred on the substrate by form coarse structure led to decrease the characteristics of mechanical strengths. In a related study, the mechanical characteristics of glass fibre and banana fibre were compared to determine which fibre was superior [29]. To enhance the qualities of the composite materials, a mechanical investigation was conducted on AA2024-T3 plates [30]. From similar study, how kenaf/glass/epoxy hybrids' mechanical characteristics are impacted by nano- and micro-TiO₂ [31].

Especially in the magnesium alloy of AZ91D, extensively used in the various industrial defense sectors due to the presence of light weight maximum strength ratio combinations and also this material is the most desirable element in rare earth elements to improve the mechanical attributes and creep resistances in the elevated room temperatures. This magnesium alloy specifically utilized in the bio medical related fields. Due to the presence of secondary phases which influenced by the galvanic reactions causes the poorer corrosion but maintain the period of primary phased in magnesium alloy is the main aspects to improve their mechanical attributes [23]. The modification of secondary phases is to enhance the corrosion and wear rates in the rare earth elements of magnesium alloys. The previous literatures exhibited that the laser cladding the most suitable method to improve the mechanical properties than the laser melting process. This technology is also the beneficial method to enhance the mechanical properties at the same time this AZ91D mg alloy was not widely utilized in these previous research and the strengthening particles of SiC also not influenced till now. Therefore, this present a study, the severe effort was achieved to complete the laser cladding process on AZ91D alloy with influence of various processing parameters. The microhardness and wear rates are evaluated scientifically. The grey relational analysis was utilized to find the optimal processing parameters through the Taguchi principles.

2. Methodology

In this present investigation, the AZ91D magnesium alloy was utilized to carry out the process of laser cladding. The chemical composition of AZ91D alloy is 9.7 of Al, 0.50 of Mn, 1 of Zn, 0.005 of Fe, 0.1 of Si, 0.002 of Ni, 0.03 of Cu, 0.02 of others and Bal of Mg, respectively. These samples were extracted from the raw plate and transformed into required dimension of 60 X 50 X 10 mm³. These plates were refined for the surfaces with various grit sizes 500 to 1500 of SiC sheets having the abraded one and cleaned with ethanol solution to prepare for cladding process. The CO₂ with cross current Han's laser having the 1060 wavelength with 100 mm of spot size specification was utilized. The selected Mg alloy was irradiated with laser power density with constant range at 60 W/cm². Meanwhile, the 3 times

having the equivalent direction throughout the entire process under the manipulation of argon gas shielding. Before that the mixing of SiC particles were blended via the mechanical mixing for about 3 hrs. Throughout the cladding process with effect of SiC powders on AZ91D alloy, there are different processing constraints like scanning speed from (3 to 5 mm/s), SiC proportions feed rate (10 to 30%) and laser output power (0.6 to 0.8 kW), respectively. Then the microhardness test and wear rates were utilized by the vicker's hardness test and pin on disc apparatus. During the hardness experimentation, ASTM E18 was used for the entire hardness test under the dwell time of 10 sec and 250 g load with minimum of three average values were taken. Similarly, the wear test was carried out by the ASTM G99 standards through the pin on disc apparatus having the counter disc made of EN 32 steel. The schematic illustration of laser cladding process is presented in Figure 1. These processing parameters are approached with taguchi L9 level for identifying the optimal laser cladding processing constraints. Table 1 shows the level of taguchi L16 with unexpanded ranges. Table 2 shows the expanded levels with three factors of laser output power, SiC proportions and scanning speed.

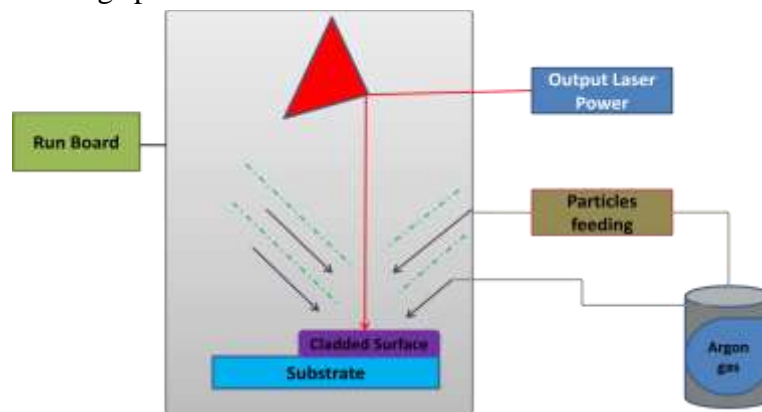


Figure 1 Laser cladding schematic representation

Table 1 laser cladding constraints with their three factors

Cladding processing constraints	Level 1	Level 2	Level 3
Scanning speed (m/s)	3	4	5
SiC proportions (%)	10	20	30
Laser output power (kW)	0.6	0.7	0.8

Table 2 Taguchi L9 array with laser cladding process parameters

Run	Scanning speed (m/s)	SiC proportions (%)	Laser output power (kW)
1	3	10	0.6
2	3	20	0.7
3	3	30	0.8
4	4	10	0.7
5	4	20	0.8
6	4	30	0.6
7	5	10	0.8
8	5	20	0.6
9	5	30	0.7

3. Results and Discussion

3.1. Mechanical properties of laser cladded AZ91D Mg alloy with SiC particles

Based on the Taguchi L9 array the entire processing was carried out which mentioned in Table 2. The mechanical properties of microhardness and wear resistances are subjected to respective investigation as discussed in section 2 and displayed in Table 3. From the table 3, runs 9 shows the better microhardness than other runs. The parameters are 5 m/s of scanning speed, 30 wt. % of SiC and 0.7 kW of output laser power. Similarly, the superior wear rates are attained at the runs 3 having the parameters at 3 m/s of scanning speed, 30 wt. % of SiC and 0.8 kW of output laser power. In both the properties were improved at increment of SiC particles with increasing of output laser power. According to the Hall Petch equation, the generated fine grains of dendritic region caused to enhance the microhardness. While in dissolution of AZ91D Mg alloy was dissolved properly to compose the solidified material. Due to the condition of lattice distortion, the solid solution gets strengthened. Figure 2 shows the hardness representation with different laser cladding processing parameters. At the same time, wear rates are improved with increasing of silicon carbide particles and homogeneous dispersion was occurred in the cladded Mg alloy and superior dilution rate was happed during the process of coating on the magnesium alloy with influence through the SiC particles. The scanning speed at 5 mm/s and maximum proportions of SiC was the major reason to enhance the wear rates. Figure 3 displays the wear rate illustration with various processing constraints.

Table 3 Microhardness and wear rates of laser cladded AZ91D alloy with their outcomes

Run	Scanning speed (m/s)	SiC proportions (%)	Laser output power (kW)	Micro hardness (HV)	Wear rate (10^{-6} mm ³ /mN)
1	3	10	0.6	144	0.00486
2	3	20	0.7	147	0.00478
3	3	30	0.8	155	0.00193
4	4	10	0.7	140	0.00514
5	4	20	0.8	142	0.00471
6	4	30	0.6	148	0.00361
7	5	10	0.8	146	0.00392
8	5	20	0.6	145	0.00357
9	5	30	0.7	159	0.00214

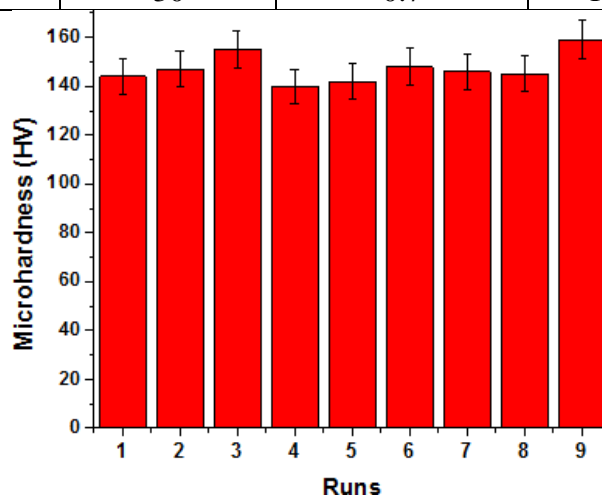


Figure 2 Microhardness on laser cladded AZ91D MG alloy

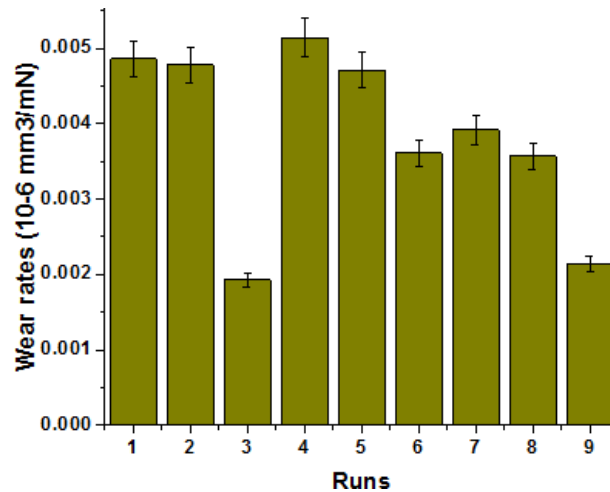


Figure 3 Wear rate on laser cladded AZ91D MG alloy

3.2 Contour analysis of microhardness and wear rates with various processing variables

Figure 4(a) to 4(c) shows the contour analysis of mechanical properties of microhardness with different laser processing constraints. Figure 4(a) exhibits the contour analysis on microhardness with scanning speed and various weight proportions of SiC. From the figure 4(a) it is implicit that the superior hardness was attained at increment of scanning speed and proportions of SiC. Figure 4(b) shows the hardness with their contour analysis with different process constraints of SiC weight proportions and laser output power. From the figure 4(b), it is understood that the increasing of microhardness with increment of SiC proportions at 30% and moderate laser power at 0.7 kW. Figure 4(c) shows the contour analysis on composed composites of AZ91D with SiC hardness with interaction of laser output power and scanning speed. From the figure 4(c), it is concluded that the superior hardness was achieved at the process parameters maximum of scanning speed at 5 m/s and moderate laser output power at 0.7 kW. From these contour analyses, maximum hardness was attained at the process parameters like scanning speed at maximum range (5 m/s), SiC proportions at 30% and laser output power at 0.7 kW, respectively.

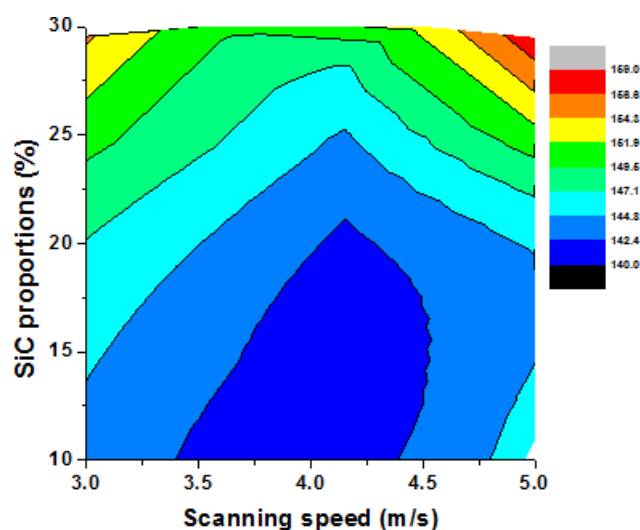


Figure 4(a) Contour analysis on hardness with scanning speed and SiC fractions

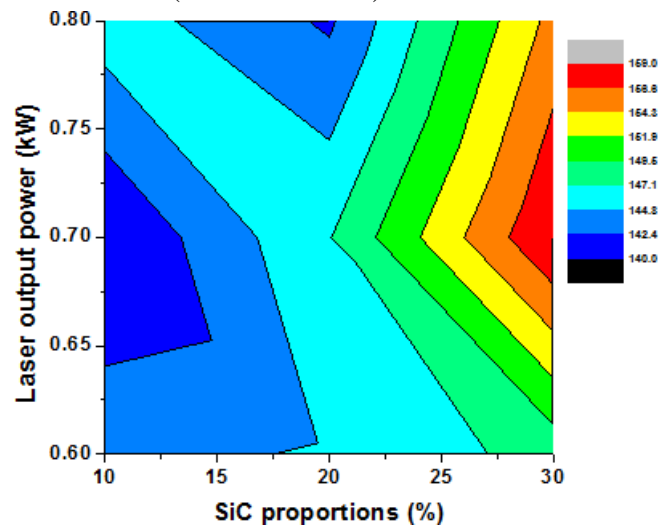


Figure 4(b) Contour analysis on hardness with SiC fractions and laser output power

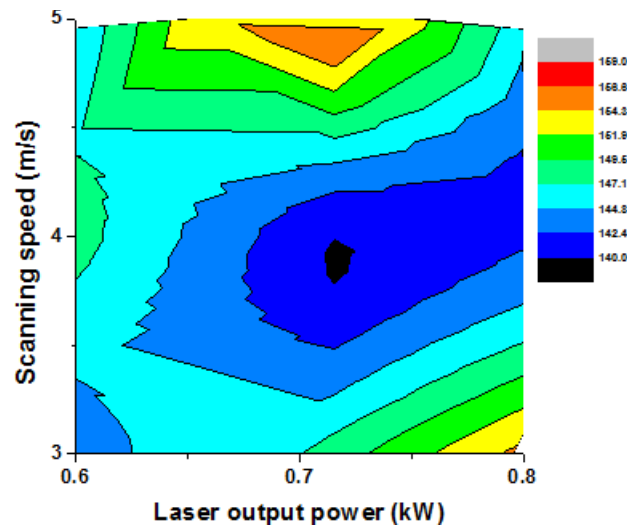


Figure 4(c) Contour analysis on hardness with laser output power and scanning speed

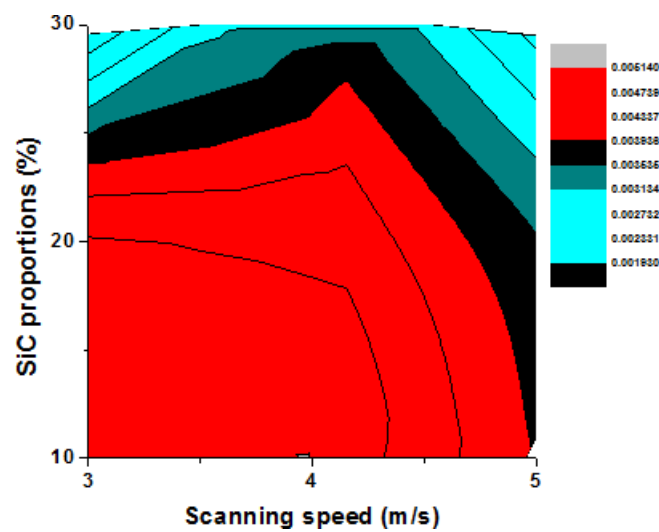


Figure 5(a) Contour analysis on wear rates with scanning speed and SiC fractions

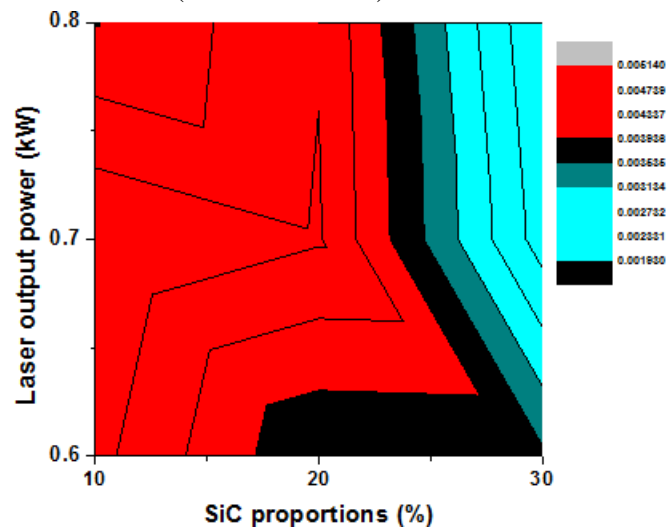


Figure 5(b) Contour analysis on wear rates with SiC fractions and laser output power

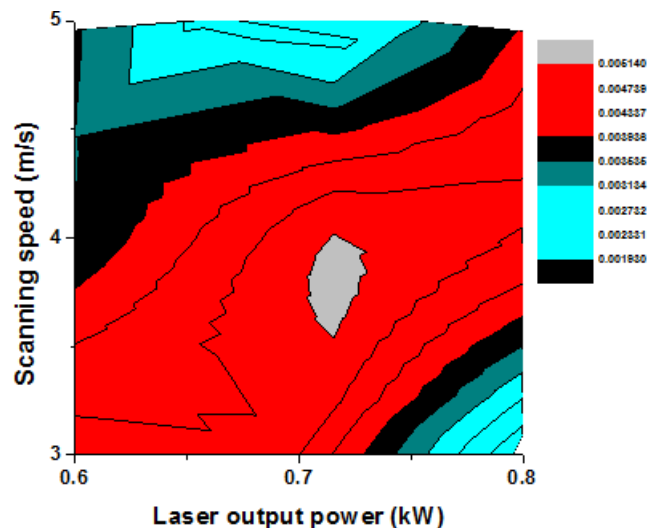


Figure 5(c) Contour analysis on wear rates with laser output power and scanning speed

Figures 5(a) to 5(c) illustrates the contour analysis of wear resistances with special laser processing parameters like scanning speed, SiC proportions and laser output power. Figure 5(a) displays the contour interpretation on wear resistances with scanning speed and different fractions of SiC. From the figure 5(a) it is showed that the enhanced wear rate was achieved at increasing of scanning speed from 4 to 5 m/s and proportions of SiC from 20 to 30%. Figure 5(b) presents the wear rates with their contour performances with laser cladding process like SiC weight proportions and laser output power. From the figure 5(b), it is understood that te enhancing of wear rates with increment of SiC proportions from 20 to 30% and laser output power from 0.7 to 0.8 kW. Figure 5(c) shows the contour analysis on composed composites of AZ91D with SiC wear rates with correlation of laser output power and scanning speed. From the figure 5(c), it is concluded that the superior wear was achieved at the process parameters maximum of scanning speed at 5 m/s and laser output power ncreased from 0.7 to 0.8 kW. From these contour analyses, superior wear rate was attained at the process parameters like scanning speed at maximum range (5 m/s), SiC proportions at 30% and laser output power at 0.8 kW, respectively.

3.3. Grey relational analysis on microhardness and wear rates with different laser cladding process parameters

In this investigation, the various parameters of laser cladding like scanning speed, SiC

proportions and laser output power. These processing constraints achieved better outcomes like microhardness and wear rates. But this conditions only significant with individual response. This study employed with various processing parameters so it is necessary to transformed into single responses from group of responses. Therefore this present study suggests grey relational approach to implement the single responses from multi responses. This grey approach is one of the best multi objective methods to identify the optimal laser cladding processing parameters [22]. The outcomes like microhardness and wear rate are the responses and it is taken as considered for choosing the options. This option is necessary to face the options like larger the better and smaller the better selection. Then this initiation is better for identifying the standardized data, grey coefficient and finally grey value with their specified rank method. The overall computed grey values with their converted single responses are presented in table 4. From the table 4, it is concludes that the maximum rank was attained at the process parameters 5 m/s of scanning speed, 30% of SiC proportions and 0.7 kW of laser output power, respectively. Figure 6 shows the GRG rank with their responses. From the figure 6, it is clearly mentioned that increasing of scanning speed, SiC proportions and medium range of laser output power was significant reason to improve the mechanical responses on the composed specimen of AZ91D Mg alloy and SiC proportions.

Table 4 Computed Grey values with their responses

Runs	Evaluation with standardized		Grey Relational Coefficient		GRG	Rank
	Microhardness	Wear	Microhardness	Wear		
1	0.789	0.913	0.388	0.354	0.3708346	7
2	0.632	0.888	0.442	0.360	0.4010649	6
3	0.211	0.000	0.704	1.000	0.8518519	2
4	1.000	1.000	0.333	0.333	0.3333333	9
5	0.895	0.866	0.358	0.366	0.3622555	8
6	0.579	0.523	0.463	0.489	0.4759996	3
7	0.684	0.620	0.422	0.446	0.4343378	5
8	0.737	0.511	0.404	0.495	0.4494312	4
9	0.000	0.065	1.000	0.884	0.9421488	1

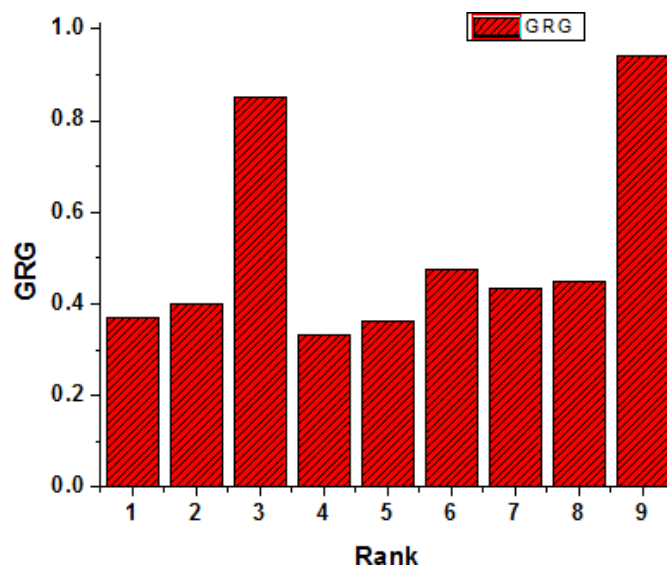


Figure 6 grey with their rank of mechanical properties

3.4 Microstructure of optimal parameter with grey responses

Figure 7 shows the SEM image of wear rates with composed composites of AZ91D Mg alloy with SiC particles. This SEM is taken as per the grey approached values with maximum and superior rank order. Therefore, this condition only met with 9th optimal runs and the parameters are 5 m/s of scanning speed, 30% of SiC proportions and 0.7 kW of laser output power, respectively. These parameters exhibit the better microhardness and wear rates and that the specified specimen is subjected for SEM analysis. From the figure 7, the worn surfaces are clearly indicates that the presence of SiC particles were occurred in maximum range with smoother grooved surfaces and better dispersion is utilized to absorbs the wear on hard carbide particles during the wear tests [20]. Some modified grains improve the wear rates and hardness with influence of superior toughness and solidification reinforced composites. Aluminium and carbide with Silicon strengthening particles presents majorly in the worn surfaces image it is one of the reason to improve the wear rates with plasticized deformation. The presence of collection agglomeration is occurred majorly in the worn surfaces. The little cut and lesser wear tracks were formed in the worn surface s due to presence of SiC particles.

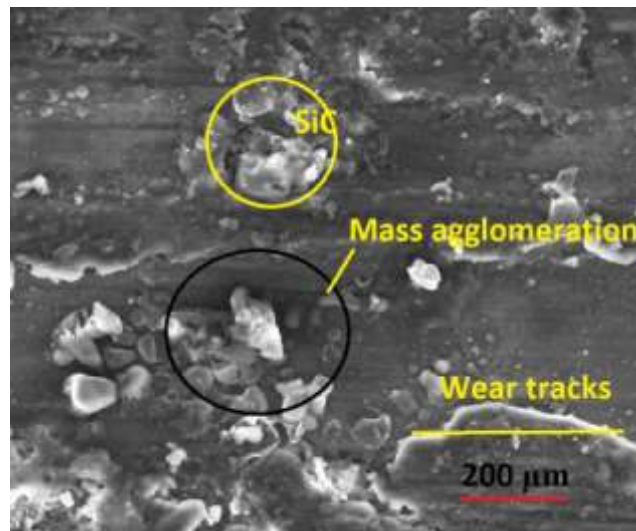


Figure 7 SEM of worn surfaces for Specimen 9

4. Conclusions

In this present study, the laser cladding process was effectively employed on AZ91D Mg alloy with influence of SiC strengthening particles through different processing constraints. The scanning speed, SiC wt. proportions and laser output power processing parameters are utilized successfully to carry out the coating process on AZ D substrates. The taguchi provides the better responses like microhardness and wear rates with single responses optimal parameters are 5 m/s of scanning speed, 30 wt. % of SiC and 0.7 kW of output laser power. Similarly, the superior wear rates are attained at the parameters 3 m/s of scanning speed, 30 wt. % of SiC and 0.8 kW of output laser power, respectively. The grey relational approach was successfully optimized the processing parameters with grey ranking procedures. The single response optimal parameters are 5 m/s of scanning speed, 30% of SiC proportions and 0.7kW of laser output power, respectively. In both the cases, maximum of SiC proportions was accumulated in the composed composite specimens due to the selected parameters and confirmation of worn surface images was verified effectively in the optimal parameter specimen. The solidification and even dispersion of SiC particles on the substrates was the

significant aspects to enhancing the wear rates.

References:

1. Ma, Z., Xia, C., Zhong, H., Yang, T., Liu, N., Liang, C., & Li, Q. (2023). Microstructure, mechanical property and corrosion resistance of FeCoCrNi-M high- entropy alloy coatings on 6061 aluminum alloy prepared by laser cladding. *Surface and Coatings Technology*, 455, 129217. <https://doi.org/10.1016/J.SURFCOAT.2022.129217>
2. Gao, Z., Geng, H., Qiao, Z., Sun, B., Gao, Z., & Zhang, C. (2023). In situ TiBX/TiXNiY/TiC reinforced Ni60 composites by laser cladding and its effect on the tribological properties. *Ceramics International*, 49(4), 6409–6418. <https://doi.org/10.1016/J.CERAMINT.2022.10.087>
3. Jiang, D., Cui, H., Chen, H., Song, X., Zhao, X., Xie, J., & Ma, G. (2023). Wear and corrosion resistance improvement of (CoCrNi)_{72-x}B₁₈Si₁₀Nb_x coatings obtained by laser cladding: Role of Nb concentration. *Materials Today Communications*, 34, 105057. <https://doi.org/10.1016/J.MTCOMM.2022.105057>
4. Yu, J., Chen, J., & Ho, H. (2023). Effect of laser cladding Ti/B₄C/dr40-based composite coatings for the surface strengthening of shaft part. *Optics & Laser Technology*, 157, 108721. <https://doi.org/10.1016/J.OPTLASTEC.2022.108721>
5. Wang, C., Li, R., Bi, X., Yuan, W., Gu, J., Chen, J., Yan, M., & Zhang, Z. (2023). Microstructure and wear resistance property of laser clad CrCoNi coatings assisted by ultrasonic impact treatment. *Journal of Materials Research and Technology*, 22, 853–864. <https://doi.org/10.1016/J.JMRT.2022.11.170>
6. Chen, X., Yao, M., Kong, F., Fu, Y., Wu, J., & Zhang, H. (2023). In-situ quality monitoring of laser hot wire cladding process based on multi-sensing diagnosis and machine learning model. *Journal of Manufacturing Processes*, 87, 183–198. <https://doi.org/10.1016/J.JMAPRO.2023.01.031>
7. Zheng, Y., Liu, F., Gao, J., Liu, F., Huang, C., Zheng, H., Wang, P., & Qiu, H. (2023). Effect of different heat input on the microstructure and mechanical properties of laser cladding repaired 300M steel. *Journal of Materials Research and Technology*, 22, 556–568. <https://doi.org/10.1016/J.JMRT.2022.11.153>
8. Zhu, Z. X., Liu, X. B., Liu, Y. F., Zhang, S. Y., Meng, Y., Zhou, H. bin, & Zhang, S. H. (2023). Effects of Cu/Si on the microstructure and tribological properties of FeCoCrNi high entropy alloy coating by laser cladding. *Wear*, 512–513, 204533. <https://doi.org/10.1016/J.WEAR.2022.204533>
9. Liang, H., Hou, J., Cao, Z., & Jiang, L. (2023). Interesting ‘island-like’ microstructure and tribological evaluation of Al_{1.5}CrFeNiW_{0.5}Ti_{0.5} high entropy alloy coating manufactured by laser cladding. *Tribology International*, 179, 108171. <https://doi.org/10.1016/J.TRIBOINT.2022.108171>
10. Hua, S. W., Pang, M., Ji, F. Q., Chen, J., & Liu, G. (2023). Microstructure and tribological properties of Ti₂AlC-B particle-enhanced self-lubricating coatings on Ti6Al4V by ultrasonic impact treatment and laser cladding. *Materials Today Communications*, 34, 105165. <https://doi.org/10.1016/J.MTCOMM.2022.105165>
11. Li, C., Xia, F., Yao, L., Li, H., & Jia, X. (2023). Investigation of the mechanical properties and corrosion behaviors of Ni-BN-TiC layers constructed via laser cladding technique. *Ceramics International*, 49(4), 6671–6677. <https://doi.org/10.1016/J.CERAMINT.2022.10.104>
12. Jiang, Y., Xiao, L., Zhai, P., Li, F., Li, Y., Zhang, Y., Zhong, Q., Cai, Z., Liu, S., & Zhao, X. (2023). Microstructure and properties of Cu-Cr-SiC in-situ composite coatings by laser cladding. *Surface and Coatings Technology*, 456, 129264. <https://doi.org/10.1016/J.SURFCOAT.2023.129264>
13. Teng, L., Shi, X. H., Wang, H. H., Li, W., Yin, X. M., & Li, H. J. (2022). A new method to improve the laser-ablation resistance of Si-SiC coating on C/C composites: Laser cladding. *Journal of the European Ceramic Society*, 42(14), 6425–6434. <https://doi.org/10.1016/J.JEURCERAMSOC.2022.07.028>
14. Rezaee Hajideh, M., & Farahani, M. (2023). Direct laser metal deposition cladding of IN718 on DIN 1.2714 tool steel reinforced by the SiC nanoparticles. *Journal of Materials Research and Technology*. <https://doi.org/10.1016/J.JMRT.2023.01.107>
15. Li, F. F., Ma, N. N., Chen, J., Zhu, M., Chen, W. H., Huang, C. C., & Huang, Z. R. (2022). SiC ceramic mirror fabricated by additive manufacturing with material extrusion and laser cladding. *Additive Manufacturing*, 58, 102994. <https://doi.org/10.1016/J.ADDMA.2022.102994>
16. Sivakumar, V. R., Kavitha, V., Sri Saravanan, N., Nanjundamoorthi, T. T., & Chanakyan, C. (2022). Tribological behavior on stir casted metal matrix composites of Al 6070 and TiC reinforcement with Taguchi S/N ratios. *Materials Today: Proceedings*. <https://doi.org/10.1016/J.MATPR.2022.11.222>
17. Jiang, F., Cheng, L., Zhang, J., & Wang, Y. (2017). Fabrication of barium-strontium aluminosilicate coatings

- on C/SiC composites via laser cladding. *Journal of Materials Science & Technology*, 33(2), 166–171. <https://doi.org/10.1016/J.JMST.2016.12.002>
18. Murmu, A. M., Parida, S. K., & Das, A. K. (2023). Evaluation of in-situ synthesised titania-zirconia-boron carbide composite cladding on Ti6Al4V substrate using continuous wave fibre laser. *Materials Chemistry and Physics*, 296, 127177. <https://doi.org/10.1016/J.MATCHEMPHYS.2022.127177>
19. Liu, J., Li, Y., He, P., Tan, N., Li, Q., Zhang, G., & Lu, B. (2022). Microstructure and properties of ZrB₂-SiC continuous gradient coating prepared by high speed laser cladding. *Tribology International*, 173, 107645. <https://doi.org/10.1016/J.TRIBOINT.2022.107645>
20. Wang, H. H., Kong, J. A., Xu, M., Zhang, P. F., Yang, L., Shi, X. H., & Li, H. J. (2022). Laser ablation behavior of SiO₂-Nd₂O₃/Si-SiC-MoSi₂ coated C/C composites repaired by laser cladding. *Corrosion Science*, 198, 110132. <https://doi.org/10.1016/J.CORSCI.2022.110132>
21. Xu, Y., Wang, G., Song, Q., Lu, X., Li, Z., Zhao, Q., & Chen, Y. (2022). Microstructure, mechanical properties, and corrosion resistance of SiC reinforced Al_xCoCrFeNiTi_{1-x} high-entropy alloy coatings prepared by laser cladding. *Surface and Coatings Technology*, 437, 128349. <https://doi.org/10.1016/J.SURFCOAT.2022.128349>
22. Alagarsamy, S.V., Chanakyan, C., Prabhakaran, P., Mathew, A.A., Senthamarai, K. (2023). Performance Studies of Process Parameters on Friction Stir Processed AA5052 by Grey Analysis. In: Vignesh, R.V., Padmanaban, R., Govindaraju, M. (eds) *Advances in Processing of Lightweight Metal Alloys and Composites. Materials Horizons: From Nature to Nanomaterials. Springer, Singapore.* https://doi.org/10.1007/978-981-19-7146-4_15
23. Riquelme, A., Rodrigo, P., Escalera-Rodríguez, M. D., & Rams, J. (2019). Characterisation and mechanical properties of Al/SiC metal matrix composite coatings formed on ZE41 magnesium alloys by laser cladding. *Results in Physics*, 13, 102160. <https://doi.org/10.1016/J.RINP.2019.102160>
24. Zhuang, D.-D., Tao, W.-W., Du, B., Zhang, S.-H., Lian, X.-L., & Wang, F. (2023). Microstructure and properties of TiC-enhanced CrMnFeCoNi high-entropy alloy coatings prepared by laser cladding. *Tribology International*, 180, 108246. <https://doi.org/10.1016/J.TRIBOINT.2023.108246>
25. Li, J., Gu, J., Zhang, Y., Wang, Z., & Zhang, G. (2023). Study on laser cladding process and friction characteristics of friction pairs of copper-based powder metallurgy materials. *Tribology International*, 177, 107953. <https://doi.org/10.1016/J.TRIBOINT.2022.107953>
26. Kong, Y., Liu, Z., Wang, X., Li, J., & Liu, Q. (2023). Evolution in microstructure and oxidation behaviors of the laser cladding C22 coatings with the Si addition concentrations. *Journal of Alloys and Compounds*, 932, 167536. <https://doi.org/10.1016/J.JALLCOM.2022.167536>
27. Wu, W.-J., Zou, Y., Li, C.-H., Li, Y.-W., Wang, Z.-Y., Chang, N., & Shi, Y.-S. (2023). Effect of impregnated phenolic resin on the properties of Si-SiC ceramic matrix composites fabricated by SLS-RMI. *Ceramics International*, 49(2), 1624–1635. <https://doi.org/10.1016/J.CERAMINT.2022.06.324>
28. Mi, G., Xiang, Y., Wang, C., Xiong, L., & Ouyang, Q. (2023). Microstructure and mechanical properties of SiCp/Al composite fabricated by concurrent wire-powder feeding laser deposition. *Journal of Materials Research and Technology*, 22, 66–79. <https://doi.org/10.1016/J.JMRT.2022.11.112>
29. Karthick, L., S. Sivakumar, A. Sasikumar, A. Prabhu, J. Senthil Kumar, and L. Vadivukarasi. (2022). A comparison and analysis of mechanical properties of glass fiber and banana fiber composite. *Materials Today: Proceedings* 52, 398-402.
30. Joseph Leon, S.L., et al., (2022). Heat Index Based Optimisation of Primary Process Parameters in Friction Stir Welding on Light Weight Materials. *Advances in Materials Science and Engineering*.
31. Karthick, L., et al. (2022). Influence of Nano-/Microfiller Addition on Mechanical and Morphological Performance of Kenaf/Glass Fibre-Reinforced Hybrid Composites. *Journal of Nanomaterials*.

Hardness and Compressive Properties on Metal Matrix Composites with Influence of Nano Ceramic Particles through Powder Metallurgy Process

N. Bhuvaneshwari¹, Muthusamy², Ravikiran Kamath Billady³, Balakrishnan S⁴,
MarximRahula Bharathi B⁵, L. Vadivukarasi⁶

¹Department of Physics, Rathinam College of Arts and Science, Coimbatore -641021.

²Department of Mechanical Engineering, Pollachi Institute of Engineering and Technology, Pollachi -642205. ³Nitte (Deemed to be University), NMAM Institute of Technology (NMAMIT), Department of Mechanical Engineering, Nitte, India.

⁴Department of Mechanical Engineering, Francis Xavier Engineering College, Tirunelveli, 627003, Tamil Nadu, India.

⁵Aditya college of Engineering, Surampalem, Andhra Pradesh.

⁶Department of Mathematics, Nandha Arts and Science College, Erode, India.

Corresponding Author: *bhuvana23mscphd@gmail.com*

Abstract: Hardness and compressive strength of metal matrix composites (MMCs) are influenced by different processing constraints like various sizes of reinforcing particles, different weight ratios and mixing time. Due to segregation of strengthening particles in the MMCs were easily occurred in the stir casting process and it is very complex to evade. Therefore, the powder metallurgy process is the significant route to prepare the composites with base matrix of aluminium alloy AA1050 and ceramic hard particles of chromium carbide (Cr_3C_2) were utilized in this research. During this process, instead of ball milling, the barrel based mixer was utilized to mixing the powders to compose quality based composites. Therefore, in this study barrel mixing time is considered as main parameters consequently the various sizes of strengthening particle and different weight proportions were utilized. The new approach of barrel mixing with different time durations from 15 to 45 min, different nano sized ceramic particles (10 to 20 nm) and various weight proportions of particles (10 to 14%) were investigated through the powder metallurgy process. finally, the maximum time at 45 min and increasing the particles from 10 to 14% and nano sizes composes better hardness and compressive strength. The contour interpretation is explained the different approaches of process parameters on the prepared composites.

Keyword: MMCs, Hardness, Compressive, Cr_3C_2 and Contour.

1. Introduction

Owing to various exclusive performances and the possibility of tailor related characteristics, the metal matrix composites possess attained from the different researchers. Some of the few exemplar properties like creep, maximum specific strength, lesser densities, and greater fatigue are specific properties which are based on the metal matrix composites and advances to traditional materials [1-2]. The generally composed metal matrix composites might exhibit the lesser thermal expansion and maximum wear resistances to appropriate for utilize in packaging sections, nuclear components for aerospace applications. There are various applications in the automotive sectors like, pistons, transmission shafts and turbine blades are the components and it's also implemented MMCs in the different automobile companies [3-
Dept. of Mech. Engg.

4].

The different ceramic particles like aluminium oxide, titanium carbide, and chromium oxide, chromium carbide and silicon carbide are strengthened into aluminium based alloy and other magnesium alloy or aluminium alloy matrix. The incorporation of magnesium in the ceramic particulates of Cr_3O_2 or Cr_3C_2 related MMC can participate important aspects in the maintaining tailored made characteristics like creep strength, yield strength and tensile strength [5]. The preferred properties of metal matrix composites could be obtained by the different shapes, categories and proportions of strengthened particulate. When compared to other process for the production of metal matrix composites, the powder metallurgy method provides better manufacturing and also gives reliable technique [6-7]. For example, the stir casting process normally produces the wettability issues but in powder metallurgy process some free defects like temperature gradient, surface tension, density issues and other chemical reactions and mass agglomeration. During the powder metallurgy process, the appropriated powders were wellmixed into the base material; the fore mentioned defects are not produced [8].

The proper blending of matrix material is the major advancing process and the strengthened particles could obtain in solid state and it is the major reasonable management from the other processing constraints. It leads to composes defect free intermetallic surface without any change of phase in the processed materials and chemical responses. When utilizing the powder metallurgy process, reinforcement isolation is not produced and it is one of the major disadvantages in stir casting process [9-10]. The powder metallurgy process is most suited technique to produce the metal matrix composites and it is a clear cut process and valuable processing ways to achieve the end product. It is far sighted to identify that the reinforcement particle sizes and its dimensions will change the characteristic of objective metal matrix composite material. Similarly, the compaction pressure may be influenced by the size of the particles and potency of strengthening particle. Next to compaction, the sintering process is the most significant one for resolving the creation of large angle grain boundary and porosities in the MMCs [11-12].

The essential mechanical tool is also straightforward when it is contrasted to other techniques like PVD, infiltration spray deposition process, CVD and other specific methods like rapid prototyping process. In powder metallurgy process, the above issues will easily solve. The better arrangement of metal and non metals to compose the different metal matrix composites are offered by the powder metallurgy process [14-15]. Usually, in the process of liquid metallurgy reaction products and their creations will easily formed and these overcomes are rectified in this powder metallurgy process. The superiority of processed MMCs based components and their mechanical properties are very much reliant on the blending and evenly scattered distribution of strengthening particles is composed via the powder metallurgy process. There are various researchers have specified advances in the mixing of powders in the powder metallurgy process. The following steps like, blending powders; compaction and post processing are required to compose the MMCs. Therefore, the most advantages of this process are mixing of powders to get the desired MMCs without defects [16-18].

Mulisa et al. [19] reported that the fabricated Fe based MMCs through the powder metallurgy process are developed in hardness strength and corrosion performances. The increasing amount of reinforcing particles improves the strength and reduces density. Chufan et al. [20] fabricated the lamellar structure in Ti-Ta alloys under the sintering pressure of $1600\text{ }^\circ\text{C}$. The

mechanical properties were enhanced by the increasing of Ta content through the powder metallurgy process. Dinaharan et al. [21] prepared the copper matrix composites through the powder metallurgy process with different industrial waste ceramic materials. It is concluded that the copper and boron carbide particles presented composites had better mechanical strength when compared to the other combinations of copper-flyash and copper-W. Mofijul et al. [22] conducted the EDM on the composites by the powder metallurgy process. During the process, various sintering and compaction loads were applied on the SiC-nano graphite on the aluminium alloy and strengthen the characteristics. By increasing the content of ceramic particles improves the hardness and enhances the surface roughness. Dinesh kumar et al. [23] synthesized the MMCs by increasing of SiC into the magnesium powders. The mixing of SiC powders with 12% enhances the mechanical strength. The maintaining of ball mill at 10 min improves the grain refinement and strengthens the MMCs. From these reviews, carbide based ceramic particles strengthens the MMCs and improves the wear rates which is clearly indicated in the above mentioned literatures.

From the detailed literatures, metal matrix composites can be composed defect free by the route of powder metallurgy process. The segregation of reinforcement is easily avoided during this process. At the same time, appropriated reinforcement in solid state and permitting allowable control from the different processing constraints. Considering these issues, the aim of this current work is to investigate the influence of different processing variables like particles proportions, mixing time and particle sizes are the significant key aspects which can affect that the blending characteristics of the selected nano powders [24-26]. From the similar research, the mechanical properties of glass fiber and banana fiber was analysed and found the better fiber [27]. The mechanical study was carried out on AA2024-T3 plates to improve the properties of the composite materials [28]. From another study, to ascertain how nano-/micro-TiO₂ affects the mechanical properties of kenaf/glass/epoxy hybrids [29].

In this research, barrel based mixer was utilized to mixing the powders with different time period. Owing to this method, clustering of powder is easily removed and led to produce the superior blending behaviors when utilizing the barrel based mixer. The different researchers proved that the blending by the barrel based mixers composes better hardness and compressive strength on the processed MMCs. Consequently, the novel method is achieved in the blending of nano powders are approached in this research. Moreover, this works also explored the impact of different proportion of Cr₃C₂ and particle different dimensions on the hardness and compressive strength of the composed metal matrix composites. Utilizing these processing constraints, the defect free metal matrix composites are developed during the powder metallurgy process by the influence of chromium carbide particles. It is cleared from the literatures; the barrel mixing time and different strengthening particulates of chromium carbide through the powder metallurgy process is not conducted so far. Similarly, the Taguchi combinations with contour analysis is effectively implemented with their different parameters is done in previous research.

2. Materials and Methods

The selected essential powders of AA1050 aluminium alloy and chromium carbide have been utilized to arrange the metal matrix composites. From the various strengthening particulates, chromium carbide is extensively approached in the production of metal matrix composites material. The accessibility of Cr₃C₂ in the form of powder in various sizes and

cleanliness is an added motive to desire Cr₃C₂ among the other strengthening particles. The average size of Cr₃C₂ particle having the sizes of 10, 15 and 20 nm is used for powder metallurgy process. The moisture content test is utilized for each and every sample of chromium oxide powder and AA1050 aluminium alloy powder. Around 15% of chromium oxide powder of lesser reinforcing size which is less than 30 nm and it takes the better advancement in the particle sizes added much potency in the processed composites. The powder metallurgy composes the green compacted composites in the sintering steps which influenced by intermetallic region with particle size. The Cr₃C₂ is added into the AA1050 aluminium alloy with three ratios like 10, 12 and 14%. The barrel mixing with stimulated shear is utilized to mixing both powders to generate the quality of composites. The schematic illustration of present research is displayed in figure 1.

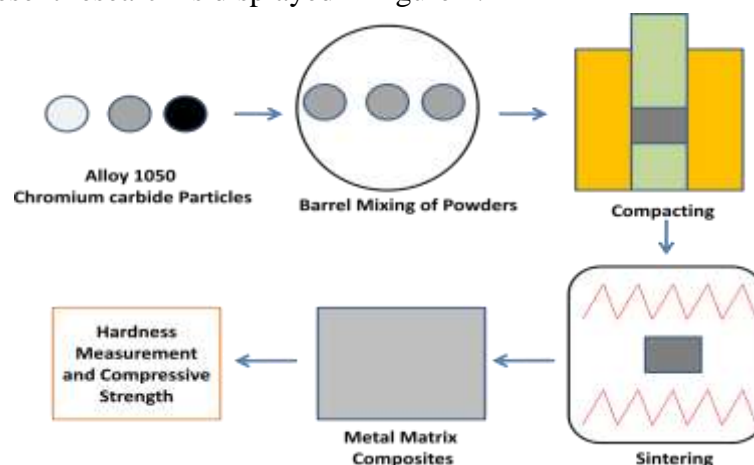


Figure 1 Schematic illustration compose composites through powder metallurgy process

The barrel based mixer having components of agitator, the both components are rotating oppositedirection to get desired composites mixing without agglomeration and clustering in the localized region. These issues were easily eradicated during the mixing process. After adding the different proportions of Cr₃C₂ into the aluminium alloy by barrel mixer, the proposed green MMCs were fabricated by powder metallurgy process. The mixed powders were poured into circular die with support of steel punch machine by maintain of 200 MPa pressure. After that the completed specimens were taken for sintering process with utilizing of argon gas inert atmosphere by 600⁰C of sintering temperature at holding time 60 min. Subsequently, water quenching and drying is approached for all the samples. The microstructure is used to analyze the presence of chromium carbide particles by the following procedures like 100 to 800 grit size emery paper and diamondpaste having the 2 micro meters to takes place in the processed samples for attaining the uniform dispersion in MMCs. The processing constraints like different chromium carbide particle sizes, different proportions and barrel mixing time are approached into Taguchi design for arranging the levels of parameters. It is considered that above levels, L9 Taguchi method is suitable for that. Then the processed composites samples were accounted for investigating hardness and compressive strength. Table 1 shows the different processing parameters for present powder metallurgy process.

Table 1 Various processing variable in powder metallurgy process

Sample No	Nano Cr ₃ C ₂ sizes	Weight ratio of Cr ₃ C ₂	Barrel Mixing duration (min)
-----------	---	--	------------------------------

1	10	10	15
2	10	12	30
3	10	14	45
4	15	10	30
5	15	12	45
6	15	14	15
7	20	10	45
8	20	12	15
9	20	14	30

3. Results and Discussion

3.1 Hardness measurements and compressive strength on MMCs

The required properties of MMCs are only achieved with support of hardness measurement. The hardness property is one of the significant one for processed materials. The occurrence of hard particles in the soft matrix alloy consequently enhances the hardness and also improves with increment of weight proportions of the ceramic hard particles. There are many investigates revealed that the increment of weight proportions of ceramic particles improves the surface hardness of the MMCs. In some special cases, the blending of powders were composed by some traditional techniques like ball milling are employed to form the intense deformation, even dispersion and fine refinement. This forwarded to the advancement of MMCs hardness and the maximum hardness of ceramic hard particulates involves improving the hardness as the shifting of load to the ceramic particle of MMCs. Nevertheless, the particulates dimensions were too superior, the contribution of improvement in hardness of MMCs were arrived from ceramic based hard particles and interfacial bonding among the strengthening particulates and matrix alloy also improves the hardness without voids and porosities.

From the table 2, it is understood that the increasing of chromium carbide particles enhances the hardness in the metal matrix composites. By increasing of chromium carbide content in the MMCs, attained with maximum hardness at the same time mixing time with longer duration takes place the better effectiveness when mixing chromium particles and matrix alloy and the dispersion of ceramic particles also achieves the better strength and Cr₃C₂ particles were dispersed evenly in the processed matrix composites. Especially the sample number 5 shows that the hardness were maximum at the processing constraints of 15 nm of Cr₃C₂ particle sizes, 12% of weight ratios and 45 min of barrel mixing. Figure 2 show the evidence of hardness measurement in the metal matrix composites. Similarly, the lesser barrel mixing time with lesser proportions of chromium carbide particles reduces the hardness on the MMCs due to less uniform dispersion of reinforcing particles on the matrix alloy. It is concluded that the barrel mixer improves the dispersion evenly in the matrix composites and indentation of maximum load is withstand highly during the hardness test on the composites.

As per the micromechanical model, the metal matrix composites of aluminium alloy AA1050 were improved by the strengthening of chromium carbide reinforcements. The increment of chromium carbide particles improves the mechanical strength when added to the aluminium alloy matrix. Similarly, the dislocation density and shear modulus are the key factor to improve the MMCs potency. Therefore, the strengthening particles with maximum value of

shear modulus are enhanced to the alloy of matrix material and it forward straight effect on the strength. Owing to fine grain sizes, compressive strength is maximized as per the estimated Hall petch equation. The hardness is initiated when blending the powders and the particle sizes. The nano particles influence the maximum work hardening. When increases the ratio from 10 to 14% chromium carbide particles, the compressive strength also increased and the Cr₃C₂ particles restricts the cracks with loading during the compressive test and the severe plastic defroamtion was takes place in the processed MMCs composites. From the table 2, the specimen 4 with processing variable at 10 nm of particle sizes, 14% weight ratio and 45 min barrel mixing composes the better compressive properties in the composites. Figure 2 shows the compressive strength on MMCs with different proportions and sizes of chromium carbide particles.

Table 2 Various processing variable on hardness and compressive strength

Sample No	Nano Cr ₃ C ₂ sizes (nm)	Weight ratio of Cr ₃ C ₂ (%)	Barrel Mixing duration (min)	Hardness (HV)	Compressive Strength (MPa)
1	10	10	15	63	165
2	10	12	30	66	168
3	10	14	45	68	181
4	15	10	30	73	175
5	15	12	45	82	179
6	15	14	15	70	169
7	20	10	45	76	177
8	20	12	15	78	174
9	20	14	30	80	176

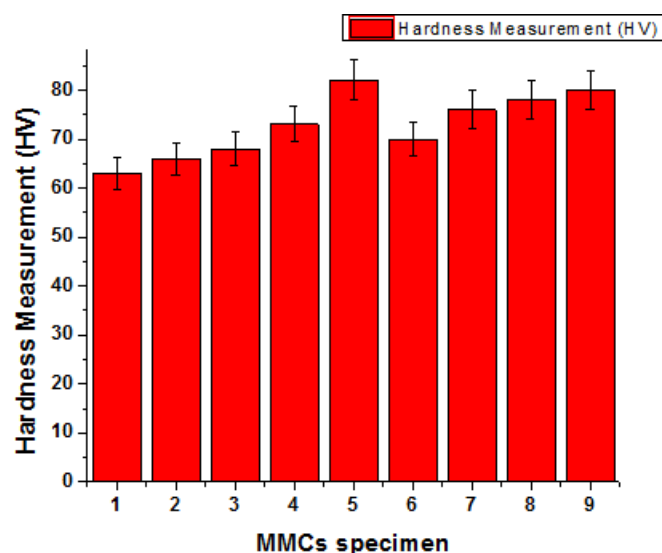


Figure 2 Hardness measurement of processed MMCs

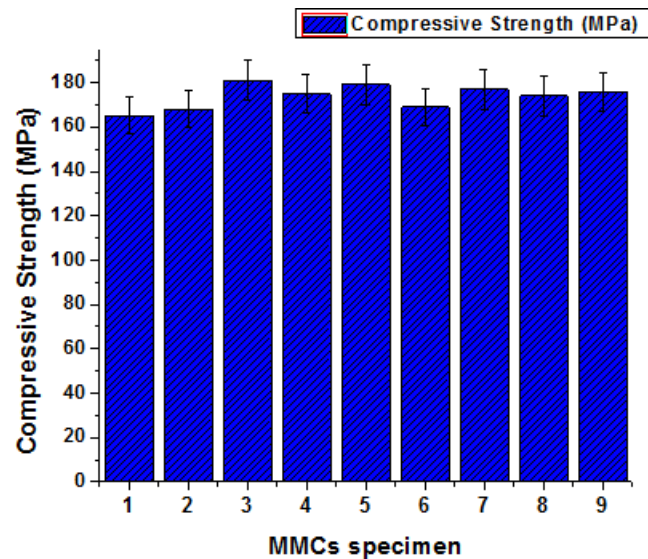


Figure 3 Compressive strength of processed MMCs

3.2 Contour analysis of hardness measurement and compressive strength on AA1050 and chromium carbide composites

Figure 4(a) to 4(c) shows the contour analysis of different processing constraints of metal matrix composites. From these figure, it is understood that the interpretation of different processing parameters with surface hardness on processed composites are clearly indicated. Figure 4(a) shows the hardness measurement by the influence of different chromium carbide particle sizes and various weight proportions. From the figure 4(a), it is implicit that the improved surface hardness was increased by the influence increment of nano chromium carbide particles from 10 to 15 and their weight proportion from 10 to 12%. Figure 4(b) shows the surface hardness on matrix composites under the parameters at weight ratio of Cr₃C₂ particulates and barrel mixing of matrix alloy and reinforcing particles. It is clearly understood that the enhanced hardness is developed from increasing of mixing time at maximum level and maximum weight proportion of chromium carbide particulates. Figure 4(c) shows the relation between the parameters of barrel mixing duration and nano reinforcing particles. From the figure 4(c), it is explored that the increasing of mixing time and increment of reinforcing particles sizes are the major reason to enhance hardness strength on the MMCs.

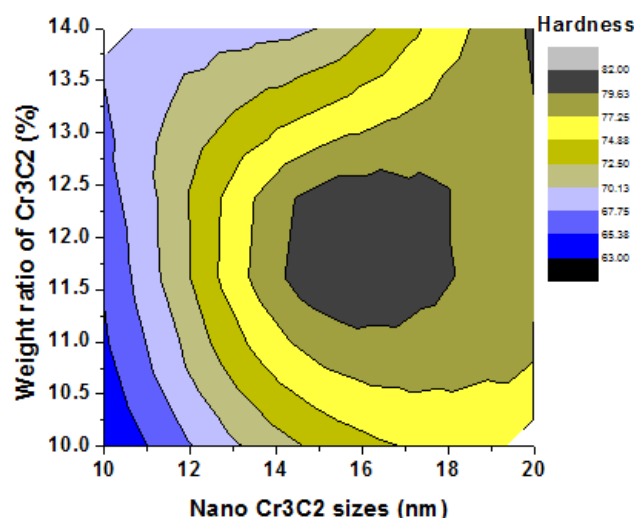


Figure 4(a) Chromium carbide particle with various sizes and proportion of composites

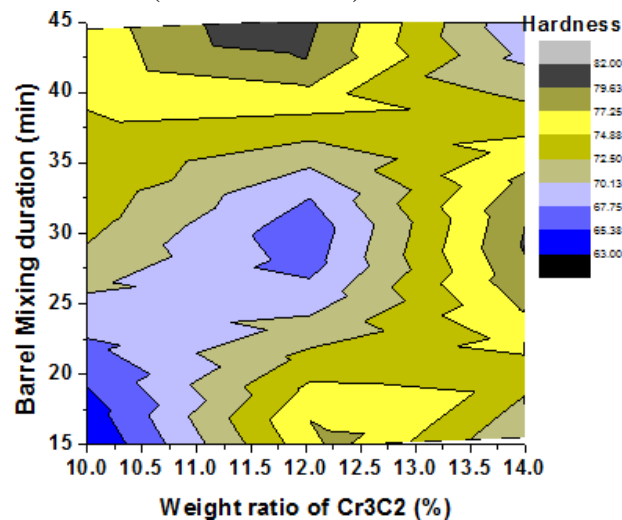


Figure 4(b) Reinforcing particle with various proportion and blending time of composites

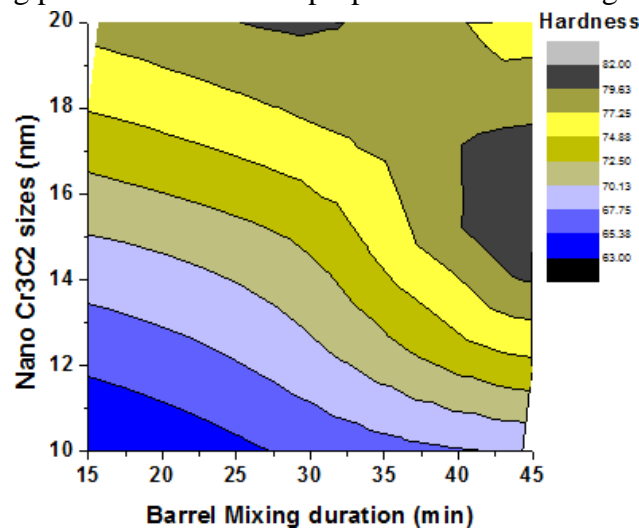


Figure 4(c) Barrel blending time and different nano particle dimensions of composites

Figure 5(a) to 5(c) exhibits the contour analysis of special processing constraints of metal matrix composites. From these figure, it is unstated that the analysis of various processing parameters with compressive strength on processed composites are evidently specified in this section. Figure 5(a) displays the compressive strength on composites by the utilizing of various chromium carbide particle sizes and different weight proportions. From the figure 5(a), it is understood that the superior compressive strength is improved by the increasing of nano chromium carbide particles from 15 to 20 nm and their weight proportion from 12 to 14%. Figure 5(b) exhibits the compressive strength on prepared matrix composites under the different parameters at weight proportion of Cr₃C₂ particulates and barrel mixing of matrix alloy and reinforcing particles. It is evidently implicit that the enhanced compressive strength is expanded from increasing of mixing time at higher range at 45 min and maximum weight proportion (14%) of chromium carbide particulates. Figure 5(c) shows the correlation between the parameters of barrel mixing time and nano carbide reinforcing particles. From the figure 5(c), it is investigated that the rising of blending time of alloy matrix and its reinforcement and addition of reinforcing particles sizes are the main significant reason to enhance compressive strength on prepared MMCs through powder metallurgy process.

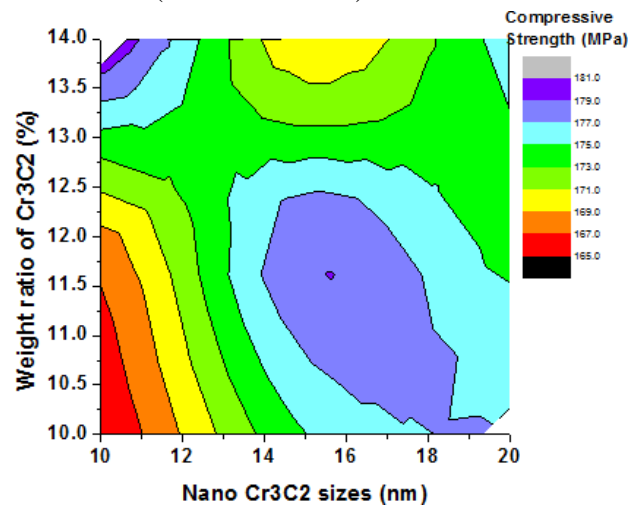


Figure 5(a) Compressive strength at different sizes and weight ratio of reinforcing particles

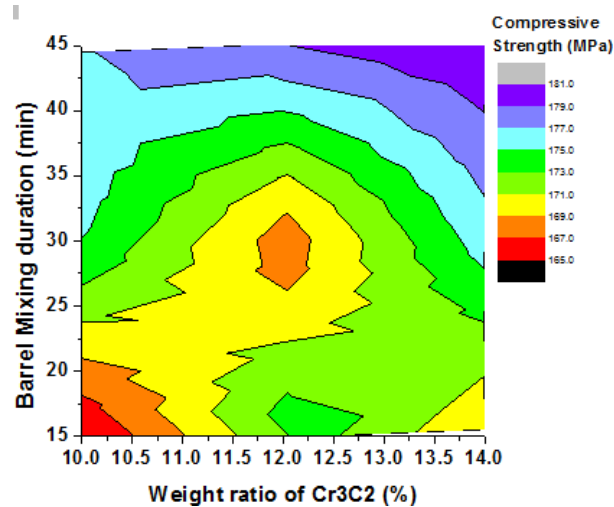


Figure 5(b) Compressive strength at various proportions and blending time of composites

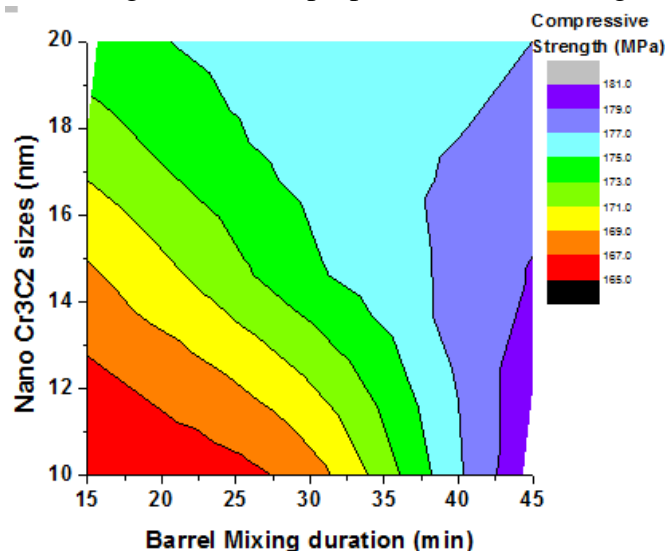


Figure 5(c) Compressive strength at Barrel blending time and various sizes of particles

4. Conclusions

In this research, the powder metallurgy processing was successfully produced the metal matrix composites from the alloy of AA1050 and chromium carbide particles. Especially the mixing of barrel is effectively composes the blended powder to make the effectiveness in the form of fine dispersion and severe plastic deformation is occurred during the process of

powder metallurgy. The different processing constraints like different proportion of nano Cr₃C₂ particles, various sizes and mixing time was effectively conducted on the processed metal matrix composites. Particularly, the mixing of barrel in powders at maximum range of time duration is the major significant aspects for improving the mechanical properties like hardness measurement and compressive strength. The process parameter at maximum sizes of Cr₃C₂ particles, 12 weight ratio and maximum mixing time at 45 min composes the better hardness on the prepared composites. Similarly, lesser size of chromium carbide particles, maximum weight proportion of particles and high level of mixing time at 45 min, produces the greater compressive strength.

References

1. V. Govindarajan et al., "Effect of Tungsten Carbide Addition on the Microstructure and Mechanical Behavior of Titanium Matrix Developed by Powder Metallurgy Route," *Advances in Materials Science and Engineering*, vol. 2022, 2022, doi: 10.1155/2022/2266951.
2. D. D. Radev, "Nickel-Containing Alloys for Medical Application Obtained by Methods of Mechanochemistry and Powder Metallurgy," *ISRN Metallurgy*, vol. 2012, p. 464089, 2012, doi: 10.5402/2012/464089.
3. K. Moeinfar, F. Khodabakhshi, S. F. Kashani-bozorg, M. Mohammadi, and A. P. Gerlich, "A review on metallurgical aspects of laser additive manufacturing (LAM): Stainless steels, nickel superalloys, and titanium alloys," *Journal of Materials Research and Technology*, vol. 16, pp. 1029–1068, 2022, doi: 10.1016/j.jmrt.2021.12.039.
4. O. S. Onwuka, G. O. Unachukwu, and S. C. Nwanya, "Design and development of a brush atomization machine for metal powder production," *Scientific African*, vol. 14, p. e00986, 2021, doi: 10.1016/j.sciaf.2021.e00986.
5. W. Abd-Elaziem et al., "On the current research progress of metallic materials fabricated by laser powder bed fusion process: a review," *Journal of Materials Research and Technology*, vol. 20, pp. 681–707, 2022, doi: 10.1016/j.jmrt.2022.07.085.
6. S. Narayan and A. Rajeshkannan, "Workability Behaviour of Powder Metallurgy Aluminium Composites," *Journal of Powder Technology*, vol. 2014, p. 368721, 2014, doi:10.1155/2014/368721.
7. Z. Jiang and C. Zhou, "Automatic Measurement of Nanoimage Based on Machine Vision and Powder Metallurgy Materials," *Advances in Materials Science and Engineering*, vol. 2022, p. 8975190, 2022, doi: 10.1155/2022/8975190.
8. D. Yang, L. Lu, and Z. Wan, "Material Removal Mechanism of Green Machining on Powder Metallurgy Parts during Orthogonal Cutting," *Advances in Materials Science and Engineering*, vol. 2020, p. 1962602, 2020, doi: 10.1155/2020/1962602.
9. K. Kondoh, T. Threrujirapong, H. Imai, J. Umeda, and B. Fugetsu, "CNTs/TiC Reinforced Titanium Matrix Nanocomposites via Powder Metallurgy and Its Microstructural and Mechanical Properties," *Journal of Nanomaterials*, vol. 2008, p.127538, 2008, doi: 10.1155/2008/127538.
10. B. Stalin et al., "Investigations on Microstructure, Mechanical, Thermal, and Tribological Behavior of Cu-MWCNT Composites Processed by Powder Metallurgy," *Journal of Nanomaterials*, vol. 2021, p. 3913601, 2021, doi: 10.1155/2021/3913601.
11. W. Yu et al., "Influence of Nitrogen Content on the Corrosion Behavior of Powder Metallurgy Nickel-Free Austenitic Stainless Steel," *Advances in Materials Science and Engineering*, vol. 2021, p. 7808070, 2021, doi: 10.1155/2021/7808070.
12. W.-N. Hsu, T.-S. Shih, and M.-Y. Lin, "Preparation of Al-Mg Alloy Electrodes by Using Powder Metallurgy and Their Application for Hydrogen Production," *Advances in Materials Science and Engineering*, vol. 2014, p. 594984, 2014, doi:10.1155/2014/594984.
13. X. Feng, A. Tao, and Z. Song, "Construction and Performance Research of Reinforced Iron-Based Powder Metallurgy Materials Based on Phyllanthin as Drug Transport Carriers," *Advances in Materials Science and Engineering*, vol. 2022, p. 8528074, 2022, doi: 10.1155/2022/8528074.
14. S. Pradeep Devaneyan, R. Ganesh, and T. Senthilvelan, "On the Mechanical Properties of Hybrid Aluminium 7075 Matrix Composite Material Reinforced with SiC and TiC Produced by Powder Metallurgy Method," *Indian Journal of Materials Science*, vol. 2017, p. 3067257, 2017, doi: 10.1155/2017/3067257.
15. P. Gupta, D. Kumar, O. Parkash, and A. K. Jha, "Sintering and Hardness Behavior of Fe- Al₂O₃ Metal Matrix Nanocomposites Prepared by Powder Metallurgy," *Journal of Composites*, vol. 2014, p. 145973, 2014, doi: 10.1155/2014/145973.
16. X. feng Guo, L. Jia, Z. lin Lu, Z. guo Xing, H. Xie, and K. Kondoh, "Preparation of Cu/CrB₂ composites with well-balanced mechanical properties and electrical conductivity by ex-situ powder metallurgy,"

Two-day International Conference on Recent Advances in Mechanical and Industrial Engineering – 2023
(ICRAMIE-2023)

- Journal of Materials Research and Technology, vol. 17, pp. 1605–1615, 2022, doi: 10.1016/j.jmrt.2022.01.112.
17. L. E. Murr, “Metallurgy principles applied to powder bed fusion 3D printing/additive manufacturing of personalized and optimized metal and alloy biomedical implants: An overview,” Journal of Materials Research and Technology, vol. 9, no. 1, pp. 1087–1103, 2020, doi: 10.1016/j.jmrt.2019.12.015.
 18. T. Panneerselvam, T. K. Kandavel, and P. Kishore, “Experimental Investigation on Cutting Tool Performance of Newly Synthesized P/M Alloy Steel Under Turning Operation,” Arabian Journal for Science and Engineering, vol. 44, no. 6, pp. 5801–5809, Jun. 2019, doi: 10.1007/s13369-019-03763-4.
 19. Mulisa Olani, Devendra Kumar, Getinet Asrat, Mechanical and corrosion properties of Fe–SiC–ZrO₂ hybrid composite fabricated through powder metallurgy process, Results in Engineering, Volume 17, 2023, 100866, <https://doi.org/10.1016/j.rineng.2022.100866>.
 20. Chufan Wang, Qi Cai, Jinxu Liu, Xifeng Yan, Strengthening mechanism of lamellar-structured Ti–Ta alloys prepared by powder metallurgy, Journal of Materials Research and Technology, Volume 21, 2022, Pages 2868–2879, <https://doi.org/10.1016/j.jmrt.2022.10.095>.
 21. Isaac Dinaharan, Thangadurai Albert, Effect of reinforcement type on microstructural evolution and wear performance of copper matrix composites via powder metallurgy, Materials Today Communications, Volume 34, 2023, 105250, <https://doi.org/10.1016/j.mtcomm.2022.105250>.
 22. Mofijul Islam, Abhijit Bhowmik, Shamim Haidar, Srijit Biswas, Machining performance of Nano SiC and graphite powder mixed aluminum matrix composites fabricated by powder metallurgy using EDM, Materials Today: Proceedings, 2022, <https://doi.org/10.1016/j.matpr.2022.11.123>.
 23. S. Dinesh Kumar, et al., “Mechanical properties of magnesium-silicon carbide composite fabricated through powder metallurgy route,” Materials Today: Proceedings, Volume 27, Part 2, 2020, Pages 1137–1141, ISSN 2214-7853, <https://doi.org/10.1016/j.matpr.2020.01.592>.
 24. P. Kishore, P. M. Kumar, and D. Dinesh, “Wear analysis of Al 5052 alloy with varying percentage of tungsten carbide,” AIP Conference Proceedings, vol. 2128, no. 1, p. 040003, Jul. 2019, doi: 10.1063/1.5117965.
 25. D. Srinivasan et al., “Tribological Behavior of Al/Nanomagnesium/Aluminum Nitride Composite Synthesized through Liquid Metallurgy Technique,” Journal of Nanomaterials, vol. 2022, p. 7840939, 2022, doi: 10.1155/2022/7840939
 26. V.R. Sivakumar, V. Kavitha, N. Sri Saravanan, T.T. Nanjundamoorthi, C. Chanakyan, Tribological behavior on stir casted metal matrix composites of Al 6070 and TiC reinforcement with Taguchi S/N ratios, Materials Today: Proceedings, 2022, <https://doi.org/10.1016/j.matpr.2022.11.222>.
 27. Karthick, L., S. Sivakumar, A. Sasikumar, A. Prabhu, J. Senthil Kumar, and L. Vadivukarasi. "A comparison and analysis of mechanical properties of glass fiber and banana fiber composite." Materials Today: Proceedings 52 (2022): 398-402.
 28. Joseph Leon, S.L., et al., “Heat Index Based Optimisation of Primary Process Parameters in Friction Stir Welding on Light Weight Materials”. Advances in Materials Science and Engineering, 2022.
 29. Karthick, L., et al. "Influence of Nano-/Microfiller Addition on Mechanical and Morphological Performance of Kenaf/Glass Fibre-Reinforced Hybrid Composites." Journal of Nanomaterials 2022.

Robopill for Enhanced Drug L-Carnitine Delivery in the Gastrointestinal Tract

Vikram Vinayakrao Nimbalkar^{1*}, Niraj S Vyawahare², Manoj Maruti Jagdale³,
Pandurang M. Gaikwad⁴

^{1,4}Department of Pharmacology, DRVVPF'S College of Pharmacy, Ahmednagar,
Maharashtra -414111.

²Department of Pharmacology, Pad. Dr. D. Y. Patil College of Pharmacy, Akurdi, Pune
411044

³Department of Medicine, Late. Yashwantrao Chavan Dental College and Hospital,
Ahmednagar

**Corresponding Author Email: rajevikram@gmail.com*

Abstract: Parenteral administration of these drugs is required since the gastrointestinal tract's degradative environment and poor absorption limit the oral drug distribution of proteins. Luminal mucus is one of the initial steric and dynamic obstacles to absorption. This article will cover the Robopill, a robotic oral drug delivery capsule that enhances luminal mixing, eliminates localized mucus layer blockages, and topically delivers the drug payload throughout the small intestine to enhance drug absorption. The plicae circulares, villi, and mucus are removed and churned by the robopill's internal motor and surface properties working together. L-carnitine treatment with Robopill resulted in improved bioavailability that was 20–40 times larger than standard oral dosage in *ex vivo* and *in vivo* pig models. The therapeutic hypoglycemia brought on by insulin delivery via the Robopill is further evidence of the Robopill's potential to permit oral administration of drugs that are often restricted by absorption constraints.

Keywords: *micropill, microneedles, L-Carnitine, iontophoresis, ultrasound and epithelial layer*

1. INTRODUCTION

The capacity of medication to dissolve in GI fluid, traverse the tough belly's acid, maintain stability no matter the intestine's constantly converting microbiota in addition to degradative enzymes, avoid being absorbed lower back by using efflux pumps, and accomplish healing bioavailability are all important [1]. due to the sub - therapeutic bioavailability levels of many capsules, more, time-consuming administration strategies are required. For instance, millions of diabetes patients global want to take insulin each day, a peptide with a bioavailability within the mouth of less than 1%. Subcutaneous injections are required for this, which can also motive anxiety, discomfort, and nonadherence because of the injection procedure [2]. Because of the bad oral bioavailability of vancomycin, a tiny drug typically used to deal with extreme Gram-effective bacterial infections, intravenous treatment and a high priced clinic stay are required [3]. technology have a great capacity to assist sufferers gather necessary pharmacological therapy and assist the pharmaceutical enterprise in creating more widely established medicinal drugs by using putting off boundaries to absorption, distribution, metabolism, and removal [4].

In the beyond, micro stirrers were developed to carry out in-situ stirring, and that they have

established the capability to hurry up bioavailability and absorption [5, 6]. Nano biotechnology techniques, along with tubular μm in diameter lined with pH-responsive polymers, have shown centered distribution and better retention in stomach tissues and mucosa, but their utilization is confined to pick pharmaceutical classes and has now not but been scaled as much as huge mouse models or people [7]. Higher tissue permeability is provided via PEGylated liposomes which can go mucus, although they require time-consuming drug-unique tailoring. Although ultrasonic vibrations and low-frequency micro vibrations have proven promise in mechanically reaching better delivery charges, scientific programs require greater realistic transport techniques. Drug transport fees through viscous mucus can be extended via enhancing drug dispersion, producing mucus layer mixing, and momentarily exposing the epithelial layer [8].



Figure 1. Prototype Robopill

This article will cover the creation of the RoboCap, a robot oral pharmaceutical delivery device that enhances blending, topically distributes the drug payload, and reduces localized mucus to promote drug absorption (figure 1). Small intestine (SI) plicae, villi, and mucus fast interact with surface elements at the RoboCap to provide spinning and churning motions. We anticipate that using the RoboCap as adverse to conventional oral shipping will significantly growth the drug's bioavailability. We examine the RoboCap's performance in administering the version peptide medicines, insulin and vancomycin in vivo on pigs and Franz cell diffusion [9].

The Section II of the remaining portions of the report discussed the numerous robopill-related work. The recommended technique of the study in this article was presented in Section III. The outcomes of the suggested work are displayed and discussed in section IV. The intended work was completed in Section V.

2. LITERATURE SURVEY

The gastrointestinal machine can be used to physically distribute remedy via an expansion of various drug management methods. Warmth has been proven to significantly enhance physical routes of medication delivery [10]. The stratum corneum has been removed by means of direct laser ablation the use of targeted microsecond heat pulses which will create microchannel with a diameter of between 10 and a hundred μm within the pores and skin for transdermal distribution. Additionally, hyperthermia has been utilized for most cancer remedy for a long time, and localized heating using magnetic nanoparticles has been investigated as a technique to improve remedy delivery [11]. Further to the physical switch of warmth to tissue to start or beautify drug transport, heat has also been studied as a trigger mechanism for managed drug management in the GI tract [12]. Using this technique, medicine transport drugs have been blanketed from the pH variations within the GI tract surroundings through being wrapped in a wax that included nanoparticles. Magnetic

hyperthermia changed into used to motive heating within the wax by way of nanoparticle movement, exposing the capsule to create warmth and cause the drug shipping mechanism. Further to at once handing over heat by means of laser ablation or magnetic hyperthermia, close to-infrared radiation (NIR) has been validated to be a useful method for starting bodily remedy delivery [14]. The possibility for a reliable and at ease outside triggering mechanism is suggested through the capacity of NIR waves from 650 to 900 nm to permeate tissue as much as centimeters deep with little or no of the tissue that absorbs these wavelengths. It has been tested that using gold nanoparticles that absorb NIR has substantial benefits for the drug transport method [15].

Research has also been performed on magnetic drug delivery techniques [16]. These strategies normally hire a magnetically nanoparticle that acts because the particle's center and which reason the machine to move or prompt while faced with an external magnetic area. Then, a protecting cloth like silica or a chemical coating is applied to this particle. Then, a natural linkage molecule and an energetic biomolecule are connected to the protective coating's floor at every give up. The issues posed by using hypoxic zone in cancer treatment had been efficiently addressed via this tactic [17]. This approach should make it feasible to create customized drug delivery profiles, which have been proved to be efficient in treating precise ailments. For instance, it has been confirmed that pulsatile transport styles are effective in overcoming adaptive resistance displayed via most cancers cells exposed to remedy. If you want to create these ferrogels, an alginate hydrogel is first blended with iron oxide powder earlier than being forged as a pure segment fabric. So one can create biphasic systems and entice all of the iron pozzolanic materials to 1 facet all through the casting method, the ferrogel may be exposed to a magnetic area [18].

Additionally, bodily drug transport techniques can make use of electric fields [19]. Hydrogels can be created with a view to de-swell whilst uncovered to an electric powered field that allows you to generate a pressure gradient that releases the remedy. Those hydrogels work on the identical standards because the previously said ferrogels. In reality, those materials work as smooth actuators. Due to the simplicity of establishing gadgets that can produce an electrical stimulus, electric powered fields can be useful for GI drug transport alternatives. That is especially authentic whilst as compared to magnetic triggers, which frequently need large external tools [20].

Convective-greater transport is a much less studied physical drug shipping approach that might be beneficial in GI remedy transport [21]. In preference to diffusive drift produced via a concentration gradient, this technique makes use of most emission pushed by a stress distinction throughout the drug-shipping catheter. By way of using this technique, it isn't essential to apply the surprisingly excessive drug concentrations required to set off viscous dissipation flow into tissue. Convective-primarily based flow is also impartial of molecular weight, whereas big molecules may diffuse slowly or under no circumstances in diffusive glide. Therapeutics are actually administered to the main frightened gadget using this technique [22].

The various technology discussed here haven't undergone medical trying out. To increase these innovations into scientific utility, there are some of troubles that ought to be resolved, such as device transport uniformity and protection. The GI tract may also benefit from the constancy of dose supplied through microneedle management and jetting gadgets. There's a threat of intestinal wall rupture if a tool meant for delivery in the stomachs deploys inside the small gut [23]. The production of cavitation at the same time as minimizing damage to

the luminal wall is one of the foremost issues for ultrasonic transport. On-device electronics are present in iontophoretic gadgets and ought to be guarded and restricted. The scale of the drug molecule furnished and the depth of drug penetration are additional elements for iontophoretic gadgets. One shipping episode can most effectively deliver a certain quantity of medicine, therefore numerous episodes can be required. Last but not longer least, the scale of the drug molecule limits drug transport making use of iontophoresis, favoring smaller drug molecules for management [24].

3. PROPOSED METHODOLOGY

The Robopill, which has the size of a triple-zero pill and can contain up to 342.6 mm³ of drug payload in its cargo compartment, is ingestible. To shield the surface structure from abrasion or pain during swallowing, a gelatinous protecting is applied (Fig. 1). The Robopill's surface traits are then made visible whilst it passes through the stomach's gastric juice (Fig. 2). The pH of the organic fluids inside the small intestine reasons a soluble activation membrane to open the Robopill's onboard circuit and activate the device. The centripetal pressure, F_c , produced via an offsetting weight laterally located on a motor in the Robopill causes it to rotate and vibrate in competition to floor friction, F_{cf} , which pushes the Robopill outward and alters its orientation theta with offset eq (1).

$$F_c = m_{weight} * \omega^2 * r_{weight} \quad (1)$$

$$f = \frac{\omega_{weight}}{2 * \pi} \quad (2)$$

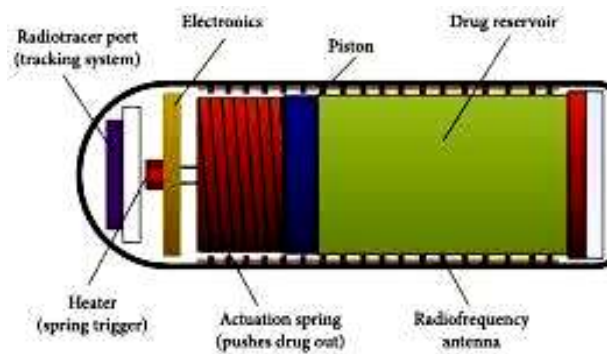


Figure 1. Schematic Robopill

$$\sum L = L_{weight} + L_{cap} = 0 \quad (3)$$

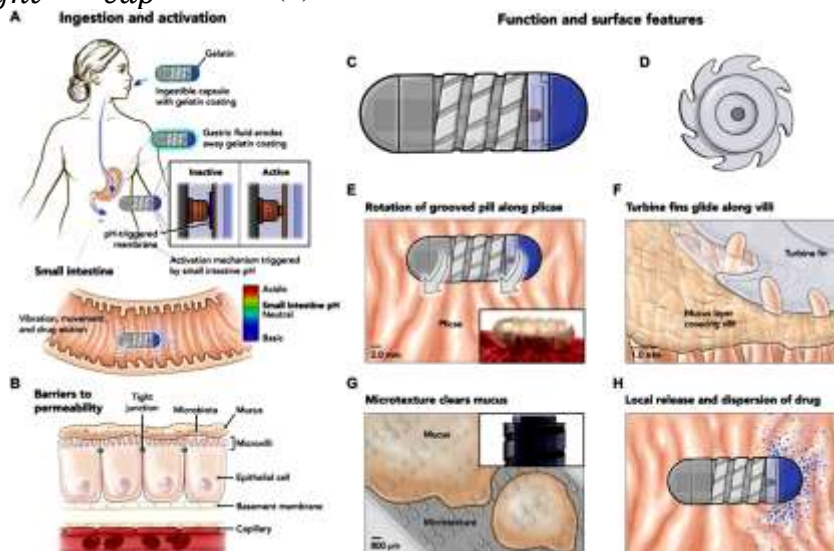


Figure 3. Process of Robopill mechanism [25]

The speed at which the capsule spins is determined via the conservation of energy and momentum within the machine. with a view to counter the spin of its inner motor, which rotates at weight in a frictionless environment, the tablet will generate an angular pace pill that is withoutdelay proportionate to the motor's rotational price and expanded via a ratio of the weight's secondof inertia Iweight, to the capsule's second of inertia, Icapsule. Observe S2 substantially investigates the outcomes of gravity in addition to the engine at the Robopill's movement. The Robopill improves medication distribution in a ramification of methods by means of physically interacting with intestinal epithelium, villi, or plicae as it rotates. Rotation is made easier by using the exteriorhelix's (1.0 mm) most beneficial touch with the plicae's (1 to 10 mm) interface and the rounded slits' (0.5 mm) touch with the villi's (0.2 to 0.8 mm) floor. Additionally, the curved floor enhances mucosal surface touch, permitting the five hundred–800 m thick layer of mucus that covers the epithelium to be churned and cleared by using microtextured (200–300 m) studs located on the recessed surfaces. The drug load deposits drug debris as it erodes away layer by using layer with every revolution. The Robopill movements thru the tract via peristalsis for round 35 minutes before being surpassed via feces. Designing the Robopill took under consideration functionality to allow for plenty makes use of. For example, the medicine payload is located at one quit of the pill, making it easy for pharmacists to load any medicinal drug in theirdeciding on. Through adjusting the characteristics of the dissolvable membrane, the pH sensitivity of the RoboCap can also be adjusted to goal special components of the GI tract [26].

4. RESULTS AND DISCUSSION

We contrasted surface designs with spiral, helical, and studded characteristics with a smooth exterior in order to maximize rotation. As the Robopill rotated on newly removed SI tissue, the rate of rotation was recorded. When compared to a smooth exterior, the rotation rate was found to be considerably higher with a helical groove (6.9 1.6 revolutions per minute (rpm), P 0.01, two- tailed heteroscedastic t test). This was probably caused by alignment with plicae and accentuation of the oscillatory effect [27, 28].

Table 1. Technical specifications or drug delivery systems [29].

DDS	Dimension (mm)	Reservoir Volume (ml)	Release Mechanism
MAARS	18.2 × 7.7	0.34	Passive
RaniPill™	26.1 × 10	-	Passive
IntelliCap®	27 × 11	0.3	Active
Groening prototype	28 × 8.5	0.17	Active
MASCE	40 × 15	0.17	Active

To interrupt up mucus beds whilst the Robopill strokes the floor, studs had been made and placed in the crevices of the helical outer frame. The potential of studs to wick and do away with mucus was evaluated for heights between two hundred and 800 m. (Fig. 2F). These had been contrasted with a nice manipulate in which mucus became physically removed from the tissue through being rubbed across it ten times with a steady downward pressure. Moreover assessed was a poor control that had no Robopill or mucus elimination [30].

5. CONCLUSION

Robot tablets are about to enter the mainstream. Soon, pills might not be used only for

diagnostic imaging functions. Similar to how the platform's development in the subject of digestive diagnostics changed into motivated by using the country of improvement of the essential technologies, its progress in the field of drugs administration has taken longer because of the diploma of readiness of the essential integrated modules. The usage of powerful medicines and hemostatic powder or a similar spray formula, sensing/turning in robots, for example, can be used to deal with a localized GI tract ailment without the need for a painful intervention or systemic unfavourable consequences. The distribution of prescription drugs that have to be taken orally, which include insulin or chemotherapeutic treatments, might be some other helpful use. Moreover, a robot capsule delivery system that mixes neighborhood and systemic remedy management would be useful for treating autoimmune-mediated bowel disorders.

REFERENCES:

1. Sharma, V.K. The future is wireless: Advances in wireless diagnostic and therapeutic technologies in gastroenterology. *Gastroenterology* 2009, 137, 434–439, <https://doi.org/10.1053/j.gastro.2009.06.029>.
2. Yadav, K.S.; Kapse- Mistry, S.; Peters, G.J.; Mayur, Y.C. E- drug delivery: A futuristic approach. *Drug Discov. Today* 2019, 24, 1023–1030, <https://doi.org/10.1016/j.drudis.2019.02.005>.
3. Swain, C.P.; Gong, F.; Mills, T.N. Wireless transmission of a colour television moving image from the stomach using a miniature CCD camera, light source and microwave transmitter. *Gastrointest. Endosc.* 1997, 45, AB40, <https://doi.org/10.1016/S0016-510780063-6>.
4. Iddan, G.; Meron, G.; Glukhovskiy, A.; Swain, P. Wireless capsule endoscopy. *Nature* 2000, 405, 417, <https://doi.org/10.1038/35013140>.
5. Eliakim, R.; Yassin, K.; Shlomi, I.; Suissa, A.; Eisen, G.M. A novel diagnostic tool for detecting oesophageal pathology: The PillCam oesophageal video capsule. *Aliment. Pharm. Ther.* 2004, 20, 1083–1089, <https://doi.org/10.1111/j.1365-2036.2004.02206.x>.
6. Eliakim, R.; Fireman, Z.; Gralnek, I.M.; Yassin, K.; Waterman, M.; Kopelman, Y.; Lachter, J.; Koslowsky, B.; Adler, S.N. Evaluation of the PillCam Colon capsule in the detection of colonic pathology: Results of the first multicenter, prospective, comparative study. *Endoscopy* 2006, 38, 963–970, <https://doi.org/10.1055/s-2006-944832>.
7. Eliakim, R. Where do I see minimally invasive endoscopy in 2020: Clock is ticking. *Ann. Transl. Med.* 2017, 5, 202, <https://doi.org/10.21037/atm.2017.04.17>.
8. Munoz, F.; Alici, G.; Li, W. A review of drug delivery systems for capsule endoscopy. *Adv. Drug Deliv. Rev.* 2014, 71, 77–85, <https://doi.org/10.1016/j.addr.2013.12.007>.
9. Connor, A. Location, location, location: Gastrointestinal delivery site and its impact on absorption. *Ther. Deliv.* 2012, 3, 575–578, <https://doi.org/10.4155/tde.12.34>.
10. Lee, H.J.; Choi, N.; Yoon, E.S.; Cho, I.J. MEMS devices for drug delivery. *Adv. Drug Deliv. Rev.* 2018, 128, 132–147, <https://doi.org/10.1016/j.addr.2017.11.003>.
11. Prior, D.V.; Connor, A.L.; Wilding, I.R. Human Drug Absorption Studies in Early Development. In *Application of Pharmacokinetic Principles and Drug Development*; Krishna, R., Ed.; Springer: New York, NY, USA, 2004; pp. 177–194.
12. Horst Staib, A.; Beermann, D.; Harder, S.; Fuhr, U.; Liermann, D. Absorption differences of ciprofloxacin along the human gastrointestinal tract determined using a remote-control drug delivery device (HF- capsule). *Am. J. Med.* 1989, 87, S66–S69, <https://doi.org/10.1016/0002-934390026-0>.
13. Pithavala, Y.K.; Heizer, W.D.; Parr, A.F.; O'Connor- Semmes, R.L.; Brouwer, K.L. Use of the IntelliSite capsule to study ranitidine absorption from various sites within the human intestinal tract. *Pharm. Res.* 1998, 15, 1869–1875, <https://doi.org/10.1023/a:1011910223812>.
14. Dietzel, C.T.; Richert, H.; Abert, S.; Merkel, U.; Hippus, M.; Stallmach, A. Magnetic Active Agent Release System (MAARS): Evaluation of a new way for a reproducible, externally controlled drug release into the small intestine. *J. Control. Release* 2012, 161, 722–727, <https://doi.org/10.1016/j.jconrel.2012.04.047>.
15. Dhalla, A.K.; Al- Shamsie, Z.; Beraki, S.; Dasari, A.; Fung, L.C.; Fusaro, L.; Garapaty, A.; Gutierrez, B.;

- Gratta, D.; Hashim, M.; et al. A robotic pill for oral delivery of biotherapeutics: Safety, tolerability, and performance in healthy subjects. *Drug Deliv. Transl. Res.* (in press 2021), <https://doi.org/10.1007/s13346-021-00938-1>.
16. Becker, D.; Zhang, J.; Heimbach, T.; Penland, R.C.; Wanke, C.; Shimizu, J.; Kulmatycki, K. Novel orally swallowable IntelliCap® device to quantify regional drug absorption in human GI tract using diltiazem as model drug. *AAPS PharmSciTech* 2014, 15, 1490–1497, <https://doi.org/10.1208/s12249-014-0172-1>.
 17. van der Schaar, P.J.; Dijkman, J.F.; Broekhuizen-de Gast, H.; Shimizu, J.; van Lelyveld, N.; Zou, H.; Iordanov, V.; Wanke, C.; Siersema, P.D. A novel ingestible electronic drug delivery and monitoring device. *Gastrointest. Endosc.* 2013, 78, 520–528, <https://doi.org/10.1016/j.gie.2013.03.170>.
 18. Steiger, C.; Abramson, A.; Nadeau, P.; Chandrakasan, A.P.; Langer, R.; Traverso, G. Ingestible electronics for diagnostics and therapy. *Nat. Rev. Mater.* 2019, 4, 83–98, <https://doi.org/10.1038/s41578-018-0070-3>.
 19. Söderlind, E.; Abrahamsson, B.; Erlandsson, F.; Wanke, C.; Iordanov, V.; von Corswant, C. Validation of the IntelliCap® system as a tool to evaluate extended release profiles in human GI tract using metoprolol as model drug. *J. Control. Release* 2015, 217, 300–307, <https://doi.org/10.1016/j.jconrel.2015.09.024>.
 20. Groening, R.; Bensmann, H. High frequency controlled capsules with integrated gas producing cells. *Eur. J. Pharm. Biopharm.* 2009, 72, 282–284, <https://doi.org/10.1016/j.ejpb.2009.01.003>.
 21. Yim, S.; Sitti, M. Design and Rolling Locomotion of a Magnetically Actuated Soft Capsule Endoscope. *IEEE Trans. Robot.* 2012, 28, 183–194, <https://doi.org/10.1109/TRO.2011.2163861>.
 22. Wilding, I.; Hirst, P.; Connor, A. Development of a new engineering- based capsule for human drug absorption studies. *Pharm. Sci. Technol. Today* 2000, 3, 385–392, <https://doi.org/10.1016/s1461-534700311-4>.
 23. Pi, X.; Lin, Y.; Wei, K.; Liu, H.; Wang, G.; Zheng, X.; Wen, Z.; Li, D. A novel micro- fabricated thruster for drug release in remote controlled capsule. *Sens. Actuators A Phys.* 2010, 159, 227–232, <https://doi.org/10.1016/j.sna.2010.03.035>.
 24. Pi, X.; Zheng, X.; Peng, C.; Hou, W.; Liu, H. A Novel Remote Controlled Capsule for Human Drug Absorption studies. In *Proceedings of the IEEE Engineering in Medicine and Biology 27th Annual Conference, IEEE Shanghai, China, 2005*; pp. 5066– 5068, <https://doi.org/10.1109/IEMBS.2005.1615615>.
 25. Woods, S.P.; Constandinou, T.G. Wireless capsule endoscope for targeted drug delivery: Mechanics and design considerations. *IEEE Trans. Biomed. Eng.* 2013, 60, 945–953, <https://doi.org/10.1109/TBME.2012.2228647>.
 26. Connor, A.; Evans, P.; Doto, J.; Ellis, C.; Martin, D.E. An Oral Human Drug Absorption Study to Assess the Impact of Site of Delivery on the Bioavailability of Bevirimat. *J. Clin. Pharm.* 2009, 49, 606–612, <https://doi.org/10.1177/0091270009333488>.
 27. Le, V.H.; Rodriguez, H.L.; Lee, C.; Go, G.; Zhen, J.; Nguyen, V.D.; Choi, H.; Ko, S.- Y.; Park, J.O.; Park, S. A soft- magnet- based drug- delivery module for active locomotive intestinal capsule endoscopy using an electromagnetic actuation system. *Sens. Actuators A Phys.* 2016, 243, 81–89, <https://doi.org/10.1016/j.sna.2016.03.020>.
 28. Lee, C.; Choi, H.; Go, G.; Jeong, S.; Ko, S.Y.; Park, J.O.; Park, S. Active Locomotive Intestinal Capsule Endoscope (ALICE) System: A Prospective Feasibility Study. *IEEE ASME Trans. Mechatron.* 2015, 20, 2067–2074, <https://doi.org/10.1109/TMECH.2014.2362117>.
 29. Stewart, F.; Cox, B.F.; Wang, G.; Huang, Z.; Newton, I.P.; Nathke, I.S.; Thanou, M.; Cochran, S. An in vitro sonication system for applications in ultrasound- mediated targeted drug delivery. In *Proceedings of the IEEE International Ultrasonics Symposium (IUS), IEEE, Tours, France, 2016*; pp. 1–4, <https://doi.org/10.1109/ULTSYM.2016.7728701>.
 30. Stewart, F. Capsule- Based Ultrasound- Mediated Targeted Drug Delivery. PhD. Thesis, University of Dundee, Dundee, UK, 2018. Available online: <https://discovery.dundee.ac.uk/en/studentTheses/capsule-based-ultrasound-mediated-targeted-drug-delivery>. (accessed on 1st November 2021).

A Novel PCB prototype for smart garden

Mr. Koteswara Rao Unnam¹, Dr. P. Venu Madhav², Bommu Tarun Kumar³,
Karra Jagadeesh³, Kandula Naveen³, Mallampalli Kushwanth³

¹Associate Professor, Dept. of ME, PVP Siddhartha Institute of Technology, Vijayawada

²Asst. Professor, Dept. of ECE, PVP Siddhartha Institute of Technology, Vijayawada

³U.G student, Dept. of ME, PVP Siddhartha Institute of Technology, Vijayawada

Abstract: Utilization of natural resources like water and sunlight for home gardens and public gardens is an everyday challenge where unrestricted or accessed utilization of natural resources often happen. For example, electrical lighting is periodically left on in public gardens, plants are not watered, or the water tank is spilled and empty due to human or operational error, resulting in massive use of power and other natural resources. The present paper proposes a solution that relies on a controller to help address these problems. The controller manages the water in the garden as well as the lighting system using sensors in a timely manner and avoids unnecessary wastage of resources. The controller is in charge of overseeing all other linked devices, with flexible programming and regulating the entire set of activities. The overall outcome of the work is finally presented on a PCB prototype integrated with the controller and makes it easier to maintain household & public gardens lawns.

Keywords: Controllers, Garden maintenance, Electricity, Gardening operational error

INTRODUCTION:

The smart gardening system project is a cutting-edge solution for modern agriculture and gardening. It gives a complete and efficient approach to garden management by merging innovative technologies and data analysis. The device monitors environmental elements like humidity and sunshine and utilizes this data to improve plant growth and save waste. This project makes gardening accessible and convenient for everyone, from urban balcony gardeners to large-scale users, thanks to its user-friendly interface, real-time monitoring, and automatic watering and lighting system. The literature understanding is presented as two categories, smart watering and adaptive lighting for the effective use of natural resource.

A smart device that can convey data on the water level of installed household tanks to a smartphone was created by the Smart water company [1]. This device can instantly identify wastage of water which happen inside of homes (for example, leaks caused by sanitation, etc.). By comparing the difference between the total water flow from the tanks and the actual amount of water utilized by users (using smart meters), a similar examination is conducted to discover leaks in the society's large water tanks [2].

In many parts of the world, there is a major problem with water shortage [3] that has to be handled. Using sensor technology, SWS offers online monitoring, assisting in the efficient management of water resources. Reduced water losses in WDS are the result of SWT's analysis of sensor data for effective pressure control, pipeline leak detection, and identification of commercial water losses. Water that was before lost as a result of financial and material losses can now be used to assist others who need it. This may help to ease the

world's water shortage.

For machine-to-machine communication to be created, smart water devices [4] must have a common standardized module and platform. The platform and module that will be utilized in smart water devices should be standardized. Researchers may want to focus on the creation of smart portable gadgets.

Societal constraints

There are not only technical and scientific limitations that prevent the use of smart water technology, but there are also economical limitations, such as a lack of funding. Even when funds are available, there may not always be enough technical support (based on location) to adequately maintain such technology. The local administration decides whether to employ such technologies to advance the city. Hence, a lack of knowledge in local government may deter people from utilizing such tools [5].

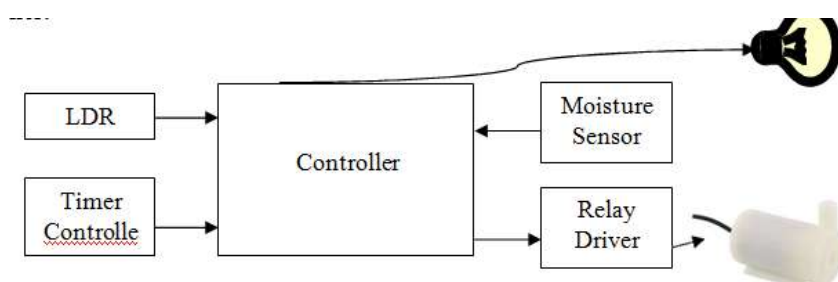
A study on an automated [6] and real-time plant watering system for smart gardens shows how to set up a smart garden without the need for human input. A real-time plant watering system, an automated plant watering system with a soil moisture sensor, remote garden management, an intruder sensor with a camera, and a relay light function are the main topics of the work. As it can cover a far larger area than a sonar sensor, the study used a Passive Infrared Sensor (PIR) to detect human presence. The development of an automated garden maintenance system proved successful

A smart garden monitoring system based on the Internet of Things was shown by Thamaraimanalan et al. [7]. In the study, metrics from sensors connected to a Wi-Fi network, such as wetness, temperature, humidity, and ultrasonic, are derived using a mobile application called fire-base.

Proposed solution:

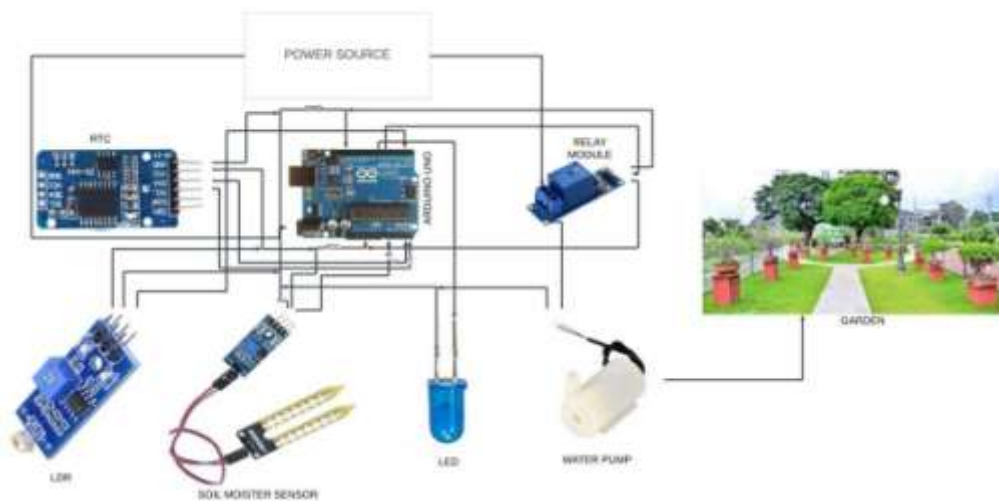
Functional Block:

The functional block outlines the approach to solve the problem. In phased manner the first step is to identify the operation of the LDR module with the controller and to check its validity by the triggering signal to turn the Led ON when fading of light in an open environment. Under full lighting condition the LDR should generate the low pulses thus making the turn OFF. The water pump and moisture sensor are controlled by the timer controller. The moisture sensors continuously evaluates a soil moisture condition and upon getting a below a threshold for low moisture will initiate the controller to trigger a relay circuit which in turn turn ON the water motor pump for pumping of water. The timer controller is programmed to activate the motor controller relay at a specified time interval. During the time interval the moisture sensor continuously detects the soil moisture and upon reaching the upper threshold will disable the triggering input to relay module with the help of controller.



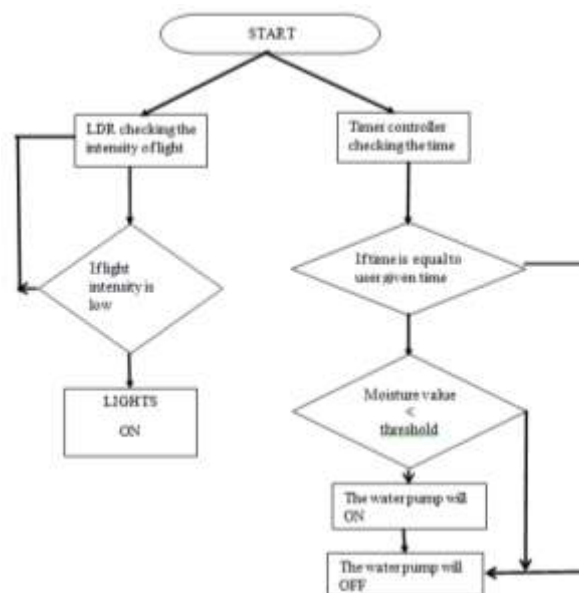
Components integration:

GND, VCC, SDA, and SCL are the four pins that make up the timer module. As the controller's is, GND and G connections GND and G VCC and connections. The GND and VCC connections connections. The GND and G G. SDA (serial data pin) is linked to the controller's SDA analogue input pin, while SCL (serial clock pin) is connected to the Arduinosystem. The GND, VCC, and digital output pins are the 3 pins on the LDR module. The GND and VCC are linked to the controller's output power supply, and the digital output pin is connected to the controller's digital input pin. The GND, VCC, and analogue signal pins are the three pins on the moisture sensor. The analogue output pin of the module is linked to the analogue input pin of the controller, and the GND and VCC are connected to the controller's output power supply. The positive and negative terminals of the LED are linked to the controller's digital output pin and GND, respectively. The LED has two terminals: positive and negative. The controller's output power source is connected to the GND and VCC of the relay module, and the controller's digital output pin is connected to the input pin of the relay module. The relay module has seven pins total: ANODE, CATHODE, GND, VCC, input pin, and output pins (ANODE, CATHODE, AND 2 NC pins). Water pump and power supply are linked to the anode and cathode pins, respectively.



Workflow:

Flow chart:



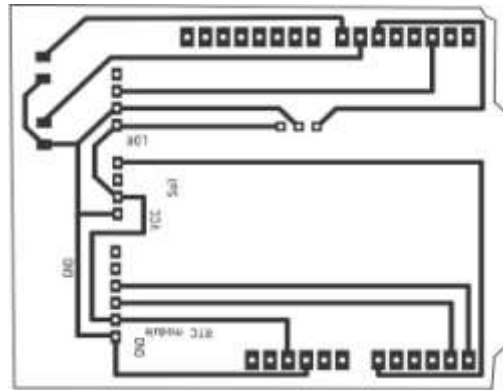


Fig.: PCB layout

Custom Code: -

Step-1: include the libraries of RTC module Step-2: initiate the pin numbers of the sensor
Soil sensor=A0 Ldrsensord=2 Ldrsensord value =0 Soil sensor value =0

Step-3: setup of Arduino

Use pins 6,7 for output from the Arduino to connect the sensors

Step-4: Setting of loop to continuously running of program and conditions to work

```
If (Ldrsensord Value==1)
{
Digital Write (7, HIGH);
}
Else
{
Digital Write (7, LOW);
}
if (st1=="15:30")
{
If (soil sensor Value<500)
{
digital Write (6, LOW);
}
else
{
digital Write (6, HIGH);
}
}
if(time=="15:50")
{
digital Write (6, LOW);
}
}
```

Testing:

The following results are obtained in the serial monitor while using the prototype

Two-day International Conference on Recent Advances in Mechanical and Industrial Engineering – 2023
(ICRAMIE-2023)

Event	Status on serial monitor
<p style="text-align: center;">Timer</p> <p>When the time is not equal to user giventime so the motor is in OFF position</p>	<pre>Lights OFF Date/Time: 11:47:31 15/02/2023 11:47 977 3 Lights OFF Date/Time: 11:47:32 15/02/2023 11:47 976</pre>
<p style="text-align: center;">Motor ON</p> <p>The moisture level is less than threshold value than the motor will ON</p>	<pre>Motor ON Date/Time: 11:51:17 11 : 51 971 O Lights OFF Motor ON Date/Time: 11:51:18 11 : 51 971 15/02/2o23 15/02/2023 O Lights OFF Motor ON Date/Txme : 11:51 11:51:19 15/02/2023 970 O Lights OFF Motor ON</pre>
<p style="text-align: center;">MOTOR OFF</p> <p>If the moisture level exceeds the threshold,the motor will turn off.</p>	<pre>Lights OFF Motor OFF Date/Time: 11:55:09 15/02/2023 11:55 468 3 Lights OFF Motor OFF Date/Time: 11:55:10 15/02/2023 11:55 458 3 Lights OFF Motor OFF</pre>
<p style="text-align: center;">LED ON</p> <p>At low light the LEDs are triggered to ON state</p>	<pre>Date/Time: 11:42:40 15/02/2023 11:42 1001 1 Lights ON Date/Time: 11:42:41 15/02/2023 11:42 1001 1 Lights ON</pre>

<p style="text-align: center;">LED OFF</p> <p>When the light is normal the LEDs are in OFF state</p>	<p>Light3 OFF Date/Time: 11:46:09 15/02/2023 11:46 966 3 Lights OFF Date/Time: 11:46:10 15/02/2023 11:46 966 3 Lights OFF Date/Time: 11:46:11 15/02/2023 11:46 966 3 Lights OFF</p>
--	---

Discussion on outcome:

The PCB prototype that was built has the adaptability of updating the code for any modifications for the timer to handle the triggering event of the motor controller, provides additional expansion capacity of up to 8 sensors with minor circuit changes for the hardware. During the design aspect the dimensions of the sensors that are to be attached to the PCB are also taken into consideration. Since common voltage values of 5V and a ground has to be mixed with the sensors like timer, relay module, LED and moisture level measurement precautions during the circuit layout need to be identified and accordingly the position of the components layout on the PCB is handled. The overall dimension of the PCB layout thus attained is 2.78 inches X 2.26 inches (LxW) and equals to the size of the controller board. As part of this study, the environmental factors affecting both private gardens and public gardens were taken into account, and a workable solution was created. The work's objectives are determined by reading a variety of literary works, and a simpler, easier-to-use system for automating the garden is developed.

CONCLUSION

Prototype of the Smart PCB By incorporating methods and instructions that are sent to the automation device remotely or as specified per job, a garden automation system brings the user closer to the plants they wish. For a productive result, more PCB prototypes for pesticide spraying can be made. Prediction modelling may be used to estimate maintenance operations based on sensor data, expanding the project's scope. Notwithstanding the fact that dynamic sensor allocation and data extraction from dynamic sensors are challenging problems. The algorithmic evolution of dynamic sensor allocation still needs a great deal of study. The wireless data flow from the sensor could cause interference with other gadgets.

References

1. Hope, R.; Foster, T.; Money, A.; Rouse, M.; Money, N.; Thomas, M. Smart Water Systems. In *Project Report to UK DFID*; Oxford University: Oxford, UK, April 2011. Available online: https://assets.publishing.service.gov.uk/media/57a08ab9e5274a31e000073c/SmartWaterSystems_FinalReport-Main_Reduced_April2011.pdf(accessed on 10 August 2020).
2. Kumar, S.; Yadav, S.; Yashaswini, H.; Salvi, S. An IoT-Based Smart Water Microgrid and Smart Water Tank Management System. In *Emerging Research in Computing, Information, Communication and Applications*; Springer: Berlin, Germany, 2019; pp. 417–431. [Google Scholar]

Two-day International Conference on Recent Advances in Mechanical and Industrial Engineering – 2023
(ICRAMIE-2023)

3. Gupta, A.; Mishra, S.; Bokde, N.; Kulat, K. Need of smart water systems in India. *Int. J. Appl. Eng. Res.* **2016**, *11*, 2216–2223. [[Google Scholar](#)]
4. Whittle, A.J.; Allen, M.; Preis, A.; Iqbal, M. Sensor networks for monitoring and control of water distribution systems. In Proceedings of the 6th International Conference on Structural Health Monitoring of Intelligent Infrastructure (SHMII 2013), Hong Kong, China, 9 December 2013. [[Google Scholar](#)]
5. Araral, E. Why do cities adopt smart technologies? Contingency theory and evidence from the United States. *Cities* **2020**, *106*, 102873. [[Google Scholar](#)] [[CrossRef](#)]
6. Olawepo, Samuel & Adebisi, Ayodele & Adebisi, Marion & Okesola, Olatunji. (2020). An Overview of Smart Garden Automation. 1-6. 10.1109/ICMCECS47690.2020.240892.
7. Thamaraimanalan, T., Vivekk, S.P., Satheeshkumar, G., and Saravanan, P.(2018). Smart garden monitoring system using IOT, Asian Journal of Applied Science and Technology (AJAST), Volume2, Issue 2, pp 186-192.

Experimental Analysis on FDM - 3D Printing Process Parameters Optimization to Enhance Tensile Strength with PLA Material

Raffik R¹, Akila K², Sabitha B³, Sivaguru J⁴, Naveen C⁵, Sakira Parveen A⁶

^{1,2,3,4}Department of Mechatronics Engineering, Kumaraguru College of Technology, Coimbatore, Tamilnadu, India ⁵Department of Mechatronics Engineering, Kongu Engineering College, Perundurai, Erode, Tamilnadu, India ⁶Department of Electronics and Communication Engineering, Aditya Institute of Technology, Coimbatore, Tamilnadu, India

Abstract: Numerous industries use 3D printing technology to construct buildings, manufacture vehicles and create medical products. Fusion deposition modeling (FDM) is an emerging additive manufacturing (AM) technique used to manufacture functional components and prototypes with complex geometries. It is also known as manufacturing with fused filaments. It is gaining popularity due to its capacity to shorten product development cycles without the use of expensive instruments and tools. However, low dimensional precision, substandard surface quality, inadequate part strength, and insufficient mechanical properties limit the use of FDM in numerous industrial applications. Different process parameters, like layer thickness, raster width, build orientation, and print speed, influence the characteristics of FDM-created components and parts. The optimal and best possible combinations of process parameters must be selected. There are numerous techniques for optimizing and selecting the appropriate FDM process parameters. A comprehensive review of pre-processing is required to evaluate the printed component's qualities. In accordance with the components of FDM machines, the range of process parameters must be determined. The various parameters vary based on the type of machine, nozzle diameter, and filament type. Setting the process settings properly is believed to enhance the quality of a three-dimensional (3D) printed component, which may also reduce post-manufacturing efforts. This study article explores the least studied parameter combinations and provides the optimal FDM parameter range.

Keywords: FDM Process, Process Parameter Optimization, Tensile Strength, Layer Thickness, Printing Speed, and Infill Pattern.

1. Introduction

The term 3D printing refers to the additive manufacturing processes formerly known as Rapid Prototyping (RPT). Fused Deposition Modeling is becoming the emerging bottom-up manufacturing technique implemented to produce finished products by creating layer-by-layer patterns automatically using CAD-generated design [2],[3]. Additive Manufacturing Technologies are rapidly expanding in the manufacturing and industrial sectors. FDM is the most popular AM technique; it employs inexpensive polymeric materials that are simple to print in 3D [4] and have numerous applications. FDM components have disadvantages such as surface roughness[5], part strength[6], and dimensional inaccuracies[7, 8]. To counteract these disadvantages, process parameter optimization is performed [9], [10]. Using the FDM process, a variety of underwater systems [11], robots [12], and drones [13] are designed and marketed for various applications. It is also employed to create medical equipment [14], medical infrastructure coatings [17], weaving loom components [18], and automation system

casings [27]. UAVs (Unmanned Aerial Vehicles) and robot components deployed in agricultural fields for pesticide or weedicide spraying processes are also created [20],[21]. The FDM technology is displayed in Fig.1. Continuously heated filaments are extruded onto a heated bed or deposited over the printed layers. The CAD design is used to generate the STL file, which controls the movement of the printer nozzle along the X and Y axes. The functional model is constructed by layering a semi- molten filament.[19] The thermo-plasticity of the polymer filament is essential for this technique because it enables the filaments to bond and then solidified at room temperature. It is essential to identify the part strength that influences process parameters and their correlation.[20]

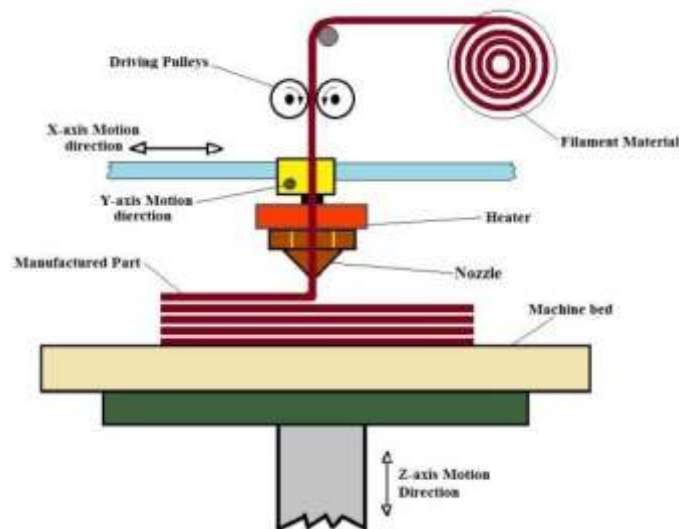


Fig.1. Fusion Deposition Modeling Process

2. Materials and Procedures

Process Materials for FDM Components

ABS and PLA are the two most extensive and popular FDM process materials. Instead of ABS and PLA, other filament materials such as PETG, Nylon,[16] Polyphenylsulfone (PPS), polycarbonate (PC), and other polymer composites are used to create functional parts and research projects, providing researchers and makers of functional parts with a wider range of material options.

Extensive research is conducted on process variables such as build orientation, layer thickness, raster orientation, and raster width. Less thoroughly examined process parameters are printing speed, infill pattern, extrusion nozzle temperature, and shell width [15]. Therefore, it simultaneously maximized the features of multiple sections [22] even though few investigations occurred. In this research examination, the least understood process variables such as print speed, infill pattern, and extrusion temperature are considered. FDM is a complex 3D printing technique with a variety of process parameters. [23]. Future research with multi-objective process parameter adjustments is necessary to enhance the consistency of FDM-printed parts during the design and manufacturing processes [25], [26], [28].

Polylactic Acid is used as the filament material in this research. PLA (Polylactic Acid) is a biodegradable, renewable, and food-safe organic polymer. Due to its versatility and ease of use, it is the most common filament used in Fusion Filament Fabrication (FFF) 3D printers, especially for non-mechanically or thermally demanding applications. The advantages of using PLA material include a shiny exterior finish, superior tensile strength, superior UV resistance, the ability to withstand operating temperatures up to 50 °C, and low humidity

resistance.[24]

3. Fabrication, Evaluation, and Optimization

A 1.75mm diameter PLA filament is used to create ASTM D638 tensile specimens. This study modifies the optimization settings, such as infill pattern, printing speed, and nozzle temperature, to produce a homogenous sample of nine ASTM D638 tensile specimens.[29] This identifies the optimal FDM process parameter combination for producing objects with the highest tensile strength. A Creality CR-10 S5 FDM printer produces each of the nine specimens. This device can utilize materials with a temperature degradation range of 2300C to 2500C degrees Celsius. In this study, temperatures between 200°C and 220°C have been utilized. In addition, the ambient temperature is used as the minimum temperature for the bed or platform. Tables 2 and 3 lists the selected parameter ranges and parameter combinations for the L9 orthogonal array, respectively.

Test Specimen

Table 1. ASTM D638 – Type I Specimen Dimensions

S. No	Dimension	Tolerance
1	Overall Length, mm	165
2	Width at ends, mm	19+6.4
3	Length of narrow section, mm	57±0.5
4	Gauge Length, mm	50+0.25
5	Distance between grips, mm	115±5
6	Radius of fillet, mm	76±1
7	Thickness, mm	3±0.4
8	Width of narrow section, mm	13±0.5
9	Cross-sectional area of the narrow	35 to 48.6
10	section, mm ² Perimeter of the narrow section, mm	30.6 to 34.2

The American Society for Testing and Materials (ASTM) has established standard specimen profiles and dimensional specifications for the tensile testing of materials.[19] The profile and dimensions vary for metals, plastics, ceramics, composites, etc. ASTM D638 should be used for plastics and polymers. ASTM D68 contains five types of specimens, with Type I being the most common. The ASTM D638 Type I specimen is depicted in Figure 2. Table 1 contains the dimensions and dimensions of the profile.

Selected Process Variables:

The least investigated parameters nozzle temperature and infill pattern are considered with layer thickness.

The selected parameters are as follows.

- Layer Thickness
- Nozzle Temperature
- Printing Speed
- *Layer Thickness:* The distance vertically covered by a single layer of deposition.
- *Nozzle Temperature:* The extruding nozzle temperature that transforms the thermoplastic PLA filament into a semi-solid state to create the parts.
- *Printing Speed:* The rate at which the extrusion nozzle traverses the part-building platform/bed.

Optimization Steps for FDM Process Parameters

The process flow of FDM process parameter optimization is depicted in Figure 3. Figure 4

depicts the experimental setup for tensile testing using a universal testing machine. The tested specimens are shown in Figure 5.

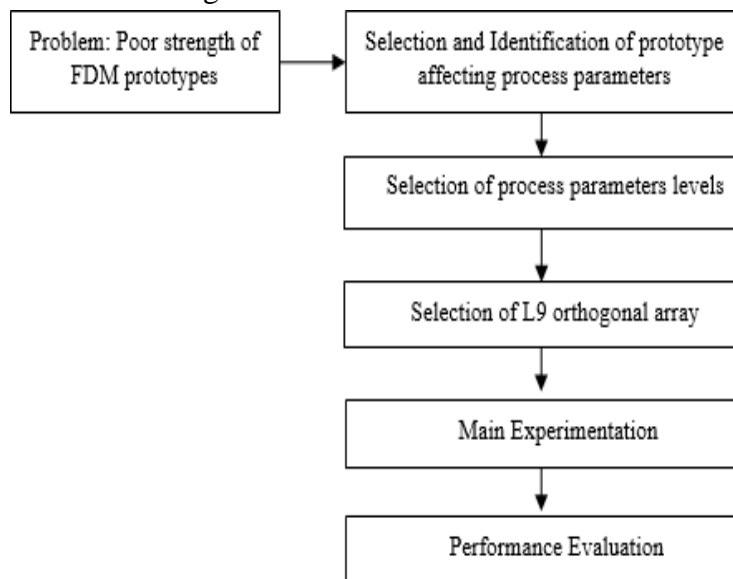


Fig. 3. Steps for Optimizing FDM process parameters.

Parameter Range:

Table 2. Selected Parameter range

Parameter Levels	Levels		
	Level 1	Level 2	Level 3
Layer thickness (mm)	0.15	0.2	0.25
Infill Pattern	Grid	Concentric	Tri-Hexagon
Print speed (mm/sec)	100	75	50

Combination of parameters for the L9 orthogonal array:

Three values were picked for each of the three selected parameters based on their range as maximum, minimum, and mean values, as shown in Table 2. This yields a total of nine values utilized for the L9 orthogonal array combination as indicated in Table 3. [29]

Table 3. L9 Orthogonal array with Parameter combination

Specimen Number	Layer thickness (mm)	Infill Pattern	Print speed (mm/sec)
1	0.15	grid	100
2	0.15	concentric	75
3	0.15	tri-hexagon	50
4	0.20	grid	75
5	0.20	concentric	50
6	0.20	tri-hexagon	100
7	0.25	grid	50
8	0.25	concentric	100
9	0.25	tri-hexagon	75

Tensile Testing Process for Optimization of FDM Process Parameters



Fig. 4. Specimen Test by using Universal Testing Machine



Fig. 5. Tested Specimens using Universal Testing Machine

3. Results and Discussion

The specimen is loaded and constantly pulled until it fails. The purpose of the tensile test was to determine the ultimate load and breaking load. Utilizing the Dak Systems Test bench, a universal testing machine, the tensile tests are undertaken. The testing speed has been set at 5mm/min in accordance with ASTM standards. For each orthogonal array configuration, the maximum load, ultimate tensile strength, and elongation % are calculated and tabulated. Table 4 provides the ultimate tensile load, elongation, ultimate tensile strength, and elongation percentages for each of the nine L9 orthogonal specimens. The ultimate tensile strength and elongation percentages are calculated using the formulas provided below, and the calculated values are tabulated in Table 4.

Ultimate Tensile Strength = Maximum Load / Cross-Section Area

Elongation % = Strain linear at failure X 100

Tensile Test Results:

Table 4. Tensile test – Experimental results

Specimen No.	Ultimate Tensile Load (N)	Ultimate Strength (N/mm ²)	Elongation (mm)	Elongation %
1	684.883	17.561	2.920	5.840
2	626.250	16.058	3.020	6.039

3	684.422	17.549	2.730	5.460
4	747.169	19.158	3.530	7.060
5	881.441	22.601	3.950	7.901
6	706.112	18.105	2.540	5.079
7	817.350	20.958	4.451	8.902
8	817.978	20.974	3.490	6.980
9	786.164	20.158	2.850	5.701

Results of ANOVA analysis for Ultimate Tensile Load

Table 5 - ANOVA Analysis of Variance for S-N ratios

Source	DF	Seq. SS	Adj. SS	Adj. MS	F	P	Contribution %
Layer Thickness	2	4.7422	4.7422	2.3721	5.08	0.165	65.626
Infill Pattern	2	0.3766	0.3766	0.1883	0.413	0.713	5.212
Printing Speed	2	1.1708	1.1708	0.5854	1.2544	0.444	16.202
Residual Error	2	0.9344	0.9344	0.4672			12.931
Total	8	7.2261					

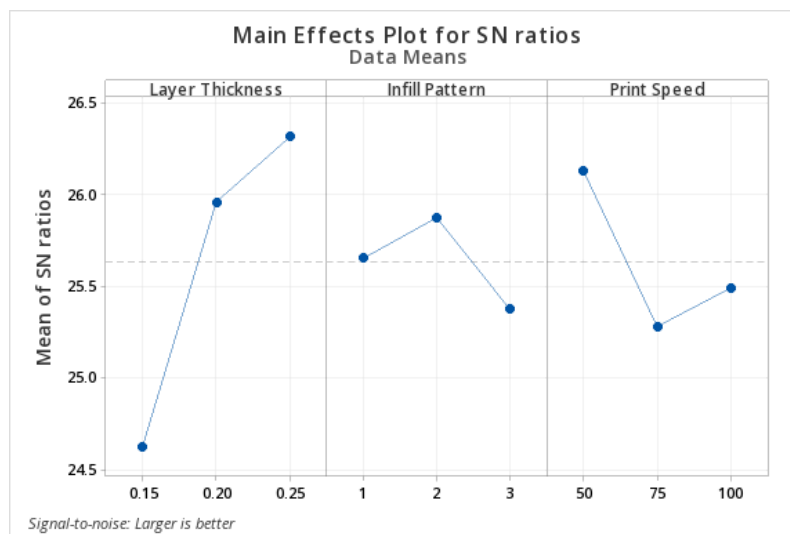


Fig. 6. ANOVA Analysis - SN Ratio for Ultimate Tensile Strength

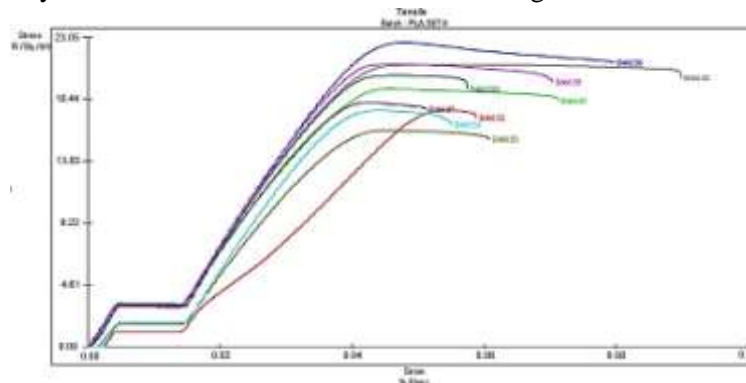


Fig. 7. Stress-Strain Response Curves for Specimens
Dept. of Mech. Engg.

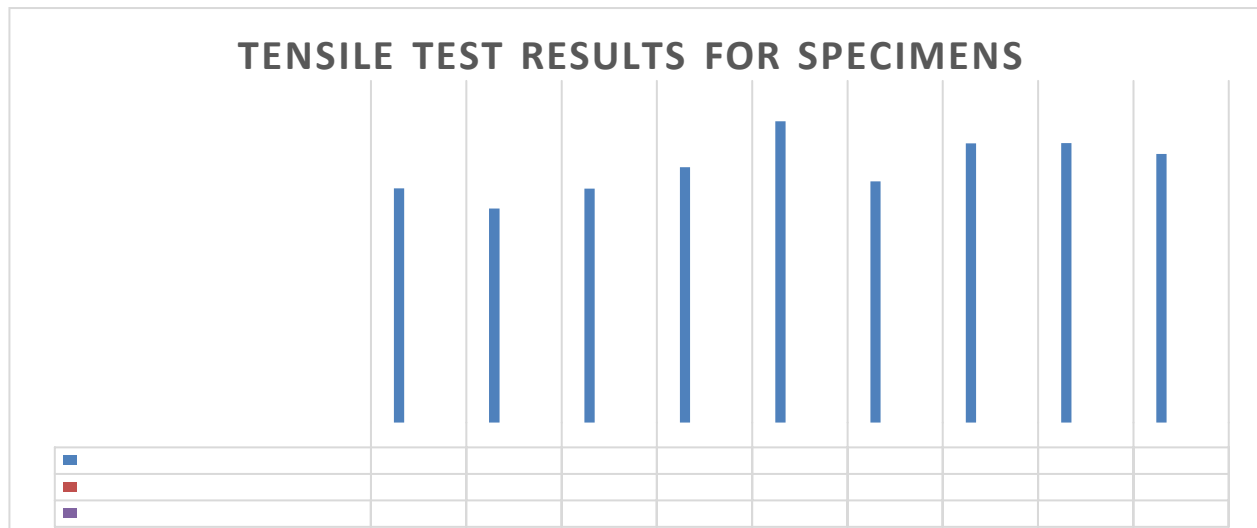


Fig. 8. Tensile Test Results for L9 Orthogonal Array Specimens

4. Conclusions

Empirical Analysis

- In all fast multilayer 3D manufacturing applications, part strength is a critical attribute.
- Fig. 7 depicts the stress-strain curve for all nine samples, while Fig. 8 gives the specimen's maximum load, maximum tensile strength, and percentage of elongation.
- Ultimate load is 881.441 N and Ultimate Tensile Strength is 22.601 MPa.
- The combination of parameters for the fifth specimen is, Layer thickness – 0.20 millimeters Infill Pattern - Concentric Speed of Printing - 50 mm/sec
- These parameter settings will increase the tensile strength of the manufactured components.

ANOVA Analysis

- Layer thickness contributes more to the load-bearing capacity of FDM prototypes under tensile loading conditions, as determined by the ANOVA analysis.
- Figure 5 and Table 6 depict the variances of the S-N ratios and the process parameter modifications, as well as their influencing percentages and effects on achieving better tensile strength.
- The optimal parameter combination to get greater tensile strength is, Layer thickness – 0.25 millimeters Infill Pattern - Concentric Speed of Printing - 50 mm/sec.
- The most influential process parameter is layer thickness, followed by printing speed, and the least influential is the infill pattern.
- Layer thickness contributes 65.63%, printing speed affects approximately 16.20%, infill pattern has the least impact at 5.21%, and other parameters and errors contribute approximately 12.93% to the ultimate tensile load handling capacity of 3D-printed PLA prototypes.

References

- [1]. Dey A, Yodo N. A Systematic Survey of FDM Process Parameter Optimization and Their Influence on Part Characteristics. *Journal of Manufacturing and Materials Processing*. 3(3), 64. (2019). <https://doi.org/10.3390/jmmp3030064>
- [2]. Patel, R., Jani, S. & Joshi, A. Review on multi-objective optimization of FDM process parameters for composite materials. *International Journal on Interactive Design and Manufacturing* (2022). <https://doi.org/10.1007/s12008-022-01111-9>
- [3]. Rehman, R.U., Zaman, U.K.u., Aziz, S., Jabbar, H., Shujah, A., Khaleequzzaman, S., Hamza, A., Qamar, Dept. of Mech. Engg.

U., Jung, D.W. Process Parameter Optimization of Additively Manufactured Parts Using Intelligent Manufacturing.

Sustainability, 14, 15475. (2022). <https://doi.org/10.3390/su142215475>

[4]. Huiqun Zhou, Guoxiang Zhao. Error Analysis and Process Parameter Optimization of Impeller Model Manufactured by FDM Process. In: 8th Annual International Conference on Geo-Spatial Knowledge and Intelligence. 693012069. IOP Conference Series: Earth and Environmental Science. IOP Publishing Ltd. China. (2021)

[5]. Saad, M.S., Mohd Nor, A., Abd Rahim, I. et al. Optimization of FDM process parameters to minimize surface roughness with integrated artificial neural network model and symbiotic organism search. Neural Computing & Applications, 34, 17423–17439 (2022).

[6]. Panda, S. K., Padhee, S., Anoop Kumar, S. O. O. D., & Mahapatra, S. S. Optimization of fused deposition modelling (FDM) process parameters using bacterial foraging technique. Intelligent information management, 1(02),89. (2009).

[7]. Equbal, A., Sood, A. K., Ansari, A. R., & Equbal, A. Optimization of process parameters of FDM part for minimizing its dimensional inaccuracy. International Journal of Mechanical and Production Engineering Research and Development, 7(2), 57-65. (2017).

[8]. Deswal, S., Narang, R., & Chhabra, D. (2019). Modeling and parametric optimization of FDM 3D printing process using hybrid techniques for enhancing dimensional precision. International Journal on Interactive Design and Manufacturing (IJIDeM), 13(3), 1197-1214. (2019).

[9]. Gao, G., Xu, F., & Xu, J. Parametric optimization of FDM process for improving mechanical strengths using Taguchi method and response surface method: A comparative investigation. Machines, 10(9), 750. (2022).

[10]. Shankar, A. N., Jagota, V., Jamadon, N. H., Raffik, R., Suneetha, V. L., Samori, I. A., & Karnan, L. An AHP- TOPSIS Approach for Optimizing the Mechanical Performance of Natural Fiber-Based Green Composites. Advances in Materials Science and Engineering, (2022).

[11]. Raffik, R., Kamal, S. S., Arun, S., Raja, P. P., & Kumar, R. M. Automatic Tank Cleaner. International Journal of Mechanical and Production Engineering Research and Development, 8(113). (2018).

[12]. Raffik, R., Mayukha, S., Hemchander, J., Abishek, D., Tharun, R., & Kumar, S. D. Autonomous Weeding Robot for Organic Farming Fields. In 2021 International Conference on Advancements in Electrical, Electronics, Communication, Computing and Automation (ICAECA) (pp. 1-4). IEEE. (2021).

[13]. Ezhil, V. S., Sriram, B. R., Vijay, R. C., Yeshwant, S., Sabareesh, R. K., Dakshesh, G., & Raffik, R. Investigation on PID controller usage on Unmanned Aerial Vehicle for stability control. Materials Today: Proceedings, 66(3), 1313-1318, (2022).

[14]. Rakesh, D., Keerthivaasan, R. K. V., Mohan, A., Samvasan, P., Ganesan, P., & Raffik, R. Automated Public Screening and Health Vitals Monitoring Station. In 2021 International Conference on Advancements in Electrical, Electronics, Communication, Computing and Automation (ICAECA) (pp. 1-6). IEEE. (2021)

[15]. Rayegani, F., & Onwubolu, G. C. (2014). Fused deposition modelling (FDM) process parameter prediction and optimization using group method for data handling (GMDH) and differential evolution (DE). The International Journal of Advanced Manufacturing Technology, 73(1), 509-519. (2014).

[16]. Ramesh, M., & Panneerselvam, K. Mechanical investigation and optimization of parameter selection for Nylon material processed by FDM. Materials Today: Proceedings, 46, 9303-9307. (2021).

[17]. Zhang, J., Liu, T., Hu, X., Raffik, R., Bhatt, M. W., & Ofori, I. Anti-cracking performance test of thick steel structure fireproof coating under vibration fatigue load for critical health infrastructure. The Journal of Engineering, 1086-1094. (2022).

[18]. Raffik, R., Naveen, C., Siyaguru, J., & Vijayanandh, R. Performance analysis of modified shuttle mechanism in polymerized bag weaving circular loom. In AIP Conference Proceedings (Vol. 2446, No. 1, p. 180028). AIP Publishing LLC. (2022).

[19]. Soundararajan, R., Raffik, R., & Karthikeyan, S. Mechanical Properties Enhancement of A356 Alloy Hybrid Composite by FSP and SP Route (No. 2022-28-0541). SAE Technical Paper. (2022).

[20]. Senthilkumar, S., Anushree, G., Kumar, J. D., Vijayanandh, R., Raffik, R., Kesavan, K., & Prasanth, S. I. Design, Dynamics, Development and Deployment of Hexacopter for Agricultural Applications. In 2021 International Conference on Advancements in Electrical, Electronics, Communication, Computing and Automation (ICAECA) (pp.1-6). IEEE. (2021).

[21]. An, Z., Wang, C., Raj, B., Eswaran, S., Raffik, R., Debnath, S., & Rahin, S. A. Application of New Technology of Intelligent Robot Plant Protection in Ecological Agriculture. Journal of Food Quality, (2022).

[22]. Jin, L., Zhou, Z., Li, K., Zhang, G., Liu, Q., Yao, B., & Fang, Y. (2022). Applying Evolutionary Multitasking for Process Parameter Optimization in Polymerization Process of Carbon Fiber Production. Applied Sciences, 12(18),9378. (2022).

[23]. Wang, Z., Li, J., Wu, W., Zhang, D., & Yu, N. Multitemperature parameter optimization for fused deposition modeling based on response surface methodology. AIP Advances, 11(5), 055315. (2021).

[24]. Raja, S., Agrawal, A. P., Patil, P., Timothy, P., Capangpangan, R. Y., Singhal, P., & Wotango, M. T. Optimization of 3D Printing Process Parameters of Polylactic Acid Filament Based on the Mechanical Test.

International Journal of Chemical Engineering, (2022).

[25]. Malviya, M., & Desai, K. Build orientation optimization for strength enhancement of FDM parts using machinelearning based algorithm. Computer Design Applications, 17, 783-796. (2019).

[26]. Alam, N., Alam, M., & Ahmad, S. Optimization of Fused Deposition Modelling process parameters using Teaching Learning Based Optimization (TLBO) algorithm. In IOP Con-ference Series: Materials Science and Engineering (Vol. 1149, No. 1, p. 012014). IOP Pub-lishing. (2021).

[27]. Sharma, B. B., Raffik, R., Chaturvedi, A., Geeitha, S., Akram, P. S., Natrayan, L., ... & Sathyamurthy, R. (2022). Designing and implementing a smart transplanting framework using programmable logic controller and photoelectricsensor. Energy Reports, 8, 430-444. (2022).

[28]. Yadav, D., Chhabra, D., Garg, R. K., Ahlawat, A., & Phogat, A. Optimization of FDM 3D printing process parameters for multi-material using artificial neural network. Materials To-day: Proceedings, 21, 1583-1591. (2020).

[29]. Tura, A. D., Mamo, H. B., & Rao, D. K. Study on the effect of fused deposition modelling (FDM) process parameters on tensile strength and their optimal selection. International Journal of Engineering and Artificial Intelligence. Vol.2, No.2, 81–91. (2021).

Pre Detection of Fire Accidents in Locomotive with Micro controller

M.Bala Chennaiah¹, G Dilli Babu², M Sumalatha³, K Dillip Kumar⁴, T. Srinivasa Rao⁵

^{1,2,3}V. R. Siddhartha Engineering College, Department of Mechanical Engineering,
Vijayawada, Andhra Pradesh, India.

⁴Lakireddy Balireddy College of Engineering, Department of Mechanical Engineering,
Mylavaram, Andhra Pradesh, India.

⁵Vasireddy Venkatadri Institute of Technology, Department of Mechanical Engineering,
Guntur, Andhra Pradesh, India.

ABSTRACT: The main objective of the paper is to diminish the fire accidents and to send the information to the control room, locating the place where the accident occurs. This work is helped to find the short circuit place before the short circuit occurs and also detects the fire if it occurs due to multiple reasons. The model is also used to stop the train before the short circuit occurs and is also used to send the information to the LOCO pilot and to the control room.

Key Words: Fire Detector, LED, Micro Processor, Pump

1. Introduction

Safety in travel is main concern for everyone. Present day's fire accidents are the majority often happening in trains. When these accidents are going on in isolated areas or throughout night times the defeat or spoil being caused is at higher rates. The spoil is heavier due to improper attain of service at right time due to improper communication and time delay is causing heavier spoil. That's way eliminating the time between when an accident occurs and when first responders are dispatched to the scene decreases the damage. One approach to eliminate the delay is by identifying the fire accident and notifying the concerned the system, loco pilot and passenger with in no time. Passengers will be notified by ringing the buzzer and loco pilot will be notified showing the message in the LCD display fitted in the engine along with alarm.

2. Literature Survey

According to our survey analysis for long distance communication people prefer rail transport when compared to air and road. The reason for that because rail transport is sophisticated way to travel. Now-a-days the accidents are occurs in the railways periodically. The accidents means it can occurs in detection, collision, bomb disaster and fire in the compartments. Out of all the parameters we are going to discuss about fire safety system alone. Fire safety system (FSS) can be implemented through automation techniques. The parameters and analysis is allowed for only Indian railway networks alone [1]. The usages of vehicles are rapidly increasing and at the same time the occurrence accident is also increased. No one can prevent the accident, but can save their life by expediting the ambulance to the hospital in time. A new vivid scheme called Intelligent Transportation System (ITS) is introduced. The objective of this scheme is to minimize the delay caused by traffic congestion and to provide the smooth flow of emergency vehicles. The concept of this scheme is to green the traffic signal in the path of ambulance automatically with the

help of RF module. So that the ambulance can reach the spot in time and human life can be saved and the accident location is identified sends the accident location immediately to the main server. The main server finds the nearest ambulance to the accident zone and sends the exact accident location to the emergency vehicle. The control unit monitors the ambulance and provides the shortest path to the ambulance at the same time it controls the traffic light according to the ambulance location and thus arriving at the hospital safely [2]. Early detection is of great importance as the consequences of a fire are catastrophic. Towards this direction this project envisages the deployment of Wireless Sensor Networks at the “Urban-Rural-Interface” (URI) and uses sensor fusion techniques to enhance the performance of the early fire detection and fire location estimation processes. [3] The use of NNs for automatic detection of smoke is also proposed. A system for wildfire monitoring using a wireless sensor network (WSN) that collects temperature relative humidity and barometric pressure is described. The wireless networked nodes communicate with a base station that collects the sensed data. Satellite based monitoring is another method to detect forest fires but the scan period and the low resolution of satellite images make this method incapable for real-time detection[4].

In highly populated Countries like India, everyday people lose their lives because of accidents and poor emergency facilities. These lives could have been saved if medical facilities are provided at the right time. This paper implies system which is a solution to this drawback. Accelerometer sensor can be used in car security system to sense vibrations in vehicle and GPS to give location of vehicle, so dangerous driving can be detected. When accident occurs, Accelerometer will detect signal and will send signal to AVR controller, microcontroller will enable airbag to blow and message with accident location is sent to preprogrammed numbers such as ambulance, police station, etc via GSM [5]. In this paper, a remedy to reduce the death loss occurring due to fire accidents in trains is presented. Fire on a running train is more catastrophic than on a stationary one, since fanning by winds helps spread the fire to other coaches. When these accidents are occurring in remote areas or during night times the loss or damage being caused is at higher rates. The damage is heavier due to improper reach of service at right time due to improper communication. This projects help in notifying the passengers and emergency services. The project consists of a microcontroller which is interfaced with the GPS module, GSM modem and fire sensors. Once the sensors attached in the compartments of train senses the smoke detection, it assumes a fire accident. The controller assumes it as an emergency and starts the buzzer, LCD display and GSM modem in the engine sending the latitude and longitude information to the specified mobile number and emergency services, by fetching the information from the GPS [6]. The increased growth in the railway sector has resulted in an increase in the train traffic density across the world. This has resulted in the increase in the number of accidents involving trains. In this paper, the proposed system includes several features which prevent train accidents. It includes automatic speed controlling in curves, collision detection, fire detection, detaching of couch automatically when fire is detected in it, automatic railway gate control and track continuity. This system makes use of IR sensors, fire sensor, Zigbee and other embedded systems [7].

3. Model Development

In existing system we detect fire using smoke sensors, temperature sensors etc., then we activate buzzer and send signal to LOCO pilot to stop the train. It takes some time for train to stop. In the mean while, the damage occurs. In our proposal we pre-detect the places where short circuit/fire occurs and send message to the control room and then to LOCO pilot. So, we can

take necessary actions before the fire occurs.

3.1 Block / Short Circuit Diagram

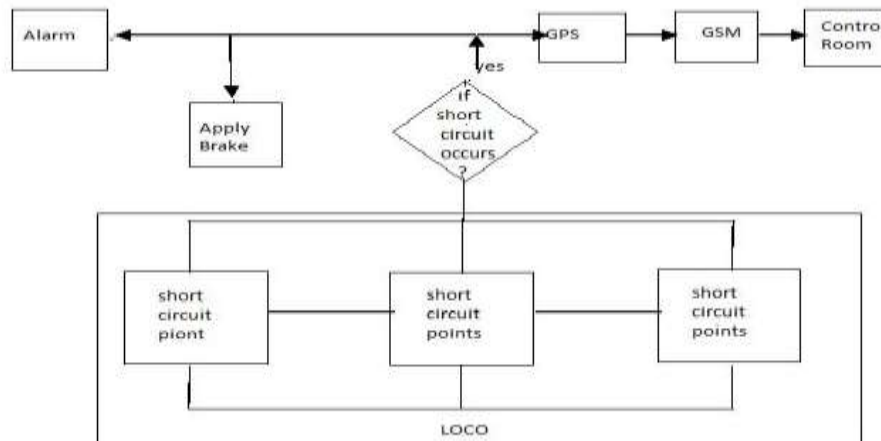


Fig-1: Short circuit system

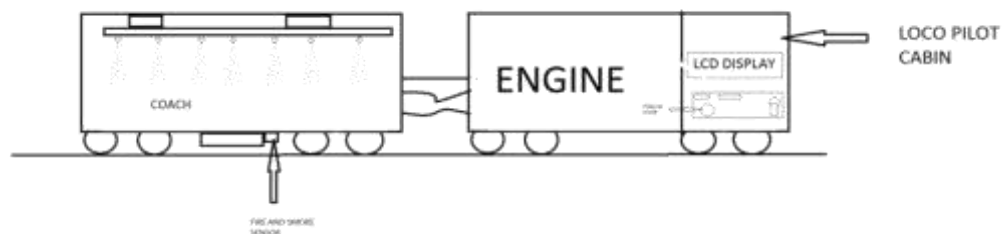
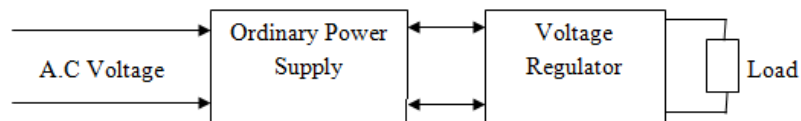


Fig-2: Fire and smoke detection system

3.2 Fire Pre Detection System & Components

3.2.1 Supply of power

The given power supply is the +5V D.C. The external power is 230V A.C and there is a required to convert the above supply it into +5V D.C.

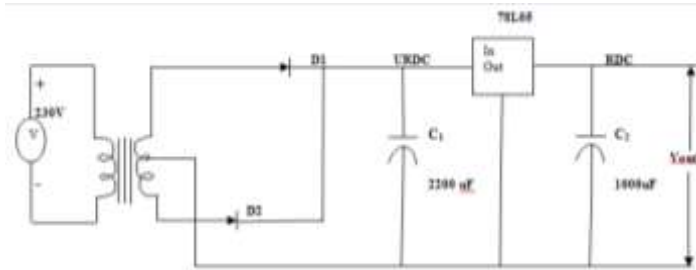


Circuit 1: Block Diagram of R.P.S

The input power supply is step down from 230V to 9V. The rectifier consists of diodes D_1 and D_2 makes the direct current supply. The output from rectifier is a URDC, whose value is 13V peak to peak. The voltage regulator makes this Ultra remote driver cabinet to Remote Device Control of +5V. The capacitor C_1 is used to maintain constant voltage between two successive positive cycles where as C_2 is used to eliminate the fluctuations caused by regulator. Here we are selecting 13V as a peak value. Because of fluctuations, the peak voltage may decrease, then control device cannot step up to +5V. If we select peak value, a higher one, then the problem can be overcome. A regulated power supply which maintains the output voltage steady irrespective of A.C. mains fluctuations or load variations is known as regulated power supply. A regulated power supply means it combination of an ordinary power supply and voltage regulating device. The output of ordinary power supply is fed to the voltage regulator which produces the final output. The output voltage remains constant whether the load current changes or there are fluctuations in the input A.C. voltage.

The rectifier converts secondary voltage into pulsating voltage. The pulsating D.C. voltage is applied to the capacitor filter. This filter reduces the pulsations in the rectifier D.C. output

voltage. Finally, it reduces the variations in the filtered output voltage.



Circuit 2: Power supply regulator



Fig 3: Pre Fire detection Circuit

3.3 Microcontroller - 89C52

3.3.1 Pin Diagram and its explanation

The microcontroller common part number in point of fact includes a whole family of microcontrollers that have information ranging from 8031 to 8751 and are available in N-Channel NMOS (Metal Oxide Silicon) and CMOS (Complementary Metal Oxide Silicon) construction in a selection of enclosure types. With 4K bytes of Flash Programmable and Erasable Read Only Memory (PEROM). The device is manufactured using Atmel's high density nonvolatile memory technology and is compatible with the industry standard MCS-51 instruction set and pin out. The on-chip Flash allows the program memory to be reprogrammed in-system or by a conventional nonvolatile memory programmer. By combining a versatile 8-bit CPU with Flash on a monolithic chip shown in fig 4, the Atmel AT89C52 is a powerful microcomputer which provides a highly flexible and cost effective solution to many embedded control applications. The AT89C52 provides the following standard features: 4 Kbytes of Flash, 256 bytes of RAM, 32 I/O lines, two 16-bit timer/counters, five vector two-level interrupt architecture, a full duplex serial port, on-chip oscillator and clock circuitry.

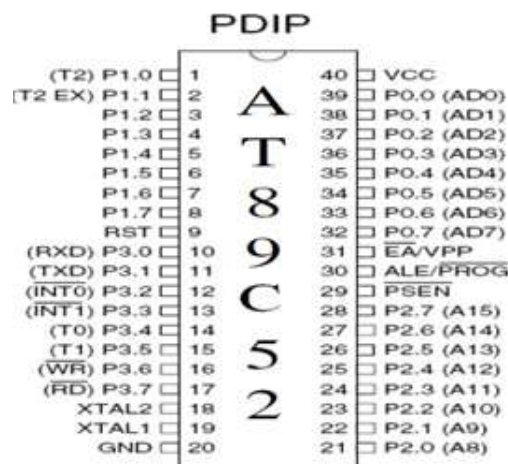


Fig 4: Pin Diagram and Description of AT89C52

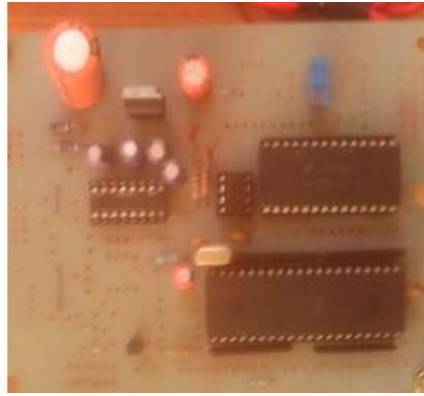


Fig 5: Micro controller and ADC modules

In addition, the AT89C52 is designed with static logic for operation down to zero frequency and supports two software selectable power saving modes. The Idle Mode stops the CPU while allowing the RAM, timer/counters, serial port and interrupt system to continue functioning. The Power down Mode saves the RAM contents but freezes the oscillator disabling all other chip functions until the next hardware reset. The semiconductor diode is a radioactive recombination type. It requires a specific amount of power to generate an electron-hole pair. The same power is released when an electron recombines with a hole. This released power may result in the discharge of photon and such a recombination. Finally, the amount of power released when the electro again from the transmission band to the valence band appears in the form of radiation. Alternatively the released power may result in a series of photons causing lattice deliverance. Finally the released power may be transferred to another electron. The recombination power may be lie down in the infra-red and observable light spectrum. In forward is peaked around the band gap power and the phenomenon called insertion luminescence. In a junction biased in the sudden large amount break down region, there results a spectrum of photons transportation much higher energies. Approximately White light subsequently gets emitted from micro plasma collapse region in silicon junction.

Diodes having radioactive recombination are termed as Light Emitting Diode, abbreviated as LEDs as shown in fig 5. In gallium arsenide diode, recombination is predominantly a radiation recombination and the probability of this radioactive recombination far exceeds that in either germanium or silicon. Hence Ga As LED has much higher efficiency in terms of Photons emitted per carrier. The internal efficiency of Ga as LED may be very close to 100% but because of high index of refraction, only a small fraction of the internal radiation can usually come out of the device surface. In spite of this low efficiency of actually radiated light, these LEDs are efficiency used as light emitters in visual display units and in optically coupled circuits, the efficiency of light generation increases with the increase of injected current and with decreases in temperature. The light so generated is concentrated near the junction since most of the charge carriers are obtained within one diffusion length of the diode junction.

Results

In this Paper a prototype for PRE DETECTION OF FIRE SYSTEM in loco has been developed successfully. This is well suitable for present INDIAN RAILWAY SYSTEM with little adjustments. The short circuit places, favorably to take place are identified and the protecting methods are discussed

References

- [1] Rail Parameters Monitoring For The Fire Safety System In The Compartments Using Automation Technology.
- [2] S. Ramesh Accident Identification With Automatic Ambulance Rescue System -Srajan Saxena Vit University ,Vellore,India.
- [3] Fire Detection In The Urban Rural Interface Through Fusion Techniques E. Zervas,Dept. Of Electronics,TEI-Athens.
- [4] O. Sekkas, S. Hadjieftymiades, C. Anagnostopoulos,Dept. Of Informatics And Telecommunications,University Of Athens.
- [5] Vehicle Accident Detection And Reporting System Using GPS And GSM Aboli Ravindra Wakure, Apurva Rajendra Patkar, Manisha Vitthal Dagale, Priyanka Pradeepkumar Solanki.
- [6] Fire Detection And Notification System In Trains Kuncham Viswa Tej, Suresh Angadi,Final Year B.Tech, Dept. Of ECE, K L University, Vaddeswaram,A.P, India. Assistant Professor, B.Tech, Dept. Of ECE, K L University, Vaddeswaram, A.P, India.
- [7] Advanced Railway Accident Prevention System Using Sensor Networks M.D.Anil1, Sangeetha.S, Divya.B ,Niranjana.B, Shruthi. K.S Assistant Professor, TCE Department, GSSSIETW, Mysore, India.

Strength Analysis of Aircraft Composite Structure due to Air loads during flight by Finite Element Method

Sd. Abdul Kalam¹, Sk. Ziaavulla², Sk. Abdul Rahman², Sk. Karim², R. Santhosh²

¹ Assistant Professor, PVP Siddhartha Institute of Technology, Vijayawada, Andhra Pradesh, India

² Student, PVP Siddhartha Institute of Technology, Vijayawada, Andhra Pradesh, India
Corresponding mail: sdak77@gmail.com

Abstract. A bird strike occurs during the takeoff and landing of an aeroplane. Bird strike is a common flight safety issue that results in significant losses each year. Front-facing component, such as the nosecone structure, is one of the most vulnerable area of an aeroplane to bird hit, according to statistics. The Federal Aviation Administration (FAA) in the United States and the European Aviation Safety Agency (EASA) in Europe set certification standards that involve assessing the structural integrity of airframes composed mostly of composite materials.

In this present investigation strength prediction analysis is done as per FAA and EASA during aircraft flight condition on composite structure which is required prior to the impact analysis of bird strike while takeoff and landing of the aircraft. Composite failure load estimations are critical for ensuring flight safety during service periods. The finite element approach was used to analyse the strength of a typical composite structure. In this, an improved finite element model has been developed for an engine composite nosecone which is a roof structure of an aircraft covers all engine parts. This structure has to withstand under air loads during flight condition. It is necessary to know about the stresses and strains in a structure in order to estimate failure load. Failure theories are used to predict the strength of composite laminates. The comparative study of numerical results with theoretical values was carried out. These results were shown good agreement between them.

Keywords: Composite structures, Finite Element Approach, Strength Prediction.

1. Introduction

Before analysing the damage behaviour of forward facing composite structure of a typical aircraft under high velocity bird impact, it is mandatory to evaluate the strength prediction under critical flight condition [1]. Composite materials are becoming more prevalent in the aviation industry every year as they outperform metallic materials in many ways. Composites have structural strengths comparable to metals yet are lighter, improving aircraft performance and efficiency [2].

Following specific types of high-energy bird hit on forward-facing components made up of tailor-made composite materials, an aircraft must demonstrate compliance with "continued safe flying and landing" requirements. A thorough grasp of the behaviours of various aircraft components is required for designing a bird-proof aeroplane [3].

Experimental tests are still important in the development and design of new materials, whereas numerical tests are commonly employed to validate aircraft components against bird strike, either alone or in conjunction with experimental tests [4]. To tackle this class of

problems, explicit nonlinear finite element programmes (such as AUTODYNE, LSDYNA, PAM-CRASH, PAM-SHOCK, DYNA3D, ABAQUS, PW/WHAM, RADIOSS) that are accessible as advanced commercial FE solvers have been used. Intra-ply failures and inter-laminar delamination transmit the damage downward, forming a pine tree-shaped damage region [5].

The deformation and damage characteristics of unidirectional composite plates caused by a bird-strike impact were studied by Nishikawa [6]. To determine how these deformations cause damage, Nishikawa assessed the damaged elements using the "failure criteria" developed by Hou, Petrinic, Ruiz, and Hallett [7], which include:

To make a laminate, the numerous unidirectional layers are piled together. Fig. 1.1 depicts a typical lamination.

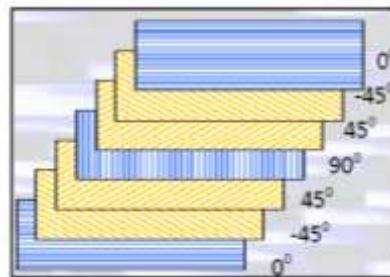


Fig.1.1. Exploded view of Laminate

2. Failure Criteria

Hashin criteria are often applied to point stress calculations using a two-dimensional classical lamination technique with ply discounting as the material degradation model. Hashin criterion failure indices are based on fibre and matrix failures and include four failure categories. The maximum stress criteria are utilised for the transverse normal stress component in three-dimensional situations, where the maximum stress criteria are applied.

Hashin's criterion [8] include the following failure modes:

The Tensile fibre failure for $\sigma_{11} \geq 0$

$$\left(\frac{\sigma_{11}}{X_T}\right)^2 + \frac{\sigma_{12}^2 + \sigma_{13}^2}{S_{12}^2} = \begin{cases} \geq 1 & \text{failure} \\ < 1 & \text{no failure} \end{cases} \quad (2.1)$$

The compressive fibre failure for $\sigma_{11} < 0$

$$\left(\frac{\sigma_{11}}{X_C}\right)^2 = \begin{cases} \geq 1 & \text{failure} \\ < 1 & \text{no failure} \end{cases} \quad (2.2)$$

The tensile matrix failure for $\sigma_{22} + \sigma_{33} > 0$

$$\frac{(\sigma_{11} + \sigma_{22})^2}{Y_T^2} + \frac{\sigma_{23}^2 - \sigma_{22}\sigma_{33}}{S_{23}^2} + \frac{\sigma_{12}^2 + \sigma_{13}^2}{S_{12}^2} = \begin{cases} \geq 1 & \text{failure} \\ < 1 & \text{no failure} \end{cases} \quad (2.3)$$

The compressive matrix failure for $\sigma_{22} + \sigma_{33} < 0$

$$\left[\left(\frac{Y_C}{2S_{23}}\right)^2 - 1\right] \left(\frac{\sigma_{22} + \sigma_{33}}{Y_C}\right) \frac{(\sigma_{22} + \sigma_{33})^2}{4S_{23}^2} + \frac{\sigma_{23}^2 - \sigma_{22}\sigma_{33}}{S_{23}^2} + \frac{\sigma_{12}^2 + \sigma_{13}^2}{S_{12}^2} = \begin{cases} \geq 1 & \text{failure} \\ < 1 & \text{no failure} \end{cases} \quad (2.4)$$

The interlaminar tensile failure for $\sigma_{33} > 0$

$$\left(\frac{\sigma_{33}}{Z_T}\right)^2 = \begin{cases} \geq 1 & \text{failure} \\ < 1 & \text{no failure} \end{cases} \quad (2.5)$$

The stress components σ_{ij} are denoted by subscripts 1, 2 and 3, while the tensile and compressive permissible strengths for lamina are indicated by subscripts T and C. The tensile strengths in three material directions are denoted by the letters X_T , Y_T , and Z_T . Similarly, the letters X_C , Y_C , and Z_C stand for the allowed compressive strengths in three

different material directions. S_{12} , S_{13} , and S_{23} also indicate acceptable shear strengths in the corresponding main material orientations. In a typical aircraft nosecone is provided to cover all the equipment/parts that are placed on the roof structure of the fuselage. It is a secondary structure and is made out of composite sandwich construction and monolith skin. During flight it is subjected to air loads and is attached to the fuselage by means of quick release camloc fasteners all along its length to facilitate easy removal for inspection or maintenance if any. The applicable compliance is FAR 29.351 and FAR 29.1193(a). The nosecone sandwich structure with each face sheet is of 2 layers of Kevlar prepreg, each layer has 0.24 mm thick and a Nomex flex core of 10 mm thickness. The geometry details of nosecone are shown in Fig. 2.1.

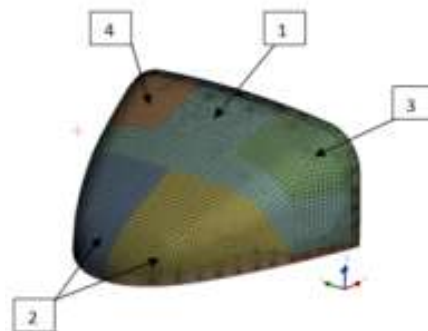
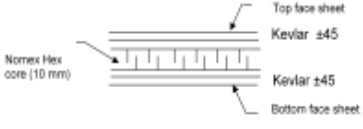
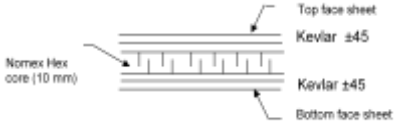
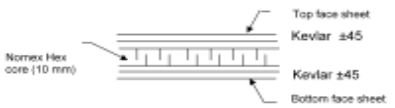


Fig. 2.1. Geometry details of nosecone
The lay-up scheme at various regions is given in table 2.1

S. No.	Region	Lay-up scheme
1	Monolith	 KEVLAR
2	Sandwich Core- Forward	
3	Sandwich Core- Left	
4	Sandwich Core- Right	

3. Strength Prediction

[9] ACP (Pre)/ACP (Post) is utilised to create a finite element model for stress analysis of composite laminates in this study. The pre-processor ACP is used to produce the finite element model, which includes the finite element mesh, boundary conditions, and material attributes (Pre). To anticipate the laminate's strength, post-processing is done in ACP (Post). For the purpose of analysis, the coordinate system must first be specified by the thickness, length, and width of distinct sections of the laminate. Table 3.1 lists the features of composite laminates. The mechanical properties of Honeycomb Nomex core are shown in the table 3.2. Stress analysis of nosecone structure is carried out and failure loads are predicted using failure theories.

Material properties of kevlar/epoxy and glass/epoxy are listed below.

Table 3.1 Material properties of kevlar/epoxy and glass/epoxy [10]

Property	kevlar/epoxy	glass/epoxy
Young's Modulus in fiber Direction(E_1) (MPa)	76000	54000
Young's Modulus matrix direction(E_2) (MPa)	5500	18000
Modulus of Rigidity(G_{12})(MPa)	2100	9000
Poisson Ratio (ν_{12})	0.340	0.25
Compressive Strength in fiber direction (X_C) (MPa)	276	1035
Compressive Strength in matrix direction (Y_C) (MPa)	138	138
Tensile Strength in fiber direction (X_T) (MPa)	1380	1035
Tensile Strength in matrix direction (Y_T) (MPa)	28	28
Shear Strength (S_{12}) (MPa)	44	41

Table 3.2 Mechanical properties of Honeycomb Nomex core [11]

Property	Honeycomb Nomex core
Compressive Modulus (MPa)	138
Compressive Strength (MPa)	2.24
Crush Strength (MPa)	1.34
Shear Strength (MPa)	1.21
Shear Modulus (MPa)	45
Density(kg/m^3)	48

4. Loads and Boundary conditions

The loads for any given external surface of the helicopter are determined by the pressure coefficient (C_p) obtained from the wind tunnel tests. This will be achieved by multiplying the C_p with the dynamic pressure corresponding to the flight speed. In general on conservative side the maximum C_p of a particular surface will be considered for the loads estimation on it. On the other hand the load is critical at higher angles of air approach on to the helicopter. The nosecone surface considered for the analysis face a variety of flow interaction in terms of aerodynamic load.

Helicopter flying with a velocity (V) of 270 kmph level and -4° pitch, 0 psi at an altitude of 1000 m, then the density of fluid (ρ) = 1.064 (kg/m^3). Then the expression for dynamic pressure is given as

$$\text{Dynamic pressure (q)} = 0.5 * \rho * V^2$$

The value of 'q' from above equation is 2992 N/m^2 ,

The C_p over nosecone surface at a critical section from the wind tunnel test results is taken

as -0.51 and the expression for the suction pressure on nosecone surface is given below

$$\text{Suction pressure} = q * C_p$$

The value of suction pressure from above equation is -1526 N/m^2 , (-ve sign indicates the pull outward)

Inertia load on nosecone is to be added with suction pressure. It is negligible when compared to suction pressure. Then suction pressure is applied on throughout the nosecone surface at A and fixed boundary conditions at surface B as shown below in figure 4.1.

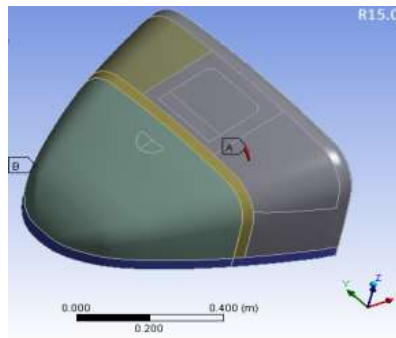


Fig.4.1 Nosecone structure

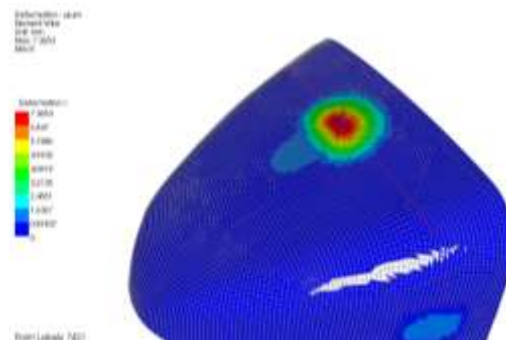


Fig. 5.1 Total deformation of nosecone structure

5. Discussion of Results

Total deformation was analyzed from the numerical simulation of nosecone structure and the resulted displacement was very small as shown in Fig. 5.1 and it is concluded that the structure is safe in terms of wind interactions. Comparison of In-plane stresses from the numerical analysis with theoretical value are presented in following table 5.1

Table 5.1 Comparison of results with allowable strength [10]

Description	Maximum stresses from numerical analysis (MPa)	Allowable strength (MPa)
Stress in fiber direction	S_{1C} (14.411), S_{1T} (21.291)	X_C (276), X_T (1380)
Stress in matrix direction	S_{2C} (41.721), S_{2T} (54.447)	Y_C (138), Y_T (28)
Stress in fiber-matrix direction	S_{12} (2.6379)	S_{12} (44)

In-plane stresses S_{1C} and S_{1T} , S_{2C} and S_{2T} , S_{12} are analyzed from the simulation of nosecone structure are plotted below (Fig.5.2).

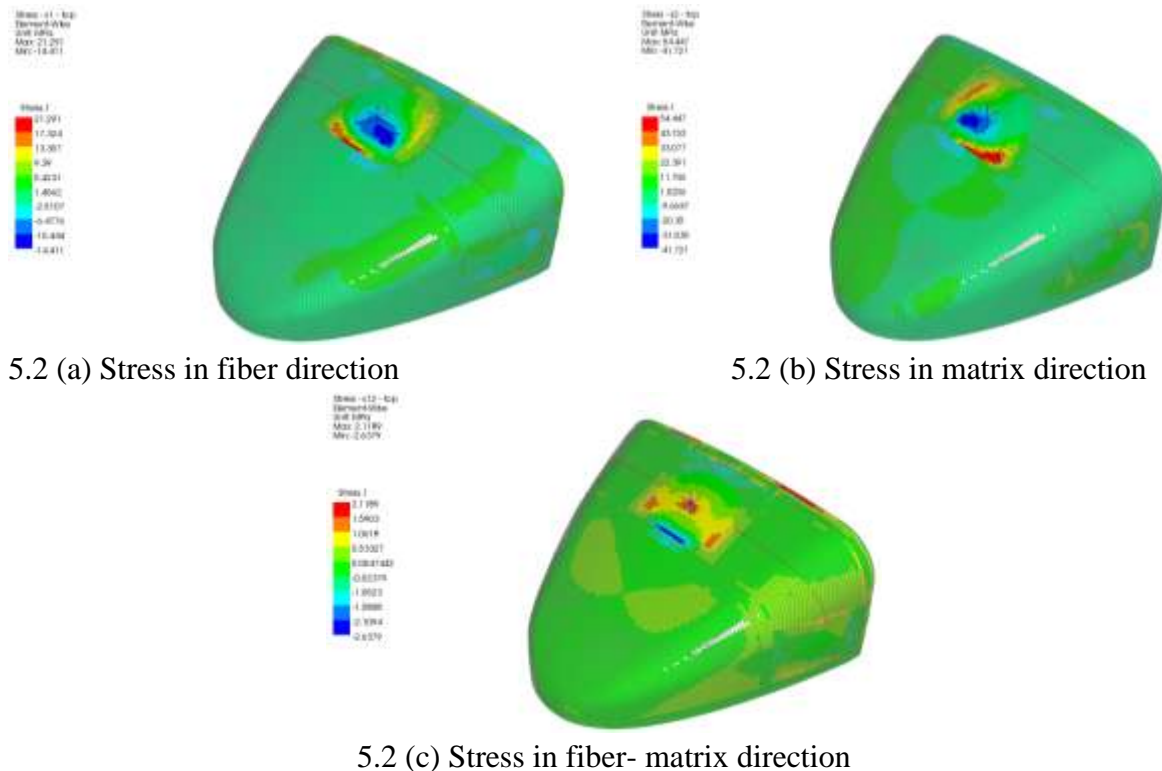


Fig.5.2 Plot of in-plane stresses

6. Conclusions

From the above analysis, it is observed that the stresses obtained from the analysis are within the strength limits, so it is confirmed that the nosecone structure has the capability to withstand the service loading conditions.

References

1. Blokpoel, H. Bird hazards to aircraft. Clarke, 1976.
2. Composites in the Aircraft Industry, Available from Appropedia: [http://www.appropedia.org/Composites in the Aircraft Industry# cite note-A-2](http://www.appropedia.org/Composites_in_the_Aircraft_Industry#cite_note-A-2), 2014.
3. Barber, J. P., Bird impact loading. The V shock and vibration: Vol. 48 , 1978. (pp. 115–122).
4. Hedayati, R., & Ziaei-Rad, S.. Effect of bird geometry and orientation on bird-target impact analysis using SPH method. International Journal of Crashworthiness, 17/4,2012a ,pp.445–459.
5. Abrate, S., Impact on composite structures. Cambridge University Press, (2005).
6. Nishikawa, M., Hemi, K., & Takeda, N., Finite-element simulation for modelling composite plates subjected to soft body, high-velocity impact for application to bird-strike problem of composite fan blades. Composite Structures, 93(5), 2011. pp.1416–1423.
7. Hou, J. P., Petrinic, N., Ruiz, C., & Hallett, S. R., Prediction of impact damage in composite plates. Composites Science and Technology, 60, 2000. 273–281.
8. [8] Hashin Z. Failure criteria for unidirectional fibre composites, ASME Journal of Applied Mechanics, Vol. 47 (2), 1980, pp 329- 334.
9. ANSYS AUTODYN user's manual theory manual, ANSYS Inc. Southpointe, 275 Technology Drive, Canonsburg, PA, USA, 2014.
10. Robert M. Jones, "Text book of Mechanics of Composite Materials", second edition, Virginia polytechnic institute and state university, blacksburg, virginia 24061-0219.
11. A. Zinno, A. Prota, E. Di Maio, C.E. Bakis, "Experimental characterization of phenolic-impregnated honeycomb sandwich structures for transportation vehicles" Composite Structures 93 (2011) 2910–2924.

Comparative Analysis of Semi Monocoque Structured Aircraft Nose Cone Made of Different Titanium Graded Alloys at different operating conditions

T J Prasanna Kumar¹, Y Ayyappa^{2a}, M Kiran Kumar^{2b}, Sk Roshan^{2c}, P Tarun
kumar^{2d}

^{1*} Assistant Professor, Department of Mechanical Engineering, PVP Siddhartha Institute of
Technology, Kanuru, Vijayawada, AP, India-520007

^{2abcd} UG Students, Department of Mechanical Engineering, PVP Siddhartha Institute of Technology,
Kanuru, Vijayawada, AP, India-520007

*Corresponding Author Email: tjpk.mech@gmail.com

Abstract: The purpose of this article is to carry static structural analysis on a semi-monocoque structured aircraft nose cone made of titanium with different graded alloys, in order to predict the optimum values for structural deformation and von mises stresses under various operational load conditions. In general the passenger aircrafts will fly at maximum altitude of about 50000 Feet and minimum at sea level and hence the environmental impact or atmospheric pressure will influence on strength of the nose cone structure when the aircraft is flying at different altitudes are considered. In present research it is proposed to design a scaled model of nose cone section with semi monocoque structure having 4 segments and each segment is a shell parabolic configuration. Among several nose cone configurations such as conical, elliptical, O-give, Parabolic, and sears hack, our investigation is carried on parabolic configuration because of less mean shear stress distribution and lowest tip temperature at various operational conditions. For the present work Titanium with graded alloys are chosen because of its excellent physical properties, which is currently most widely used in various fields, has been adopted for aircraft nose cones and has achieved good results. The main challenge faced by aerospace industries is to design the shape nose of the flying object that travels at high speeds with optimum values of air drag. This study deals with computational analysis on parabolic nose cone profiles of a commercial aircraft. The effect of change in material pure graded titanium with alloys and in turn changes in material properties on nose cone structure are studied different pressure loads. The paper objective is to identify the better Titanium graded alloy with minimum structural deformation at all operating altitudes. The scope of this paper is to develop a nose cone configuration with variable shell thickness the structure should yield optimum material strength to withstand loads at all operating conditions.

Keywords: *Nose cone, Titanium alloys, operating pressure, total deformation, vonmises stress*

1. Introduction

1.1 Nose cone material consideration

A nose cone is the conically shaped foremost section of an aircraft, rocket, and guided missile designed to modulate oncoming airflow behaviors and minimize aerodynamic drag.

The cone configurations generally used for aerospace applications are conic, spherically blunted conic, bi-conic, tangent ogive, spherically blunted tangent ogive, secant ogive, elliptic, parabolic, power series and Haack series etc. The most widely used materials for aircraft nose cone structure includes: aluminum, titanium, magnesium alloys, molybdenum, carbon-carbon composites, and hafnium diboride.

The composite materials, although being outstanding in their strength to weight characteristic have some drawbacks in the cost of raw materials, storage and available data on structural life limitations in addition to requiring in many instances, expensive methods of non-destructive inspection.

In this study, to determine the observed behaviour of these titanium materials used to build the nose of a parabolic model for aircraft, the parabolic shape was selected because the average shear stress distribution was small and the tip temperature was the lowest. First, we will focus on nose cone structural deformation at different atmospheric pressures, and then, the investigation continues to predict the optimum values of induced stresses for the subjected loads on nose cone made of different Titanium graded alloys. And comparing the above materials with their ability to withstand the Pressure loads at various operating conditions based on altitudes range from 10000 feet to 50000 feet.

2. Literature Survey

[1] P. Venkata Suresh et al, carried their investigation on aircraft nose cone at specified altitude (40,000ft) for different materials such as structural steel, stainless steel, aluminium alloy, and titanium alloy (pure grade). In present research it is proposed to design a scaled model of nose cone section with semi monocoque structure having 4 segments and each segment is a shell parabolic configuration. Among several nose cone configurations such as conical, elliptical, O-give, Parabolic, and searshack, our investigation is carried on parabolic configuration because of less mean shear stress distribution and lowest tip temperature at Mach number having 0.8 to 1.0. [2] C.M.V Priya et al, investigated aircraft nose of conical and elliptical configuration with titanium alloys at a standard pressure of 10×10^5 MPa. [4] P. V. D Aditya et. al, carried their analysis on missile nose cone of conical and elliptical configuration made of Titanium grade-I and Titanium α -alloy and concluded that total structural deformation is less for titanium grade-1 alloy when compared with titanium α -alloy. [3] M. Srinivasula et.al. new nose cone concept that promises a gain in performance over existing conventional nose cones is discussed in this paper the term nose cone is used to refer to the forward most section of a rocket, guided missile or aircraft. The cone is shaped to offer minimum aerodynamic resistance. Titanium Ti-6Al-6V-2SN Titanium grade 1 the remainder titanium. These are significantly stronger than commercially pure titanium. While having the same stiffness and thermal properties a structural-loaded, a pressure sudden impact loads and a foam nose-cone concept Results from analysis of the nose cone are used in structural analysis performed with ANSYS. [8] A Sanjay Varma, et.al. : Comparison of various nose profiles is to be carried out to know performance over existing conventional nose profiles is discussed in this paper. The paper objective was to identify the types of nose profiles and its specific aerodynamic characteristics with minimum pressure coefficient and critical Mach number. The scope of this paper is to develop some prototype profiles with outstanding aerodynamic qualities and low cost for use in construction projects for missile increasing their range and effect on target. For the present work Titanium with graded alloys are chosen because of its excellent physical properties, which is currently most widely used in various fields, has been adopted for aircraft nose cones and has achieved good results. [7] The main challenge faced by aerospace industries is to design the shape nose of the flying object that travels at high speeds with optimum values of air drag. This study deals with computational analysis on parabolic nose cone profiles of a commercial aircraft. The effect of change in material properties on nose cone structure is studied different pressure loads.

3. Titanium Alloys and their Material Properties

Titanium is a prominent metal generally regarded as one of the strongest metals; titanium is used in a variety of industrial forms and is in great demand today. Titanium material has more advantages and best used when parts require high strength and light weight. Titanium can also withstand high temperatures and is highly resistant to corrosion. These properties make titanium ideal for many industries including transportation, medical, military and defense, and aerospace.

3.1 Properties of Titanium

Proper forging of titanium requires knowledge of the metallurgical properties and what happens to the material when it is heated in order to prepare it for the forging process at the micro-structural level. There are two phases associated with titanium and titanium alloys that occur in the material during heating.

These phases are known as alpha and beta phases and it is very important to have a good understanding of these phases in order to properly forge titanium.

3.1.1 Alpha (α) Phase

The alpha phase is a low-temperature allomorph with a hexagonal close-packed structure. The alpha phase exists from room temperature to 1625°F. "Alpha" grade titanium has the highest corrosion resistance of any other grade of titanium.

3.1.2 Beta (β) Phase

Titanium transforms at 1625°F into its high-temperature allomorph, the body-centered cubic beta phase, and retains the beta phase up to a melting point of 3038°F. This phase is ideal for forging, heat treating and welding while retaining titanium. This phase materials attained incredible strength and high corrosion resistance.

Titanium can be easily combined with other metals to create stronger alloys, resulting in three types of titanium alloys. There are three grades of titanium alloys: alpha alloys, alpha beta alloys and beta alloys.

- Alpha alloys generally retain their original alpha phase which makes them creep resistant up to 5537.778°C. The alpha stabilizers that make up alpha titanium alloys are aluminium, oxygen, and nitrogen-carbon.
- Alpha-beta alloys combine both alpha and beta microstructures that are modified at room temperature. This alloy is capable of high-strength heat treatment and contains neutral elements such as tin and zirconium. A well-known alpha-beta alloy is Ti-6AL4V.
- Beta alloys are titanium alloys that contain enough other alloys to maintain the beta phase at room temperature and can be heat treated to very high strengths. Titanium alloys of this grade contain beta stabilizers such as vanadium, molybdenum, niobium and tantalum.

3.2 Material Properties considered for the Analysis

Table-1 Mechanical properties and real constants used for present analysis

Properties	Titanium-Gr1	Titanium-Gr2	Ti- α alloy	Ti- β alloy
Modulus of Elasticity (Pa)	1.02E+11	1.02E+11	1.10E+11	1.01E+11
Density (kg/m ³)	4540	4540	4540	4420
Poisson's Ratio	0.34	0.37	0.31	0.31
Thickness (m)	0.001	0.001	0.001	0.001

[6] (*Titanium and their alloys material properties are taken from the reference: Metals Hand Book ASM International, 1990*)

4. Method of Approach (Modeling and Analysis using ANSYS)

4.1 Introduction to Finite Element Analysis

Ansys [5] is a general-purpose finite element modeling package for the numerical solution of a wide range of mechanical problems. These problems include static/dynamic problems, structural analysis, heat transfer and fluid problems, acoustics and electromagnetic problems. In general, finite element solutions can be divided into three steps and typical general engineering problems.

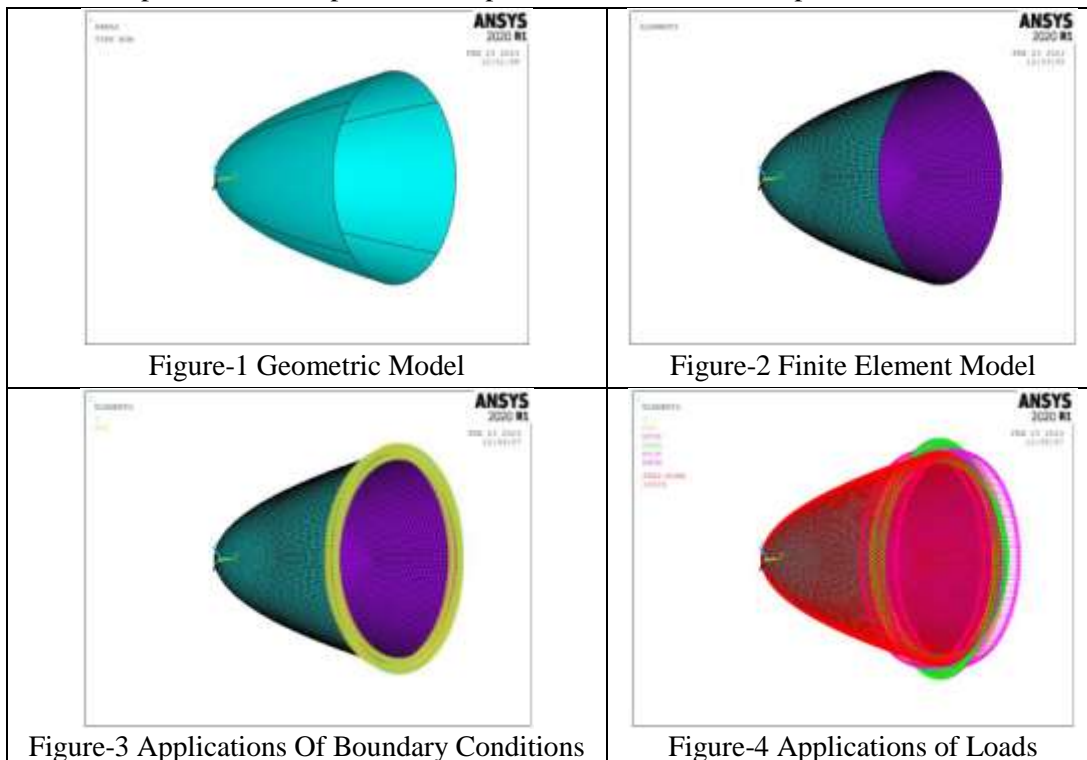
Pre-Processing: Problem Definition: The main pre-processing steps define key points/lines/areas/volumes, element types and material/geometric properties, and required mesh lines/areas/volumes. The amount of detail required depends on the analysis dimension, 1D, 2D, axisymmetric and 3D.

Solutions: Load assignments, constraints and solutions. Here you need to show the loads (point or pressure), constraints (translational and rotational) and finally solve the resulting system of equations.

Post-Processing: further processing and viewing results. At this stage, you can get a list of nodal displacements, forces and moments of elements, deflection graphs and contour stress diagrams or temperature maps. neers, metallurgists and quality personnel.

In the present investigation, the aircraft nose cone structure is proposed to model in parabolic configuration [3] in ANSYS 2020 R1 APDL to study the static structural behavior at different loading conditions.

Considering four different materials such as Titanium ASTM Grade-1(pure), Titanium ASTM Grade-2 (pure), Titanium α -Grade alloy Ti-5Al-2.5Sn, Titanium β -Grade alloy: Ti-13V-11 Cr- 3 Al with slight changes in material properties like [6] modulus of elasticity, density, poisson's ratio etc., keeping the SHELL thickness as constant ie. 0.0016 m, (presented in the above Table-1) the model is tested each time with different Pressure load conditions. Upon solving the solution at given load step, the individual structures are examined for Total Deformation and maximum- minimum vonmises stresses and respective contour plots were captured and results are compared.



5. Results and Discussions

The nose cone when it is tested under a wide range of operating conditions about 10000 ft to 50000 ft of altitudes, however the respective pressure values in Pascal's are taken from standard atmospheric table as shown below:

Table-2: Pressure values from Standard Atmospheric table

Altitude in Feet	Pressure (Pa)
10000	70326.52
20000	44126.4
30000	29647.5
40000	18615.8
50000	11031.6

ANSYS 2020 R1 tool is used to analyse this nose cone structure made of different materials with different material properties as mentioned in above Table-2. The proposed model is tested for total deformation and von mises stresses when it is operating under different loading conditions as shown in above table.

The tested model is subjected to the various ranges of Total deformation. The maximum value and minimum value of von mises stresses induced in the nose structure made of 4 different materials subjected to pressure at various altitudes are presented in the below Table-3 to 7.

Table-3 Total Deformation and vonmises results obtained from static structural analysis at an altitude of 10000 Ft

PRESSURE (Pa)		70326.52	
Material	Total Deformation	Von mises Stress	
		(max)	(min)
Ti-Gr1	0.001782	8.34E+07	9.88E+06
Ti-Gr2	0.002842	1.33E+08	1.60E+07
Ti- α alloy	0.002734	1.32E+08	1.61E+07
Ti- β alloy	0.002974	1.32E+08	1.61E+07

Table-4 Total Deformation and vonmises results obtained from static structural analysis at an altitude of 20000 Ft

PRESSURE (Pa)		44126.4	
Material	Total Deformation	Vonmises Stress	
		(max)	(min)
Ti-Gr1	0.001819	8.33E+07	1.01E+07
Ti-Gr2	0.001096	5.26E+07	6.19E+06
Ti- α alloy	0.001716	8.31E+07	1.01E+07
Ti- β alloy	0.001866	8.31E+07	1.01E+07

Table-5 Total Deformation and vonmises results obtained from static structural analysis at an altitude of 30000 Ft

PRESSURE (Pa)		29647.5	
Material	Total Deformation	Vonmises Stress	
		(max)	(min)
Ti-Gr1	8.35E-04	3.38E+07	4.21E+06
Ti-Gr2	6.81E-04	3.53E+07	4.16E+06
Ti- α alloy	7.08E-04	3.50E+07	4.17E+06
Ti- β alloy	0.001254	5.58E+07	6.77E+06

Table-6 Total Deformation and vonmises results obtained from static structural analysis at an altitude of 40000 Ft

PRESSURE (Pa)		18615.8	
Material	Total Deformation	Vonmises Stress	
		(max)	(min)
Ti-Gr1	7.68E-04	3.51E+07	4.25E+06
Ti-Gr2	7.52E-04	3.53E+07	4.25E+06
Ti- α alloy	7.24E-04	3.50E+07	4.25E+06
Ti- β alloy	7.87E-04	3.50E+07	4.25E+06

Table-7 Total Deformation and vonmises results obtained from static structural analysis at an altitude of 50000 Ft

PRESSURE (Pa)		11031.6	
Material	Total Deformation	Vonmises Stress	
		(max)	(min)
Ti-Gr1	4.55E-04	2.08E+07	2.52E+06
Ti-Gr2	4.46E-04	2.09E+07	2.52E+06
Ti- α alloy	4.29E-04	2.08E+07	2.52E+06
Ti- β alloy	4.67E-04	2.08E+07	2.52E+06

Contour Plots are captured for the above analysis carried out using Ansys 2020 R. Total Deformation and vonmises stresses maximum and minimum values are plotted in comparison with structural deformation of nose cone made of different titanium graded alloys at various operating conditions.

5.1 Contour Plots At 50000 ft, Total Deformation and vonmises stresses of Nose cone structure with different Titanium graded alloys are shown below Figure-5 & Figure-6

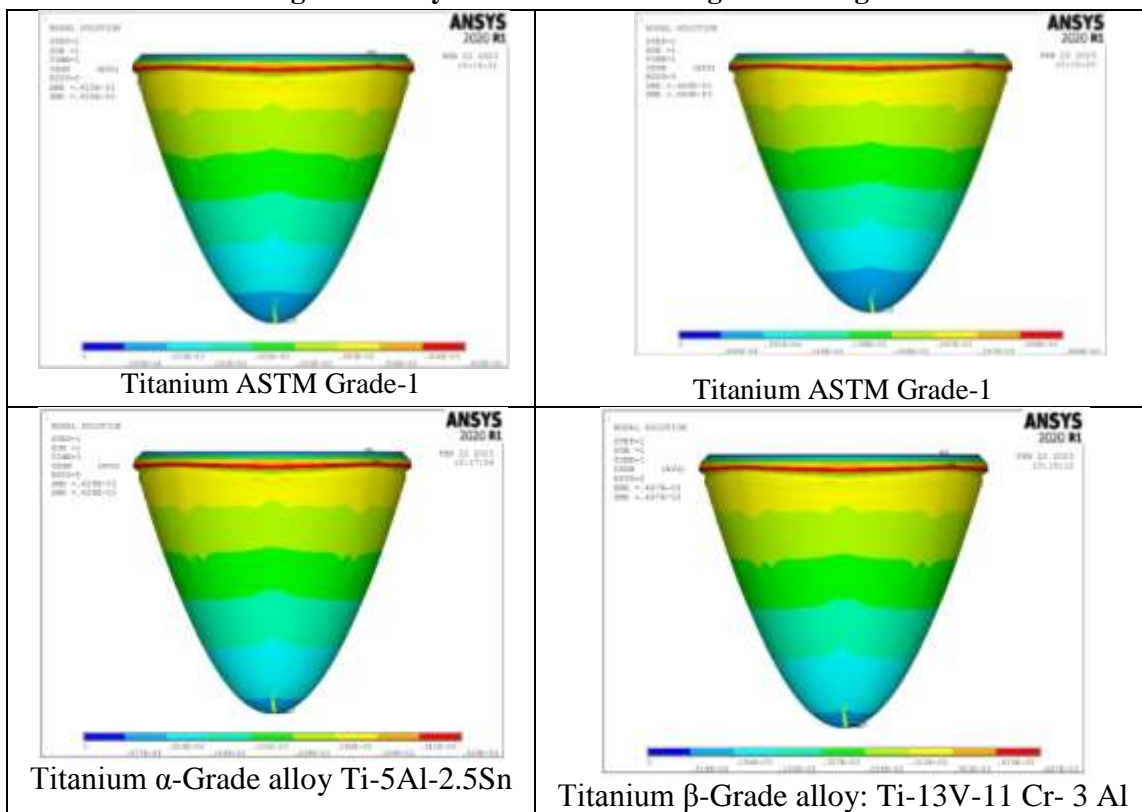
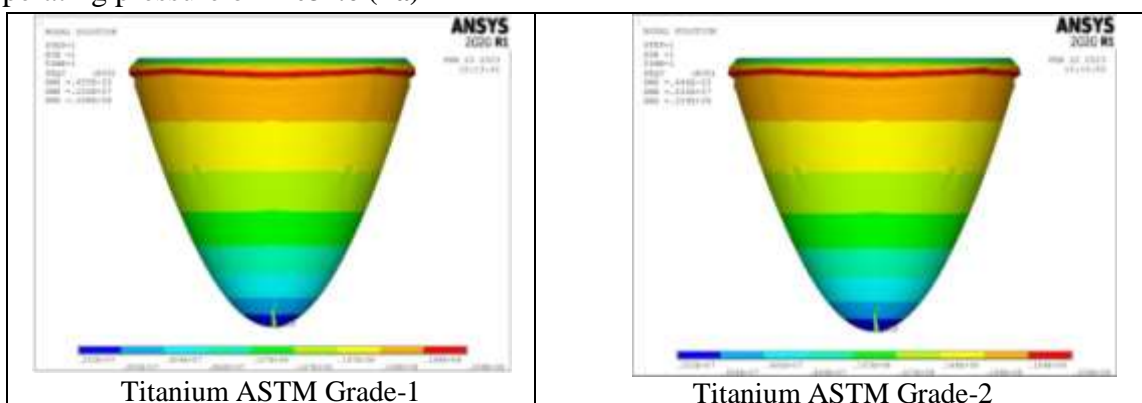


Figure-5 Contour plots for Nose cone structure subjected to Total Deformation under operating pressure of 11031.6 (Pa)



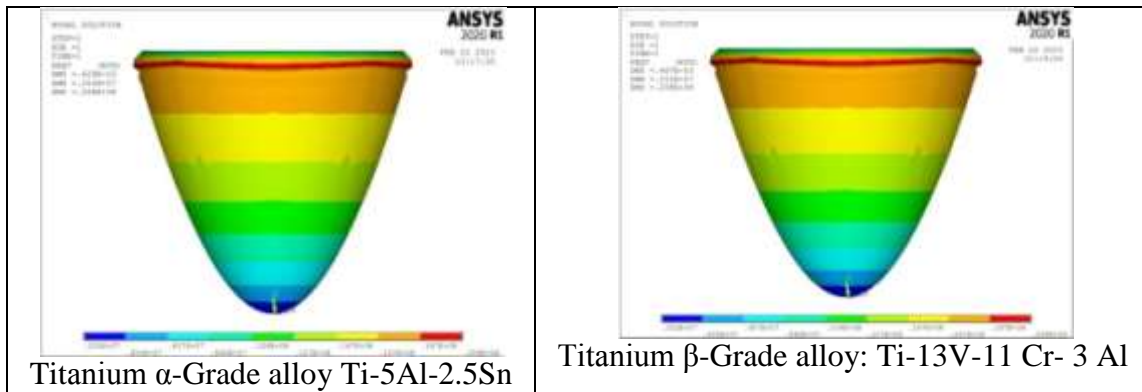


Figure-6 Contour plots for Nose cone structure subjected to vonmises stresses under operating pressure of **11031.6 (Pa)**

At an altitude of 50000 Ft and pressure of **11031.6 Pa**, the proposed nose cone model with different Titanium Graded alloys yielded promisable values. However the model made of Ti- α alloy has less total deformation of $4.29E-04$ m when compared with Ti-Gr1, Ti-Gr2 and Ti- β alloy. It is also noticed that the nose cone structure with Gr-1, Ti- α alloy and Ti- β alloy are induced with less vonmises stress about $2.08E+07$ Pa.

5.2 Contour Plots At 40000 ft, Total Deformation and vonmises stresses of Nose cone structure with different Titanium graded alloys are shown below Figure-7 & Figure-8

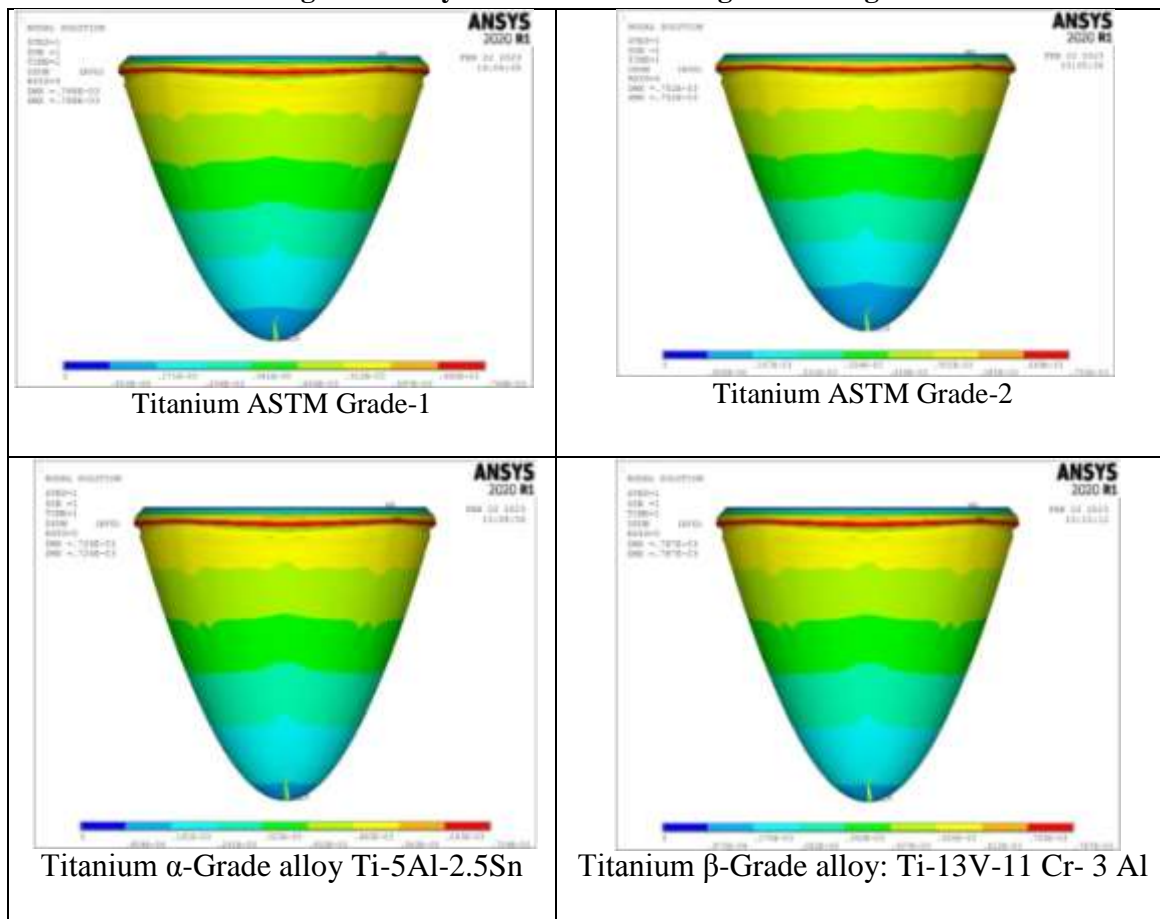


Figure-7 Contour plots for Nose cone structure subjected to Total Deformation under operating pressure of **18658.2 (Pa)**

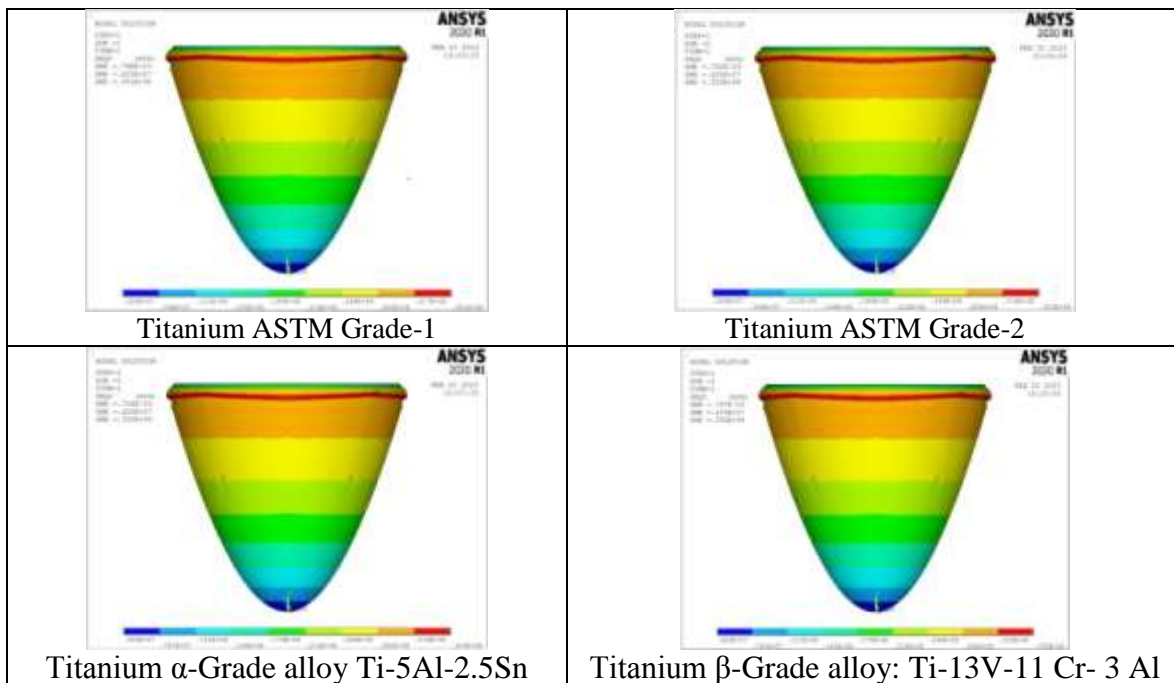


Figure-8 Contour plots for Nose cone structure subjected to vonmises stresses under operating pressure of **18658.2 (Pa)**

From the above contour plot results, at an altitude of 40000 Ft and pressure of **18615.8 Pa**, the proposed nose cone model with different Titanium Graded alloys yielded promisable values. However the model made of Ti- α alloy has less total deformation of $7.24E-04$ m when compared with Ti-Gr1, Ti-Gr2 and Ti- β alloy. It is also noticed that the nose cone structure with Ti- α alloy and Ti- β alloy are induced with less vonmises stress about $3.50E+07$ Pa.

5.3 Contour Plots At 30000 ft, Total Deformation and vonmises stresses of Nose cone structure with different Titanium graded alloys are shown below Figure-9 & Figure-10

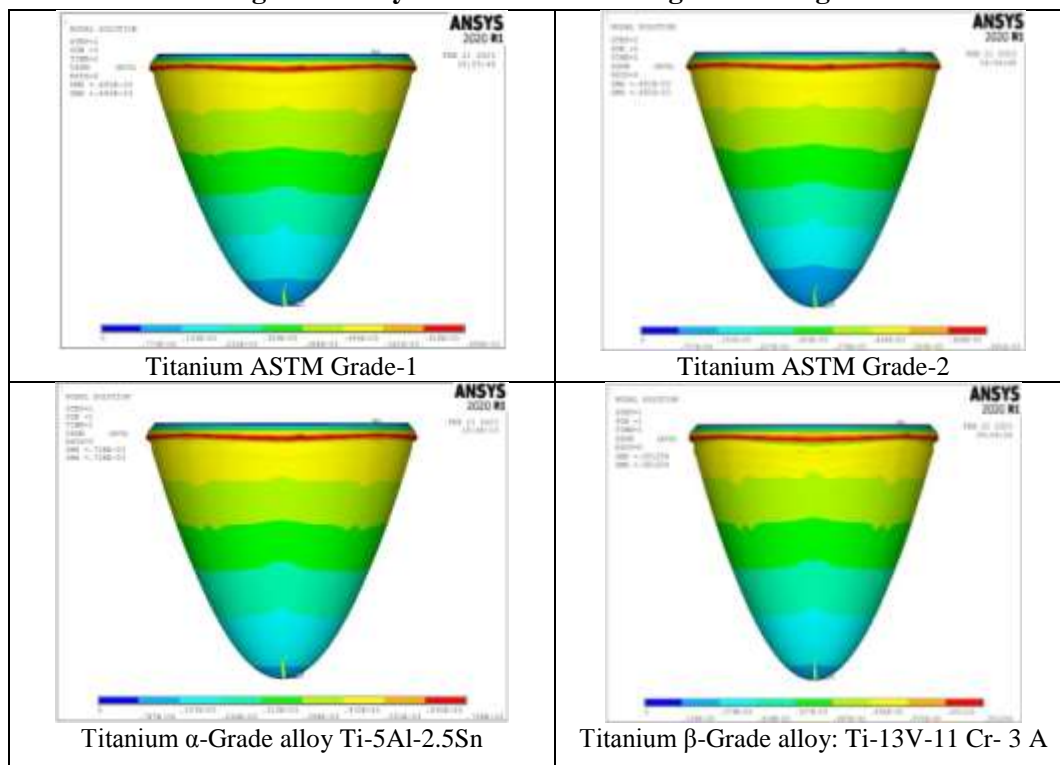


Figure-9 Contour plots for Nose cone structure subjected to Total Deformation under operating pressure of **29647.5 (Pa)**

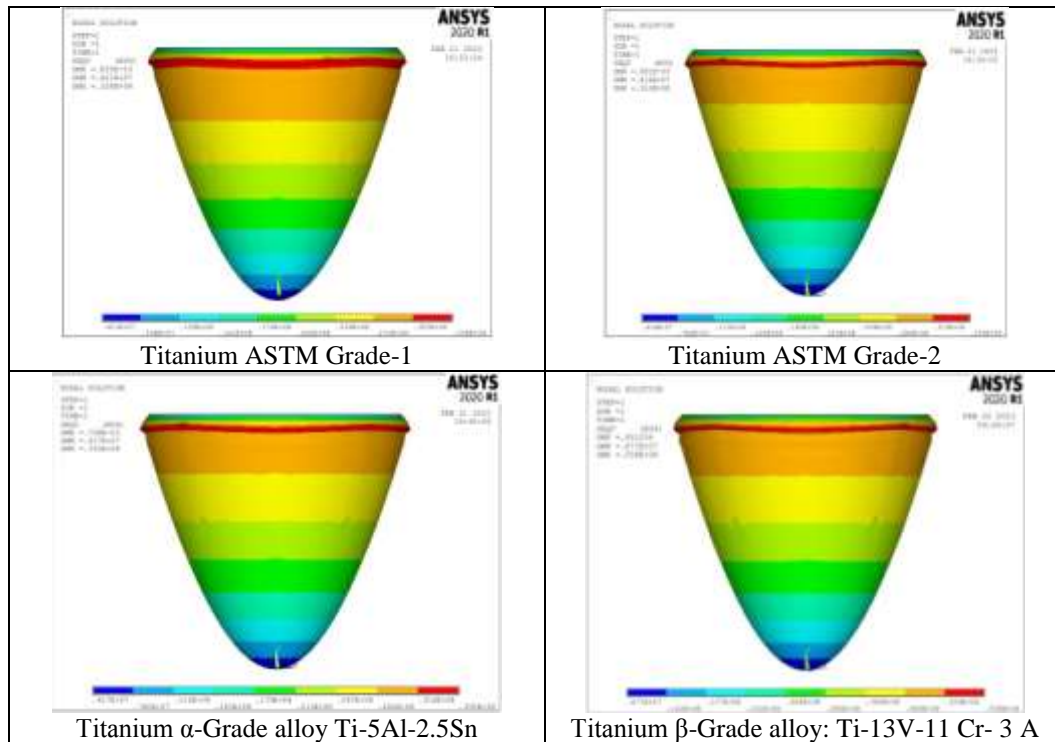


Figure-10 Contour plots for Nose cone structure subjected to vonmises stresses under operating pressure of **29647.5 (Pa)**

When compared at an altitude of 30000 Ft and pressure of **29647.5 Pa**, the proposed nose cone model with different Titanium Graded alloys yielded promisable values. However the model made of Ti- β alloy has less total deformation of 0.001254 m when compared with Ti-Gr1, Ti-Gr2 and Ti- α alloy. It is also noticed that the same structure is induced with less vonmises stress about $5.58E+07$ Pa.

5.4 Contour Plots At 20000 ft, Total Deformation and vonmises stresses of Nose cone structure with different Titanium graded alloys are shown below Figure-11 & Figure-12

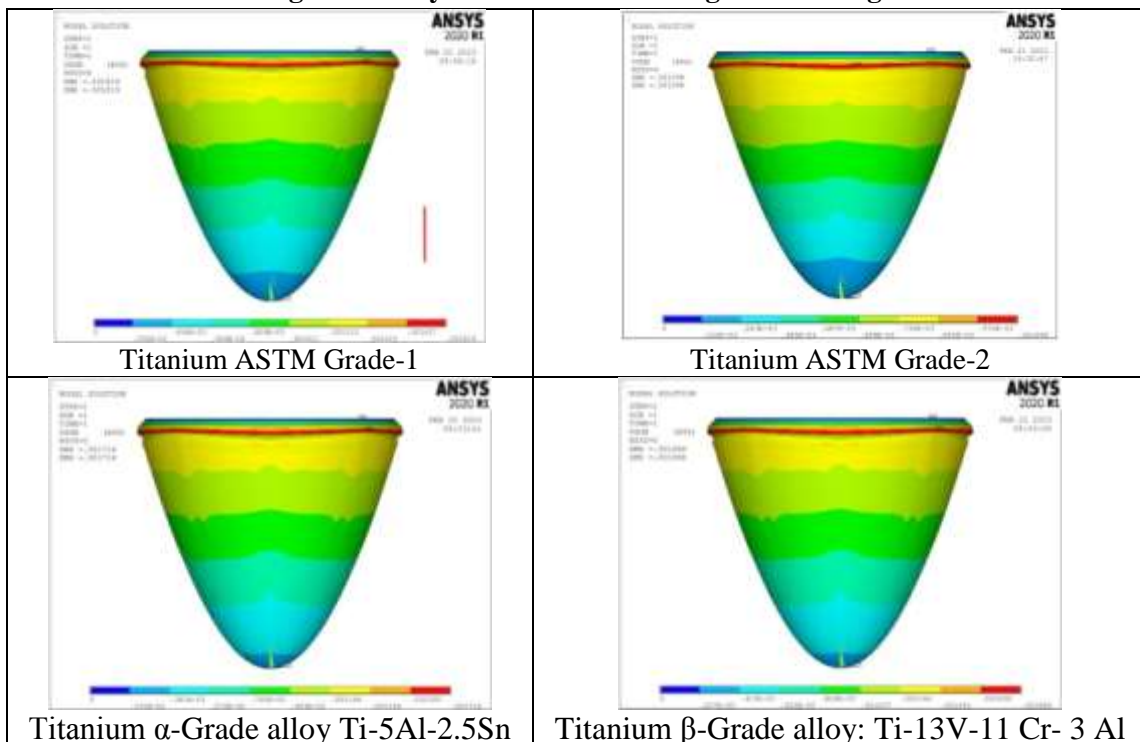


Figure-11 Contour plots for Nose cone structure subjected to Total Deformation under operating pressure of **44126.4 (Pa)**

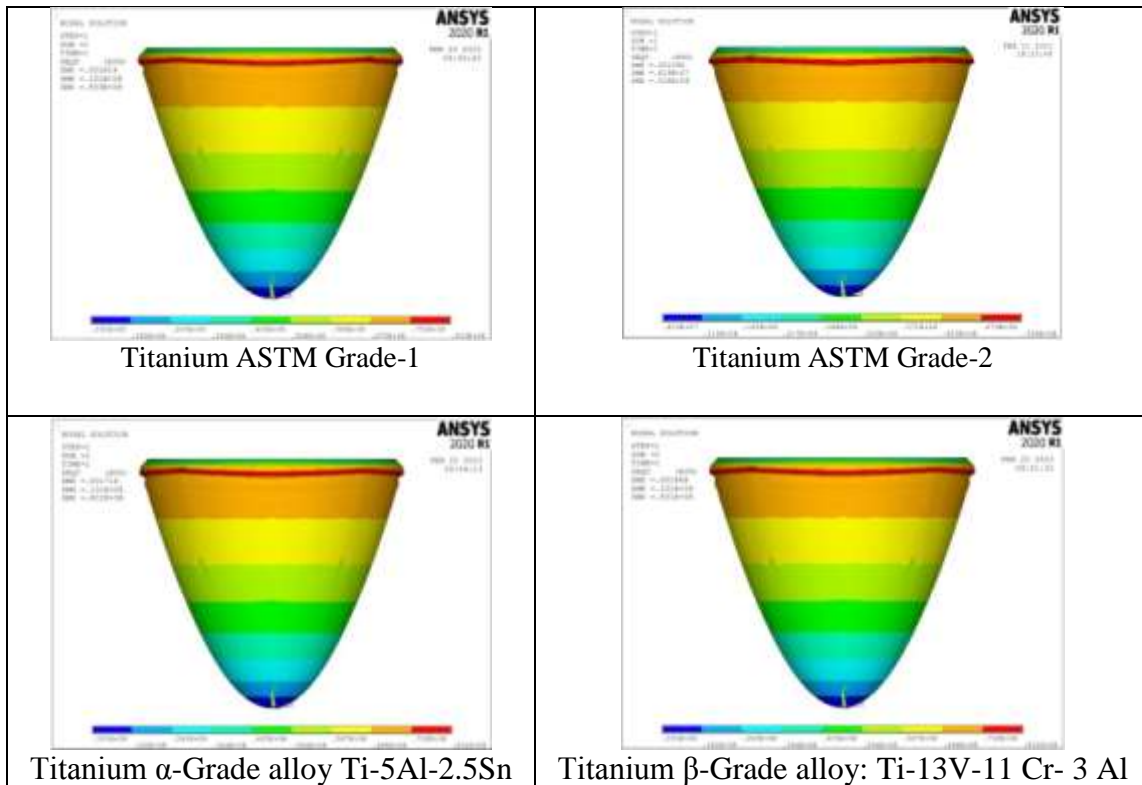


Figure-12 Contour plots for Nose cone structure subjected to vonmises stresses under operating pressure of **44126.4 (Pa)**

Similarly, at an altitude of 20000 Ft and pressure of **44126.4 Pa**, the proposed nose cone model with different Titanium Graded alloys yielded promisable values. However the model made of Ti-Gr2 has less total deformation of 0.001096 m when compared with Ti-Gr1, Ti- α alloy and Ti- β alloys. It is also noticed that the same structure is induced with less vonmises stress about $5.26E+07$ Pa.

5.5 Contour Plots At 10000 ft, Total Deformation and vonmises stresses of Nose cone structure with different Titanium graded alloys are shown below Figure-13 & Figure-14

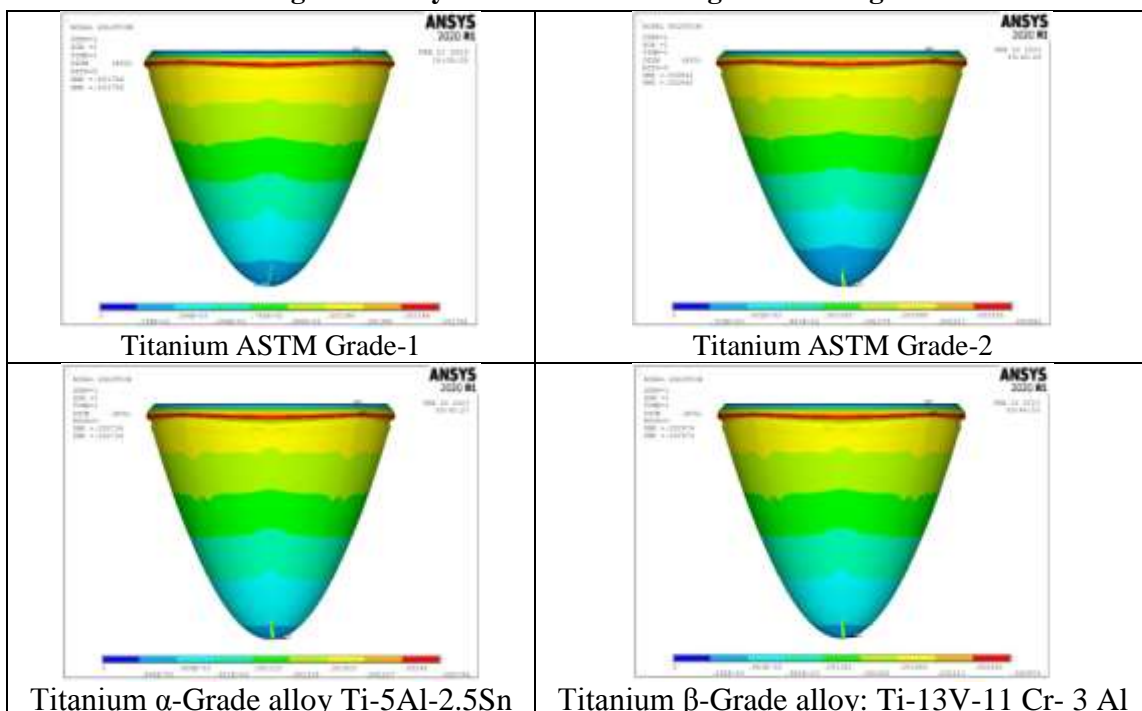


Figure-13 Contour plots for Nose cone structure subjected to Total Deformation under operating pressure of **70326.2 (Pa)**

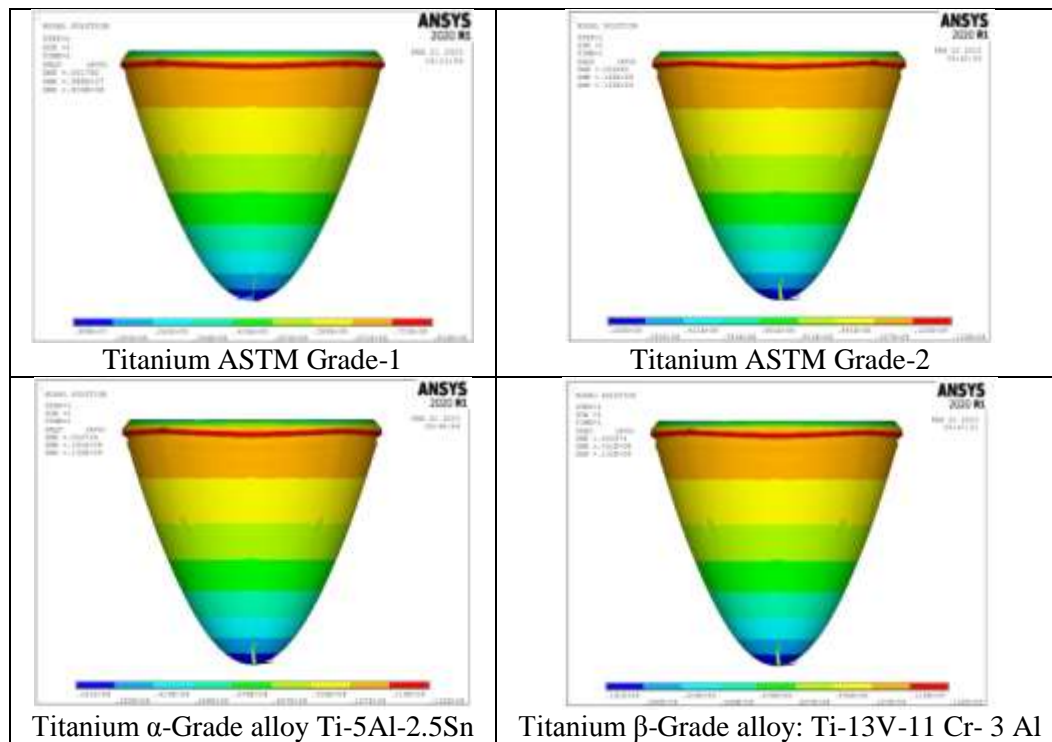


Figure-14 Contour plots for Nose cone structure subjected to vonmises stresses under operating pressure of **70326.2 (Pa)**

From the above observations, it is noticed that at an altitude of 10000 Ft and pressure of 70326.2 Pa, the proposed nose cone model with different Titanium Graded alloys yielded promisable values. However the model made of Ti-Gr1 has less total deformation of 0.001782 m when compared with Ti-Gr2, Ti- α alloy and Ti- β alloys. It is also noticed that the same structure is induced with less vonmises stress about $8.34E+07$ Pa.

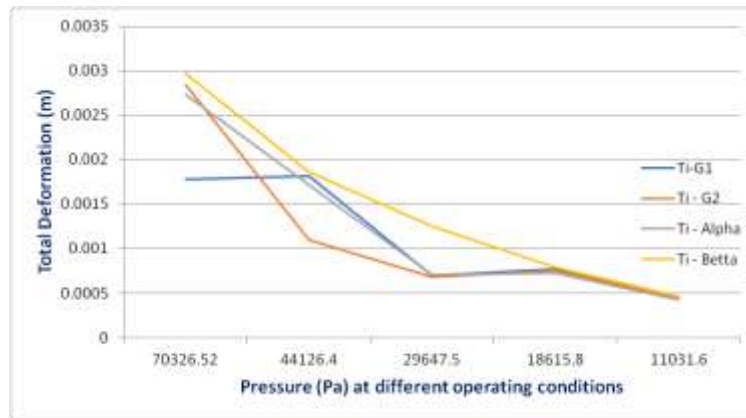
6. Comparison Plots for nose cone structure made of Titanium graded alloys subjected to Total Deformation and Vonmises stresses at different operating conditions

Table-8: Total Deformation values for nose cone structure noticed for 4 different Ti grade and alloy materials

Total Deformation of nose cone with different materials at various operational conditions				
Pressure (Pa)	Ti - Gr1	Ti-Gr2	Ti- α alloy	Ti- β alloy
70326.52	0.001782	0.002842	0.002734	0.002974
44126.4	0.001819	0.001096	0.001716	0.001866
29647.5	6.95E-04	6.81E-04	7.08E-04	0.001254
18615.8	7.68E-04	7.52E-04	7.24E-04	7.87E-04
11031.6	4.55E-04	4.46E-04	4.29E-04	4.67E-04

The nose cone with Titanium-Grade1, Titanium- Grade2, Titanium- α alloy and Titanium- β alloy materials are modeled and analyzed in Ansys tool to investigate the Total deformation and vonmises stress values. In contrast from the obtained results, a comparison graph was plotted and presented for different operating conditions such as 10000 Ft to 50000 Ft.

From the Graph Total Deformation Vs Pressure, it is noticed that almost all titanium graded alloy structures have gradual increment in Total deformation as the (Pressure) increases and altitude decreases. However Among these Titanium family nose cone structure made of Titanium Grade-2 has yielded optimum values of less total deformation for the operating conditions range from 10000 Ft to 30000 Ft.

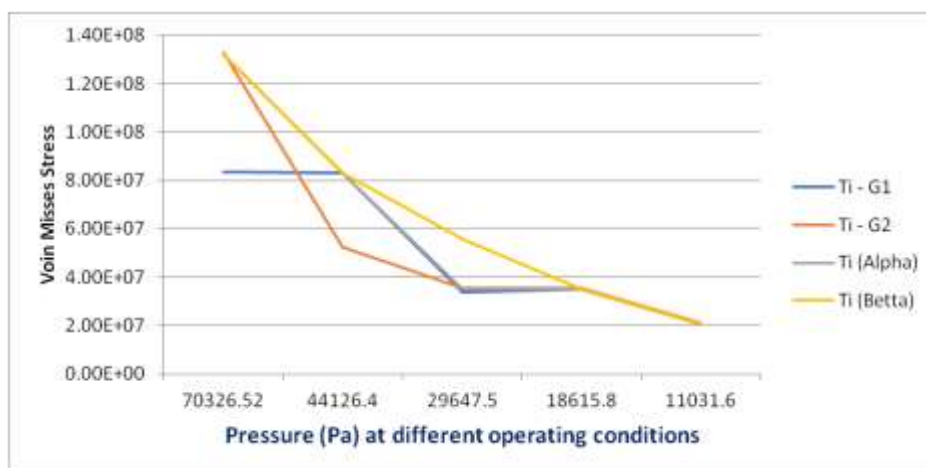


Graph-1 Total Deformation Vs Pressure (Pa) of nose cone with 4 different Ti Gr & alloys

Whereas cone structure made of Titanium Grade-1 and Titanium- α alloy both has decrement in total deformation range from 20000 Ft to 30000 Ft linearly. However at a range from 30000 Ft to 40000 ft nose cone structure made of Ti- Gr1, Ti- Gr2 and Ti- α alloy materials have increment in total deformation. Also observed that at a range from 40000 Ft to 50000 Ft structure made of all Titanium graded alloys have decrement in total deformation.

Table-9: Maximum vonmises stress values for nose cone structure captured for 4 different Ti grade and alloy materials

Von mises stress values of nose cone structure with different materials at various operational conditions				
Pressure (Pa)	Ti - G1	Ti-G2	Ti- α alloy	Ti- β alloy
70326.52	8.34E+07	1.33E+08	1.32E+08	1.32E+08
44126.4	8.33E+07	5.26E+07	8.31E+07	8.31E+07
29647.5	3.38E+07	3.53E+07	3.50E+07	5.58E+07
18615.8	3.51E+07	3.53E+07	3.50E+07	3.50E+07
11031.6	2.08E+07	2.09E+07	2.08E+07	2.08E+07



Graph-2 vonmises stress Vs Pressure (Pa) for a nose cone model tested with 4 different Ti Gr & alloys

From the Graph vonmises stresses Vs Pressure, it is noticed that almost all titanium graded alloy structures have gradual increment in vonmises stresses as the (Pressure) increases and altitude decreases. However Among these Titanium family nose cone structure made of Titanium Grade-2 has yielded optimum values of minimum vonmises stress for the operating conditions range from 10000 Ft to 30000 Ft.

Whereas cone structure made of Titanium Grade-1 and Titanium- α alloy both have decrement in stresses at range from 20000 Ft to 30000 Ft linearly. However at a range from 30000 Ft to 40000 ft

nose cone structure made of Ti- Gr1, Ti- Gr2 and Ti- α alloy material have increment in stresses. Also observed that at a range about 40000 Ft to 50000 Ft, the structure made of all Titanium graded alloys have decrement in vonmises stresses.

7. Conclusion & Future Scope

In the present study, the nose cone is modelled and analyzed using Finite Element tool ANSYS. From the above results, Titanium- grade 1 and Titanium grade 2 materials yielded less total deformation at specified operational conditions ie,. At higher altitudes range about 40000 Ft to 50000 Ft and at lower altitudes about 10000 Ft to 30000 Ft, these materials failed to withstand high pressures and yields maximum vonmises stresses and subjected to maximum total deformation.

On the other side, the nose cone structure made of Titanium α alloy: Ti-5Al-2.5Sn and Titanium β alloy: Ti-13V-11 Cr- 3 Al have better strength than pure grade titanium materials since these materials yielded less vonmises stress and a gradual increment in Total deformation as the pressure load increases and vise-versa. After overall observation of obtained results, the Titanium β alloy: Ti-13V-11 Cr- 3 Al material is preferable and also it has high quality, low weight proportion and great erosion resistance over wide range of operating conditions.

Future scope: The scope of this paper is to develop a nose cone configuration with variable shell thickness the structure should yield optimum material strength to withstand loads at all operating conditions. Similarly, the longerons and bulkheads of the nose cone structure made with different material and can be analyzed to predict the strength of such materials under all operating conditions.

References

- [1] P. Venkata Suresh, K. Ayyappa, V. Anjalee Kumari, M. Koteswararao, J. Venumurali, Design of an Air Craft Nose Cone and Analysis of Deformation under the Specified Conditions with Different Materials using ANSYS, International Journal of Engineering Research & Technology (IJERT), ISSN: 2278-0181, Vol. 4 Issue 02, February-2015
- [2] C.M.Vamsi Priya, New Aerodynamic Design and Structural Analysis of Missile Nose Cone using different materials, JETIR May 2019, Volume 6, Issue 5, ISSN-2349-5162
- [3] M. Sreenivasula reddy, Keerthi, "Design and Structural Analysis Of Missile Nose Cone", Australian Journal of Basic and Applied Sciences, 11(11) August 2017, Pages: 30-40, ISSN: 1991-8178
- [4] P. V. Devendra Aditya, Y. Rajesh Kumar, "Design and Structural Analysis of Missile Nose Cone Using Different Materials", International Journal of Advanced Technology and Innovative Research Volume- 10, IssueNo.12, December-2018, Pages: 1147-115, ISSN 2348–2370
- [5] Adrian Bogdan Şimon-Marinică1 , Nicolae-Ioan Vlasin1 , Florin Manea1 , Gheorghe-Daniel Florea Finite element method to solve engineering problems using ansys, MATEC Web of Conferences 342, 01015 (2021), UNIVERSITARIA SIMPRO 2021
- [6] Metals Hand Book, Properties & Selection Iron, Steel, and High Performance Alloys, ASM International 1990.
- [7] A.Yeshwanth, P V.Senthiil, "Nose Cone Design And Analysis Of An Avion", International Journal of Pure and Applied Mathematics, Volume 119 No. 12 2018, 15581-15589 ISSN: 1314-3395
- [8] A Sanjay Varma, ,G Sai Satyanarayana, Sandeep "CFD ANALYSIS OF VARIOUS NOSE PROFILES", International Journal of Aerospace and Mechanical Engineering , ISSN (O): 2393-8609, Volume 3 – No.3, June 2016

A study on the impact of a proximity-sensor-based leaf jig for a flange to enhance productivity

B. Kiran Kumar^{1,*}, K. Venkatesan², B Saikrishna Srikar³

¹Associate Professor, Department of Mechanical Engineering, Koneru Lakshmaiah Education Foundation, Vaddeswaram, AP, India

²Professor, Department of Automobile Engineering, Bharath Institute of Higher Education and Research, Chennai, Tamil Nadu, India

³Assistant System Engineer, Tata Consultancy Services

*Corresponding author; E-mail: buragaddakirankumar15@gmail.com

Abstract: This article introduces the revolutionary design of a leaf jig equipped with proximity sensors that significantly reduce the cycle time during the flange drilling process. By attaching proximity sensors to a leaf jig, it is possible to drill an array of holes on the flange. It verifies proper seating while locating the jig plate prior to drilling. Reduced cycle times are possible in the mass manufacturing of flanges by lowering the overhead time for positioning, adjusting, and inspecting. Two flow-process diagrams for drilling operations are created utilizing template and leaf jigs. According to the flow-chart analysis, the verification of flange seating using a feeler gauge is eliminated in the leaf jig, while the production rate rises by 17%.

Keywords: flange, flow process charts, leaf jig, production rate

1. Introduction

Leaf jigs are production tools that are identified by their hinged cover, or leaf, which swings open to load or unload the jig. After positioning the workpiece inside the jig, the leaf is tightly closed and secured with thumbscrews. Leaf jigs are quick to load and unload and are ideal for complex workpieces with uneven curves. The hinge plate of this jig is precision-machined to assure precise alignments, and the joints comprise heat-treated pins and bushings to prevent excessive wear. The flanges are manufactured by casting, turning, and drilling hole patterns. The drilling of holes is traditionally accomplished by hole-center marking, punching, piloting, and final drilling, all of which require longer cycle times and have inconsistent results. Drill jigs aid in their performance. There will always be a need to reduce cycle times in this process (Donaldson, 2012).

Pandit et al. (2017) discussed the modeling and analysis of drill jigs for the mounting casing of an electric motor using Catia 5R20 and Ansys 14.5, respectively. They found that the maximum permissible value of the stress of the structural steel was 250 MPa. As the stress value acting on the drill jig was less than the permissible stress of the material, the design was safe. Rahul et al. (2016) studied the fabrication and analysis of a leaf exchangeable jig and concluded that the leaf can be interchangeable to drill different types of patterns. Ashish et al. (2015) and Rama et al. (2016) carried out an experimental study on the design and analysis of a drill jig with variable materials and found that steel experiences less deformation than to gray forged iron and aluminum alloy. Prassetiyo et al. (2019) and Varatharajulu et al. (2020) chose an industrial manufacturing problem and designed a drill jig for the side-plate component. Through the implementation of the drill jig, the part rejection was reduced from 20% to zero, the setup time was reduced from 0.97 min to 0.30 min, and the total production was increased per hour/day. Patil et al. (2016) and Raghavendra et al. (2018) presented the design and development of a drill jig for spinning rings used in the textile industry and an indexing drill jig, respectively. Ritesh et al. (2022) worked on the concepts of delamination and

measurement in the drilling process. Francis et al. (2022) further investigated increases in shear strength through chemical processing, in order to overcome the delamination issues encountered while drilling. Hongbo et al. (2016) developed a reconfigurable jig with adaptive clamping that requires a strong construction and discussed this requirement in detail. It was concluded that through the usage of the drill jig, the life of the drill bit improved as the tool was guided in its operation and total cycle time was reduced.

Mohammed et al. (2013) presented the design and analysis of a drill jig for a shaft using ANSYS. It was found in the analysis that the steel shaft withstood 200N, while the aluminum shaft only withstood a load of 150N. It was also determined that by using software tools such as Pro E and Ansys, it is possible to precisely construct any model and obtain exact stresses with much greater precision and in less time than with manual computation. Apai et al. (2021) emphasized the need for secondary stress conditions while performing structural analysis in CAE software. Kiran et al. (2018) presented research on the design, fabrication, and automation of an indexing drill jig. The drilling operation was carried out on fiber, aluminum, mild steel, and cast-iron materials, and the machining time for each material was determined and compared with the conventional machining time. It was concluded that high accuracy and a reduced consumption of time were achieved with the automated indexing drill jig compared to conventional machining. Bhatwadekar et al. (2018) developed a turning fixture and drill jig for an exhaust manifold. It was concluded that through the use of these tools, the overall machining cost was reduced, and the interchangeability of the parts was increased. The indexing set-up for the actuator support component drill jig was designed and built by Kulkarni et al. (2016). A comparison between manual and hydraulic indexing cycle times was also performed. Hydraulic indexing saved an average of 71.94% of the time.

Kumar et al. (2019) developed a modular jig for winding cone 1 with error proofing for effective CNC use. The redesigned jig increased the efficiency by 32% by machining 12 parts every cycle. Furthermore, by modifying the fixture design and using Renishaw probing procedures on HMC, Siva et al. (2020) improved the productivity of the planet carrier component by 85%. Kumar et al. (2020) developed a re-engineered fixture that allowed them to load two jobs into a single fixture, lowering the production time by 4 minutes each job. Rajesh et al. (2021) created a drill jig for brake-lining components of three different sizes. When three distinct jigs are built, the aim is to minimize the time it takes to replace a jig for each component for spring hole drilling. Lam et al. (2017) studied how to reduce the setup time in a CNC machine in three phases by redesigning existing jigs and fixtures. Tripathi et al. (2019) estimated that redesigning and testing the engine fixture would increase manufacturing capacity from 650 to 700 units per hour. Gebray et al. (2018) analyzed how to increase assembly productivity for the AK103 by reducing the assembly time and lowering the production costs, which are high due to crack wastage.

Yazdi et al. (2018) used a time study approach to assess the overall equipment effectiveness (OEE) and identify issues that needed to be handled and optimized to raise the OEE percentage while maintaining system sustainability. By conducting a time analysis for each of the firm's activities and collecting bottlenecks in each process, Kumar et al. (2020) proposed solutions for greater productivity rates compared to the existing setup. Time-study approaches, such as sequences of operations, task reassignment to workstations, and line balancing at set cycle times, were utilized by Babar et al. (2020) to improve the productivity of a garment production line in a work-wear manufacturing facility. To improve the machinability of alloys, the current industrial trend is to look for efficient strategies or techniques (Davim, 2018). Industrial integration is advancing manufacturing techniques, and their applications have reached a high level of production maturity (Davim, 2014). To achieve desired quality and target forms, composite materials require careful machining. By evaluating the most recent advancements made in the scientific literature critically, the machining aspects for fibrous composites are set out (Davim, 2022).

Mgbemena et al. (2020) created a proximity-warning system that decreases the likelihood of shop-floor accidents by monitoring the distance between an object and a worker and providing both audio

and visual feedback. Kidsanapong et al. (2021) developed a sensor system in the presence of water. This concept is highly important in drilling processes, since the presence of cutting fluids is essential in drilling. Haque et al. (2022) developed a coplanar capacitive proximity-sensor system for measuring the space between dielectric foil edges.

From the literature review, it is understood that cycle time and accuracy are important factors to maximize the production rates of drill jigs. Therefore, in this work, proximity sensors were integrated into the suggested design to address some of the cycle-time challenges associated with these jigs.

2. Objectives

To investigate the current drilling process of a flange component and suggest a strategy to reduce the production-cycle time and maintain consistency in flange-drilling quality. A further objective was to increase operator safety in flange machining during drilling.

3. Materials and methods

For this experiment, a common industrial component flange was chosen, and its dimensions were measured. The approach presented in this study, involving the drilling of four clamping holes, was examined, and a flow-process chart was developed.

3.1 Component section

The flange component is typically completed on a lathe, with the exception of four clamping holes. The typical procedure involves marking and drilling the hole centers. The component selected is depicted in detail in Figure 1. The purpose of this lesson is to drill using a drill jig.



Figure 1. Component details of flange selected

3.2 Component dimensions

Dimensions of the flange component were measured by vernier caliper, as indicated in Figure 2. The component's material is mild steel.

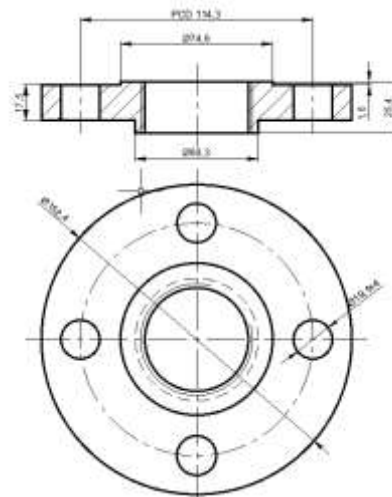


Figure 2. Dimensions of flange selected (in mm).

3.3 Experimental study

The drilling-cycle time of a flange on a radial drilling machine was determined through an experiment. Figure 3 illustrates how flanges were clamped using a template jig, as well as how their seating was evaluated using a feeler gauge. Plate seating was randomly tested and clamped to ensure there were no gaps in the four quadrants.



Figure 3. Inspection of flange seating with template jig

After the pilot drilling, the template jig was removed, the flange was reclamped, and the position of each hole was located to drill the final holes in the correct size. Figure 4 depicts the flange-drilling process.



Figure 4. Pilot drilling of the flange using template jig

A flow chart was generated for the flange-drilling procedure. In this drill cycle, the flange was positioned, the template jig was mounted, the seating on the machine table was inspected, and the flange was clamped and drilled. A stopwatch is used to collect and record the average time of 5 samples for each operation. Figure 5 depicts a drill-cycle flow chart employing a flange template jig.

3.4 Design of leaf jig

This study's major goal was to improve the present drill jig to reduce the cycle time in the completion of four-hole drilling without compromising the quality of the flange. The following factors were taken into consideration while designing the leaf jig.

a. Development of rigid body

Jig body should be strong enough to withstand all forces applied to it and must also resist deflection, which would destroy its accuracy. Deflection may occur as the result of excessive tightening or loosening of clamps that hold the workpiece in place. The body must also be supported so that it does not bend under drilling pressure. Cast iron body was chosen in the design.

b. Location and clamping

As locating a component is the primary function of drill jigs, they are designed in such a way that the workpiece can be fitted into the nest without difficulty. Clamping methods should be rapid and positive, and the clamps should be in a position that offers the greatest convenience to the operator. A screw clamp with a floating pad was selected in the design.

c. Design of jig bushings

Jig bushings are used to guide drills, reamers, and other cutting tools into the proper position on the workpiece.

As the hole diameter on the flange was big, it was planned to drill a pilot hole before determining the final size of the hole. A renewable bush was used for this purpose.

d. Miscellaneous considerations

Sufficient space is required between the bottom of jig bushing and work to control chip movement. This prevents chip packing in drill flutes, allowing more coolant to reach the cutting edge of the drill. Four jig feet were added to the base of the body to avoid surface resting. For the quick removal of part, an ejector was included in the design.

3.4.1 Modeling of Leaf Jig

Figure 6 shows the modeling of the leaf jig, which was performed with Auto CAD software.

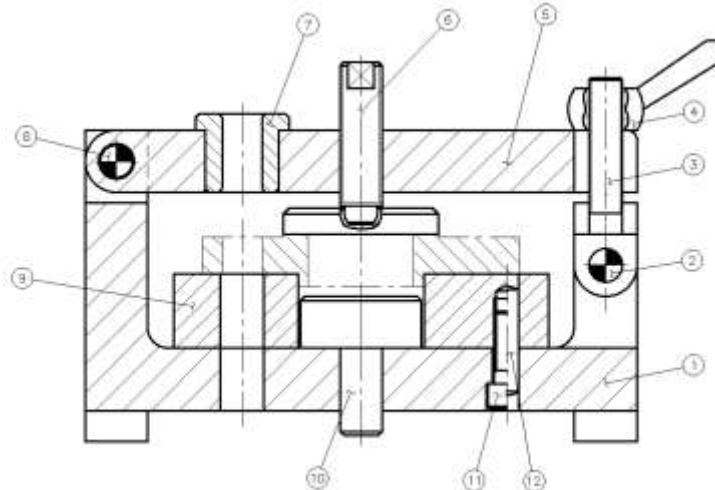


Figure 6. CAD model of the leaf jig assembly

FLOW PROCESS CHART					MATERIAL TYPE		
Chart No.1 Sheet No.1		SUMMARY					
Subject charted: Drilling	ACTIVITY	PRESENT	PROPOSED	SAVING			
	Operation	9					
Chart begins: Work piece	Transport	0					
	Delay	0					
Chart ends: Inspection	Inspection	7					
	Storage	2					
Method: Present	Distance (m)	-					
Charted by :	Time (man – sec)	963					
Approved by :	date:	Total Production units (per shift)	29				
	Symbols				Distance (m)	Time (sec)	Remarks
Description	●	➔	⬇	■	▼		
Collecting of work piece						10	By Hand
Positioning of clamping bolt and work piece on drilling machine						25	"
Placing of Template Jig on work piece						12	"
Clamping the Jig assembly						15	"
Verification of butting surfaces using feeler gauge at 1 st corner						12	"
Verification of butting surfaces using feeler gauge at 2 nd corner						12	"
Verification of butting surfaces using feeler gauge at 3 rd corner						12	"
Verification of butting surfaces using feeler gauge at 4 th corner						12	"
Loosen the Jig assembly, adjust and reclamp						25	"
Verification of butting surfaces at 4 corners						24	"
Drilling of pilot holes at 4 places						240	"
Removal of template jig						90	"
Clamping of workpiece on drilling machine						40	"
Locating each predrilled hole and drill to finish 4 holes						360	"
Final inspection of workpiece						24	"
Loosen the clamping bolt to remove the work piece						30	"
Cleaning of metal chips						10	"
Placing the workpiece in tray						10	"
Total	9	-	-	7	2	963	

Figure 5. Flow-process chart for flange using template jig
Dept. of Mech. Engg. PVPSIT

3.4.2 Parts List

Table 1 includes the names and materials of the parts of the leaf jig designed (Donaldson, 2012).

Table 1. Parts list

Serial No.	Component		
	Name	Material	Quantity
1	Jig body	CI	1
2	Dowel	STD	2
3	Clamping bolt	EN8	1
4	Clamping nut	EN8	1
5	Jig plate	EN31	1
6	Screw clamp	EN8	1
7	Jig bush and renewable bush	EN31	4
8	Clamping screw	EN8	4
9	Locator	EN31	1
10	Ejector	EN8	1
11	SHCS	STD	4
12	Dowel	STD	2

3.5 Analysis of drill jig

The suggested design of the drill jig will result in faster setup times than the existing process. The predicted cycle time was determined using a flow-process chart when drilling the flanges with leaf jig.

The previous flange setup time (i.e., butting surface verification) using a template jig has a direct effect on the working time of the component whose speed is to be increased. The manual method of verification can be further improved by the addition of sensors, which indicate the butting surface throughout the drilling operation. Proximity sensors, shown in Figure 7, can be used for this purpose. Figure 8 indicates the position of four proximity sensors below the flange component in the leaf jig.



Figure 7. Proximity sensor

In the design of the leaf jig, four proximity sensors were included in the locator plate, and they were connected. Once the flange component was located and clamped in the drill jig, the sensor caused the LED lights to glow to indicate the correct seating of the flange. Figure 9 shows the estimated flow-process chart of the drill jig using proximity sensors.

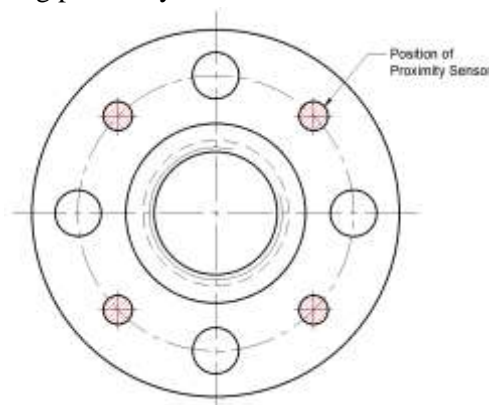


Figure 8. Position of four proximity sensors in leaf jig

4. Results and Discussion

The objective of modifying the existing template jig was to reduce the production time and the overhead work. In the present drilling process of a flange using a template jig, the workpiece is picked and placed a jig manually and clamped. It is also inspected for seating of workpiece on the jig at quadrants and corrected. It is pilot drilled and enlarged to Ø19.1hole size. For the present system, a flow-process chart was created. The proposed system uses a leaf jig with proximity sensors to drill a flange. During this procedure, the workpiece was positioned on a leaf jig, clamped, and drilled to size using automated sensing of its seating. A flow-process chart was also made for the suggested system. Two flow-process charts for drilling operations were compared with the number of operations to be performed. Their process times in seconds are shown in Figures 10(a) and (b), respectively.

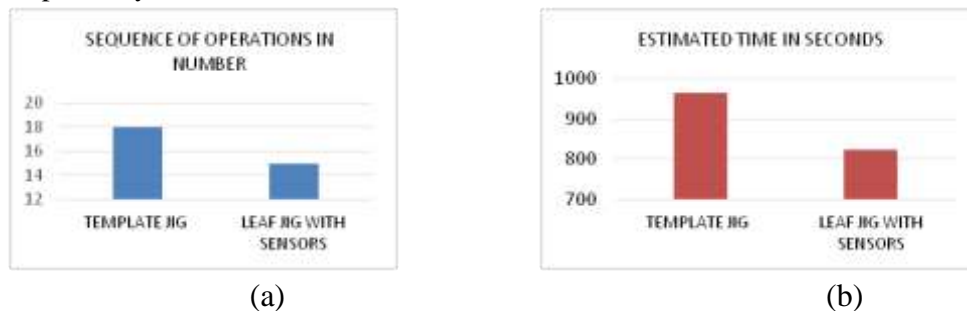


Figure 10. Comparison of two drilling processes using jigs on a flange, From two flow-process charts shown in Figure 5 and Figure 9, it can be observed that the number of operations was reduced by 3, from 18 to 15, and the cycle time was reduced by 140 seconds, from 963 to 823 seconds, which shows an improvement in the production time. A comparison of the times for the two drill jigs and the productivity is given in Table 2.

Table 2. Setup times and productivity.

Drilling Method	Process Time (seconds)	Production/shift (units)	Production/day (units)	Percentage of improvement
Template jig	963	29	87	-
Leaf jig with	823	34	102	17%

FLOW PROCESS CHART		SUMMARY			MATERIAL TYPE	
Chart No.2 Sheet No.1						
Subject charted: Drilling		ACTIVITY	PRESENT	PROPOSED	SAVING	
	Operation	●	9	9	-	
Chart begins: Work piece	Transport	➡	0	0	-	
	Delay	●	0	0	-	
Chart ends: Inspection	Inspection	■	7	4	3	
	Storage	▼	2	2	-	
Method: Proposed	Distance (m)	-	-	-	-	
Charted by :	Time (man-sec)	963	823	140		
Approved by : date:	Total Production units (per shift)	29	34	5		
		Symbols	Distance (m)	Time (sec)	Remarks	
Description	● ➡ ● ■ ▼					
Selecting of work piece	● ➡			10	By Hand	
Opening of Leaf jig	➡			20	"	
Load the work piece on Locator	➡			15	"	
Clamping the Work piece	➡			20	"	
Verification of butting surfaces	➡			12	"	
Open leaf jig to adjust of workpiece and reclamp.	➡			25	"	
Verification of butting surfaces	➡			12	"	
Drilling of pilot holes at 4 places	➡			200	"	
Removal of Renewable bushes (4Nos.)	➡			120	"	
Checking of workpiece position	➡			12	"	
Drilling to finish 4 holes	➡			320	"	
Final Inspection of workpiece	➡			12	"	
Open the Leaf jig to unload the workpiece	➡			25	"	
Cleaning of metal chips	➡			10	"	
Placing the workpiece in tray	➡			10	"	
Total		9	-	4	2	823

Figure 9. Flow-process chart for drill jig with proximity sensor

5. Conclusion

In the present study, a template jig is used to drill holes into the flanges for four clamping points. According to our research, this is the first attempt to use proximity sensors in a leaf jig to drill the aforementioned holes. To ensure accuracy, adaptability, and increased productivity by cutting down on inefficient time, four proximity sensors are installed in the leaf jig locator plate at non-drilling sections of the flange. By including proximity sensors in the design and analysis of a leaf jig for flange component, the component positioning may be promptly verified and rectified when compared to an existing design. The new design minimizes the number of operations from 18 to 15. Additionally, this innovative design reduces the cycle time from 963 to 823 seconds, saving 140 seconds for each cycle. The routine output rate improves by 17%. The leaf jig's design with sensors for the flange component makes it significantly safer and faster to operate. It is an excellent design for manufacturing comparable components in industry.

6. Acknowledgment

We would like to express our gratitude to Venkateshwara Engineerings, Nidamanuru, Vijayawada, for providing us with the best facilities and a working atmosphere that was conducive to the development of our project.

References

- Apai Benchaphong, Rattanasak Hongthong, Sutera Benchanukrom, & Nirut Konkong (2021). Determination of the secondary bending stress in cold-formed steel connection. *Journal of current science and technology*, 11(2), 287-298. DOI: 10.14456/jcst.2021.29
- Ashish Mourya, Chandrashekhar Patil, Priyanka Chavan, Manjur Sande, Sarang Pisal (2015) "Automatic Indexing Mechanism For Drilling Machine". *International Journal of Advance Research in Science and Engineering*, 4(1).
- Babar, M., Shafiq, M., Rasheed, A., Salman, M., & Mario, M. (2020). Productivity Improvement Through Time Study Approach: A Case Study from an Apparel Manufacturing Industry of Pakistan. *Procedia Manufacturing*, 39(2019), 1447–1454. <https://doi.org/10.1016/j.promfg.2020.01.306>
- Bhatwadekar, D. S. G., Yadav, M. A. A., & Ghodake, M. Y. R. (2018). Design and Fabrication of Turning Fixture and Drilling Jig for Exhaust Manifold. *International Journal of Trend in Scientific Research and Development*, 2(3), 1224–1231. DOI: <https://doi.org/10.31142/ijtsrd10891>
- Davim, J. P. (2014). *Modern mechanical engineering*. Berlin, Heidelberg: Springer Berlin Heidelberg.
- Davim, J. P. (Ed.). (2018). *Introduction to mechanical engineering*. Springer.
- Davim, J. P. (Ed.). (2022). *Mechanical and industrial engineering: Historical aspects and future directions*. Springer Nature.
- Donaldson, C., LeCain, G. H., Goold, V. C., and Ghose, J. (2012). *Tool design*. Tata McGraw-Hill Education. pp 542-544
- Francis Xavier Joseph, Sudeshkumar Moranahali Ponnusamy, M. P. Natarajan, Jayabalakrishnan Duravelu, Jayaseelan Veerasundaram, Ramasamy Nallamuthu (2022) Interlaminar shear strength of chemically treated Kevlar/Cucurbitaceae fiber metal laminated hybrid composites. *Journal of current science and technology*, 12(1), 102-109. DOI: 10.14456/jcst.2022.10
- Gebray, T., & Thakur, A. (2018). Productivity improvement of AK 103 assembly line. *International Journal of Current Engineering and Technology*, 8(04), 935–947. <https://doi.org/10.14741/ijcet/v.8.4.7>
- Haque, R. I., Lubej, M., & Briand, D. (2022). Design and printing of a coplanar capacitive proximity sensor to detect the gap between dielectric foils edges. *Sensors and Actuators A: Physical*, 337(September 2021), 113424. <https://doi.org/10.1016/j.sna.2022.113424>
- Hongbo Zhang, Lianyu Zheng, Xiwei Chen & Haiji Huang (2016). A Novel Reconfigurable Assembly Jig Based on Stable Agile Joints and Adaptive Positioning-Clamping Bolts. *Procedia CIRP*, 44, 316-321.
- Lam, P. X., Prakash, J., & Lai, K. C. (2017). Setup Time Reduction in a CNC Production Facility through Redesign of Jigs and Fixtures. *AIP Conference Proceedings* 1902, 020061. <https://doi.org/10.1063/1.5010678>
- Kidsanapong Puntsri, Ekkaphol Khansalee & Puripong Suttisopapan (2021), Underwater environment sensors with visible light communication systems. *Journal of current science and technology*, 11(2), 269-276. DOI: 10.14456/jcst.2021.27
- Kiran, S. M., & S, S. M. (2018). Design, Fabrication and Automation of Indexing Drill Jig, *International Journal of Scientific & Engineering Research*, 9(5), 70–76.

- Kulkarni, V. V. (2016). Design and Fabrication of Indexing Set Up for Drill Jig. *International Research Journal of Engineering and Technology*, 3(6), 1–8.
- Kumar, S., Campilho, R. D. S. G., & Silva, F. J. G. (2019). Rethinking modular jigs' design regarding the optimization of machining times. *Procedia Manufacturing*, 38(2019), 876–883. <https://doi.org/10.1016/j.promfg.2020.01.169>
- Kumar, S. R., S, D. K., Gowthamaan, K. K., Mouli, D. C., Chakravarthi, K. C., & Balasubramanian, T. (2020). Development of a Re-engineered fixture to reduce operation time in a machining process. *Materials Today: Proceedings*. <https://doi.org/10.1016/j.matpr.2020.09.056>
- Kumar, S. R., Nathan, V. N., Ashique, S. I. M., Rajkumar, V., & Karthick, P. A. (2020). Productivity enhancement and cycle time reduction in toyota production system through jishuken activity - Case study. *Materials Today: Proceedings*, 37(Part 2), 964–966. <https://doi.org/10.1016/j.matpr.2020.06.181>
- Mgbemena, C. E., Onuoha, D. O., Okpala, C. C., & Mgbemena, C. O. (2020). Design and development of a proximity warning system for improved safety on the manufacturing shop floor. *Journal of King Saud University - Engineering Sciences*. <https://doi.org/10.1016/j.jksues.2020.11.004>
- Mohammed, A. J., & Tariq, D. M. (2013). Design and Analysis of Drill Jig for a Shaft using ANSYS. *International Journal of Scientific Engineering and Technology Research*, 2(18), 2059-2066.
- Pandit, G. P., Patil, S. B., Shinde, R. V., & Amale, S. B. (2017). Modelling and analysis of drilling jig for mounting casing of electric motor. *Int J Eng Res Technol (IJERT)*, 6(02).
- Patil, R. K., Shinde, S. C., Takale, S. M., & Choudhary, B. (2016). Design and Development of Drilling Jig for Spinning Rings used in Textile Industry. *Proceedings of the International Conference on Industrial Engineering and Operations Management*, 3067–3075.
- Prasetyo, H., Septiana, R., & Kurniawati, M. (2019). Design of Drilling Jig for Side Plate Component. *International European Extended Enablement in Science, Engineering & Management*, 7(8), 238–243.
- Raghavendra H, Shanti kiran M & Sunitha M S (2018) Design, Fabrication and Automation of Indexing Drill Jig. *International Journal of Scientific & Engineering Research*, 9(5), 70-76.
- Rahul, K., & Prathap, S. (2016). Fabrication and Analysis of Leaf Exchangeable JIG. *International Journal of Research in Engineering, Science and Technologies*. 2(1), 6-9
- Rajesh, S., Ramnath, B. V., Parswajinan, C., Vishnu, K., & Sridhar, R. (2021). Multi Component Drill Jig for Brake Lining Component. *Materials Today: Proceedings*. <https://doi.org/10.1016/j.matpr.2021.02.342>
- Rama, K., Reddy, S., Scholar, P. G., & Kumar Babu, S. R. (2016). Design and Analysis of Drill Jig at Variable Materials. *International Research Journal of Engineering and Technology*, 2022–2029.
- Ritesh Bhat, Nanjangud Mohan, & Sathyashankara Sharma (2022), Revised adjusted factor for delamination measurement in drilling of composites. *Journal of current science and technology*, 12(1), 32-42. DOI: 10.14456/jcst.2022.4
- Siva, R., Siddardha, B., Yuvaraja, S., & Karthikeyan, P. (2020). Improving the productivity and tool life by fixture modification and renishaw probe technique. *Materials Today: Proceedings*, 24, 782–787. <https://doi.org/10.1016/j.matpr.2020.04.386>
- Tripathi, A., & Patel, A. S. (2019). A Study of Flexible Fixture Using Computer Aided Fixture Design Need and Application of Reconfigurable Fixture Design, *International Research Journal of Engineering & Applied Sciences*. 7(2), 14–18.
- Varatharajulu, M, G. Jayaprakash, N. Baskar and A. Saravanan. (2020) “Genetic algorithm assisted artificial neural network for the estimation of drilling parameters of magnesium AZ91 in vertical milling machine”. Vol. 27, No. 10, *Surface Review and Letters*. <https://doi.org/10.1142/S0218625X19502214> ISSN 0218-625X
- Yazdi, P. G., Azizi, A., & Hashemipour, M. (2018). An empirical investigation of the relationship between overall equipment efficiency (OEE) and manufacturing sustainability in industry 4.0 with time study approach. *Sustainability (Switzerland)*, 10(9). <https://doi.org/10.3390/su10093031>

Finding Approximate Solution to a Very Large-scale Open Vehicle Routing Problem

Vangipurapu Bapi Raju^{a*}, Mallapuram Bala Chennaiah^a, Govada Rambabu^b

^aVelagapudi Ramakrishna Siddhartha Engineering College, Kanuru, Vijayawada, Andhra Pradesh 520007, India

^bDept. of Mechanical Engg, Andhra University, Visakhapatnam, 530003, AP, India

Abstract: Extremely large-scale open vehicle routing problem (OVRP) has received little attention from researchers though such problems exist in real life. In this paper, a deterministic heuristic method is developed for obtaining approximate solutions to an extremely large-scale inconsistent OVRP with stringent delivery times. The new method proposed is based on the sweep algorithm and obtains an approximate solution to a large-scale OVRP. This method is first tested on OVRP test instances of a relatively smaller size for which comparison can be done with other methods. It is found that the new method produces quick approximate solutions even when the number of customers is nearly 500. The deviation of the best of the approximate solutions is not more than 5% of the corresponding best-known solutions (BKS). The heuristic is then tested on 10 sets of standard benchmark instances having thousands of customers. It is found that the heuristic provides approximate solutions consuming a very small amount of CPU time and having a minimum number of vehicles.

Key words: Open Vehicle Routing Problem, Very large scale, approximate solution

1. Introduction

The vehicle routing problem can be formulated as follows. Starting from a depot several customers should be visited in such a way that the length of the resulting tour(s) is minimized. In the capacitated vehicle routing problem (CVRP) the capacity of the used vehicles is limited. The open vehicle routing problem (OVRP) is a variant of CVRP where the distance from the last customer to the depot is not considered as the vehicle will not return to the depot.

There are three main categories of methods to solve OVRP namely exact methods, heuristics, and metaheuristics. Exact methods can only solve problems with a limited number of customers (Laporte, 1992). On the other hand, although heuristics find a solution quickly, they are far from finding an accurate solution. Therefore, a major research stream on the design of metaheuristics for the OVRP has evolved over the past two decades (Elshaer and Awad, 2020). These metaheuristics find high-quality solutions in a reasonable amount of computing time. However, most of this research on metaheuristics has focused on developing algorithms that can solve VRP problems of at most a few hundred customers. For a long time instances by Golden et al. (1998) which contain up to 483 customers were treated as ‘large OVRP’ by many researchers. Rarely did anyone try to go beyond this. Kytöjoki (2007) developed the variable neighborhood search specifically aimed at solving very large-scale real-life vehicle routing problems. Later Uchoa et al. (2017) developed test instances that contained up to 1000 customers. More recently Arnold et al. (2019) developed test instances having thousands of customers. Normally metaheuristics use heuristics like the insertion method for the generation of approximate initial solutions. The effectiveness of most of these metaheuristics depends to a large extent on good initial solutions. For example, Van Breedam (2001) states that the performance of the tabu search heuristic is

highly dependent on the quality of the initial solutions. As there is no heuristic to generate initial solutions to a very large-scale OVRP as of today an attempt is made in this direction. The rest of the document is organized as follows. In section 2 existing methods to generate an initial solution and their limitations are discussed. section 3 describes the problem and the assumptions made. In section 4 the modified sweep method is explained. In section 5 the methodology that is used to obtain some approximate solutions for large-scale OVRP is explained. Section 6 describes the experimental tests that were conducted. In section 7 a discussion is carried out on the results that were obtained. Finally, in section 8 the conclusion of this work is presented.

2. Literature Survey

In this section, various heuristics used to generate initial solutions, their advantages, and limitations w.r.t handling large-scale OVRP are discussed below.

Sariklis and Powell (2000) used the insertion method used to get initial solutions while solving OVRP by CFRS method. The balancing of clusters is computationally intensive hence this method is not suitable to solve large-scale OVRP. Fu et al. (2005) used the Farthest first heuristic (FFH) to get initial solutions to solve OVRP by TSF. This method is computationally intensive and hence cannot be used to solve large-scale OVRP. The nearest neighbor heuristic (NNH) is used in metaheuristics like TSAK and TSAN by Brandão (2004). This has a computational time complexity of $O(n^2)$ as per Brandão (2004). Then there are those which generate the initial solutions on a random basis. Examples include TSR by Fu et al. (2005), Ant colony system by X Li and Tian (2006), Particle swarm), A memetic algorithm by Fung et al. (2013), Bumble Bees Mating Optimization(BBMO) algorithm by Marinakis and Marinaki (2014), Gravitational search algorithm by Hosseinabadi et al. (2016), hybrid ant colony optimization by Ge et al. (2016), random key genetic algorithm by Ruiz et.al. (2019) and so on. Since the initial solution is generated randomly there is no guarantee that the solution will be accurate enough. Also, there is no guarantee that the initial solutions will have a minimum number of vehicles. Şevkli and Güler (2017) used the K-means clustering algorithm to construct an initial solution. However, the K-means algorithm is computationally intensive (computational time complexity of $O(n^2)$) and hence is not suitable for a large-scale OVRP. Tarantilis et al. (2004) start the initial solution by dispatching one vehicle to each customer and consequently start the local search. Since the number of vehicles in the initial solution is extremely large, local search for improving the solution is not possible practically since the number of customers runs into thousands. Bapi Raju et al. (2020,2021) developed the modified sweep which can result in an approximate solution with the minimum number of vehicles within a reasonable amount of time even for a large size CVRP. However there is not heuristic to generate an approximate solution for a large size OVRP.

From the above discussion, it is clear that as of now there is no single heuristic to generate approximate solutions for OVRP that is capable of solving extremely large-scale OVRP with reasonable accuracy. Hence an attempt is made in this direction.

3. Problem Definitions and Assumptions

3.1 Hierarchical OVRP description

The OVRP can be defined over a complete graph $G = (V, A)$, in which $V = \{0, 1, \dots, n\}$ is a

set of vertices containing the depot 0 and the clients $v = \{1, \dots, n\} \subset V$. The Set of edges between the nodes in V is represented by $E = \{(vi, vj) : vi, vj \in V, i \neq j, j \neq 0\}$. Each node v_i in $(0 \leq i \leq n)$ has an associated demand $d_i \geq 0$; that must be delivered. The demand of v_0 (the depot) is 0, i.e $d_0 = 0$. Each edge E has an associated cost $c_{ij} > 0$ which represents the Euclidian distance between the two customers. There is a set of vehicles each of which has a maximum load equal Q . The vehicles are denoted by $M = \{m_1, m_2, \dots, m_t\}$ where t is defined by

$$t = \sum_{i=1}^n \frac{d_i}{Q}$$

Vehicles are initially located at v_0 .

The problem has the following are constraints

(a) Each path starts from the v_0 .

(b) Each node other than v_0 is assigned to a single-vehicle.

It is required to generate a set of approximate solutions for large size problem using a heuristic each of which is a Hamiltonian path.

3.2 Assumptions

In formulating the above mathematical model, the following assumptions have been made:

- There is only a single warehouse from which all the products are sent to the consumers.
- The number of customers and demand for each customer is not known until a few hours before the start of the trip (generally known only at the cut-off time for same-day delivery).
- Identical vehicles with known capacities Q are used.
- All vehicles travel with identical constant velocity.
- Each customer is to be serviced by one and only one vehicle (there is no split delivery).
- The total demand of any customer is not more than the capacity of the vehicle.

4. Modified sweep algorithm

The modified sweep algorithm by Bapi Raju et al (2021) is good at obtaining an approximate solution for a CVRP. This heuristic is modified to generate an approximate solution for OVRP as mentioned below by developing a new method to solve travelling salesman problem as mentioned below.

4.1 Solving the individual route by open traveling salesman problem (OTSP).

For finding the individual routes of the vehicles the following method is employed.

Using the nearest neighbor algorithm an initial route is generated. The selected path is improved by applying the 2-opt improvement method in 3 different ways as explained below.

- a. Keeping depot and the farthest customer from depot fixed, 2-opt improvement is applied for the rest of the customers. The total distance of the open traveling salesman problem is calculated. For example, in Fig. 1 the customer '37' is fixed as the last customer and the depot as the first customer.
- b. Customers in the current vehicle are arranged as per the polar angle from any reference line passing through the depot. The positions of the customer which is first in the list and the depot are fixed and 2-opt improvement is applied for the rest of the customers. If there is a tie in selecting the customer node to be fixed, then the customer which is farthest from the depot is selected. The total distance of the open traveling salesman problem is calculated. For example, in Fig. 1 the customer '26' is fixed as the last customer and the depot as the first customer.

- c. Customers in the current vehicle are arranged as per the polar angle from any reference line passing through the depot. The positions of the customer which is last in the list and the depot are fixed and 2-opt improvement is applied for the rest of the customers. If there is a tie in selecting the customer node to be fixed, then the customer which is farthest from the depot is selected. The total distance of the open traveling salesman problem is calculated. For example, in Fig. 1 the customer '27' is fixed as the last customer and the depot as the first customer. The best among the above 3 solutions (having the least distance) is taken as the solution.

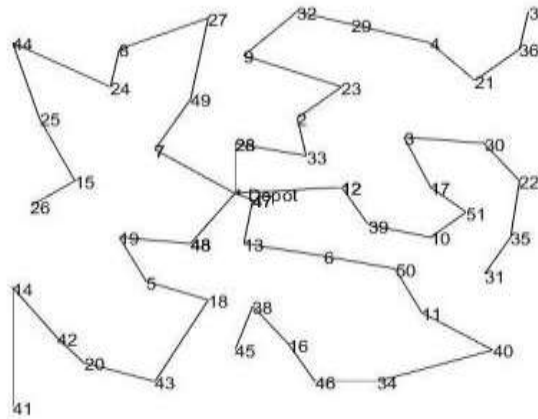


Fig. 1. Fixing the last customer and depot before solving the open TSP

5. Proposed Method

The following algorithm describes the method to get approximate solutions to extremely large-scale OVRP.

- 1) Locate the depot as the center. Compute the polar coordinates of all customers
- 2) The number of divisions (concentric rings) into which the customers must be divided to minimize the distance is determined by the following algorithm.

Let N be the number of divisions into which the customers are divided.

Do until no more improvement is done consecutively for 5 iterations starting with $N=2$

- Sort all customers as per the distance from the depot.
- Divide customers into N equal divisions. Thus they are divided into N concentric rings
- Sort customers in the first division as per the polar coordinates in the clockwise direction. Sort customers in the next division as per the polar coordinates in an anti-clockwise direction. This process of sorting in the clockwise and anti-clockwise direction is continued until all the divisions are sorted. Now all the divisions are joined one by one in the same order so that we get a total list of customers in one particular order.
- Starting from the first customer modified sweep algorithm is applied to get the first solution in the iteration. Starting from the last customer modified sweep algorithm is applied in the reverse direction to get a second solution. Best solution is taken as the solution for the iteration
- N is increased to $N+1$

End do

Let the optimum number of divisions, determined from the previous step be N_{opt} . The approximate solutions are obtained by the following method.

Divide the customers into ' N_{opt} ' divisions. Let the number of customers be n . Then ' n ' approximate solutions are obtained by using every customer as the starting point of the modified sweep and sweeping the customers in the clockwise direction. Another set of ' n ' approximate solutions is obtained by using every customer as the starting point of the modified sweep and sweeping the

customers in the anticlockwise direction. From these, those solutions which do not yield a minimum number of vehicles are ignored and the remaining solutions are taken.

6. Experimental tests

The modified sweep algorithm is designed to solve extremely large-scale OVRP. An algorithm to find large-scale OVRP containing thousands of customers could not be found in the literature for comparison purposes. The largest test instances so far used for solving OVRP are those by Golden et al (1998). Hence this heuristic is first tested on 8 test instances from and Golden et al for which solutions from other methods exist for comparison. Later on, the algorithm is tested on large-scale vehicle routing problem data of Arnold (2019) (<http://neo.lcc.uma.es/vrp/vrp-instances>) which consists of thousands of customers. The new algorithms are implemented using MATLAB software. The experiments have been done on a PC (Intel Core i7-8550U CPU @ 1.80 GHz , 8GB RAM) with Windows 10 OS.

7. Results & Discussion

The output from the modified sweep algorithm after it is run on the test instances by Golden et al (2019) is tabulated in Table 1. This output is compared with the outputs of the genetic algorithm by Ruiz, E.(2019) which is considered as the final solution for comparison purposes. The number of approximate solutions produced is approximately twice the total number of customers. All the solutions have a minimum number of vehicles. The CPU time taken is also relatively less. For example to generate 960 solutions for the test instance G8 the CPU time taken is approximately 23 seconds. The deviation of the best of each set of approximate solutions is less than 5% from its corresponding final value. Thus all the objectives are met. A sample of approximate solutions is presented in Appendix A.

Table 1: Comparison between modified sweep algorithm results and previous research for test instances of Golden et al. (1998)

Instanc e	Nu mber of cust ome rs	Mini mum No of vehic les	Vehi cle Capa city	Nu mber of solu tion s	Best	Worst	CPU time(se c)	Final Solution by GA (Ruiz, E et al)	CPU time	% Deviation of best from Final Solution
G1	200	5	900	400	6117.7	7136	3.65	6003.08	2081.37	1.91
G2	240	9	550	480	4757.8	5184.4	5	4609.25	4028.96	3.22
G3	280	7	900	560	8077.1	8674.6	6.83	7735.16	7200	4.42
G4	320	10	700	640	7414.7	7762.9	8.56	7280.98	7200	1.84
G5	360	8	900	720	9604.7	10439.1	15.17	9178.13	7200	4.65
G6	400	9	900	798	9951.4	10446.5	14	9847	7200	1.06
G7	440	10	900	880	10637.2	11288.5	23.41	10444.7	7200	1.84
G8	480	10	1000	960	12835.4	13600.7	22.81	12449.6	7200	3.1

Now the modified sweep algorithm is run on test instances by Arnold (2019) which contains thousands of customers. First, the algorithm is run to produce only a single solution. This is obtained by running the modified sweep algorithm with a single starting point. In the next case, it is run to produce nearly 10 approximate solutions. This is obtained by running the modified sweep algorithm with 5 different equidistant starting points. Finally, it is run to produce approximately 40 approximate solutions. This is obtained by running the modified

sweep algorithm with 20 different equidistant starting points. It can be observed the CPU time taken to produce approximate solutions increases approximately linearly with the number of approximate solutions produced. The modified sweep algorithm produced the solutions having the minimum number of vehicles in all the cases. The results are tabulated in Table 2. As can be seen from this table for larger instances, the difference between the best and worst cases of approximate solutions obtained are insignificant. However, these solutions can be used as some of the approximate solutions required to solve very large-scale OVRP having thousands of customers.

A sample of approximate solutions is presented in Appendix B.

Table 2 Output of modified sweep algorithm on extremely large instances by Arnold (2019)

Instance	No of customers	Minimum No of Vehicles	Capacity	Case 1		Case 2				Case 3			
				One solution	CPU time (sec)	No of solutions	Best	Worst	CPU time (sec)	No of solutions	Best	Worst	CPU time (sec)
A1	3001	203	25	118271	3	10	118214	119298	5	40	117876	119543	10
A2	4001	46	150	83764	5	10	83764	85673	10	40	83764	86150	23
A3	6001	343	30	286747	6	10	286518	287964	9	40	286457	287977	19
A4	7001	120	100	201811	6	10	201811	202976	11	40	200465	203316	26
A5	10001	485	35	284906	13	10	284755	285909	16	40	284679	286004	37
A6	11001	110	170	181255	18	10	180962	181690	48	39	180797	181786	88
A7	15001	512	50	321800	21	10	321436	322529	54	40	320852	322723	52
A8	16001	182	150	244029	31	10	243685	244818	98	37	243834	245245	100
A9	20001	684	50	4326326	46	10	4326326	4358618	75	39	4326326	4365523	92
A10	30001	256	200	3051656	120	10	3051656	3076562	274	40	3051656	3082930	316

8. Conclusion

In this paper, a new heuristic algorithm based on modified sweep is developed to get some approximate solutions to very large-scale inconsistent OVRP. The output from the heuristic generally has the least number of vehicles in most of the cases and slightly more than the least number of vehicles in some rare cases. These solutions can be used to complement the approximate solutions produced by any other method, to solve very large-scale inconsistent OVRP. In case sufficient time is not available to improve the solution then the best of these approximate solutions can be taken as the final solution.

Appendix A

The best approximate solution for one of the Golden's instances is shown below. For clarity, the line joining the first customer and the depot is not shown.

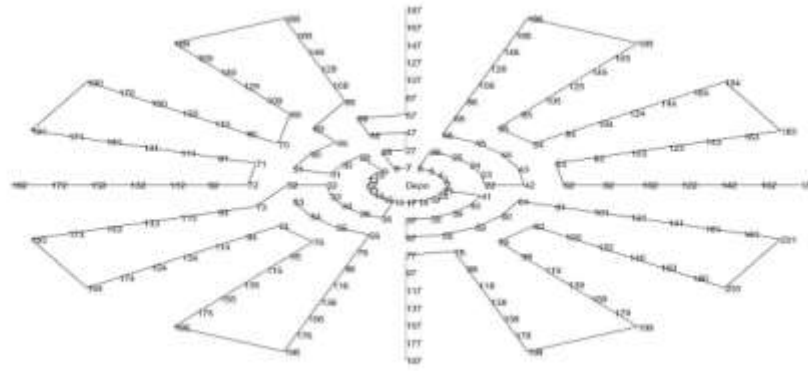


Fig. 2. An approximate Solution for G1.

Appendix B

The best approximate solution for one of the Arnold's instances is shown below. For clarity, the line joining the first customer and the depot is not shown.



Fig. 3. An approximate Solution for A1

References

1. Arnold, F., Gendreau, M., & Sörensen, K. (2019). Efficiently solving very large-scale routing problems. *Computers & Operations Research*, 107, 32-42.
2. Brandão, J. (2004). A tabu search algorithm for the open vehicle routing problem. *European Journal of Operational Research*, 157(3), 552-564.
3. Elshaer, R., & Awad, H. (2020). A taxonomic review of metaheuristic algorithms for solving the vehicle routing problem and its variants. *Computers & Industrial Engineering*, 140, 106242.
4. Fu, Z., Eglese, R., & Li, L. Y. (2005). A new tabu search heuristic for the open vehicle routing problem. *Journal of the Operational Research Society*, 56(3), 267-274.
5. Fung, R. Y., Liu, R., & Jiang, Z. (2013). A memetic algorithm for the open capacitated arc routing problem. *Transportation Research Part E: Logistics and Transportation Review*, 50, 53-67.
6. Ge, B., Han, Y., & Bian, C. (2016). Hybrid ant colony optimization algorithm for solving the open vehicle routing problem. *Journal of Computers*, 27(4), 41-54.
7. Golden, B. L., Wasil, E. A., Kelly, J. P., & Chao, I. M. (1998). The impact of metaheuristics on solving the vehicle routing problem: algorithms, problem sets, and computational results. In *Fleet management and logistics* (pp. 33-56). Springer, Boston, MA.
8. Hosseinabadi, A. A. R., Kardgar, M., Shojafar, M., Shamshirband, S., & Abraham, A. (2016). Gravitational search algorithm to solve open vehicle routing problem. In *Innovations in bio-inspired computing and applications* (pp. 93-103). Springer, Cham.
9. Kytöjoki, J., Nuortio, T., Bräysy, O., & Gendreau, M. (2007). An efficient variable neighborhood search heuristic for very large scale vehicle routing problems. *Computers & operations research*, 34(9), 2743-2757.
10. Laporte, G. (1992). The vehicle routing problem: An overview of exact and approximate algorithms. *European journal of operational research*, 59(3), 345-358.
11. Marinakis, Y., & Marinaki, M. (2014). A bumble bees mating optimization algorithm for the open vehicle routing problem. *Swarm and Evolutionary Computation*, 15, 80-94.

12. Ruiz, E., Soto-Mendoza, V., Barbosa, A. E. R., & Reyes, R. (2019). Solving the open vehicle routing problem with capacity and distance constraints with a biased random key genetic algorithm. *Computers & Industrial Engineering*, 133, 207-219.
13. Sariklis, D., & Powell, S. (2000). A heuristic method for the open vehicle routing problem. *Journal of the Operational Research Society*, 51(5), 564-573.
14. Şevkli, A. Z., & Güler, B. (2017). A multi-phase oscillated variable neighbourhood search algorithm for a real-world open vehicle routing problem. *Applied Soft Computing*, 58, 128-144.
15. Tarantilis, C. D., Ioannou, G., Kiranoudis, C. T., & Prastacos, G. P. (2004). A threshold accepting approach to the open vehicle routing problem. *RAIRO-Operations Research*, 38(4), 345-360.
16. Test data source. [\url{http://neo.lcc.uma.es/vrp/vrp-instances/}](http://neo.lcc.uma.es/vrp/vrp-instances/)
17. Uchoa, E., Pecin, D., Pessoa, A., Poggi, M., Vidal, T., & Subramanian, A. (2017). New benchmark instances for the capacitated vehicle routing problem. *European Journal of Operational Research*, 257(3), 845-858.
18. Van Breedam, A. (2001). Comparing descent heuristics and metaheuristics for the vehicle routing problem. *Computers & Operations Research*, 28(4), 289-315.
19. Vangipurapu, B. R., Govada, R., & Kandukuri, N. R. (2020). A New Heuristic for Solving Open Vehicle Routing Problem with Capacity Constraints. In *Innovative Product Design and Intelligent Manufacturing Systems* (pp. 897-906). Springer, Singapore.
20. Vangipurapu, B. R., & Govada, R. (2021). A construction heuristic for finding an initial solution to a very large-scale capacitated vehicle routing problem. *RAIRO-Operations Research*, 55(4), 2265-2283.

Design and fabrication of Multipurpose Manual Controlled Robotic Arm (MMCRA)

B. Kiran Kumar^{1,*}, K. Venkatesan², B Saikrishna Srikar³

¹Associate Professor, Department of Mechanical Engineering, Koneru Lakshmaiah
Education Foundation, Vaddeswaram, AP, India

²Professor, Department of Automobile Engineering, Bharath Institute of Higher Education
and Research, Chennai, Tamil Nadu, India

³Assistant System Engineer, Tata Consultancy Services

*Corresponding author; E-mail: buragaddakirankumar15@gmail.com

Abstract: With the increasing technology, the industries are moving from the current state to automation in Industry 4.0 to maximize productivity and maintain consistency in quality. A robotic manipulator with 3 to 5 degrees of freedom is the most frequently employed robot in the industry. They have movable joints and links suitable for industrial and household applications. This work presents a design and fabrication of a multipurpose manual controlled robotic arm (MMCRA) and its control is as simple as operating with a remote. Its applications will exist at pick and place, painting, drilling operations by changing the end effector or gripper of the arm. In the first phase of this study, the modelling and finite element analysis is done by using Unigraphics NX software. In the second phase, the materials are selected by comparing their nodal stresses, deflections of different elements, and a prototype is fabricated. It is validated through real-time applications.

Keywords: *Robotic manipulator, DOF, Kinematic chain, End effector, Unigraphics NX, Finite element analysis.*

1. INTRODUCTION

Mechanical engineering is one of the branches of engineering and technology related to machinery based on its design, manufacturing, and application. Robotics is also a part of mechanical engineering that embeds software, electronics, and mechanics. The main scope of today's robotics and its development is towards the systems that reveal modularity, extended software environment, fault-tolerance, redundancy, flexibility, and smooth, logical connectivity with other machines. In most routine and often carried out industrial tasks, automation plays a critical role in saving human effort. The flexible and generally high cost of automation systems is used in big industries used for several tasks ^[5].

The robots are broadly divided into industrial and service robots. International Federation of Robotics (IFR) defines a service robot as a robot based on a semi or fully automated service that benefits human well-being and equipment, excluding manufacturing operations. Those robots are used in various applications, including office, military areas, hospitals, agriculture. Moreover, particular jobs such as picking up explosive chemicals, defusing bombs, selecting and putting the bomb somewhere for containment, and repeating pick and place activity in industries may be challenging or risky for people. As a result, humans can take the position of robots in the workplace. In some layouts, links can be compared with human anatomy as wrist, upper arm, and forearm with the joint at shoulder and elbow. A wrist joint connects to an end effector at the end of the arm, which may be a tool or a gripper or end effector, or any other device to work ^{[1][2]}.

A robotic manipulator is a programmed mechanical arm that performs functions similar to a human arm. The links of those manipulators are connected by joints permitting either rotational motion or translational displacement ^{[6][7]}. Figure.1 shows various types of mechanical arms with motion links.

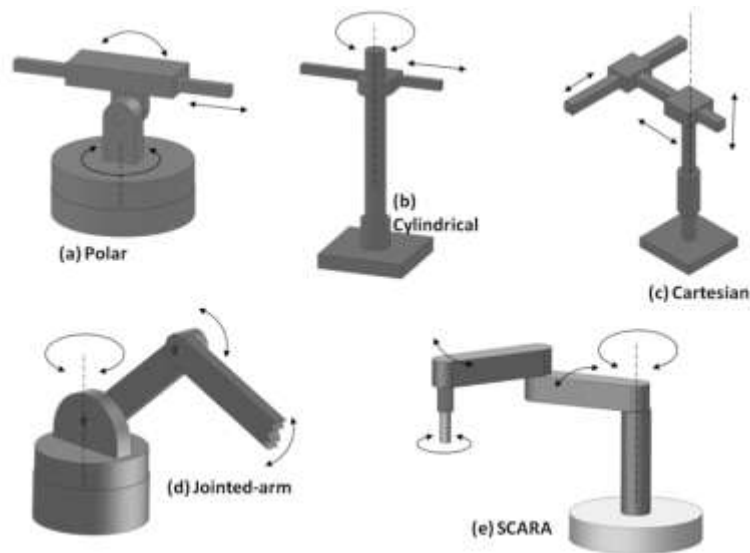


Figure.1: Different types of arms based on their motion.

Degrees Of Freedom (DOF) refers to the freedom of movement of a rigid body in 3D space. There is a total of 6 degrees of freedom i.e., three rotation moments, and three linear movements along the x, y, and z axes^{[8][9]}.

The Kinematic chain of the manipulator can be expressed as a combination of links. The end effector is a replica of the human hand that serves as the final link in the manipulator's kinematic chain.^[10]

An end effector may be created to do any activity, including gripping, welding, and spinning. It contains various sensors based on the task in which it is used^{[2][5][8]}.

Unigraphics NX (also known as Siemens NX) is advanced CAD/CAM/CAE software and is used for the modelling and finite element analysis of the MMCRA.

The literature on robotic arms and their industrial applications is reviewed in Section 2. Designing a robotic arm is covered in Sections 3 and 4, respectively. The suggested robotic arm's specs are shown in Section 5. The analysis of robotic arm elements and its selection are explained in Section 6. The proposed robotic arm and its suggested applications are shown in Sections 7 and 8. The major conclusions of the present research work and the potential for future work are covered in sections 9 and 10, respectively.

2. LITERATURE REVIEW

Ghadge et al. (2018)^[5] proposed the fabrication of a robotic arm that can pick and place items using Node MCU controller based on microchip technology as the control system to guide the device. The input signal is sent from the android application to MCU, and the arm reacts according to it.

Gautam et al. (2017)^[6] discussed industrial robots in the areas such as wood, consumer goods, plastic, food, etc. His approach is to develop a lightweight robot by using carbon fiber and aluminum material and with the help of a stepper motor for movements.

Yusoff et al. (2012)^[7] presented the wireless mobile robotic arm for pick and place operations using the wireless PS2 controller. The Arduino Mega interface platform is used in the development of an arm and is intended to solve the challenges of item placing and picking. Singh et al. (2013)^[8] carried the Design of a Robotic Arm with a gripper & end effector for Spot Welding using an AC motor along with spur gear and threaded shaft arrangements. The end effectors of his design are used for various tasks like holding, picking, grasping objects, and spot welding with a fixed base.

Mourya et al. (2015)^[9] proposed a design and implementation of a 4-DOF pick and placed robotic arm. This model is self-operational in controlling simple tasks like lifting, gripping, Dept. of Mech. Engg.

and placing. It consists of revolute links for angular motion and four serial servo motors are used to perform four degrees of freedom.

Abdulkareem et al. (2019) ^[10] reported the design and implementation of a robotic arm used for pick and place tasks. Its control is based on the Arduino microcontroller having a slave configuration. The model is developed by using various motors and tracked wheels for the transportation of the arm.

Omijeh et al. (2014) ^[11] worked on a Design Analysis of a Remote Controlled "Pick and Place" Robotic Vehicle. It is used for handling some objects and specific tasks in hazardous environments. This model contains a 5-DOF arm with a base resting on the vehicle.

Liang et al. (2018) ^[12] presented a Soft Robotic Arm (SRA), which is a potential alternative for a domestic robotic arm, as it is constructed of low-cost fabrics and flexible plastics. It contains two joints and a gripper. They characterized the force output of the bending modality and demonstrated the result of the SRA in object manipulation.

Kumar et al. (2016) ^[13] worked on the design and execution of a mechanical and vacuum gripper-based multi-handling pick and place robotic arm. It is a self-operated device used for lifting, sucking, and placing. The angular movement between adjacent is incubated by using revolute joints.

Wongphati et al. (2012) ^[14] shared their views on how the robotic arm is used in daily lives. They surveyed to know the people thinking about the use of a robotic arm worldwide and concluded that most of the people suggested use in the workplace and the household.

Kadir et al. (2012) ^[15] presented an Internet Controlled Robotic Arm and arm movement that is controlled with the help of Arduino Uno by using the internet.

Rushikeshwar et al. (2019) ^[16] studied on Bio-Mimetic Portable Robotic Arm. They briefed that robots can be used in place of a human in various dangerous places like coal mines, deep tunnels, defense tasks, etc. The control system of this Robotic-arm consists of microcontroller DC motors, Motor Drivers, Servo motors, potentiometers, and joystick controls.

It is clear from the literature review that robotics has a wide range of applications. This study's goal is to improve the robotic arm and broaden its range of applications.

3. DESIGN STEPS OF ROBOTIC ARM

Figure.2 illustrates the multiple steps involved in the creation of a Robotic arm.

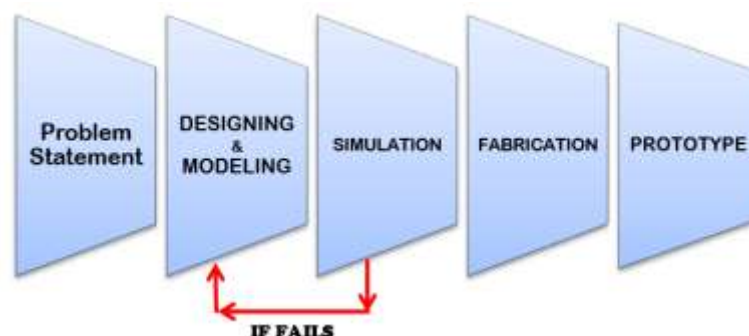


Figure.2: Various steps of designing a Robotic Arm

Problem Statement

The robotic arms are fit for industrial and household applications. Some of the inconveniences caused by modern industrial robotic manipulators are listed below.

- Very expensive
- Require additional maintenance
- Need a skilled person to operate
- Fixed and cannot be moved

- Program is mandatory for the robotic arm
- **Not intelligent or sentient**

A design of a new robotic manipulator will be useful to overcome the disruptions

Features of the proposed Robotic Arm

It includes the features of both Cartesian Mechanical and Articulated Mechanical arms. Each link is having 2-DOF, in which both linear and rotation movements can be obtained at once or simultaneously.

In this model, the arm is directly connected at the remote (controller) front end, and the person himself manually operates for the movement. In this context, links can resemble human anatomy as wrist, upper arm, and forearm with the joint at shoulder and elbow. A wrist joint connects to an end effector at the end of the arm, which may be a tool or a gripper, or any other device to work.

The model includes a telescopic arrangement for linear motion by using the **nut and bolt principle**, and for rotary motion is obtained by using DC gear motors of different capacities (i.e., 45, 60,100 RPMs). To operate the total unit, DC rechargeable batteries of 12 volts are used.

General components used in Mechanical Arm ^[2]

Structure

An arm's structure is a type of kinematic chain. The chain is a collection of links, joints, and actuators capable of supporting one or more degrees of freedom. The majority of modern arms employ open serial chains, in which each link connects to the next. These arms are frequently modelled like human arms. An end effector is positioned on the end link of the manipulator. Figure.3 shows a Robotic arm structure.

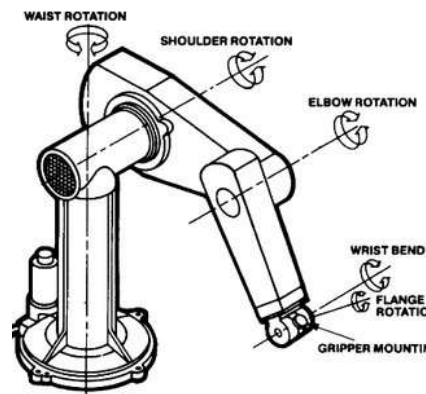


Figure.3: Robotic arm structure

Power Sources

Rechargeable battery is generally more sustainable and sensible type power source. The current is created due to a chemical reaction between the elements inside the battery. After using power from the battery, it can be charged by using AC/DC adapter. Nickel-cadmium, Lead Acid, and nickel-metal hydride are the widely used chemical combinations for rechargeable batteries.

Actuator

Actuators are also known as muscles of the arm, and they convert the stored energy into work by creating the required movements. The most popular actuators are electric motors which are used to spin a wheel or gear. Nevertheless, several recent advancements in alternative actuators use electricity, chemicals, or compressed air as a source of power.

Figure.4 shows the actuators being used in Industries.



Figure.4. Industrial actuators

Gear Motor

Motors are the devices that are used to rotate the parts mounted on the motor shaft. Servo motor, stepper motor, a gear motor is some of the widely used motors. Gear motors have mechanisms that regulate the speed of electric motors by having an arrangement like sun planet type, worm & worm gear type. The main aim of this kind of gear motor is to increase or decrease the speed of the gear to the pinion or vice versa and is depicted in Figure.5.



Figure. 5: Gear Motor

Controller

It controls the manipulator by sending the input signal as per the given program in the form of commands and receives back the signal in the form of feedback from the manipulator.

End Effector

The end effector is the arm's final connection. i.e., the part situated at the end of the arm, in which the end effector mainly does every task done by the arm. Figure.6 shows a model End Effector.



Figure.6: Model End Effector

Mechanical Gripper

The gripper mechanism is based on simple kinematic mechanical connections. The most basic gripper has merely two or three fingers that open and close to pick up and position tiny

things. Here we used spur gear meshed with worm gear type of system is used for construction of gripper. Figure.7 shows a Mechanical Gripper.

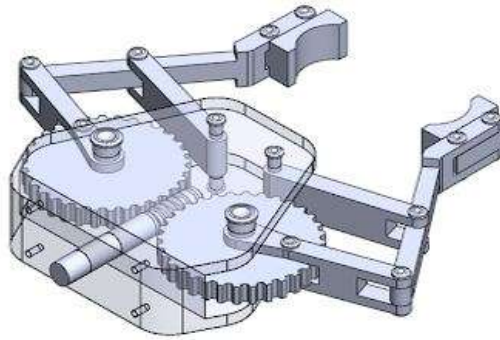


Figure. 7: Mechanical gripper

4. DESIGN OF ROBOTIC ARM

The proposed Multipurpose Manual Controlled Robotic Arm (MMCRA) is designed by using the elements listed below. It is aimed to operate manually.

- Motor
- Controller & Controller Casing
- Motor Couplings
- Outer Shaft
- Screw Coupling
- Stud & Nut
- Inner Shaft
- Nut Holding Coupling
- Clearance Reducer Coupling
- Elbow Coupler
- Elbow
- Gripper

Modeling of Robotic Arm

All the elements of the Robotic arm are designed and assembled by using NX Design Software. Figure 8 depicts the proposed Robotic Arm, which was created using NX. The telescopic arrangement with nut and bolt principle between outer and inner shafts is shown in Figure.9

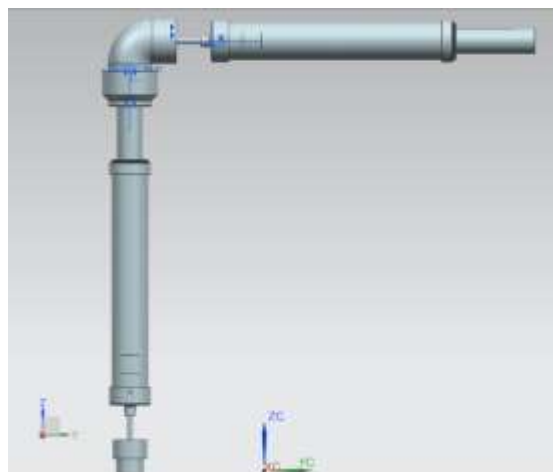


Figure.8: Assembly model of Robotic Arm

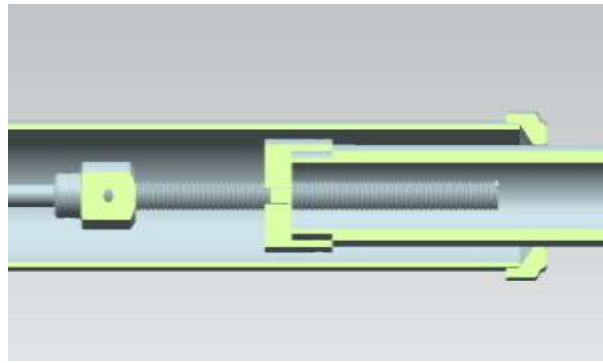


Figure.9: Cut sectional view of Telescopic arrangement

Drafting of Robotic Arm elements

Two dimensional & three dimensional drawings are drafted for each element of the Robotic arm in NX software. It includes all the necessary views and dimensions that are necessary for the fabrication of these elements. Figure.10 shows the 2D & 3D drawing of a Gear motor.

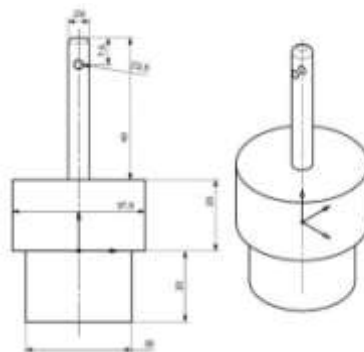


Figure. 10: 2D & 3D drawing of Gear Motor

5. SPECIFICATIONS OF THE ROBOTIC ARM

Table 1 lists the features for the proposed Multipurpose Manual Controlled Robotic Arm (MMCRA).

Table.1: Specifications of the MMCRA

DOF per link	2
Payload capacity	400g (Experimentally)
Total weight	2.5 kg
Motor Speeds	
• Rotational	45 rpm
• Linear	60 rpm
• Gripper	100m
Motor Shaft diameter	12mm
No. of links	4 (2 rotary + 2 linear)
Hardware interface	2 pin connector
Battery (Rechargeable)	
• Capacity	7.5 AH
• Charging time	6 to 10 h

• Voltage	12 V
• Life	2000 to 3000 cycles
Length of link	
Minimum	240mm
Maximum	360mm

6. SIMULATION OF ROBOTIC ARM ELEMENTS

Simulation is an approximate analysis of the body at any instant point of time due to structural, thermal, and vibration behaviour, i.e., the application of loads, temperature, noise. Using this type of analysis, the approximate lifetime of the body, occurrence of failure in the region and strength will be known ^[4].

Materials for Robotic Arm elements

While choosing the materials for the prototype of a robotic arm, the mechanical properties, manufacturing characteristics, appearance, and cost are to be considered ^{[9][10]}. The mechanical properties of the materials include:

- Density
- Strength
- Elasticity
- Hardness & Toughness
- Durability & Malleability
- Temperature and moisture resistance
- Corrosion & Wear resistance

The most commonly used Metallic and Non-metallic materials are Aluminum, Mild steel, Stainless steel, and ABS plastic, PVC respectively.

Theoretical analysis

In this study, a comparison of nodal stress and deformation values obtained from the theoretical calculation and NX software is done to confirm the closeness of their values and to find the location of major stress-induced on a simple cantilever.

In this simulation, Aluminium specimen of size 100 * 20 * 5mm is considered

$$\text{Deflection in beam } (\delta) = \frac{FL^3}{3EI}$$

where F = Load applied, L = Length of material, E= Young's Modulus, and I = Moment of Inertia

$$\delta = \frac{40 * 100^3}{3 * 68 * 10^3 * 208.33} = 0.9411\text{mm}$$

$$\text{Max stress-induced } (\sigma) = \frac{y * M}{I}$$

where y = Vertical distance away from the neutral axis, M = Bending Moment and I = Moment of Inertia

$$\sigma = \frac{2.5 * 40 * 10^2}{208.33} = 48.0379 \text{ MPa}$$

The Displacement and Nodal stress simulations are shown in Figure.11 and Figure.12 respectively. Table. 2 depicts the values obtained from both theoretical and analysis by NX software.

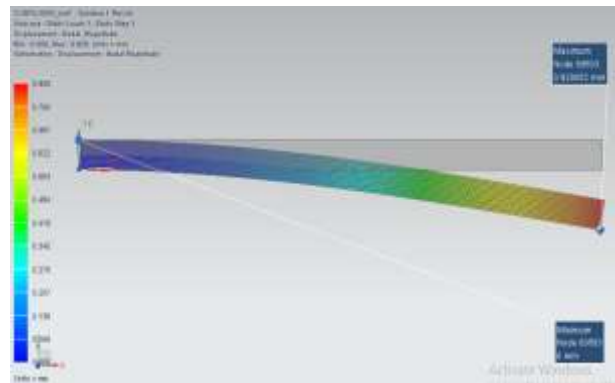


Figure.11: Displace simulation of Aluminium beam

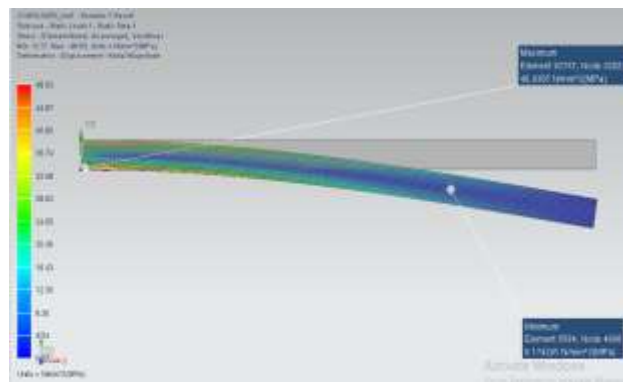


Figure.12: Nodal Stress simulation of Aluminium beam

Table.2: Deflection and Stress values

Solutions	Theoretical	NX Software
Max Deflection (mm)	0.9411	0.829052
Max Stress (MPa)	48.0379	48.9305

By comparing the solutions of theoretical and NX software values, it is clear that they are very close. Hence, it is concluded that NX data can be taken directly for further study. It reflects that the failure occurs at the constrained location or position and needs to be more focused on the constrained area.

In the design of the Robotic arm, a motor coupling connects the motor with the outer shaft. Study includes material selection and design of a motor coupling. Four different kinds of Motor coupling designs and Five materials (i.e, Metallic and non-metallic materials) are considered for the simulation purpose.

Motor Coupling materials and Loads considered

The total load is the sum of self-load and a payload of 400gms will be acting on a motor coupling. The self-load is mainly dependent on the properties of material like density and volume of the arm. Table.3 shows different kinds of motor coupling materials, properties, and the loads applied on them.

Table.3: Motor Coupling materials and loads

S. No.	Materials	Density (Kg/m ³)	Max Tensile Strength (MPa)	Young Modules (GPa)	Load Applied (N)
1	Aluminum	2707	90	68	80

2	ABS Plastic	1050	60	-	30
3	PVC	1380	62	190	40
4	Mild Steel	7850	490	215	240
5	Stainless Steel	7850	540	190	240

Motor Coupling Design

Table.4 lists four different motor coupling designs for simulation purposes.

Table.4: Different design of Motor couplings

Design	3D Drawing of the coupling
I	
II	
III	
IV	

Simulation for Displacement and Nodal Stress

Simulation carried on all four designs of Motor couplings for displacement and Nodal stress values by using NX software. It is carried for all five different kinds of materials listed in Table.3. Figure.13 and Figure.14 shows simulations for the Aluminium material. For all twenty models (i.e., 4 designs x 5 materials) the Displacement and Nodal stress values obtained from NX software are tabulated in Table.5 and Table.6 respectively.

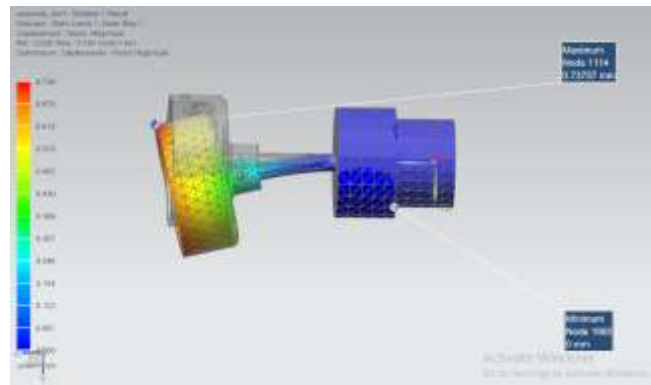


Figure.13: Simulation for Displacement on Aluminium Design I coupling

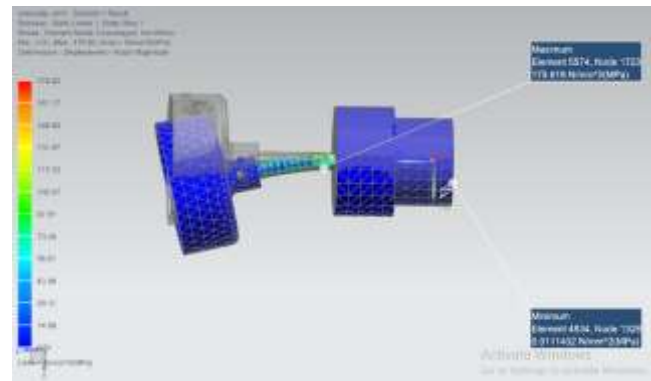


Figure.14: Simulation for Nodal Stress on Aluminium Design I coupling

Table.5: Displacement values of twenty models

Displacement (in mm)										
Design/ Material	Aluminium		ABS		PVC		Mild Steel		Stainless Steel	
	min	max	min	max	min	max	min	max	min	max
I	0	0.7376	0	0.3635	0	0.4595	0	2.109	0	2.101
II	0	1.2407	0	0.8221	0	0.9745	0	3.602	0	3.619
III	0	1.1562	0	0.6128	0	0.74862	0	3.4004	0	3.39232
IV	0	1.9295	0	0.9081	0	0.85291	0	5.5363	0	5.65878

Table.6: Nodal Stress values of twenty models

Nodal Stress values (in MPa)										
Design / Material	Aluminum		ABS		PVC		Mild Steel		Stainless Steel	
	min	max	min	max	min	max	min	max	min	max
I	0.0114	175.82	0.005	65.626	0.00557	87.9093	0.03756	525.01	0.0375	525.009
II	0.0135	178.89	0.005	67.083	0.0067	89.441	0.04045	536.67	0.0405	536.665
III	0.0189	176.84	0.004	66.875	0.0049	89.1972	0.03931	535.3	0.04852	530.531
IV	0.0201	236.73	0.008	88.775	0.00582	98.1094	0.04513	782.44	0.05624	710.199

By referring to the values of Table.5 & Table.6, it is found that ABS material has less deformation and stress values for Design I. This motor coupling is fabricated by a 3D printing process.

7. PROPOSED ROBOTIC ARM PROTOTYPE

As per the design shown in Section 4, all the elements are suitably fabricated as per the design and assembled. The prototype of the proposed Multipurpose Manual Controlled Robotic Arm with a controller is depicted in Figure.15. Figure.16 shows an enlarged picture of the gripper.



Figure.15: Prototype of a Multipurpose Manual Controlled Robotic Arm

This arm is the combination of cartesian and articulated robotic arm in which each link has both linear and rotary motion simultaneously. The control is done manually by the person operating it. The nut and bolt mechanism is employed for cartesian motion and different capacity gear motors for the articulated motion. This arm can be used for various purposes by changing the end effector i.e., mechanical gripper, vacuum gripper or any other types of customized grippers.



Figure. 16: Prototype of the Gripper of Robotic arm

8. SUGGESTED APPLICATIONS OF MMCRA

- Pick and place
- Nursing homes
- Home quarantine patients
- Drilling, spraying, painting, welding operations
- Hot metals handling in industries
- Plucking of fruits and vegetables from plants
- Household works, such as cleaning, moving, and placing of objects

9. CONCLUSION

The progression of robotic arm will increase the aptness of its applications in Manufacturing, Health care, Agriculture, Space Exploration. Based on the application the gripper needs to be altered.

- The objective of this study is to provide a design and prototype implementation of a Multipurpose Manual Controlled Robotic Arm (MMCRA) that increases its versatility. This arm combines the features of both Cartesian and Articulated Mechanical Arms.
- It is proved that the nodal stress and deformation values obtained from theoretical and analytical methods are very close and concluded that analytical value could be taken for further study.
- Also concluded that ABS is the best material in the fabrication of motor coupling.
- Having both linear and rotary movements at each link of the arm, facilitates in increasing the suitability of its application.

10. FUTURE SCOPE

- The type of sensors utilized has an impact on job accuracy. and also hybrid sensor brings more efficiency.
- In the next level Robotic arm can be attached to drones for various applications.
- Optimization of material is another area need to be focused, consumption of materials may increase or decrease the efficiency and good research need to be conducted on best combination.
- Nano coating need to be considered on arm and gripper.

References

- [1] Robotic Engineering by Richard D.Klafter, Prentice-Hall, Tata Mc Graw-Hill, 1995.
- [2] Industrial Robotics by Mikell P.Groover, Tata Mc Graw-Hill, 1986.
- [3] Bansal, R. K. (2008). A Textbook of Strength of Materials. *Laxmi Publications (P) Ltd*, <https://books.google.com/books?id=2IHEqp8dNWwC&pgis=1>
- [4] Reddy, G. R., & Eranki, V. K. P. (2016). *Design and Structural Analysis of a Robotic Arm*. 101. <http://www.diva-portal.org/smash/get/diva2:1068547/FULLTEXT02>
- [5] Ghadge, K., More, S., Gaikwad, P., & Chillal, S. (2018). Robotic ARM for pick and place application. *International Journal of Mechanical Engineering and Technology*, 9(1), 125–133.
- [6] Gautam, R., Gedam, A., Zade, A., & Mahawadiwar, A. (2017). Review on Development of Industrial Robotic Arm. *International Research Journal of Engineering and Technology (IRJET)*, 4(3), 1752–1755. <https://irjet.net/archives/V4/i3/IRJET-V4I3402.pdf>
- [7] Yusoff, M. A. K., Samin, R. E., & Ibrahim, B. S. K. (2012). Wireless mobile robotic arm. *Procedia Engineering*, 41(Iris), 1072–1078. <https://doi.org/10.1016/j.proeng.2012.07.285>
- [8] Singh, P., Kumar, A., & Vashisth, M. (2013). Design of a Robotic Arm with Gripper & End Effector for Spot Welding. *Universal Journal of Mechanical Engineering*, 1(3), 92–97. <https://doi.org/10.13189/ujme.2013.010303>
- [9] Mourya, R., Shelke, A., Satpute, S., Kakade, S., & Botre, M. (2015). Design and Implementation of Pick and Place Robotic Arm. *International Journal of Recent Research in Civil and Mechanical Engineering (IJRRCME)*, 2(1), 232–240.
- [10] Abdulkareem, A., Ladenegan, O., Agbetuyi, A. F., & Awosope, C. O. A. (2019). Design and implementation of a prototype remote-controlled pick and place robot. *International Journal of Mechanical Engineering and Technology*, 10(2), 235–247.
- [11] Omijeh, B. O., Uhunmwangho, R., & Eikhamenle, M. (2014). Design Analysis of a Remote Controlled Pick and Place Robotic Vehicle. *International Journal of Engineering Research and Development*, 10(5), 2278–67. http://www.ijerd.com/paper/vol10-issue5/Version_1/J1055768.pdf
- [12] Liang, X., Cheong, H., Sun, Y., Guo, J., Chui, C. K., & Yeow, C. H. (2018). Design, Characterization, and Implementation of a Two-DOF Fabric-Based Soft Robotic Arm. *IEEE Robotics and Automation Letters*, 3(3), 2702–2709. <https://doi.org/10.1109/LRA.2018.2831723>

Two-day International Conference on Recent Advances in Mechanical and Industrial Engineering – 2023
(ICRAMIE-2023)

- [13] Kumar, S. P., Varman, K. S., & murugan, R. B. (2016). Design and Implementation of multi handling Pick and Place Robotic Arm. *International Journal of Engineering Trends and Technology*, 33(3), 164–166. <https://doi.org/10.14445/22315381/ijett-v33p230>
- [14] Wongphati, M., Matsuda, Y., Osawa, H., & Imai, M. (2012). Where do you want to use a robotic arm? and what do you want from the robot? *Proceedings - IEEE International Workshop on Robot and Human Interactive Communication*, 322–327. <https://doi.org/10.1109/ROMAN.2012.6343773>
- [15] Kadir, W. M. H. W., Samin, R. E., & Ibrahim, B. S. K. (2012). Internet-controlled robotic arm. *Procedia Engineering*, 41(Iris), 1065–1071. <https://doi.org/10.1016/j.proeng.2012.07.284>
- [16] Rushikeshwar, B. N. S., Shanthi, T. M. V., & Shailendra, K. (n.d.). *Study on BioMimetic Portable Robotic Arm*.

Design of a Self Guarded Drone and Analysis Using Fusion 360

Sivananda Uddagiri¹, Aishwarya Nalluri¹, Pradeep Sathivada¹, Kali Prasad Potluri¹, P.Mastan Rao²

¹UG Students, Department of Mechanical Engineering, Prasad V Potluri Siddhartha Institute of Technology, Kanuru, Vijayawada, Andhra Pradesh, India.

²Assistant Professor, Department of Mechanical Engineering, Prasad V Potluri Siddhartha Institute of Technology, Kanuru, Vijayawada, Andhra Pradesh, India.

Corresponding author: mastan_pb@yahoo.com

Abstract: Various drones with distinct features are available on the market. This paper focuses on designing and analyzing a self-guarded drone using Fusion 360 software. Drones typically have a propulsion system with multiple rotors and having multiple technological and build features. The collisions with rigid objects can damage the system, rendering the drone inoperable. To prevent this, suitable materials and design can protect the props and enable the drone to fly again after a collision. The drone's design is to withstand impact loads and avoid damage to the propulsion system in case of a sudden collision.

Keywords: Drones, Self-guarded drones, Fusion 360 software, Propulsion system, Impact loads, collision damage, Multiple rotors, Prop protection

INTRODUCTION

A drone refers to any aerial vehicle that receives remote commands from a drone pilot or relies on software for autonomous flight. Many drones are equipped with features like cameras for collecting visual data and propellers for stabilizing their flight. Drones are controlled by ground control stations and typically have rotors or fixed wings, as well as sensors, navigational systems, and gyroscopes for stability. Drones, or UAVs, are unmanned aerial vehicles. They can be operated with a pilot at a ground station or with varying levels of autonomy. They are currently utilized in several important industries, including transportation, security, and agriculture. Drones are often constructed with carbon-fiber composites, which sets them apart from piloted flights, where a significant portion of the construction is made from carbon fiber composites, aluminum, and titanium. It is possible to use 3D printing to create a drone, which can reduce the need for multiple parts assembly and enable rapid prototyping. However, 3D printing can also reduce the drone's durability. The FAA, or Federal Aviation Administration, regulates all aspects of civil aviation in the surrounding air and is responsible for research and developing systems for safe air navigation and traffic control over drone aviation. When making drones, manufacturers must follow FAA drone manufacturing regulations. Nowadays, drones often lack mechanical safety features, and instead rely on onboard sensors for added safety. However, there is a risk of accidents if the drone sensor fails unexpectedly. To address this, drone manufacturers must design drones to be mechanically safe and able to withstand impact loads. One way to do this is by designing a drone (quadcopter) with a self-guarded feature.

DESIGN OF A DRONE

Design is the process of creating a virtual or physical element using creativity, knowledge, and skills. Before drawing a sketch, several factors must be considered, including weight. Weight refers to the mass of a particular body acting downwards due to gravity on Earth. Basic keep out sketch: For a flying vehicle to operate correctly, the weight must be evenly distributed in all directions. The total weight of the vehicle rotates around its center of gravity, which is the point where the weight is distributed evenly to maintain balance. Designing a drone needs a geometry with this drone can be modeled. When designing a quadcopter, four rotors are required. Drawing a perfect sketch is a critical step in modeling a drone. To ensure accuracy, it is essential to consider basic dimensions and use sketch tools in the drawing panel of Fusion 360 Design workspace.

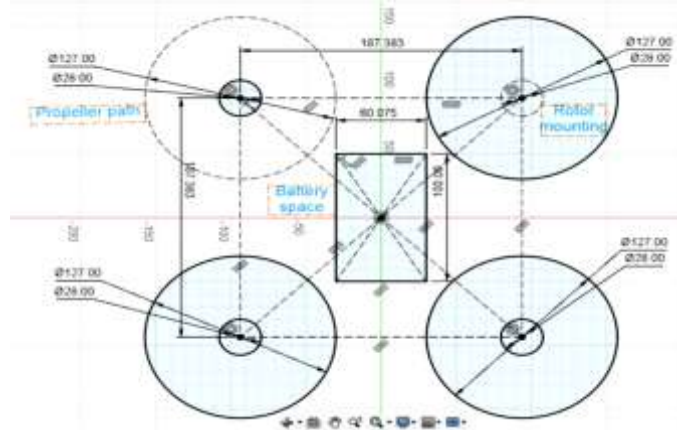


Fig-1: Basic Keep out sketch

Front Profile view sketch: The front profile view sketch maintained some curve shape. This shape helps reduce drag when lifting the vehicle. Also with this below sketch a minimum ground clearance is maintained.

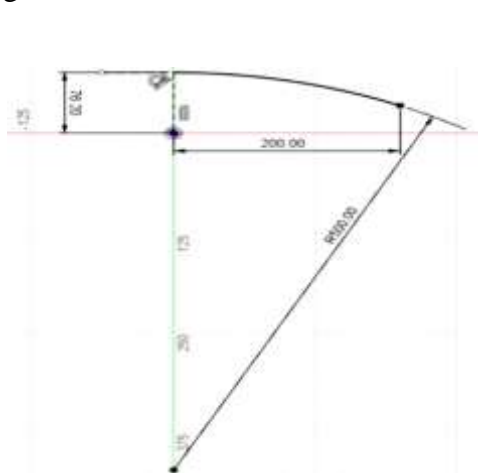


Fig-2: Front profile view sketch

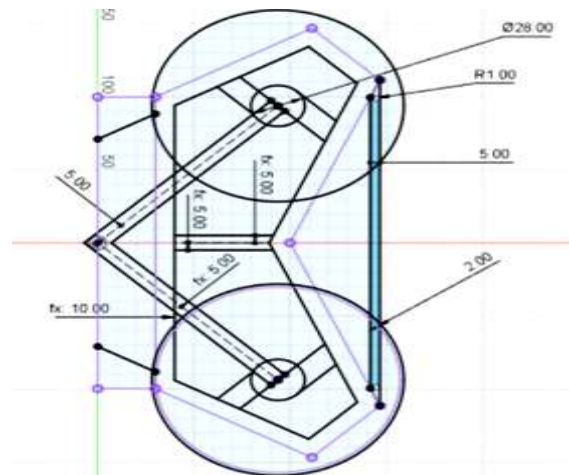


Fig-3: Top down cut view sketch

Top Down cut view sketch: It is the sketch geometry for the Box X frame formation. Box X frame is nothing but shape of the drone from the top view, it seems to be like an Box x shape. Motor mounting specifications: Brush-less motor is used in multi rotors. For this design the motors are going to mount on the frame in the reverse direction. That means the motor propellers are in downside. Considered FPV racer motor DYS 2205-2300 KV.

Extruding the above sketches will get box X frame shape. The landing leg is very important for most of the drones with this it can able to land properly on the ground. Here in this design landing leg should be act like protective guard to the inside propeller. Sketch drawn with

some dimensions from the corners of box x frame and lofted a surface from corner edge to the landing leg sketch. Then by extrude cut the surface with reference to the sketch obtains a nice shape. Then the components can be combined with the tool. Apply round fillets with a radius of 2 mm to all the edges of the frame. Mirror all the Landing leg features to the other side, and similarly mirror the half-modeled frame through the origin axis. Use the combine tool to merge the mirrored bodies into a single entity.

The frame design has several gaps in the body that can be filled using a generative mesh arrangement. It's nothing but arranging a mesh like structure using form tool. Resulting in a more aesthetically pleasing design. This mesh helps to improve the air flow during takeoff and landing also covers the in and out way. Create a compartment below the frame for the battery and other components. Sketch a front view of the design and extrude it to a length of 100 mm, 34 mm height, thickness 1 mm, width 63 mm taking into account from the factors such as the propeller path, clearance from propeller path to battery base height. By symmetrically extruding the above battery compartment sketch will get the battery space. Make sure sketch must be drawn at the center.

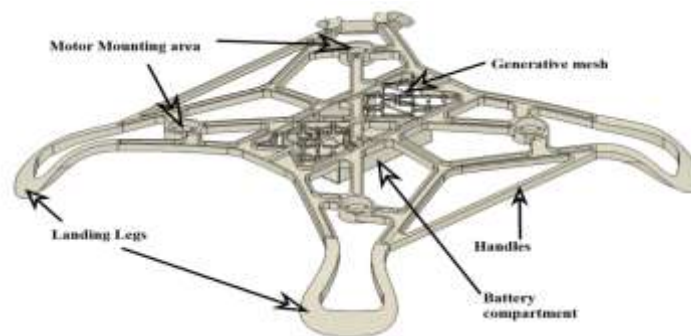


Fig-4: Modeled drone

Table - 1 drone properties after the adding the materials

Material - 1		Material - 2	
Physical Material	Nylon 6/6	Physical Material	Nylon 12
Density	0.001 g / mm ³	Density	0.001 g / mm ³
Area	1.906E+05 mm ²	Area	1.906E+05 mm ²
Mass	231.293 g	Mass	207.754 g
Volume	2.047E+05 mm ³	Volume	2.047E+05 mm ³
<u>Bounding Box</u>		<u>Bounding Box</u>	
Length	424.66 mm	Length	424.66 mm
Width	452.176 mm	Width	452.176 mm
Height	77.271 mm	Height	77.271 mm
Center of Mass	-0.14 mm, 5.884 mm, 36.836 mm	Center of Mass	-0.14 mm, 5.884 mm, 36.836 mm
Moment of Inertia at Center of mass (g mm ²)	Ixx = 3.074E+06 Ixy = 319.019 Ixz = 31883.739 Iyx = 319.019 Iyy = 3.185E+06 Iyz = -50042.692 Izx = 31883.739 Izy = -50042.692 Izz = 6.544E+06	Moment of Inertia at Center of mass (g mm ²)	Ixx = 2.761E+06 Ixy = 286.553 Ixz = 28638.934 Iyx = 286.553 Iyy = 2.861E+06 Iyz = -44949.851 Izx = 28638.934 Izy = -44949.851 Izz = 5.878E+06
Moment of Inertia at Origin (g mm ²)	Ixx = 3.630E+06 Ixy = 308.635 Ixz = 1211.012 Iyx = 308.635 Iyy = 3.744E+06	Moment of Inertia at Origin (g mm ²)	Ixx = 3.261E+06 Ixy = 277.225 Ixz = 1087.767 Iyx = 277.225 Iyy = 3.363E+06

	Iyz = -50231.099 Izx = 1211.012 Izy = -50231.099 Izz = 6.545E+06		Iyz = -45119.085 Izx = 1087.767 Izy = -45119.085 Izz = 5.879E+06
--	---	--	---

ANALYSIS

Once the Drone is modeled then open modeled file in the simulation workspace.

Material Properties:

Table - 2 Marble Properties

Density	2.69E-06 Kg/mm ³
Young's Modulus	54 Gpa
Poisson's Ratio	0.2
Yield strength and Ultimate tensile strength	9 Mpa

Table - 3 Nylon 6/6 Material Properties

Density	1.13E-06 Kg/mm ³
Young's Modulus	2930 Mpa
Poisson's Ratio	0.35
Yield strength and Ultimate tensile strength	82.75 Mpa

Table - 4 Nylon 12 (With Form Labs Fuse 1 3D printer) Material Properties

Density	1.015E-06 Kg/mm ³
Young's Modulus	1850 Mpa
Poisson's Ratio	0.35
Yield strength	46 Mpa
Ultimate tensile strength	50 Mpa

(Static)Center load Test on Nylon 6/6 material



Fig-5: Safety Factor of center Load test

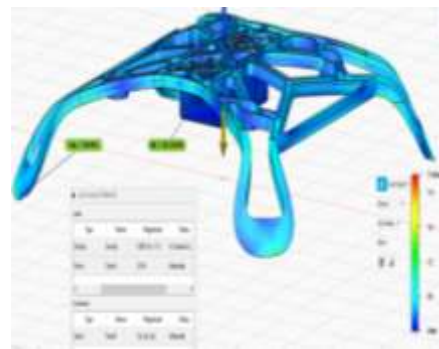


Fig-6: Von Mises stress distribution

(Static)Center load Test on Nylon12(Form labs) material



Fig-7: Center load case safety factor

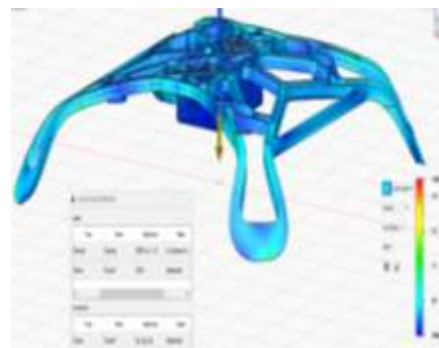


Fig-8: Center load case Von Mises Stress distribution

(Static)Battery compartment Load test on Nylon 6/6 material

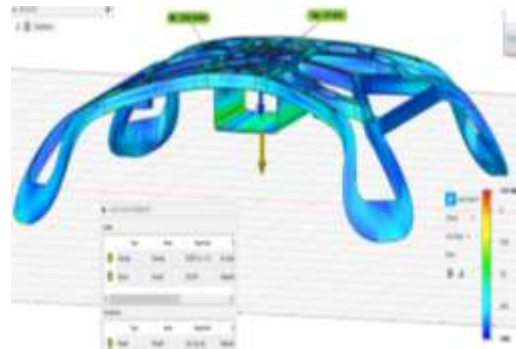


Fig-9: Safety Factor of Battery Compartment Fig-10: Von Mises Stress of Battery Compartment
(Static)Battery compartment Load test on Nylon 12(Form Labs) material

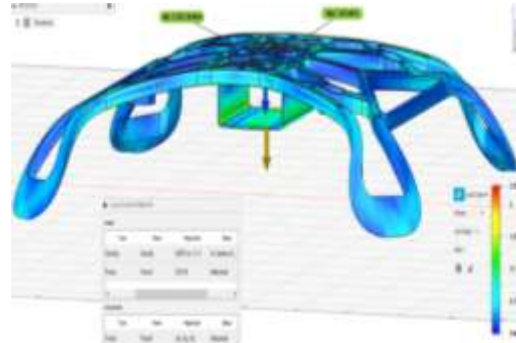


Fig-11: Safety Factor of Battery Compartment Fig-12: Von Mises Stress of Battery Compartment

Dynamic analysis(Crash Test)

Table - 5 Simulation information

Movement	Dynamic (Considers inertia)
Total event duration	0.001s
Number of result intervals	25
Drone Material (Crash test1)	Nylon 6/6
Drone Material (Crash test2)	Nylon 12
Rigid Body material	Marble

Table - 6 Load Case

Constraints Fixed	Ux, Uy, Uz, Rx, Ry, Rz
Loads	
Gravity Magnitude	9.807 m/s ²
Initial Linear Velocity	100 Mph (44.7m/s)

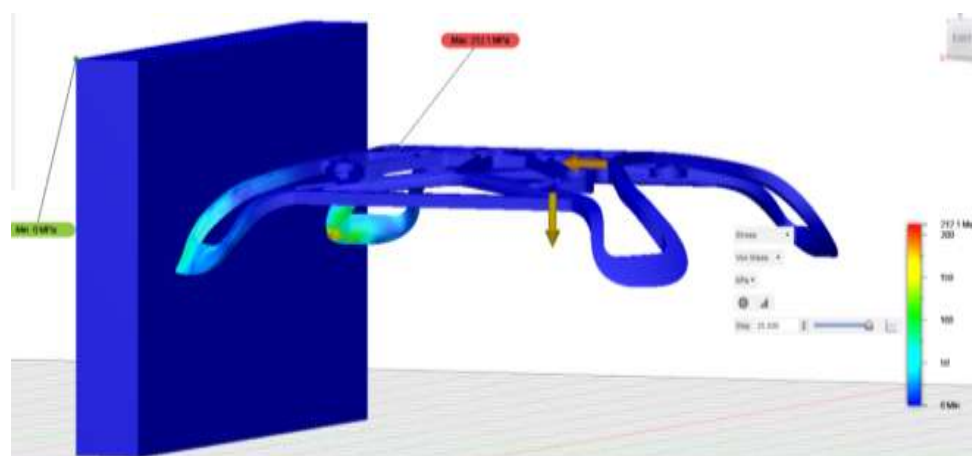


Fig-13: Nylon 6/6 with Rigid Marble Body (Crash test)

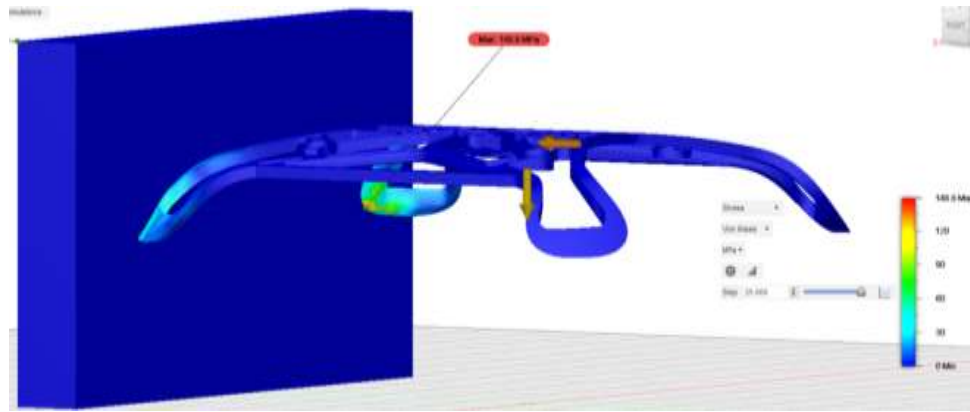


Fig-14: Nylon 12 (Form Labs) with Rigid Marble Body

Stress is raised in the drone due to rapid transfer of energy that occurs during the collision with rigid body. Rigid body is the body that does not deform under stress. When object strikes the rigid body, the kinetic energy of moving object is rapidly transferred to the rigid body. Result in sudden and intense force being applied to the rigid body. The reaction that produces high levels of stress and deformation within the body in above scenario.

Below the values are obtained by Fusion 360 Simulation

Table - 7 Simulation Values from the static and dynamic analysis

	Nylon 6/6	Nylon 12 (Form Labs)
Center load test Safety factor Von Mises stress	15 Max: 3.433 Mpa Min: 2.16E-06 Mpa (negligible)	15 Max: 2.688 Mpa Min: negligible
Battery compartment test Safety Factor Von Mises stress	15 Max: 3.451 Mpa Min: 2.983E-06 Mpa (negligible)	15 Max: 3.433 Mpa Min: 3.161E-06 Mpa (negligible)
Crash Test (Von Mises Stress)	212.1 Mpa	148.8 Mpa

Note: Crash test can be done as per FAA (Federal Aviation Administration) speed regulation.

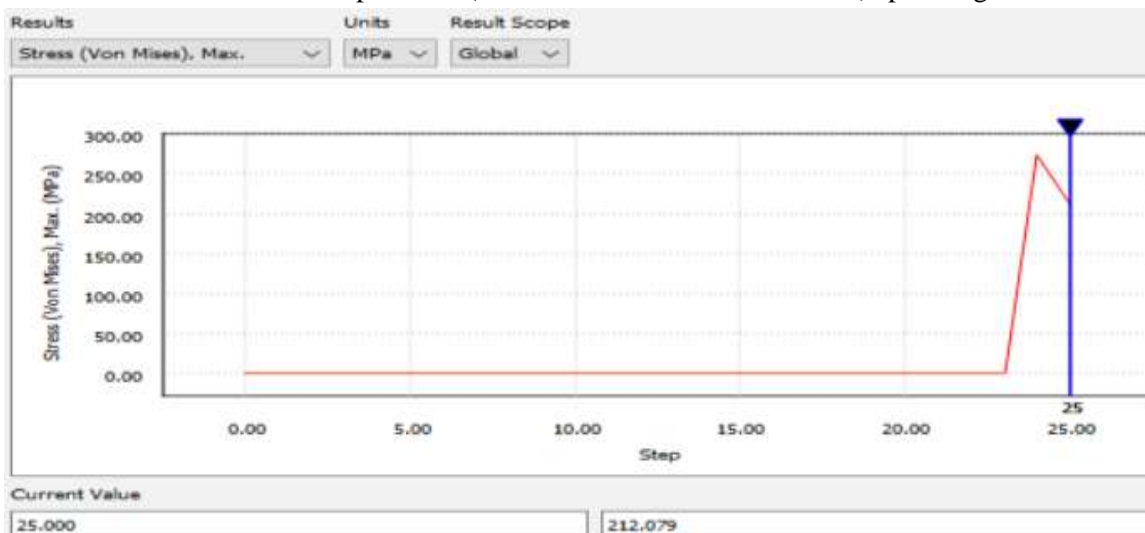


Fig-15: Graph of stress in Nylon 6/6 material



Fig-16: Graph of stress in Nylon 12(Form Labs) material

CONCLUSION

After conducting the thorough analysis, it has been determined that the use of this design and Nylon 12(Form Labs Fuse 1 3D printer) is the most effective solution for crash testing and other performances assessments. By utilizing this material the drone design that can withstand collisions with rigid bodies without damaging the propulsion system. This conclusion came from the observation of actual deformation view. This finding Highlights the importance of selecting the appropriate materials for drone design to ensure both safety and efficiency. These results provides valuable guidance for future design decisions, with the potential to lead to the development of even better and safer drones.

REFERENCES

- [1]. <https://interestingengineering.com/innovation/a-brief-history-of-drones-the-remote-controlled-unmanned-aerial-vehicles-uavs>
- [2]. <https://cfdflowengineering.com/classification-and-application-of-drones/>
- [3]. <https://yourtechdiet.com/blogs/drone-technology-and-its-future-uses-and-applications/>
- [4]. <https://www.jouav.com/blog/drone-types.html>
- [5]. <https://www.techtarget.com/iotagenda/definition/drone#:~:text=Essentially%2C%20a%20drone%20is%20a,often%20associated%20with%20the%20military.>
- [6]. <https://builtin.com/drones>
- [7]. <https://www.sculpteo.com/en/industries/drones/3d-printed-drone/>
- [8]. <https://www.instructables.com/Design-a-Micro-Drone-in-Autodesk-Fusion-360/>
- [9]. <https://cormack.xyz/GenerativeDrone/>
- [10]. <https://uavsystemsinternational.com/blogs/drone-guides/recreational-use-of-drones>
- [11]. <https://drones.stackexchange.com/questions/1094/how-does-the-center-of-gravity-affect-a-quadcopter>
- [12]. Autodesk Fusion 360 User manual 2021-22.

Design and Fabrication of Total Emissivity Measuring Apparatus

Dr.M.Naga Swapna Sri¹, Dr.P.Anusha², Rumalla Haranath³, Dr.K.Srividya⁴,
Neelapu Nikhil Babu⁵,Pajjuru Jaswanth Rakesh⁶,Nimmakuri Vineeth⁷, Pamu
Rahul⁸, Muppalla Praveen Chowdary⁹

^{1,2}Assistant Professor, Department of Mechanical Engineering, P V P Siddhartha Institute of
Technology, Vijayawada, India.

³Assistant Professor, Maturi venkata subba rao(MVSR) Engineering college, Hyderabad.

⁴Associate Professor, Department of Mechanical Engineering, P V P Siddhartha Institute of
Technology, Vijayawada, India.

^{5,6,7,8,9}B.Tech Student, Department of Mechanical Engineering, P V P Siddhartha Institute of
Technology, Vijayawada, India.

Abstract: The invention of the present work is to find out the emissivity of a test specimen by comparing with the reference specimen of known emissivity. The primary objective of the present work is to determine the total emissivity of the given sample to high accuracy using simple and economical experimental setup. In this experiment used in black body at a specified temperature and wave length no surface can emit more energy than a black body. It absorbs all incident radiation, regardless of wavelength and direction, and gray body used it uses all the real surfaces are approximated as gray surfaces. The heat emitted from the surface passes through the heat flux sensor, the hemispherical total emissivity of the surface can be calculated using the Stephen-Boltzmen law of radiation. Emissivities of metals at high temperatures influence the energy balance in a wide range of manufacturing process as well as research and development activities and there by determine performance even economic viability. Accurate and comprehensive measurements of metals thermal emissivity have always been a challenge due to numerous influential factors. An experimental setup for emittance measurement in air at high temperature was developed during the course study. Thermostats and temperature sensors can be mounted directly on the heaters for direct temperature control. Substances absorb different frequencies and radiate out lower frequencies due to collision consumption. Emissivity is also dependent on the temperature of the object and the incident wavelength of light on the material. The total emissivity measuring apparatus is designed and analyzed based on geometrical and thermal constrains. Suitable materials were selected based on their mechanical properties, cost and availability in the market. The efficiency of the equipment increases with increase in operating temperature. The calibrated efficiency is found to be higher than the previous equipment's.

Keywords — Emissivity, black body, gray body, incident radiation, Innovation

1. Introduction

The overall capacity of its surface to produce energy by radiation is the emissivity of material (generally composed ϵ or e). Emissivity is the proportion of at similar temperatures, the energy emanated by a specific material to the energy transmitted by a dark body. A genuine dark body has an emissivity(ϵ) = 1 while any genuine item has emissivity(ϵ) < 1. Emissivity is a dimensionless amount. Emissivity relies upon factors like temperature, frequency, and discharge point. That a surface phantom emissivity and absorptive don't rely upon frequency

is an average designing presumption, so the emissivity is consistent. This is known as the "gray body presumption".

$$\varepsilon = \frac{\text{Emissive Power Of Body}}{\text{Emissive Power Of Blackbody}} = \frac{E}{E_b}$$

Giovanni Tanda [1] examined the estimation of absolute hemispherical emittance and explicit warmth of aluminium and Inconel 718 by a calorimetric method. S Moghaddam [2] examined the Heat Flux-Based Emissivity Measurement. Zhang R-H [3] concentrated on emissivity scaling and relativity of homogeneity of surface temperature. RuiPitarma [4] assessed wood emissivity by a methodology technique. Petra Honnerova Jiri [5] examined the emissivity estimation strategy for cloudy coatings at encompassing temperature. Seban R.A. [6] introduced the emissivity of progress metals in the infrared. Yunus A Cengel [7] printed a book on warmth and mass exchange. Naga Swapna M [8-10] contemplated the Radiation Effect of MHD Casson liquid stream straightly permeable extending sheet in the presence of substance response.

2. Theory

Preceding beginning the essential target of the paper is to decide the all-out emissivity of the offered test to high exactness utilizing basic and practical test arrangement.

The exact estimation of emissivity is needed in different applications like:

Thermography:- Thermal imaging cameras identify radiation in the infrared scope of the electromagnetic range (around 9000–14,000 nanometres or 9–14 μm) and produce pictures of that radiation, which is called thermo grams. To make a temperature estimation of an item, the thermograph alludes to the emissivity table to pick the emissivity estimation of the article and afterward went into the camera. The camera's calculation rectifies the temperature by utilizing the emissivity to figure a temperature that all the more intently coordinates with the real contact temperature of the article.

Brilliant barriers:- or (intelligent hindrances) forestall heat move by warm radiation. Brilliant hindrance materials have low emissivity (generally 0.1 or less) at the frequencies to which they are relied upon to work. Brilliant Barriers has different applications like space investigation, materials fire vicinitysuit, space cover,thermolite, window medicines, developments.

Sun-based thermal collectors:- The surface coatings of sunlight-based level plate gatherers ought to consistently be made of materials that have high emissivity esteem almost to that of the dark body i.e $\varepsilon = \text{one}$.

The emissivity estimated in this methodology is the absolute emissivity of the test by comparison with the reference test of higher emissivity were the two examples are having the same measurements. This methodology is unique concerning the ordinary one utilized in emissimeters which is worried about the estimation of otherworldly emissivity of the radiation. The technique utilized in this paper can be utilized to decide the absolute emissivity of various materials of square state of side 0.028m and 0.001m thickness. The extent of the paper includes a plan and depiction of the device, which is introduced in detail in the coming sections.

3. Design considerations

A. Design considerations

1. Area of the specimen $\leq (1/1000)$ X Total Surface area of the enclosure

- Enclosure is cuboidal in shape
where Length (l) = 1m or 1000mm,
Breadth (b) = 0.75m or 750mm,
Height (h) = 1m or 1000mm.
- Total surface area of enclosure = $2(lb+bh+hl)$
 $= 2(1 \times 0.75 + 1 \times 0.75 + 1 \times 1) = 5 \text{ m}^2$ or $5 \times 10^6 \text{ mm}^2$
- $(1/1000) \times$ Total Surface area of the enclosure = $5/1000 = 0.005 \text{ m}^2$ or 5000 mm^2
- Area of the square shaped specimen = $0.028 \times 0.028 = 0.000784 \text{ m}^2$ or 784 mm^2

2. The temperature difference between specimen and surrounding is maintained as high as possible.

- Temperature at the specimen surface, $T_s \geq 100^\circ\text{C}$
- Temperature in the surrounding, T_a or $T_\infty = 27^\circ\text{C}$

B. Design parameters

Power parameters

- Power rating of heater: 3.3W to 11.36W
- Input Voltage range: 10V to 18V AC
- Resistance of heater: 28.5Ω
- Current carrying capability of heater: 0.35 to 0.63A

Geometric parameters

- Geometric Shape of specimen: Square
- Side length: 28mm or 0.028m
- Area of cross section of specimen: 784 mm^2 or 0.000784 m^2
- Thickness of specimen: 1mm or 0.001m
- Size of enclosure: Length (l) = 1m or 1000mm,
Breadth (b) = 0.75m or 750mm, Height (h) = 1m or 1000mm.
- Total surface area of enclosure: $5 \times 10^6 \text{ mm}^2$ or 5 m^2

Thermal parameters

- Maximum operating temperature of heater: 120°C
- Maximum value of Syndanio insulation temperature: 350°C
- Maximum value of ceramic fiber blanket insulation temperature: 983°C
- Maximum temperature which alumina plate can withstand: 1750°C
- Temperature measuring range of FeK thermocouple: -50 to 900°C

C. Specimen holder

The example holder is made of syndanio cover block. Two square scores of 28 mm^2 are sliced up to a profundity of 9mm is cut. For this reason, 2 syndanio sheets 9mm and 12mm are utilized independently. Absolutely 6 subset screws alongside nuts are utilized to hold it. The earthenware fiber up to a thickness of 2mm is set inside the sections to give protection just as padding impacts the base size of the heater. The warmer is put on it. The alumina plate of 1mm thick is set on the heater to forestall direct contact between the heating component (silver palladium) and aluminium plate else it will prompt short out. On the highest point of a warmer sandwich aluminium plate of 4mm thick plate is set which gives a

Dept. of Mech. Engg. PVPSIT 223

stage to put test and reference examples. This aluminium plate is put in the furrows. The two thermocouples are utilized to decide the temperature of the test and reference examples. Third thermocouple is utilized for estimating encompassing temperature inside the container. The specimen holder sectional, top view and 3D views are shown in Figure.1 (a),(b) and Figure.2.

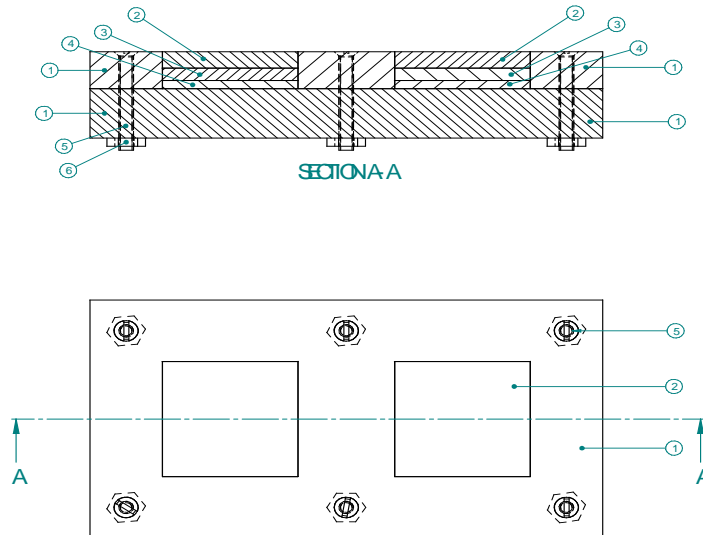


Figure 1 Specimen holder (a) Sectional view (b) Top view

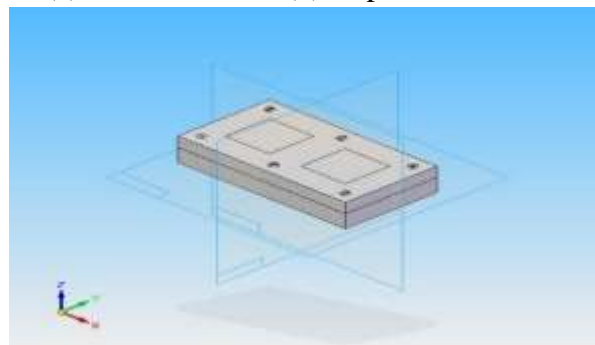


Figure 2 Specimen holder 3-dimensional view

Table 1 Part Labeling Table

Comp. No.	Name	Qty	Breadth (in mm)	Length (in mm)	Thickness (in mm)	Other Specifications
1	Syndanio	1	58	106	21	
2	Aluminium	2	28	28	4	
3	Heater + Alumina plate	2	28	28	3	
4	Ceramic Fiber Blanket	2	28	28	2	
5	Counter sink screws	6	-	-	-	8mm diameter 390mm length Counter sink angle $\alpha = 120^\circ$
6	Nuts	6	-	-	-	5mm hole

D. Test cabinet

The test bureau comprises of fenced-in area and control board shown in Figure.3. The whole bureau is made of gentle steel CR. To forestall rusting of gentle steel it is painted. Within dividers of the nook is painted with a dark matte paint to assimilate heat. To keep the warmed surface from seeing its appearance on the lower part of the chamber, within dividers of the nook are covered with 2 layers of steel wire network. The nook is furnished with 2 ways to approach the examples which are put on the example holder and part labelling detail shown in Table.1. and Cross sectional view of test cabinet is illustrated in Figure.4.

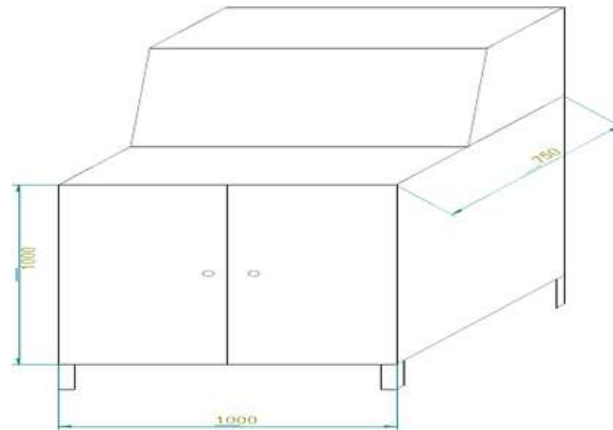


Figure 3 Test cabinet

Overall dimensions of enclosure:-

Length = 1m or 1000mm

Breadth = 0.75 or 750mm

Height = 1m or 1000mm

Total surface area = 5 m^2 or $5 \times 10^6 \text{ mm}^2$

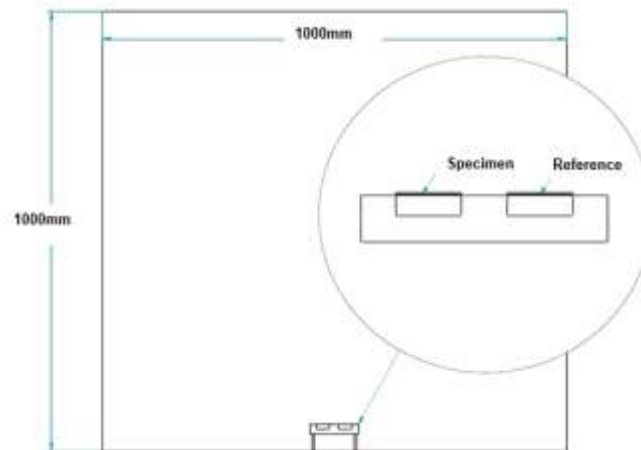


Figure 4 Cross sectional view of test cabinet Inset: enlarged view of specimen setup

E. Electric circuit diagram

The circuit for every heater is the same. The power supply which is an auto variable transformer (230V AC to 0-20 V AC) is utilized to work warmer. The single-stage voltmeter and ammeter are associated in equal and arrangement to the warmer to gauge voltage and current separately provided to the heater. The computerized temperature regulator is utilized to control the temperature from the warmer. Three thermocouples are utilized, one each for heater and the other for encompassing is utilized and the list of electric components used for the study displayed in Table.2.

Table 2 List of electric components used

Serial No.	Component Name	Quantity (In No's)
1	POWER SUPPLY	2
2	AMMETER	2
3	VOLTMETER	2
4	DIGITAL TEMPERATURE CONTROLLER	2
5	THERMOCOUPLES	3

Figure. (5-13) showed the View of finished apparatus, Specimen Holder, Anodized Aluminium, Alumina ceramic substrate, Aluminium plate, Mild Steel, Syndanio board, Ceramic Fiber Blanket, Screen printed ceramic heater, FeK thermocouple for this experimental work



Figure 5 View of finished apparatus

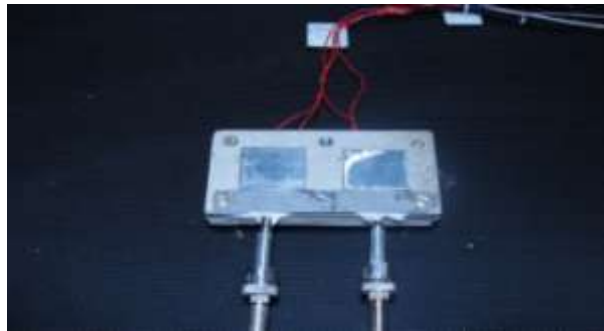


Figure 6 View of Specimen Holder

4. Materials Used

A. Reference specimen

Anodized aluminium having $\epsilon = 0.84$ is utilized as a reference example. The aluminium was anodized up to 6 microns profundity. Softening place of anodized aluminium is 2050°C and a lot higher than unadulterated aluminium is 658°C .

Benefits of Anodizing: -

To increment consumption opposition.

To increment surface hardness.

To permit coloring

Improved lubrication

Improved adhesion.

Anodized coatings have a much lower thermal conductivity and coefficient of linear expansion aluminium.

Anodizing: -

Anodizing is an electrolytic passivation measure used to build the thickness of the normal oxide layer on the outside of metal parts. The part to be dealt with structures the anode-cathode of an electric circuit.

In commonplace business aluminium anodization measures, the aluminium oxide is become down into the surface and out from the surface by equivalent sums. So anodizing will expand the part measurements on each surface by half of the oxide thickness. Anodized aluminium surfaces are more diligently than aluminium yet have low to direct wear opposition.



Figure 7 Anodized Aluminium (black)

B. Test specimen

Alumina which is otherwise called aluminium oxide is utilized as test example. There is 98% of Al_2O_3 . Aluminium oxide is an electrical encasing however has a generally high warm conductivity ($30 \text{ Wm}^{-1}\text{K}^{-1}$). Its hardness makes it reasonable for use as a grating and as a segment in cutting apparatuses.



Figure 8 Alumina ceramic substrate

Specimen holding surface

Aluminium is utilized as a base surface on which test example and reference examples are set. pure aluminum is soft, ductile, and erosion safe and has electrical conductivity. It is generally utilized for foil and conductor links.

Advantages:

- Lighter metal
- Good thermal conductivity of 204.2 W/mK



Figure 9 Aluminium

4. Test cabinet

Mild steel (CR) is utilized to make the whole assemblage of the testing bureau. Carbon steel is once in a while alluded to as 'mild steel' or 'plain carbon steel'. Regularly carbon preparations are strong and stiff. Anyway, welding carbon steel presents far fewer issues than welding treated steel. The consumption opposition of carbon prepares is poor (for example they rust) thus to forestall this they are painted.

Benefits: -

Cheap

Wide assortment accessible with various properties

High stiffness
Magnetic properties
Most carbon prepares are easy to machine and weld



Figure 10 Mild Steel

E. Syndanio insulation board

The example holder is made of syndanio. It is made of asbestos fiber and Portland concrete under high tension. It can withstand temperature up to 350°C.

Benefits: -

- Mechanically strong
- Good curve and heat-resisting qualities
- Good machine capacity



Figure 11 Syndanio board

F. Ceramic fiber insulation

The base side of the heater is covered with ceramic fiber which goes about as a separator and gives padding impact to forestall harm to the heater. The ceramic fiber of thickness 0.002m or 2mm and 0.028 x 0.028 m² or 28 x 28 mm² area is utilized. It is a protecting material and can withstand 983°C.

Benefits: -

- Non-flammable
- Non-toxic
- Resistant to erosion
- Low thermal conductivity 0.06 W/m-k
- Low weight by volume
- Light and meager subsequently permits more space as valuable floor territory



Figure 12 Ceramic Fiber Blanket

Electrical devices

G. Screen-printed ceramic heater

A screen-printed ceramic heater is a kind of heating component that changes overpower into heat through the interaction of Joule heating. Electric flow through the component experiences obstruction, bringing about the heating of the component. By using printed thick film innovation the heaters can all the more productively spread the warmth across the surface, and are more savvy frameworks when contrasted with carved foil or wire components.

The plan consolidates printed thick film innovation as the dynamic warmth source. The ink can be planned in different examples and densities, concentrating power precisely where it is required. The element traces can be widened or narrowed to allow for cut-outs and holes.

Thick film technology

Thick film innovation began as half and half circuits for military and car applications are given their high unwavering quality. The expression "thick film" identifies with the circuit or heating component that is saved through screen printing (.005 inches thick) on the substrate. Inks made by blending earthenware production and metals (known as cermet inks) are utilized to make the resistors and transmitters. Regularly, these are metallic materials like silver, gold, silver palladium, gold platinum, copper, and ruthenium.

Clay inks are additionally utilized for the dielectric layer (glass under the circuit) and typify over the circuit layers.

A common thick film interaction would comprise of the accompanying stages:

(1) Ink preparation: -

Inks for cathodes, terminals, resistors, dielectric layers, and so forth are ordinarily set up by blending the metal or ceramic powders needed with a natural vehicle to deliver glue for screen-printing. To accomplish a homogeneous ink the blended segments of the ink might be gone through a three-move plant. On the other hand, instant inks might be acquired from one of the numerous organizations offering items for the thick film technologist.



Figure 13 Screen printed ceramic heater

(2) Screen Printing: -

Screen-printing is the way toward pushing ink through a designed woven cross-section screen or stencil utilizing a wiper.

(3) Drying/Curing: -

In the wake of permitting a timeframe after printing for the settling of the ink to happen, each layer of ink that is saved is typically dried at a respectably high temperature (50 to 200°C) to dissipate the fluid part of the ink and fix the layer incidentally in position on the substrate so it very well may be taken care of or put away before conclusive preparing. For inks dependent on polymers and some bind glues that fix at these temperatures this might be the last advance that is required. A few inks likewise require relief by openness to UV light.

(4) Firing: -

For large numbers of the metal, clay, and glass inks utilized in thick film measures a high temperature (typically more prominent than 800°C) terminating is needed to fix the layers in position for all time on the substrate.

Benefits: -

Uniform and proficient heating

High temperature can be acquired (100-120°C for our situation)

Small dimensions

Low power utilization 3.3 to 11.36W Faster heating capacity

H. Digital temperature regulator

Thermostats and temperature sensors can be mounted straightforwardly on the warmers for direct temperature control. Warm wires/TCO'S are accessible for over-temperature/runaway condition security. The UDIAN TC is utilized in our paper that can gauge the temperature in the reach 0-999°C. It has 0.3%FS $\pm 1\text{oC}$ precision, power supply voltage 100-240V AC and force utilization is $\leq 2\text{W}$.

I. Power supply

The auto variable variac transformer which can change 230V AC over to 20V AC with 2A current rating is utilized.

J. Voltmeter

The single-stage 0-30V ANALOG voltmeter is utilized forestimating applied voltage across the warmer.

K. Ammeter

The single-stage 0-2A ANALOG ammeter is utilized for estimating current going through the radiator.

L. Thermocouple

A thermocouple is utilized for estimating temperature. It comprises 2 unique metals, combined toward one side. At the point when the intersection of the two metals is warmed or cooled a voltage is created that can be associated back to the temperature. J type Iron Constantantan having temperature range - 40 to 750°C yet higher affectability $55\mu\text{V}/^\circ\text{C}$ is utilized. Table.3 shows thermocouple observation.



Figure 14 FeK thermocouple

5. Calculations &Inference

A. Sample

Test plate: Alumina,Reference plate: Anodized aluminium and Table.4 displayed the total emissivity of various material surfaces

Table .3 Thermocouple Observations: -

Particulars		
Test plate	V_t in Volts	12
	I_t in Amps	0.36
Temperature on test plate $^\circ\text{C}$		88
Reference plate	V_r in Volts	13
	I_r in Amps	0.36
Temperature on reference plate in $^\circ\text{C}$		87
Ambient temperature T_a in $^\circ\text{C}$		27

Emissivity of test plate ϵ	0.62
-------------------------------------	------

Table.4 Total emissivity of various material surfaces

Material	Temperature $^{\circ}\text{C}$	emissivity
Stainless steel	216	0.44
Steel	500	0.35
Silver	200	0.02
Brass	200	0.03
Asbestos	200	0.96
Ceramic	93	0.90
Copper	20	0.07
Graphite	3600	0.80
Glass	200	0.95

B. Improvements achieved over the previous equipment

- The heat misfortune through the radiators is limited toward all paths aside from one, along these lines making unidirectional warmth stream.
- This strategy gives exact outcomes than the prior one because of a decrease in heat misfortunes because of convection by utilizing the example of more modest measurements.
- Efficient and uniform warming of screen printed ceramic radiators when contrasted with mica warmers.
- In the prior technique the reference and test example were fixed. In this technique, various examples can be utilized.
- Power utilization is 6W, which is low contrasted with the past one, which is 120W and the each parameter notation are shown in Table.5.

Table.5 Nomenclature of each parameters

NOMENCLATURE			
ϵ	Emissivity	V_t	Test plate in volts
E	Emissive power of body	V_r	Reference plate in volts
E_b	Emissive power of black body	I_t	Test plate in Amps
T_s	Temperature at the specimen surface	I_r	Reference plate in Amps
T_a or T_{∞}	Temperature in the surrounding (Ambient Temperature)	A_t	Test plate area
l	Length (size of enclosure)	A_r	Reference plate area
b	Breadth (size of enclosure)	T_t	Test plate temperature
h	Height (size of enclosure)	T_r	Reference plate temperature
σ	Stefan-Boltzmann constant	ϵ_t	Test plate emissivity
Q	Rate of Heat transfer	ϵ_r	Reference plate emissivity

6. Conclusions

The absolute emissivity estimating contraction is planned and broke down dependent on mathematical and warm limitations. Appropriate materials were chosen dependent on their mechanical properties, cost, and accessibility on the lookout. The plan is finished utilizing SOLID EDGE v18. The manufacture was done dependent on the plan boundaries. Protection

for the whole contraction is never really a heat misfortune. To accomplish a serious level of precision touchy thermocouples are utilized. The effectiveness of the hardware increments with expansion in working temperature. The adjusted effectiveness is discovered to be higher than the past hardware.

Following steps can be implemented in future to improve the accuracy of the apparatus:

- Better and exact, electronic and electrical estimating instruments can be utilized
- Vacuum siphon can be utilized to empty the air from the fenced in area where the example is kept. With this the impacts of the convection can be diminished.
- Heater with better plan can be utilized.

References

- [1] Giovanni Tanda & Mario Misale, Measurement of total Hemispherical Emissivity and Specific Heat of Aluminium and Inconel 718 by a Calorimetric Technique, *J. Heat Transfer*, vol.128, no.3, pp.302-306, 2006, doi:10.1115/1.2150840.
- [2] Saeed Moghaddam, John Lawler, Collin McCaffery & Jungho Kim, Heat Flux-Based Emissivity Measurement, *AIP Conference Proceedings*, vol. 746, 32, 2005, doi.org/10.1063/1.1867115.
- [3] Zhang. R.-H., Zhao-Liang Li, Tang.X.-Z., & Xiaomin Sun, Study of Emissivity Scaling and Relativity of Homogeneity of Surface Temperature, *International Journal of Remote Sensing*, vol. 25, pp.249-259, 2010, doi:10.1080/0143116031000115184.
- [4] Rui Pitarma & João Crisóstomo, An Approach Method to Evaluate Wood Emissivity, *Journal of Engineering*, pp.1-9, 2019, doi:10.1155/2019/4925056.
- [5] Petra Honnerová, Jiří Martan, Zdeněk Veselý, & Milan Honner, Method for emissivity measurement of semitransparent coatings at ambient temperature, *Scientific reports*. Article number 1386, 2017, doi:10.1038/s41598-017-01574-x.
- [6] Seban, R. A., The Emissivity of Transition Metals in the Infrared, *J. Heat Transfer*, vol.87, no.2, pp.173-176, 1965, doi.org/10.1115/1.3689067.
- [7] Yunus A Cengel, & Afshin J. Ghajar, *Heat and Mass Transfer: Fundamentals and Applications*, Book, 2017.
- [8] S P Samrat, CSulochana, G P Ashwinkumar, Impact of Thermal Radiation on an Unsteady Casson Nanofluid Flow Over a Stretching Surface, *International Journal of Applied and Computational Mathematics*, vol.5, no.2, 2019, doi.org/10.1007/s40819-019-0606-2.
- [9] S Idowu Amos, T Mojeed Akolade, Jos U. Abubakar and Bidemi O Falodun. MHD free convective heat and mass transfer flow of dissipative Casson fluid with variable viscosity and thermal conductivity effects, *Journal of Taibah University for Science*, vol.14, no.1, pp.851-862, 2020, doi: 10.1080/16583655.2020.1781431.
- [10] Ullah, K Bhattacharyya, S Shafie, I Khan. Unsteady MHD Mixed Convection Slip Flow of Casson Fluid over Nonlinearly Stretching Sheet Embedded in a Porous Medium with Chemical Reaction, Thermal Radiation, Heat Generation/ Absorption and Convective Boundary Conditions. *PLoS ONE*, vol. 11, no.10, 2016, doi:10.1371/journal.pone.0165348.

Landmine Detection Robotic Vehicle with GPS Positioning

Dr. T. HARITHA¹, L. DORA BABU², P. PUJITHA³, M. NIHARIKA⁴

¹Associate Professor, Dept of ECE, Prasad V. Potluri Siddhartha Institute of Technology,
Vijayawada, AP, India,

^{2,3,4}UG Students, Dept of ECE, Prasad V. Potluri Siddhartha Institute of Technology,
Vijayawada, AP, India

E-mail: harithat4770@gmail.com

Abstract: Landmines are explosive devices that will explode when triggered by pressure. It is approximated that there are nearly 110 million unexploded landmines around the world. When these landmines explode they will cause severe damage to the people and economy. To avoid these consequences a robot is designed, which is capable of detecting landmines. The robot starts moving in the field and it senses the metal elements nearby, it sends an image along with its GPS coordinates to the nearby monitoring station. The robot also uses a camera for navigating purposes to avoid human interaction within the field.

Introduction:

As we know now, a landmine is an explosive device buried under or on the ground to defeat enemies but also harms the people's existence [2]. When it detonates, these fragments can kill up to 35 meters or more from the landmine and harsh injuries at more than 100 meters. After the explosion of a landmine, it can act for up to 50 years. Landmines are inexpensive and effective when deployed, but are expensive and dangerous to remove. It is approximated that there are 110 million landmines in the ground right now [1]. This purpose is pleased by employing a robot. A robot possesses a metal detector that will spot the line, GPS (Global positioning system) [3] to pursue the location of the mine which is covered and then sends the GPS co-ordinates along with the captured image to the monitoring station for further processing.

Landmines are explosive devices made of plastic, metal, and other materials, containing explosives or sometimes pieces of metal concealed under or on the ground that explode when applied to external pressure to destroy the target. These landmines are extensively used in war times and have an indefinite life and may cause horrific personnel injuries, and economic losses for decades even after the war was finished. To prevent the consequences like casualties, land degradation, loss of biodiversity, and chemical contamination, countries that are most affected by the mines follow various traditional mine detection techniques like using dogs and rats and prodders [4].

Dogs have been used in landmine detection. They are almost a million times more sensitive compared to humans in detecting chemicals, but their true capability is unknown. Well-trained mine detection dogs can sniff out explosive chemicals. Rats have the advantage of being far lower in mass compared to dogs resulting in less probability to set off mines. The main disadvantage of this approach is that the thick vegetation can disturb them and they get confused if there is a high density of mines. Prodder on the other hand is a rod-like structure inserted into the ground about 30cm that makes acoustic or electromagnetic measurements during insertion. The echo received gives information about the type of material detected. Both these techniques involve humans at the site which involves reduced safety, accuracy, and a time-consuming process [6].

Over 60 countries are affected by landmines and face severe consequences with the presence of them regularly. The majority of casualties occur in countries like Egypt, Iran, Iraq, Syria, Afghanistan, and others most of which are economically on the weaker side [7]. Over 110 million landmines are estimated to be buried, covering around 3000 Km² land worldwide. Deactivation at a pace of 1 lakh landmines per year results in the clearance of land to be

completed in 500 years, excluding the 2 million mines installed each year. This poses a difficult task in front of the countries most affected in the world [7].

To detect the mines in the world without the need for endangering personnel and operation being economically feasible for poor regions of the world [5], and at a faster pace compared to the traditional methodologies in landmines detection, we proposed a project “Land Mine Detection using UGV [Unmanned Ground Vehicle]”. This project produces a prototype for landmine detection and marking robot that uses GPS localization, a prototype for metal detection, and a landmarking system using GPS. This robot detects the presence of mines using a metal detector and marks the mine presence spot and sends the GPS coordinates to the base station.

Tools required

Jetson nano Development Board:

The ports on this Jetson nano board are as follows: a 40-pin header, a Micro-USB port for 5v power input, a Gigabit Ethernet port, a USB 3.0 port, an output port, a microSD card slot for primary storage, a USB 3.0 port, a display port connector for tasks like speech processing, object detection, object segmentation, and image classification [9]. A Jetson nano board is a small computer that operates in multiple networks simultaneously. It has a quad-core ARM A57 64-bit CPU, a 128-core Maxwell GPU, 4GB of memory, and a DC power adapter built in. A low-power system is the Jetson Nano Board.

Metal detector:

A metal detector is an electronic device that locates metal in the area [8]. They are frequently employed in the detection of landmines or to uncover hidden metal inclusions. Fine buried metal components, which are made up of a proximity sensor probe that can be swept across the ground. A buzzer indicates whether the sensor detects any nearby metal. It also gives information about the distance i.e., how close the metal is present by increase or decrease in the volume of the buzzer. Typically, a well- equipped device can find metal materials up to 6 to 10 inches underground.

L298N motor driver:

A DC motor can be driven in either direction and its speed can be managed using the motor driver integrated chip (IC), model number L298N. We can drive up to two DC motors with a single L298N. There are two H-bridge circuits in L298N [12]. Each motor can be driven by one of the two enable pins, two input pins, and two output pins. The module has an on-board 78M05 5v regulator. When the power supply is less than or equal to 12V, then the internal circuitry will be powered by the voltage regulator.

Wi-Fi dongle:

Dongles are compact, mobile Wi-Fi USB sticks that can be connected to laptops, smartphones, or tablets to give them easy access to the internet while they are in motion. It performs the role of a portable internet modem, so when a dongle is plugged into a computer, the device is essentially connecting to a modem. USB stick for those who travel frequently or work from a computer and require constant internet access, Wi-Fi is a very helpful tool. An easy-to-use plug-and-play gadget called a Wi-Fi dongle enables you to use the internet while you're on the road.

Camera module:

A lightweight, portable Logitech USB webcam that works with Jetson nano development board for live monitoring and image capturing has been employed in the project. It uses the USB interface protocol to talk to the Jetson nano development board. The usual applications for it are in surveillance, machine learning, and image processing. It is commonly used in surveillance drones since the payload of a camera is very less. In addition to these modules, Jetson nano can make use of CSI interface specially designed Camera sensors developed by Jetson nano community.

Neo 6M GPS Module:

Global Positioning is a satellite-based navigation system that consists of at least 24 satellites orbiting around the earth every 24 hours in 6 orbitals. Neo-6M GPS module is a GPS receiver that is able to track 22 satellites. It consists of a high- performance u-blox 6 positioning engines. Antenna is firmly attached to the module via U.FL connector [10].

Work Done

Detection:

While the rover is in motion, metal detector keeps on identifying the surrounding metal objects buried on the ground. Whenever there is a metal object identified with in the detector's range, it provides a signal through a buzzer along with control signal to Jetson nano, which indicates the camera to capture an image of the surrounding place of the ground and the Neo-6M module provides the GPS co-ordinates of the place the image was taken. The image along with the GPS co-ordinates were sent to the monitoring station for further processing like identifying the type of mine, and it's demining technique which can be included in the future scope.

Rover Control:

Using the complete potential of Jetson nano development board, the mounted camera module has been used for real- time monitoring from the monitoring station over a remote hand. A Web page developed has been used for the controlling the rover manually from a remote location by monitoring the visuals from the camera module [11].

Result

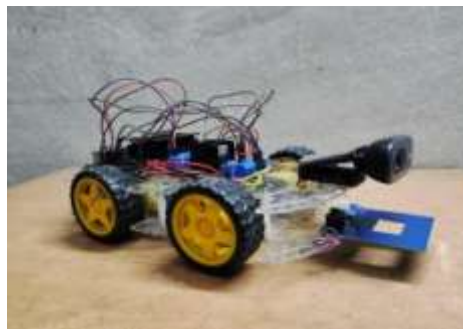


Fig-1 Landmine Detection Rover Profile

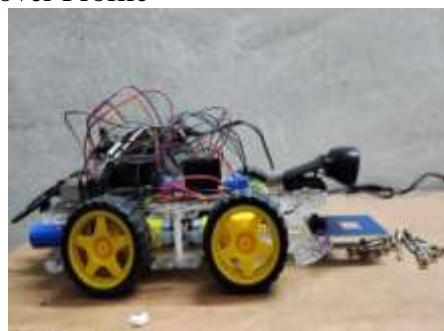


Fig-2 Landmine Detection Rover detected metal objects on the ground



Fig-3 Captured image by the camera equipped on Landmine Detection Rover

Reference

1. V. Prakash and P. Sreedharan, "Landmine Detection Using A Mobile Robot," 2021 IEEE 9th Region 10 Humanitarian Technology Conference (R10-HTC), Bangalore, India, 2021, pp. 01-05, doi: 10.1109/R10-HTC53172.2021.9641540.
2. Ebada, Ahmed & Elmogy, Mohammed & El-Bakry, Hazem. (2014). Landmines Detection Using Autonomous Robots: A Survey. International Journal of Emerging Trends & Technology in Computer Science (IJETTCS). 3. 183-187.
3. V. Abilash and J. P. C. Kumar, "Arduinio controlled landmine detection robot," 2017 Third International Conference on Science Technology Engineering & Management (ICONSTEM), Chennai, India, 2017, pp.1077-1082, doi: 10.1109/ICONSTEM.2017.8261366.
4. Rocks, Trevor Anthony, and Brendan Devon Casey. Landmine Detection Rover. : Worcester Polytechnic Institute, 2017.
5. M. K. Habib, "Mine detection and sensing technologies-new development potentials in the context of humanitarian demining," IECON'01. 27th Annual Conference of the IEEE Industrial Electronics Society (Cat. No.37243), Denver, CO, USA, 2001, pp. 1612-1621 vol.3, doi:10.1109/IECON.2001.975531.
6. Y. S. Alqudsi, A. S. Alsharafi and A. Mohamed, "A Review of Airborne Landmine Detection Technologies: Unmanned Aerial Vehicle-Based Approach," 2021 International Congress of Advanced Technology and Engineering (ICOTEN), Taiz, Yemen, 2021, pp. 1-5, doi: 10.1109/ICOTEN52080.2021.9493528.
7. M. Zucchetti, M. Khoder, I. Makki, R. Younes, C. Francis and T. Bianchi, "Landmines," 2017 First International Conference on Landmine: Detection, Clearance and Legislations (LDCL), Beirut, Lebanon, 2017, pp. 1-6, doi: 10.1109/LDCL.2017.7976954.
8. C. L. Brown, A. M. Zoubir, I. J. Chant and C. Abeynayake, "Landmine detection using single sensor metal detectors," 2002 IEEE International Conference on Acoustics, Speech, and Signal Processing, Orlando, FL, USA, 2002, pp. IV-3948-IV-3951, doi:10.1109/ICASSP.2002.5745521.
9. S. Cass, "Nvidia makes it easy to embed AI: The Jetson nano packs a lot of machine-learning power into DIY projects - [Hands on]," in IEEE Spectrum, vol. 57, no. 7, pp. 14-16, July2020, doi:10.1109/MSPEC.2020.9126102.
10. A. M. Luthfi, N. Karna and R. Mayasari, "Google Maps API Implementation On IOT Platform For Tracking an Object Using GPS," 2019 IEEE Asia Pacific Conference on Wireless and Mobile (APWiMob), Bali, Indonesia, 2019, pp. 126-131, doi:10.1109/APWiMob48441.2019.8964139.
11. M. R. Guggilla, K. Deepa and M. Nithya, "Internet Based Real Time Control of Rover Using Live Video Streaming," 2022 International Conference on Innovations in Science and Technology for Sustainable Development (ICISTSD), Kollam, India, 2022, pp. 325-329, doi: 10.1109/ICISTSD55159.2022.10010523.
K. Ren, J. Lin and S. Cai, "The design of networked DC motor speed control platform based on WiFi," 2017 Chinese Automation Congress (CAC), Jinan, China, 2017, pp. 5613-5618, doi: 10.1109/CAC.2017.8243783.

Simulation of Heat Stratification in Thermal Energy Storage Tank Using Fluent

¹Dr.G. Naga Malleswara Rao, ²Shaik Chand Mabhu Subhani

¹Principal & Professor, ²Assistant Professor, Dept. of Mechanical Engg, Eswar College of Engineering, Kesanupalli(Po), Narasaraopet(Md), Palanadu(Dt), AP,
Email:gnmr26@gmail.com, skcmsubhani@gmail.com

Abstract: Heat energy is major energy source which generate the power and used in all applications of human needs in case of transportation, house hold, domestic & power plants etc. A water storage tank maintains the sensible heat transfer & it is the best choice to heat addition in thermal energy systems. These type of tanks have the advantages of low maintenance and high thermal conductivity. The hot water from the mantle heat exchanger is collected at bottom inlet portion of the tank and a heat stratification arrives due to difference in temperature which gives rise of hot water to a weight variation in the different locations of water. This article presents the analysis of thermal stratification in heat exchange water tank by three dimensional fluent analysis methods. Especially, this paper concentrates on both steady state and transient analysis. In this analysis the steady state condition takes place at different inlet temperatures of mantle fluid and at different intervals of time were considered. A different outside drum sizes, by changing the inside drum material such as stainless steel, copper and inlet temperature of working fluid was used and compared with each other by using the ANSYS fluent methods. It may be expected from its calculation that the Validation of results with experimental data will have a good consistency. Results from the paper may guide the engineers to establish this type of heat energy storage tanks in heat integration and distributed systems. The effectiveness of the storage tanks was calculated.

Keywords: *Heat Energy Storage, HVAC system, ANSYS Fluent, Drum size & Materials, Working fluid*

Introduction

The Thermal energy storage tank is a necessary concept that the way of increasing the heat stratification. In many applications, the Separation of different fluids which have different temperatures will interact with each other in the heat stratification tank and the hot fluid of the inner tank will move up due to loss of density.

Water is the one best fluid for sensible heat transfer in tanks. The heat storage tank is an important mechanical device for heat interaction between two fluids. The effectiveness, inlet mantle fluid and inner tank water properties are terms in performance of the tank.

The factors effecting the stratifications are

- Energy interaction between storage tank and outside atmosphere.
- Leakages of tank causing the mixing of two fluids
- Thermal diffusion and conduction
- Length to diameter ratio of both tanks
- Variation in the tank thickness

Thermal energy storage tank with Solar water heater

A Thermal energy storage tank is vessel of cylindrical shape having two tanks immersed one in another (tank in tank). The outer tank is called as mantle tank and middle tank is called the inner tank. The inner tank is filled with the cold water. The mantle tank is filled with the mantle fluid with different temperatures. The cold water flow rate in inner tank will maintained at zero and the mass flow rate of mantle fluid is in mantle tank. The temperature

of cold water in inner tank is the ambient temperature where as the temperature maintained by mantle fluid is high. The total tank is insulated & there is no heat interaction with surrounding.

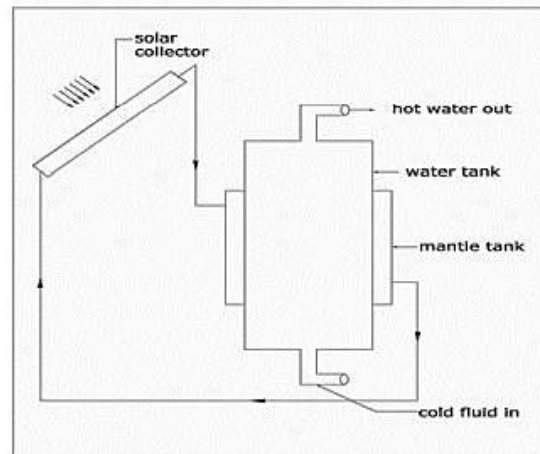


Fig 1: Thermal energy storage tank with solar water heater

Literature Review

Zurigat [1], Shyu, [2] investigated the factors influencing the thermal stratification degradation in solar energy tanks are forced convection flow through the tank, heat loss to the surrounding environment, thermal mixing at inlet, natural convection flow induced by conduction within the tank walls and heat diffusion inside the tank due to the vertical temperature gradient within the tank.

Lavan and Thompson [3] performed an experimental study on a thermally stratified, vertical hot water storage tank. Experimental measurements were made on various height/diameter ratios, inlet port location and geometry, inlet-outlet temperature difference and different mass-flow rate. Their study showed that better thermal stratification can be obtained by increasing the ratio of the tank height to its diameter, increasing the diameter of the inlet port, or increasing the difference between the inlet and outlet water temperature.

Cole and Bellinger [4] concluded that maximum thermal stratification could be achieved inside the storage tank with a height to diameter ratio of four. The studies of Ismail et al. [5] and Hahne and Chen [6] confirmed Cole and Bllinger's conclusion while Nelson et al. [7] suggested aspect ratio of three for the best thermal stratification.

Lightstone et al. [8] showed that in the dynamic mode, the effect of wall thermal conductance on the thermal stratification degradation is negligible. Mixing flow in the inlet opening is considered one of the most important parameters in the degradation of thermal stratification. Therefore, in order to reduce the inlet mixing, different inlet configurations were considered and studied.

EXPERIMENTAL SETUP

Description of experiment

In this paper, the heat interaction takes place between the mantle fluid and the inner tank cold water were investigated under certain boundary conditions. In this analysis, the convection analysis of the cases steady state and transient in between the both tanks were analyzed. This is not only sufficient to analyze about the heat interaction between to fluids and the study of heat stratification at different locations of the inner tank also done.

The theme of this paper is to find the overall characteristics in stratification process in thermal energy storage tank at different cases and conditions were considered. The analysis is performed in ANSYS modeling package.

Table 1: Details of Thermal Energy Storage Tank (Mantle Tank)

Data Of Mantle Tank	
Volume of inner tank [mm ³]	31000000
Inner tank volume from end of the mantle [mm ³]	16000000
Inner tank diameter [mm]	200
Wall thickness of both tanks [mm]	1
Mantle tank diameter[mm]	260
Mantle upper portion height from bottom of the inner tank [mm]	500
Mantle bottom portion height from bottom of the inner tank [mm]	100
Mantle inlet valve position from top of mantle[mm]	10
Mantle inlet valve diameter [mm]	12.5
Mantle tank volume[mm ³]	8700000
Inner tank inlet size[mm]	25

Experimental methodology

The mantle is connected to the cold water circulation inner tank at 100 mm above from bottom of the tank. The two fluids in these experiments consider are water and water. The cases considered are mass flow rates of mantle fluid at 1ltr/sec at inlet temperature are 50⁰C, 65⁰C & 75⁰C and for cold water is 25⁰C.

The cases for analysis consider are as shown in Table

Table 2: Details of Experimental cases

S.No	Type Of Analysis	Material (Mantle & Inner Tank)	Mantle Fluid Inlet Temperature(⁰ c)	Cold Water Inlet Temperature (⁰ c)	Mass Flow Rate (Liter/Sec)
1	Steady State	Steel & Steel	50 ⁰ c	25 ⁰ c	Mass Flow Rate Of Mantle Fluid Is 1 Liter/Sec
2			65 ⁰ c		
3			75 ⁰ c		
4	Steady State	Copper & Copper	50 ⁰ c	25 ⁰ c	
5			65 ⁰ c		
6			75 ⁰ c		
7	Transient	Steel & Steel	50 ⁰ c	25 ⁰ c	Mass Flow Rate Of Mantle Fluid Is 1kg/Sec
8			65 ⁰ c		
9			75 ⁰ c		
10	Transient	Copper & Copper	50 ⁰ c	25 ⁰ c	
11			65 ⁰ c		
12			75 ⁰ c		

Measurement of experimental parameters

The analyzed parameters are:

- The mantle fluid flow rate at inlet and out let
- The inlet temperature of mantle fluid
- The mantle fluid outlet temperature
- The cold water temperature in inner tank
- The temperature at different points in inner tank
- The temperature distribution at different time periods.

MODELLING OF THERMAL ENERGY STORAGE TANK

The modeling of the thermal energy storage tank performed by using ansys fluent with the dimensions mentioned in table 1.

By using the ansys, several engineering problems will get solved with the fractional variation. Ansys fluent is the place where the computation fluid dynamics, fluid flow, heat interactions analysis performed.

The fluent techniques used in this work use ANSYS 15.0 for modeling the thermal energy storage tank and analysis also takes place. This is a finite element based technique uses a mesh containing tetrahedral and prism elements. This has the benefit that the reduction of local numerical diffusion take place and also suitable for complex flows.

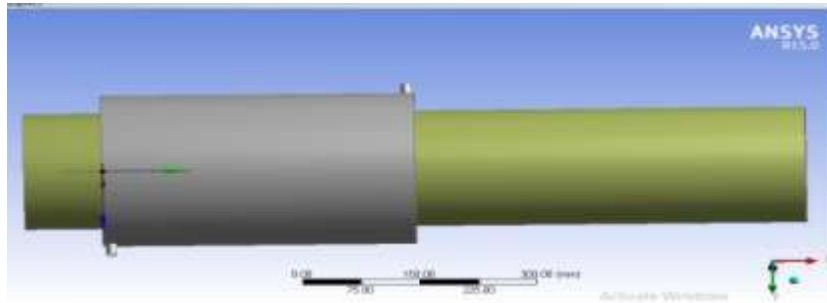


Fig 2: ANSYS Model of Thermal energy storage tank system

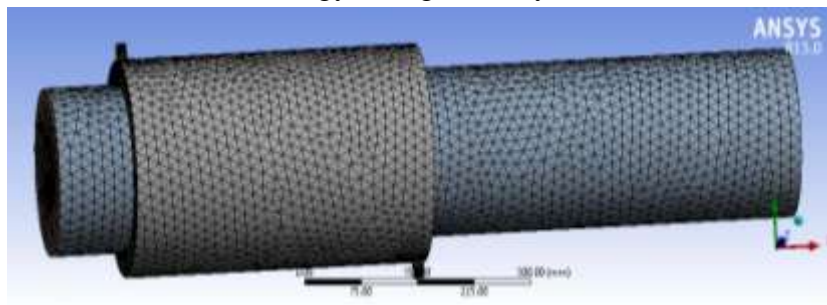


Fig 3: ANSYS Meshed Model of thermal energy storage tank system

ANALYSIS AND RESULTS

In this paper, the transient analysis and steady state analysis were performed. The material of mantle and inner tank is steel-steel and copper –copper . by considering zero mass flow rate of cold water at 25°C and 1 kg/sec mass flow rate of mantle fluid at a 50°C , 65°C & 75°C . The transient and steady state analysis results are shown below

Transient analysis

Case 1: in this case of consideration that the temperature of mantle fluid(Mantle inlet) is consider as 50°C , the materials of mantle and inner tank are steel and steel. The variation of temperature distrubution at different time intervals were recorded

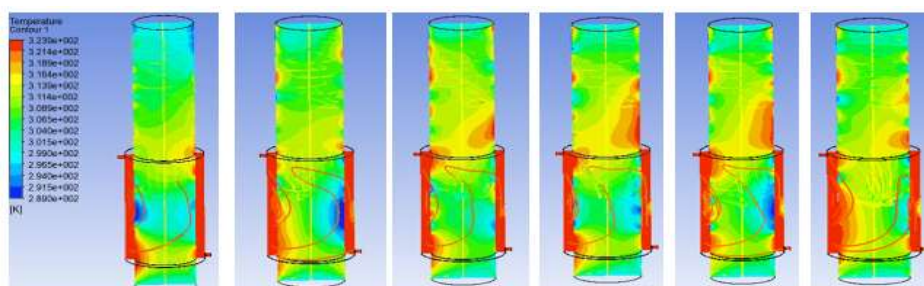
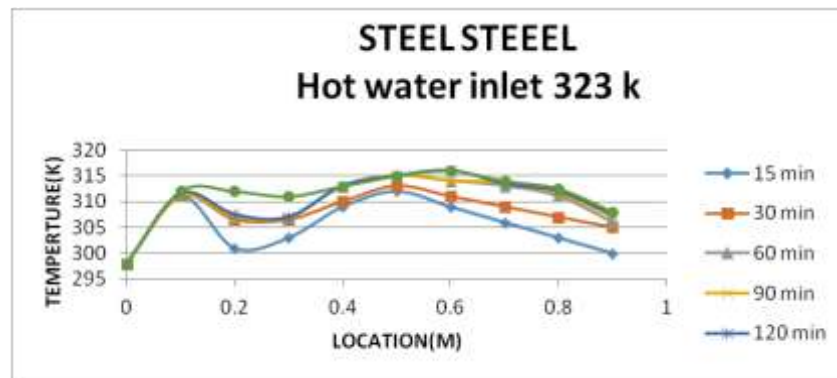


Fig 4: Temperature distribution in mantle system after time 15, 30, 60, 90, 120, 180 min at 50°C of mantle fluid flow



Graph 1: Temperature distribution in mantle at different times in steel tank 50⁰c mantle flow
From the above graph, the cold water has the temperature of 298K at entrance of the tank and increased at beginning of the mantle portion. In middle of the mantle portion there will be a slight decrease in the temperature due to resistance in tank material i.e. steel. And heated water is moved to the top of the tank by stratification process. Cold water on the top of the tank is moved to the down due to density difference between mantle fluid and cold water. After 120 min the maximum temperature reached is 317K.

Case 2: in this case of consideration that the temperature of Mantle fluid is consider as 65⁰C, the materials of mantle and tank are steel and steel. The variation of temperature distribution at different time intervals were recorded

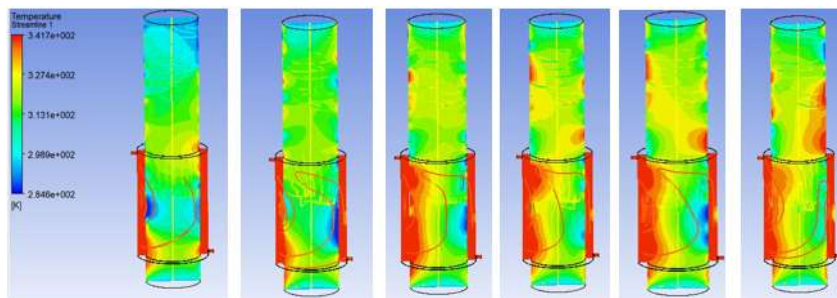
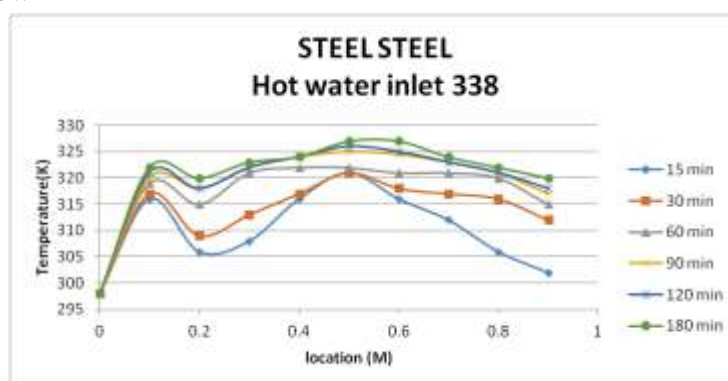


Fig 5: Temperature distribution in mantle system after time 15 ,30,60,90,120,180 min at 65⁰c of mantle fluid flow



Graph 2: Temperature distribution in mantle at different times in steel tank 65⁰c mantle flow
From the above graph, there was a variation of heat distribution from time to time and at different places of the tank. In this case the maximum temperature reached at the top of the mantle and low at the 100 mm above the bottom of the mantle. Due to the resistance of heat transfer in steel the variation in temperature takes place. The maximum temperature reached is 328K. And heated water is moved to the top of the tank by stratification process. Cold water on the top of the tank is moved to the down due to density difference between mantle fluid and cold water

Case 3: in this case consideration that the temperature of Mantle fluid is consider as 75°C , the materials of mantle and tank are steel and steel. The variation of temperature distrubution at different time intervals were recorded

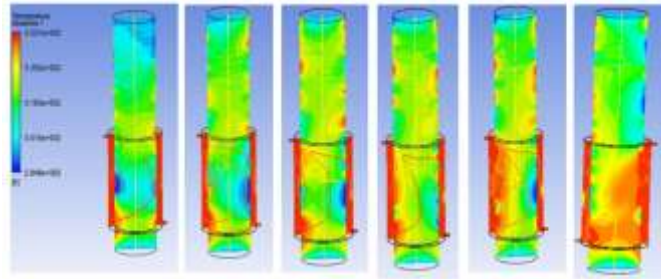
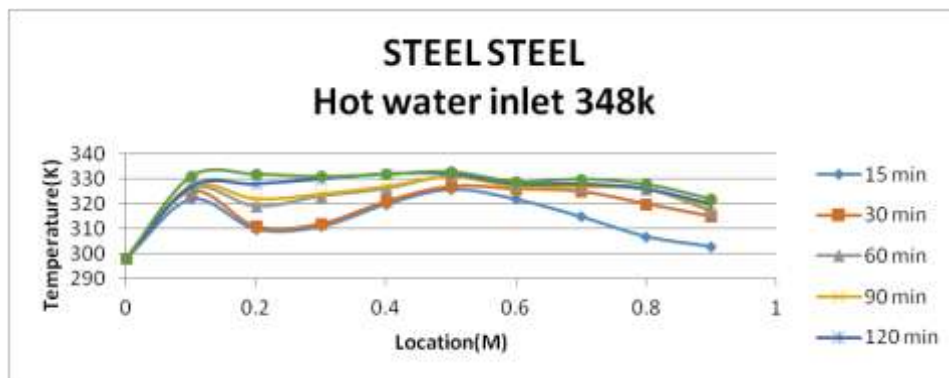


Fig 6: Temperature distribution in mantle system after time 15 ,30,60,90,120,180 min at 75°C of mantle fluid flow



Graph 3: Temperature distribution in mantle at different times in steel tank 75°C mantle flow

Case 4: in this case consideration that the temperature of Mantle fluid is consider as 50°C , the materials of mantle and tank are copper-copper. The variation of temperature distrubution at different time intervals were recorded

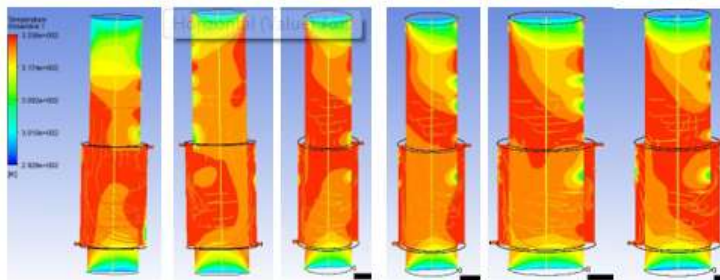
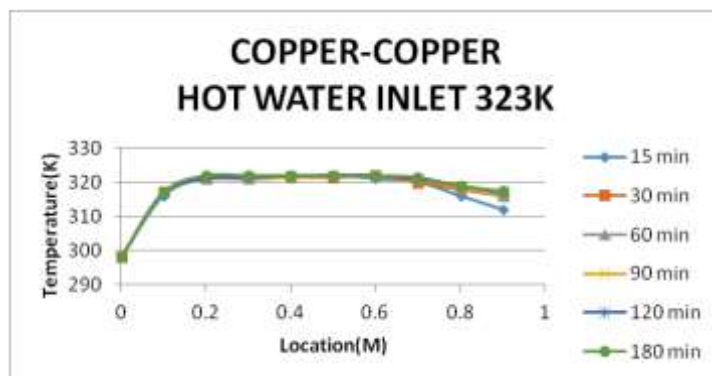


Fig 7: Temperature distribution in Mantle system after time 15,30,60,90,120,180 min at 50°C of Mantle fluid flow



Graph 4: Temperature distribution in mantle at different times in steel tank 50°C mantle flow

In this case, at the beginning of the tank have the initial temperature of 298K. the temperature gradually increased 100mm above the bottom of the mantle. After that it was nearly constant up to the top of the tank. This is happening because of the good thermal conductivity of material. heated water is moved to the top of the tank by stratification process. Cold water on the top of the tank is moved to the down due to density difference between mantle fluid and cold water.

Case 5: in this case of consideration that the temperature of Mantle fluid is consider as 65⁰C, the materials of mantle and tank are copper-copper. The variation of temperature distrubution at different time intervals were recorded.

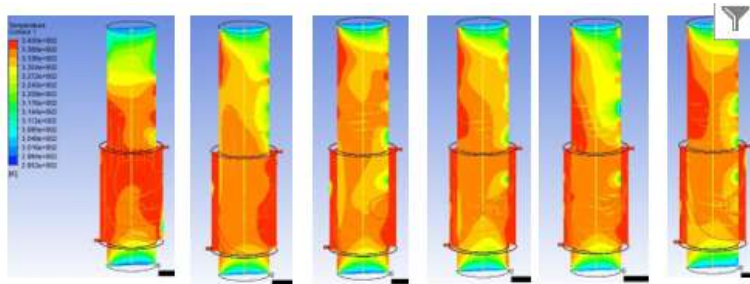
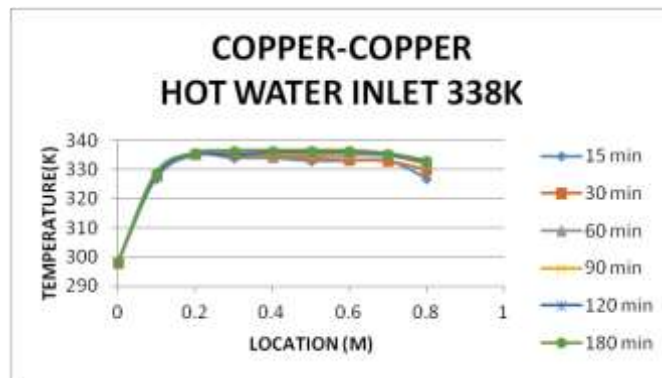


Fig 8: Temperature distribution in Mantle system after time 15 ,30,60,90,120,180 min at 65⁰c of Mantle fluid flow



Graph 5: Temperature distribution in mantle at different times in steel tank 65⁰c mantle flow
The inlet of the cold water is at 298K in the tank of Mantle system. At the distance of 200 mm from the bottom of the tank the water reached to a temperature of 332K due to the effect of mantle fluid and the transfer of heat through the copper tank. In the rest of the water in tank above the 200mm from bottom the temperature was nearly constant. The stratification takes place in the tank.

Case 6: in this case consideration that the temperature of Mantle fluid is consider as 75⁰C, the materials of mantle and tank are copper-copper. The variation of temperature distrubution at different time intervals were recorded.

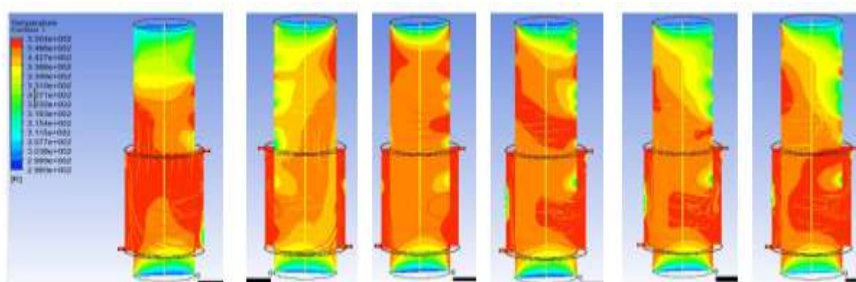
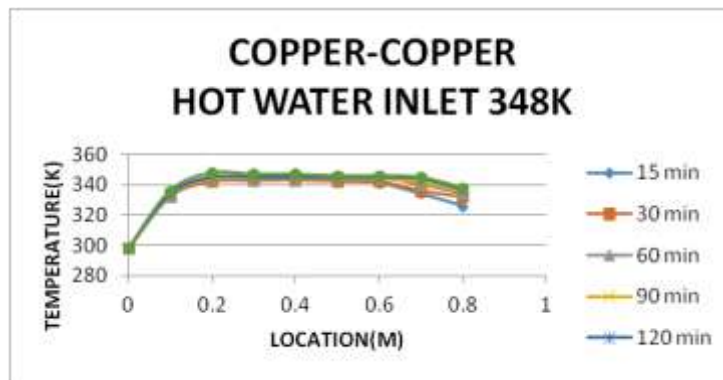


Fig 9: Temperature distribution in Mantle system after time 15 ,30,60,90,120,180 min at 75⁰c of Mantle fluid flow



Graph 6: Temperature distribution in mantle at different times in steel tank 65⁰c mantle flow
From the graph 6, the stratification process takes place for 120min. in that process the variation of temperature from bottom of the tank to top of the tank takes place. The nearly constant temperature was maintained in rest of the length of 200 mm from the bottom. The heat interaction takes place between cold water and mantle fluid because of the copper have good thermal conductivity.

STEADY STATE ANALYSIS

The following analysis report shown that for cases

Case 1: STEEL – STEEL

The mass flow rate of mantle fluid is 1kg/sec having temperature of 50⁰ C, 65⁰C & 75⁰C and no mass flow rate for cold water and the temperature consider for cold water is 25⁰C. the steady state result as shown in below.

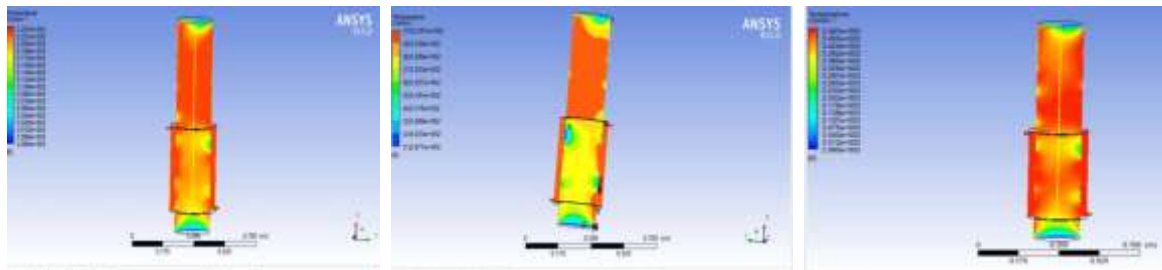
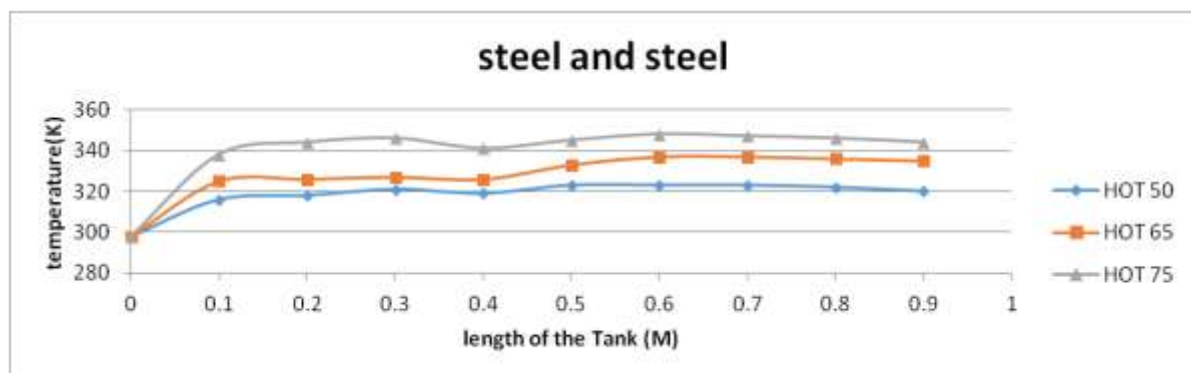


Fig 10: Temperature distribution in cold water for different mantle fluid inlets of 50⁰ C, 65⁰C & 75⁰C



Graph 7: Temperature distribution for the case steel and steel

The inlet for the above the three cases is neglected mass flow rate for cold water and the temperature is 298K . The above figure shows the temperature distribution for that three cases. The 323K, 337K and 348K are the highest temperature only at few points . the teperature distribution verses length of the tank as shown in graph.

Case 2: COPPER-COPPER

The mass flow rate of mantle fluid is 1kg/sec having temperature of 50⁰ C, 65⁰C & 75⁰C and no mass flow rate for cold water and the temperature consider for cold water is 25⁰C. the steady state result as shown in below

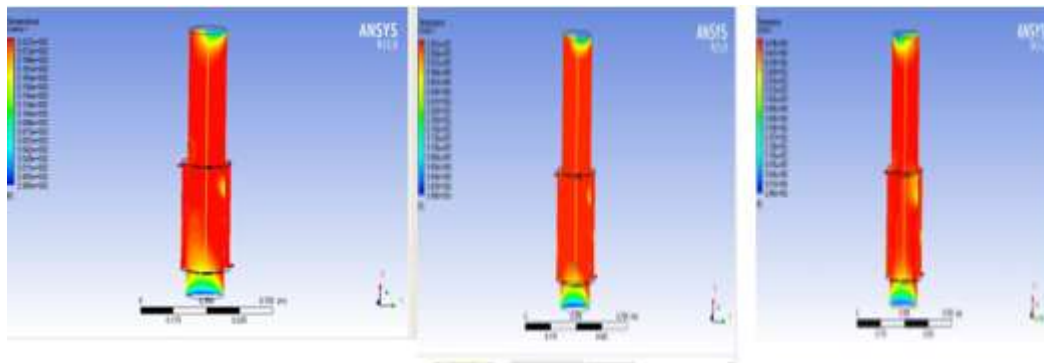
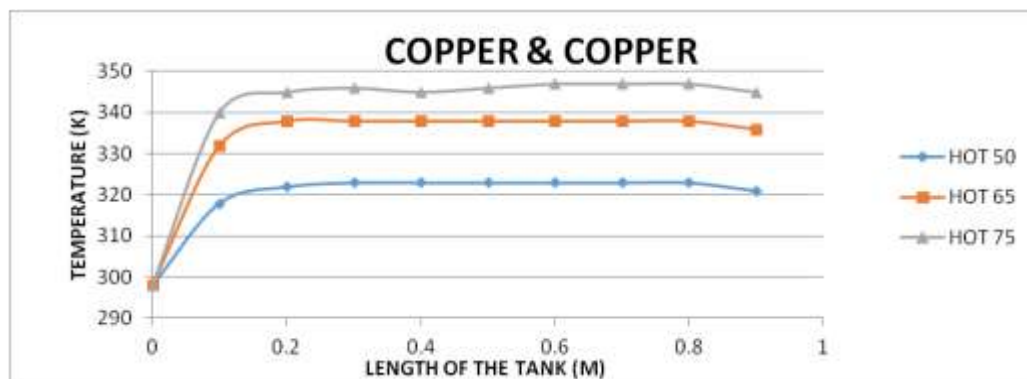


Fig 11 : Temperature distribution in cold water for different mantle fluid inlets of 50⁰ C, 65⁰C & 75⁰C



Graph 8: Temperature distribution for the case copper and copper

The inlet for the above the three cases is neglected mass flow rate of cold water and the temperature is 298K . The above figure shows the temperature distribution for that three cases. The 323K, 337K and 348K are got at maximum length of the tank. The temperature distribution versus length of the tank as shown in graph.

EFFECTIVENESS THE THERMAL ENERGY STORAGE TANK

The effectiveness (ϵ) of a heat exchanger is defined as the possibility of transfer of heat between two fluids.

$$\epsilon = \frac{Q_{actual}}{Q_{max\ possible}}$$

Q_{actual} = Heat lost by hot fluid = Heat gained by cold fluid

$$Q_{actual} = m_h c_{ph} (T_{hi} - T_{ho}) = m_c c_{pc} (T_{co} - T_{ci})$$

Substituting values of Q_{actual} and $Q_{max\ possible}$ from equations

$$\epsilon = \frac{m_c c_{pc} (T_{co} - T_{ci})}{c_{min} (T_{hi} - T_{ci})} = \frac{c_c (T_{co} - T_{ci})}{c_{min} (T_{hi} - T_{ci})}$$

if $C_h < C_c$ then $C_h = C_{min}$, the effectiveness can be expressed as

$$\epsilon = \frac{c_{min} (T_{hi} - T_{ho})}{c_{min} (T_{hi} - T_{ci})} = \frac{(T_{hi} - T_{ho})}{(T_{hi} - T_{ci})}$$

if $C_c < C_h$ then $C_c = C_{min}$, the effectiveness can be expressed as

$$\epsilon = \frac{c_{min} (T_{co} - T_{ci})}{c_{min} (T_{hi} - T_{ci})} = \frac{(T_{co} - T_{ci})}{(T_{hi} - T_{ci})}$$

The Effectiveness calculated for the Thermal energy storage tank by using the above expression C_c is less than the C_h Mantle water inlet of 75°C after stratification time of 120 min.

S.NO	MATERIAL Mantle-Tank	T_{CO} (K)	T_{ci} (K)	T_{hi} (K)	Effectiveness (ϵ)
1	Steel –Steel	333	298	348	0.7
2	Copper -copper	341	298	348	0.86

CONCLUSIONS

The fluent analysis of stratification process in thermal energy storage tank have the following conclusions are

1. In case of steel and steel material of tank and mantle, the heat distribution is low at 200 mm above the bottom of the tank due to resistance in the material.
2. In case of copper and copper material of tank and mantle, the heat distribution is small at 200 mm above the bottom of the tank and nearly constant at all times of the simulation and at all locations of the tank due to good thermal conductivity of copper.
3. Higher inlet velocity and temperature for mantle fluid result in increased stratification process.
4. TES tanks have major height to diameter ratio (aspect ratio). It increases the process of stratification between the layers of cold water in inner tank
5. Higher temperature differences between inlet water and mantle water gives greater density differences between layers.
6. The effectiveness of the steel and steel material of mantle and inner tank is less than the material of copper and copper.
7. In complete analysis, fluent is most accurate and effective package to perform the stratification in thermal energy storage tank. It increases the importance of the thermal energy storage system effectiveness and performance with suitable design

REFERENCES

- [1] Zurigat, Y.H., "A comparison study of one-dimensional models for stratified thermal storage tanks", ASME J. Solar Energy Eng. 111, 205-210.
- [2] Shyu, R.J., J.Y. Lin, and L.J. Fang. "Thermal analysis of stratified storage tanks". ASMEJ. Solar Energy Eng. 111, 54-61.
- [3] Lavan, Z. and Y. Thompson, "Experimental study of thermally stratified hot water storage tanks". Solar Energy 19,519-524.
- [4] Cole R.L. and Bellinger F.O., "Thermally stratified tanks", ASHRAE Transactions 88, 1005-1017.
- [5] Ismail, K.A.R., Leal, J.F.B., Zanardi, M.A., "Models of Liquid Storage Tanks". International Journal of Energy Research 22,805-815.
- [6] Hahne, E. and Y. Chen, "Numerical study of flow and heat transfer characteristics in hot water stores". Solar Energy 64,9-18.
- [7] Nelson, J.E.B., Balakrishnan, A.R. and Murthy, "Experiments on Stratified Chilled Water Tanks". International Journal of Refrigeration, Vol. 22, 216-234.
- [8] Lightstone, M.F., Raithby G.D., and Hollands K.G.T., "Numerical simulation of the charging of liquid storage tanks: comparison with experiment", Journal of Solar Energy Engineering 111, 225-231,
- [9] Shah, L.J. and Furbo, S. "Entrance Effects in Solar Storage Tanks", Solar Energy, Vol. 75, 337-348,
- [10] Robert Huhn. "Correlation of Design. Material, "Plow conditions and the thermodynamic losses in hot water storage tanks". 10 International Symposium on District Heating and Cooling.
- [11] Moffat R.J., (1988). "Describing the uncertainties in experimental results", Experimental Thermal and Fluid Science, pp: 3-17.

- [12] G. Naga Malleshwara Rao, K. Hema Chandra Reddy , M. Sreenivasa Reddy, Influencing parameters on performance of a mantle heat exchanger for a solar water heater - a simulation study, *International Journal of Engineering, Science and Technology*, Vol. 2, No. 2, 2010, pp. 155-164.
- [13] Lavan Z., Thompson J. 1977. Experimental study of thermally stratified hot water storage tanks. *Solar Energy* 19, 519-524.
- [14] G. Angrisani, M. Canelli, C. Roselli, M. Sasso, Calibration and validation of a thermal energy storage model: Influence on simulation results, *Applied Thermal Engineering* 67 (2) (2014) 190–200.
- [15] Sunliang, C., State of the art thermal energy storage solutions for high performance buildings, Master`s thesis, University of Jyvaskyla, Finland, 2010
- [16] Tamme, R., Bauer, T., Hahne, E. (2009) Heat Storage Media, *Ullmann's Encyclopedia of Industrial Chemistry*, Wiley-VCH Verlag GmbH & Co. KGaA
- [17] C. Nielson, A. Akbarzede, J. Andrews, Humberto R Becerra L and P. Golding, “The History of Solar Pond Science & Technology,” *Proceedings of the International Solar Energy Society*, 2005.
- [18] Research Institute for Sustainable Energy (RISE), “Solar ponds,” Research Institute for Sustainable Energy. [Online]. Available: <http://www.rise.org.au/info/Tech/lowtemp/ponds.html>. [Accessed April 22, 2010].
- [19] “Texas Renewable Energy Projects,” Texas State Energy Conservation Office. [Online]. Available: <http://www.infinitepower.org/projects.htm>. [Accessed April 22, 2010].
- [20] H. Singh, R. P. Saini, J. S. Saini, “A review on packed bed solar energy storage systems,” *Renewable and Sustainable Energy Reviews*, Vol. 14, pp. 1059-1069, 2010.
- [21] D. Jain, “Modeling the performance of greenhouse with packed bed thermal storage on crop drying application,” *Journal of Food Engineering*, Vol. 71, pp. 170-178, 2005.

Exploration of Novel Materials to Achieve Best Performance of Solar Collector for usage in Solar Water Heating

Markndeyulu Vuggirala¹, N. Alagappan², CH V K N S N Moorthy^{3*}

¹Research Scholar, Annamalai University, Chidambaram, Tamilnadu, India

²Annamalai University, Annamalai Nagar, Chidambaram, Tamil Nadu, India

³Vasavi College of Engineering, Ibrahimbagh, Hyderabad, Telangana State, India

^{3*}Corresponding Author: krishna.turbo@gmail.com

Abstract. Fossil fuels exhaust faster than the expected, if the current rate of using fossil fuels with the available reserves continued. As a result, solar energy is regarded as a very good alternative to traditional sources of energy due to its zero emissions and renewable nature. The collector is a crucial component of any solar heater. It absorbs solar energy and transfers the heat to a fluid that is passing through the collector. The purpose of this article is to provide a thorough, integrated assessment of the potential uses of various types of solar collectors for solar water heaters. In light of these findings, it is suggested that Evacuated Tube Collectors (ETCs) are best suited for Solar Water Heating. Further, it is suggested that nanofluids be used in various solar collectors for solar water heating and identified a need for more insight into the applications of various nanofluids for solar heating.

Keywords: Solar Water Heater; Nanofluids; Solar Collectors; Performance Enhancement; Heat Transfer Fluids

1. Introduction

Natural resources have always been a source of power generation and has been in use for the past few decades. The source of energy has always been a concern for the environment, due to its emissions and harmful effects. In general, The Natural resources used to produce power are hydroelectric, nuclear, natural gas, coal, wind energy, solar energy, Geothermal energy so on and so forth, but most of the power is generated by burning of fossil fuels. The fossil fuels contain carbon atoms in them which when burnt releases a few harmful gases (Greenhouse gasses) and therefore indirectly increase the surface temperature of earth. The main problem arises when the fossil fuels are extracted from the ground. Mining causes a lot of land degradation and is the main cause of deforestation. By deforestation there is a lot of temperature increase on the surface of earth and is one of the causes of Global Warming.

Another main issue with the non-renewable source of energy is that it is limited in nature, and it takes many thousands of years to regenerate them. There was an oil crisis in 1973 which caused the whole world to rethink the source of energy they use. Oil is one of the most imported natural resources, about 83% of the oil is imported from other countries and is a drain on the economy for India. The use of renewable energy helps mankind to overcome all such problems. Renewable sources of energy are the sources that can be renewed or regenerated in nature in a limited period of time. The advantage from the use of most of the sources of renewable energy is they are eco friendly and non-polluting. A few examples of renewable sources of energy are solar energy, wind energy, biogas, geothermal energy, etc. Out of all the mentioned energy sources Solar energy is unlimited, free of cost, and most importantly it's abundant in nature. Solar energy can be harnessed and used for both power generation and domestic purposes. The conversion of solar energy is evident and helpful as it has both commercial values and has no bad environmental impact. In general, the 2 methods of using solar energy for the generation of electrical energy are: solar-thermal conversion

and solar–electric conversion. A few of the advantages of using solar energy are as follows: It reduces the electricity bills. The power generated by solar is available all through the year, sustainable, clean, green and more importantly doesn't cause any emission of greenhouse gases. Diminished reliance on oil and petroleum products for power. It has very less maintenance cost and the return on investment is fast. Siddharth Suman, Mohd. Kaleem Khan n, Manabendra Pathak [1]

2. Solar Water Heater

An average family with four to five members expends one fifth of their total power consumption for heating the water only. So, water heating systems using solar energy are proven to be the cheapest and pollution free energy that can be utilized by the household people for the hot water requirement of the total family. The utilization of solar water heating has been increasing rapidly since last two to three decades and the solar water heaters are being used extensively all over the globe irrespective of the climatic conditions. Usually during summer seasons, the requirements of the solar water heating are completely satisfied, and 100% water heating can be done using solar systems due to the obvious continuous and more solar radiation availability. However, this is quite reverse and up to a maximum of 50% during the winter seasons. During rainy months, the possibility of the solar radiation availability is further lesser[15]. Consequently, a storage system for the solar radiation or heat is necessary during winter and rainy seasons for effective and complete utilization of the solar water heating.

The principle of solar water heater is that it uses only the renewable solar radiation to heat the water[10]. This solar radiation will be converted into heat energy when the sunlight falls on an absorbing surface[17]. The fluid which is in contact with that absorbing surface gets heated up. If the fluid is water, then the water gets direct heating, and the corresponding system is called direct system [4]. Else, the fluid may be other than water such as glycol-water mixture, or it may be a heat transfer fluid such as a glycol/water mixture, which first absorbs heat from the absorbing surface and transfers that heat to water for heating through a heat exchanger [8]. As the water is not heated directly, this system is called an indirect system.

The solar water heating systems whether it is direct or indirect can be developed in three basic types depending upon the principle of fluid flow as follows:

1. Active systems or forced convection systems
2. Passive Systems or natural convection systems
3. Batch Systems or passive systems with storage.

2.1 Active Systems

The principle of circulating water or any other fluid for heat transfer in active systems is forced convection[9]. That is, the fluids are being circulated forcefully with external mechanical devices such as controllers, valves, and hydraulic pumps. These systems can be of two sub-types as follows:

- Direct or Open-loop system
- Indirect or Closed-loop System

2.1.1 Direct or Open-loop Active System

The water is circulated through solar collectors and directly gets heated from the heat generated by the absorption of the solar radiation at the solar collectors as shown in the figure 1. As the water is directly in contact with the collector it is direct or open-loop active systems. Such systems are proven to be having good efficiency and also reduce the operating or maintenance cost due to a smaller number of components and simple in design. However, if the water is acidic or hard, then corrosion and scaling of the components spoil the surfaces and damage the total system. In addition, these systems are proven to be more successful and apt for the climates where the minimum temperatures are not the higher than the freezing temperature of the water for the same reason.

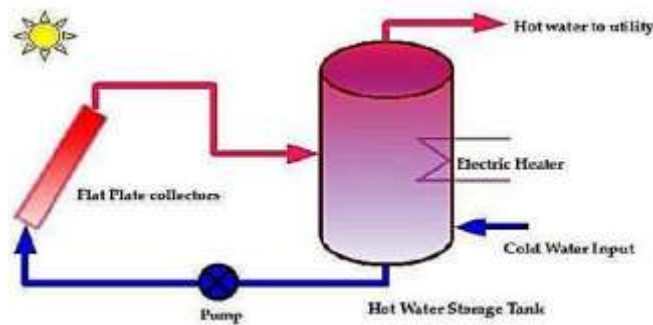


Fig. 1. Open-loop (Direct) Active System [25]

2.1.2. Closed loop (Indirect) Active System

Contrast to the direct systems, a fluid other than water is circulated through the solar collectors for the absorption of the heat energy. This absorbed heat then is transferred to water in a heat exchanger as shown in figure 2. As the water is not in contact directly with the heat source it is termed as indirect system. The heat transfer does not take place with direct contact of water with either solar collector or the working fluid and hence closed loop or indirect system[7]. Usually, the working fluids are chosen such that they have extended temperatures of freezing such as glycol-water blends as they give excellent protection from freezing.

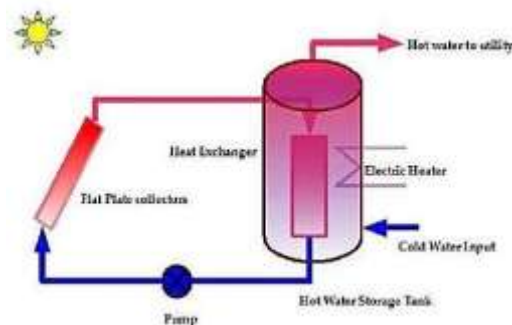


Fig. 2. Closed loop (Indirect) Active System [25]

2.2 Passive Systems

Compared to active systems, the passive systems also have the circulation of working fluid or water not with any external mechanical device but due to natural convection created from the elevation and density differences. The fluid storage tank will be arranged above the solar collector. When the fluid pass through the solar collector, it gets heated up. Consequently, the density of the fluid decreases and rises to the top of the collector from where it is sent to a storage tank. As the working fluid rejects heat to the water, it gets cooled and collected at the bottom of the storage tank because of the increase in the density of the working fluid. Finally, the water gets heated. The cost of the passive systems is very less and easily affordable due to the absence of major mechanical components. However, they perform less efficient when compared to the active systems. The best existing solar water heater with passive system is thermosiphon system.

2.2.1 Thermosiphon Systems

As shown in figure 3, the working of the thermosiphon system follows the principles of natural circulation and convection. First, the normal water is supplied to the overhead tank which is situated above to the solar collector. Due to the elevation difference the water then, is directed to the solar collector to its bottom by natural circulation [13]. The heating of the water makes it rise to the top and sent again to the top of the overhead tank from where it can be drained out at high temperature. This circulation of water continues till the collector absorbs the solar radiation and heats the water. This system is very simple as the operation is simple, natural, low maintenance and absence of the mechanical moving components. The variation of the temperatures related to the collector and ambient is directly proportional to the efficiency of the thermosiphon system and inversely with the solar radiation intensity [16].

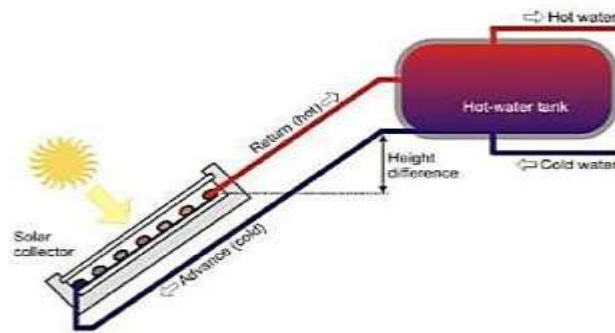


Fig .3. Thermosiphon system – An example of Passive System [25]

2.3 Batch Systems

These are in principle simple passive systems but with number of storage tanks as per the seasonal optimization. Hence, these are also called “Integral Collector Storage Systems”. These storage systems are placed in a box which is insulated on three sides and one side is glazed to face the sun and receive the radiation as shown in figure 4. Consequently, these systems perform both the functions of solar absorption and storage. Usually, due to no moving parts or pumps are installed in these systems which lead to less failures and maintenance.

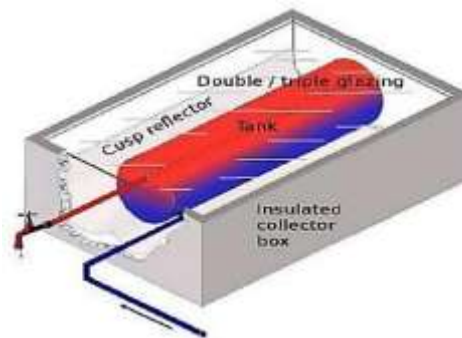


Fig 4. Batch System (integral collector storage systems) [25]

3. Components of Solar Water Heating System

The components of the solar water heater include

- a panel to collector solar radiation,
- a tank to storage the energy,
- a pump to circulate fluids,
- a heat exchanger for the transfer of fluid from the working fluid to water,
- piping units for the circulation and
- an auxiliary heating unit if required.

However, the performance of any solar collector depends majorly on only two components viz., the solar collector which decides the amount of solar radiation converted to useful heat and heat transfer fluid which decides the heat that is transferred to water.

3.1 Solar Collector

Solar collector is a gadget that gathers thermal energy from solar insolation by captivating them. The heat is put away and channelised by a streaming liquid which is used for some particular purposes. A few of the purposes include domestic water heating and steam generation for the production of electricity. Solar collectors are broadly classified into 2 types which are non-tracking or stationary type and Tracking or moving type. Non-tracking solar collectors are simple stationary solar collectors. They work until the solar energy is incident on the plates. The efficiency of the stationary solar collectors is less as the working time is less for them. They are non- moving and fixed to the ground. All the different types of solar collectors are classified in fig 1. Tracking solar collectors are designed in such a way that they move along with the movement of sun. They are not fixed to the ground and are having a tracking system. They are designed such that the solar radiation falls on the collectors perpendicularly. The need of tracking system is to increase the efficiency of the solar

collector as there is more time of solar insolation on the solar collector. The main motive of tracking system is to improve the efficiency of the solar collector by facing the sun to absorb the solar rays for a longer period of time. The tracking type solar collectors are additionally classified as one axis tracking and two axes tracking collectors. The tracking system is used if and only if the power generated by the solar collector is significantly more than the power consumed by it to use the tracking system. Based on the working fluid the solar collectors are divided into 2 types based on working fluid viz, water and air as Solar Water Heater and Solar Air Heater (SAH) respectively.

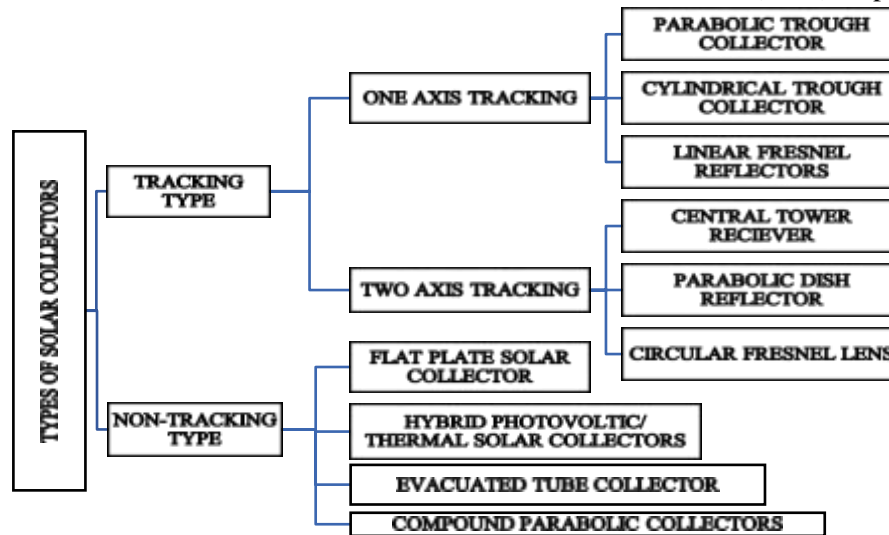


Fig .5. Types of Solar Collectors

3.1.1 Basic Solar Collectors used in Solar Water Heaters

Many types of solar collectors are used and developed for the solar water heating. The selection of the type of collector depends majorly on the atmospheric conditions of the place where the solar water heater is to be established and the requirements of the heating capacity. In broad and basic, three typical types of solar collectors are used in solar water heating viz., flat plate, evacuated tube and concentrated solar collectors.

3.1.1.1 Flat plate solar collectors

A flat plate collector consists of an absorber plate with a parallel back plate and a transparent glass cover. The flow passage is developed depending upon the type of fluid. The passage for the fluid flow is made through the volume between the black and absorber plates in the case of air [20]. In the case of water, the tubes made from copper placed on the absorber plate are used for the flow. To reduce the loss of heat the collector is blackened from the sides as well as from the bottom. During prolonged usage of the collectors a layer of dust is accumulated on the glass plate on the top of the collector, which decreases the performance of the solar collector. Cleaning or removal of the dust on the glass is mandatory to maximize the efficiency of the solar collector. The distinctive method of residue expulsion or cleaning are as expressed: (a) washing by water stream, (b) pushing the dust by pressurised stream of air, (c) straightening the collector to make the dust fall down due to gravity, (d) using of pre-programmed machine wipers, and (e) use of hydrophilic Nano-film, (used so that no dust particle settles on the smooth glass surface. Himangshu Bhowmik, Ruhul Amin [2] have stated that the efficiency of a flat plate collector can be improved by the use of reflectors and their experiment shows that they had some effective increase in the performance of the solar collector. G. Alvarez J. Arce, L. Lira, M.R. Heras. [3] developed a flat plate collector for solar air heater in which the absorber plate was replaced by an array of recyclable aluminium cans painted black. They tracked down that the maximum efficiency which could be obtained was 74%. The benefits offered by this novel collector are reusing of waste cans, being less expensive, and giving a cleaner climate.

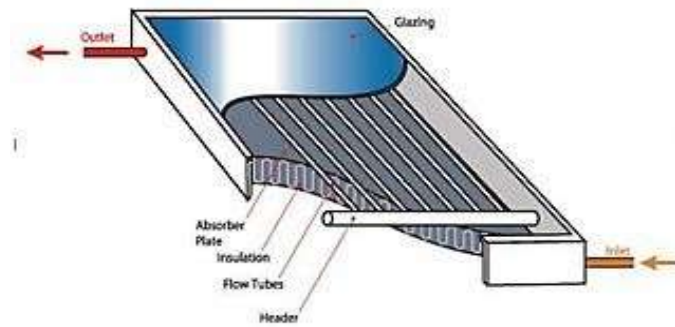


Fig.6. Solar Flat Plate Collector [25]

3.1.1.2 Evacuated Tube Collectors

The evacuated tube collector comprises of a heat pipe kept inside a glass nook. The heat pipe utilizes fluid like ethanol, methanol, water and so forth to catch warmth of sun powered insolation and this fluid exchange heat to some other working liquid while going through evaporation–condensation cycles. The hot liquid rises due to its low density (buoyancy) and the cold liquid falls down due to gravity. The hot fluid becomes fume and ascends to the heat transferring segment and moves the heat to the functioning liquid. After the heat is lost from the vapour it cools down and becomes a liquid and due gravity the liquid falls down back to the tube collector, and then the cycle continues to flow (evaporation-condensation cycle). The glass enclosure is cleared to limit the heat loss because of convection and to prevent the impact of environment within parts. It even prevents rusting. Frequently, heat pipes are likewise emptied to permit stage change of the internal fluid at low temperatures. Its effectiveness isn't essentially influenced by the adjustment in incidence angle of the sun's radiation. This component of ETC gives adaptability to tube direction from 25 degrees to 60 degrees at the hour of establishment. Various number of evacuated tubes are incorporated and associated with a typical header to accomplish high coolant temperatures. Single tube ETCs are once in a while utilized practically speaking. The two sorts of plans are normally utilized for ETCs: H-type and T-type collectors. Likewise, be noticed that T-type collectors gather marginally more radiation contrasted with H-type authorities on a yearly basis.

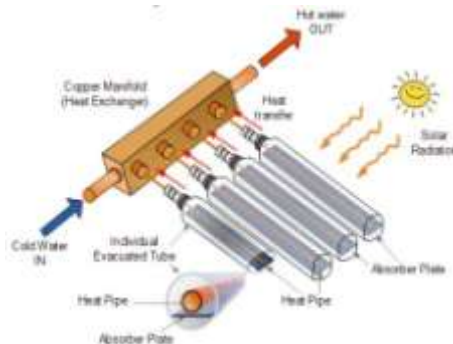


Fig.7. Evacuated Tube Collectors [25]

3.1.1.3 Parabolic Trough Collector

The parabolic trough collector comprises of a parabolic reflecting surface with an absorber tube set along its central line. The placement of the sun is followed for typical rate of solar radiations at any moment of time. This type of technology is robust, but to be able to use it when there is a budget constraint, we must bring down the cost of the solar collector. Since this type of solar collector is huge and heavy, it can be used in steam power plants, for the direct production of steam. The main motive for us to move towards renewable sources of energy is the harm it causes to the environment, if the parabolic trough collector can solve the problem then we can simply use these kinds of collectors to produce steam. The working fluid can reach the temperatures of around 400 degrees. The parabolic trough collector is generally utilized for enormous scope power production. Nonetheless, it very well may be additionally utilized for limited scope direct steam production. V.K. Jebasingh, G.M. Joselin Herbert,[6] says that there is a vast application of Parabolic trough collectors in the power generation

sector and the other major application is in refrigeration systems. The author has clearly explained the temperatures required in different industries for which solar collectors can be integrated to meet their required temperatures without changing the working systems of the industry. In Fig 5, we can clearly understand the working of the tracking system and the working of the fluid in the PTC.

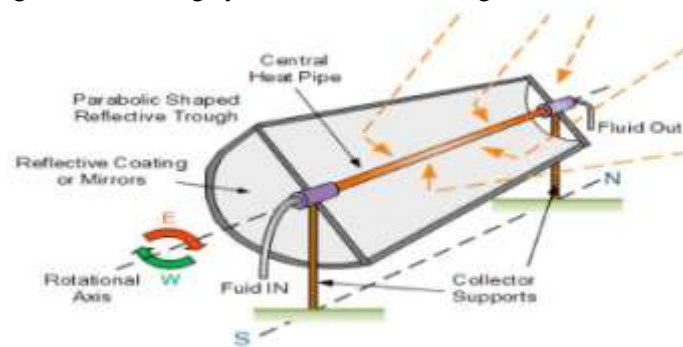


Fig.8. Parabolic trough collector (PTC) with one axis tracking [12]

4. Storage Tank

The storage tanks play a vital role in the solar water heaters. The requirement majorly depends on the atmospheric conditions as per the seasons [18]. The tank used for the storage is made up of stainless steel with high pressure resistance and covered with aluminum foil and fiber for insulation. The storage tank insulation is vital criteria for the effective storage of the energy. Another feature required in solar water heaters especially which will be installed in the environments of very low temperatures is to protect the flow from freezing [19]. To achieve this, pumps are used for recirculation of the warm water taken from the storage tanks and exposed to the piping via solar collectors.

5. Heat Transfer Fluid

The heat generated at the collector from the absorption of the solar radiation need to be transferred to the water either via the heat exchanger or directly. The fluid that is used for this purpose is the heat transfer fluid. In order to have an efficient SHW configuration, the fluid should have high specific heat capacity, high thermal conductivity, low viscosity, and low thermal expansion coefficient, anti-corrosive property and above all low cost. Among the common heat transfer fluids such as water, glycol, silicon oils and hydrocarbon oils, the water turns out to be the best among the fluids. Water is the cheapest, most readily available and thermally efficient fluid but does freeze and can cause corrosion.

5.1 Nanofluids

The performance of solar collectors will be improved by using nanofluids as a working fluid. The use of nanofluids increases the various thermophysical properties such as viscosity, density and thermal conductivity. Nanofluids are the base fluids which are dispersed with solid particles of size at nanometer scale and form a colloidal suspension [28,34]. Base fluids can be water, ethylene glycol, engine oil, etc. nanoparticles can be metallic or non-metallic particles and they are ranged from 10nm to 200nm [35-37]. Better optical and thermophysical properties will be developed by using nanofluids [35-37]. The nanoparticles have better properties than base fluids due to low specific heat capacity [35-37].

Advantages of Nanofluids:

- It has high thermal conductivity and fast transferability of heat.
- It possesses better stability even at high temperatures.
- It reduces clogging and erosion.
- It has better observing characteristics.
- It has a high heat transfer rate and reduction in pumping power

6. Conclusion

This review leads to the following key conclusions

1. The type of solar collector type may be chosen depending upon the capacity requirement.
2. Parabolic trough collectors (PTCs) are observed to be giving best outcome compared to the flat plate and evacuated tube collectors.
3. However, PTCs are huge and heavy and are generally utilized for enormous scope power production
4. Hence for small purposes such as solar water heater Evacuated Tube Collectors (ETCs) are best suited.
5. The heat pipe utilizes fluid like ethanol, methanol, water and so forth to catch warmth of sun powered insolation and this fluid exchange heat to some other working liquid while going through evaporation–condensation cycles.
6. Nanofluids are found to be performing best in the augmentation of the heat transfer performance by the heat transfer fluids.
7. Consequently, a more insight study is needed to be done on the use of nanofluids in solar collectors for solar water heating.
8. Though, the performance analysis can be carried out using theoretical modelling, software simulation, experimental study is suggested for having a complete and real outcome.

References

- [1] Siddharth Suman, Mohd. Kaleem Khan, Manabendra Pathak, Performance enhancement of solar collectors- A review, *Renewable and Sustainable Energy Reviews*, Volume 49, 2015, Pages 192-210. <https://doi.org/10.1016/j.rser.2015.04.087>.
- [2] Himangshu Bhowmik, Ruhul Amin. Efficiency improvement of flat plate solar collector using reflector. 16 August 2017 Published by Elsevier Ltd <https://doi.org/10.1016/j.egy.2017.08.002>
- [3] G. Alvarez J. Arce, L. Lira, M.R. Heras. Thermal performance of an air solar collector with an absorber plate made of recyclable aluminium cans. 18 March 2004 <https://doi.org/10.1016/j.solener.2004.02.007>
- [4] Jaehnig D, Isaksson C. Solar integration: five easy ways to incorporate solar thermal into conventional heating systems. *Renew Energy World* 2006;6:66–72
- [5] IEA. Renewable energy – market and policy trends in IEA countries. UK: OECD/ IEA; 2004
- [6] V.K. Jebasingh, G.M. Joselin Herbert, A review of solar parabolic trough collector, 21 October 2015, <https://doi.org/10.1016/j.rser.2015.10.043>.
- [7] Kalogirou S. Solar thermal collectors and applications. *Prog Energy Combust Sci* 2004;30:231–95
- [8] Jeong K, Kessen MJ, Bilirgen H, Levy EK. Analytical modeling of water condensation in condensing heat exchanger. *Int J Heat Mass Transf* 2010;53: 2361e8.
- [9] Nehrir MH, LaMeres BJ. A multiple-block fuzzy logic-based electric water heater demand-side management strategy for leveling distribution feeder demand profile. *Elec Power Syst Res* 2000;56:225e30.
- [10] De Gracia A, Oró E, Farid MM, Cabeza LF. Thermal analysis of including phase change material in a domestic hot water cylinder. *Appl Therm Eng* 2011;31: 3938e45.
- [11]] Kuang YH, Wang RZ. Performance of a multi-functional direct-expansion solar assisted heat pump system. *Sol Energy* 2006;80:795e803
- [12] Olia, H.; Torabi, M.; Bahiraei, M.; Ahmadi, M.H.; Goodarzi, M.; Safaei, M.R. Application of Nanofluids in Thermal Performance Enhancement of Parabolic Trough Solar Collector: State-of-the-Art. *Appl. Sci.* 2019, 9, 463. <https://doi.org/10.3390/app9030463>
- [13] Huang BJ, Lee JP, Chyng JP. Heat-pipe enhanced solar-assisted heat pump water heater. *Sol Energy* 2005;78:375e81
- [14] Roonprasang N, Namprakai P, Pratinthong N. Experimental studies of a new solar water heater system using a solar water pump. *Energy* 2008;33:639e46
- [15] Al-Madani, Hussain (2006). “The performance of a cylindrical solar water heater.” *Renewable Energy* Vol. 31, pp 1751-1763.
- [16] B Sivaraman and N Krishna Mohan (2005). “Experimental analysis of heat pipe solar collector with different L/di ratio of heat pipe”, *Journal of Scientific & Industrial Research*, Vol. 64, pp 698-701
- [17] Charles Smith (1995). “History of Solar Energy Revisiting, Past Solar Power Technology Review”

- [18] Duffie J.A and Beckman W.A. (1991). "Solar Engineering of Thermal Processes", Second Edition, Wiley-Interscience, New York.
- [19] Harrison J, Tiedeman T (1997). "Solar Water Heating Options in Florida", Florida Solar Energy Centre. Rpt: FSEC-EN-9-85.
- [20] K. Sivakumar, N. Krishna Mohan and B. Sivaraman (2005) "Performance analysis of elliptical heat pipe solar collector" Indian Journal of Science and Technology.
- [21] Soteris A. Kalogirou (2004). "Solar thermal collectors and applications.", Progress in Energy and Combustion Science 30, pp 231–295.
- [22] Rehana Nasrin, M. A. Alim, "THERMAL PERFORMANCE OF NANOFLUID FILLED SOLAR FLAT PLATE COLLECTOR", INTERNATIONAL JOURNAL OF HEAT AND TECHNOLOGY, Vol.33,No.2, Pages 17-24, Jan-15, <https://doi.org/10.18280/ijht.330203>.
- [23] Vikrant Khullar, Himanshu Tyagi, "A study on environmental impact of nanofluid-based concentrating solar water heating system", International Journal of Environmental Studies, Vol. 69, Issue 2, Pages 220-232, Apr-12, <https://doi.org/10.1080/00207233.2012.663227>.
- [24] Dilip Johari, Ashok Yadav, Ravi Verma —Study of solar water heaters based on exergy analysis Proceedings of the National Conference on Trends and Advances in Mechanical Engineering, YMCA University of Science & Technology, Faridabad, Haryana, Oct 19-20, 2012
- [25] D.N. Korres, C. Tzivanidis, Numerical investigation and optimization of an experimentally analyzed solar CPC, Energy, Volume 172, 2019, Pages 57- 67. <https://doi.org/10.1016/j.energy.2019.01.119>.
- [26] U. Ortobasi, W.M. Buehl, An internal cusp reflector for an evacuated tubular heat pipe solar thermal collector, Solar Energy, Volume 25, Issue 1, 1980, Pages 67-78. [https://doi.org/10.1016/0038-092X\(80\)90407-7](https://doi.org/10.1016/0038-092X(80)90407-7).
- [27] M. Gajic, N. Karwa, A. Mojiri, and G. Rosengarten, Modeling reflection loss from an evacuated tube inside a compound parabolic concentrator with a cylindrical receiver, Opt. Express, Volume 23, 2015, Pages 493-501. <https://doi.org/10.1364/OE.23.00A493>.
- [28] Srinivas, V., Moorthy, C. V. K. N. S. N., Dedeepya, V., Manikanta, P. V., & Satish, V. (2016). Nanofluids with CNTs for automotive applications. Heat and Mass Transfer/Waerme- Und Stoffuebertragung, 52(4), 701-712. doi:10.1007/s00231-015-1588-1.
- [29] Wandong Zheng, Lin Yang, Huan Zhang, Shijun You, Chunguang Zhu, Numerical and experimental investigation on a new type of compound parabolic concentrator solar collector, Energy Conversion and Management, Volume 129, 2016, Pages 11-22. <https://doi.org/10.1016/j.enconman.2016.10.013>.
- [30] Yu, L.; Wang, J.; Zhang, Y. Two-stage concentrating CPC. CN Patent CN201020022517.8, 13 January 2010
- [31] Y Tripanagnostopoulos, M Souliotis, Th Nousia, CPC type integrated collector storage systems, Solar Energy, Volume 72, Issue 4, 2002, Pages 327-350. [https://doi.org/10.1016/S0038-092X\(02\)00005-1](https://doi.org/10.1016/S0038-092X(02)00005-1).
- [32] Kessentini, H., and Bouden, C. Numerical Simulation, Design, and Construction of a Double-Glazed Compound Parabolic Concentrators-Type Integrated Collector Storage Water Heater. ASME. J. Sol. Energy Eng. 2016; Volume 138(1): 014501. <https://doi.org/10.1115/1.4032141>
- [33] Wattana Ratismith, Yann Favre, Maxime Canaff, John Briggs, A non-tracking concentrating collector for solar thermal applications, Applied Energy, Volume 200, 2017, Pages 39-46. <https://doi.org/10.1016/j.apenergy.2017.05.044>.
- [34] Teja, S. R., Moorthy, C. V. K. N. S. N., Jayakumar, S., Kumar, A. K., & Srinivas, V. (2020). Ethylene glycol-based nanofluids – estimation of stability and thermophysical properties. Frontiers in Heat and Mass Transfer, 15, 1-9. doi:10.5098/hmt.15.7
- [35] Moorthy, C. V. K. N. S. N., & Srinivas, V. (2018). Discretization analysis of a composite GFRP cylinder. International Journal of Engineering and Technology(UAE), 7(4), 277-279. doi:10.14419/ijet.v7i4.5.20088
- [36] V, S., A, J., V.S.N, V., H, R., & Ch. V. K. N. S. N,M. (2020). Mechanical, corrosion and cavitation erosion properties of LM 9 grade aluminium– multi-walled carbon nanotubes composites. Australian Journal of Mechanical Engineering, doi:10.1080/14484846.2020.1784557.
- [37] Moorthy, C. V. K. N. S. N., Kumar, G. N., Srinivas, V., Kumar, M. A., Reddy, K. R. R. M., Vasundhara, D. N., . . . Said, S. M. (2020). Metallography, microstructure, and wear analysis of AA 6063/TiC composites for augmented dry sliding property at room temperature. Metallography, Microstructure, and Analysis, 9(2), 140-151. doi:10.1007/s13632-020-00625-6

- [38] Helal O., Benrejeb R., Chaouachi B. Comparative Study of Two Integrated Solar Collectors with Symmetric and Asymmetric CPC Reflectors Based on a Ray Trace Analysis. *Environment Impact Assessment and Potential Solutions*. Springer 2018, Cham. https://doi.org/10.1007/978-3-319-62575-1_65.
- [39] Srikanth Madala, Robert F. Boehm, "Effect of reflection losses on stationary dielectric-filled nonimaging concentrators," *J. Photon. Energy* (2016). Volume 6 (Issue 4) 047002. <https://doi.org/10.1117/1.JPE.6.047002>.
- [40] Kok-Keong Chong, Sing-Liong Lau, Tiong-Keat Yew, Philip Chee-LinTan, Design and development in optics of concentrator photovoltaic system, *Renewable and Sustainable Energy Reviews*, Volume 19, 2013, Pages 598-612. <https://doi.org/10.1016/j.rser.2012.11.005>.
- [41] Baljit Singh Sarban Singh, Chan Hoy Yen, Saleem Hussain Zaidi, KamaruzzamanSopian. Part II: Enhanced Performance of Concentrating Photovoltaic-Thermal Air Collector with Fresnel Lens and Compound Parabolic Concentrator (CPC). *Journal of Advanced Research in Fluid Mechanics and Thermal Sciences* (2018). Volume 47 Issue 1. Pages 16-24.
- [42] Li, Guiqiang, Gang Pei, Jie Ji, YuehongSu, Hang Zhou, and Jingyong Cai. "Structure optimization and annual performance analysis of the lens-walled compound parabolic concentrator." *International Journal of Green Energy* 13, no. 9 (2016): 944-950. <https://doi.org/10.1080/15435075.2015.1109514>.
- [43] Babar, Hamza; Ali, Hafiz Muhammad (2019). Airfoil shaped pin-fin heat sink: Potential evaluation of ferric oxide and titania nanofluids. *Energy Conversion and Management*, 202(),112194–.doi:10.1016/j.enconman.2019.112194
- [44] Vishal G. Shelke, Chinmay V. Patil, and Kishor R. Sontakke, "Solar Water Heating Systems: A Review", *International Journal of Scientific Engineering and Research (IJSER)*, Vol.3, Issue 4, 2015

New Approach of Generation of Power by Using Wind Energy

Dr. K. Srividya¹, Dr. J. Ravindra Babu², CH. Ravi Kiran³, B. Raghu Ram³, B. Ravindra Naik³, K. Varun Sai³

¹ Associate Professor, Mechanical Engineering Department, Prasad V Potluri Siddhartha Institute of Technology, Vijayawada, India.

² Associate Professor, Electronics and Communication Engineering Department, Prasad V Potluri Siddhartha Institute of Technology, Vijayawada, India.

³ IV B.Tech students, Mechanical Engineering Department, Prasad V Potluri Siddhartha Institute of Technology, Vijayawada, India.

Abstract: Now a day's power requirement is more due to operation of many components' need electricity to perform certain work. To meet the demand of power we burnt lots of fossil fuels which are non-renewable energy resource for power generation. These are depleting day by day. We need to depend on renewable energy resource for generating electricity. By using wind as a renewable energy resource, we are using horizontal and vertical wind mills for power generation. Due to usage of this type of wind mills there is a possibility of damage towards bird life and when maintenance of this turbine at 500 feet may cost the human life to avoid these consequences. We have designed a bladeless wind turbine to avoid the limitations of both horizontal and vertical axis wind turbines. This is economical and it is easily available to individuals to set up at top of the building and it is simple in design. This way of generation of power will meet the demand of power in the society.

Keywords: Bladeless wind turbine, Power circuit, Bladeless wind turbine-assembly.

INTRODUCTION

The invention of bladeless wind turbine describes the generation of electricity without using blades of traditional wind mill. It is a non-conventional type of wind mill. It is very advantageous to environment to save the bird life and balance the eco-system. This invention plays a crucial role in making the use of bladeless windmills near the load centres and reduce the transmission system and we can utilize maximum wind potential in the location.

The non-renewable energy resources are exhaustible in nature. Due to usage of non-renewable energy resources like fossil fuels, coal and petroleum products for generation of power, these sources may emit toxic gases to environment and this may damage different ecosystems on earth. Due to exhaust of non-renewable energy resources humans are depending upon the renewable energy resources like solar, wind, geothermal, biomass and ocean thermal energy for power generation. The renewable energy resources are inexhaustible in nature and freely available for many years. [1] discussed how to design the bladeless wind turbine and how it generates the power by using vibrations of mast by motion of wind. [2] presented the various applications of bladeless wind turbine in the field of power utilising components like electronics and electrical appliances like fan, light setc. [3] shows the behaviour of a wind turbine and its dynamic characteristics of turbine under working and taking design considerations when designing of bladeless and bladed turbine. [4] presented the outline parameters of wind and potential of energy which can be predicted by using

Dept. of Mech. Engg. PVPSIT 258

previous data for analysing.[5] investigated the future dependence on renewable energy resources for generation of power and showing different approach for bladeless wind turbine. [6] discussed the evolution of bladeless wind turbine the flow of vortex of air or fluid creates a small vibration of mast or disturbance on surface of body this creates a new approach of generation of power by using bladeless wind turbine. [7] invented the jiggling effect of mast creates a motion of parts of bladeless wind turbine to generate electricity with arrangement setup. [8] discussed how the vortex bladeless wind turbine working under the flow of wind how the parts are responding and it analyse the power output based on velocity of wind. [9] presented the new approach of design and it shows is that possible to create a wind turbine without bladeless and discuss how it will generate power by operation.

1. THEORY: COMPONENTS OF BLADELESS WIND TURBINE



Figure 1. Bladeless wind turbine

1.1 Parts and their working

1.1.1 Base

The base is made up of cast iron used to with stand all the forces of bladeless wind turbine. The base is used to support the all-othercomponents like mast, copper coils,magnetsand power transmission circuit.

1.1.2 Mast

The mast is made up of polyvinyl chloride or plastic material. It's the major component in bladeless wind turbine. Due to the flow of wind the mast oscillates around the fixed axis with help of weight balancer. Theoscillations of mast are directly proportional to the wind speed.

1.1.3 Weight balancer

The weight balancer is used to balance the weight of mast for oscillation motion if the arrangement of weight balancer is not done accurately whole structure will collapse.

1.1.4 Arc-shaped pendulum

An arc-shaped pendulum is made to carry the copper coils and oscillate with mast.

1.1.5 Magnetic poles stand

A magnetic poles stand is made up of glass frame or fiber frame to hold the magnetic poles of north and south. The magnets of north and south attracts each other due to this attraction between poles a strong magnetic field is generated. Due to the arrangement of copper coils between the magnetic field creates a change in flux due to change in flux an electro motive force(EMF) is generated.

1.1.6 Rectifier

A rectifier is an electronic device which converts alternating current in to direct current.

1.1.7 Battery

A Battery is a source of electric power which stores direct current.

1.1.8 Inverter

An inverter is an electronic device which converts direct current in to alternating current.

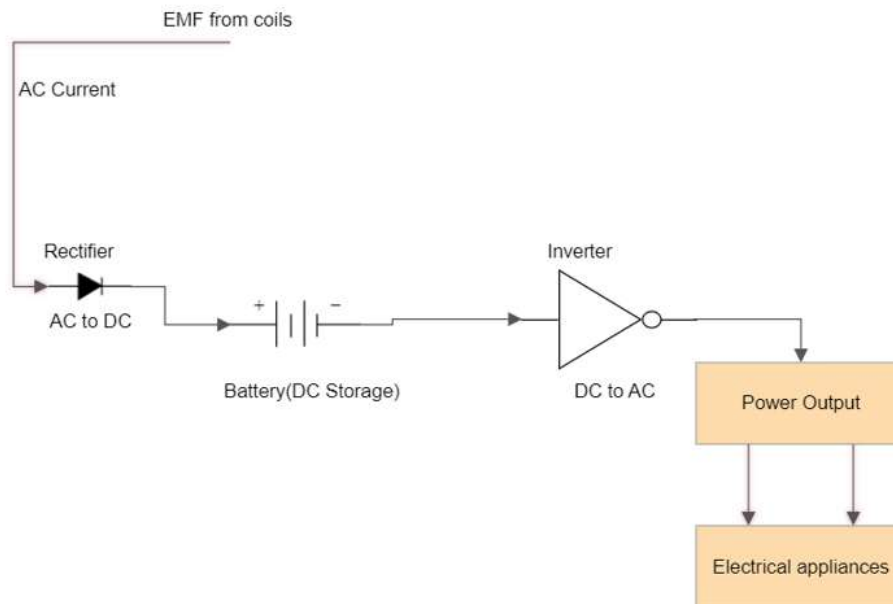


Figure 2. Power circuit

1.1.9 Power Circuit

An emf generated from coils is in alternating current form this is converted in to direct current by using rectifier. Because the battery is used to store the energy in the form of direct current only. When we require power for utilizing, we extract energy from battery. we convert direct current to alternating current by using inverter. in this way we utilize power when required and store power when not require.

2. CONSTRUCTION AND WORKING

2.1 Construction procedure

All the components are assembled according to the design. The base is fixed to ground by bolted joints and magnetic poles stand is attached to the base. The mast is fixed to the base and weight balancer is used to balance the weight of all other components. The special attachment between arc pendulum and mast is done and copper coils are attached to arc – shaped pendulum for oscillation between the magnetic field in these all-other components are assembled according to design of bladeless wind turbine.

2.2 Circuit construction

To utilize the power which is generated from bladeless wind turbine we have designed a power circuit to store the energy when not require and utilize when required. Due to the working of bladeless wind turbine an emf is generated from copper coils this emf is in alternating current form and we can directly utilize when required if power is not required for utilization we can store the energy in the form of battery for future utilization, for that we can use a rectifier to convert AC to DC and store the energy in the battery. For utilization we use an inverter to convert DC to AC this is conversion is done because all electronic components work with alternating current and battery stores direct current in this way we can store and utilize energy when required.

VIEWS OF BLADELESS WIND TURBINE

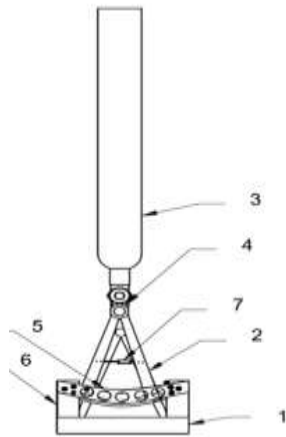


Figure.3 Front View

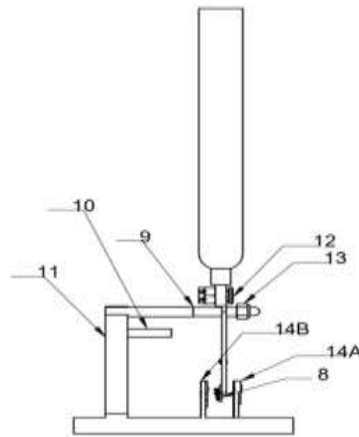


Figure.4 Side View

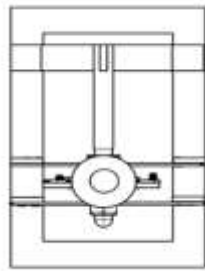


Figure.5 Top View



Figure.6 Isometric View

S.NO.	PART NO.	PART NAME
1	1	BASE
2	2	ARC-SHAPED PENDULUM
3	3	MAST
4	4	CONNECTING ROD SUPPORT
5	5	MAGNETIC-MATERIAL
6	6	MAGNETIC SUPPORT STAND
7	7	WEIGHT BALANCER
8	8	COPPER COIL
9	9	CONNECTING ROD
10	10	WEIGHT BALANCER SUPPORT
11	11	COLUMN
12	12,13	BOLT AND NUT
13	14A,14B	MAGNETIC POLES (NORTH AND SOUTH POLES)

3. RESULT & DISCUSSION

3.1 Normal condition

The bladeless wind turbine is placed on top of the building or beside of the road due to the flow of wind or motion of wind passes from high pressure to low pressure due to this phenomenon a pressure difference is created due to the mast is oscillates around a fixed axis due to motion of mast in too and fro motion the copper coils oscillates with arc shaped pendulum. The magnetic poles stand is used to hold the north and south poles with some

distance generally the opposite poles attract each other and creates a strong magnetic field this field is cuts by copper coils with the motion of mast due to this change in magnetic flux there is an emf generation.in this way power is generated by using bladeless wind turbine.



Figure 7. Normal condition

3.2 Actuated Power circuit

When high flow of wind strikes the mast, it oscillates more and more power is generated. Based on the wind potential on the region the amount of electricity is generated. This is fully renewable energy resource and it will not create any environmental crises.if this system gets uncontrollable winds, then other attachments like chains are used to stop the system.

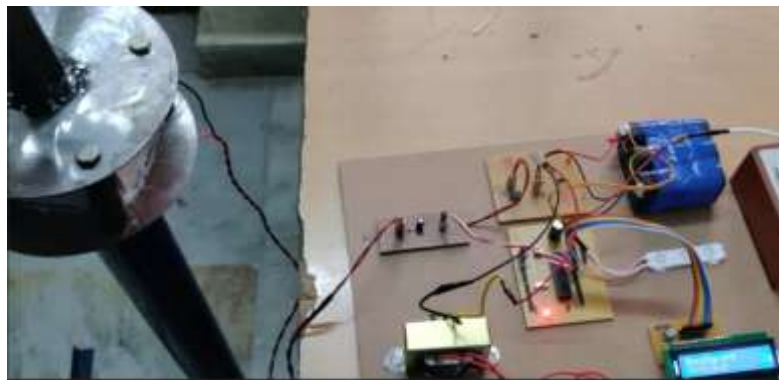


Figure 8. Actual power circuit

3.3 When working on field

When the bladeless wind turbine starts working then the power generation will start and flow according the circuit diagram. We have done a prototype of bladeless wind turbine with total height of 5 feet. There the base will be 3 feet and the mast will be 2.5 feet and remaining 0.5 feet will be the spring and magnetic setup. Its start working and power generation will be done and this power will be utilised or it can store through a battery

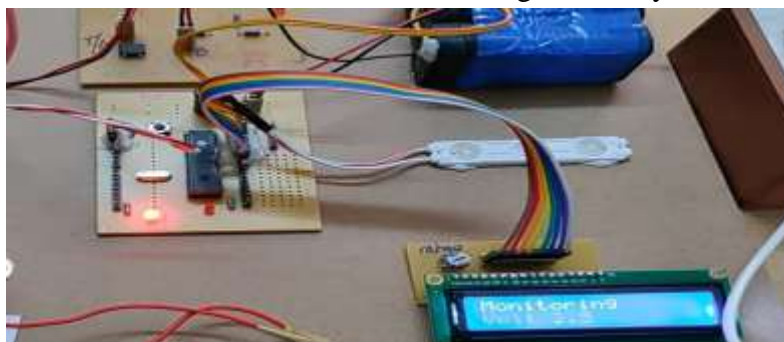


Figure 9. Power output display

CONCLUSIONS

This bladeless wind turbine system consists of mast, magnetic coil setup, base, arc shaped pendulum with copper winding and connecting rod. Once it starts working on the field it will not stop or come to rest until we stopped with an external force the performance of system depends on various parameters regarding to wind potential and wind velocity on the region. The following are the conclusions of this report:

- We can able to design and develop a model on bladeless wind turbine.
- By using bladeless wind turbine, generate power for individual purpose by self-installation at their place.
- By using this system, save the birdlife and we can reduce the disturbance in bio-life.
- The bladeless wind turbine is fully eco-friendly and it is a renewable energy resource. it is inexhaustible in nature
- Mainly this project can operate at any location based on wind potential of location. the wind energy is freely available in nature.
- Main advantage in this project is to meet the power demand on earth through renewable energy resource and reduce the consumption of non-renewable energy resource.

References

- [1] Younis, A., Dong, Z., ElBadawy, M., AlAnazi, A., Salem, H. and AlAwadhi, A., 2022, "Design and Development of Bladeless Vibration-Based Piezoelectric Energy-Harvesting Wind Turbine", Applied Sciences, 12(15), pp.7769.
- [2] Asre, C.M., Kurkute, V.K. and Kanu, N.J., 2022, "Power generation with the application of vortex wind turbine", Materials Today: Proceedings, 56, pp.2428-2436.
- [3] Jokar, H., Mahzoon, M. and Vatankhah, R., 2022, "Nonlinear dynamic characteristics of horizontal-axis wind turbine blades including pre-twist", Ocean Engineering, 256, pp.111441.
- [4] DehghanManshadi M, Ghassemi M, Mousavi SM, Mosavi AH, Kovacs L., 2021, "Predicting the Parameters of Vortex Bladeless Wind Turbine Using Deep Learning Method of Long Short-Term Memory", 14(16), pp.4867.
- [5] Frangoul, Anmar (21 September 2017). "The future of wind turbines could be bladeless". CNBC. Retrieved 11 December 2018.
- [6] "Vortex Bladeless biography". Vortex Bladeless. 14 May 2018. Retrieved 11 December 2018.
- [7] Wanshel, Elyse (25 May 2016). "These Jiggling Bladeless Turbines are a Breath of Fresh Air". Huffington Post. Retrieved 13 December 2018.
- [8] Spendlove, Tom (4 June 2015). "Vortex Bladeless Generates Power from Wind without Blades". Engineering.com. Retrieved 13 November 2016.
- [9] Patel, Sonal (1 July 2015). "New Approach Powers Bladeless Wind Turbine". Power Magazine. Retrieved 27 June 2018 – via EBSCOHost.

Overview of Ample Investigation on Renewable Energy Sources: Types of Sources, Tasks and Implications: A Review

Senthil Murugan V¹, Hassan Majeed Hassoon ALDelfi², Kaushal Kumar³,
SSSV Gopala Raju⁴, Sumanth Ratna. Kandavalli⁵, Pradeep Johnson⁶

¹Department of Mechanical Engineering, Hindusthan College of Engineering and
Technology, Coimbatore 641032, India

²Interior design Department, Faculty of Engineering, Tishk International University, Erbil,
Kurdistan Region, Iraq.

³Research Scholar, Department of Botany, School of Life Sciences, Mahatma Gandhi Central
University, Bihar-845401

⁴Department of Civil Engineering, RGUKT Nuzvid, Andhra Pradesh.

⁵Department of Mechanical Engineering, Tandon School of Engineering, New York
University, Brooklyn, 6 Metro Tech Center, NY, 11201, United States of America.

⁶Department of Mechatronics Engineering, Hindusthan college of Engineering and
Technology, Valley Campus Coimbatore -641032

Corresponding Author: vsena11@gmail.com

Abstract: Sustainable, renewable and green energy is necessity to develop the ecological health, social activities and economical situations causes to production and improvement in economic. This review paper reveals the renewable energies to supports in improvement of ecological health and climatic modification effectively. This research focused to identify the renewable energy is workable and investigate how to change from traditional energies to renewable energies could supports in modifying the climatic and its effect. In the bio mass energy, the lignocellulosic based bio fuels are widely applied in different methods to compose the bio reactors and bio refineries to the chemical migrating process and it act as the sustainable energy. To beneficially develop the potential strength of bio refineries and the government regulations were followed in universities and various related industrial sectors that can support to compose the maximum value of fuels and different products from different bio mass energies. This work is suited for future researchers who are initiating the renewable energies in the nest level and also assess the economic progress, social awareness, eco health and climatic changes.

Keywords: biomass, geothermal, renewable, energy, sustain

1. Introduction

Owing to increasing demands electrical energies in worldwide in the developing and developed countries, therefore the sustainable energy demand necessity is more to reinstate traditional electricity sources of fossil fuel. This fossil fuel based sources of energy composes the environmental based problems to produce the climatic modification and global warming. From the past decades, the emission of green house gas from the power making has established frequently. The present environmental problems to be resolved with help of renewable energy methods to generate the electricity. The methods are wind, solar, hydrogen, geothermal, biomass and hydro [1-3].

The zero emission concepts is more significant in this renewable energy to advance in eco friendly attributes and capable to produce the more electric power. So it will cause to increase the motivational awareness to the social responsible societies. The renewable energy also improves the economy rate in overall countries and also diminishes the expensive rates in creation of electricity which is significant to recognize the priority to nation by utilizing

the natural resources. This is promoting to compose secondary income for those who are integrated with generation of electric power source to the main power grid [4-6].

Owing to increasing the overall cost of renewable energy setup cost, the renewable energy sources for electric power creation is developed and more power creation is currently executed with usages of traditional fossil fuel sources. There are many devices are utilized to produce the electric power generation in the renewable energy sources [7-9]. For example, the photovoltaic system and wind based turbines are fully employed with sufficient of sunlight sources and hydro only worked with available of potential energy with adequate flow of water. But some researchers focused many issues which are related to the renewable energy sources and similarly it has disadvantages for achieving the efficiency in power production.

In the normal day to day life due to increasing of power generation with fossil fuel based sources from the last decades, there are so many green house gases are formed and it affects the global warming. The global warming causes severe affects in economic development and human health issues and the climatic modification also achieved by manmade situations. From the various researches composes the detailed review in the global warming which is related to the environmental scenario, easily access the water and food fabrication and it is severely affected in internal human damages. Owing to intense climatic alteration, some infectious diseases like malaria, dengue and diarrhea which are mentioned by the medical sciences and this will be serious issues by upcoming days. Due to generation of power from the traditional methods and pollution which comes from the industrial area severely affects the human body internal functions like heart issues and respiratory problems and similarly, the severe air pollution also major reason for that [10-13].

On the other side, the modification of ozone layer and increasing of sea ranges also causes to farming areas and human health is indirectly affected due to poor nutrition. There is an alternate solutions are required to replace the conventional method for power generation like sources of fossil fuel, natural gases and traditional coal sources as a fuel. Therefore normal day to day life the conventional methods are replacing with reliability of renewable energy sources. So this renewable method better to resist to environment and it will transform into environment sustainability with green energy [14-16]. Replacing fossil fuel sources with non-fossil fuel sources is quite a challenging task. This task is more difficult to replacing the fossil fuels with unconventional energy sources. The controlling the essential aspects like polluted energy sources and effectiveness of energy is not simple to accomplish in real investigations in the regions of industrial and laboratory. Subsequently, the most important concern is to identify the easy routes to diminish the carbon dioxide based pollutants or other pollutants like sulfur dioxide, nitrogen oxide and PM based pollutants like PM_{2.5} and PM₁₀, respectively. These pollutants are migrated to the environment and it influencing significantly in the deprivation of pure air which is directly affects the other living and human living things [17-20].

From the last decades there are different methods are focused to reinstate polluting fuels with unconventional renewable energies with various ratios in the upcoming decades at the international global range. Nevertheless, due to believe in storage capacity, creation of power and installation procedures are need to planned for designing in the establishment of renewable energy. But in the current state, the development of this renewable system has been transforming rapidly [21-22]. There is some cases, now a days the new technology is converted from the older method to making the desirable methods to commercially with possible factors. The maximum capital expense is other constraints to concern when executing these renewable based technologies. On the other hand, the government sectors in the worldwide are giving the financial supports to encourage renewable based energies.

In the recent decades there is severe supports has received from the government to initiate the companies, photovoltaic system, other startup based firms and wind mills related has received. Based on the climatic conditions some technologies like wind and solar based methods are really utilized with flexibility and easily approach as the alternative sources based on the geographic zones. In some countries like Africa and Latin America, wind energy is improving progressively. Solar based energy

is broadly utilized in South Africa, North Africa and Middle East countries when compared to western countries. There are significant supports to assist the renewable energies with financially, various useful policies and enhanced technological assistance. Therefore the sustainable future is based on above the significant criteria which are implemented in renewable energies. The overall effect of conventional processing for composing the power generation is severely impact to human health [23]. The heat pump water heater assisted solar still are used to improve the productivity [39]. The researchers have explored and used efficient refrigerants in a variety of applications. [40].

Based on the human health risk there are different clusters are generated. For example burning of coal, natural gas, wood and oil consumption creates the extensive quantity for air pollution and solid waste. Next the solar, wind and hydro are other groups of renewable sources of energies which include the lesser energy density. These systems include lesser probability accidents, lesser emission and easily predictable risk factors. On the other hand, it has different limitations like less public risks, installed in particular zones, enhanced facilities and more expensive during the installation [24-25]. Lastly the nuclear based energies produced the maximum energy densities are characterized in the composed fuel with dependent to lesser quantity of fuel and create the minimum wastes to converting. So these energies emit various toxic from their energies in specified types and we reduce their levels from each classification.

In this manner, the entire life cycle methods with progressive statements are utilized to investigate the potential effects on man health issues and environmental loads. The normalized method has been utilized to analyze for computing the loads of ecological and probable impacts on human physical condition and present environment owing to formation and utilization goods and services. This system is appropriate for appreciative the valuation of fossil, renewable and nuclear related energies with ecological attributes with their self characteristics. Therefore, we lastly implicit that the initiation of ethanol, blends, biodiesel and electric vehicles reduces the emission of hydrocarbons and carbon monoxide higher than the quantity emitted in petrol and diesel engine. While in using the biodiesel engines, nitrogen oxide emission minimization is very difficult to diminish but in electric vehicles like charging inadequate and electronic hardware system malfunctions are faced by the customers. Moreover, we acknowledged the issues for solar and wind power system, maximum initial cost and insufficient efficiency. Subsequently, to conclude with renewable systems, we could do with maximum awareness and enhanced systems that steadiness with all processing factors from funds to fabrication. Figure 1 illustrates the renewable energy sources.

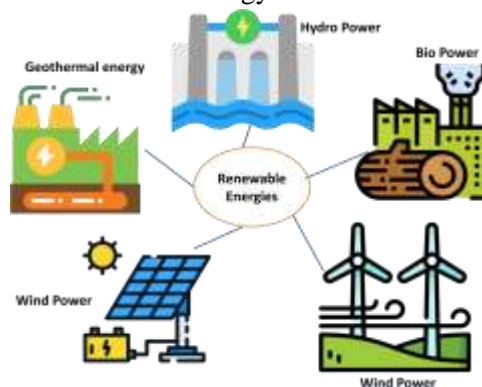


Figure 1 Schematic representation of various renewable sources of energy

2. Renewable Green Energy

Renewable green energy is comprises the sources of energy that are not exhausted through the utilization. The following renewable types like solar energy, biomass, geothermal, wind and hydroelectric energy and it is extraction from sunlight, plants, earth minerals, air and water flowing, respectively. The green energy is also called as the renewable energy and other additional energy was not composed. The fossil based fuel was not produced and pollution free. But in renewable energy sources produces the lesser green house gases and carbon traces. In current years, the green energy has been familiar at various countries and more financial supports are much

attention in reducing their addiction on maximum contaminated fossil fuels. From the present scenario, the electrical requirements of worldwide are 28 percentages from 96 percentages. The following section clearly exhibits the various types of renewable energies with their limits, benefits and challenging issues [26-28].

2.1 Solar energy

The solar energy is most precious system which is collected from the sunlight or light energy and it is transformed into electrical energy through the solar system via the photovoltaic cells (PV). By the assists of wind power to composes the lesser carbon energy with appropriated methodologies. To establishing the sources of renewable energy is a complicated work for human livings till now the tasks is to surpass the insufficient for green with energy and diminish the fossil fuel with world's belief. From the various types of renewable energies, the solar is one of the significant method due to their attributes like eco-friendly, maximum storage capacity, unique, long life and hopeful. While in expected solar irradiation is irregular and denationalized, the current usages of solar utilizing the green and enhanced technology for important tasks [29-31].

The photovoltaic cells are main one for receiving and storing the electrical energy. There are different components like direct to alternative current, DC connecting link and three phase line are fitted with appropriated circuit breakers and suitable transformer are mainly utilized. The entire system was manipulated by through the proper communication system and the transformed energy was saved in appropriated batteries or other thermal based saving methodologies to shifting the power to the maximum grade of AC power system. Now the current system develops the power which is transferred to end applications through the fiber optic cable. Through this system, there are main elements like photo voltaic, photo thermal and photo catalytic energy are the important mechanism for producing the electricity, therapy and polluted water. Therefore, the PV cells convert the energy which is based on photon and formed into thermal energy by concentrator equipments. To improve the effectiveness of solar energy is transformed into electrical energy by using the thin solar films with various alterations via the solar cells, solar cells and sensible solar cells within the devices of energy savings. Till now the year of 2010, more than 90 % of the photovoltaic trending of global towards the silicon based solar cells. The worth of effectiveness in the solar cells hasforwarded from more than 5 to 25 % next for the alteration which includes silicon based cells. The various establishments of creation of PV based solar for the first to fourth generation was concentrated to enhancing the surface and reducing the losses like electrical, photon and carrier loss. Figure 2 displays the photovoltaic system for electric power.

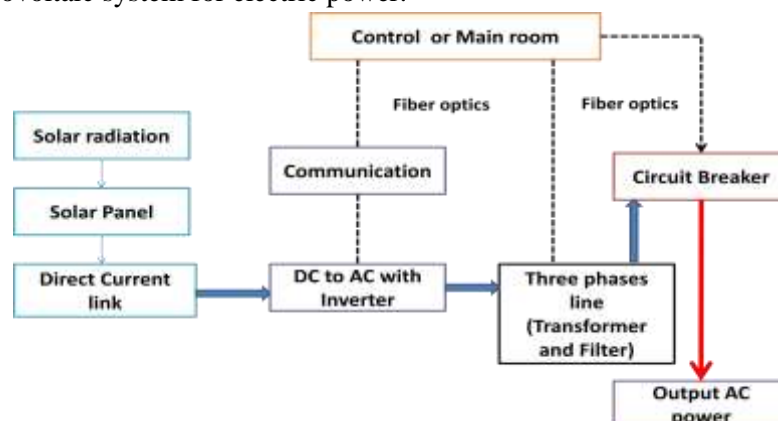


Figure 2 Generation of electric power through PV system

The thin film solar cells is second generation based solar which is manufactured by dropped over the surfaces of the films and it might appropriate and reliability towards the suitable for marketing at 5%. The greater efficiency was accumulated in thin film surfaces having the material of copper and cadmium but in the toxic level is not diminished and it is one of the limitations while using thin surface films. Sensitized solar cells are comes under the generation of third, this method composes the lesser expensive cells and it it was reported in the year of 1991. In this work, even the winter

seasons, the photovoltaic system develops the energies and produces the more efficiency by utilizing the silicon based cells and the efficiency is about 60 to 250 % which is higher than the thin film solar cells [32-34].

2.2 Bio Energy

The animal and plant material wastes are composed of the energy which is derived from their wastes and forms the bio energy like materials ethanol, biodiesel, hydrocarbons and bio oil. The following wastages like food, chicken, animal, farming, organic, fish waste, municipal, house, wood are included to bio mass energies. From the feed stocks biodiesels are generated and it is useful for vehicles to transmit the logistics. Similarly, the various bio fuels which are formed from micro algae based biomass for present generation and utilized as a bio fuels. The fabrication of various bio fuels with assisting of microalgae gives the supplementary intakes to assist the carbon dioxide and it might balance in the environmental atmosphere to save the health and environment clean through the process of sequestration. Figure 3 shows the bio resources energy [35-37].



Figure 3 Biomass with their resources of energy

Those micro algae based bio fuels form the better advantages for making the green house gases and forming the renewable sources of energy and maintainable for the production of bio fuel with bio mass energies. Some of the following micro algae like *Chlorella* sp, *Chlorella vulgaris*, *Spirulina* sp., *Chlorella sorokiniana*, *Scenedesmus* sp., *Dunaliella tertiolecta*, *Chlorella kessleri* are various fixation capacities with carbon dioxide to produce the bio mass energies. The wastages of bio fuel productivities material is act as the substitute materials for fertilizers in the agricultural sectors and remaining fuel is act as the bio mass energies. Similarly, the waste products are utilized to fill the land for farming and remaining waste are might be act as the disposal method to decompose the material [38].

2.3 Wind Energy

The motion of air with kinetic energy is the reason for producing the wind energies with supports of wind turbines and other transforming systems and similarly electric energy is converted from the kinetic energy. Wind energy is most exceptional energy sources and it is approached for saving the nature and maintaining itself and utilized well from the various countries by the supports of government agencies and it is most the centralized idea for employing this works. In this manner, all the central and state government sincerely worked intense to establish the generation of wind and sequence development is taken with newer methods. Wind energy is commonly used as the mechanical energy to produce the electrical energy which is not directly. Normally the wind energy production is attained with various elements or components having gear trains, rectifiers, and control boards with inverters, filters and transformer. The gear trains is used as the operating the velocities, control board are the main for entire operation and finally the transformer is act as the final unit to transfer the current from one sources to other regions. Figure 4 shows the wind energy schematic representation.

The wind mills having common two types like vertical and horizontal based on the requirements and flowing of wind it will be varied. There are various suitable components are required to connect into the wind turbines with appropriated high power generators to produce the maximum efficiency wind

power and it was reported by the various researchers. The unique design with turbine blade attracts the winds with assist of kinetic energy to revolute it. Due to the help of shaft, rotating blades with mechanical energy capacities is converted into rotor based generator for improving the efficiency of wind turbine. Therefore the electrical energy was transformed from the mechanical energy by utilizing the specially made generators and then electrical energy is shifted to the inaccessible load via the transformer. The entire control boards of wind energy are more crucial to improve the effectiveness with generation of electric power. The maximum manipulated systems approached in various plants and its secondary systems of wind energy [30].

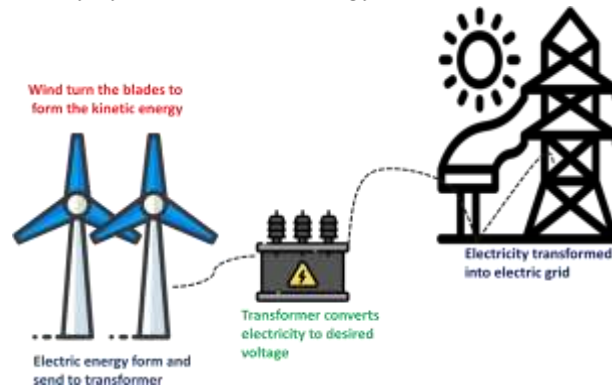


Figure 4 Schematic representation of wind energy

2.4 Hydro energy systems

From the last two decades, total capacity with maximum of 70% was increased which is performed for electricity generation with one sixth in globally. Therefore the hydro energy is third largest renewable sources of energy especially for generating the electricity afterwards for gas and coal. There are two classification was attained in hydro power that is tidal and traditional hydro power. Due to gravitational pull forces which comes from flowing of water and it is referred as the hydro electricity and converts the electrical energies. Running river, dams, pumped water are some categories which is comes under the hydro power. Therefore, based on the initialization hydro power design, dam and flowing of riverside is constructed which is basic necessity for capital investments [35]. Utilizing the hard forces of water which comes from the tides, ocean energy is formed and generates the hydro power. When contrasted to solar and wind power, tidal power is more forecasted and easily identified. But in the real scenario compared to hydro power tidal power is still used partially. There is still maximization margin of utilization in tides for composing the energies.

The UNESCO contributes agreement between the Paris with international association of hydropower in 7th world hydro power congress in the year of 2019. This agreement is fully relates to maintain the climatic conditions and improve the hydropower and interconnecting is attained to worldwide hydro power. Continuously, the year 2021 November before assignment was seriously reported and watched by the committee. Then summit conference in the year of March 2021, the international energy agency is discussed the global road map for net zero in the year 2050 [37].

There various arrangements were followed by the committee and the points were discussed below. Enhance the revenues, follow the installations, reducing the capital cost without wastages while in installations,, reduce the emission with maximum energy utilization, list of priorities are enlisted which is based on the climatic conditions and energies. The improvisation is must watched and compared with traditional system to enhance the flexibility and reliability also evades the situation of catastrophic in the nearby plant. The electrical security with mechanism is the critical aspects for hydro power generation. The other important role is to give more subsidy and assist the financial in under developing countries for maintain the establishment of hydro power. From the international energy agency, the advantages of hydropower in structure of cost also approached. In some regions like mountains and islands are difficult to reach these facilities due to grid connections and the small hydro power systems easily interconnects the grid and it is one of the suitable solutions for upcoming projects.

2.5 Geothermal energy

Geo thermal energy is also called as the natural thermal energy from the earth's minerals. In this process, the pumps are utilized to dig out the hot water or steam into the level of earth's surfaces. From the earth's crust, the steam was generated in the form of heat energy and maximum effectiveness is shifted to turbine blades to transform the applicable energy into the electrical via the appropriated generator and finally converted into suitable grid for industrial and domestic usages [38]. The steam, binary cycle and dry steam plants are the some processing methods for improving the geothermal power efficiency. Normally the geothermal energy plant has some constraints like availability and maintained predictable system for enhancing the resources of energies. Figure 5 shows the geothermal system.

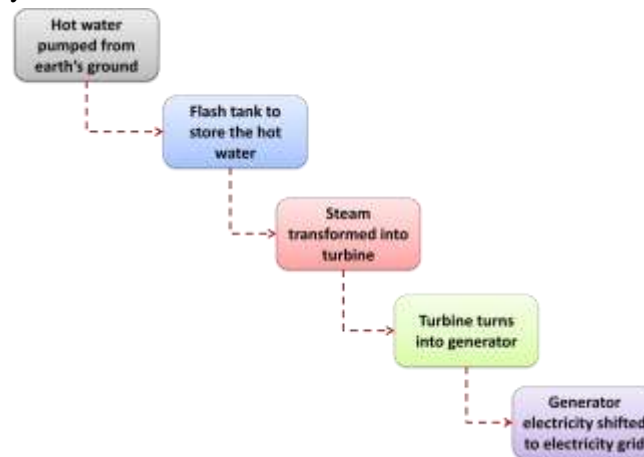


Figure 5 Illustration of geothermal energy principle

Conclusion

Renewable energy is most indispensable method to enhance, maintain and sustaining the global ecological health. The broad replacement is required for traditional energy sources like fossil fuel method with unconventional renewable energy sources. Therefore the various changes must be followed which is more valuable for the people and it is associated with risk factors. Those serious tasks like government policies, infrastructure, installation and construction expenses, corporate politics and political issues are including. The government taken the serious action for those critical issues and provides opportunities to the public those who are willing to initiate the projects which are relate to the renewable energy sources. Similarly, the business sectors provide the job to the skilled peoples to do the work in renewable sources of energies and applying various skills for operating the process. The bio reactors and bio refinery methods for the transformation of chemical process is maintained for the composing of energies from the bio fuels under the advanced methods. So the government must takes the innovative works projects to the students and get the novel result that assist in financial supports to do the project in real time and join with some industries. The utilization of solar panels in residential zones might be converted and optimistic to establish the market and approval from the common people. Similarly the health maintains is major for aquatic and marine applications to obtain the maximum advantages from the hydro power system.

References

1. Jiang, W., Liu, Y., Fang, G., & Ding, Z. (2023). Research on short-term optimal scheduling of hydro-wind-solar multi-energy power system based on deep reinforcement learning. *Journal of Cleaner Production*, 385, 135704. <https://doi.org/10.1016/J.JCLEPRO.2022.135704>
2. Li, S., Wu, Y., Dao, M. U., Dragoi, E.-N., & Xia, C. (2023). Spotlighting of the role of catalysis for biomass conversion to green fuels towards a sustainable environment: Latest innovation avenues, insights, challenges, and future perspectives. *Chemosphere*, 318, 137954. <https://doi.org/10.1016/J.CHEMOSPHERE.2023.137954>
3. Li, J., Gan, C., Zhou, J., & Novakovic, V. (2023). Performance analysis of biomass direct combustion heating and centralized biogas supply system for rural districts in China. *Energy Conversion and Management*, 278, Dept. of Mech. Engg.

116730. <https://doi.org/10.1016/J.ENCONMAN.2023.116730>

4. Hussain, B., Asif Ali Naqvi, S., Anwar, S., & Usman, M. (2023). Effect of wind and solar energy production, and economic development on the environmental quality: Is this the solution to climate change? *Gondwana Research*. <https://doi.org/10.1016/J.GR.2023.01.012>
5. Campos, I., Brito, M., & Luz, G. (2023). Scales of solar energy: Exploring citizen satisfaction, interest, and values in a comparison of regions in Portugal and Spain. *Energy Research & Social Science*, 97, 102952. <https://doi.org/10.1016/J.ERSS.2023.102952>
6. Zhang, M., Tang, Y., Liu, L., Jin, J., & Zhou, D. (2023). Is asset securitization an effective means of financing China's renewable energy enterprises? A systematic overview. *Energy Reports*, 9, 859–872. <https://doi.org/10.1016/J.EGYR.2022.12.032>
7. Sun, B., Li, M., Wang, F., & Xie, J. (2023). An incentive mechanism to promote residential renewable energy consumption in China's electricity retail market: A two-level Stackelberg game approach. *Energy*, 269, 126861. <https://doi.org/10.1016/J.ENERGY.2023.126861>
8. Hossain, M. R., Singh, S., Sharma, G. D., Apostu, S.-A., & Bansal, P. (2023). Overcoming the shock of energy depletion for energy policy? Tracing the missing link between energy depletion, renewable energy development and decarbonization in the USA. *Energy Policy*, 174, 113469. <https://doi.org/10.1016/J.ENPOL.2023.113469>
9. Reffat, R. M., & Ezzat, R. (2023). Impacts of design configurations and movements of PV attached to building facades on increasing generated renewable energy. *Solar Energy*, 252, 50–71. <https://doi.org/10.1016/J.SOLENER.2023.01.040>
10. Dar, J., & Asif, M. (2023). Environmental feasibility of a gradual shift from fossil fuels to renewable energy in India: Evidence from multiple structural breaks cointegration. *Renewable Energy*, 202, 589–601. <https://doi.org/10.1016/J.RENENE.2022.10.131>
11. Zhang, Z., Zhao, Y., Cai, H., & Ajaz, T. (2023). Influence of renewable energy infrastructure, Chinese outward FDI, and technical efficiency on ecological sustainability in belt and road node economies. *Renewable Energy*. <https://doi.org/10.1016/J.RENENE.2023.01.060>
12. Lee, C. C., Zhang, J., & Hou, S. (2023). The impact of regional renewable energy development on environmental sustainability in China. *Resources Policy*, 80, 103245. <https://doi.org/10.1016/J.RESOURPOL.2022.103245>
13. Regueiro-Ferreira, R. M., & Alonso-Fernández, P. (2023). Interaction between renewable energy consumption and dematerialization: Insights based on the material footprint and the Environmental Kuznets Curve. *Energy*, 266, 126477. <https://doi.org/10.1016/J.ENERGY.2022.126477>
14. Abbas, J., Wang, L., Belgacem, S. ben, Pawar, P. S., Najam, H., & Abbas, J. (2023). Investment in renewable energy and electricity output: Role of green finance, environmental tax, and geopolitical risk: Empirical evidence from China. *Energy*, 126683. <https://doi.org/10.1016/J.ENERGY.2023.126683>
15. Habiba, U., & Xinbang, C. (2023). The contribution of different aspects of financial development to renewable energy consumption in E7 countries: The transition to a sustainable future. *Renewable Energy*, 203, 703–714. <https://doi.org/10.1016/J.RENENE.2022.12.088>
16. Alola, A. A., Olanipekun, I. O., & Shah, M. I. (2023). Examining the drivers of alternative energy in leading energy sustainable economies: The trilemma of energy efficiency, energy intensity and renewables expenses. *Renewable Energy*, 202, 1190–1197. <https://doi.org/10.1016/J.RENENE.2022.11.045>
17. Bei, J., & Wang, C. (2023). Renewable energy resources and sustainable development goals: Evidence based on green finance, clean energy and environmentally friendly investment. *Resources Policy*, 80, 103194. <https://doi.org/10.1016/J.RESOURPOL.2022.103194>
18. Liu, Y., & Feng, C. (2023). Promoting renewable energy through national energylegislation. *Energy Economics*, 118, 106504. <https://doi.org/10.1016/J.ENERGY.2023.106504>
19. Yi, S., Raghutla, C., Chittedi, K. R., & Fareed, Z. (2023). How economic policy uncertainty and financial development contribute to renewable energy consumption? The importance of economic globalization. *Renewable Energy*, 202, 1357–1367. <https://doi.org/10.1016/J.RENENE.2022.11.089>
20. Dong, W., Li, Y., Gao, P., & Sun, Y. (2023). Role of trade and green bond market in renewable energy deployment in Southeast Asia. *Renewable Energy*, 204, 313–319. <https://doi.org/10.1016/J.RENENE.2023.01.022>
21. Nan, S., Huang, J., Wu, J., & Li, C. (2022). Does globalization change the renewable energy consumption and CO2 emissions nexus for OECD countries? New evidence based on the nonlinear PSTR model. *Energy Strategy Reviews*, 44, 100995. <https://doi.org/10.1016/J.ESR.2022.100995>

22. Bianchi, F. R., Bosio, B., Conte, F., Massucco, S., Mosaico, G., Natrella, G., & Saviozzi, M. (2023). Modelling and optimal management of renewable energy communities using reversible solid oxide cells. *Applied Energy*, 334, 120657. <https://doi.org/10.1016/J.APENERGY.2023.120657>
23. Alharbi, S. S., al Mamun, M., Boubaker, S., & Rizvi, S. K. A. (2023). Green finance and renewable energy: A worldwide evidence. *Energy Economics*, 118, 106499. <https://doi.org/10.1016/J.ENERCO.2022.106499>
24. Dogan, E., Hodžić, S., & Šikić, T. F. (2023). Do energy and environmental taxes stimulate or inhibit renewable energy deployment in the European Union? *Renewable Energy*, 202, 1138–1145. <https://doi.org/10.1016/J.RENENE.2022.11.107>
25. Wang, S., Dong, Q., Zhang, J., Sun, J., Gu, X., & Chen, C. (2023). Robustness assessment of power network with renewable energy. *Electric Power Systems Research*, 217, 109138. <https://doi.org/10.1016/J.EPSR.2023.109138>
26. Wang, Q., Guo, J., Li, R., & Jiang, X. ting. (2023). Exploring the role of nuclear energy in the energy transition: A comparative perspective of the effects of coal, oil, natural gas, renewable energy, and nuclear power on economic growth and carbon emissions. *Environmental Research*, 221, 115290. <https://doi.org/10.1016/J.ENVRES.2023.115290>
27. Johannsen, R. M., Mathiesen, B. V., Kermeli, K., Crijns-Graus, W., & Østergaard, P. A. (2023). Exploring pathways to 100% renewable energy in European industry. *Energy*, 268, 126687. <https://doi.org/10.1016/J.ENERGY.2023.126687>
28. Wang, Z., Yao-Ping Peng, M., Anser, M. K., & Chen, Z. (2023). Research on the impact of green finance and renewable energy on energy efficiency: The case study E-7economies. *Renewable Energy*, 205, 166–173. <https://doi.org/10.1016/J.RENENE.2022.12.077>
29. Corakci, A., & Omay, T. (2023). Is there convergence in renewable energy deployment? Evidence from a new panel unit root test with smooth and sharp structural breaks. *Renewable Energy*. <https://doi.org/10.1016/J.RENENE.2023.01.119>
30. Shan, Y., & Ren, Z. (2023). Does tourism development and renewable energy consumption drive high quality economic development? *Resources Policy*, 80, 103270. <https://doi.org/10.1016/J.RESOURPOL.2022.103270>
31. Pizza, G., Bracco, S., Delfino, F., Somma, M. di, & Graditi, G. (2023). Impact of electric mobility on the design of renewable energy collective self-consumers. *Sustainable Energy, Grids and Networks*, 33, 100963. <https://doi.org/10.1016/J.SEGAN.2022.100963>
32. Xu, Y., Ji, M., Klemeš, J. J., Tao, H., Zhu, B., Varbanov, P. S., Yuan, M., & Wang, B. (2023). Optimal renewable energy export strategies of islands: Hydrogen or electricity? *Energy*, 269, 126750. <https://doi.org/10.1016/J.ENERGY.2023.126750>
33. Simionescu, M. (2023). The renewable and nuclear energy-economic growth nexus in the context of quality of governance. *Progress in Nuclear Energy*, 157, 104590. <https://doi.org/10.1016/J.PNUCENE.2023.104590>
34. Siddik, A. B., Khan, S., Khan, U., Yong, L., & Murshed, M. (2023). The role of renewable energy finance in achieving low-carbon growth: Contextual evidence from leading renewable energy investing countries. *Energy*, 126864. <https://doi.org/10.1016/J.ENERGY.2023.126864>
35. Park, H., Kim, J.-K., & Yi, S. C. (2023). Optimization of site utility systems for renewable energy integration. *Energy*, 269, 126799. <https://doi.org/10.1016/J.ENERGY.2023.126799>
36. Matallah, S., Matallah, A., Benlahcene, L., & Djelil, Z. (2023). The lure of oil rents and the lack of innovation: Barriers to the roll-out of renewable energy in oil-rich MENA countries. *Fuel*, 341, 127651. <https://doi.org/10.1016/J.FUEL.2023.127651>
37. Nchofoung, T. N., Fotio, H. K., & Miamo, C. W. (2023). Green taxation and renewable energy technologies adoption: A global evidence. *Renewable Energy Focus*, 44, 334–343. <https://doi.org/10.1016/J.REF.2023.01.010>
38. Zhang, W., & Chiu, Y.-B. (2023). Country risks, government subsidies, and Chinese renewable energy firm performance: New evidence from a quantile regression. *Energy Economics*, 106540. <https://doi.org/10.1016/J.ENERCO.2023.106540>
39. Mohanraj, M., Karthick, L., Dhivagar, R. (2019) Performance and economic analysis of a heat pump water heater assisted regenerative solar still using latent heat storage. *Applied Thermal Engineering*, 196, 117263. <https://doi.org/10.1016/j.applthermaleng.2021.117263>.
40. Karthick, L., Murugan, V.S., Leon, S.L.J., Mallampati, M., Ahamed, M.I. and Loganathan, G.B., (2022). Energy performance of a compression refrigeration cycle using environment-friendly refrigerants. *Materials Today: Proceedings*, 66, pp.1519- 1525.

Comprehensive review and recent advancement in dairy process through solar based thermal energy techniques

L. Karthick^{1*}, Sanchit Kumar Khare², Parmod Kumar³, Mohd Yunus Khan⁴,
R. Prasanna Venkatesh⁵, Liana Mihaela Fericean⁶

¹Department of Mechanical Engineering, Hindusthan College of Engineering and Technology, Coimbatore 641032, India.

²Department of Mechanical Engineering, Institute of Technology and Management, GORAKHPUR-273209, U.P., India

³Department of Electronics and Information Engineering, Jiangxi University of Engineering, Xinyu City, Jiangxi Province 338000, China.

⁴Department of Mechanical Engineering, National Institute of Technical Teachers Training and Research (NITTTR), Chandigarh, India.

⁵Department of Mechanical Engineering, SACS MAVMM Engineering College, Madurai - 25301.

⁶Biology and Plant Protection Department, Faculty of Agriculture University of Life Sciences “King Michael I of Romania” from Timisoara, Romania.

*Corresponding Author *Email: bemechkarthick@gmail.com*

Abstract: The necessity of appropriated energies like thermal and electrical is utilized to conduct the demanding thermal processes like heating, cooling and cleaning are used in the dairy fabrication industries. There is some complex issues to choose and incorporation of the equipments which utilized for the solar processing system including the extensive components like solar collectors with different types, solar heating sources and related cooling components. While in solar thermal energy, temperature maintain is about maximum at 200 °C that can be strongly mechanized in this dairy processes. During the heating process, the maintaining of temperature is about 300 to 400 °C significantly utilizing the solar collectors with different categorize like flat plate and parabolic collectors. During the cooling processes, the Fresnel reflectors are used through the solar absorption chillers. The additional energy in thermal based solar energy system is about 200 °C. This research significantly reviewed the thermal necessity of the dairy based industries. The obtainable solar thermal usages and suggested the conception of design and procedures are incorporated by the existing collection of data. This conceptual design contains the relationship of the thermal energy and solar collector's storage to the pipe line of thermal energy via the steam drum and absorption chiller. This advantage gives feasibility of the shifting the heat fluids, the unique solar energy fabrication to conventional fabrication are explained in this paper and different methods are elaborately reviewed.

Keyword: Dairy, direct, solar, cooling, heating and Fluid

1. Introduction

From the 2020 year, our world is suffering severe transforms that will resume among the upcoming decades to affect the food sectors in global wise and needs of energy. Owing to urbanization, increasing population and climatic modification are main reasons to meet the food demand. In the industrial sectors, consumption of global energy is very tedious which is the heat consumes above 70 % of the overall industrial require of energy and the heating need is about above 50% of total energy and the temperature range is maintain between 50 to 250 °C. Presently, the renewable energy resources demand is attained only at 9% for the industrial utilization out of more than 700 units of industrial that utilize solar heat with overall region of solar receivers of 560 MWth and it is reported

in the year of 2019. The purposes of solar based thermal energy in the industrial sectors towards to prolong fabrication [1-2].

The following process like solar potential, environmental evaluation, solar thermal component performance evaluation, integration of solar heat, economic, expensive, present state of methodology and related case studies are implicit to solar thermal energy related industrial process which is discussed in following sections. Out of global in food fabrication and its supply lie between 10 to 20% for energy consumption [3-4]. The global energy approximate is nearly equal to 170000 TWh in the year of 2019 and its more than 50% is contrasted to last 20 years. But in the blending of energy of non renewable sources are extracted from fossil fuels. While increasing the resources of energy is essential to promote alongside rapid increasing requirement and it is attained by substantial task in environmental which also required to be revised. These comprise the loss of biodiversity, degradation of environmental, global warming incident, lessening of natural sources and environmental deprivation. It is not adequate to diminish consumption of energy and the concentration required to be transforming to construction blocks to compose food fabrication with sufficient energy effectiveness and supply method [5-6].

Due to increasing the world population, our planet also modified by environmental pollution and the increasing of food demand and agricultural production which is reported by the food and agricultural organization (FAO). This organization alerts that a increasing of food production will be necessity to envelop the needs and it is anticipated to achieve the growth in food production in 2050 by 70%. This projected increase in food supply as expected towards to respected growth in energy need in the supply chain of food industries [7-8]. The other significant future warning to the food sector is climate modification, which is predictably affecting the world's fabrication of agriculture and it is a severe impacts for food sector, containing quality, insecurity for food capacity, safety and protection. To ensure the sufficient delivery of food supply needs additional energy and similarly the climatic changes need to be addressed [9-10].

There are three key role is utilized to follow the dairy sectors will be significantly recognized. The first way is analyzing the global warming effects that will not be undesirable in all places, a respected increment of deficiency incidents is projected across the global impacting the crop growth and as an outcome diminishing accessibility of animal feed. The increasing temperature from global warming region that will affect the growth of crop and resulting in reducing milk fabrication and developed humanity risk [11-12]. Lastly, the food protection relates a significance of food borne pathogens acclimatizing to global warming issues and the reproduction rates will be reduced or modified as per the heat resistance. In some cases, the present pasteurization system might no lengthy and the accomplishment of food safety procedures could be unavoidable. The steps may be like lesser refrigeration temperatures and maximum heat treatment. These tasks to the dairy sectors are already in live and required to be resolved via the supply chain of dairy prior their outcomes turn into unruly and effect of safety and surplus supply. Even though the dairy industry endures the causes of global warming and it is concomitantly responsible for considerable discharge of emission of green house gas, which influence to the global warming incident [13-14].

As expected in the year of 2007, food product fabrication, supply chain of dairy sector and farm based activities are subjected to green house gas emission at 2.7% by the report of FAO in the year of 2010. These are extracted from broad fossil fuel and fermentation of bovine enteric procedures beside with supply chain. Undesirably, between the year of 2005 and 2015 green house emission are rapidly raised by 18% as per the report of GDP in 2018. The dairy products make the significant aspects in the human diets which are major sources of minerals, proteins and vitamins. The secondary products of diary like butter, cheese and milk are another intake of energy and it is accounted for developed countries from the total consumption at 14% and developing countries at 5%, respectively [15-17].

The rapid developing world population from the different organization views, the maximum capita income develops the diet tendency in eastern countries. Similarly, the major development in needs of

dairy based products locates the long term maintainability of dairy sectors. In the decades like 2020 to 2030, anticipated increment of 1.0% is predicted for new dairy products. Even though the dairy based products are crucial in human diets, utilization of energy, green house gas emission is related to meat and fabrication of dairy are much maximum than the plant related food products [18-20]. Figure 1 shows the food processing methods with renewable techniques.

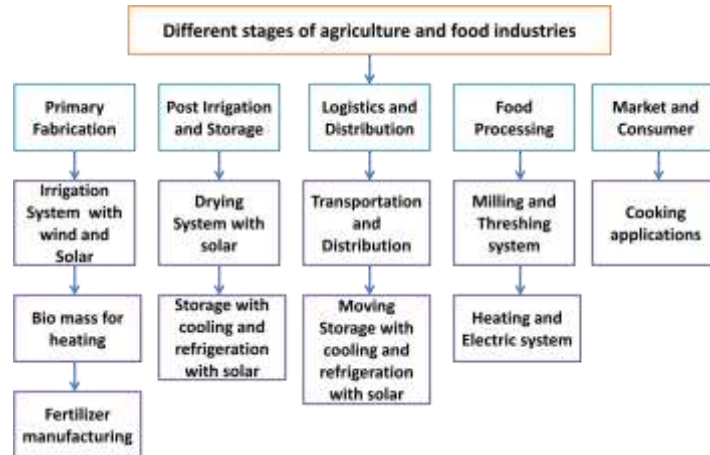


Figure 1 Food processing chain with solar and other renewable energy

Some researchers analyzed in the western regions, the populations are improving rapidly which is feared about animal welfare, environmental impact, vegetarian diets and low meat trending. Consequently, that green house gas emission of vegetarian based diets about semi that of meat-eaters' diet. Transforming habits of eating of plant diets considerably adds to environment maintainability. The zero gas emission targets are required to face in meet year of 2050 due to rise in global temperature and climatic modification, it exhibits that the government has set the target. From the outcomes, the more number of concurrence and its instructions for the utilization of renewable sources of energy has been achieved on the nontraditional energy resources of energy and unprotect emission. Among the various resources appropriated renewable techniques that have been extensively utilized for creating warm water and normal heating by the sources of solar energy. It is the beneficial potential to be applied to the food based sectors and it is one of top most energy demanding in the renewable industrial sectors. The dairy based units, in especially necessitate important thermal energy for cooling, heating, fermentation, cleaning, evaporation, washing, drying and pasteurization [21]. The application of heat pump assisted water heater also useful for dairy process [35]. The cooling cycles and effective refrigerants are studied and applied in various applications [36].

The combination of thermal with solar energy is mainly utilized for dairy process that employ only on solar thermal. During this investigate, this research approach of both thermal with solar based cooling and heating process for the fabrication of cheese, yoghurt, milky drinks, milk, milkpowder and cream. Therefore, the main aim of this research is to evaluate the present requirement of thermal of the dairy routes, analyze the prospective of utilizing solar thermal methods, proposed an interpretation approach for solar thermal application to the dairy routes and estimate the respective cost of heat and various techniques in solar related methodologies.

2. Necessity of solar techniques in dairy process

This section reviews the solar related components like electrical and thermal energy necessity of the dairy for the fabrication with different dairy manufactured goods. The important attributes of solar energy applications is solar classification and quantities of mass flow streams. There are different main steps like fabrication of milk, steam to process of cooling and heating and coolant to cooling process. The pasteurization and pre treatment of raw milk is the main process for maintain the temperatures. This raw milk is maintained about the temperatures 4 to 90 degree Celsius. In some

region of raw milk is utilized for milk powder fabrication is maintained about the temperature is about 200 degrees Celsius which is completed next to pasteurization [22].

The following fluid elements like ammonia, brine, water and mixture of glycol for cooling stream is utilizes through the piping system which is comes from the buffer tank and itscirculated through this pipe line. Owing to food safety apprehension, the stream of heating posse's water which is transformed interested in steam to the boilers and it driven to process. Nevertheless, the considerable quantity of water cannot be reused in the cycle. The additional heat losses also extracted from the hot water which is discharged from heating processes.

The electrical energy is majorly utilized for powering purpose that the components like lighting, pumps, refrigerators, control units and compressor. The processes like homogenization, separation with centrifugal and sterilization are the electrical energy purposes. Especially, the specific energy consumption which based on thermal and electrical researches was analyzed by different researchers [23]. During the production of cheese, maximum specific energy consumption thermal at 7.66 MJ/kg is measured for milk proportion. The significant factors influences the specific energy consumption milk products are energy effectiveness. Similarly, specific energy consumption electrical at 2.95 MJ/kg is estimated in favor of milk fabrication with whey powder. The necessity of temperature at 200 °C is the maximum for solar collector selection. Figure 2 exhibits the thermal processing methods in dairy units.

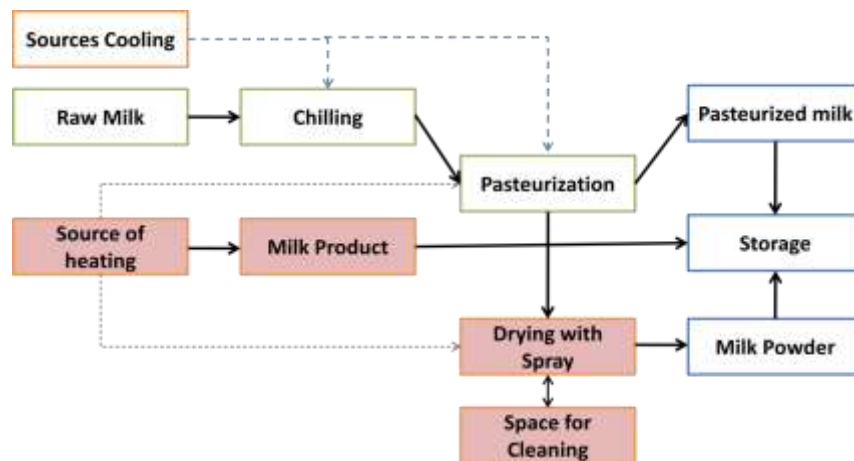


Figure 2 Thermal processing systems in dairy process plant

The cooling is essential for keep in store and storing of the dairy goods while the high temperature is essential for fermentation, clean-up, drying and pasteurization. In the spraying process, the lesser and maximum temperature in refrigeration was measured at 4 and 200 degree Celsius. This is the normal method in food industries to compose the steam at maximum temperature then diminish to target ranges to face the necessities. The temperatures between 80 to 150 °C are maintained for yoghurt fabrication because the steam might be approached to the process of fermentation, sterilization, cleaning and pasteurization. The production capacity of dairy plants for power necessities is differed from 76 to 6200 kW and based on the process; the power may be slightly changed [24-25].

3. Dairy process with integration of solar energy

Solar thermal cooling and heating are categorized by the four steps like indirect and direct steam fabrication, milk by direct heating and cooling through solar method. From the detail analyzed literatures, there is no common methods were not attained for solar thermal energy into the dairy processes. Normally, the application of heat exchanger toward shifts heat into the diary routes through maximum necessities of temperatures could not practicable for cooling processes. Dueto low temperature application was utilized in that process. On the next side, the incorporation ofsupply level focused to shift energy to the offered cooling and heating supply lines to creates the utilize of solar based mechanical driven chiller box for supplying the breezing essential routes. The major significant usage of the contribute level contains, evading of component alteration like boiler,

pasteurizer. Due to alteration on the pressurized devices like boiler might need regulated certification of the modified component. Next, while in installation time, interruption might be sorted during the production time. Finally, the control system must be recognized [26].

The solar energy option is the key role to produce the dairy based products with effect of quantity flow with magnitudes of various streams. The small scale industries produce the initial products like cream and milk. But in the integration of supply range could be the suitable option of more quantity flow sections on the production line. The evading methods like evaporation, spray drying and fermentation. Besides, much dairy plants the pasteurization process temperatures about 85 degrees Celsius is maintained in some dairy [27].

The moderate and huge dairy units composes the broad assortment of dairy goods like cheese, special powders and yoghurt has various branches or categorizes in their fabrication sections for different process. The maximum quantity flows with maximum temperature need could construct the level of supply which is more in flexible. In the view of industrial processes in European based sectors, the dairy demands cannot be meet to required solar thermal methods includes spraying and maximum temperature needs for evaporation. Figure 3 shows the outline of solar energy integration with dairy process.

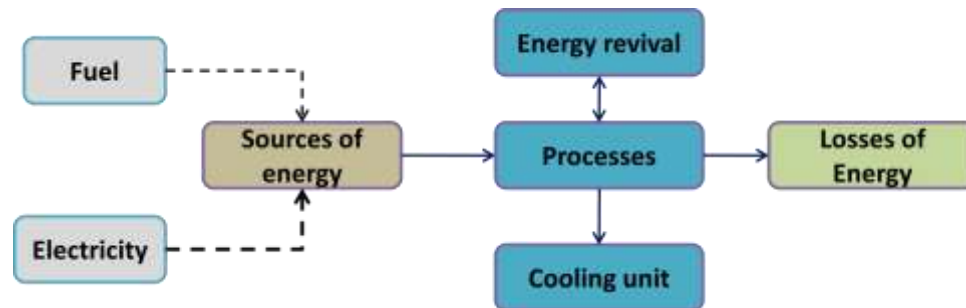


Figure 3 Solar energy integration in dairy process

4. Steam production by indirect method

This method utilizes the heat excluding the water for shifting the fluid in the thermal based solar collectors and it has mechanized component to produces the steam. Below the figure showed that the steam production method with supports of closed tank, kettle boiler, heat exchanger, steam could mechanized by the solar to fabricate the steam. Some researchers investigated the indirect steam production through parabolic tough collectors having the 10 Sq. Meters with solar concentrator region and utilized thermal oil. Another researcher investigated with flat plat collectors to compose the solar heat for the production of dairy in 2000 Sq. meter area. The PV based solar system to exploit thermal potency for pasteurization systems. These procedures were only attained in the medium scale industries and its production rate of milk is about 4000 liters per day [28]. The kettle boilers and steam drum is the common component which is integration for the indirect steam fabrication in thermal based solar applications. Figure 4 displays the indirect technology for steam fabrication.

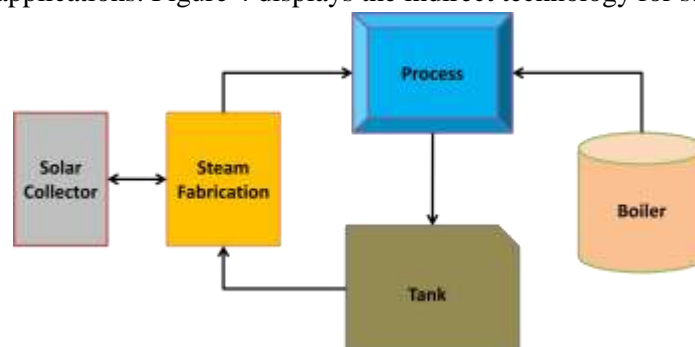


Figure 4 Steam fabrications by indirect method

The combination of steam and water blender was utilized to pass the water through route of external exchanger of heat having the traditional convection system to transform water into steam

production. The kettle boilers approached with tube having the shell type has been utilized to pass the heat transfer fluid to alter to steam from water [29]. The fabrication of indirect steam utilized broadly for heating method which especially in dairy industries. The advancement of present study is utilized of thermal based oil for heat transfer fluid owing to enhancements of thermal efficiency.

5. Steam production by direct method

The below figure showed the fabrication of steam which utilize as the water in heat transfer fluid in the solar collectors to compose the steam for the direct process. The direct steam fabrication might be approached to enhance the cost efficient methods. Especially, the U type heating pipe line was utilized for the direct method to produce the steam fabrication that was passed via the parabolic trough collector [30]. The usual boiler is altered in the proper way that parabolic trough method collects the water from the drum which is transformed into steam and drive back into the boiler having maintaining at pressure of 0.75 MPa with greater thermal efficiency at 40%. The major drawbacks were occurred in tracking system which is related to cost in the certain location and recognized certification of the altered boilers. Some studies were attained in the glass type tube collectors to compose about 2 kg/Sq. meter at 130 degree Celsius having the effectiveness which is greater than 40 percentages for heating process. Figure 5 shows the steam fabrications through direct system.

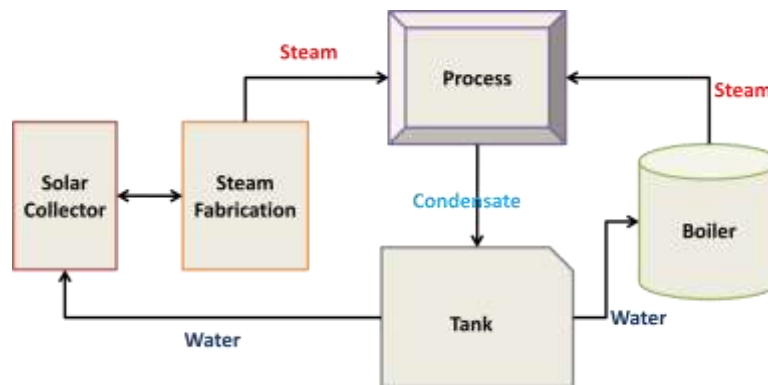


Figure 5 Steam fabrications by direct method

Even this system can be approached as common route to direct steam method for the steam fabrication exclude any requirement of tracking system and boiler alteration, the modified boilers. The moderate temperatures levels are improbable to be appropriated on the big industries of dairy units owing to needs of maximum temperatures for the processes of spray drying and evaporation in their dairy process. In the pasteurization process, PV system with incorporation of parabolic concentrator having the partial covering was utilized. The PV panels are implanted at the mid portion of the parabolic collectors to compose the electrical energy which is intended for pumps beside with thermal energy [31].

It is concluded that the experimented methods was proficient to pasteurize with milk of 216 kg which contains 5 kWh of electrical energy composed with three elements having the area at 4.2 Sq. meter with polycrystalline PV panels utilized for pumps. There are three various methods are initiated with solar integration of direct method for dairy sectors. The steps are connecting the conventional heater with collectors in the arrangements of parallel, prior to hot tank solar collector is fitted and after the heat tank solar collectors is combined in series arrangements [32].

The significant competent decision is verified to the next one with solar heating average at 2.3 MW which is contrasted to decision 1 at 1 MW. It can be stated that the fabrication of steam is extensively utilized in application of solar thermal for the different dairy process. The drawbacks of this system for heat transfer fluid for the water usages vaporizes about 100 degree Celsius and this phase were converted from liquid to steam stages. The enhanced heat transfer fluid like thermal oil which posse's maximum boiling temperatures and it kept as a fluid with maximum temperature necessity.

6. Solar cooling system

The majority of normal solar mechanized cooling methods are utilized on the real time market. From the literature, the chillers having the absorption are the appropriated and extensively utilized methods for the solar based thermal utilization for cooling. It consists of generator, condenser, evaporator, pump, absorber and expansion valves having the potency to be utilized for storage the milk and cooling. Instead of electrical energy, thermal energy with solar technique was suited for this process and the absorbent and refrigerant as fluids which are utilized in this dairy process [33].

The absorbent fluid suck up the vapors with refrigerant towards intake to pump so as to working at the phase of liquid and it turns to minimize the input of work. The single and double chillers on coolant of bromine and lithium combination is attain that the mixing techniques are appropriated for dairy process in cooling. The lithium bromide absorption chillers are mechanized by altered flat plate collectors having the 500 Sq. meter area with supporting of 100 kW. The outlet temperature about 75 degree Celsius is utilized to intake the chiller absorption that cooling the water at 9 degree Celsius. Similarly, various capacities like 100 to 350 kW of absorption chiller were mechanized by relinquished tube collectors of solar having the mentioned areas of 500 to 650 Sq. meter range. These approaches gives the collectors which having the outlet temperatures at 80 to 90 degree Celsius. It is utilized to feed chillers in absorption to give cold water at various temperatures from 8 to 15 degree Celsius. Even though this methods has been utilized for space cooling purposes with lesser temperatures. It is not suited for dairy processes when using the minimum temperature and the fluid as the mixing of ammonia and water through the parabolic trough collector. Figure 6 shows the solar mechanized cooling system.

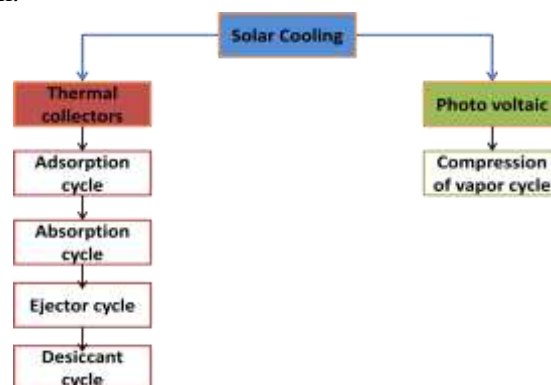


Figure 6 Solar cooling system

The extra benefits has utilized to reducing the maintenance for eradicating the defects of legionella and excluding the additional water spending. In the dairy industries, absorption chillers are used for feeding the mixture of ammonia and water fluid which is appropriated for dairy processes. But there are restricted data in the application of cooling process through the solar based thermal applications. In some literatures, one exceptional investigation was analyzed by the pinch analysis method in the dairy industries which is attained in the Austria. The studied related about the heating methods in the dairy methods to need cooling and heating at lesser capacities of 95 and 624 kW.

7. Utilization of solar collector to heat the milk by direct method

There is restricted data is accessible about utilizing the solar collectors for warming the milk for dairy process. During the process of heating milk through this solar collector for pasteurize at 72 degree Celsius with 50 liters per day. While in process, the milk was passed through this collector with horizontal tubes which is having black colored painted matt and it is located in this horizontal tubes maintain the distance 10 cm from each [34]. This method looks practical by technically, it could be approached to the pasteurization process having the steps like mixing, separation and cooling needs the lesser temperature at 5°C which is impossible to attain. Figure 7 shows the direct concept method for solar collectors to heat the fresh milk.



Figure 7 Heating milk through direct method

8. Conclusion

In this research, more number of literatures were utilized and reviewed seriously and concluded overall processes with different procedures were analyzed. In this study, overall demanding of renewable energy is more needed in this recent world demands for dairy process. The solar thermal energy incorporation also analyzed through the heating and cooling processes with solar based applications. The food processing chains with different methodologies were analyzed significantly. The composing the dairy products through the pasteurization process with heating and it is the major noteworthy methods to maintain the temperatures at 150 °C. The fermentation and cooling process need the lesser temperatures at 40°C. During the drying with support of spraying processes is maintained about the temperatures is 180 °C. Finally, this research concluded with some important points like complex to attain maintained collectors owing to maximum temperature modifications, thermal loss in solar receivers was attained with various lengths of pipe; loop flow rate of solar is restricted to manipulated and deficient in solar thermal energy storage. This paper much reviewed significantly and it is very much utilize for future researchers.

References

1. Blanchet, C. A. C., Pantaleo, A. M., & van Dam, K. H. (2019). A process systems engineering approach to designing a solar/biomass hybrid energy system for dairy farms in Argentina. *Computer Aided Chemical Engineering*, *46*, 1609–1614. <https://doi.org/10.1016/B978-0-12-818634-3.50269-1>
2. Kirim, Y., Sadikoglu, H., & Melikoglu, M. (2022). Technical and economic analysis of biogas and solar photovoltaic (PV) hybrid renewable energy system for dairy cattle barns. *Renewable Energy*, *188*, 873–889. <https://doi.org/10.1016/J.RENENE.2022.02.082>
3. Sakhare, K. P., Kiran, Balsoriya, H., & Kesari, J. P. (2022). Opportunities for solar thermal systems across dairy, agricultural, hotel & automobile industries. *Materials Today: Proceedings*, *56*, 3656–3668. <https://doi.org/10.1016/J.MATPR.2021.12.353>
4. Cetina-Quiñones, A. J., Bassam, A., Carrillo, J. G., Pérez-Quintana, I., Ricalde, L. J., & San- Pedro, L. (2022). 4E analysis for the implementation of parabolic trough solar collectors in Mexican dairy industry sector: An optimization approach including passive heat transfer methods. *Sustainable Energy Technologies and Assessments*, *53*, 102532. <https://doi.org/10.1016/J.SETA.2022.102532>
5. Blanchet, C. A. C., Pantaleo, A. M., & van Dam, K. H. (2019). A process systems engineering approach to designing a solar/biomass hybrid energy system for dairy farms in Argentina. *Computer Aided Chemical Engineering*, *46*, 1609–1614. <https://doi.org/10.1016/B978-0-12-818634-3.50269-1>
6. Kelly, P., Bertsch, R., Brazzale, P., Kulozik, U., Marx, M., & Felon, M. (2022). Sustainable Processing: Energy Conservation in Dairy Processing. *Encyclopedia of Dairy Sciences: Third Edition*, *4*, 836–845. <https://doi.org/10.1016/B978-0-12-818766-1.00393-7>
7. Sharma, A. K., Sharma, C., Mullick, S. C., & Kandpal, T. C. (2017). Potential of solar industrial process heating in dairy industry in India and consequent carbon mitigation. *Journal of Cleaner Production*, *140*, 714–724. <https://doi.org/10.1016/J.JCLEPRO.2016.07.157>
8. Zhang, C., Campana, P., Yang, J., Zhang, J., & Yan, J. (2017). Can Solar Energy be an Alternative Choice

- of Milk Production in Dairy Farms? ---A Case study of Integrated PVWP System with Alfalfa and Milk Production in Dairy Farms in China. *Energy Procedia*, 105, 3953–3959. <https://doi.org/10.1016/J.EGYPRO.2017.03.822>
9. Sharpe, K. T., Heins, B. J., Buchanan, E. S., & Reese, M. H. (2021). Evaluation of solar photovoltaic systems to shade cows in a pasture-based dairy herd. *Journal of Dairy Science*, 104(3), 2794–2806. <https://doi.org/10.3168/JDS.2020-18821>
 10. Vutukuru, R., Pegallapati, A. S., & Maddali, R. (2019). Thermodynamic studies on a solar assisted transcritical CO₂ based tri-generation system with an ejector for dairy applications. *International Journal of Refrigeration*, 108, 113–123. <https://doi.org/10.1016/J.IJREFRIG.2019.08.031>
 11. Moerkerken, A., Duijndam, S., Blasch, J., van Beukering, P., & Smit, A. (2021). Determinants of energy efficiency in the Dutch dairy sector: dilemmas for sustainability. *Journal of Cleaner Production*, 293, 126095. <https://doi.org/10.1016/J.JCLEPRO.2021.126095>
 12. Wallerand, A. S., Kermani, M., Voillat, R., Kantor, I., & Maréchal, F. (2018). Optimal design of solar-assisted industrial processes considering heat pumping: Case study of a dairy. *Renewable Energy*, 128, 565–585. <https://doi.org/10.1016/J.RENENE.2017.07.027>
 13. Quijera, J. A., Alriols, M. G., & Labidi, J. (2011). Integration of a solar thermal system in a dairy process. *Renewable Energy*, 36(6), 1843–1853. <https://doi.org/10.1016/J.RENENE.2010.11.029>
 14. Luqman, M., & Al-Ansari, T. (2022). Energy, water and food security through a waste- driven polygeneration system for sustainable dairy production. *International Journal of Hydrogen Energy*, 47(5), 3185–3210. <https://doi.org/10.1016/J.IJHYDENE.2021.10.214>
 15. Villarroel-Schneider, J., Höglund-Isaksson, L., Mainali, B., Martí-Herrero, J., Cardozo, E., Malmquist, A., & Martin, A. (2022). Energy self-sufficiency and greenhouse gas emission reductions in Latin American dairy farms through massive implementation of biogas-based solutions. *Energy Conversion and Management*, 261, 115670. <https://doi.org/10.1016/J.ENCONMAN.2022.115670>
 16. Egas, D., Ponsá, S., Llenas, L., & Colón, J. (2021). Towards energy-efficient small dairy production systems: An environmental and economic assessment. *Sustainable Production and Consumption*, 28, 39–51. <https://doi.org/10.1016/J.SPC.2021.03.021>
 17. Kumar, M., Kumar Choubey, V., Deepak, A., Gedam, V. v., & Raut, R. D. (2021). Life cycle assessment (LCA) of dairy processing industry: A case study of North India. *Journal of Cleaner Production*, 326, 129331. <https://doi.org/10.1016/J.JCLEPRO.2021.129331>
 18. Stanek, B., Wang, W., & Bartela, Ł. (2023). A potential solution in reducing the parabolic trough based solar industrial process heat system cost by partially replacing absorbers coatings with non-selective ones in initial loop sections. *Applied Energy*, 331, 120472. <https://doi.org/10.1016/J.APENERGY.2022.120472>
 19. Kumar Awasthi, M., Paul, A., Kumar, V., Sar, T., Kumar, D., Sarsaiya, S., Liu, H., Zhang, Z., Binod, P., Sindhu, R., Kumar, V., & Taherzadeh, M. J. (2022). Recent trends and developments on integrated biochemical conversion process for valorization of dairy waste to value added bioproducts: A review. *Bioresource Technology*, 344, 126193. <https://doi.org/10.1016/J.BIORTECH.2021.126193>
 20. Alvarez, V. B., Eastridge, M. L., Lee, C., & Sarantis, S. D. (2022). Sustainable Processing: Minimizing the Impact of the Dairy Industry on the Environment – Toward Zero Carbon Footprint. *Encyclopedia of Dairy Sciences: Third Edition*, 4, 846–854. <https://doi.org/10.1016/B978-0-12-818766-1.00307-X>
 21. Wang, K., Pantaleo, A. M., Herrando, M., Faccia, M., Pasmazoglou, I., Franchetti, B. M., & Markides, C. N. (2020). Spectral-splitting hybrid PV-thermal (PVT) systems for combined heat and power provision to dairy farms. *Renewable Energy*, 159, 1047–1065. <https://doi.org/10.1016/J.RENENE.2020.05.120>
 22. Das, R., & Ganguly, S. (2022). A comprehensive review on solar pond research in India: Past, present and future. *Solar Energy*, 247, 55–72. <https://doi.org/10.1016/J.SOLENER.2022.10.008>
 23. Zhou, M., Groot Koerkamp, P. W. G., Huynh, T. T. T., & Aarnink, A. J. A. (2022). Development and evaluation of a thermoregulatory model for predicting thermal responses of dairy cows. *Biosystems Engineering*, 223, 295–308. <https://doi.org/10.1016/J.BIOSYSTEMSENG.2022.09.010>
 24. Rajesh Banu, J., Anandan, S., Kaliappan, S., & Yeom, I. T. (2008). Treatment of dairy wastewater using anaerobic and solar photocatalytic methods. *Solar Energy*, 82(9), 812–819. <https://doi.org/10.1016/J.SOLENER.2008.02.015>
 25. Ravi Kumar, K., Krishna Chaitanya, N. V. V., & Sendhil Kumar, N. (2021). Solar thermal energy technologies and its applications for process heating and power generation – A review. *Journal of Cleaner Production*, 282, 125296. <https://doi.org/10.1016/J.JCLEPRO.2020.125296>

26. Fu, X., Zhang, Y., Zhang, Y. G., Yin, Y. L., Yan, S. C., Zhao, Y. Z., & Shen, W. Z. (2022). Research and application of a new multilevel fuzzy comprehensive evaluation method for cold stress in dairy cows. *Journal of Dairy Science*, 105(11), 9137–9161. <https://doi.org/10.3168/JDS.2022-21828>
27. Yan, G., Shi, Z., Cui, B., & Li, H. (2022). Developing a new thermal comfort prediction model and web-based application for heat stress assessment in dairy cows. *Biosystems Engineering*, 214, 72–89. <https://doi.org/10.1016/J.BIOSYSTEMSENG.2021.12.006>
28. Gil, J. D., Topa, A., Álvarez, J. D., Torres, J. L., & Pérez, M. (2022). A review from design to control of solar systems for supplying heat in industrial process applications. *Renewable and Sustainable Energy Reviews*, 163, 112461. <https://doi.org/10.1016/J.RSER.2022.112461>
29. Sandoval, M. A., & Salazar, R. (2021). Electrochemical treatment of slaughterhouse and dairy wastewater: Toward making a sustainable process. *Current Opinion in Electrochemistry*, 26, 100662. <https://doi.org/10.1016/J.COEELEC.2020.100662>
30. Quijera, J. A., & Labidi, J. (2013). Pinch and exergy based thermosolar integration in a dairy process. *Applied Thermal Engineering*, 50(1), 464–474. <https://doi.org/10.1016/J.APPLTHERMALENG.2012.06.044>
31. Vieira Costa, J. A., Cruz, C. G., & Centeno da Rosa, A. P. (2021). Insights into the technology utilized to cultivate microalgae in dairy effluents. *Biocatalysis and Agricultural Biotechnology*, 35, 102106. <https://doi.org/10.1016/J.BCAB.2021.102106>
32. Luqman, M., & Al-Ansari, T. (2021). A novel solution towards zero waste in dairy farms: A thermodynamic study of an integrated polygeneration approach. *Energy Conversion and Management*, 230, 113753. <https://doi.org/10.1016/J.ENCONMAN.2020.113753>
33. Pachori, H., Choudhary, T., & Sheorey, T. (2022). Significance of thermal energy storage material in solar air heaters. *Materials Today: Proceedings*, 56, 126–134. <https://doi.org/10.1016/J.MATPR.2021.12.516>
34. Ismail, M. I., Yunus, N. A., & Hashim, H. (2021). Integration of solar heating systems for low-temperature heat demand in food processing industry – A review. *Renewable and Sustainable Energy Reviews*, 147, 111192. <https://doi.org/10.1016/J.RSER.2021.111192>
35. Mohanraj, M., Karthick, L., Dhivagar, R. (2019) Performance and economic analysis of a heat pump water heater assisted regenerative solar still using latent heat storage, *Applied Thermal Engineering*, 196, 117263. <https://doi.org/10.1016/j.applthermaleng.2021.117263>.
36. Karthick, L., Murugan, V.S., Leon, S.L.J., Mallampati, M., Ahamed, M.I. and Loganathan, G.B., 2022. Energy performance of a compression refrigeration cycle using environment- friendly refrigerants. *Materials Today: Proceedings*, 66, pp.1519-1525.

A Role of Design and Development on Mechanical, Wear and Thermal Characterization of Areca Fiber Reinforced Polymer Composites

G Dilli Babu¹, M. Bala Chennaiah², K Dilip Kumar³, T. Srinivasa Rao⁴, K Sivaji Babu⁵

^{1,2}Mechanical Engineering Dept., V. R. Siddhartha Engineering College, Vijayawada, AP-India

³Mechanical Engineering Dept., Lakireddy Balireddy College of Engg., Mylavaram, AP-India

⁴Mechanical Engineering Dept., Vasireddy Venkatadri Institute of Technology, Guntur, AP-India

⁵Mechanical Engineering Dept., Prasad V. Potluri Siddhartha Institute of Technology, Vijayawada, AP-India

Abstract: Synthetic fiber reinforced polymer composite products have very large decomposition periods and the gases released by them are very harmful to the environment and human beings due to their low biodegradable nature. Now a day, the use of agro and natural fiber reinforced polymer composites which are more commercialized owing to a lot of advantages like natural resource availability, low cost of processing, less weight, and acceptance range value in stiffness to weight ratio. Recently manufacturing industries shows huge interest in the areas of natural fiber (jute, sisal, hemp, bamboo fiber, etc.) reinforced polymer composites. In the present work, Areca Fiber Reinforced Polymer Composites (AFRPC) was manufactured by using hand Lay-up process, and their mechanical properties like tensile, flexural, impact and wear properties were evaluated experimentally. The composite specimens were fabricated at various levels of fiber volume fraction loading of 0%, 5%, 15%, and 30%. The results showed that the mechanical properties are gradually improved with the increase of fiber volume fraction in the composites. Also, the thermal conductivity of AFRPC were studied by using thermal conductivity meter. The results shows that the areca fiber-reinforced composites made up of hand lay-up process can also be used as one of the alternative materials in the field of mechanical and thermal insulation applications.

Keywords: Areca Fiber, Hand Lay-up Method, Mechanical Properties, Thermal Conductivity, Wear Characteristics.

I. INTRODUCTION

Increasing concern towards environmental problems influenced by polymers, reinforcement of natural fibers in the polymers has shown curiosity to most of the materials researchers. The important benefits of the natural fibers are low weight to strength ration, biodegradable, less cost and effective properties [1-3].

In recent years, many authors were showing lot of interest in developing of new type polymer composite materials by reinforcing various natural fibers to identify with their effects in properties likely in mechanical, thermal, wear, water absorption, machining characteristics and also nature of fracture failure [4-11].

Srinivasa C. V et al. evaluated the impact strength of areca fiber composites for raw and alkali treated with KOH (potassium hydroxide) in three different types of matrix materials (melamine urea formaldehyde, epoxy resin and urea formaldehyde) by 50% and 60% fiberweight percentages loading. Found better impact properties with treated fibers as compare with untreated fibers. Noticed the 60% fiber volume fraction epoxy composites shows better performance as compared

with other matrix-based composites in Chapry and Izord tests [4]. Chama Ajay et al. fabricated new thermos set plastic composites by reinforcing the calotropisgigientia fruit fibers in a polyester matrix by hand lay-up method. It was reported that the machining and mechanical properties for various fiber loadings of calotropisgigientia fruit fibers respectively. It was observed that the better mechanical properties at 30% of fiber loading compared to pure polyester matrix [5].

Chethan et al. developed the untreated areca sheath fiber reinforced polymer composites. They studied the tensile strength and tensile modulus properties. Test specimens are fabricated using Hand lay-up method and properties were studied at various volume fraction of the composites. Results were validated by using finite element analysis (FEA) made through ANSYS [6].

C.V. Srinivasa et al. used 10% KOH (Potassium Hydroxide) for treating of areca fibers for 36 hours, these treated fibers again neutralized using acetic acid with 2% weight to maintain fibers pH value approximately at 7 as neutral, then after that fibers dried 48 hours at room temperature. The authors developed treated area fiber reinforced epoxy polymer composites for two weight proportion levels at 50 and 60% with random orientation. The results showed that clear identification of increment values in impact strength and hardness for treated fiber at 60% volume fraction [7].

Dhanalakshmi et al. used compression molding technique for preparation of composites for untreated and treated (potassium permanganate, benzoyl chloride, Sodium hydroxide and acrylic acid) areca fiber reinforced polymer composites to identify the flexural and impact strengths at different fiber volume fractions. Observed that treated fibers significantly influenced on flexural properties compare to untreated fibers [8].

K Ramanaiah et al. reported the extraction of Typhaangustifolia fibers and their reinforcement in varied volume fraction in a polyester resin matrix to fabricate the composites. They studied the mechanical and thermal conductivity properties of Typhaangustifolia fiber reinforced polymer composites. They concluded that the mechanical properties are increasing with respect to the increase of volume fraction of fiber content. Found decrease of thermal conductivity with increase of fiber volume fraction. They showed that the thermal conductivity values are more similar in both empirical models and experimental values [9].

Mansour Rokbi et al. investigated the mechanical properties of treated and untreated Alfa natural fibers reinforced polyester matrix composites. Alkali treatment (NaOH) was applied at various levels (1, 5, and 10%) over a period of 24 and 48 hours at room temperature. The composite specimens were made with 40 wt% fiber loadings by hand lay-up method. Found better flexural strength and modulus values at 10% treated fiber composites, but decreased in both flexural strength and modulus for 5% NaOH treated fibers [10].

Sunil Kumar M et al. studied the mechanical and physical properties of areca fiber reinforced composites. The areca fiber shows predominant properties in terms of compressive and lower density in merge of Vinyl ester as compare with epoxy composites for the same areca fiber reinforcement. The areca fiber reinforced epoxy composites shows less water absorption for all fiber fraction loadings compare to Vinyl ester composites [11].

N. Vijaya Kumar et al. investigated the wear characteristics of jute fiber reinforced polymer composites varying the loads and sliding velocities. He observed that, the values of coefficient of friction drops with increasing of load. He also identified that the increase of fiber percentage in the composites increases the coefficient of friction [12].

Dipa Ray et al. studied the Wear characteristics of vinyl ester matrix composites filled with flyash. He observed that, the fly ash filled composites are exhibiting good wear resistant than for pure resin [13].

Kim et al. studied the thermal conductivity of various fiber (hemp, flex, sisal, kenaf, etc.,) reinforced with polypropylene matrix. The results shows that natural fiber reinforced composites are having good insulation properties and these composites can be used a insulating material for thermal applications [14]. In the literature, thermal conductivity of synthetic fiber reinforced composites are widely available [15-17] but the thermal conductivity of natural fibers are available with less quantity.

Chandrika et al. [18] studied the mechanical characterization of kenaf and waste saw dust reinforced composites for automobile applications. Based on the results the kenaf and saw dust reinforced hybrid composites are having good mechanical properties (tensile and flexural strength) than the other natural fiber reinforced composites.

Montalvo et al. [19] studied the mechanical and thermal characteristics of wood flour reinforced composites using additive manufacturing technique. The specimens were fabricated using screw extrusion method. Obtained results are compared with injection molding process. Optimum temperature for additive manufacturing processing of composite specimen fabrications was studied. They concluded that wood flour composites may be used for automobile exterior body part fabrication.

From the literature, there are some studies on mechanical characterization of areca fiber reinforced composite materials and these materials are used in some structural applications like automobile interior and exterior body building, partition walls, furniture body [20-23]. But in-depth experimental study on mechanical, thermal and wear characterizations is very limited.

The present paper describes the preparation of raw areca fiber reinforced polyester composites through conventional Hand lay-up method. The various fiber percentage volume of Areca fiber (10%, 15%, 20%, 25% and 30%) have been added to polyester matrix to fabricate the composites. The fiber loading effect on some of the mechanical properties like Tensile, Impact, flexural and wear properties were reported and compared with Peepal Fiber Reinforced Polyester Composites (PFRPC) and Esculentus Cyperus fiber Reinforced Polypropylene Composites (ECFRPC) available in the literature [24-25]. Wear and thermal conductivity of Areca fiber reinforced polyester in matrix composites was not reported in the literature. Hence, the wear and thermal conductivity of AFRPC was also studied and reported in this paper.

2. EXPERIMENTAL METHODOLOGY

2.1 Fabrication of Composites Specimens

Figure 1 shows the preparation of mould for the test specimens. ASTM D 638 M standard was followed for the tensile test and ASTM D790M-86 standard is followed for the flexural test [24]. Impact test specimens are prepared as per the ASTM D 638 M standard [24].



Figure 1: Test Specimen Mould preparation

The present work was focused on the preparation of natural fiber reinforced polymer composites. Areca fibers were used as reinforcing material and polyester resin was used as matrix material to prepare composite specimens. The triggering elements like catalyst and accelerator are mixed to the polyester matrix at atmosphere temperature with quantity of 1ml per 100 ml of polyester matrix. The composite specimens were prepared by using wet lay-up processes as shown in figure 2. With the use of a hand roller member polyester matrix was uniformly distributed over the fiber surface for good adhesion bonding interaction among fiber and matrix. Getting a good quality, good surface finish and minimal fiber deformation of unidirectional fiber polymer composites, it was needed to apply external compressive load of approximately 441.29 N was applied on the top surface of the mold over a period 24 hours. In the present work five levels of Areca fiber volume fraction (10%, 15%, 20%, 25% and 30%) composite specimens were prepared.



Figure 2: Preparation of composite specimens

2.2 Testing of Composite Specimens

2.2.1 Tensile Testing

The tensile specimens were tested on Tensometer, M/s Microtech, and Pune, India. Experiments were conducted as per ASTM D 638 M standard. Recorded the ultimate tensile load and specimen elongated length where the composite samples are fractured. The experimental set up and fractured tensile specimens were shown in figure 3.



Figure 3: Tensile test and fractured specimens

2.2.2 Flexural Testing

The flexural specimens were tested on Tensometer, M/s Microtech, Pune, India. Experiments were conducted as per ASTM D790M-86 standard. Recorded the ultimate flexural load and specimen bending elongated length where the composite samples are fractured. The experimental set up and fractured flexural specimens were shown in figure 4.

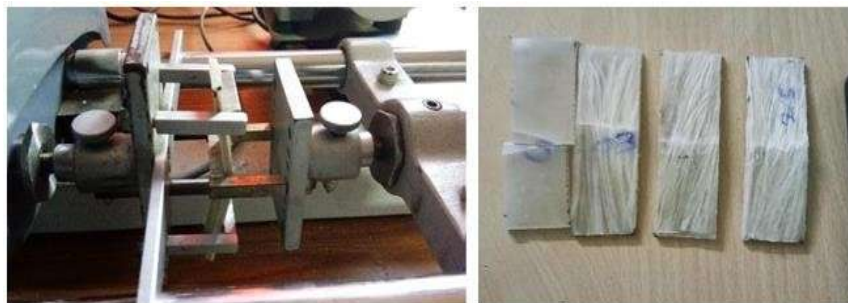


Figure 4: Flexural test and fractured specimens

2.2.3 Impact Testing

The Impact specimens were tested on Izod impact tester, M/s International Equipments, Mumbai, India. Experiments were conducted as per ASTM D256-97 standard. Recorded the energy observed by the specimen on impact load. The experimental set up and fractured flexural specimens were shown in figure 5.



Figure 5: Impact test and fractured specimens

2.2.4 Wear Testing

The wear characterization of areca fiber reinforced polyester composites was studied using pin on disc DUCOM Tribometer. Wear is calculated by finding the wear groove with a profile meter. Wear test equipment and specimens are shown in figure 6.



Figure 6: Pin on disc Tribometer and specimens

2.2.5 Thermal Conductivity

Thermal conductivity of the areca fiber reinforced polyester composites was studied by using Unit herm Model 2022 thermal conductivity meter. Experiments are conducted as per ASTM E 1530 Standard guidelines. For ASTM E1530–99, the experimental specimen of diameter 50 mm and thickness of 10 mm were fabricated by using hand lay-up method. Below mathematical relations shows the evaluation of thermal conductivity in the composites materials. Thermal conductivity meter equipment and specimen are shown in the figure 7.

$$Q = \frac{(T_1 - T_2)}{L} \quad R = \frac{(T_1 - T_2)}{Q} \quad K = \frac{L}{R}$$

Where k = thermal conductivity in W/mK , q = Heat flux Wm^2 , $T_1 - T_2$ = temperature difference in K ,
 L = sample thickness in metre, R = sample thermal resistance in m^2K/W



Figure 7: Thermal conductivity meter equipment and specimen

3. RESULTS AND DISCUSSION

3.1 Tensile Properties

The tensile strength and tensile modulus results for the unidirectional areca fiber reinforced polyester composites with different fiber volume fractions are shown in figure 8 with the data available in the Dept. of Mech. Engg. PVPSIT 287

literature [24-25]. From figure 8, it is very clear that the tensile characteristics are gradually increasing with an increase in fiber volume fraction. Maximum tensile strength was observed at a 30% volume fraction of the fiber. The Tensile strength value for the 30% fiber volume fraction is 66.86 MPa which is 57.57% more compared with the 0% volume fraction of fiber. Maximum tensile modulus were also observed at a 30% volume fraction of the fiber. The Tensile modulus for the 30% fiber volume fraction are 2.53GPa which is 80.45% more compared with the 0% volume fraction of fiber. From the results, it is clear that the areca fiber reinforced polyester composites can be used in the area of mechanical and constructional applications.

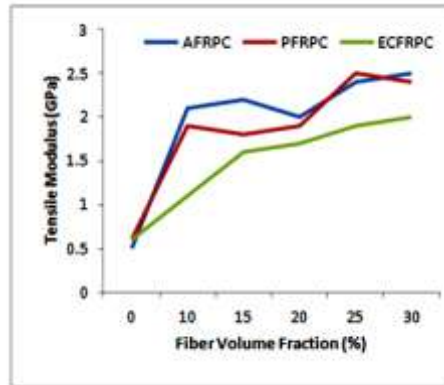


Figure 8: Variation of tensile strength and tensile modulus with fiber volume fraction

3.2 Flexural Properties

The flexural strength and flexural modulus results for the areca fiber reinforced polyester composites with different fiber volume fractions are shown in figure 9. From figure 9, it is very clear that the flexural characteristics are increasing with an increase in fiber volume fraction. Maximum flexural strength was observed at a 30% volume fraction of the fiber. The flexural strength value for the 30% fiber volume fraction is 260.66 MPa which is 67.30% more compared with the 0% volume fraction of fiber. Maximum flexural modulus was observed at a 30% volume fraction of the fiber. The flexural modulus for the 30% fiber volume fraction was 12.1GPa which is 80.83% more compared with the 0% volume fraction of fiber. From the results, it is clear that the areca fiber reinforced polyester composites are possessing good flexural properties when compared with pure polyester.

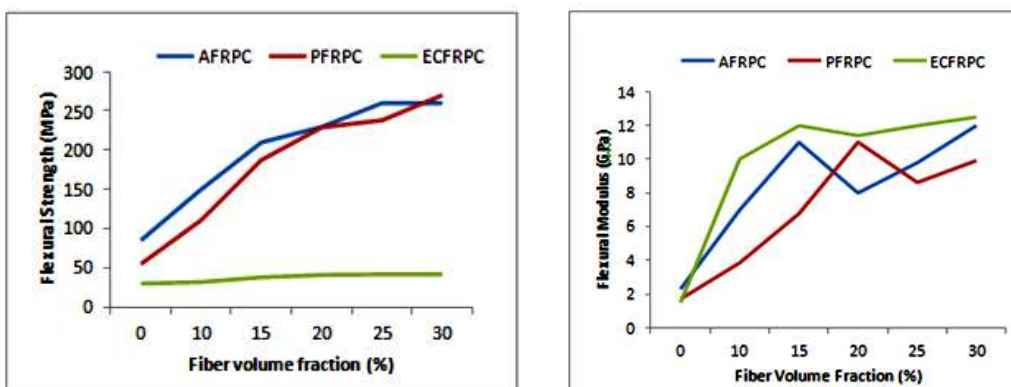


Figure 9: Variation of Flexural strength and flexural modulus with fiber volume fraction

3.3 Impact Properties

The impact strength results for the areca fiber reinforced polyester composites with different fiber volume fractions are shown in figure 10. From figure 10, it is clear that the impact strength was increasing with an increase in fiber volume fraction. Maximum impact strength was observed at a 30% volume fraction of the fiber. The impact strength for the 30% fiber volume fraction was 39.04 KJ/m² which is 87.18% more compared with the 0% volume fraction of fiber. From the results, it is clear that most natural fibers have better load bearing capacity.

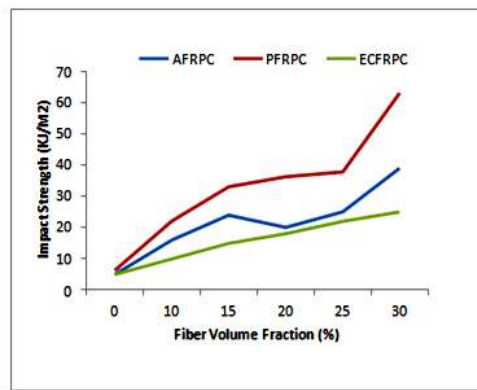


Figure 10: Variation of Impact strength with fiber volume fraction

3.4 Wear Characteristic

Wear is studied by adopting a pin-on-disk or stick-on-plate sort contact and information acquisition framework on the wear screen. The circular material is hardened ground steel with a hardness of 65 HRC and a surface roughness of 0.5 μ m. The machine is allowed to run for 10 minutes to maintain a constant sliding speed of 60 cm/sec. The procedure was reshaped for alternative examples with a circle sliding speed of 120 cm/s. Characteristics of wear rate and coefficient of friction were represented with different weight percentage fibers (figure 11).

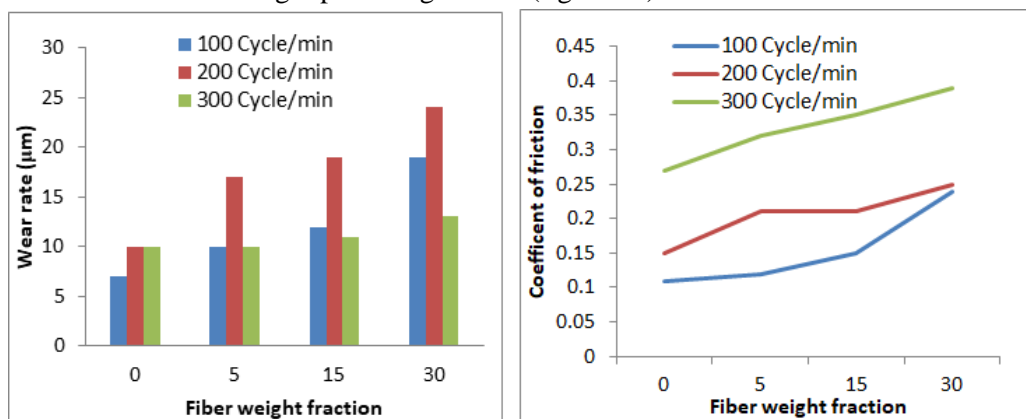


Figure 11: wear rate and coefficient of friction with fiber volume fraction at different cycle times

3.5 Thermal conductivity

Thermal conductivity of areca fiber reinforced polyester composites is tested and the results are shown in figure 12. The thermal conductivity of the composites decreases with increase of the fiber volume fraction in the composites. From the results it is observed that the AFRP composites are having good thermal insulating property. So, these composites may be used as insulating material for air-conditioning rooms to decrease the energy consumption.

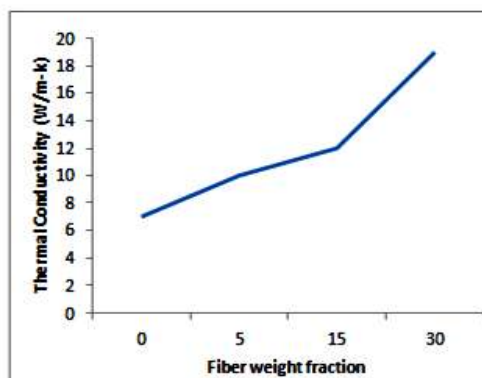


Fig.12. Thermal conductivity w.r.t. fiber volume fraction of fibers in the composites.

4. CONCLUSION

- In this work, areca fiber reinforced polyester composites were fabricated and the mechanical characteristics were experimentally studied.
- The behavior of the areca fiber reinforced polyester composites with different fiber volume fractions for tensile, flexural and impact strength characteristics were studied.
- Areca fiber reinforced polyester composites possess 57.57% more tensile strength and 80.45% more tensile modulus when compared with pure polyester resin.
- Areca fiber reinforced polyester composites possess 67.30% more flexural strength and 80.83% more flexural modulus when compared with pure polyester resin.
- Areca fiber reinforced polyester composites possess 87.18% more impact strength when compared with pure polyester resin.
- The AFRPC shows similar trend in the mechanical properties of the other composites studied in the paper namely PFRPC and ECFRPC.
- Subjecting to the wear test the areca fiber reinforced polyester composites are having the better wear characteristics.
- The thermal conductivity of the composites has decreased with increase in volume fraction of fibers. Based on the results, the AFRPC can be used as good insulators.
- This improvement was observed because the polyester matrix distributed with better external loads and stress transfer to the reinforcing fibers. Hence, areca fiber reinforced polyester composites can also be used as one of the alternative material for the lightweight application like automobile interior parts, electronics cabinets, and general purpose domestic furniture.

References

1. J. Biagiotti, D. Puglia, Jose M. Kenny, "A Review on Natural Fibre-Based Composites-Part I, Journal of Natural Fibers", 1(2), pp. 37-68, 2004.
2. S. V. Joshi, L. T. Drzal, A. K. Mohanty, and S. Arora, "Study of Mechanical Properties of Raffia Palm Fibre/Groundnut Shell Reinforced Epoxy Hybrid Composites", Composites Part A: Applied Science and Manufacturing, 35, pp. 371- 376, 2014.
3. Madsen B, Thygesen A, Lilholt H, "Plant Fibre Composites-Porosity and Stiffness", Composites Science and Technology, 69, pp.1057-1069, 2009.
4. Srinivasa, Chikkol V. and K. N. Bharath. "Effect of Alkali Treatment on Impact Behavior of Areca Fibers Reinforced Polymer Composites", International Journal of Chemical, Molecular, Nuclear, Materials and Metallurgical Engineering, 7, pp. 240- 244, 2013.
5. A. Srinivas and G. Dilli Babu, "Mechanical and Machining Characteristics Of Calotropis Gigentea Fruit Fiber Reinforced Plastics", International Journal of Engineering Research & Technology, 2 (6), pp. 1524-1530, 2013.
6. S. G. G. K. Chethan M R, "Effect of Fiber Length on Tensile Characteristics of Untreated Natural Areca Sheath FRP Green Composites", International Journal of Mechanical and Production Engineering, 1(Special Issue), pp. 90–92, 2016.
7. C. V. Srinivasa and K. N. Bharath, "Impact and hardness properties of areca fiber- epoxy reinforced composites", Journal of Materials and Environmental Science, 2(4), pp. 351–356, 2011.
8. P. Ramadevi and B. Basavaraju, "Research Article a Study of Influence of Chemical Treatments on Flexural Strength and Impact Strength of Areca Fiber Reinforced Natural Rubber Composites", International Journal of Recent Scientific Research, 6, pp. 4833–4839, 2015.
9. K. Ramaiah, A. V. Ratna Prasad, and K. Hema Chandra Reddy, "Mechanical properties and thermal conductivity of typhaangustifolia natural fiber-reinforced polyester composites", International Journal of Polymer Analysis and Characterization, 16(7), pp. 496–503, 2011.
10. M. Rokbi, H. Osmani, A. Imad, and N. Benseddq, "Effect of chemical treatment on flexure properties of natural fiber-reinforced polyester composite", Procedia Engineering, 10, pp. 2092-2097, 2011.

11. Sunil Kumar .M, S.G.Gopalakrishna, Shivakumar H.R, K.S Rai, “Preparation and Characterization of Short Areca Leaf Fiber Reinforced Epoxy and Vinyl Ester Composites”, *International Journal of Advance Research in Science and Engineering*,4(1), pp. 1635–1646, 2015.
12. Vijayakumari, Gowthamipriyanka, K. Srikanth, “Evolution of Wear Properties of Jute Reinforced Polypropylene Composites”. *International Journal of Engineering Research & Technology (IJERT)*, 3(1), pp.1212-1215, 2014.
13. Dipa Ray, R Gnanamoorthy, Friction and wear Behaviour of Vinelyster Resin Matrix Composites Filled with Fly Ash Particles, *Journal of Reinforced Plastics and Composites*, Vol 26(1), pp.5-12, 2007.
14. S. W. Kim, S. H. Lee, J. S. Kang and K. H. Kang, Thermal conductivity of thermoplastics reinforced with natural fibers, *Int. J. Thermophys.* Vol 27(6), pp.1873- 1881, 2006.
15. K.Ramanaiah, A.V.Ratna Prasad, K.Hemachandra Reddy, Experimental study on thermo physical properties of biodegradable borassus fruit fiber-reinforced polyester composites, *Materials Today: Proceedings*, 44(1), pp.1857-1859, 2021.
16. K.Ramanaiah, A.V.Ratna Prasad, K.HemaChandra Reddy, Thermo physical properties of elephant grass fiber reinforced polyester composites, *Materials Letters*, 89(1), pp.156-158, 2012.
17. K.Ramanaiah, A.V.Ratna Prasad, K.Hema Chandra Reddy, Thermo physical and fire properties of vakka fiber-reinforced polyester composites, *Journal of reinforced plastics and composites*, 13(15), pp.1092-1098, 2013.
18. Chandrika, S., Kumar, T.R.H. & Mahesh, V. Physio-mechanical characterization of kenaf/saw dust reinforced polymer matrix composite and selection of optimal configuration using MADM-VIKOR approach. *Int J Interact Des Manuf.*, <https://doi.org/10.1007/s12008-022-01078-7>, 2022.
19. MontalvoNavarrete, J.I., Hidalgo-Salazar, M.A., Escobar Nunez, E., Thermal and mechanical behavior of bio composites using additive manufacturing. *Int J Interact Des Manuf.*, 12, pp.449–458, 2018.
20. Girisha.C, Sanjeevamurthy, GuntiRangasrinivas, Manu.S., Mechanical Performance Of Natural Fiber-Reinforced Epoxy Hybrid Composites, *International Journal of Engineering Research and Applications (IJERA)*, 2(5), pp.615-619, 2012.
21. Ashok R. Banagar, Srinivasa Chikkol Venkateshappa, Sakshi Shantharam Kamath, Basavaraju Bennehalli, Tensile and flexural properties of areca sheath fibers, *Materials Today: Proceedings*, 5(14), pp.28080-28088,2018.
22. Chikkol Venkateshappa, Srinivasa, Bharath, K N., Effect of Alkali Treatment on Impact Behavior of Areca Fibers Reinforced Polymer Composites, *Journal of Materials Engineering*, 7(4), pp.874-879, 2013.
23. Srinivasa, C.V. and Bharath, K.N., Impact and Hardness Properties of Areca Fiber- Epoxy Reinforced Composites. *Journal of Materials and Environment Science*, 2(4), pp.351-356, 2011.
24. G. Dilli Babu, S.P. Kumar Gudapati, A.V. Ratna Prasad, K. Sivaji Babu, Experimental investigation on mechanical and thermal properties of Esculentus Cyperus fiber reinforced polypropylene composites, *Materials Today: Proceedings*, 23, pp.557–560, 2020.
25. Obulasu Tapela, G. Dilli Babu, Ginka Ranga Janardhana, An Analysis of the Behavior of Peepal Fiber Reinforced Polyester Composites for Tensile, Flexural and Impact Strengths, *Recent Trends in Product Design and Intelligent Manufacturing Systems, Lecture Notes in Mechanical Engineering*, Springer, IPDIMS 2021, pp 417– 428, 2022.

Experimental Investigation of Solar Water Heating System

Kamala Priya B¹, K Lohinadh², K Karthik², S Stalin², P Adi Narayana²

¹ Department of Mechanical Engineering, Assistant Professor, Lakireddy Bali Reddy College of Engineering, Mylavaram, Andhra Pradesh, India.

² Department of Mechanical Engineering, IV Year Student, Lakireddy Bali Reddy College of Engineering, Mylavaram, Andhra Pradesh, India.
kamala.jkp@gmail.com

Abstract: The energy harnessed from the power and heat of the sun's rays is named as solar energy which is renewable, eco-friendly having an easily convertible nature and hence called as green source of energy. The solar energy into heat energy transformation will be used to generate electricity where it can be utilized for wide range of applications like water heating, preheating of water in boiler systems, power generation etc. In the present investigation, fabrication of solar water heating system has been developed. Tests are made, by heating of water for 1 hour i.e., 12pm-1pm (noon), performed in 2 days. First day, the experimentation done by using 4 glow plugs in heating of water and in second day 2 glow plugs are used for heating. At the end of both experimentations, we came to know the rate of change in temperature with respect to time and also the maximum temperatures obtained at the end of experimentation time i.e., the maximum temperature at the end of 1 hour.

Key words: Solar Energy, Glow Plugs, Solar Panels, Heating System

INTRODUCTION

Solar water heating systems are used to collect solar energy or radiation through solar collectors and utilize this energy for water heating ranges from 60 – 80 degree centigrade. The resulted hot water from solar water heating system is utilized for wide range of applications like water preheaters in economizers, boiler systems, power generation and also in various chemical industries. In our Solar water heating system, we are used to replace the solar collectors by solar panels, and addition of energy bypass and storage system by battery and charge regulators which makes the solar heating system to give effective output and heating system works even in nighttime or in no solar radiation in particular intervals of times. Reza Alayi [1] concludes the amount of atmospheric CO₂ set of possible measures and the economic and technical prioritization. And the result PS TRNSYS software used in technical analyze the solar water heater system. And also, the reduction of renewable energy sources. Different design modifications of solar air collector have been discussed. Modifications include increase in number of fluid passes, corrugating and roughening the absorber plate, adaption in top cover plate, employing photo-voltaic/thermal (PV/T) panels and use of phase change materials. Roughness and corrugation on the absorber plate improved the thermal performance of the conventional solar collector. The top cover of the solar collector is generally glazed which helps in trapping the reflected solar radiations from the absorber plate. Solar air collectors having PCM provided increased working time during the off-sunshine hours.

Through Ajay Prakash [2] research, we understand the basic modifications that can be applied on the absorber plate of the solar collector to improve its thermal performance in a simple manner. To produce the consumable hot water, solar water is used. Based on the Mohammad Hossein Ahamdi [3] analysis it is observed that the Solar water heaters are one of the most effective and easy to use solar energy. And the result of the thermal energy required to supply the consumable hot water is supplied by solar energy through a gas-fired boiler. Study of solar water heating system to produce the importance the energy of solar water heating systems, various resources are used for heating water and steam manufacturing. Energy sources are usually categorized energy sources, sunlight, wind, water. A solar Dept. of Mech. Engg.

water heating scheme (SWHS) consists of several significant. More solar collectors, a pump, a heat exchanger. And by the result of Manish Jouhri [4] the right solar water heating system for a facility of climate, water and budget. And to produce the solar water heating system. Aidah M J Mahdi [5] fabricated and give the experimentation results on half circular trough solar water heater system using forced circulation system is proposed. Integration the solar absorber with the easily fabricated half circular trough reflector can improve the performance of a solar water heater system. The practical results have shown that very promising measures in thermal efficiency. The maximum water temperature achieved in April-2018 was 54°C while the incoming water was 21°. These encouraging results Calls for rethinking the use of solar water heaters to reduce waste of electricity. Investigation of solar water by using flat plate collector and evacuated tubes” proposed by J.J. Jayakanth [6] suggested the usage of flat plate collector and evacuated tube to provide a solar water heating system. The designed system is capable of collecting, storing, and utilization of produced nonconventional energy source for household purposes. This system uses copper tubes alternative for G.I. sheets resulting in low cost of production and high capacity.

This system also includes a stainless-steel tank, dense PUF insulation, toughened glass, etc. The capacity of this system is increased by using pebbles as the medium of heat. Thus, the system is helpful to replace an electric-depend water heater with eco-friendly water. Vishal G. Shelke [7] provides a review of existing solar water heaters. The work also specifies the hindrance that occurred to the limited availability of solar power. The author also mentions the usage of solar energy for different purposes in households and industries. The paper shows a great evaluation of innumerable mechanisms used to develop a solar water heater.

The present investigation was to evaluate the thermal and environmental analysis of solar water heating system to obtain maximum temperature's at different time intervals.

DESIGN AND FABRICATION

In this solar water heating system, a solar panel [40 watt & 18v] is connected to a battery [32 amp & 12v], the energy produced by solar panel is stored in battery this acts as a power source, a set of glow plugs [12v] are connected to battery which generates heat by utilizing power from solar panel & battery. This set of glow plugs are placed in an insulation tank, this insulation tank acts as a storage tank where the water or fluid gets heated in this tank. For experimentation purpose a digital thermal sensor, timer and an input measuring tank with water pump is placed beside the insulation tank. The insulation tank, input measuring tank are placed on a supporting stand.



Fig 1: Fabrication of solar water heating system using solar panels and glow plugs

EXPERIMENTATION PROCEDURE

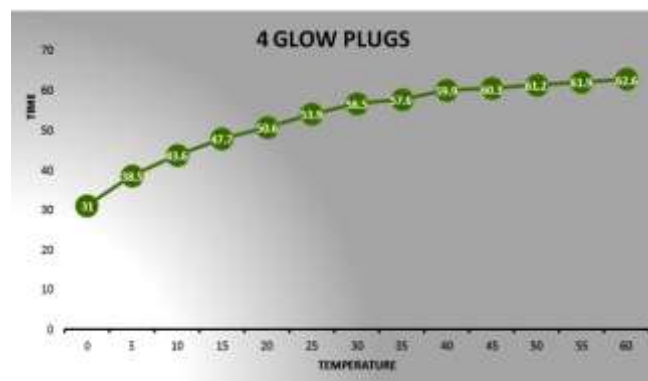
1. Connect all the connections between solar panels, battery and glow plugs.
2. Then fill 2 liters of water in the input measuring tank and then turn on the pump to circulate water from measuring tank to insulated tank.

3. Note down the initial temperature of water in insulation tank.
4. And then switch on the 4 glow plugs and also start the timer at a time.
5. Observe the increasing water temperature for every 5 minutes at insulation tank thermos sensor.
6. Stop the timer when the time reaches 1 hour i.e., 60 minutes and note down the maximum temperature obtained.
7. Repeat this step for testing of heater by using 2 glow plugs and note down the temperature with respect to time and also note the maximum temperature obtained.

RESULTS

Experimentation results by using 4 glow plugs:

SL.NO	TIME IN MINUTES	TEMPERATURE IN DEGREE CENTIGRADE
1	0	31
2	5	38.5
3	10	43.6
4	15	47.7
5	20	50.6
6	25	53.9
7	30	56.5
8	35	57.6
9	40	59.9
10	45	60.3
11	50	61.2
12	55	61.9
13	60	62.6

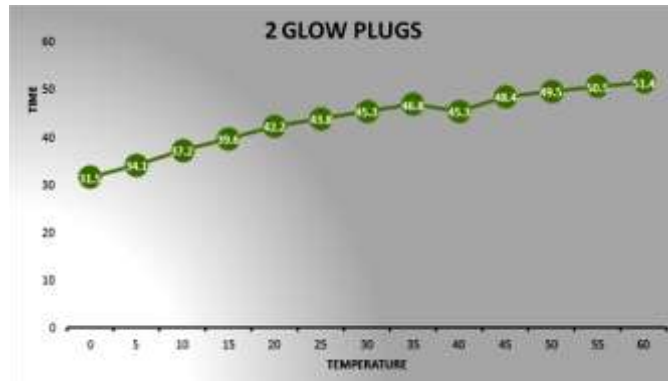


Graph 1: 4- Glow Plugs Time Vs Temperature

Experimentation results by using 2 glow plugs:

SL.NO	TIME IN MINUTES	TEMPERATURE IN DEGREE CENTIGRADE
1	0	31.5
2	5	34.1
3	10	37.2
4	15	39.6
5	20	42.2
6	25	43.8
7	30	45.3
8	35	46.8

9	40	45.3
10	45	48.4
11	50	49.5
12	55	50.5
13	60	51.4



Graph 2: 2- Glow Plugs Time Vs Temperature

CONCLUSION

This experimental investigation presents the results of solar water heating system using solar panels and glow plugs, the experiments were carried out in two days in noon time from 1pm-2pm by taking 2 liter of water on fabricated solar water heater and tested by using 4 glow plugs and 2 glow plugs. It was found that the maximum temperature obtained is 62.6 °C when 4 glow plugs are used for heating and the maximum temperature of 51.4 °C is obtained when 2 glow plugs are used for heating. Concerning the results, the solar water heater works effectively when the number of glow plugs are increased.

REFERENCES

1. Reza Alayi, 'technical and environmental analysis of photovoltaic and solar water heater cogeneration system': a case study of saveh city, 2021, 16, 447-453
2. Ajay Prakash, 'review on solar flat plate air collector with different design modifications', 2021
3. Reza Alayi, 'thermal and environmental analysis on solar water heater system for residential buildings', 2021
4. Manisha Johri, 'a review study on solar water heating system', vol 6, June 2019
5. Aidah MJ Mahdi, 'the performance of an effective solar water enhancement based on experimental study, 4(7):50-54, 2017
6. JJ Jayakanth, 'investigation of solar water heater by using flat plate collector and evacuated tubes', iop publications ltd, 2017
7. Vishal G. Shelke, 'a review on solar water heating systems', vol:3, 4 april, 2015.

Electro thermal experimental analysis on Li-Ion battery for electric vehicles

G.Sainath¹, Srinivas Prasad Sanaka², CH.Balaji³, MD.Ameer⁴, G.Ganesh⁵

¹⁻⁵Department of Mechanical engineering, V R Siddhartha Engineering College,
Vijayawada, India,
Corresponding author:nadhg2003@gmail.com

Abstract: Electric vehicles are a promising technology for attaining a sustainable mobility sector in the future due to their zero carbon emissions characteristics, simplicity, low noise, high efficiency, reliability, cost, comfort. Battery is the primary energy storage device used for driving an electric motor. The performance and the life of the battery are directly influenced by the temperature developed in the battery during the charging and discharging conditions. The Li-ion battery pack was designed to deliver the power output of 0.374 kW with 24Volts and 36 Nickel Manganese cobalt (NMC) cells are used in the battery pack. A 48Volts, 20Amps motor is used as load to discharge the battery. Experiments are carried out on battery and the results reveal that the temperature developed on battery at low voltage is high and the maximum temperature developed on the external surface of the battery pack is 50⁰C. The study is useful to select suitable battery thermal management system. The automatic active forced air cooling system will be activated by the developed control system. The temperature developed is inversely proportional to the voltage.

Keywords: Battery thermal management, Li-ion Battery, Electric Vehicle

1. Introduction

Battery is the main source of the energy for electric vehicles. Few batteries are subjected to fire hazards due to overheating caused by electron's movements during chemical reactions during the charging process in elevated temperatures and can lead to fatal destruction of the batteries. But the safety of battery during charging is the most important. Lead-acid and Nickel-cadmium, Lithium ion (LIBs) batteries have outstanding properties like high energy density, power density and high operating voltage [1]. But, the main factor that governs the performance of LIBs batteries is temperature. The adequate temperature range for LIBs is -20 °C to 40 °C [2]. Once this temperature range is exceeded, LIBs will degrade fast with increases danger of facing the problems temperature can be categorized into low temperature effects and high temperature effects. Low temperature effects are caused in high-altitude countries like Russia, Canada and higher temperature effects are caused in low-altitude countries like India, China [4]. Thermal runaway occurs in the battery due to the high temperature effects [5]. Battery aging is mostly triggered by the establishment of solid electrolyte interphase film at the electrolyte/electrode surface, lithium deposition, electrode assembly destruction, a phase transformation of electrode material, termination of active material and electrolyte disintegration [6]. A good battery thermal management is essential to overcome the higher temperature effects. The most vital purpose of the BTMS is to maintain an optimal operating temperature range and a uniform temperature distribution within the battery cell, module and pack at high discharge/ charge/ rates [7]. Air cooling is employed to carry away the heat that is generated in the battery [8]. A battery works on the oxidation and

reduction reaction of an electrolyte with metals. During charging the reduction reaction takes place at cathode and electrons are released and are moved towards the anode through the external circuit [9] and the positive ions formed are moved in the direction of anode through electrolyte. The electrons gained at anode through oxidation are stored in the anode collector. Similarly during discharging the reduction reaction takes place at anode and electrons are released towards cathode, here in cathode oxidation reaction occurs and electrons are gained. Bandhauer et al. [10] have published the capacity and power fade of various positive electrode materials under high temperature cycling and storage, it showed the capacity appeared to degrade when the temperature increased greater than 50°C. A large amount of heat generated within the battery during operation will lead to a drastic rise in the battery temperature, which contribute to low life expectancy of battery and even explosion [11]. Battery thermal management system (BTMS) was proposed to maintain the temperature of battery within the optimum range during operation. Smart et al. [12] published that it was very hard to charge the cell once the temperature fell down to -10 °C this also causes the energy and power degradation of the cell. The temperature distribution on battery is important. Christophe Forgez [13] studied and acknowledged that a difference of 10°C was observed between the core of the battery and the surface with the help of embedded thermocouple. The battery thermal management system is required to control the battery temperature. [14] Documented that the battery pack with Natural air convection is not sufficient for the larger capacity batteries and leads to develop unacceptable high temperature. Zhang [15] suggested various methods to improve the low temperature performance of lithium ion batteries. Fenfang Chen [16] studied the forced air and phase change material cooling for the battery pack. Jiateng Zhao [17] had proposed a mini channel cooling system for the cylindrical batteries observed that the temperature can be maintained constant by increasing the flow rate of fluid through the pipes.

2. Description of battery pack used for the experiment

The battery pack is designed by connecting the cells in series and parallel to obtain the required voltage and current. In this study the Li-ion battery pack was designed to deliver the power output of 0.374 kW with 24 Volts. The total number of cells used for the battery pack are 36. One individual battery cell is shown in in figure1. Each row of battery pack has 6 cells and the six rows of battery are connected in parallel. All batteries are connected by Nickel and are spot welded and the battery pack designed is shown in Figure 2.



Figure1: Battery cell



Figure2: Battery pack

3. Experimental Description

The battery pack is tested during the discharge of battery by applying the load using D.C motor with 48 Volts and 20 amps. The voltage supplied by the battery is increased due to increase of load.

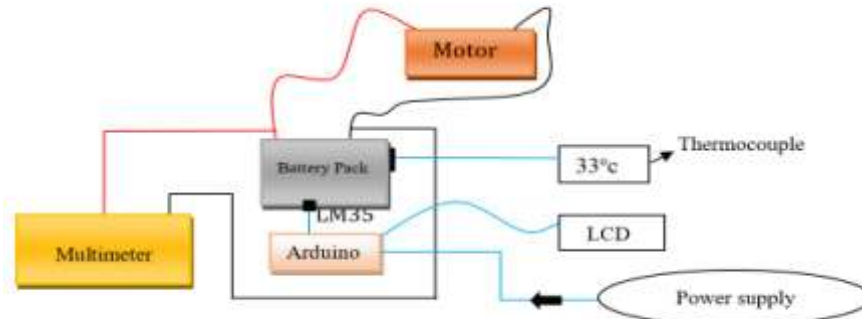


Fig 3: Circuit diagram for battery discharging

During this discharge process the maximum temperature obtained on the surface of the battery is at 10.7Volts. This temperature is controlled by installing the forced automatic air cooling with the help of Arduino UNO. The input power supply to the Arduino UNO is 5V. The temperature input to the Arduino UNO is provided by the LM35 sensor. The Arduino UNO checks the input temperature is whether within the temperature range set. If the temperature exceeds the set temperature it triggers the forced air cooling battery thermal management system till the temperature is equal to the set value. Finally, the temperature of the battery surface is noted at different voltage values.

4. Results and Discussion

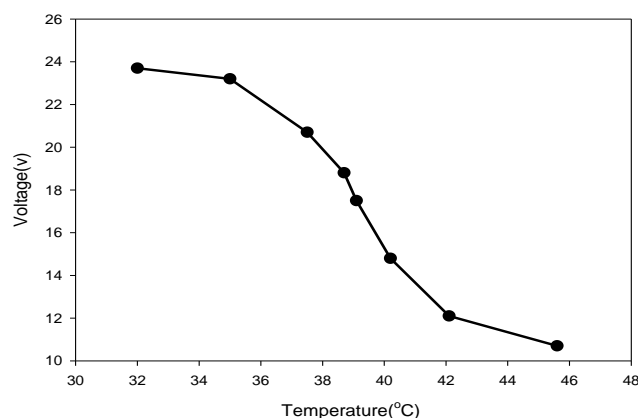


Fig 4: Voltage Vs Temperature of the battery pack

Figure 4 show the characteristic curve between the temperature and the voltage of the battery pack during the discharge. Obviously it can be seen that, the temperature increases with decrease in the voltage. So the curve can be treated as non-linear, slope of the curve is negative. It is perceived that the temperature increased by 13.6°C with the decrease of battery voltage from 23.7 V – 10.7 V. This means that there is 54.6% of voltage is reduced to produce a temperature change of around 29.82%. The maximum temperature is obtained at 10.7 Volts. The voltage-temperature curve of a lithium-ion battery can also be used to design the charging and discharging circuits for the battery, in order to ensure that the battery is charged and discharged safely and efficiently within its temperature limits. Therefore, the

voltage-temperature curve is an important characteristic of a lithium-ion battery and is used extensively in the testing, and operation of these batteries. The curve can be used to monitor the battery's temperature during operation, which is important for ensuring safe and efficient operation, as well as detecting potential problems such as overcharging or overheating.

Conclusions

- For the safety performance of the battery pack, BTMS is required to ensure the power source operating within the optimum temperature range. The BTMS based on forced-air convection is popular with its low maintenance, ease of use, and simple integration.
- The battery pack has been designed to deliver the power with 24Volts the battery pack contains 36 battery cells (NMC) these are designed to deliver a power of 0.384 Kw
- The preliminary experimental analysis is carried out to understand the cause and effect of battery thermal management.
- Thermal analysis is done successfully on battery surface temperature the temperature of the specified points has been measured.
- The discharging characteristics of the battery are plotted and the result reveals the output characteristics are similar and the temperature developed on the surface result reveals that at low voltage the temperature develops are high.
- The magnitude of maximum temperature develop on the external surface of the battery pack is nearly 50°C in the range of voltage.
- For the proposed system the air cooling can control the temperature of the battery depending upon the battery power requirements based on the temperatures developed PCM cooling systems can be employed on batteries which further helps in better battery thermal management of the battery pack.

Refernces

1. Ma, S., Jiang, M., Tao, P., Song, C., Wu, J., Wang, J., Shang, W. (2018). Temperature effect and thermal impact in lithium-ion batteries: A review. Progress in Natural Science: Materials International. <https://doi.org/10.1016/j.pnsc.2018.11.002>
2. Liao, L., Zuo, P., Ma, Y., Chen, X., An, Y., Gao, Y., & Yin, G. (2012). Effects of temperature on charge/discharge behaviors of LiFePO₄ cathode for Li-ion batteries. <https://doi.org/10.1016/j.electacta.2011.11.041>
3. Thermal Runaway: Identifying the Cause of Rupture of Li-Ion Batteries during Thermal Runaway (Adv. Sci. 1/2018) <https://doi.org/10.1002/advs.201870003>
4. Wang, Q., Ping, P., Zhao, X., Chu, G., Sun, J., & Chen, C. (2012). Thermal runaway caused fire and explosion of lithium ion battery. Journal of Power Sources, 208, 210–224. <https://doi.org/10.1016/j.jpowsour.2012.02.038>
5. M. Broussely , Ph. Biensan , F. Bonhomme , Ph. Blanchard ,S. Herreyre , K. Nechev , R.J. Staniewicz”Main aging mechanisms in Li ion batteries <https://doi.org/10.1016/j.jpowsour.2005.03.172>
6. D. Adair, K. Ismailov, Z. Bakenov, Thermal Management of Lithium-ion, Battery Packs. (2014). <http://nur.nu.edu.kz/handle/123456789/852>
7. Wang, M., Teng, S., Xi, H., & Li, Y. (2021). Cooling performance optimization of air-cooled battery thermal management system Applied Thermal Engineering, 195, 117242. <https://doi.org/10.1016/j.applthermaleng.2021.117242>
8. Jilte, Ravindra D.; Kumar, Ravinder; Ahmadi, Mohammad H.; Chen, Lingen (2019). Battery thermal management system employing phase change material with cell-to-cell air cooling. Applied Thermal Engineering, 114199. <https://doi.org/10.1016/j.applthermaleng.2019.114199>
9. Banguero, Edison; Correcher, Antonio; Pérez-Navarro, Ángel; Morant, Francisco; Aristizabal, Andrés (2018). A Review on Battery Charging and Discharging Control Strategies: Application to Renewable Energy Systems.

Energies, 11(4), 1021. <https://doi.org/10.3390/en11041021>

10 Bandhauer TM, Garimella S, Fuller TF. A critical review of thermal issues in lithium-ion batteries. *J Electrochem Soc* 2011; 158:R1–25. <https://doi.org/10.1149/1.3515880>

11. Kizilel R, Sabbah R, Selman JR, Al-Hallaj S. An alternative cooling system to enhance the safety of Li-ion battery packs. *J Power Sources* 2009; 194(2):1105–12 <https://doi.org/10.1016/j.jpowsour.2009.06.074>

12. M.C. Smart; B.V. Ratnakumar; L.D. Whitcanack; K.B. Chin; S. Surampudi; H. Croft; D. Tice; R. Staniewicz (2003). Improved low-temperature performance of lithium-ion cells with quaternary carbonate-based electrolytes. [https://doi.org/10.1016/S0378-7753\(03\)00154-X](https://doi.org/10.1016/S0378-7753(03)00154-X)

13. Pesaran AA., Sanathanagopalan S, Kim G H(). Addressing the impact of temperature extremes on large format Li-ion batteries for vehicle applications. <https://www.nrel.gov/docs/fy13osti/58145.pdf>

14. G. Karimi X. Li (2012). Thermal management of lithium-ion batteries for electric vehicles <https://doi.org/10.1002/er.1956>

15. Zhang, X., Li, Z., Luo, L., Fan, Y., & Du, Z. (2022). A review on thermal management of lithium-ion batteries for electric vehicles *Energy* <https://doi.org/10.1016/j.energy.2021.121652>

16. Chen, Fenfang; Huang, Rui; Wang, Chongming; Yu, Xiaoli; Liu, Huijun; Wu, Qichao; Qian, Keyu; Bhagat, Rohit (2020). Air and PCM Cooling for Battery Thermal Management Considering Battery Cycle Life. *Applied Thermal Engineering*, (), 115154 <https://doi.org/10.1016/j.applthermaleng.2020.115154>

17. Zhao, J., Rao, Z., & Li, Y. (2015). Thermal performance of mini-channel liquid cooled cylinder based battery thermal management for cylindrical lithium-ion power battery. *Energy Conversion and Management*, 103, 157–165. <https://doi.org/10.1016/j.enconman.2015.06.056>

Comparative Heat Transfer Analysis of Horizontal Cylindrical Jet Impinging on Vertical Flat Plate

K. Siva Satya Mohan¹, K. Ravi Kumar², P Ravi kumar³, K.P.V. Krishna Varma⁴, M.Rambabu⁵, P V S Muralikrishna⁶

¹Associate Professor, Department of Mechanical Engineering, Aditya College of Engineering & Technology, Surampalem, Andhra Pradesh, India,

²Assistant Professor, Department of Mechanical Engineering, V RSiddhartha Engineering college, Vijayawada, Andhra Pradesh, India

³Professor, Department of Mechanical Engineering, CMR College of Engineering & Technology, Telangana, India,

⁴Associate Professor, Department of Mechanical Engineering, Raghu Engineering College, Visakhapatnam, India,

⁵Assistant Professor, Department of Mechanical Engineering, Aditya College of Engineering & Technology, Surampalem, Andhra Pradesh, India,

⁶Sr. Assistant Professor, Department of Mechanical Engineering, Aditya College of Engineering & Technology, Surampalem, Andhra Pradesh, India.

¹kunapulivisa46@gmail.com ²ravi_24k@yahoo.com ³pravikamar@cmrcet.ac.in

⁴varmamtech2005@gmail.com ⁵rambabuthermal@gmail.com ⁶krishna4bi@gmail.com

Abstract: The present paper is a comparison of heat transfer analysis with a cylindrical horizontal jet which impinges on flat plate. Experimental investigation and CFD simulation is analyzed the heat transfer for hot fluid in a cylindrical horizontal jet on a flat vertical surface. The tests were conducted by taking the jet diameter of 12mm and the distance of horizontal jet to vertical plate surface were 6, 12, 18 and 24mm. H/D ratios ranging from 0.5 to 2 and Reynolds numbers ranging from 3.07×10^5 to 13.03×10^5 are considered in this analysis. Air is compared with CO₂ gas. Experimental investigations are compared with CFD simulation. It is found that CFD simulation gives better results than experimental results. Results shows that heat flux at H/D=0.5 for both air and CO₂ gives better value than H/D=1, 1.5 and 2.

Keywords: CFD, H/D ratio, Flat plate, Heat flux, Jet Impingement

Nomenclature

ρ Density, kg/m³

K Thermal conductivity, W/mK

Pr Prandtl number

Re Reynolds number

Nu Nusselt number

h Convective heat transfer coefficient (W/m²K)

V Velocity of the fluid, m/s

C_p Specific heat, J/kg K

μ Dynamic viscosity, Ns/m²

D_1 Diameter of cylinder, mm

L_1 Length of the cylinder, mm

D Diameter of the jet (mm)

L_2 Length of the plate, mm

H Distance from nozzle exit to stagnation point

CFD Computational fluid dynamics

ΔT Change in temperature (K)

T_∞ Ambient temperature (K)

T_s Temperature of the surface (K)

1. Introduction

Jet impingement heat transfer is a well established technique for heating, cooling or drying a surface. Impinging jets provide an effective and flexible way to transfer heat in industrial applications. Keyon *et al.* [1] explained the factors on the fluid flow and heat transfer both experimentally and numerically. From the results it shows that greater the blowing ratio higher the cooling effectiveness. The results also shows that the staggered-holes arrangement has a lower temperature on the outer surface of the leading edge and has improved the cooling effectiveness. Gokulnath. [2] explained about Jet impingement cooling mechanism with pulsating impinging jet array has proved to be one of the most efficient heat transfer mechanism for cooling applications. Results shows that impingement heat transfer is to obtain the higher heat transfer coefficients from a given surface with limited area by means of the high velocity of the jets. Khudheyer. [3] explained computational study for thermal and hydrodynamic analysis of the impingement cooling inside a channel backward facing step flow performed numerically. Results shows that the rate of the heat transfer is significantly enhanced due to the presence of impinging slot jets compared with conventional backward-facing step problem. Also it is found that the heat transfer rate increases as the jet size increases.

Akshay. [4] explained about theoretical and experimental developments in heat transfer by jet impingement method and the parameters which affects heat transfer. The results shows that large amount of removal of heat for better performance and jet impingement method provides better way of extracting large heat fluxes from high temperature components. Muhsincan. [5] explained about the effects of a vertical nano structured plate on single and two phase heat transfer enhancement via jet impingement cooling device. The results also shows that vertical nano rods integrated to the copper thin film layer on silicon wafer act as nano scale pin fins and introduce enhanced surface area. Pallavi and Ashish. [6] experimented and simulated to achieve an elementary perceptible. The heat transfer characteristics for copper square plate with nozzle diameter are 6 and 8 mm, when a jet of water is impinged on it for varying mass flow rate. Results also shows that heat transfer improvement is achieved by varying the parameters like nozzle diameters, h/d ratio and flow rate of water. Vipin *et al.* [7] studied enhancement of heat transfer in pulsed jet impingement cooling at different frequencies. From results it is observed that there is a considerable increase in average Nusselt number. Mahesh. [8] studied standard k- ϵ turbulent model which give most accurate result with minimum complexity in calculations. The results are, r_{ib} with highest number of perforation has higher Nusslet number than the other cases. Chaina. [9] numerically studied the single impinging jet through cylindrical and converging conical hole on concave surface. The results also shows that increase in Reynolds number increases the Nusselt number at jet impinging point as well as along the curvature. Reji Kumar. [10] investigated the jet impingement cooling to improve the heat transfer coefficient, interface temperature, pressure drop characteristics in a rectangular plate heat sink with inline array

jets. It can be concluded that jet impingement cooling scheme is compact in nature and hence used for high power density applications. The main objective of the work is to compare the heat flux of air and CO₂ for different H/D ratios and mass flow rates. This experimental study is compared with CFD simulation.

2. Materials and Methodology

The components used, their materials and working fluids used for the present analysis were as shown in Table 2.1. Three different jets were fabricated with different diameters. Parameters considered and their ranges are pivoted in Table.2.

Specifications of the jet and plate used for the analysis were pivoted in Table 2.2. Thermal properties of fluids at 30⁰C temperature are shown in the Table 2.3. It shows that thermal conductivity of air is more than that of CO₂.

Table 1 Materials and working substance

Component	Material	Working substance
Cylinder and jet	Steel	Air
Plate	Copper	CO ₂

Table 2.1 Parameters and their ranges

Parameter	Value
Surface temperature range, T _{s, ∞} °C	30- 80 ⁰ C
Diameter of nozzle, mm	10, 12, and 14
Nozzle to plate distance to jet diameter (H/D)	0.5 – 2

Table 2.2 Specifications of jet and plate

D1(mm)	L1(mm)	D(mm)	H(mm)	H/D	L2(mm)
76	140	10, 12 and 14	5, 6 and 7	0.5	180
76	140	10, 12 and 14	10, 12 and 14	1	180
76	140	10, 12 and 14	15, 18 and 21	1.5	180
76	140	10, 12 and 14	20, 24 and 28	2	180

Table. 2.3 Thermal properties of fluids

Property	Density (kg/m ³)	Specific heat (J/kgK)	Thermal Conductivity (W/mK)	Coefficient of viscosity μ (Ns/m ²)	Prandtl number (Pr)
Air	1.0445	1006.43	0.02931	20.345 x 10 ⁻⁶	0.695
CO ₂	1.773	851	0.01655	149 x 10 ⁻⁷	0.766

2.1 Experimental Set up and Procedure

Fig.1 shows the proposed experimental set up for Horizontal jet impingement on vertical flat plate



Fig 1 Pictorial view of horizontal jet on flat plate
Dept. of Mech. Engg.

2.2 Data Reduction

Heat flux is calculated by the following equation

$$\text{Heat flux (q)} = h \times (\Delta T) = h (T_{\infty} - T_s), \text{ W/m}^2 \quad (3.1)$$

Heat transfer coefficient (h) is calculated by using Nusselt number

$$\text{Heat transfer coefficient (h)} = (\text{Nu} \times K)/D, \text{ W/m}^2\text{k} \quad (3.2)$$

$$\text{Nusselt number (Nu)} = 0.023(\text{Re}^{0.8}) (\text{Pr}^n) \quad (3.3)$$

Where n = 0.4 for hot fluids

$$\text{Reynolds number (Re)} = (\rho V D)/\mu \quad (3.4)$$

Table 4 Reynolds number of air and CO₂ for $\theta = 90^\circ, \alpha = 0^\circ$ and $\theta = 0^\circ, \alpha = 90^\circ$ at D=10mm

		Re		h, W/m ² K	
		Air	CO ₂	Air	CO ₂
H/D	0.5	6.25 x 10 ⁵	8.54 x 10 ⁵	2527	1903
	1	9.38 x 10 ⁵	12.81 x 10 ⁵	3497	2633
	1.5	12.51 x 10 ⁵	17.08 x 10 ⁵	4399	3313
	2	15.64 x 10 ⁵	21.35 x 10 ⁵	5261	3962

Table 5 Reynolds number of air and CO₂ for $\theta = 90^\circ, \alpha = 0^\circ$ and $\theta = 0^\circ, \alpha = 90^\circ$ at D=12mm

		Re		h, W/m ² K	
		Air	CO ₂	Air	CO ₂
H/D	0.5	5.21 x 10 ⁵	3.07 x 10 ⁵	1820	1370
	1	7.82 x 10 ⁵	4.60 x 10 ⁵	2517	1896
	1.5	10.42 x 10 ⁵	6.14 x 10 ⁵	3168	2386
	2	13.03 x 10 ⁵	7.68 x 10 ⁵	3788	2853

Table 6 Reynolds number of air and CO₂ for $\theta = 90^\circ, \alpha = 0^\circ$ and $\theta = 0^\circ, \alpha = 90^\circ$ at D=14mm

		Re		h, W/m ² K	
		Air	CO ₂	Air	CO ₂
H/D	0.5	4.47 x 10 ⁵	6.10 x 10 ⁵	1380	1039
	1	6.70 x 10 ⁵	9.16 x 10 ⁵	1907	1437
	1.5	8.94 x 10 ⁵	12.21 x 10 ⁵	2401	1809
	2	11.17 x 10 ⁵	15.25 x 10 ⁵	2870	2162

2.3 Flow diagram of horizontal jet to vertical plate in CFD

Figure 3 and 4 shows model and meshing of horizontal jet impinging on vertical plate.

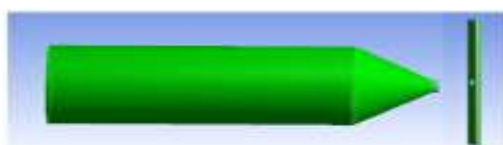


Figure 2 Horizontal jet & plate



Figure 3 Meshing

2.4 Boundary conditions in CFD

Boundary conditions are the inlet and outlet conditions for which analysis is to be done.

Table 3 shows boundary conditions of the jet

Table 7 Boundary conditions

Inlet	Velocity inlet
Outlet	Pressure outlet

3. Results and Discussion

3.1 Experimental Results and Discussion

3.1.1 Experimental results and discussion for air at D=10mm

Fig. 4 shows the heat flux variation at various H/D ratios and at various Reynolds numbers. Heat flux decreases as H/D ratio increases and mass flow rate increases. Heat flux is more at H/D=0.5 and Reynolds number of 13.03×10^5 .

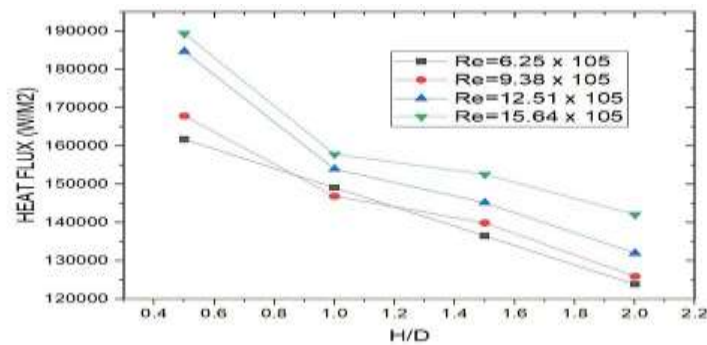


Fig. 4 Heat flux vs H/D at different Reynolds numbers at D=10mm

3.1.2 Experimental results and discussion for CO₂ at D=10mm

Fig.5 shows the heat flux variation at various H/D ratios and at various Reynolds numbers. Heat flux decreases as H/D ratio increases and mass flow rate increases. heat flux is more at H/D=0.5 and Re= 17.79×10^5

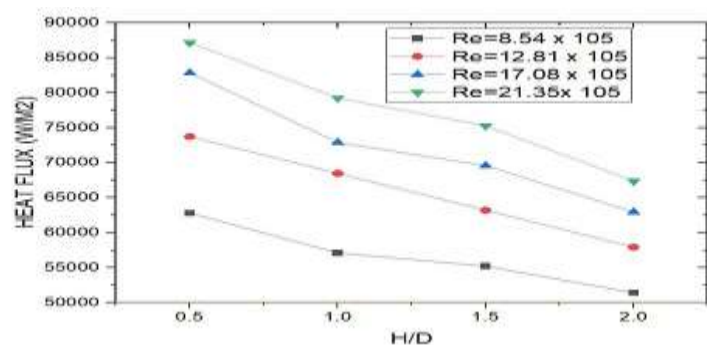


Fig. 5 Heat flux vs H/D at different Reynolds numbers at D=10mm

3.1.3 Experimental results and discussion for air at D=12mm

Fig.6 shows the heat flux variation at various H/D ratios and at various Reynolds numbers. Heat flux decreases as H/D ratio increases and mass flow rate increases. Heat flux is more at H/D=0.5 and Reynolds number of 13.03×10^5 .

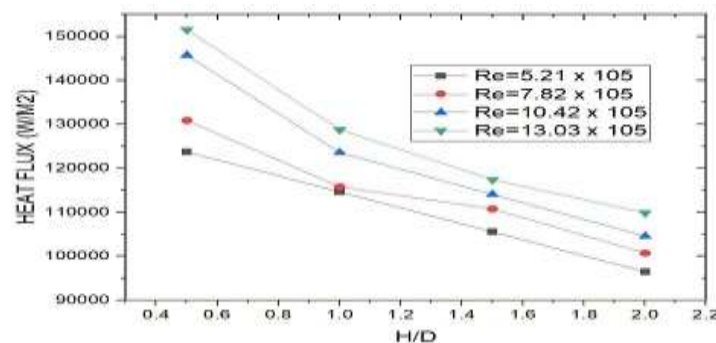


Fig. 6 Heat flux vs H/D at different Reynolds numbers at D=12mm

3.1.4 Experimental results and discussion for CO₂ at D=12mm

Fig. 7 shows the heat flux variation at various H/D ratios and at various Reynolds numbers. Heat flux decreases as H/D ratio increases and mass flow rate increases. Heat flux is more at H/D=0.5 and Re= 17.79×10^5

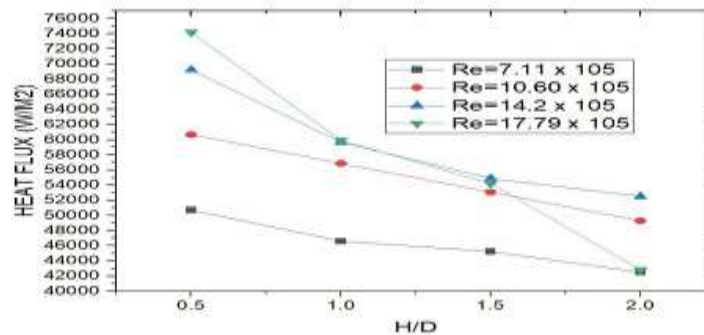


Fig. 7 Heat flux vs H/D at different Reynolds numbers at D=12mm

3.1.5 Experimental results and discussion for air at D=14mm

Fig. 8 shows the heat flux variation at various H/D ratios and at various Reynolds numbers. Heat flux decreases as H/D ratio increases and mass flow rate increases. Heat flux is more at H/D=0.5 and Reynolds number of 11.17×10^5 .

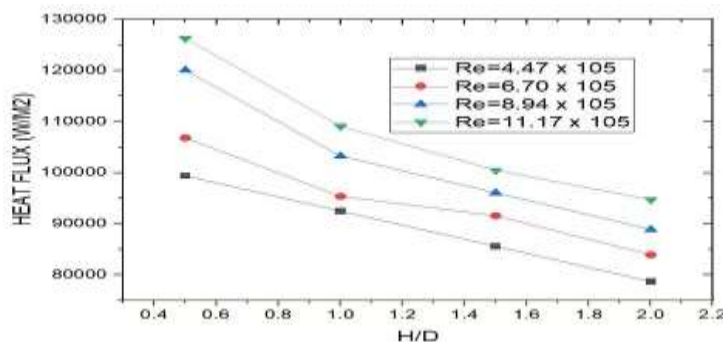


Fig. 8 Heat flux vs H/D at different Reynolds numbers at D=14mm

3.1.6 Experimental results and discussion for CO₂ at D=14mm

Fig. 9 below shows the heat flux variation at various H/D ratios and at various Reynolds numbers. Heat flux decreases as H/D ratio increases and mass flow rate increases. Heat flux is more at H/D=0.5 and $Re=15.25 \times 10^5$.

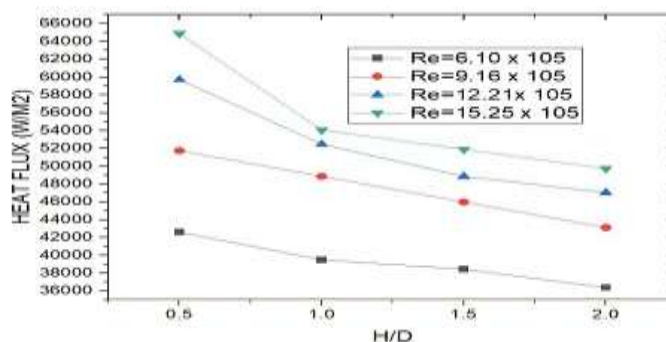


Fig. 9 Heat flux vs H/D at different Reynolds numbers for CO₂ at D=14mm

3.2 CFD Results and Discussion

3.2.1 CFD Results and discussion for air at D=10mm

Heat flux values are generated in CFD software for different H/D ratios with different Reynolds numbers for air is shown. Fig.10 shows the heat flux variation at various H/D ratios and at various Reynolds numbers. Heat flux decreases as H/D ratio increases and mass flow rate increases. Heat flux increases at H/D=0.5 and $Re=15.64 \times 10^5$.

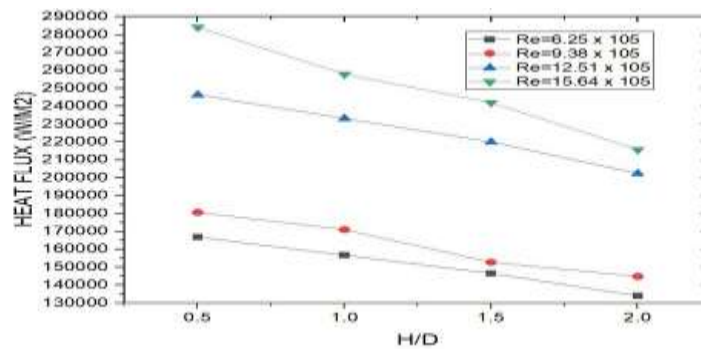


Fig. 10 Heat flux vs H/D at different Re

By comparing the CFD results with experimental results it shows that CFD results gave higher values of heat flux and were also maximum at $H/D=0.5$ and $Re=13.03 \times 10^5$. Fig.11 shows the outlet temperature distribution of the cylinder jet. In fig.12 shows the heat flux of the flat plate for different values of H/D and Reynolds number is given

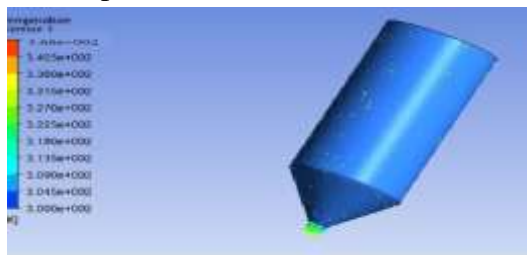


Figure 11 Outlet temperature of Jet

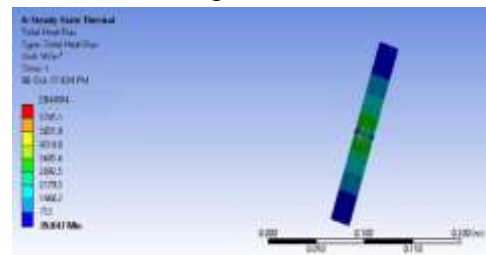


Figure 12 Total heat flux of flat plate

3.2.2 CFD Results and discussion for CO₂ at D=10mm

Heat flux values are found in CFD software for different H/D ratios with different Reynolds numbers for CO₂ is shown. Fig 13 shows the heat flux variation at various H/D ratios and at various Reynolds numbers. Heat flux decreases as H/D ratio increases and mass flow rate increases. Heat flux is more at $H/D=0.5$ and $Re=21.35 \times 10^5$

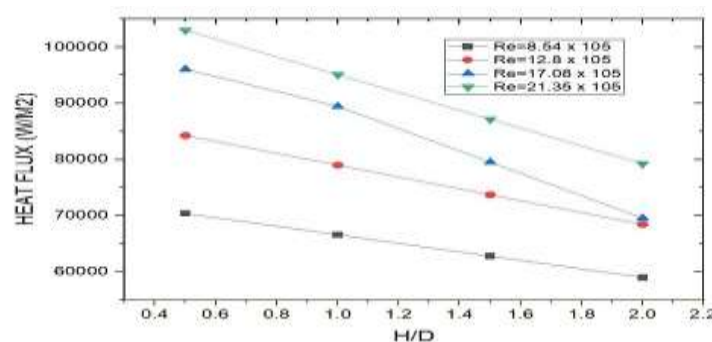


Fig. 13 Heat flux vs H/D at different Re

From the analysis, CFD results gives more value of heat flux than experiemntal results and are maximum at $H/D=0.5$ and $Re=21.35 \times 10^5$. Fig.14 and 15 are the outlet conditions of the jet and plate at $H/D=0.5$ and $Re=21.35 \times 10^5$

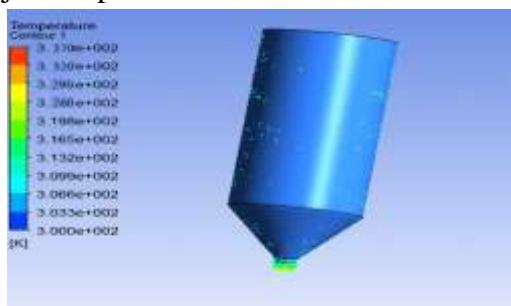


Fig. 14 Outlet temperature of jet

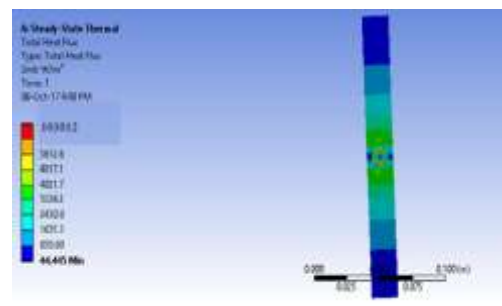


Fig.15 Total heat flux of flat plate

3.2.3 CFD results and discussion for air at D=12mm

Heat flux values are generated in CFD software for different H/D ratios with different Reynolds numbers for air is shown. Fig.16 shows the heat flux variation at various H/D ratios and at various Reynolds numbers. Heat flux decreases as H/D ratio increases and mass flow rate increases. Heat flux increases at H/D=0.5 and $Re=13.03 \times 10^5$

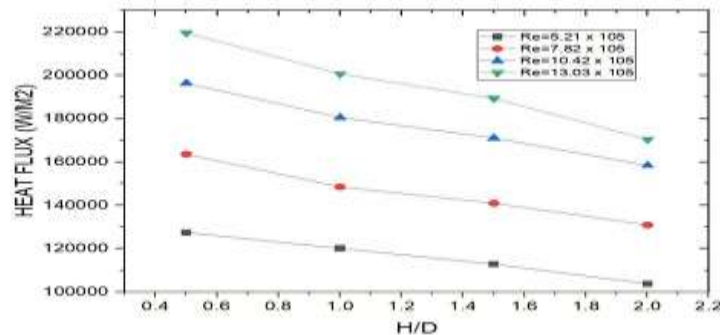


Fig. 16 Heat flux vs H/D at different Re

By comparing the CFD results with experimental results it shows that CFD results gave higher values of heat flux and were also maximum at H/D=0.5 and $Re=13.03 \times 10^5$. Fig.17 shows the outlet temperature distribution of the cylinder jet. In Fig.18 the heat flux of the flat plate for different values of H/D and Reynolds number is given

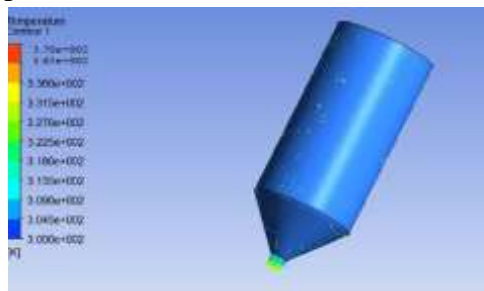


Fig. 17 Outlet temperature of Jet

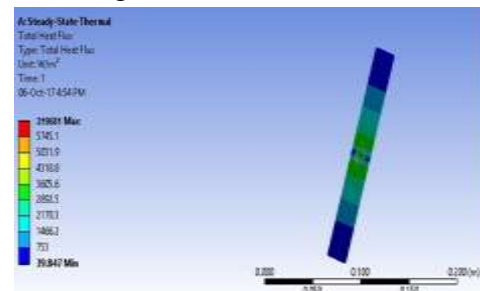


Fig. 18 Total heat flux of flat plate

3.2.4 CFD Results and discussion for CO₂ at D=12mm

Heat flux values are found in CFD software for different H/D ratios with different Reynolds numbers for CO₂ is shown below. Fig. 19 shows the variation of heat flux with different H/D ratios and Re. Heat flux decreases as H/D ratio increases and mass flow rate increases. Heat flux is more at H/D=0.5 and $Re=17.79 \times 10^5$

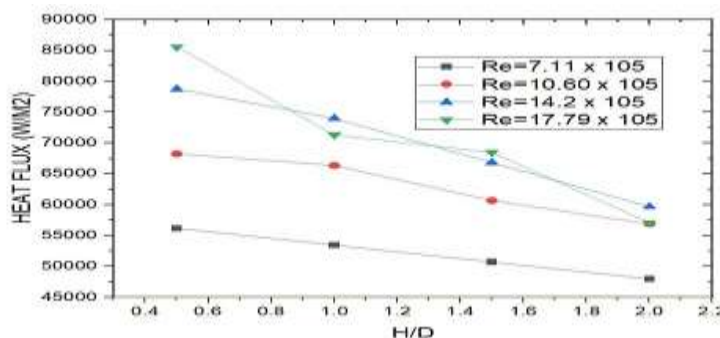


Fig. 19 Heat flux vs H/D at different Re

From the analysis, CFD results gives more value of heat flux than experimental results and are maximum at H/D=0.5 and $Re=17.79 \times 10^5$. Fig. 20 and 21 shows the outlet conditions of the jet and plate at H/D=0.5 and $Re=17.79 \times 10^5$

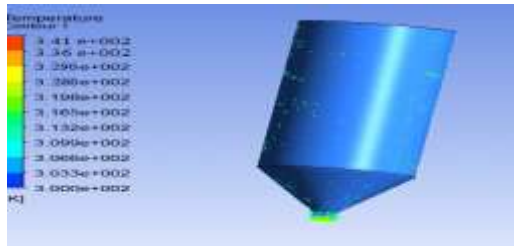


Figure 20 Outlet temp.of cylindrical jet

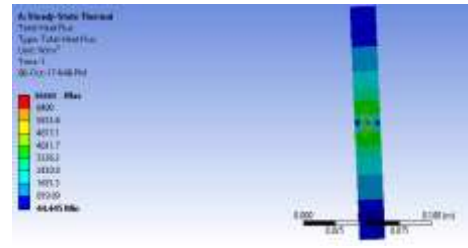


Figure 21 Total heat flux of flat plate

3.2.5 CFD Results and discussion for air at D=14mm

Heat flux values are generated in CFD software for different H/D ratios with different Reynolds numbers for air is shown below. Fig.22 shows the variation of heat flux at different H/D ratios and at different mass flow rates. Heat flux decreases as H/D ratio increases and mass flow rate increases. Heat flux increases at H/D=0.5 and $Re=15.64 \times 10^5$

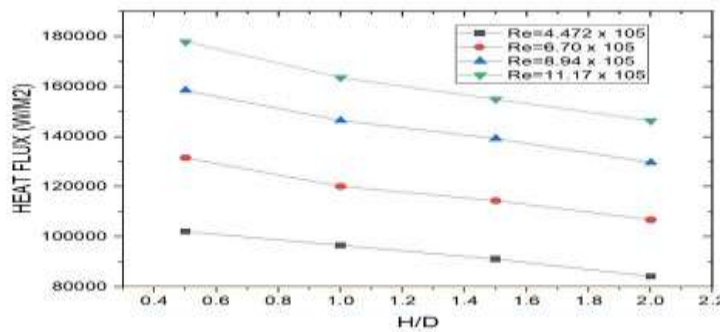


Figure 22 Heat flux vs H/D at different Re

By comparing the CFD results with experimental results it shows that CFD results gave higher values of heat flux and were also maximum at H/D=0.5 and $Re=11.17 \times 10^5$. Fig.23 shows the outlet temperature distribution of the cylinder jet. Fig.24 shows heat flux of the flat plate for different values of H/D and Reynolds number is given

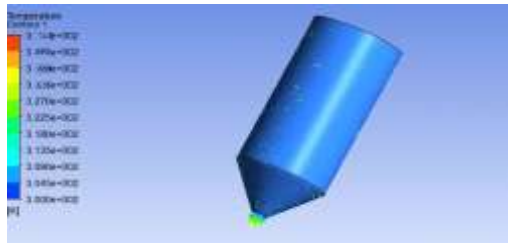


Figure 23 Outlet Temp. of cylindrical Jet

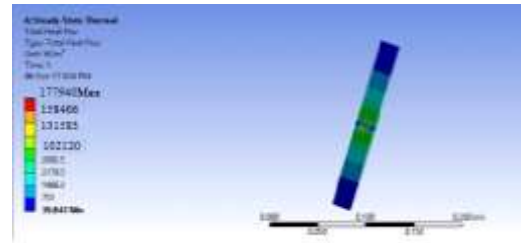


Figure 24 Total heat flux of flat plate

3.2.6 CFD results and discussion for CO₂ at D=14mm

Heat flux values are found in CFD software for different H/D ratios with different Reynolds numbers for CO₂ is shown below. Fig 25 below shows the variation of heat flux at different H/D ratios and at different mass flow rates. Heat flux decreases as H/D ratio increases and mass flow rate increases. Heat flux is more at H/D=0.5 and $Re=21.35 \times 10^5$

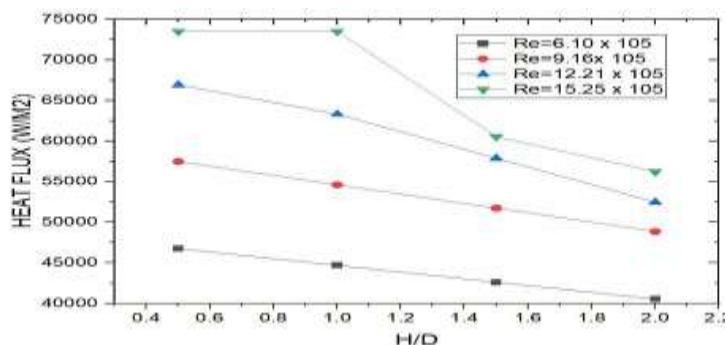


Fig. 25 Heat flux vs H/D at different Re

From the analysis, CFD results gives more value of heat flux than experimental results and are maximum at $H/D=0.5$ and $Re=21.35 \times 10^5$. Fig.26 and 27 are the outlet conditions of the jet and plate at $H/D=0.5$ and $Re=21.35 \times 10^5$

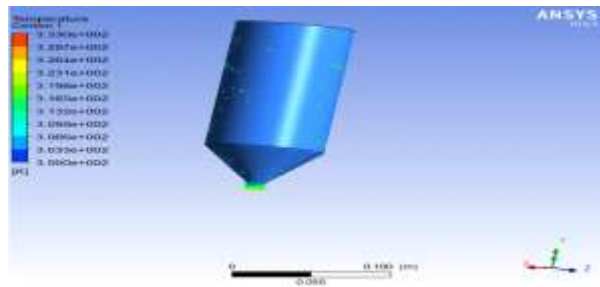


Fig. 26 Outlet temperature of cylindrical jet

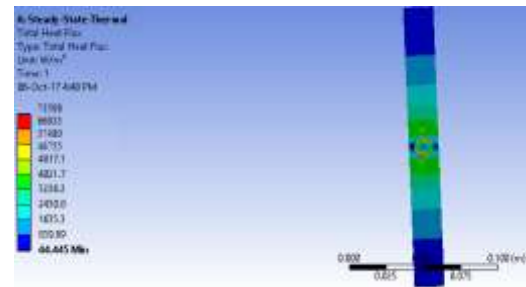


Fig. 27 Total heat flux of flat plate

3.3 Comparison of results for air and CO₂

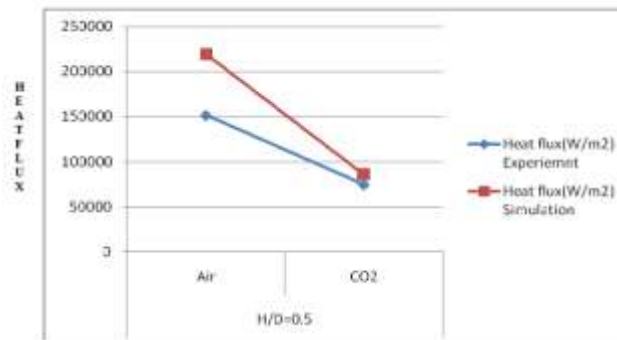


Fig. 28 Comparison of CFD and Experimental results for air and CO₂

4. CONCLUSIONS AND RECOMMENDATIONS

- From results it is observed that there is a correlation of 31% between experimental and CFD values for air.
- From it is observed that there is a correlation of 13.3% between experimental and CFD values for CO₂.
- From results is is shown that $H/D=0.5$ gives more heat flux than $H/D=1,1.5$ nd 2.
- From results it is shown that at massflow rate of 0.25kg/s gives more heat flux than 0.1, 0.15 and 0.2kg/s.
- It is concluded that CFD is validation is correlated to exerimental value and is more for air. Therefore it is recommended that CFD is the better tool used to find Heat flux calculations
- Finally it is recommended that air has more heat transfer rate than CO₂ gas

References

1. Keyon Cheng, XiulanHuai, Jun Cai, Zixionguo “Numerical simulation of Impinging Cooling on the leading edge of a Turbine blade” *International Mechanical Engineering Congress and Exposition*, 10, 2011.
2. GokulnathR“ Review on Jet Impingement Cooling of Heated Plate” *International Journal of Innovative and Emerging Research in Engineering*, 4(5), 2017.
3. Khudheyer S. Mushatet. “Thermal and Hydrodynamic Analysis of the Impingement Cooling inside a Backward Facing Step Flow” *Research Journal of Recent Sciences* , 1, 2012.
4. Akshay R. Nangare. ”Multiple Jet Impingement: A Promising method of cooling” *International journal of latest trends in engineering and technology*, 6(4), 2016.
5. Muhsincan S. “Submerged jet impingement cooling using nano structured plates” *International Journal of Heat and Mass Transfer*, 59, 2013.

Two-day International Conference on Recent Advances in Mechanical and Industrial Engineering – 2023
(ICRAMIE-2023)

6. Pallavi C. Chaudhari, Ashish N. Sarode. "Performance analysis of jet impingement cooling on copper square plate" *International Conference Proceeding ICGTETM*, 2017.
7. Vipin .R , Sabu .Kurian , Tide P. S. "STUDY ON PULSED JET IMPINGEMENT COOLING" *International Journal of Science, Engineering and Technology Research (IJSETR)*, 4(10), 2015.
8. Mahesh T. "A numerical investigation on jet impingement cooling aided with cross flow and ribs on target plate", *International Journal of Science, Engineering and Technology Research (IJSETR)*, 4(10), 2015.
9. Chaina Ram. "computational study of leading edge jet impingement cooling with a conical converging hole for blade cooling" *ARPJ Journal of Engineering and Applied Sciences*, 12(22), 2017.
10. RejiKumar "Inline Array Jet Impingement Cooling Using Al₂O₃ / Water Nanofluid In A Plate Finned Electronic Heat Sink" *American Journal of Engineering Research (AJER)*, 03(03),2014.

Colour Importance in Radiation Heat Transfer-An Experimental Work

Dr.P.Anusha, Dr.M.Naga Swapna Sri, Dr.K.Srividya, V.Sravani, Vemulapalli Chinmai, Saggurthi Ramadevi, Shaik Khiser Siddiq, Tellam Venkanna babu, Muppalla Praveen Chowdary

Department of Mechanical Engineering, P V P Siddhartha Institute of Technology,
Vijayawada, India.

Abstract: Colour is the quality of things that are caused by differing behavior of light being reflected or emitted by them. We know that Heat can be transferred in three different modes. In this, Radiation plays a major role as for the simple reason that it needs no material medium to propagate through. The best example is how we feel the heat of the sun though it is in a vacuum from our perception. For a desirable rate of Heat Transfer, literature talks about Insulation and the factors affecting it, such as thickness and type of material; but there are no traces of importance of colours. Present work deals with the effect of colours on Thermal Radiation, by conducting a simple experiment. By using experimental results the maximum wavelength, Monochromatic Emissive power, and Emissive power of different coloured objects were calculated. We observe that the colour of the body is also influencing the heat absorption capacity of the fluid inside the coloured body.

1. Introduction

Heat transfer in radiation takes place mainly in the form of electromagnetic waves in infrared region. The radiation emitted by an object is the result of the thermal motion of the molecules that make up the object. Radiation heat transfer can be explained by a reference term called 'black body'. A blackbody is defined as an object that absorbs all the radiation that hits its surface. A true blackbody does not exist in nature. A blackbody is a fictitious object that completely absorbs the heat radiation of all wavelengths incident on it. Such objects do not reflect light and will appear black if the temperature is low enough that they cannot emit light. All blackbody heated to a certain temperature emits heat radiation.

1.1 Effect of Colours on Radiation

The visible spectrum is a portion of the electromagnetic spectrum that can be detected by the human eye. Electromagnetic radiation in this wavelength band is called visible light /Light wavelengths from about 390 to 700 nm can be detected by the human eye.

1.2 The influence of colour on Radiation

The energy carried by the light doesn't just disappear, when light is absorbed by an object, but rather increases the energy of the object by absorption. The object now releases this absorbed energy by emitting long wavelengths and minimum energy infrared heat. This transformation of light into heat is based on the law of conservation of energy. The material that absorbs the most light is the one that gains the most energy and heats up more. If a material absorbs the majority of the light it receives, it seems dark. Conversely, the material looks brighter if it reflects most of the light that hits it. Different wavelengths (colours) of light have different amounts of energy. Hence, Radiation is dependent on the colour of the object. Good absorbers and emitters for items around room temperature that emit far-infrared radiation. Human skin is a good example; regardless of colour, human skin is an excellent

absorber and emitter of far infrared. As a result, no matter what colour your skin is, infrared sees you as BLACK. But, silvery metals don't behave in this way. They reflect visible as well as infrared radiation. [1]The literature says that the colour which has fewer wavelengths absorbs more heat energy and vice-versa. Hence, violet absorbs more energy in the spectrum. And red has opposite properties. Black is not exactly a particular colour. Rather, it is the absence of light. Hence, Black has no definitive wavelength. White, on the other hand, is a mixture of all the colours of the visible spectrum. Hence, BLACK and WHITE does not have a definitive set of wavelengths.

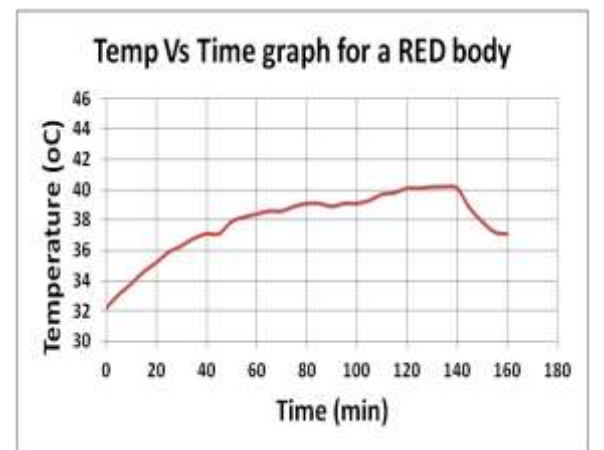
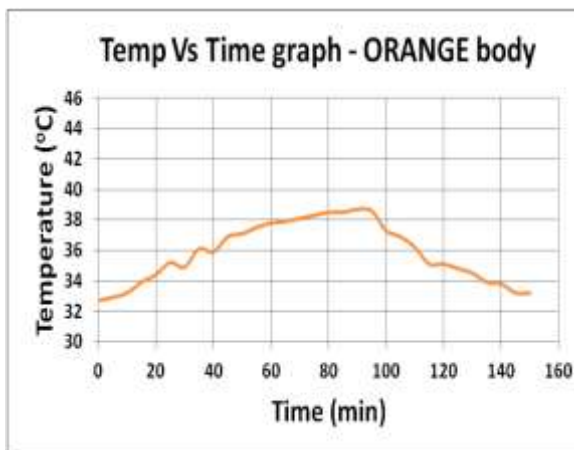
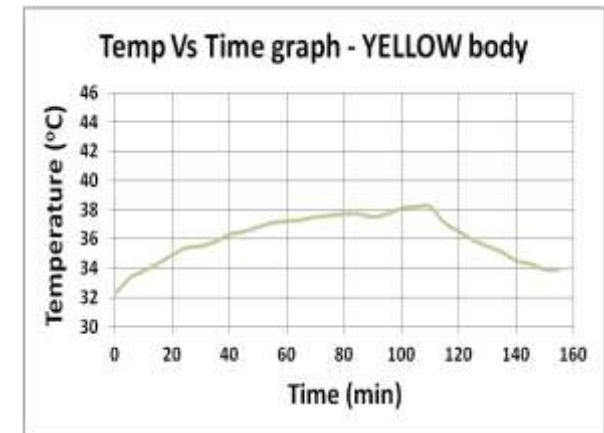
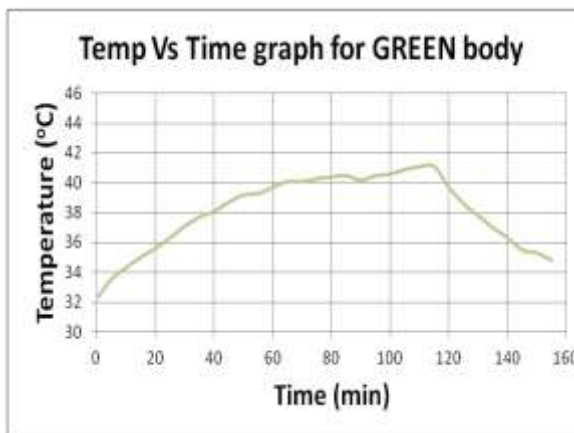
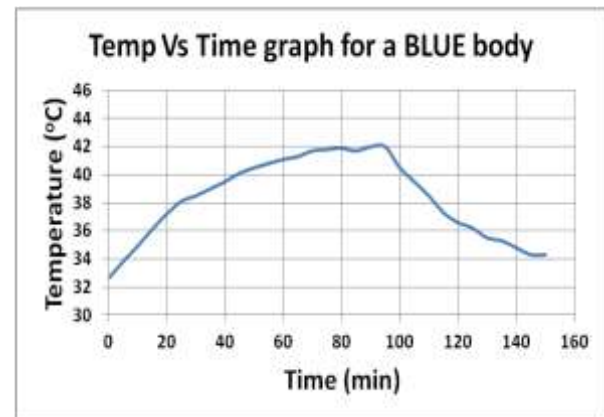
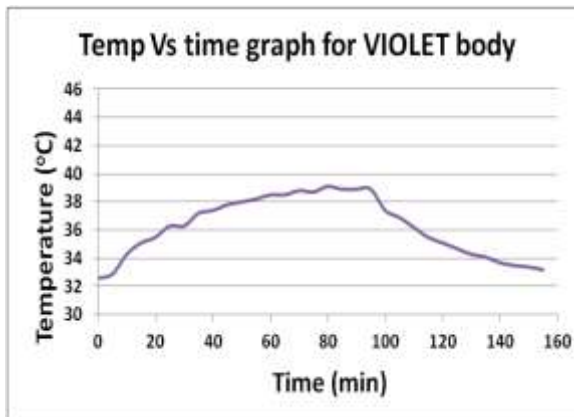
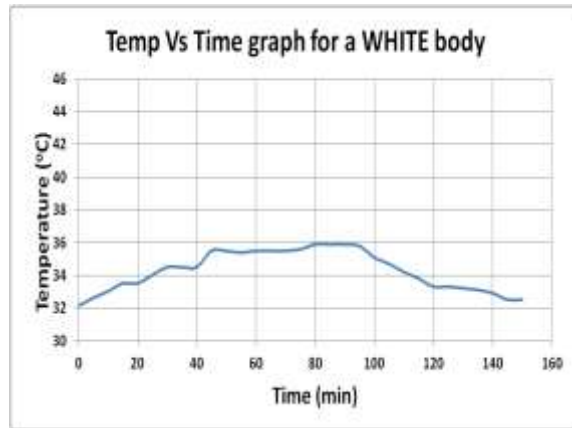
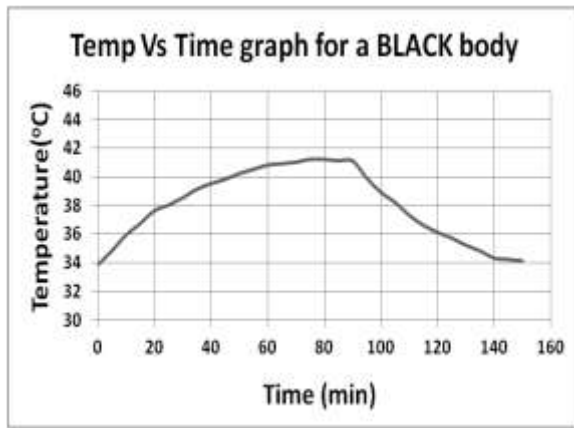
2. Experimental Setup and Process

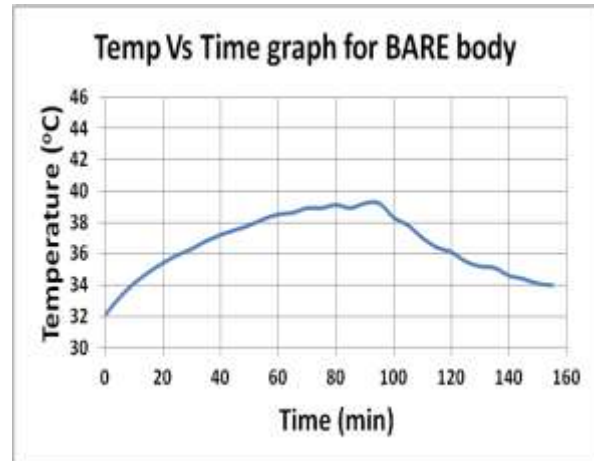
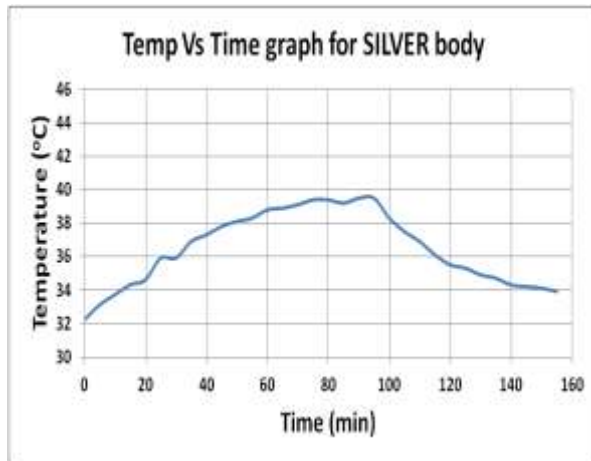
Different colours were applied to the cylinder that was filled with water in this experiment setup. A digital thermometer was used to record the temperature data as shown in fig1. This is how the experiment was carried out.

1. Coated the water filled cylinder with black colour paint and placed it under sunlight as shown in fig1.
2. Readings were noted at regular intervals until the water heats up with the help of digital thermometer.
3. Above two steps will be repeated for different colours as shown in fig 1 to observe the heat absorbing capacity.
4. Now take the cylinders away from the heat source.
5. Repeat the same experiment but now while cooling.
6. Record the temperatures and the time at which the temperatures were observed in a tabular form as shown in Table1.
7. To compare the results, graph the temperature versus time with the dependent variable TEMPERATURE on the y-axis and the independent variable TIME on the x-axis.



Fig1 various colours were coated to a water-filled cylinder





These graphs illustrate temperature vs. time for various colours coated on the water filled cylinder, with TEMPERATURE on the y-axis and TIME on the x-axis.

Experimental Values

Table 1 the table illustrate the temperatures with respect of time at different colours

S.NO	TIME IN (min)	BLACK	WHITE	VIOLET	BLUE	GREEN	YELLOW	ORANGE	RED	SILVER	BARE
1	0	32.1	32.1	32.6	32.6	32.2	32.2	32.7	32.2	32.2	32.1
2	5	33.8	32.6	32.9	33.8	33.5	33.2	32.9	33.1	33.1	33.2
3	10	34.8	33	34.3	34.9	34.3	33.8	33.2	33.8	33.7	34.1
4	15	35.9	33.5	35.1	36.1	35	34.3	33.9	34.6	34.3	34.8
5	20	36.7	33.5	35.5	37.2	35.6	34.9	34.4	35.2	34.6	35.4
6	25	37.6	34.1	36.3	38.1	36.3	35.4	35.2	35.9	35.9	35.9
7	30	38	34.5	36.3	38.5	37.1	35.5	34.9	36.3	35.9	36.3
8	35	38.5	34.5	37.2	39	37.7	35.8	36.1	36.8	36.9	36.8
9	40	39.1	34.5	37.4	39.5	38.1	36.3	35.9	37.1	37.3	37.2
10	45	39.5	35.5	37.8	40.1	38.7	36.5	36.9	37.3	37.8	37.5
11	50	39.8	35.5	38	40.5	39.2	36.8	37.1	37.9	38.1	37.8
12	55	40.2	35.4	38.2	40.8	39.3	37.1	37.5	38.2	38.3	38.2
13	60	40.5	35.5	38.5	41.1	39.7	37.2	37.8	38.4	38.8	38.5
14	65	40.8	35.5	38.5	41.3	40.1	37.3	37.9	38.6	38.9	38.6
15	70	40.9	35.5	38.8	41.7	40.1	37.5	38.1	38.6	39.1	38.9
16	75	41.0	35.6	38.7	41.8	40.3	37.6	38.3	38.9	39.4	38.9
17	80	41.2	35.9	39.1	41.9	40.4	37.7	38.5	39.1	39.4	39.1
18	85	41.2	35.9	38.9	41.7	40.5	37.7	38.5	39.1	39.2	38.9
19	90	41.1	35.9	38.9	42	40.2	37.5	38.7	38.9	39.5	39.2
20	95	41.1	35.8	38.9	42	40.5	37.7	38.6	39.1	39.5	39.2
21	100	39.9	35.1	37.4	40.5	40.5	38.1	37.3	39.1	38.3	38.3
22	105	38.9	34.7	36.9	39.5	40.9	38.2	36.9	39.3	37.5	37.8
23	110	38.2	34.2	36.2	38.5	41.1	38.2	36.2	39.7	36.9	37
24	115	37.3	33.8	35.5	37.3	41.1	37.1	35.1	39.8	36.1	36.4
25	120	36.6	33.3	35.1	36.6	39.7	36.5	35.1	40.1	35.5	36.1
26	125	36.1	33.3	34.7	36.2	38.6	35.9	34.8	40.1	35.3	35.5
27	130	35.7	33.2	34.3	35.5	37.8	35.5	34.5	40.2	34.9	35.2
28	135	35.2	33.1	34.1	35.3	37	35.1	33.9	40.2	34.7	35.1
29	140	34.8	32.9	33.7	34.8	36.3	34.5	33.8	40.1	34.3	34.6
30	145	34.3	32.5	33.5	34.3	35.5	34.3	33.2	38.8	34.2	34.4
31	150	34.2	32.5	33.4	34.3	35.3	33.9	33.2	37.9	34.1	34.1
32	155	34.1		33.2	34.3	34.8	33.9		37.2	34	34
33	160					34.8			37.1		
34	165					34.8			36.9		

35	170								36.5		
36	175								36.1		
37	180								35.9		
40	185								35.6		
41	190								35.3		

3. Formulae for Analysis:

3.1 Wien's Displacement Law,

This law establishes a link between a black body's temperature and the wavelength at which monochromatic emissive power reaches its highest value.

$$\lambda_{max} T = 2.9 * 10^{-3} mK \quad [1]$$

3.2 Max Planck Distribution Law,

The spectral or monochromatic emissive power for a black surface is highest at every wavelength at any given temperature and it is given by Max Planck's distribution law as,

$$E_b \lambda_{max} = \frac{C_1 * \lambda^{-5}}{\left[\exp \frac{C_2}{\lambda * T} \right] - 1} \quad [2]$$

3.3 Emissive Power,

Total Emissive Power is the total quantity of radiation released by a body per unit area and time.

$$E = \sigma T^4 \quad W/m^2 \quad [3]$$

4. Results and Discussions

Experimental values are used to calculate the Maximum wavelength, Monochromatic Emissive power and Emissive power of different coloured objects and the results were tabulated as,

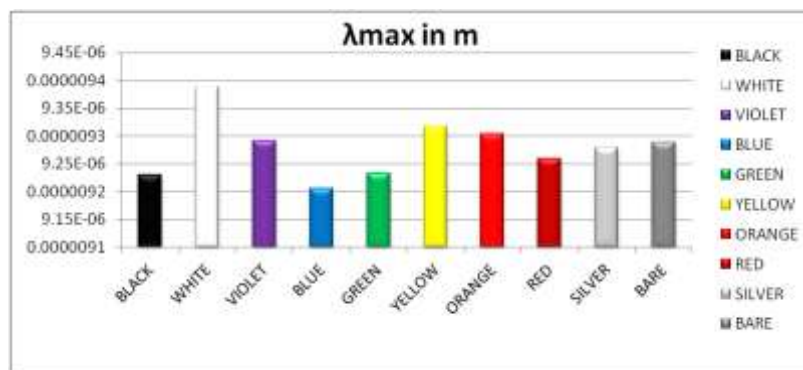


Fig 2. Variation of Maximum Wavelength Values for Different coloured Bodies

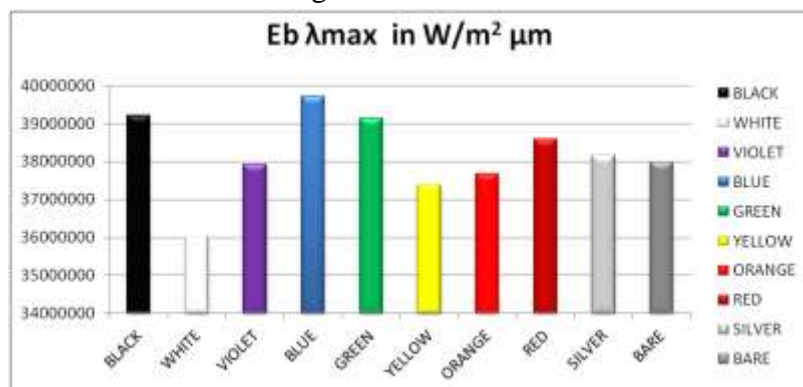


Fig 3. Variation of Spectral Emissive Power for Different coloured Bodies

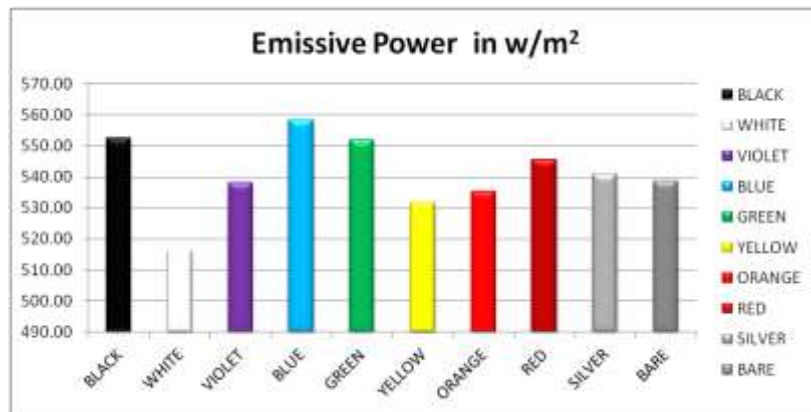


Fig 4. Variation of Emissive Power for Different coloured Bodies

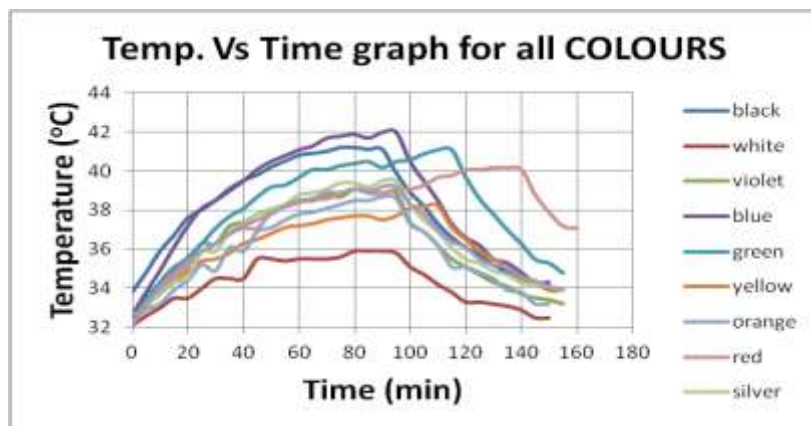


Fig 5. Variation of Temperature Values with Time for Different coloured Bodies

5. Conclusions

Started this work in search of projects in Radiation and Effect of colours in Radiation heat transfer. But hardly founded about the effects of Black, White and Shiny surfaces only. From Visible Spectrum, we can find VIBGYOR colours with specific wavelengths. Present work deals with the effect of colours on Thermal Radiation in all applications, by conducting a simple experiment on different wavelengths of visible spectrum. From the experiment, the observations from Fig [5] are, the black coated body achieved the highest temperature whereas a white coated body achieved the lowest temperature, which was true according to theory. One can coat a body with colour yellow and orange when the cooling has to be fast. Body can be coated with violet colour when the cooling has to be slow. The colours Blue, Green and Red also competed with a Black coated body, showing properties near to it. These observations were clearly understood from the experiment which slightly went off track from the theory. As expected from the theory, the bare cylinder attained the maximum temperature fast and cooled fast as well. The silver coated object reflected the light falling on it. Heating and cooling curves for individual colours are obtained. Planck's Law curve in the visible has been drawn from the observations. Understood that the experimented observations are very precise to the theoretical values. We believe that this work will be very useful for future generations who wish to work in Radiation Heat Transfer.

Future Scope

1. Aviation: At high altitudes the radiation effect is very high, hence in aviation if the colour importance in radiation is keenly implemented; a lot of variations can be observed.
2. Food preservation: Food can preserve in packets of colours which do not take in much light,

hence food can be saved from contamination noticeably.

3. Flying Cars: In future we have a scope for flying cars. Hence the colour coating importance is remarkable needed in this respect.

4. Thermal insulation: Where all we prefer thermal insulation, there we can go with colour coatings.

5. Industries: In industries, to the chimneys and cooling towers if this colour theory is applied, the variation will be remarkable.

Acknowledgements

We would like to thank SAGTE, for providing Financial Assistance in Carrying out this work successfully.

Nomenclatures

T Temperature in K

A The emitting body's surface area in m^2

C1 Value that remains constant = $0.374 \cdot 10^{-15}$
 Wm^3

C2 Value that remains constant = $14.4 \cdot 10^{-3}$ m
K

Greek Symbols

σ Constant Stefan Boltzmann, $5.67 \cdot 10^{-8}$
 w/m^2K^4

λ Wavelength

References

1. S. Del Bino and F. Bernerd, "Variations in skin colour and the biological consequences of ultraviolet radiation exposure", British Journal of Dermatology (2013) 169 (Suppl. 3), pp33–40.

Computational analysis on the PEM Fuel cell using COMSOL

Gandham Dhanya Lahari¹, Srinivas Prasad Sanaka², Landa Balajee³, Chittineni BalaManikanta⁴, Mendem Beulah Pratibha⁵ and Boji Srikar⁶

Mechanical Engineering Department, Velagapudi Ramakrishna Siddhartha Engineering College, Kanuru, Vijayawada, Andhra Pradesh.

dhanyagandham@gmail.com¹, drssp1974@gmail.com², landabalajee52@gmail.com³,
balamanikantachittineni@gmail.com⁴, srikarsrikar15@gmail.com⁶ and
beulahmendem@gmail.com⁵

ABSTRACT: Fuel cells are energy conversion devices that directly convert chemical energy of fuels such as hydrogen to useful work with negligible environmental impact and high efficiency. Proton Exchange Membrane Fuel Cell (PEMFC) is a promising power generating device to use for automobile applications, this is due to their higher efficiency and zero emissions. The performance of Proton Exchange Membrane fuel cell (PEMFC) depends on a lot of physical and chemical factors including the operation conditions, transport phenomena inside the cell and kinetics of the electrochemical reactions, membrane electrode assembly but the design of the flow channels is one of the most important factors affecting the performance of fuel cells. The homogeneous distribution of the reactive gases over the flow field channels and catalyst surface, it leads to improve the chemical reactions and thus to improve the performance of the fuel cell. The flow distributor channels are responsible for both supplying fresh reactants to, and removing product water from the reaction zones. The objective of the paper is to investigate the effect of operating temperature on the performance of fuel cell. The simulations are carried out using COMSOL Multiphysics software. The results are validated and they are in good agreement with the experimental data. The computations are carried out at operating temperatures of 70°C, 80°C, 90°C.

KEYWORDS: PEMFC, Flow Channels, COMSOL Multiphysics software.

1. INTRODUCTION

A fuel cell is a device that employs a chemical reaction to generate electricity. Every fuel cell has two electrodes, one positive and one negative, which refer to as anode and cathode, respectively. The electrodes are where the reactions that generate electricity take place. Every fuel cell also consists of an electrolyte, which transports electrically charged ions from one electrode to the other. A catalyst layer accelerates the reactions at the electrodes. Although hydrogen is the most basic fuel, fuel cells also require oxygen. Proton Exchange Membrane Fuel Cells (PEMFC), are energy efficient and environmentally friendly alternative to conventional energy conversion for various applications in stationary power plants, portable power device and transportation. PEM fuel cells provide low operating temperature and high-energy efficiency with near zero emission [1]. Work on the PEMFC was dated back to 1839. After more than a century the first PEM fuel cell was developed. In this effort, many critical issues of PEMFC technology need to be addressed. One of the key issues is the performance enhancement of fuel cell by studying the influence of various operating and design parameters [2]. Badreddine Larbi et al studied the effect of porosity and pressure and they concluded that higher backing layer porosity is required for better performance. A simple analytical model of a high temperature PEM fuel cell was developed, which is a valuable tool for the processing of experimental data. Wei-Mon Yan et al studied the effect of flow channel designs on

performance of PEMFC and concluded that the interdigitated flow field having 1.4 times better power output than the conventional flow field design. Dyi-Huey Chang et al studied the effect of flow channel depth and flow rates on performance of miniature PEMFC. They concluded that optimum flow rate was essential for shallow channel depth to maintain sufficient pressure to force reactant into channel and also to have proper water balance [3-6]. Shimpalee et al investigated the effect of number of gas paths on a 200 cm² serpentine flow field design. Also, the effect of flow channel dimensions and rib widths for performance studies on PEMFC were studied [7]. Atul Kumar et al optimized the flow channel dimensions and shape in the flow field of end plates in a single pass flow field design. Also, when humidification temperatures are less than cell temperature, the PEMFC performance deteriorates. The liquid water transport within the Gas Diffusion Layer (GDL) and liquid water removal from the surface of the GDL play a crucial role in determining the performance of cell. P. Karthikeyan et al optimized the ten operating and design parameters of PEMFC using L27 orthogonal array with three levels by Taguchi method. So proper balancing of the water in the membrane is playing a vital role [8-11]. P. Karthikeyan et al. investigated the water impact on performance of PEMFC with porous flow channels. They concluded that the porous flow channels had 48% more power output than non-porous flow channels due to water accumulation in non-porous flow channels. M. Muthu Kumar et al investigated the effect of two, three and four pass serpentine flow field design and concluded that the PEMFC with three pass serpentine channel has produced the high performance [12-14]. V. Lakshmi Narayanan et al numerically investigated the effect of six cross sections of single flow channel of PEMFC. Thus, proper water management is essential for enhanced fuel cell performance. Also, water and thermal management issues were severely affected by proper selection of design and operating parameters. So, there is an exigent need of analysing the simultaneous effect of operating and design parameters. In this paper, the PEMFC with four different Landing to Channel width were analysed to study the effect of design parameters on the performance of PEM fuel cell [14-15]. Badreddine Larbi et al studied the effect of porosity and pressure and they concluded that higher backing layer porosity is required for better performance [16]. Wei-Mon Yan et al studied the effect of flow channel designs on performance of PEMFC and concluded that the interdigitated flow field had 1.4 times better power output than the conventional flow field design. Dyi-Huey Chang et al studied the effect of flow channel depth and flow rates on performance of miniature PEMFC [17-18]. Ferng et al have studied the effect of the flow channel patterns on PEM fuel cell performance in an experiment on a three-dimensional numerical model. The studied fields have been parallel and serpentine, respectively. The obtained results show that the serpentine channel has higher efficiency over parallel channels Ghanbarian et al has studied the effect of block in channel on the performance of fuel cells. They have used various types of blocks such as square, semi-circular and trapezoid and reported that in high flow densities, the effect of block is so significant. Also, the trapezoid blocks have shown more increase in the net power. Perng et al numerically studied the cross rectangular blocks in the PEM fuel cell flow channel and found out that the efficiency of the fuel cell has been increased [19-21].

2. Simulation Model

A single channel Serpentine flow field in a Proton Exchange Membrane Fuel Cell (PEMFC) have been created using COMSOL shown in fig 2.1. The basic assumptions for the 3D model were (i) the PEMFC operates under steady state and isothermal conditions, (ii) all reactants and products are in gaseous phase and follow ideal gas law, (iii) the flow in gas channel is

laminar, (iv) the electrochemical reactions occurs only in the Catalyst Layer (CL), (v) Gas Diffusion Membrane (GDM), CL's, Membrane are isotropic and homogeneous, (vi) no cross over of reactant gases and (vii) Water transports through the membrane (Electro-Osmotic Drag).

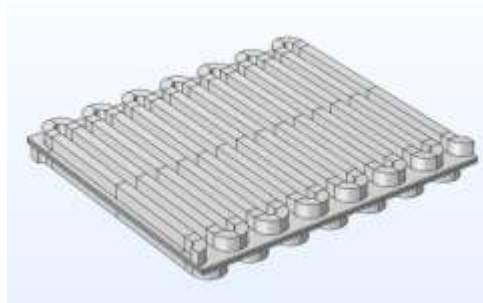


Fig 2.1 Single Channel Serpentine Flow PEMFC

All the input parameters for creating a 3D model of the single channel Serpentine PEMFC are listed in the table 2.1. The corresponding physics parameters such as species transport, molar fractions, viscosities, Temperatures, Pressures etc. are listed in table 2.2.

Table 2.1 Geometry Parameters

Geometry parameters:	
No. of Channels	1
No. of passes	14
Channel Width	0.8[mm]
Channel Depth	1.016[mm]
Land Width	0.8[mm]
Gas Diffusion Layer Thickness	0.2[mm]
Catalyst Layer Thickness	15[um]
Membrane Thickness	30[um]

Table 2.2 Physics Parameters

Physics Parameters:	
Temperature	353[K]
Pressure	100 [kPa]
HOR Exchange Current Density	0.3 [A/cm ²]
ORR Exchange Current Density	2.47e-8 [A/cm ²]
Charge Transfer Coefficient	1.0
Active Specific area	5e3 [1/m]
Porosity of GDL	0.4
Permeability of GDL	6e12 [m ²]
Porosity of CL	0.397
Permeability of CL	1.2e-12
Anode Viscosity	1.09e-5 [Pa S]
Cathode Viscosity	1.76e-5 [Pa S]

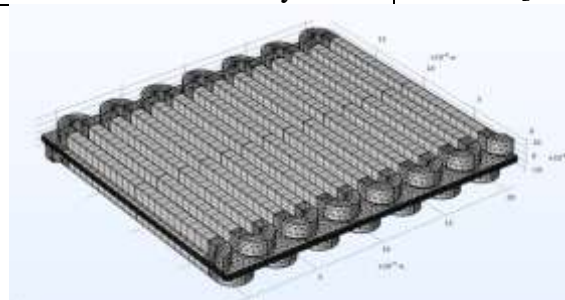


Fig 2.2 Mesh view of Single channel Serpentine PEMFC

3. Results and Discussion

The fuel cell experimental study results were taken from a literature paper [23]. In this study the simulation model of Proton Exchange Membrane Fuel Cell with serpentine flow field has been created for this experimental setup by using COMSOL Multiphysics software.

3.1 Polarisation Curves

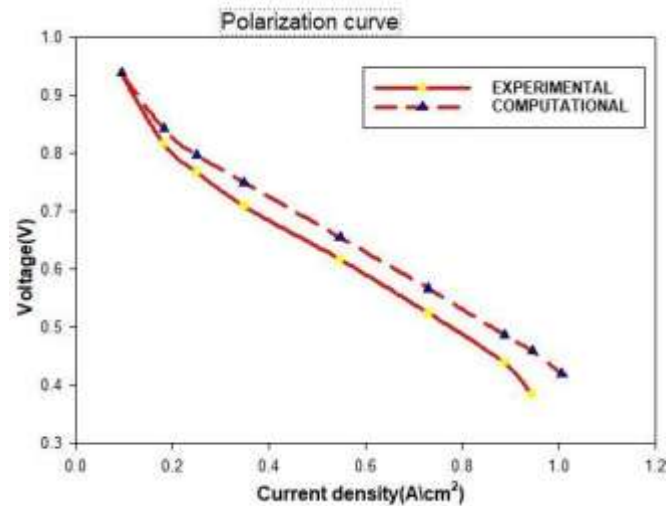


Fig 3.1 Polarisation Curve

The V-I characteristics at 80°C and 90°C were studied. Fig 3.1 shows the polarisation curve of the simulation data. Polarization curves are obtained with the following simulation results where different temperatures are taken i.e., (70°C, 80°C, 90°C) for the process. The line graph of current density against voltage represents the V-I characteristics which determines the voltage generated by the cell. The simulation results are compared with the experimental results in which the prediction shows a pretty good agreement with the obtained experimental data.

3.2 Electrolyte Conductivity

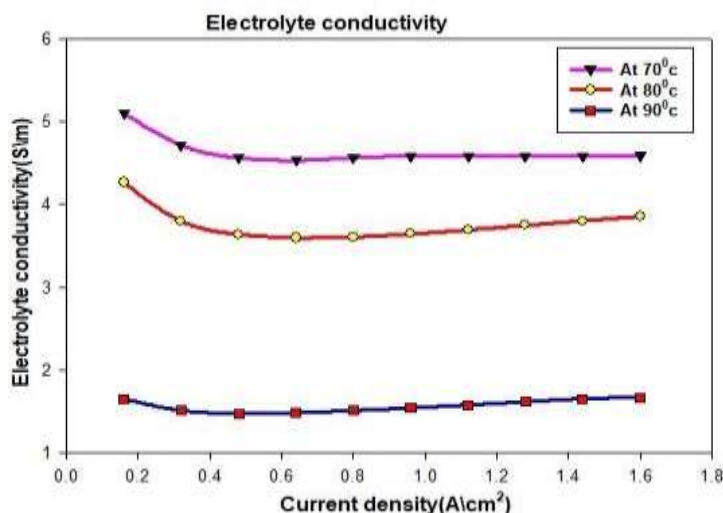


Fig 3.2 Electrolyte conductivity

As the temperature increases, the ion mobility also increases, resulting in an increase in the electrolyte conductivity. However, at high temperatures such as 90°C, the conductivity decrease due to an increase in membrane dehydration, which can reduce the water content and proton conductivity of the membrane. The electrolyte conductivity of a PEMFC plays an important role in determining its performance, as it affects the ability of protons to move through the membrane and generate electricity. At low temperatures such as 70°C, 80°C shows the higher electrolyte conductivity and higher electrolyte conductivity leads to better PEMFC performance, as it allows for faster proton transport and more efficient electrochemical reactions.

3.3 Mole Fraction of H_2

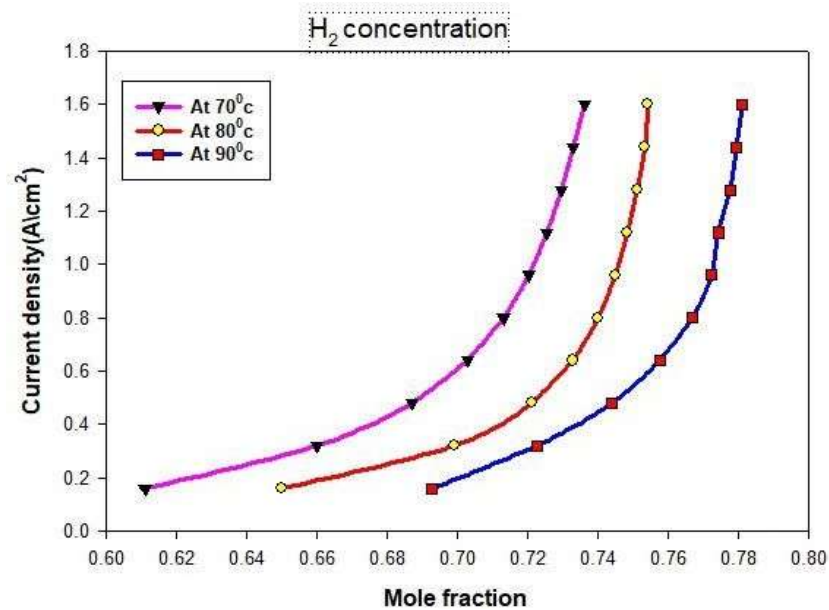


Fig 3.3 Mole Fraction of H_2

Fig 3.3 shows the mole fraction of H_2 . When the mole fraction of H_2 is increased in the anode flow field of a PEMFC, it can lead to a higher electrochemical reaction rate and increased fuel cell performance. This is because the rate of the electrochemical reaction at the anode is proportional to the concentration of H_2 molecules in the anode gas stream. At higher temperatures of about $90^\circ C$, it is observed that the mole fraction of H_2 increases gradually therefore increasing the rate of electrochemical reactions and higher fuel cell power output. If the mole fraction of H_2 becomes too high, it can lead to flooding of the anode and subsequent reduction in fuel cell performance. This is because the water produced during the electrochemical reaction can accumulate in the anode flow field blocking the flow of gas and electrolyte through the fuel cell. In rectification at temperatures of $70^\circ C, 80^\circ C$ exhibits better performance where flooding of the anode is much diminished.

3.4 Mole Fraction of O_2

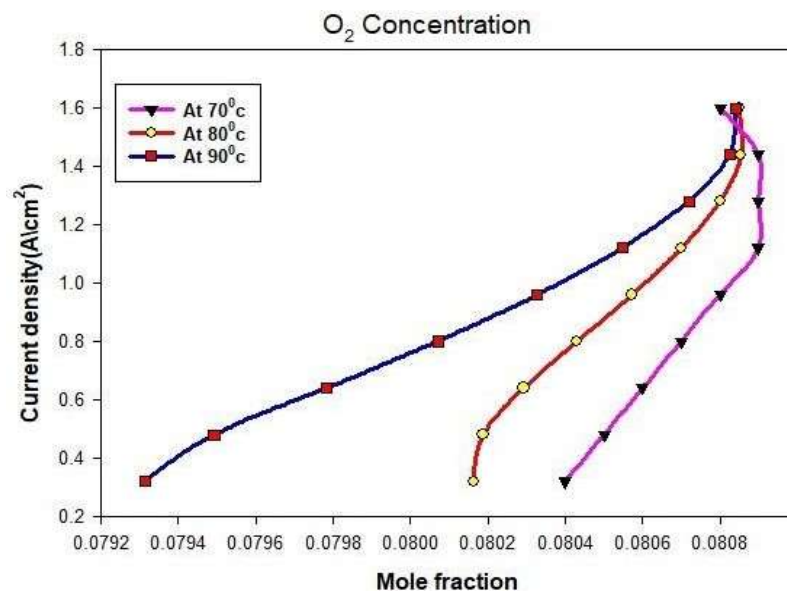
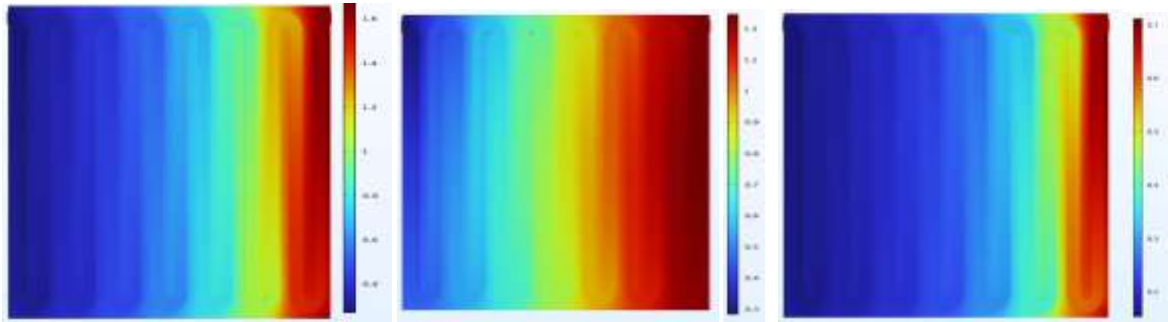


Fig 3.4 Mole Fraction of O_2

At $80^\circ C$ it is observed that there is an increase in the mole fraction of O_2 in the cathode flow field which leads to the enhancement of fuel cell performance, as it increases the availability of oxygen for the electrochemical reaction at the cathode that further leads to higher current densities and higher fuel cell power output.

3.5 Relative Humidity



a) Relative Humidity at 70°C b) Relative Humidity at 80°C c) Relative Humidity at 90°C

The relative humidity of the reactant gases affects the amount of water produced at the cathode, which in turn affects the proton conductivity of the membrane and thus the cell performance. The reactant gases flow through the channel, they pick up water from the cathode and carry it to the anode. This water is then used to help ionize the hydrogen fuel and generate electricity. At 90°C the relative humidity of the reactant gases is relatively low as the cathode becomes too dry thus decreasing the proton conductivity of the membrane which further decreases the cell performance. At 70°C the relative humidity is too high, the cathode becomes flooded, which decreases the performance. At 80°C it is observed that there is an adequate amount of relative humidity that allows an efficient water management.

4. CONCLUSIONS

The single channel serpentine flow PEMFC is modelled using COMSOL Multiphysics software. A series of performance analysis are performed by changing the operating temperatures at **70°C, 80°C, 90°C**. The Electrolyte conductivity, mole fractions of inlet gases (O_2 , H_2), Relative humidity at these parameters, operating temperatures were studied. The Fuel cell at 80°C shows the better performance when compared to **70°C, 90°C**. The electrolyte conductivity is the most significant parameter identified from the analysis to enhance the performance of the fuel cell.

References

1. Ibrahim Dincer, Hydrogen and Fuel Cell Technologies for Sustainable Future, Jordan Journal of Mechanical and Industrial Engineering, 2008.
2. Badreddine Larbi, Wael Alimi, Effect of porosity and pressure on the PEM fuel cell performance, J. Hydrogen Energy, 38 (2013) pp.8542- 8549.
3. O.Sharmardina, A.Chertovich, A simple model of a high temperature PEM fuel cell, J. Hydrogen Energy, (2009) pp.1-9.
4. Wei-Mon Yan, Chi-Yen Chen, Sheng-Chin Mei, Chyi-Yeou Soong, Falin Chen, Effects of operating conditions on cell performance of PEM fuel cells with conventional or interdigitated flow field, J. Power Sources, 162 (2006) pp.1157-1164.
5. Dyi-Huey Chang, Jung-Chung Hung, Effects of Channel Depths and Anode Flow Rates on the Performance of Miniature Proton Exchange Membrane Fuel Cells, J. Applied Science and Engineering, (2012) pp. 273280.
6. Shimpalee. S, Greenway. S, Van Zee. J.W, The impact of channel path length on PEMFC flow field design, J. Power Sources, 160 (2006) pp.398-406.
7. Shimpalee. S, Numerical studies on rib & channel dimension of flow field on PEMFC performance, J. Hydrogen Energy, 32 (2007) pp. 842-856.
8. Akira Nishimura, Satoru Kamiya, Tatsuya Okado, Yusuke Sato, Masafumi Hirota, Mohan Lal Kolhe - Heat and mass transfer analysis in single cell of PEFC using different PEM and GDL at higher temperature 2019.
9. Janovic A., Haas R. Economic prospects and policy framework for hydrogen as fuel in the transport sector. Energy Policy. 2018; 123:280–288. doi: 10.1016/j.enpol.2018.08.063.
10. Lei Yu, Shichen Jia & Qinyi Shi (2009) Research on Transportation-Related Emissions: Current Status and Future Directions, Journal of the Air & Waste Management Association, 59:2, 183-195, DOI: 10.3155/1047-3289.59.2.183

11. Barth, M.J.; Collins, J.; Scora, G.; Davis, N.; Norbeck, J. Measuring and Modeling Emissions from Extremely Low-Emitting Vehicles; *Trans. Res. Rec.* 2006, 1987, 21- 31.
12. A. Baroutaji, J. G. Carton – “Materials in PEM Fuel Cells” – 2019.
13. Md. Siddikur Rahman¹, Ridwan Rashid Riadh and Shuva Paul, November 2015 made a journal on “Investigate the output behaviour of alkaline fuel cell’s (AFC’s) parameters : flow rate & supply pressure” from the Department of Electrical and Electronic Engineering at American International University-Bangladesh, Dhaka, Bangladesh, *An International Journal (ELELIJ)* Vol 4
14. Bruno S. Machado, Nilanjan Chakraborty, Prodip K. Das, September 2016 made a journal on “Influences of flow direction, temperature and relative humidity on the performance of a representative anion exchange membrane fuel cell: A computational analysis”. *International Journal of Hydrogen Energy* Volume 42, Issue 9, 2 March 2017, Pages 6310-6323
15. Kartik Jain, June 2021 Emphasis on Proton Exchange Membrane (PEM) and different types of fuel cells from research development of hydrogen components from Indian Institute of Technology, Guwahati, ISSN: 2455-6211
16. Mohammad Talha, March 2021 research on Fuel cell Technology from Khwaja Fareed University of Engineering DOI: 10.13140/RG.2.2.15011.17442
17. San ping Jiang, January 2020, research on Fuels of the fuel cells and energy conversion techniques from *International Journal Book of Fuel cell technology* DOI:10.1007/978-981- 10-7626-8_4
18. Vladimir S. Bagotsky on July 2008, research on Alkaline fuel cell in the book: problems and solutions DOI:10.1002/9780470432204.ch6
19. J.G. Pharoah, O.S. Burheim - On the temperature distribution in polymer electrolyte fuel cells, *Journal of Power Sources* 195 (2010) 5235–5245.
20. Guoxiong Wang, Gongquan Sun, Qi Wang, Suli Wang, Hai Sun, Qin Xin - Effect of carbon black additive in Pt black cathode catalyst layer on direct methanol fuel cell performance, *International Journal of Hydrogen Energy* 35 (2010) 11245 – 11253.
21. Abhishek Raj, Tariq Shamim - Investigation of the effect of multidimensionality in PEM fuel cells, *Energy Conversion and Management* 86 (2014) 443–452.
22. H. Li, J. Zhang – “Encyclopedia of Electrochemical Power Sources” – 2009; pg: 941-950. <https://doi.org/10.1016/B978-044452745-5.00874-1>
23. N. P. Brandon – “Encyclopedia of Materials: Science and Technology (2nd Edition)”– 2004; pg:1-5. <https://doi.org/10.1016/B0-08-043152-6/01912>
24. F. Mojica¹, Md. A. Rahman¹, J. M. Mora², J. D. Ocon^{2,3}, P.-Y. A. Chuang¹ “Experimental Study of Three Channel Designs with Model Comparison in a PEM Fuel Cell”.

Comprehensive Study of Phase Change Materials for Solar Thermal Energy Storage

Nimmani Venkata Narasimha Rao¹, N. Alagappan², CH V K N S N Moorthy^{3*}

¹Research Scholar, Department of Mechanical Engineering, Annamalai University, Annamalai Nagar, Chidambaram, Tamil Nadu, India

²Associate Professor, Department of Mechanical Engineering, Annamalai University, Annamalai Nagar, Chidambaram, Tamil Nadu, India

³Professor, Department of Mechanical Engineering, Vasavi College of Engineering, Ibrahimbagh, Hyderabad, Telangana State, India

*Corresponding Author: krishna.turbo@gmail.com

Abstract: The researchers have a clear focus on thermal energy storage (TES) employing phase change materials (PCMs). The increasing quantity of in-depth articles published in the last few years might be used as ornamentation for the significance in this research field. This extensive review explores the most recent research on phase change materials investigations and their use in thermal energy storage. Important academic articles on the features and uses of PCMs are offered. This article might be interesting in directing investigators toward a brief analysis of the state of PCM science and technology at the moment.

1. Introduction

In order to preserve SE (solar energy), which has gained impressive recognition as a natural resource and is predicted to become the most significant source of energy, provides a clean environment for the next generation. The planet can only contain a little proportion (1.7 X 10¹⁴ kilowatts) of the sun's entire output of 3.8 X 10²⁰ mega watts, or 63 Mega Watt/m² of its surface. The amount of a fragment that the earth can capture is thought to complement the solar radiation that will hit the planet in 30 minutes and will supply all the energy needed for a year. All forms and energy sources on the planet, such as wood, coal, natural gas, and oil created through the photorespiration process, are derived from the sun. SE (Solar energy) has the benefit over other sources of energy in that it is pure, safe for the environment, and would not cause poverty. The only drawback of solar energy is that large solar energy plants need more space and are only inconvenient around sunrise.

Solar energy has the benefit over other sources of energy in that it is pure, safe for the environment, and would not cause poverty. The only drawback of solar energy is that large solar energy plants need more space and are only inconvenient around sunrise. Therefore, utilizing sources of renewable energy is essential to ensure economic growth without destroying the environment. Due to their comprehensiveness, satisfaction, and effectiveness, more emphasis has been given to the STE (Thermal solar energy) applications. The issue of intermittent SE (Solar energy) can be resolved by a transferable system based on phase change material that links the total energy demand and supply aspects. A solid understanding of SSTE (Storage of Solar Thermal Energy), which generates a big amount of energy from a little amount of mass and volume of material is therefore crucial. Compared to STSHS (Systems for Traditionally Sensible Heat Storage), TLHS (Thermal Latent Heat Storage) systems offer additional benefits.

2. Phase Change Materials

Heat in the form of latent heat of fusion is both emitted and absorbed by the phase change materials during the phase-transition process. The temperatures at which this reversible process occurs are

nearly constant. LTS (Latent thermal storage) is an effective choice for energy storing because it can offer a storehouse with higher energy densities than sensible storage. Phase change materials come in a vast variety, making them suitable for a variety of applications.

2.1 Characteristics of Phase Change Materials

PCMs are used for storage of thermal energy operations, mostly for SE (solar energy) storage, and they have an amazing record of performance in energy-sustaining industries including the textile, culinary, biomedical, agro, and waste heat recovery industries. Through S-G (solid to gas), S-L (solid to liquid), L-S (liquid to solid), and L-G (liquid to gas) phase changes, a phase transition material can provide latent heat. Despite the fact that it is a powerful and practical system, the S-L (solid to liquid) phase transition system. L-G (Liquid to gas) phase transfers are not practical for use in Storage of thermal systems, despite the gas phase's large volume and the high intensity of the gases it can handle. Phase transitions from S-S (solid to solid) are undesirable because of their low and slow heat of conversion.

The following characteristics are used to identify phase transition materials for applications involving latent heat storage.

1. Thermal properties
2. Physical properties
3. Kinetic properties
4. Chemical Properties

Table 2.1: Phase Change Materials Characteristics

Thermal	Physical	Kinetic	Chemical
Optimum temperature for phase transformation. High energy's latent heat of fusion latent. Increased Thermal conductivity Both phases have a large heat capacity.	Good phase equilibrium Density high. Volume change small. Vapor pressure low. Counterpart melting.	Defection of super cooling. Excellent crystallization and nucleation rates	Consistent with container material Intermittent chemical cycling solidity Very non toxic, non explosive , and non flammable

2.2 Classifications of PCMs

There are different types of Phase Transition Materials (PCM/PTM) following chemical character as organic, inorganic, or eutectic based on their chemical makeup, or according to the phase transitions they go through, such as S-L (solid- to-liquid) PCMs, S-S (solid-to-solid) PCMs, and L-G (liquid-to-gas) PCMs below (Fig:1). The chemical makeup PCMs can be a) O (organic): paraffin-free or paraffin-containing substances such FA (fatty acids), E (esters), A (alcohols), EG (glycols), or PM (polymers), such as Poly ethylene glycol, b) IG (Inorganic) refers to metals and alloys, salt hydrates, or both. c) Inorganic to inorganic, organic to organic, and inorganic to organic mixed PCMs are necessary for eutectics. PCMs are used according to their operating temperature selection (-20°C - $+200^{\circ}\text{C}$ or above) (Fig: 1). According to the application, 4 distinct temperature ranges occur: range of low temperature (-20°C - $+5^{\circ}\text{C}$) to the extent that the PCMs are by and large utilized for business and homegrown refrigeration, moderate low-temperature range (5°C - 40°C) where the PCMs generally relate for applications for less warm (cooling) and warming in structures, the acceptable range of temperatures for boiling water, sun powered based warming and

hardware applications (40°C - 80°C) and range of high-temperature (80°C - 200°C or morethan) for squander heat recuperation, assimilation cooling, and power age.

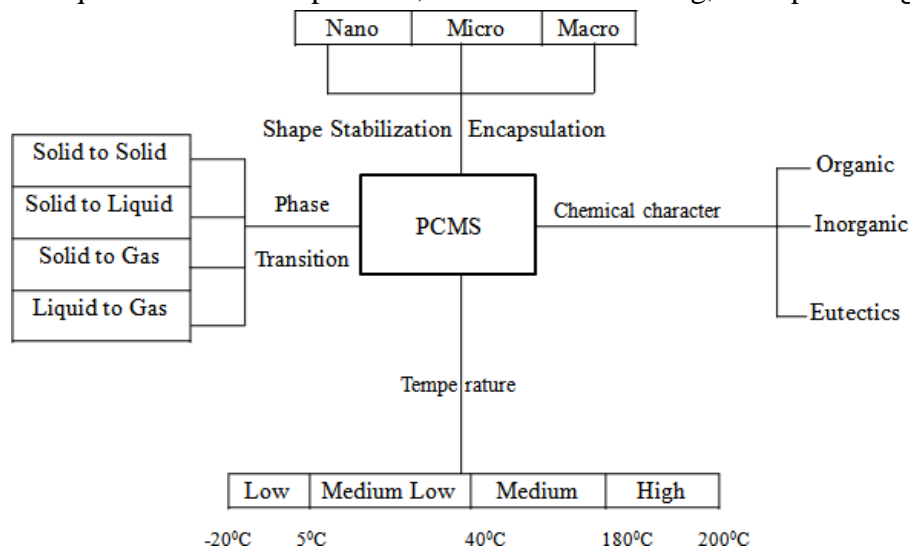


Fig: 1 Classification of Phase Change Materials

2.3 Applications of PCMs

- Solar cooling.
- Solar Power facilities.
- Solar stills.
- Solar water heaters.
- Solar dryers in agriculture industry.
- Solar dryers.
- Domestic refrigeration.
- Photovoltaic Power systems.
- Space industry.
- Systems for recovering waste heat .
- Food preservation.
- Pharmaceutical items.
- Home heating water.
- Latent heat thermal energy storage.

3. Thermal energy storage (TES)

Thermal energy storage systems can hold heat or cold to be used later, under varying conditions such as place, power or temperature. TES can also be used to heat and cool buildings rather of generating electricity. TES is consists in three types.

1. Sensible thermal storage
2. Latent thermal storage
3. Thermo chemical storage

1. Sensible thermal storage (STS): It is developed by controlling the temperature of the holding medium that could be ceramic, oil, or water. The amount of temperature that can be held depends on the material's specific thermal capacity. Here, temperature change & temperature have a linear connection. Today, the STS are commercialized in warm water retention on district heating networks, industrial water heaters, and residential water heaters. Low energy density and heat energy loss at any temperature are problems of STS.

2. Latent thermal storage (LTS): A phase change that occurs in a medium that is capable, precisely, and ideally, with a tiny temperature aperture, such as water, ice, paraffin or molten salt, is what LTS refers to as the response of heat transfer. S-L (Solid to liquid), L-G (liquid to gas), such as C (condensation) and E (evaporation), or S-S (solid to solid) modifications in CS (crystalline structure) are examples of phase transitions, and the choice of materials can influence the heat release or display. As a result, LTS has a high storage of energy density and is consequently far more effective than STS.

3. Thermo chemical storage (TCS): A resolvable chemical process involved in TCS's success. Energy stored is required for one type of reaction while being produced for another. Although It offers the greatest energy density of any any thermal energy storage technology, stability problems do occur. Additionally, the involved reactions do not maintain consistent efficiency over time without degrading. TCS is scarcity in-depth comprehension as little research effort is still being made.

4. Review of Literature

Charalambos N et al [1] studied the Phase change materials' properties, categories, and uses. As PCMs are make an appearance on several approaches as energy storage materials as well as requisition of our dwelling quarters and construction materials, the environment is important for maintaining our H (health) and S (safety) and should be strictly adhered to. If PCM TST (thermal storage temperatures) span may be applied year round, PCM big complex would be incredibly energy efficient. **Zahir khan et al [2]** examined the paraffins and salt hydrates thermophysical characteristics. In comparison to salt hydrates, paraffins exhibit better thermal and chemical stability. PCM melting in containers of various forms is caused by natural convection and conduction heat transmission. Geometric parameters relating to container attitude and PCM behavior, including the aspect ratio of rectangular and cylindrical containers, the radius of spherical capsules, and the eccentricity of the annular cavity. **Vikrant P et al [3]** thermodynamic and thermo economics analysis solar still with PCM was studied, paraffin wax as PCM used in passive solar still. Different types of solar stills are used like triangular pyramid, single slope solar still with corrugated absorber, single basin double slope, double basin double slope stepped solar still. The below table is Physical Properties of the organic PCM. The Paraffin wax has highest productivity and energy, exergy efficiency as 180%, 67.2% and 40% respectively.

Table 4.1: Physical properties of the organic PCM

PCM (Phase change materials)	MT (Melting temperature)	TC (Thermal conductivity)	HOF (Heat of fusion)	ρ (Density)	SPH (Specific heat)
A53	53 ⁰ C	0.22 w/m ⁰ c	130 kj/kg	910 kg/m ³	2.22 kj/kgk
A55	55 ⁰ C	0.22 w/m ⁰ c	135 kj/kg	905 kg/m ³	2.22 kj/kgk
A58	58 ⁰ C	0.22 w/m ⁰ c	130 kj/kg	910 kg/m ³	2.22 kj/kgk
A48	48 ⁰ C	0.18 w/m ⁰ c	234 kj/kg	810 kg/m ³	2.85 kj/kgk
A62	62 ⁰ C	0.22 w/m ⁰ c	145 kj/kg	910 kg/m ³	2.22 kj/kgk
A42	42 ⁰ C	0.21 w/m ⁰ c	105 kj/kg	905 kg/m ³	2.22 kj/kgk
A39	39 ⁰ C	0.22 w/m ⁰ c	105 kj/kg	900 kg/m ³	2.22 kj/kgk
A32	32 ⁰ C	0.21 w/m ⁰ c	130 kj/kg	900 kg/m ³	2.22 kj/kgk

Rishabh Chaturvedi et al [4] Sun-powered warming gadgets for water, box type sun based gatherer was utilized to fabricate and assess the result during the south and in the first part of the day to persuade the heated water requests and in natural stage, the structure was mathematically examined.

Karunesh Kant et al [5] encapsulating the PCM for thermal energy storage applications,

encapsulated PCM having different sizes like macro (above 1mm), micro (0-1000 mm) and nano (0-1000nm), different encapsulation PCM geometries (spherical, tubular, cylinder, rectangular) fig (a) and attributes of the PCM (TC (thermal conductivities), SPH (specific heat), LHF (latent heat of fusion)) were studied. **Zhangyuan Wang et al [6]** the solar water heating (SWH) systems apply PCM were inspecting two aspects i.e structural delineation and methodological analysis. As to the underlying outline, the consolidation of PCM with components of sun-oriented water warming (SWH) was inspected. For the particular component of heightened warm capacity, extensive works have been tracked down in the idle nuclear power stockpiling, and the joining of PCM with sunlight-based authority or different components of the sunlight-based water warming (SWH) framework barring the capacity can progress as the conceivable of PCM in Sun oriented water warming (SWH). Sun-oriented water warming (SWH) is energy saving and fossil fuel byproducts decrease universally. **Sara. Tahan Latibari et al [7]** PCM materials and methods for amplifying them using carbon-based materials deserving of the sun-oriented warm methodology have been executed. A wide assessment of warm and photograph-warm directing and pertinent expansion materials was addressed and the warm and sun-based warmproperties were contrasting. A few materials including dull materials like carbonaceous substances have been suggested to improve the sun-oriented and warm efficiencies of living PCMs. These materials include CNT (carbon nanotube), EC (enacted carbon), CNS (carbon nanosphere), CA (carbon aerogels), EGP (extended graphite), G (graphene), GO (graphene oxide), GA (graphene aerogel), and FG (graphite froth). **Zhaowen Huang et al [8]** Studied the T-history experiment, in this experiments different materials and T-type thermocouple were used depending upon the medium temperature. The materials are sugar alcohols, fatty acids, inorganic, sebacic acid and LiNO₃-KCl and also Using 2 PCM composites (LiNO₃-KCl/EG and SA/expanded graphite composite),. **Hongzhi Cui et al [9]** The accomplishment of a novel SATC(sodium acetate trihydrate composite) was due to the interdependent employment of NSD (nano Silicon dioxide)as the nucleating agent, SC (silicon carbide) foam as the TC (thermal conductivity) strengthener, and CNT (carbon nano tubes) as the photo - thermal reinforcer. Different sodium acetate trihydrate (SAT) composite materials (like SAT-1/4NS, SAT-1/2NS, SAT-1NS and SAT-2NS) were used in photothermal. **Vladimir Pozdin et al [10]** Two PCM TTA (Tritriacontane) and ETT (Erythritol) with 720°C and 1180°C melting points, respectively, are used with the solar collector's evacuated tube. The Table shows different PCM materials with melting temperatures and latent heat. Dual-PCM solar water heaters provide an impressive increase in efficiency when compared for both normal and stagnation operation.

Table 4.2: Materials with phase changes and high temperatures

S (Substance)	LH (Latent heat)	MT (Melting temperature)
Urea	170-258 kj/kg	133-135 ⁰ c
P-toluic acid	167 kj/kg	180 ⁰ c
Azelaic acid	228 kj/kg	130-134 ⁰ c
Pentaerythritol	287-298 kj/kg	186-187 ⁰ c
Erythritol	332-340 kj/kg	119 ⁰ c
Octadecanamide	211 kj/kg	106 ⁰ c
Dimethyl terephthalate	170 kj/kg	170 ⁰ c

Mauricio Carmona et al [11] PCM vessels are fitted in the rear of a typical PV module in the researched PVT-PCM (Photovoltaic thermal-Phase change materials) collector, which uses a similar design as a base for manufacture. The solar system's electrical conducting variables are all continuously monitored by the Maximum power point tracking charge controller. Convenient heat from the PVT-PCM module is a technique of thermal energy recuperation that is also included.

Niloufar Fadaei et al [12] In a solar chimney power plant (SCPP), the effect of latent heat storage on a test sample of a solar chimney was studied. In SCPP, paraffin wax was utilised as a PCM with a 1.5 m collector radius and a 3 m chimney height. The petroleum wax used in the collector of the setup an latent heat storage system raise the thermal efficiency (TE)of the solar collector. When there is no sunlight due to phase transition from liquid to solid, the latent heat(LH) is released, and as air moves through the setup at a higher velocity, the mass flow rate increases, releasing the latent heat and increasing the setup's latent heat. **Safi Mohamed et al [13]** Slat hydrate PCMs was used in the experimental investigation on heat characteristics of a micro SGSP (salinity-gradient solar pond) exposure a simulator solar pond. In this paper having two models of experiments were used model 1 using a rectangular Plexiglas tank and insulated material is Styrofoam or extracted polystyrene foam and solar simulator and SGSP prototype fluids were water and NaCl solution, model 2 using two plastic cylindrical, insulated material is glass wool and solar simulator and SGSP prototype with PCM and without PCM fluids were Glabuers salt ($\text{Na}_2\text{SO}_4, 10\text{H}_2$). It was determined that the maximum median temperature in the second model for the solar pond with and without PCM was greater. **Ning Wang et al [14]** the solar photovoltaic system incorporates with phase change material (like fatty acids). Temperature contrast comparisons of the photovoltaic panel with respect to time between the photovoltaic and T-PCM/PV systems during the 4-day investigation period. The external climate has an influence on temperature variance, which could increase PV panel photoelectric efficiency. **Han li et al [15]** Compound allegorical concentrators and phase change materials in PV/W (photovoltaic/warm) frameworks are fruitful methods to simultaneously foster electrical and warm impacts. The outside investigation of T-CPCM/PV is aimed between November 4, 2020, and November 24, 2020 in Tianjin, China (117.130-East, 39.220-North). Estimate the Photovoltaic unit's thermal inconsistency as a result of the concentrating arrangement's detrimental impact on temperature scattering and power generation conducting due to the irregular heat flow. The T-PCM/Photovoltaic plan's best essential energy efficiency is roughly 7.9% greater than that of the PV-PVC course of action and 10.7% greater than that ofthe PT-PCM course of action. **Duje Coko et al [16]** concentrated on the different photovoltaic warm (PVT) sun-oriented authority drafts that incorporate stage change materials as acceptable materials for heat activity and various properties relying on the stage change materials. Photovoltaic thermal-Phase change materials (PVT-PCM) collector plan and utilized coolant (water, nano, air), the electrical directing of the Photovoltaic thermal- Phase change materials (PVT-PCM) authority is by and large under 20%, while improvementin warm exhibitions goes generally from 40% to 70%.

Table 4.3: Physical properties of the primary PCM materials utilized in PVT-PCM collector

TC (Thermal conductivity)	LH (Latent heat)	SPH (Specific heat)	MT (Melting temperature)
0.19-0.24 w/mk	160-250 kj/kg	1.7-2.9 kj/kg	22-60 °C

Table 4.4 : PCMs in PV

PCM (Phase change materials)	LH (Latent heat)	MT (Melting temperature)	TC (Thermal conductivity)	SPH (Specific heat)
RT25HC	210 kj/kg	22-26 °c	0.2 w/mk	2 kj/kg
Paraffin Wax	2120kj/kg	57 °c	0.24 w/mk	2.1 kj/kg
Merck107158 (Paraffin)	220 kj/kg	57-60 °c	0.24 w/mk	2.9 kj/kg
Paraffin wax (Merck 107151)	244 kj/kg	46-48 °c	0.24 w/mk	2.9 kj/kg
PLUSICE S25	180 kj/kg	25 °c	0.54 w/mk	2.2 kj/kg

S21	170 kj/kg	23 °c	0.234 w/mk	2.2 kj/kg
RT-35HC	240 kj/kg	32-36 °c	0.2 w/mk	2 kj/kg
PCM 32/280	186 kj/kg	32 °c	0.4 w/mk	--
RT28HC	250 kj/kg	27-29 °c	0.2 w/mk	2 kj/kg
A44	242 kj/kg	44 °c	0.18 w/mk	2.15 kj/kg
RT35HC	240 kj/kg	35 °c	0.166 w/mk	2.1 kj/kg
RT50	160 kj/kg	50 °c	0.2 w/mk	2 kj/kg
OCTADECANE	244 kj/kg	28 °c	0.21 w/mk	1.9 kj/kg
RT44	168 kj/kg	41-44 °c	0.2 w/mk	2 kj/kg
LAURIC ACID	228 kj/kg	24-46 °c	0.19 w/mk	1.7 kj/kg

S. Harikrishnan et al [17] thermal performance of recently produced NEPCM (Nano-enhanced phase change material), comprise Silicon dioxide (SiO₂) NPs (nanoparticles) in mystric acid. Silicon dioxide (SiO₂) NPs (nanoparticles) with Mystric acid was prorogue in weight proportions of 1, 0.8, 0.5 and 0.2 wt%, which supply as the base in separate materials for phase change. Examination of the melting and solidification of organized Nano-enhanced phase change materials (NEPCMs) using a warming and refrigeration device. The fluid used to transport heat ranged in temperature from 200°C to 800°C and was water. Because of its acceptable thermal reliability, better TC (Thermal conductivity), and intensified heat transfer rate, nano-enhanced phase change material (NEPCM) is seen as a promising choice to implement solar energy for low-temperature heating. **Hussein A. Mohammed et al [18]** the reasonableness of PCMs for upgrading the cooking execution and warm factors of the sun-oriented cooker less time spent cooking in further evaluation of the likelihood of nighttime cooking the impact of the intensity move liquids and the comparability of the embodiment materials are additionally included. There are various kinds of sun-oriented cookers like box, concentrating, level plate gatherer, cleared tube authority, and allegorical gatherer were examined. Late-evening cooking is achievable by including PCM stockpiling frameworks in a sun-oriented cooker. Because the PCM absorbs some of the solar radiation needed for daylight cooking and late evening cooking with PCM stockpiling does not affect early afternoon cooking, late evening cooking with the PCM compartment is faster than early afternoon cooking. **Emin El et al [19]** studied the heat storage using latent heat method in a flat plate solar collector free circulation container. CaCl₂·6H₂O serves as a material that changes phases in this LH (latent heat) method because to its low phase change temperature. The melting point of calcium chloride hexahydrate is 28-35°C. From July to November, experiments were run by attaching a regular tank and a tank with a PCM to a free-convection flat-plate solar concentrator, the evaluation were continuously taken every 30 minutes. **Pavel Charvat et al [20]** using experimental observations and computational models, the possibility of utilising latent heat (LH) of fusion in phase change materials for TES in air-based solar thermal (ST) systems was examined. The analysis made use of a thermal container unit including 100 aluminium panels that were each filled with a paraffin-based PCM. Electric air heaters were used as the heat source during the measurements, which were performed in a lab setting.

5. Conclusions

The evolving matter of energy effective is improving the investigation performance throughout the last years in the field of PCMs. Numerous articles addressing various PCM properties and applicability by structure stability. Phase change materials by engineering substances still need to

be resolved before improving LHTS (latent heat thermal storage) technologies and stimulating application functionality.

Even while engineering polymers that have an impact on the markets are widely used as market items in combination with other natural Phase change materials, and they are still ripe for development in this regard. According to the studies done thus far, careful use is highly recommended. More research is required to find suitable material-specific solutions, especially when PCM operating temperatures (Fig. 1) are excessively low, high, or very low.

The development of PCMs' environmental characteristics through the evolution of natural, sustainable, recyclable, and secure PCMs that are not derived from fossil energy is, in the end, another aspect that will be of interest in the future. Health, Safety, Environmental concerns are climbing to the top of the priority list, and they should succeed in our residences and other constructions just as PCMs are expanding into new uses as storage materials for energy.

Material science seems to be under pressure to propose characteristics and capabilities that will progress PCM research and viability due to the demand for better and more efficient PCMs. Future PCM base storage of thermal energy and engineering treatments will progress toward a clean renewable energy future as a result of the rapid advancement in material science.

References

- [1] Charalambos N. Elias, Vassilis N. Stathopoulos A comprehensive review of recent advances in materials aspects of phase change materials in thermal energy storage *Energy Procedia* 161 (2019) 385–394.
- [2] Zakir Khan, Zulfiqar Khan , Abdul Ghafoor A review of performance enhancement of PCM based latent heat storage system within the context of materials, thermal stability and compatibility *Energy Conversion and Management* 115(2016) 132-158.
- [3] Vikrant P. Katekar, Sandip S. Deshmukh A review of the use of phase change materials on performance of solar stills *Journal of energy storage* 30 (2020) 101-398.
- [4] Rishabh Chaturvedi, Anas Islam, Kamal Sharma A review on the applications of PCM in thermal storage of solar energy material today *proceedings* 43 (2021) 293–297.
- [5] Karunesh Kant, A. Shukla, Atul Sharma Advancement in phase change materials for thermal energy storage applications *Solar Energy Materials and Solar Cells* <http://dx.doi.org/10.1016/j.solmat.2017.07.023>.
- [6] Zhangyuan Wang, Feng Qiu, Wansheng Yang, Xudong Zhao Applications of solar water heating system with phase change material *Renewable and sustainable energy reviews* <http://dx.doi.org/10.1016/j.rser.2015.07.1847>.
- [7] Sara. Tahan Latibari, Seyed Mojtaba Sadrameli Carbon based material included-shaped stabilized phase change materials for sunlight-driven energy conversion and storage *solar energy* <https://doi.org/10.1016/j.solener.2018.05.007>.
- [8] Zhaowen Huang, Ning Xie, Zigeng Luo, Xuenong Gao , Xiaoming Fang, Yutang Fang, Zhengguo Zhang Characterization of medium-temperature phase change materials for solar thermal energy storage using temperature history method *solar energy materials and Solar cells* 179 (2018) 152-160.
- [9] Hongzhi Cui, Pizhuang Wang , Haibin Yang, Waiching Tang Enhancing the heat transfer and photothermal conversion of salt hydrate phase change material for efficient solar energy utilization *Journal energy storage* <https://doi.org/10.1016/j.est.2022.104130>.
- [10] Alexios Papadimitratos , Sarvenaz Sobhansarbandi , Vladimir Pozdin ,Anvar Zakhidov , Fatemeh Hassanipour Evacuated tube solar collectors integrated with phase change materials *Solar Energy* <http://dx.doi.org/10.1016/j.solener.2015.12.040>.
- [11] Mauricio Carmona, Alberto Palacio Bastos, Jose Doria Garcia Experimental evaluation of a hybrid photovoltaic and thermal solar energy collector with integrated phase change material (PVT-PCM) in comparison with a traditional photovoltaic (PV) module *Renewable energy* <https://doi.org/10.1016/j.renene.2021.03.022>.
- [12] Niloufar Fadaei, Alibakhsh Kasaeian, Aliakbar Akbarzadeh, Seyed Hassan Hashemabadi Experimental investigation of solar chimney with phase change material (PCM) *Renewable energy* <https://doi.org/10.1016/j.renene.2018.01.12>.

- [13] Mahfoudh Ines, Principi Paolo, Fioretti Roberto, Safi Mohamed Experimental studies on the effect of using phase change material in a salinity-gradient solar pond under a solar simulator Solar energy 186 (2019) 335-346.
- [14] Hongtao Xu, Chenyu Zhang, Ning Wang, Zhiguo Qu, Shuanyang Zhang Experimental study on the performance of a solar photovoltaic/thermal system combined with phase change material Solar energy 198 (2020) 202-211.
- [15] Xiangfei Kong, Lanlan Zhang, Han Li, Yongzhen Wang, Man Fan Experimental thermal and electrical performance analysis of a concentrating photovoltaic/thermal system integrated with phase change material (PV/T-CPCM) Renewable energy <https://doi.org/10.1016/j.renene.2018.01.122>.
- [16] Sandro Nizetic, Miso Jurcevic, Duje Coko, Müslüm Arıcı, Anh Tuan Hoang Implementation of phase change materials for thermal regulation of photovoltaic thermal systems: Comprehensive analysis of design approaches Energy 228 (2021) 120546.
- [17] S. Harikrishnan, S. Imran Hussain, A. Devaraju, P. Sivasamy and S. Kalaiselvam Improved performance of a newly prepared nano-enhanced phase change material for solar energy storage Journal of Mechanical Science and Technology 31 (10) (2017) 4903~4910 DOI 10.1007/s12206-017-0938-y.
- [18] Adil A.M. Omar, Abuelnuor A.A. Abuelnuor, Hussein A. Mohammed, Daryoush Habibi, Obai Younis Improving solar cooker performance using phase change materials Solar energy <https://doi.org/10.1016/j.solener.2020.07.015>.
- [19] Sinem Kilickap, Emin El, Cengiz Yıldız Investigation of the effect on the efficiency of phase change material placed in solar collector tank Thermal science and energy process <http://dx.doi.org/10.1016/j.tsep.2017.10.016>.
- [20] Pavel Charvat, Lubomír Klimes, Milan Ostry Numerical and experimental investigation of a PCM-based thermal storage unit for solar air systems Energy and buildings <http://dx.doi.org/10.1016/j.enbuild.2013.10.01>.

Analysis of Welded Structure in Finite Element Method

CH.Mahesh¹, D.Sai Charan¹, Abdul Sattar¹, E.Rupesh Tarun¹, CH. Mohan Sumanth², Dr. P. Phani Prasanthi³

¹UG students, Department of Mechanical Engineering, Prasad V Potluri Siddhartha Institute of Technology, Kanuru, Vijayawada, Andhra Pradesh, India.

²Assistant Professor, Department of Mechanical Engineering, Prasad V Potluri Siddhartha Institute of Technology, Kanuru, Vijayawada, Andhra Pradesh, India.

³Associate Professor, Department of Mechanical Engineering, Prasad V Potluri Siddhartha Institute of Technology, Kanuru, Vijayawada, Andhra Pradesh, India.

Abstract: The present work deals with the analysis of simple welded structure using finite element method. In this context both thermal analysis and structural analysis of welded structure done by using aluminum, stainless steel, and copper materials. By using the above materials for welded structure at different levels of temperatures were considered to analyses the temperature distribution, temperature gradient, total heat flux under thermal analysis. In the same context by using the above specified materials for welded structure at different levels of temperatures were considered to obtain the stress and shear stress in XY, YZ, ZX planes and displacement of the plate under the structural analysis.

Keywords: Temperature, temperature gradient, total heat flux, stress, shear stress, displacement.

Introduction

Welding has to come to be one of the most standard becoming a member of techniques used with in the structural field because the several benefits it offers in terms of layout flexibility ,prices and weight financial savings. In making of structures without limits on the thickness of the jointed components and in improving the structural performance.[1]

Despite of advantages, throughout welding procedure residual stresses and distortions are brought on because of localised heating and the fallowing non-uniform cooling, as extensively define in the books with aid of Gunnert [2] and Connor [3].

Especially, residual stresses are caused by non-homogenous strains characterized with the aid of a change in extent or in form due to thermal expansions.

Residual stresses are nearly constantly un wanted because they, blended with in-service loading conditions, have a negative effect on the structural performance, causing several troubles in welded structures, reduction of quality and realibility,assembly problems, reduction of the component fatigue life(in case of tensile stresses) and reduction of buckling resistance(in case of compressive stresses). For example,Barsoum and Barsoum[4] investigated at the residual stresses distribution in both butt and t-fillet weld joints with the aid of using of a FE model, based totally on 2nd finite factors after which they implemented a recurring to expect the crack propagation below fatigue loading situation, with the LEFM concept. Zhigang et al [5] worked on the analysing the transient thermal behavior by developing the 2D axisymmetric FE model.

In T-type and double V-butt welded joints, made with the stainless steel, for this by using the nondestructive neutron diffraction technique. Residual stresses in the model was analysed by the Park et al [6].Numerous FE modelling techniques have been compared with aid of Mollicone et al.[7] to analyse on the impact of different methods of prediction functionality of the thermo-mechanical simulations.

Bhatti et al[8] investigated the have an impact on of thermo-mechanical fabric residences of different metallic grades on welding residual stresses and angular distortion in T-fillet joints, for the evaluation of residual stresses, all thermo-mechanical properties may be assumed as

consistent with the temperature, besides the yield pressure. Formerly, in a similar way, Zhu and chao[9] established that, for the aluminum, the thermo-mechanical homes can be considered steady in welding simulations, except for the yield stress that must be considered as temperature –structured. Liu et al [10] finished an intensive parametric study with the intention to look at the welding brought on residual stresses in welded h-sections of different metal grades, through knowing and calibrating an efficient FE version to carry out coupled thermo mechanical analyses.

From the above studies, some authors focused on the residual stress in structures and some authors focused on the thermal parameters. Present work was more focused on the thermal analysis of welded structure (plate) by performing temperature distribution, total heat flux and temperature gradient analysis. And in structural analysis by conducting stresses induced, shear stress in different orientations, displacement of the plate under different levels of temperature.

Problem statement and methodology

A welded structure with different materials such as aluminum, stainless steel, and copper materials are studied at different levels of temperature to estimate the temperature, temperature gradient, total heat flux under the thermal analysis. And under structural analysis of same parameters are used to determine the stress and shear stress in different planes and also displacement of the plate. Using finite element based method, the above mentioned parameters are estimated.

In this total analysis to obtain the different levels of temperature, melting temperature of different materials as taken as a reference temperature such as stainless steel-1540°C, aluminium-660°C, copper-1085°C.

Geometry:

A welded plate with 200mm length, 100mm width, 3mm thickness with V Butt joint at angle of 60 ° and width of welded portion at bottom side as 0.87 mm, top side as 1.73mm is created as shown in the figure. To obtain the different results different levels of temperature was imposed on this welded portion of the plate(Fig:1).

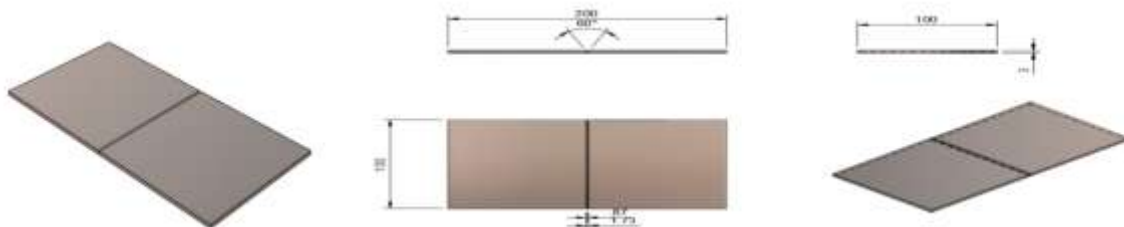


Fig:1 Finite element model of welded plate with v butt joint.

Materials considering for the analysis are aluminum, stainless steel, copper.

ALUMINUM	
Density	2.7E+06Kg/mm ³
Young's modulus	68.9Gpa
Poisson's Ratio	0.33
Yield strength	275Mpa
Ultimate Tensile Strength	310Mpa
Thermal Conductivity	0.23W/(mm C)
Thermal Expansion Coefficient	2.36E+05/C
Specific Heat	897J/(Kg C)

STAINLESS STEEL	
Density	8E+06Kg/mm ³
Young's modulus	193Gpa

Poisson's Ratio	0.3
Yield strength	250Mpa
Ultimate Tensile Strength	540Mpa
Thermal Conductivity	0.0162W/(mm C)
Thermal Expansion Coefficient	1.04E+05/C
Specific Heat	477J/(Kg C)

COPPER	
Density	8.94E+06Kg/mm ³
Young's modulus	117.5Gpa
Poisson's Ratio	0.345
Yield strength	33.3Mpa
Ultimate Tensile Strength	210Mpa
Thermal Conductivity	0.401W/(mm C)
Thermal Expansion Coefficient	1.67E+05/C
Specific Heat	450J/(Kg C)

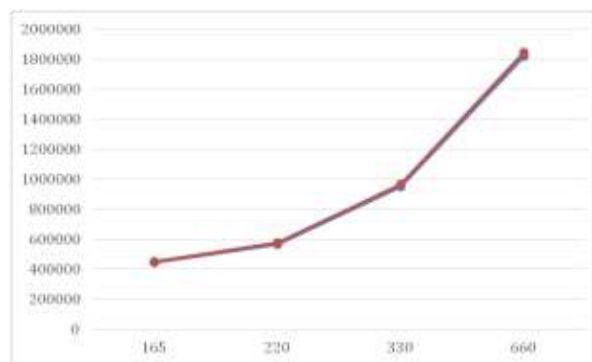
Results and Discussions

Thermal Analysis

Whenever a plate subjected to a welding there will be change in its properties due to convection process of heat to the plate. By using the thermal analysis, temperature distribution, and temperature gradient, total heat flux of a particular welded plate was obtained. The thermal analysis is performed on welded plate which is having V-butt at middle of the plate which was made up of three different materials mainly aluminum, stainless steel, copper under different levels of temperature. The temperature distribution, temperature gradient, total heat flux is estimated from the finite element results.

1. Temperature distribution (°C)

Aluminum:



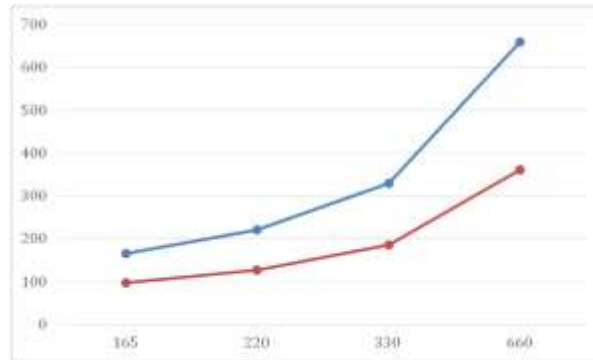
Using thermal analysis, a welded plate was analysed for the aluminium, at a temperature of 660°C, temperature distribution in that plate was obtained. In site maximum temperature was recorded at the V-butt portion with 660°C. And minimum temperature was recorded at the ends of plate with 361.2°C.

At a temperature of 330°C, temperature distribution in that plate was obtained. In site maximum temperature was recorded at the V-butt portion with 330°C. And minimum temperature was recorded at the ends of plate with 185.2°C.

At a temperature of 220°C, temperature distribution in that plate was obtained. In site maximum temperature was recorded at the V-butt portion with 220°C. And minimum temperature was recorded at the ends of plate with 126.6°C.

At a temperature of 165°C, temperature distribution in that plate was obtained. In site maximum temperature was recorded at the V-butt portion with 165°C. And minimum temperature was recorded at the ends of plate with 97.27°C.

Stainless steel:



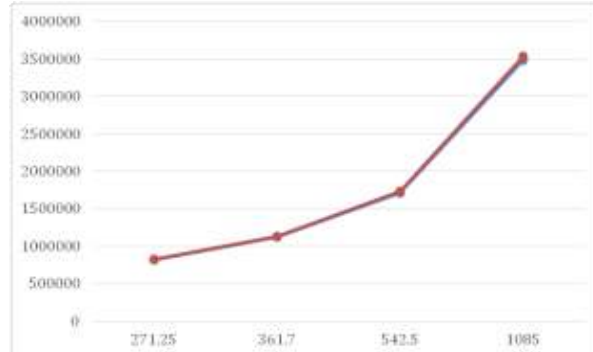
Using thermal analysis, a welded plate was analysed for the stainless steel, at a temperature of 1540°C. temperature distribution in that plate was obtained. In site maximum temperature was recorded at the V-butt portion with 1540°C. And minimum temperature was recorded at the ends of plate with 215.9°C.

At a temperature of 770°C. temperature distribution in that plate was obtained. In site maximum temperature was recorded at the V-butt portion with 770°C. And minimum temperature was recorded at the ends of plate with 116.7°C.

At a temperature of 513.33°C. temperature distribution in that plate was obtained. In site maximum temperature was recorded at the V-butt portion with 513.33°C. And minimum temperature was recorded at the ends of plate with 83.59°C.

At a temperature of 385°C. temperature distribution in that plate was obtained. In site maximum temperature was recorded at the V-butt portion with 385°C. And minimum temperature was recorded at the ends of plate with 67.05°C.

Copper:



Using thermal analysis, a welded plate was analysed for the copper, at a temperature of 1085°C. temperature distribution in that plate was obtained. In site maximum temperature was recorded at the V-butt portion with 1085°C. And minimum temperature was recorded at the ends of plate with 741.7°C.

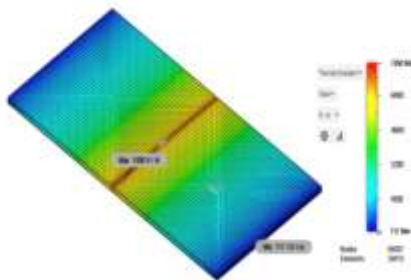
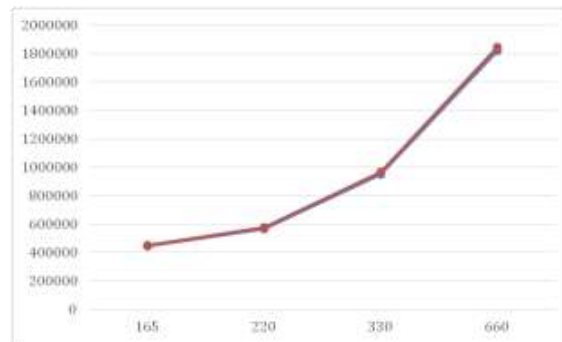
At a temperature of 542.5°C. temperature distribution in that plate was obtained. In site maximum temperature was recorded at the V-butt portion with 542.5°C. And minimum temperature was recorded at the ends of plate with 374.1°C.

At a temperature of 361.66°C. temperature distribution in that plate was obtained. In site maximum temperature was recorded at the V-butt portion with 316.66°C. And minimum temperature was recorded at the ends of plate with 251.5°C.

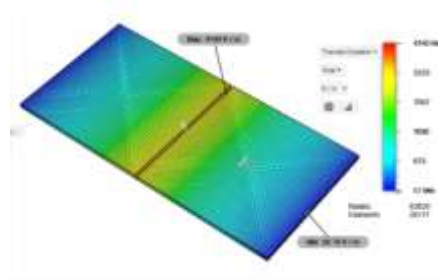
At a temperature of 271.25°C. temperature distribution in that plate was obtained. In site maximum temperature was recorded at the V-butt portion with 385°C. And minimum temperature was recorded at the ends of plate with 190.3°C.

2. Temperature gradient (K/m)

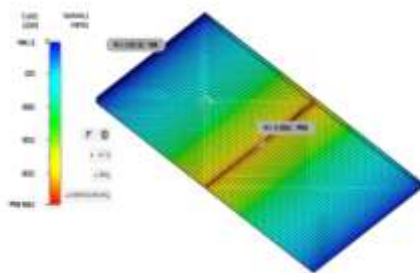
Aluminium :



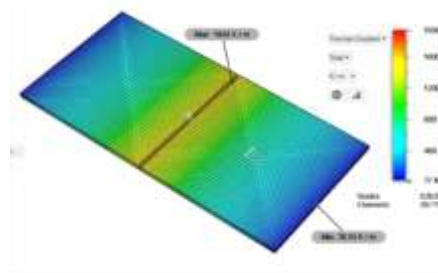
(a)



(b)



(c)



(d)

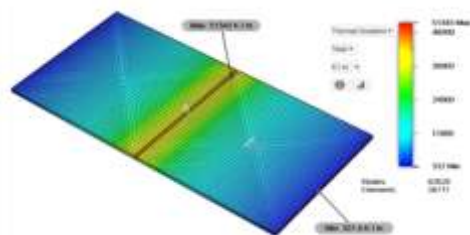
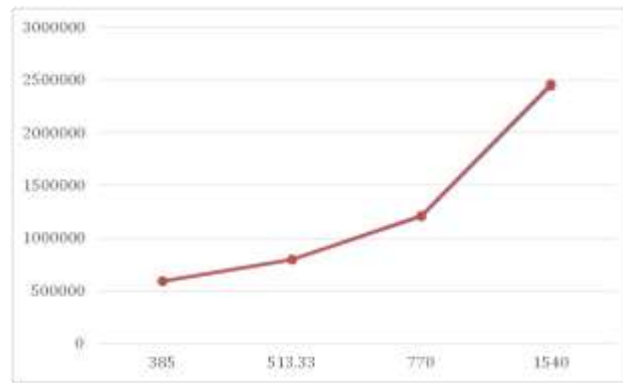
Aluminium welded plates (a) Temperature at 660°C, (b) Temperature at 330°C, Temperature at 220°C, (d) Temperature at 165°C

Using thermal analysis, a welded plate was analysed for the aluminium, at a temperature of 660°C. temperature gradient in that plate was obtained. In site maximum temperature gradient was recorded at the V-butt portion with 7890K/m. And minium temperature gradient was recorded at the ends of plate with 117.1K/m.

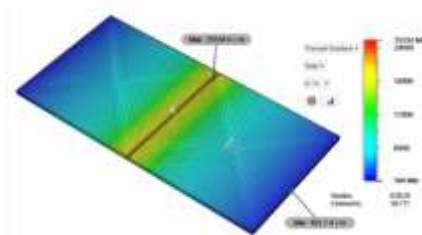
Using thermal analysis, a welded plate was analysed for the aluminium, at a temperature of 330°C. temperature gradient in that plate was obtained. In site maximum temperature gradient was recorded at the V-butt portion with 4140K/m. And minium temperature gradient was recorded at the ends of plate with 56.76K/m.

Using thermal analysis, a welded plate was analysed for the aluminium, at a temperature of 660°C. temperature gradient in that plate was obtained. In site maximum temperature gradient was recorded at the V-butt portion with 2466K/m. And minium temperature gradient was recorded at the ends of plate with 36.58K/m.

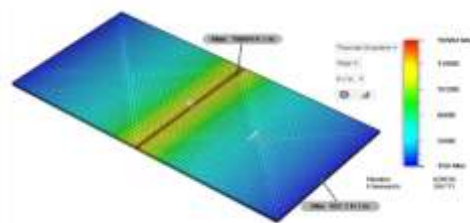
Using thermal analysis, a welded plate was analysed for the aluminium, at a temperature of 660°C. temperature gradient in that plate was obtained. In site maximum temperature gradient was recorded at the V-butt portion with 1936K/m. And minium temperature gradient was recorded at the ends of plate with 26.55K/m.



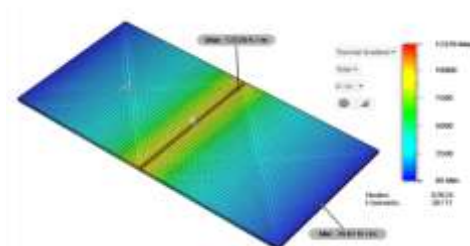
(a)



(b)



(c)



(d)

Stainless steel welded plates (a) Temperature at 1540°C, (b) Temperature at 770°C, Temperature at 513.33°C, (d) Temperature at 385°C

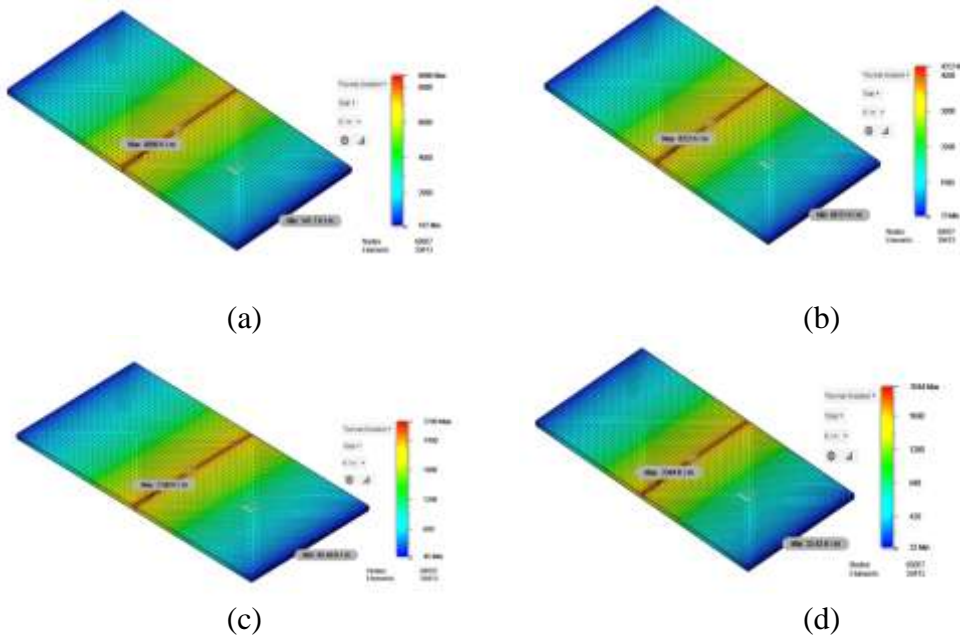
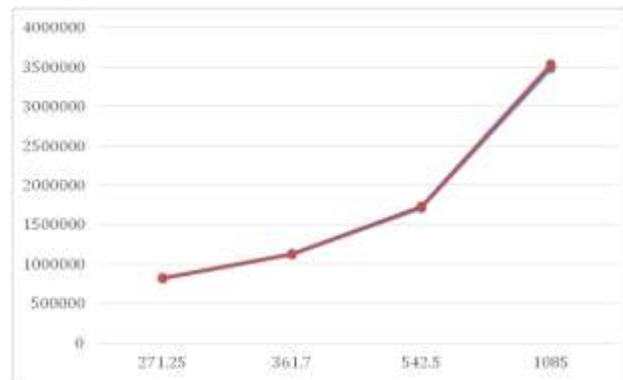
Using thermal analysis, a welded plate was analysed for the stainless steel, at a temperature of 1540°C. temperature gradient in that plate was obtained. In site maximum temperature gradient was recorded at the V-butt portion with 51343K/m. And minium temperature gradient was recorded at the ends of plate with 331.8K/m.

Using thermal analysis, a welded plate was analysed for the stainless steel, at a temperature of 770°C. temperature gradient in that plate was obtained. In site maximum temperature gradient was recorded at the V-butt portion with 25334K/m. And minium temperature gradient was recorded at the ends of plate with 163.7K/m.

Using thermal analysis, a welded plate was analysed for the stainless steel, at a temperature of 513.33°C. temperature gradient in that plate was obtained. In site maximum temperature gradient was recorded at the V-butt portion with 16664K/m. And minium temperature gradient was recorded at the ends of plate with 107.7K/m.

Using thermal analysis, a welded plate was analysed for the stainless steel, at a temperature of 385°C. temperature gradient in that plate was obtained. In site maximum temperature gradient was recorded at the V-butt portion with 12329K/m. And minium temperature gradient was recorded at the ends of plate with 79.67K/m.

Copper:



Copper welded plates (a) Temperature at 1085°C, (b) Temperature at 542.5°C, Temperature at 361.66°C, (d) Temperature at 271.25°C

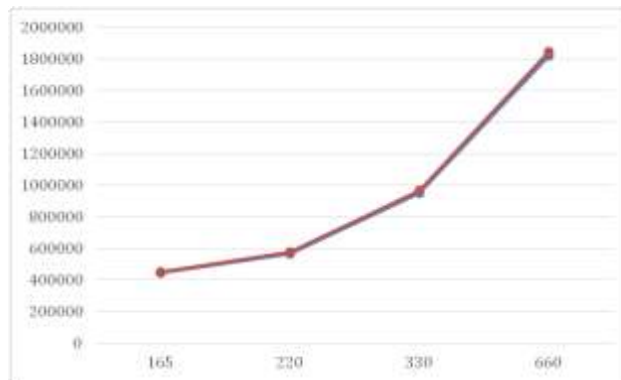
Using thermal analysis, a welded plate was analysed for the copper, at a temperature of 1085°C. temperature gradient in that plate was obtained. In site maximum temperature gradient was recorded at the V-butt portion with 8666K/m. And minium temperature gradient was recorded at the ends of plate with 141.7K/m.

Using thermal analysis, a welded plate was analysed for the copper, at a temperature of 542.5°C. temperature gradient in that plate was obtained. In site maximum temperature gradient was recorded at the V-butt portion with 4252K/m. And minium temperature gradient was recorded at the ends of plate with 69.51K/m.

Using thermal analysis, a welded plate was analysed for the copper, at a temperature of 361.66°C. temperature gradient in that plate was obtained. In site maximum temperature gradient was recorded at the V-butt portion with 2780K/m. And minium temperature gradient was recorded at the ends of plate with 45.46K/m.

Using thermal analysis, a welded plate was analysed for the copper, at a temperature of 361.66°C. temperature gradient in that plate was obtained. In site maximum temperature gradient was recorded at the V-butt portion with 2780K/m. And minium temperature gradient was recorded at the ends of plate with 45.46K/m.

3.Total heat flux(W/m²)



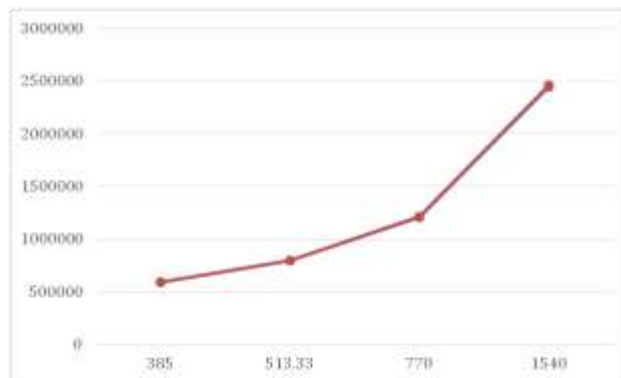
Using thermal analysis, a welded plate was analysed for the aluminium, at a temperature of 660°C. total heat flux in that plate was obtained. In site maximum total heat flux was recorded at the V-butt portion with $1.82E+06$ W/m². And minium total heat flux was recorded at the ends of plate with 26924W/m².

Using thermal analysis, a welded plate was analysed for the aluminium, at a temperature of 330°C. total heat flux in that plate was obtained. In site maximum total heat flux was recorded at the V-butt portion with 952217 W/m². And minium total heat flux was recorded at the ends of plate with 13054W/m².

Using thermal analysis, a welded plate was analysed for the aluminium, at a temperature of 220°C. total heat flux in that plate was obtained. In site maximum total heat flux was recorded at the V-butt portion with 567129 W/m². And minium total heat flux was recorded at the ends of plate with 8414W/m².

Using thermal analysis, a welded plate was analysed for the aluminium, at a temperature of 165°C. total heat flux in that plate was obtained. In site maximum total heat flux was recorded at the V-butt portion with 445392 W/m². And minium total heat flux was recorded at the ends of plate with 6106W/m².

Stainless steel:



Using thermal analysis, a welded plate was analysed for the Stainless steel, at a temperature of 1540°C. total heat flux in that plate was obtained. In site maximum total heat flux was recorded at the V-butt portion with $2.44E+06$ W/m². And minium total heat flux was recorded at the ends of plate with 15791W/m².

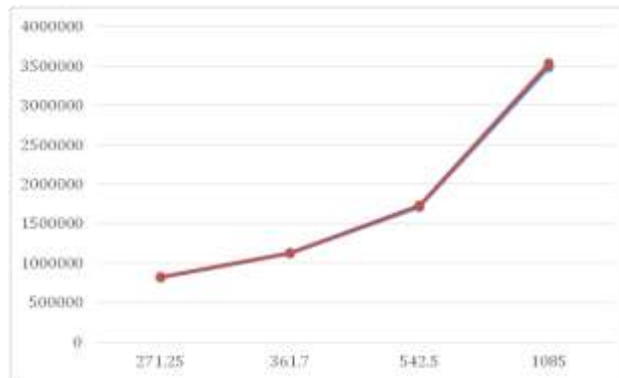
Using thermal analysis, a welded plate was analysed for the Stainless steel, at a temperature of 770°C. total heat flux in that plate was obtained. In site maximum total heat flux was recorded at the V-butt portion with $1.21E+06$ W/m². And minium total heat flux was recorded at the ends of plate with 7792W/m².

Using thermal analysis, a welded plate was analysed for the Stainless steel, at a temperature of 513.33°C. total heat flux in that plate was obtained. In site maximum total heat flux was recorded at the V-butt portion with 793204 W/m². And minium total heat flux was recorded at the ends of plate with 5125W/m².

Using thermal analysis, a welded plate was analysed for the Stainless steel, at a temperature of 385°C. total heat flux in that plate was obtained. In site maximum total heat flux was recorded at the V-butt portion with 586864 W/m². And minium total heat flux was recorded

at the ends of plate with 3792W/m^2 .

Copper:



Using thermal analysis, a welded plate was analysed for the Copper, at a temperature of 1085°C . total heat flux in that plate was obtained. In site maximum total heat flux was recorded at the V-butt portion with $3.48\text{E}+06\text{ W/m}^2$. And minium total heat flux was recorded at the ends of plate with 56818W/m^2 .

Using thermal analysis, a welded plate was analysed for the Copper, at a temperature of 542.5°C . total heat flux in that plate was obtained. In site maximum total heat flux was recorded at the V-butt portion with $1.71\text{E}+06\text{W/m}^2$. And minium total heat flux was recorded at the ends of plate with 27875W/m^2 .

Using thermal analysis, a welded plate was analysed for the Copper ,at a temperature of 361.66°C . total heat flux in that plate was obtained. In site maximum total heat flux was recorded at the V-butt portion with $1.12\text{E}+06\text{W/m}^2$. And minium total heat flux was recorded at the ends of plate with 18228W/m^2 .

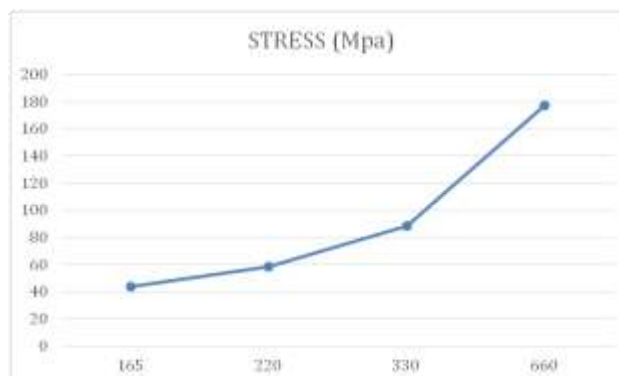
Using thermal analysis, a welded plate was analysed for the Copper ,at a temperature of 271.25°C . total heat flux in that plate was obtained. In site maximum total heat flux was recorded at the V-butt portion with 819818W/m^2 . And minium total heat flux was recorded at the ends of plate with 13404W/m^2 .

Structural Analysis

Whenever a plate subjected to a welding there will be change in its properties due to convection process of heat to the plate. By using the structural analysis, stress induced, shear stress in XY, YZ, ZX plane and displacement of a particular welded plate was obtained. The structural analysis is performed on welded plate which is having V-butt at middle of the plate which was made up of three different materials mainly aluminum, stainless steel, copper under different levels of temperature. The stress induced, shear stress in XY, YZ, ZX plane and displacement is estimated from the finite element results.

1. Stresses(Mpa)

Aluminum:



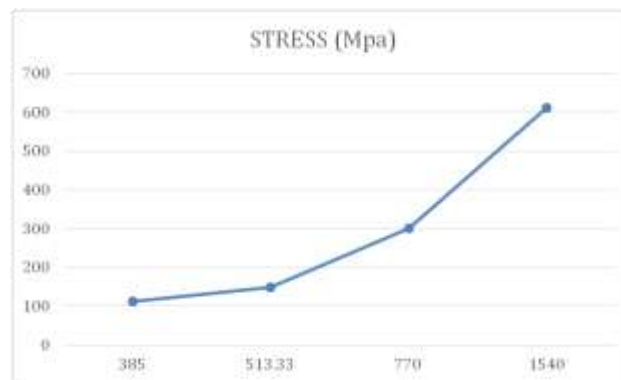
Using structural analysis, a welded plate was analysed for the Aluminum, at a temperature of 660°C . stresses in that plate was obtained. By applying 660°c at the v-butt welded portion the maximum stress of 2368Mpa was recorded in that plate.

Using structural analysis, a welded plate was analysed for the Aluminum, at a temperature of 330°C. stresses in that plate was obtained. By applying 330°C at the v-butt welded portion the maximum stress of 1147Mpa was recorded in that plate.

Using structural analysis, a welded plate was analysed for the Aluminum, at a temperature of 220°C. stresses in that plate was obtained. By applying 220°C at the v-butt welded portion the maximum stress of 739.7Mpa was recorded in that plate.

Using structural analysis, a welded plate was analysed for the Aluminum, at a temperature of 165°C. stresses in that plate was obtained. By applying 165°C at the v-butt welded portion the maximum stress of 536.2Mpa was recorded in that plate.

Stainless steel:



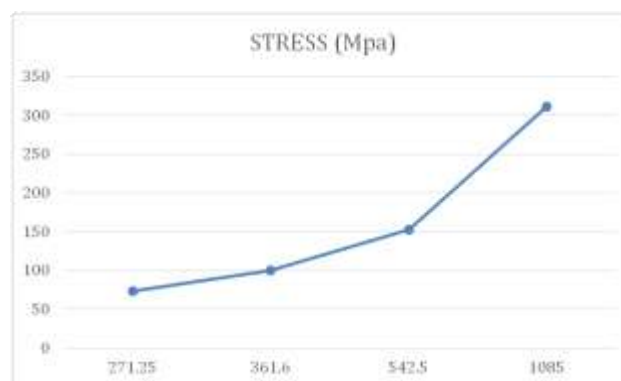
Using structural analysis, a welded plate was analysed for the Stainless steel, at a temperature of 1540°C. stresses in that plate was obtained. By applying 1540°C at the v-butt welded portion the maximum stress of 8621Mpa was recorded in that plate.

Using structural analysis, a welded plate was analysed for the Stainless steel, at a temperature of 770°C. stresses in that plate was obtained. By applying 770°C at the v-butt welded portion the maximum stress of 4254Mpa was recorded in that plate.

Using structural analysis, a welded plate was analysed for the Stainless steel, at a temperature of 513.33°C. stresses in that plate was obtained. By applying 513.33°C at the v-butt welded portion the maximum stress of 1898Mpa was recorded in that plate.

Using structural analysis, a welded plate was analysed for the Stainless steel, at a temperature of 385°C. stresses in that plate was obtained. By applying 385°C at the v-butt welded portion the maximum stress of 1404Mpa was recorded in that plate.

Copper:



Using structural analysis, a welded plate was analysed for the Copper, at a temperature of 1085°C. stresses in that plate was obtained. By applying 1085°C at the v-butt welded portion the maximum stress of 4998 Mpa was recorded in that plate.

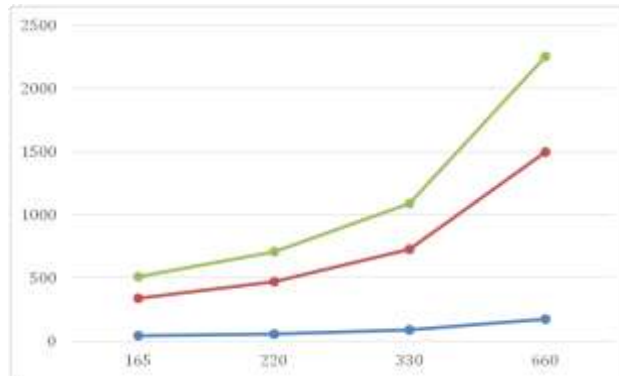
Using structural analysis, a welded plate was analysed for the Copper, at a temperature of 542.5°C. stresses in that plate was obtained. By applying 542.5°C at the v-butt welded portion the maximum stress of 2452Mpa was recorded in that plate.

Using structural analysis, a welded plate was analysed for the Copper, at a temperature of 361.66°C. stresses in that plate was obtained. By applying 361.66°C at the v-butt welded portion the maximum stress of 1603Mpa was recorded in that plate.

Using structural analysis, a welded plate was analysed for the Copper, at a temperature of 271.25°C. stresses in that plate was obtained. By applying 271.25°C at the v-butt welded portion the maximum stress of 1179Mpa was recorded in that plate.

2. Shear stress in XY,YZ,ZX (Mpa)

Aluminium:



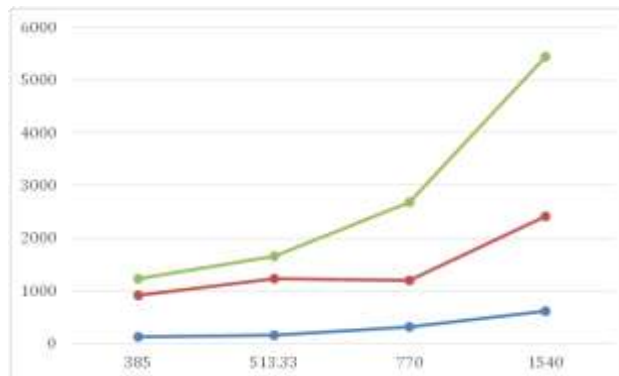
Using structural analysis, a welded plate was analysed for the aluminium, at a temperature of 660°C. shear stresses were analysed in XY,YZ,ZX direction. By applying temperature 117.5Mpa,1321Mpa,754.4Mpa respectively were obtained in that plate.

Using structural analysis, a welded plate was analysed for the aluminium, at a temperature of 330°C. shear stresses were analysed in XY,YZ,ZX direction. By applying temperature 88.27Mpa,639.8Mpa,365.4Mpa respectively were obtained in that plate.

Using structural analysis, a welded plate was analysed for the aluminium, at a temperature of 220°C. shear stresses were analysed in XY,YZ,ZX direction. By applying temperature 58.51Mpa,412.6Mpa,235.8Mpa respectively were obtained in that plate.

Using structural analysis, a welded plate was analysed for the aluminium, at a temperature of 165°C. shear stresses were analysed in XY,YZ,ZX direction. By applying temperature 43.64Mpa,299Mpa,170.9Mpa respectively were obtained in that plate.

Stainless steel:



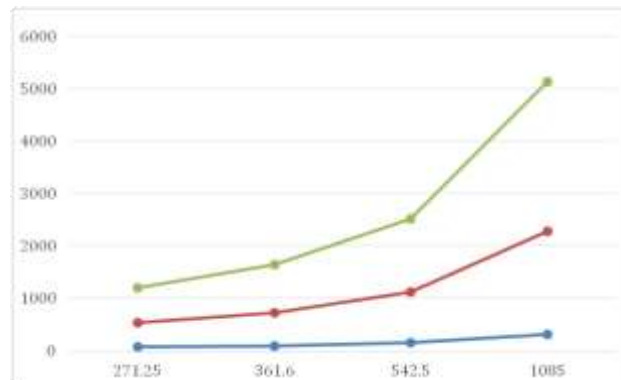
Using structural analysis, a welded plate was analysed for the Stainless steel, at a temperature of 150°C. shear stresses were analysed in XY,YZ,ZX direction. By applying temperature 612.3Mpa,1803Mpa,3029Mpa respectively were obtained in that plate.

Using structural analysis, a welded plate was analysed for the Stainless steel, at a temperature of 770°C. shear stresses were analysed in XY,YZ,ZX direction. By applying temperature 302.1Mpa,889.9Mpa,1495Mpa respectively were obtained in that plate.

Using structural analysis, a welded plate was analysed for the Stainless steel, at a temperature of 513.33°C. shear stresses were analysed in XY,YZ,ZX direction. By applying temperature 150.1Mpa,1069Mpa,441.7Mpa respectively were obtained in that plate.3

Using structural analysis, a welded plate was analysed for the Stainless steel, at a temperature of 385°C. shear stresses were analysed in XY,YZ,ZX direction. By applying temperature 112.4Mpa,790.7Mpa,326.8Mpa respectively were obtained in that plate.

copper:



Using structural analysis , a welded plate was analysed for the copper, at a temperature of 1085°C. shear stresses were analysed in XY,YZ,ZX direction. By applying temperature 311.4Mpa,1976Mpa,2851Mpa respectively were obtained in that plate.

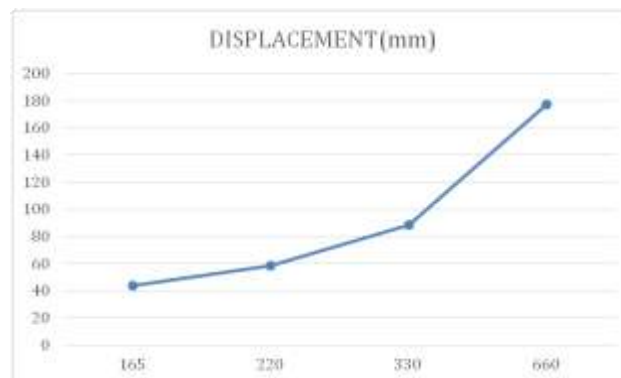
Using structural analysis , a welded plate was analysed for the copper, at a temperature of 542.5°C. shear stresses were analysed in XY,YZ,ZX direction. By applying temperature 152.8Mpa,969.5Mpa,1399Mpa respectively were obtained in that plate.

Using structural analysis , a welded plate was analysed for the copper, at a temperature of 361.66°C. shear stresses were analysed in XY,YZ,ZX direction. By applying temperature 99.86Mpa,634Mpa,914.7Mpa respectively were obtained in that plate.

Using structural analysis , a welded plate was analysed for the copper, at a temperature of 271.25°C. shear stresses were analysed in XY,YZ,ZX direction. By applying temperature 73.45Mpa,466.2Mpa,672.7Mpa respectively were obtained in that plate.

3.Displacement (mm)

Aluminum:



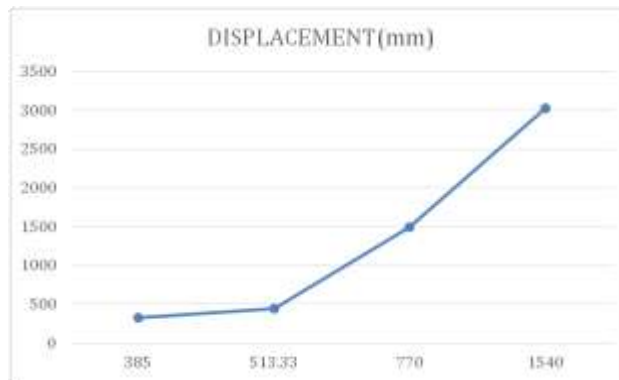
Using structural analysis, a welded plate was estimated for the aluminum, at a temperature of 660°C, displacement of the plate was obtained. By applying temperature the maximum deflection was obtained in that plate was 0.1012mm.

Using structural analysis, a welded plate was estimated for the aluminum, at a temperature of 330°C, displacement of the plate was obtained. By applying temperature the maximum deflection was obtained in that plate was 0.049mm.

Using structural analysis, a welded plate was estimated for the aluminum, at a temperature of 220°C, displacement of the plate was obtained. By applying temperature the maximum deflection was obtained in that plate was 0.0316mm.

Using structural analysis, a welded plate was estimated for the aluminum, at a temperature of 165°C, displacement of the plate was obtained. By applying temperature the maximum deflection was obtained in that plate was 0.0229mm.

Stainless steel:



Using structural analysis, a welded plate was estimated for the Stainless steel, at a temperature of 1540°C, displacement of the plate was obtained. By applying temperature the maximum deflection was obtained in that plate was 0.09931mm.

Using structural analysis, a welded plate was estimated for the Stainless steel, at a temperature of 770°C, displacement of the plate was obtained. By applying temperature the maximum deflection was obtained in that plate was 0.049mm.

Using structural analysis, a welded plate was estimated for the Stainless steel, at a temperature of 513.33°C, displacement of the plate was obtained. By applying temperature the maximum deflection was obtained in that plate was 0.0294mm.

Using structural analysis, a welded plate was estimated for the Stainless steel, at a temperature of 385°C, displacement of the plate was obtained. By applying temperature the maximum deflection was obtained in that plate was 0.0217mm.

Copper:



Using structural analysis, a welded plate was estimated for the Copper, at a temperature of 1085°C, displacement of the plate was obtained. By applying temperature the maximum deflection was obtained in that plate was 0.1226mm.

Using structural analysis, a welded plate was estimated for the Copper, at a temperature of 542.5°C, displacement of the plate was obtained. By applying temperature the maximum deflection was obtained in that plate was 0.06017mm.

Using structural analysis, a welded plate was estimated for the Copper, at a temperature of 361.66°C, displacement of the plate was obtained. By applying temperature the maximum deflection was obtained in that plate was 0.03934mm.

Using structural analysis, a welded plate was estimated for the Copper, at a temperature of 271.25°C, displacement of the plate was obtained. By applying temperature the maximum deflection was obtained in that plate was 0.02893mm.

Conclusions

- For temperature distribution in all taken materials according to the selected temperatures the maximum was allocated at the welded portion and the minimum was allocated at the ends of the plate.

- For temperature gradient in all taken materials according to the selected temperatures the maximum was allocated at the welded portion and the minimum was allocated at the ends of the plate.
- For heat flux in all taken materials according to the selected temperatures the maximum was allocated at the welded portion and the minimum was allocated at the ends of the plate.
- Structural analysis will play a key role in the welding field because stress analysis will be important in application oriented. On this view stress analysis was held in this all materials exhibit when selected temperatures increased along that stresses induced in that welded plate was also increased.
- In the point of shear stress also in the selected materials at selected temperatures as these temperatures increase the shear stress induced in all directions (XY, YZ, ZX).
- And displacement induced in the welded plates was not effect to much in this selected material welding plate according to the selected temperature ranges.

References

- [1] R. Sepe, A. Greco, A. De Luca, F. Caputo, F. Berto, Influence of thermo-mechanical material properties on the structural response of a welded butt-joint by FEM simulation and experimental tests, *Forces in Mechanics*, Volume 4, 2021, 100018, ISSN 2666-3597, <https://doi.org/10.1016/j.finmec.2021.100018>.
- [2] R. Gunnert, *Residual Welding Stressed*, Almqvist & Wiksell, Stockholm (1955)
- [3] L.P. Connor, *Welding Handbook*, (eighth ed.), American Welding Society, Miami, FL (1987)
- [4] Z. Barsoum, I. Barsoum, Residual stress effects on fatigue life of welded structures using LEFM, *Eng. Fail. Anal.*, 16 (2009), pp. 449-467
- [5] H. Zhigang, I.S. Kim, J.S. Son, H.H. Kim, J.H. Seo, K.C. Jang, D.K. Lee, J.M. Kuk, A study on numerical analysis of the resistance spot welding process, *J. Achiev. Mater. Manuf. Eng.*, 14 (2006), pp. 140-145
- [6] M.J. Park, H.N. Yang, D.Y. Jang, J.S. Kim, T.E. Jin, Residual stress measurement on welded specimen by neutron diffraction, *J. Mater. Process. Technol.* 155–156 (2004) 1171–1177.
- [7] P. Mollicone, D. Camilleri, T.G.F. Gary, T. Comlekci, Simple thermo-elastic-plastic models for welding distortion simulation, *J. Mater. Process. Technol.* 176 (2006) 77–86.
- [8] A.A. Bhatti, Z. Barsoum, H. Murakawa, I. Barsoum, Influence of thermo-mechanical material properties of different steel grades on welding residual stresses and angular distortion, *Mater. Des.* 65 (2015) 878–889.
- [9] XK Zhu, YJ Chao, Effects of temperature-dependent material properties on welding simulation, *Comput. Struct.* 80 (2002) 967–976.
- [10] X. Liu, K.F. Chung, M. Huang, G. Walg, Nethercot, Thermomechanical parametric studies on residual stresses in S355 and S690 welded H-section, *J. Constr. Steel Res.* 160 (2019) 387–401.

Estimation of Mechanical and Thermal Properties of Glass and Sisal Fiber Composites with Polyester Resin Matrix

K. Venkatarao¹, Ch. LakshmiKanth¹, A. Venkata Jayasri², Ch. Mani Kishore¹,
B. Chaitanya¹

¹Department of Mechanical Engineering, PVP Siddhartha Institute of Technology, Kanuru,
Vijayawada, A.P, India-520007.

²Department of Mechanical Engineering, Andhra University, Visakhapatnam, A.P, India-530003.

Abstract: In the present work hybrid composites using natural fibers were fabricated using hand-layup technique. The Sisal (S) and Glass (G) fibers were used as the natural reinforcements with polyester resin as the matrix material. Hybrid composites are prepared by keeping constant 30 wt% of total fibers content with various weight ratios of Glass and Sisal fibers. The test specimens were prepared as per in the ASTM standards. In this study, sisal-glass fiber reinforced polyester composites is developed and their mechanical properties such as tensile strength, flexural strength and impact strength are evaluated. The interfacial properties, internal cracks and internal structure of the fractured surfaces are evaluated by using Scanning Electron Microscope (SEM). The thermal properties were studied using Differential scanning calorimetry (DSC) and Thermo gravimetric analysis (TGA) tests. In particular, the Differential scanning calorimetric (DSC) analysis was used to measure the thermal characteristic of Sisal/Hemp composites, the TGA analysis was utilized to measure the degradation and decomposition of materials in sisal and hemp fibre, and the composites. From the results, the density of composites decreased with increasing fibre content.

Keywords: Tensile strength, Flexural strength, Impact strength, Differential scanning calorimetry (DSC), Thermo gravimetric analysis (TGA), Scanning electron microscopy (SEM).

1. Introduction

Researchers are attracted towards natural composite materials, such as plant-based natural fibres as the awareness on biodegradability increases. Natural composites have been increasingly applied in aircraft, transportation, building, musical, sports, and household applications [1-3]. Jute, hemp, banana, sisal, and bamboo are commonly used natural fibres to prepare natural composites [4].

Appropriate selection of fibre is a very important aspect in recommending natural fibre in any application. Hybridisation of natural composites is a real challenge as there are many issues related to mechanical and thermal properties.

Subrata C. Das suggested the hybridisation of natural and synthetic fibres to improve the composite laminate performance by following the correct stacking sequence [5], where these combinations improved the mechanical properties and biodegradability of the composite laminate. The tensile, flexural, and impact strength for the combination of banana and jute fibres with different stacking sequences was evaluated by conducting suitable experiments, highlighting the importance of the hybridisation of these fibres [6]. To improve the toughness of natural fibre composites, one of the approaches is through the hybridisation with synthetic fibre [7]. In the automotive industry, the brake friction composite at different composite weight fractions of natural fibres (hemp, ramie, and pineapple) was prepared and tested [8]. The hybridisation of jute, sisal, and curaua fibres was applied as natural fibre reinforcements for epoxy matrix-based composites, and the tensile, flexural, and impact strength of the new hybrid composites was assessed [9]. The importance of recent advances in the manufacturing of hybrid natural fibre composites was highlighted by Fatima-Zahra Semlali Aouragh Hassani [10]. Basket type and intra-ply hybridised composites enhanced the dynamic

mechanical properties of the composites due to the enhancement in modulus by the reinforcement [11]. The waviness of sisal fibre on the elastic modulus was also presented [12]. Considerable studies have been performed on thermogravimetric analysis (TGA) of natural fibre-reinforced composites to study the thermal behaviour of plant-based composites and a DFT study of compounds is of interest in order to gain a deeper insight of their characteristics and thus helping in the design of new materials [13]. The weight loss in natural composites due to the increase in temperature is studied using TGA. For jute/sisal hybrid composite, three significant regions of weight loss with respect to temperature were observed. [14]. The thermal decomposition of jute and bamboo fibres was observed in the temperature range of 240–260 °C [15]. The chemical composition of jute fibre was also observed [16]. From the above-mentioned studies, it is important to use different combinations of natural fibres to compete with synthetic fibre-reinforced composites. In this work, efforts have been made to identify the hybridisation effect of jute and hemp fibre-reinforced composites produced using the hand lay-up technique, and the tensile, flexural, and impact strength was evaluated using scanning electron microscopy (SEM) images. The market manageability of the each new item mostly relies upon the unrefined substance as well as usefulness. A practical completing chooses the end utilization of the items as well as upgrades the existence of the items. This paper reviews the practical completing on jute materials with unique reference to relaxing, wrinkle safe, fire retardant, and cleanliness for the fulfillment of the customer's interest are inspected [17]. This was finished to investigate the capability of decrease in energy utilization and creation time as well as colors and synthetic compounds. For this reason, our recently pre-arranged starch nanoparticles (SNPs) as a support biopolymer were integrated in cross-connecting plan of cotton textures embracing various groupings of citrus extract and cationic colors, i.e., Methylene Blue and Crystal Violet in presence of sodium hypophosphite as a capable impetus at 1500 C for 2 minutes [18]. This work deals with various surface changes of vetiver filaments to concentrate on their consequences for mechanical and warm properties. The effectiveness of every treatment has been assessed by Fourier change infra red spectroscopy, X-beam diffractometry, and checking electron microscopy. It has been seen that benzylation-treated vetiver fiber shows better execution in contrast with different medicines. [19]. In this work, jute fiber has been utilized as support and epoxy as network material to foster somewhat biodegradable green composite with the assistance of hand layup followed by compression shaping method. The impact of restoring temperature going from 80°C to 130°C on various examples was examined for different mechanical properties [20]. In this work, manufactured half breed composites utilizing artificially treated abaca, kenaf and carbon fiber supported with epoxy and teta hardener are considered. Mixture composites have four stacking successions and five layer composites comprised of hand and then the compression molding [21]. The perception led for all examples uncovers the break component of the single fiber characterized into three sorts, for example shear, tension, and joined of shear and tension [22]In this occasion was seen to be different for fluctuating fiber direction and was credited to an adjustment of solidness. The cross-employ tests had the option to oppose the effect force after delamination. The cross molded fiber breakage framed in cross-employ and round openings shaped in point handle. The predominant disappointment in cross-handle was viewed as fiber breakage (Longitudinal break). SEM pictures show that a blend of fiber-breakage and fiber-pullout alongside debonding in every one of the examples of abaca/epoxy composites cross-handle direction [23]. The results showed that the leftover gum content of the hemp utilizing GO shower is lower than that acquired utilizing water shower, and the hemp fiber had electrical conductivity, better breaking strength, warm conductivity, and great UV insurance capacity [24]. The various weight percentages of raw and optimally treated DCF composites were prepared by hand lay up and compression molding methods. In the next step the mechanical testing of prepared composites was followed as per the ASTM standard [25]. In the current review, Ceiba pentandra bark (CP) strands, attributable to their low weight-to-high strength proportion and recyclable elements have been chosen as support in thermoplastic polymer. i.e., poly (vinyl) liquor (PVA) for creation of composites to find its application in car run board and entryway board. The bark strands were synthetically adjusted with

NaOH to improve its holding property with hydrophobic polymer [26]. It was also found that the utilization of kenaf strands of various length and diameter works on the mechanical properties of cement. The discoveries from this survey affirm the plausibility of accomplishing standard substantial traits by involving the regular filaments in concrete based concrete [27]. As per the discoveries of the examination, the utilization of normal waste filaments enjoys unmistakable upper hands over manufactured strands. At last, as a result of its useful impact, this paper suggests involving jute fiber with mortar for any underlying reason [28]. At last, the measurable meaning of the not entirely set in stone through an examination of difference (ANOVA). In light of the aftereffects of the tests decided the ideal mix of fiber boundaries that gives the best shotcrete execution [29]. This writing overview proposes a top to bottom survey of the extraction techniques, compound medicines and applications for natural fiber composites. We restate the end from the different late writings and the compound treatment results other mechanical performance of the regular strands are being featured [30]. This paper presents a few regular fiber based composites (Jute, Basalt, Coir, Sisal) and their techniques for planning. By appropriate combination and treatment of normal fiber different mechanical properties of the regular fiber can be improved, which makes them reasonable for different enterprises like auto ventures, aeronautic trade, marine industry and in building development [31]. This technique can be utilized to choose great flax assortments which have high mechanical properties with a little variety, which are reasonable for a fiber support of superior execution regular fiber built up composites [32]. Inferior mechanical execution of WB/PLA composites was noticed contrasted with slick PLA. Unfortunate grip, debonding, and fiber break were the overwhelming micromechanical distortion processes in WB/PP composites, while debonding, hole, and break development because of fiber direction brought about terrible showing of WB/PLA composites. Possibilities of WB-based composites present open doors for cultivators having advantageous purposes of wheat and repaying diminished overall revenues [33]. In this review, novel ultra strong and extreme regular cellulosic fiber groups (RFs) separated from vascular tissues of manau rattan stems were gotten. The physical, mechanical, compound, warm, crystallographic, and morphological qualities of RFs with various widths were investigated [34]. The goal of the current work was to lay out process boundaries boosting the long queue fiber yield utilizing flax committed scutching and hackling gadgets. A lab-scale scutching/hackling gadget was utilized to lay out sets of cycle boundaries which best further develop the long fiber scutching yield and as a result limit the creation of tow strands [35]. Following this, this paper basically investigations the original improvement methods appropriate for natural fiber composites for harm resilience and effect obstruction ways of behaving [36]. Mechanical results showed a positive impact with incorporation of CMF in PF hybrid fiber composites. Thermal stability results showed enhancement in the degradation temperature, residual %, endothermic peak and enthalpy by the incorporation of CMF [37].

2. Materials and Methodology

Unsaturated polyester resin of grade ECMALON 4411 was purchased from ECMASS Resins Pvt., Ltd. (Hyderabad, India). The resin has a density of 1,242 kg/m³, Young's modulus of 615 MPa, tensile strength of 29.2 MPa, and elongation at break of 4.5%.

Extraction of Fibres: The extraction of fibres involved the retting process, followed by decorticating. The stems of Sisal were cut at their base and immersed in a water-retting tank for two weeks. After that, the stems were removed and the fibres were stripped from the stalks by hand, washed, and dried in the sun. After drying, any extraneous matter that might still adhere to the fibres was removed. The extracted fibres were used for composite production.

2.1 Fabrication and Testing of Composites

Fabrication of Composites: Unidirectional composites were prepared using polyester matrix to assess the reinforcing capacity of jute fibre and teak wood powder. The quantity of accelerator and catalyst added to resin at room temperature for curing was 1.5% by volume of each resin. The hand lay-up method was adopted to fill up the prepared mould with an appropriate amount of polyester

resin mixture, unidirectional jute fibre, and teak wood powder, starting and ending with layers of resin. Fibre deformation and movement should be minimised to yield good quality unidirectional fibre composites. Therefore, at the time of curing, a compressive pressure of 0.05 MPa was applied to the mould and the composite specimens were cured for 24 h. The specimens were also post-cured at 70 °C for 2 h after removal from the mould. The pycnometric procedure was adopted for measuring the density of the composite.

For determining the impact and tensile properties of the composites, the specimens were prepared according to ASTM D256 and ASTM D638 standards using the hand lay-up technique with different weight ratios.

2.2 Tensile Testing

The tensile properties of the composites were measured as per the standard test method, ASTM D638M. The test specimens were prepared with the dimensions of 160 mm long, 12.5 mm wide, and 3 mm thick. Five identical specimens were tested for each percentage weight of fibre. Overlapping aluminium tabs were attached at the end of each specimen with araldite filling the space between the tab and the specimen to prevent compression of the sample and also for effective gripping in the jaws of the chuck. The specimens were tested at a crosshead speed of 2 mm/min using an electronic tensometer.

2.3 Flexural Strength Test

The flexural strength of the composite specimens was tested as per ASTM D790M. The dimensions of the test specimens were 100 mm long, 25 mm wide, and 3 mm thick. The flexural strength and its modulus were measured by conducting a three-point bending test on a universal testing machine. The specimens were loaded until the failure occurred.

2.4 Impact Testing

Izod impact test specimens were prepared per ASTM D256M to measure impact strength. The specimens were 63.5 mm long, 12.7 mm deep, and 10 mm wide. A sharp file with an included angle of 45° was drawn across the centre of the saw cut at 90° to the sample axis to obtain a consistent starter crack. The samples were fractured and the impact toughness was calculated from the energy absorbed. The materials used to prepare the specimens were coir fibre, jute fibre, and polyester resin. To improve the bonding strength between fibre and matrix, heat treatment was conducted for jute and coir fibres. The impact study was conducted using an Izod impact testing machine.

2.5 Thermal conductivity

ASTM C177 is the standard test for measuring the thermal conductivity of a material by means of a guarded-hot-plate apparatus. For a material to be classified as a thermal insulator, it must exhibit low thermal conductivity throughout this test.

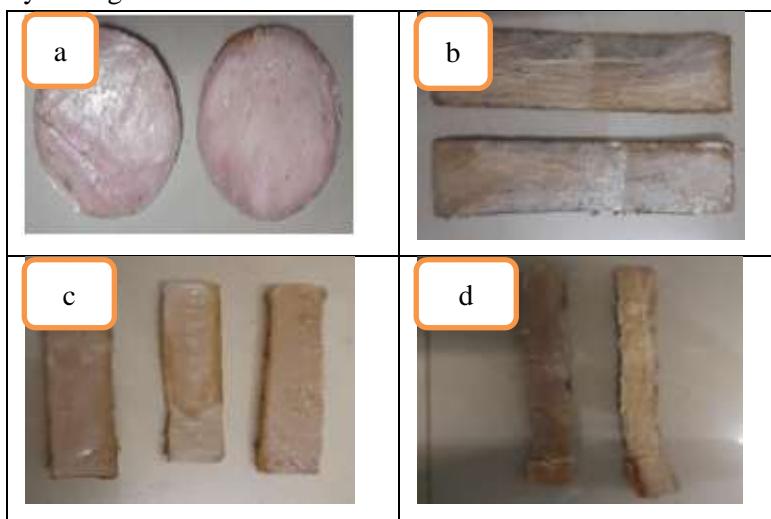


Figure 1 (a) Thermal conductivity test specimens, (b) Flexural test specimens, (c) impact test specimens (d) tensile test specimens
Dept. of Mech. Engg.

3. Results and Discussion

The effect of chemical treatment on the composite specimens shows an important role in the tensile behaviour of polyester composites, which increased gradually with an increase of the reinforcement phase. The higher tensile load-bearing capacity was recorded for T6 specimen due to excellent bonding strength and a combination of jute and coir fibres. In maximum cases, the specimen showed high strength level after chemical treatment due to enhanced surface roughness of the fibres, resulting in superior bonding strength, which was observed from the scanning electronic micrographs. The composite samples exhibited lower level displacement irrespective of load and chemical treatment. The reduced tensile strength and bearing capacity could be noted for T1 sample. Figure 2 shows the load versus displacement curves for a better understanding of the mechanical behaviour of polyester composites.

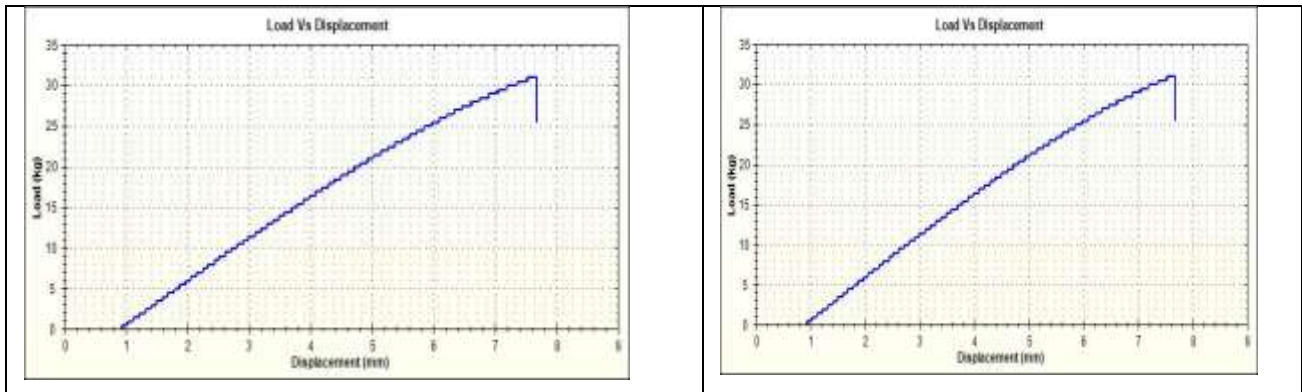


Figure 2 Tensile behaviour of composite specimens

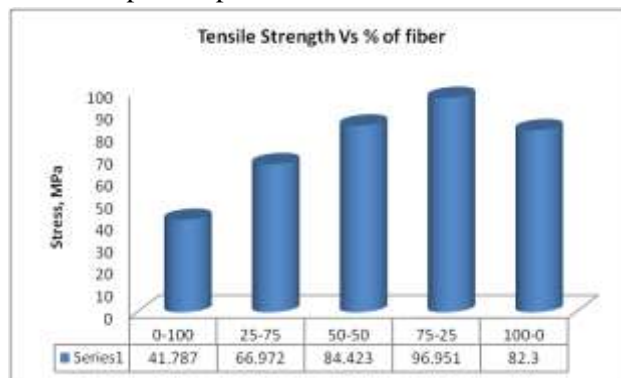


Figure 3 Tensile strength of composite specimens

From Figure 3, it can be observed that the increase in the weight fraction of Sisal and Glass fibres resulted in increased tensile strength of the proposed composite materials up to 75% glass and 25% sisal fibre. Further increase in the weight of the fibre reduced the tensile strength of the composite materials.

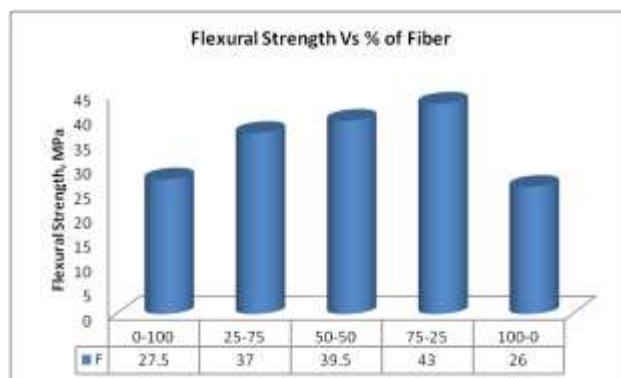


Figure 4 Flexural strength of composite specimens

From Figure 4, it can be observed that the increase in the weight of glass and sisal fibres resulted in increased flexural strength of the proposed composite materials up to 75% of glass fibre and 25% of

sisal fibre. Further increase in the weight fraction reduced the flexural strength of the composite materials.

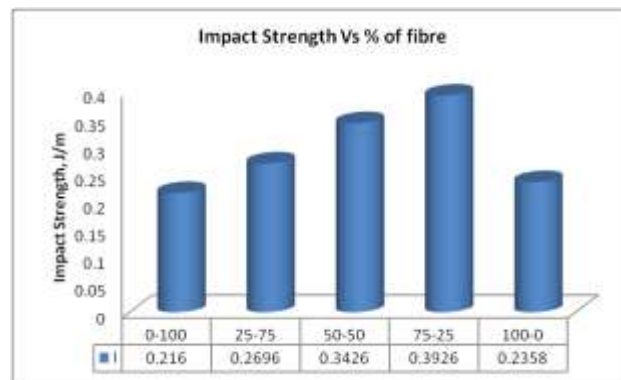


Figure 5 Impact strength of composite specimens

Figure 5 presents the impact strength of polyester composites. The maximum impact strength was observed for the combination of weight percentage 75% glass fibre and 25% of sisal specimen showed highest impact strength. The sisal fibre Specimen has showed lowest impact strength as compared to remaining the other compositions, which has lower bonding strength among the fibre and the matrix phase.

Thermal Conductivity:

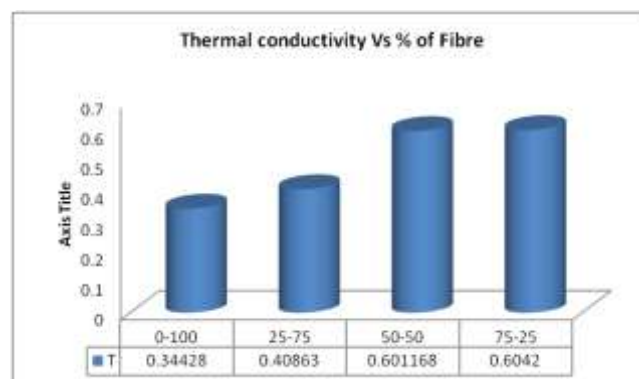


Figure6. Thermal conductivity of composite specimens

Figure 6 presents the thermal conductivity of polyester composites. The maximum thermal conductivity was observed for the combination of weight percentage 75% glass fibre and 25% of sisal specimen showed highest thermal conductivity. The sisal fibre Specimen has showed lowest thermal conductivity as compared to remaining the other compositions, which has lower bonding strength among the fibre and the matrix phase.

3.1 Fracture Analysis of Polyester-Fibre Reinforced Composites

The fracture surface was examined through the SEM micrographs of T1 and T4 specimens under tensile loading conditions. These micrographs disclose the nature of the failure of the composite specimens. Figure 7(a) shows the uniform coir fibre distribution in the polyester matrix. The internal cracks were noticed from Figure 7(b) due to tensile load and exhibited brittle failure of the specimen. The fibre pull-out and debonding could be observed in Figure 7(d) for specimen T5 under tensile load. The fibre distribution is presented in Figure 7(c).

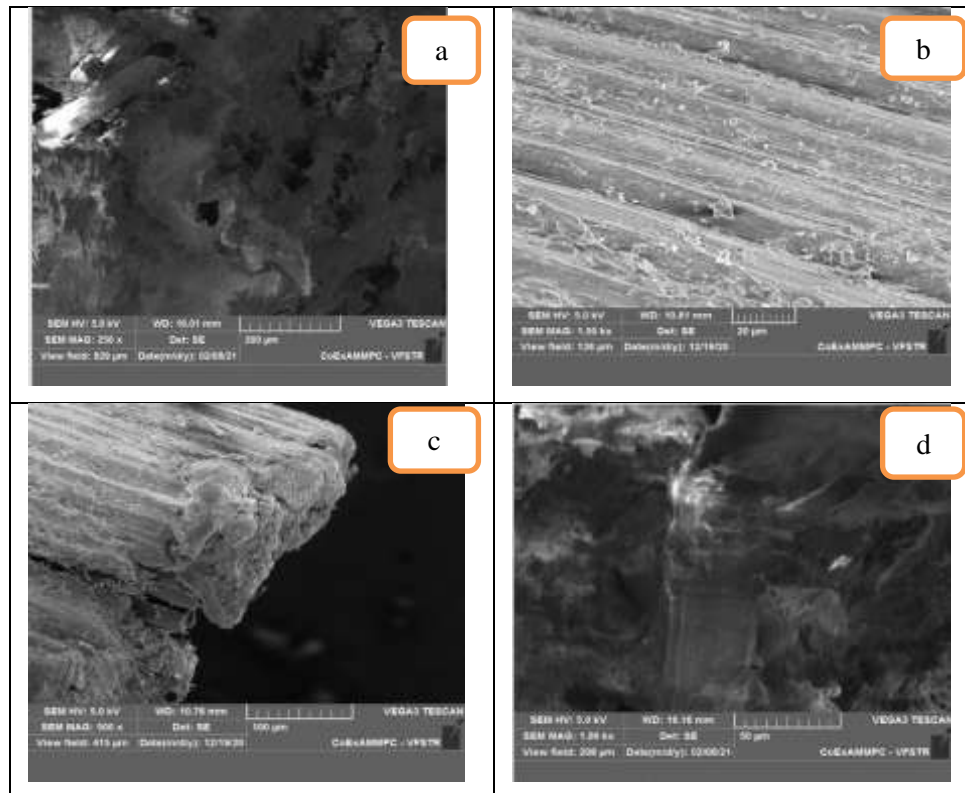


Figure 7 SEM images of impact and tensile samples

3.2 Differential scanning calorimetry:

Differential scanning calorimetry (DSC) is a technique for measuring the energy necessary to establish a nearly zero temperature difference between a substance and an inert reference material, as the two specimens are subjected to identical temperature regimes in an environment heated or cooled at a controlled rate. The biggest advantage of DSC is the ease and speed with which it can be used to see transitions in materials. Various types of DSC are Power Compensated DSC, Heat Compensated DSC, Modulated DSC, Hyper DSC, and Pressure DSC. Direct scanning calorimetry (DSC) measures the temperature and heat flux associated with material transitions as a function of temperature and time. Qualitative and quantitative information on physical and chemical changes involving endothermic (heat absorption) and exothermic (heat released) processes are provided by this technique. The exothermic and endothermic peaks and magnitudes indicate the thermal phase transformation of the composites. The result is a plot of the difference in heat (q) versus temperature (T).

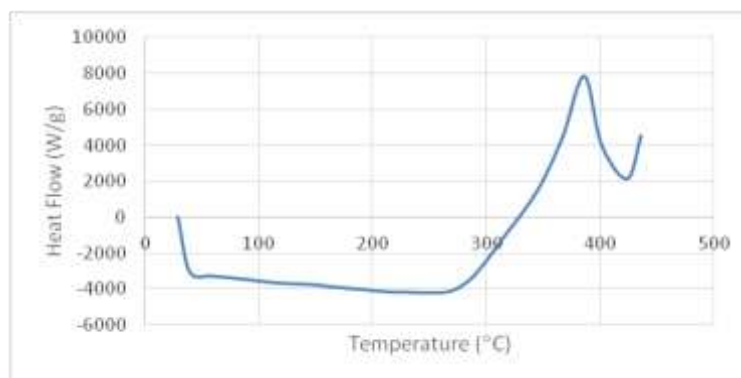


Figure 8 DSC analysis

The DSC curves of the glass and sisal fiber composites were shown in Fig.8. The glass transition (T_g) of coir and jute fiber composite at 105°C , while the melting point (T_m) at the temperature 150°C . The findings of other studies showed that the glass transition and melting point of HIPS were at 90°C and 120°C or 160°C , respectively. The glass transition (T_g) of glass and sisal fiber composite from this

study occurred at 75°C. It could be seen that the temperature of T_g HIPS/PALF composite was at 123°C, indicating that the temperature T_g of the composite increased around 18°C as compared to neat HIPS. The glass transition of the composites, denoted with CFA2, CFA4 and CFA6, was about 118°C, 104°C, and 102°C. The melting point also decreased at 149°C, 147°C, and 147°C, respectively.

Thermo gravimetric analysis (TGA)

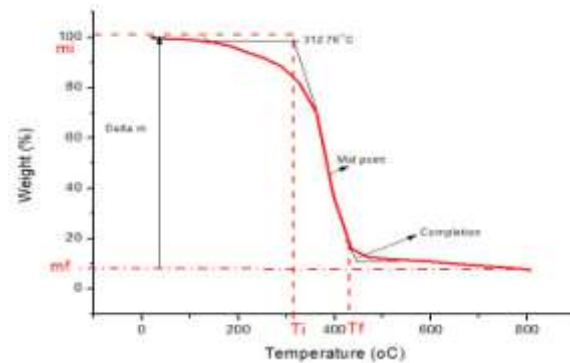


Figure 9 TGA analysis

In this study, the Thermo-gravimetric (TGA) curves were used to determine the thermal degradation and thermal stability of each material. The TG analysis of neat high impact glass fiber, sisal fibre and their composites are presented in Fig. 9. The thermal decomposition of each sample took place in a programmed temperature range of 19°C to 807°C. The combination of glass and sisal fiber showed only one stage of weight loss process, which had a transition temperature that began from 312.76°C and the final transition at 434°C, and it was clear that the peak transition temperature of glass and sisal fibre composite at 362°C. The weight loss and residual weight of 3% and 12% for the TG analysis were found to be 99% and 1.2%, respectively. By observing in this test initially there is no mass change, by increasing temperature the mass reduces very quickly and then finally the mass reduces slowly by applying temperature.

4. Conclusion

Based on the results of this study, it can be concluded that, the combination of 75% glass fibre and 25% of sisal fibre reinforced composites got high mechanical properties as compared to remaining the combinations of high-brid composites. In this work, fibre-reinforced polyester hybrid composites were prepared as per ASTM standards. Glass and sisal fibres are available abundantly in nature and offer low material density. The density of the composites decreased with increasing fibre content. Thus, the hybrid composites are light in weight with better mechanical and insulating properties. The fracture surface was studied through SEM images. The internal cracks and ductility nature of the specimens were observed from the SEM images of fractured surfaces. Orientation of fiber and its bonding with matrix is visualized by SEM and found to be good for both glass and sisal fibres. This paper provides the results of DSC analysis that can only provide the glass transition temperature. The investigation of the thermal properties of glass and sisal fibres could bring an improvement in using natural fibre composites. The investigation of thermal properties for glass and sisal fibre showed that composite has high glass transition temperature that could bring an improvement of using fibre composites. The maximum thermal conductivity was observed for the combination of weight percentage 75% glass fibre and 25% of sisal specimen showed highest thermal conductivity.

References

1. L. Prabhu, V. Krishnaraj, S. Sathish, S. Gokulkumar, N. Karthi, L. Rajeshkumar, D. Balaji, N. Vigneshkumar, K.S. Elango, A review on natural fiber reinforced hybrid composites: chemical treatments, manufacturing methods and potential applications, *Materials Today: Proceedings*, Volume 45, Part 9, 2021, Pages 8080-8085, <https://doi.org/10.1016/j.matpr.2021.01.280>.

2. Muhammad Yasir Khalid, Ans Al Rashid, Zia Ullah Arif, Waqas Ahmed, Hassan Arshad, Asad Ali Zaidi, Natural fiber reinforced composites: Sustainable materials for emerging applications, Results in Engineering, Volume 11, 2021, 100263, <https://doi.org/10.1016/j.rineng.2021.100263>.
3. P. Venkateshwar Reddy, R.V. Saikumar Reddy, J. Lakshmana Rao, D. Mohana Krishnudu, P. Rajendra Prasad, An overview on natural fiber reinforced composites for structural and non-structural applications, Materials Today: Proceedings, Volume 45, Part 7, 2021, Pages 6210-6215, ISSN 2214-7853, <https://doi.org/10.1016/j.matpr.2020.10.523>
4. Azizatul Karimah, Muhammad Rasyidur Ridho, Sasa Sofyan Munawar, Danang Sudarwoko Adi, Ismadi, Ratih Damayanti, Bambang Subiyanto, Widya Fatriasari, Ahmad Fudholi, A review on natural fibers for development of eco-friendly bio-composite: characteristics, and utilizations, Journal of Materials Research and Technology, Volume 13, 2021, Pages 2442-2458, <https://doi.org/10.1016/j.jmrt.2021.06.014>.
5. Subrata C. Das, Debasree Paul, Sotirios A. Grammatikos, Md. A.B. Siddiquee, Styliani Papatzani, Panagiota Koralli, Jahid M.M. Islam, Mubarak A. Khan, S.M. Shauddin, Ruhul A. Khan, Nectarios Vidakis, Markos Petousis, Effect of stacking sequence on the performance of hybrid natural/synthetic fiber reinforced polymer composite laminates, Composite Structures, Volume 276, 2021, 114525, <https://doi.org/10.1016/j.compstruct.2021.114525>.
6. S. Ravindran, G.G. Sozhamannan, L. Saravanan, V.S.K. Venkatachalapathy, Study on mechanical behaviour of natural fiber reinforced vinylester hybrid composites, Materials Today: Proceedings, Volume 45, Part 6, 2021, Pages 4526-4530, <https://doi.org/10.1016/j.matpr.2020.12.1077>.
7. M. Muneer Ahmed, H.N. Dhakal, Z.Y. Zhang, A. Barouni, R. Zahari, Enhancement of impact toughness and damage behaviour of natural fibre reinforced composites and their hybrids through novel improvement techniques: A critical review, Composite Structures, Volume 259, 2021, 113496, <https://doi.org/10.1016/j.compstruct.2020.113496>.
8. Tej Singh, Optimum design based on fabricated natural fiber reinforced automotive brake friction composites using hybrid CRITIC-MEW approach, Journal of Materials Research and Technology, Volume 14, 2021, Pages 81-92, <https://doi.org/10.1016/j.jmrt.2021.06.051>
9. D.K.K. Cavalcanti, M.D. Banea, J.S.S. Neto, R.A.A. Lima, L.F.M. da Silva, R.J.C. Carbas, Mechanical characterization of intralaminar natural fibre-reinforced hybrid composites, Composites Part B: Engineering, Volume 175, 2019, 107149, <https://doi.org/10.1016/j.compositesb.2019.107149>.
10. Fatima-Zahra Semlali Aouragh Hassani, Rachid Bouhfid, Abouelkacem Qaiss, Chapter Six - Recent advances in the fabrication of hybrid natural fiber composites, Editor(s): Anish Khan, Sanjay Mavinkere Rangappa, Suchart Siengchin, Mohammad Jawaid, Abdullah M. Asiri, In Woodhead Publishing Series in Composites Science and Engineering, Hybrid Natural Fiber Composites, Woodhead Publishing, 2021, Pages 113-131, <https://doi.org/10.1016/B978-0-12-819900-8.00010-6>.
11. M. Rajesh, K. Jayakrishna, M.T.H. Sultan, M. Manikandan, V. Mugeshkannan, A.U.M. Shah, S.N.A. Safri, The hydroscopic effect on dynamic and thermal properties of woven jute, banana, and intra-ply hybrid natural fiber composites, Journal of Materials Research and Technology, Volume 9, Issue 5, 2020, Pages 10305-10315, ISSN 2238-7854, <https://doi.org/10.1016/j.jmrt.2020.07.033>.
12. P. Phani Prasanthi and K. Sivaji Babu and M. S. R. Niranjan Kumar and A. Eswar Kumar, Analysis of Sisal Fiber Waviness Effect on the Elastic Properties of Natural Composites Using Analytical and Experimental Methods, Journal of Natural Fibers, pages = 1-14, 2019, <https://doi.org/10.1080/15440478.2019.1697987>
13. Selvaraj Anidha, Nachimuthu Latha, Manickam Muthukumar, Reinforcement of Aramid fiber with bagasse epoxy bio-degradable composite: investigations on mechanical properties and surface morphology, Journal of Materials Research and Technology, Volume 8, Issue 3, 2019, Pages 3198-3212, <https://doi.org/10.1016/j.jmrt.2019.05.008>.
14. M K Gupta & R K Srivastava, Mechanical, thermal and water absorption properties of hybrid sisal/jute fiber reinforced polymer composite, Indian Journal of Engineering & Materials Sciences Vol. 23, August 2016. pp. 231-238
15. Subhankar Biswas, Sweety Shahinur, Mahbub Hasan and Qumrul Ahsan, Physical, Mechanical and Thermal Properties of Jute and Bamboo Fiber Reinforced Unidirectional Epoxy Composites, 6th BSME International Conference on Thermal Engineering (ICTE 2014).
16. Sweety Shahinur, Mahbub Hasan, Qumrul Ahsan and Julfikar Haider, Effect of Chemical Treatment on Thermal Properties of Jute Fiber Used in Polymer Composites, Journal of composite science, i. 2020, 4, 132; doi:10.3390/jcs4030132.

17. "L. Ammayappan", "L. K. Nayak", "D. P. Ray", "S. Das", "A. K. Roy" [07 Dec 2013]. Functional Finishing of Jute Textiles. Pages 390-413. <https://doi.org/10.1080/15440478.2013.824849>.
18. "Kh M. Mostafa", "H. A. Ameen" (2020): Simultaneous Dyeing and Finishing of Cotton Fabric in Presence of Starch Nanoparticles as Reinforcement Agent Using Citric Acid Based Finishing Formulation, *Journal of Natural Fibers*. <https://doi.org/10.1080/15440478.2020.1848700>
19. "Pradeep Kumar Jena", "Jyoti Ranjan Mohanty", "Subhakanta Nayak" (2020): Effect of Surface Modification of Vetiver Fibers on Their Physical and Thermal Properties, *Journal of Natural Fibers*, DOI: <https://doi.org/10.1080/15440478.2020.1726249>
20. "Jai Inder Preet Singh", "Sehijpal Singh" & "Vikas Dhawan" (2017): Effect of Curing Temperature on Mechanical Properties of Natural Fiber Reinforced Polymer Composites, *Journal of Natural Fibers*, <https://doi.org/10.1080/15440478.2017.1354744>
21. "Venkatasudhahar.M" & "Ravichandran.A.T" & "Dilipraja.N" (2021). Effect of stacking sequence on mechanical and moisture absorption properties of abaca-kenaf-carbon fiber reinforced hybrid composites. *Journal of Natural Fibers*. 1-12 <https://doi.org/10.1080/15440478.2021.1944434>
22. "Ahmad, Sabri" & "Fuadi, Zahrul" & "Kurniawan, Rudi" & "Rizal, Samsul" & "Homma, Hiroomi" & "Kosukegawa, Hiroyuki" & "Takagi, Toshiyuki" & "Miki, Hiroyuki". (2021). Tensile Strength and Fracture Behavior of Single Abaca Fiber. *Journal of Natural Fibers*. 1-15. <https://doi.org/10.1080/15440478.2021.1967832>
23. "Mahaboob Subhani", "Hariharan S Subramanian" [July 2021]. An Experimental Investigation on Low-Velocity Impact Response of Abaca/Epoxy Bio-composite. *Journal of Natural Fibres*. <https://doi.org/10.1080/15440478.2021.1941485>
24. "Jin Wang", "Yintao Zhao", "Xuyu Cai", "Mingwei Tian", "Lijun Qu" & "Shifeng Zhu" (2020): Microwave-assisted One-step Degumming and Modification of Hemp Fiber with Graphene Oxide, *Journal of Natural Fibers*, <https://doi.org/10.1080/15440478.2020.1745121>
25. "P.G Baskaran", "M Kathiresan" & "P Pandiarajan" (2020): Effect of Alkali-treatment on Structural, Thermal, Tensile Properties of Dichrostachys Cinerea Bark Fiber and Its Composites, *Journal of Natural Fibers*, <https://doi.org/10.1080/15440478.2020.1745123>
26. "Subhakanta Nayak", "Sujit Kumar Khuntia", "Saumya Darsan Mohanty" & "Jagannath Mohapatra" (2020): Investigation and Fabrication of Thermo-mechanical Properties of Ceiba Pentandra Bark Fiber/Poly (Vinyl) Alcohol Composites for Automobile Dash Board and Door Panel Applications, *Journal of Natural Fibers*, <https://doi.org/10.1080/15440478.2020.1745124>
27. "Jamal A. Abdalla", "Blessen Skariah Thomas", "Rami A. Hawileh" [6 July 2022]. Use of hemp, kenaf and bamboo natural fiber in cement-based concrete. <https://doi.org/10.1016/j.matpr.2022.06.428>
28. "Jyoti Rashmi Nayak", "Jerzy Bochen", "Małgorzata Gołaszewska" [2022]. Experimental studies on the effect of natural and synthetic fibers on properties of fresh and hardened mortar. <https://doi.org/10.1016/j.conbuildmat.2022.128550>
29. "Kyong Ku Yun", "Mohammad Shakhawat Hossain", "Seungyeon Han", "Choi Seunghak" [2022]. Rheological, mechanical properties, and statistical significance analysis of shotcrete with various natural fibers and mixing ratios. <https://doi.org/10.1016/j.cscem.2021.e00833>
30. "S. Sathish", "N. Karthi", "L. Prabhu", "S. Gokulkumar", "D. Balaji", "N. Vigneshkumar", "T.S. Ajeem Farhan", "A. AkilKumar", "V.P. Dinesh" [2022]. A review of natural fiber composites: Extraction methods, chemical treatments and applications. <https://doi.org/10.1016/j.matpr.2020.12.1105>
31. "P.P. Bijlwan", "L. Prasad", "A. Sharma" [2022]. Recent advancement in the fabrication and characterization of natural fiber reinforced composite: A review. <https://doi.org/10.1016/j.matpr.2020.11.878>
32. "Anurag Pisupati", "Lies Willaert", "Frederik Goethals", "Willem Uyttendaele", "Chung Haepark" [15 October 2021]. Variety and growing condition effect on the yield and tensile strength of flax fibers. Volume 170. <https://doi.org/10.1016/j.indcrop.2021.113736>
33. "Atikur Rahaman", "Joseph Fehrenbach", "Chad Ulven", "Senay Simsek", "Khwajal Hossain" [15 November 2021]. Utilization of wheat-bran cellulosic fibres as reinforcement in bio-based polypropylene composite. Volume 172. <https://doi.org/10.1016/j.indcrop.2021.114028>
34. "Xiaoshau Han", "Linhu Ding", "Zhiwei Tian", "Weijie Wu", "Shaohua Jiang" [1 December 2021]. Extraction and characterization of novel ultrastrong and tough natural cellulosic fiber bundles from manau rattan (Calamus manan). Volume 173 <https://doi.org/10.1016/j.indcrop.2021.114103>

Two-day International Conference on Recent Advances in Mechanical and Industrial Engineering – 2023
(ICRAMIE-2023)

35. “Marie Gregoire”, “Mahadev Bar”, “Emmanuel De Luycker”, “Salvatore Musio”, “Stefano Amaducci”, “Xavier Gabrion”, “Vincent Placet”, “Pierre Ouagne” [2021]. Comparing flax and hemp fibres yield and mechanical properties after scutching/hackling processing. <https://doi.org/10.1016/j.indcrop.2021.114045>
36. “M. Muneer Ahmed”, “H.N. Dhakal”, “Z.Y. Zhang”, “A. Barouni”, “R. Zahari” [2021]. Enhancement of impact toughness and damage behaviour of natural fibre reinforced composites and their hybrids through novel improvement techniques: A critical review. <https://doi.org/10.1016/j.compstruct.2020.113496>
37. K.R. Sumesh, K. Kanthavel, V. Kavimani [2020]. Peanut oil cake-derived cellulose fiber: Extraction, application of mechanical and thermal properties in pineapple/flax natural fiber composites. <https://doi.org/10.1016/j.ijbiomac.2020.02.118>

A novel method to improve the tolerance of position in profiles using a tooling hole

B Kiran Kumar^{1*}, K Venkatesan², B Saikrishna Srikar³

¹Associate Professor, Department of Mechanical Engineering, KoneruLakshmaiah Education Foundation, Vaddeswaram, AP, India

²Professor, Department of Automobile Engineering, Bharath Institute of Higher Education and Research, Chennai, Tamil Nadu, India

³Tata Consultancy Services, Adibatla, Telangana, India

*Corresponding author: buragaddakirankumar15@gmail.com

Abstract: The die-making industry does the machining of holes by drilling, reaming, boring, grinding and EDM operations for the fitment of punches, pillars, tool inserts, etc., or assembly purposes like screw relief holes, tapped holes, and riveting holes by using standard fixturing. Normally the hole locations are given in the manufacturing drawing by taking two accurately finished perpendicular datum features. These datum features will be used in machining, inspection, reworks, and they need to be protected from damages. Any inaccuracy in the datum features like flatness, and perpendicularity leads to the wrong measurement or location of the hole, shows an inaccurate assembly. This paper presents the novel method of using tooling hole in the manufacturing drawing and illustrate the advantages through experiments. While dimensioning, the concept of tooling hole enhances the tolerance of position in profiles and permits faster machining/inspection activities; thereby increases productivity.

Keywords: Positional accuracy, datum feature, tooling hole, die-making

1. Introduction

The die-making industry makes the parts for sheet metal stamping dies, moulds, jigs, fixtures, and gauges that need to be assembled. The manufacturing drawing contains the dimensioning of hole positions and reference points for various profiles given from two datum features [1]. Figure 1 shows the sample part drawing of a die plate, and the datum features are indicated by datum references B and C, which need to be machined accurately either by milling or grinding within the tolerance of the zone of perpendicularity. These plates are often moved from machine to machine either for a series of machining operations or inspection or rework and to locate the existing hole centers from datum features. As there is no specific distance is specified in the drawing, the operator may take any point on the datum feature to move the coordinates by using the edge finder. Thereby it is difficult to get to the previously located center. There is a chance to get a deviation of 0.001mm to 0.05mm in the hole location.

To eliminate hole positioning inaccuracies, WEDM technology will be used to manufacture the entire round or special holes in the mould plate in one setup [2]. The feature-related position tolerance (also known as FRTZ) is used to manage the relationship between a group of holes. FRTZ is used to ensure that matching pieces are properly assembled. Due to the lack of a datum reference frame whose job is to impose translational and rotational constraints on the component, assessing feature-related positional inaccuracy is a tough process. A mathematical model for three-dimensional feature-related positional inaccuracy was presented by Jiang, et al. [3]. Assemblability and functional compliance of products are affected by geometric variations. Because small part differences accumulate in large-scale

assembly and cause malfunctions [4]. To address form defects, a CAD model with integrated tolerancing was created [5]. Such deviations are not acceptable in the precision machining of tool parts. The addition of material condition like MMC/LMC increases the complexity of the manufacturing process [6]. Finally, it affects the tool assembly, function, life of the tool as well as component accuracy. The danger of wrongly locating the hole center each time to be overcome. Pandya, et al. [7] developed and implemented a computer assistance to help designers in allocating design sizes and tolerances that fulfil functional translation, rotation, and assembly limitations imposed on four common datum systems. In complex assemblies the need of alternative method is anticipated, in order to ensure the assembly of the parts right at first time [8]. Attempts were also done to understand the significance of datum-oriented errors in 2D assemblies [9] and 3D assemblies [10] and non-rigid assemblies [11].

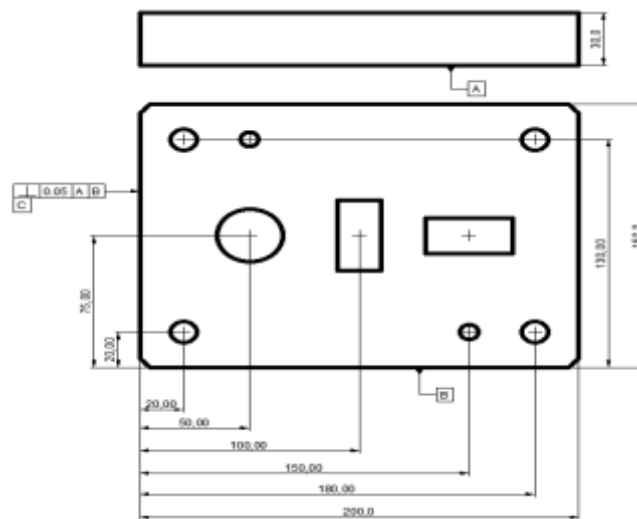


Figure 1: Sample part drawing of die plate

Section 2 of this article deals with the methodology of introducing tooling hole in the plates to overcome hole location problems. Case studies on the usage of tooling hole are discussed in Section 3 and it is concluded in Section 4.

2. Improve position tolerance utilizing Tooling Hole – Novel method

A tooling hole (TH) is an additional or existing hole placed in every plate of an assembly, which is accurately machined by reaming, boring, grinding, and WEDM operations by controlling hole cylindricity and perpendicularity. They are placed in the non-functional area of the part thickness. The tooling hole can be 5mm deep from the plate's top surface, with the rest relieved.

If the plate has to be heat treated, the TH should be finished thereafter. The tooling holes can be either one or two numbers depending on the availability of an external flat surface for pre-setting using a lever-type dial indicator. If one tooling hole is used, the hole and profile centers are located by dialing accurately machined datum feature (B) and taking the tooling hole (TH) center as the origin. This method doesn't require the machining of the second datum feature. Figure 2 shows the dimensioning of the hole and profile centers from the tooling hole center.

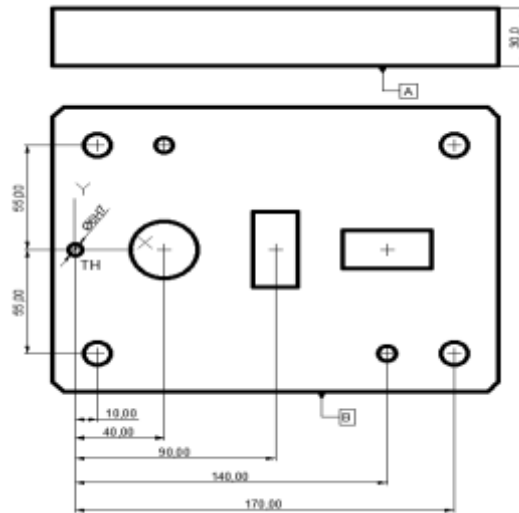


Figure:2 Dimensioning hole or profile centers from tooling hole centre

Two tooling holes are preferred when the plate size is too big to finish the datum features. Figure 3 shows the positioning of tooling holes to set the datum and also it reduces the manufacturing cost of tool parts as the accurate machining of datum feature is eliminated.

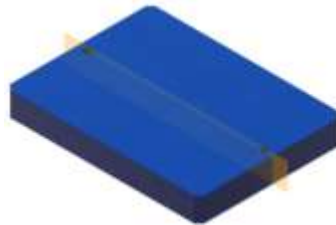


Figure: 3 Datum formed by two tooling holes

3. Case studies on Tooling hole applications

3.1 Part having uneven external profiles

Parts like machine housings, bodies, etc are processed primarily from casting. A sample diagram is shown in Figure 4, and it is not having any external flat surfaces. If the fixturing is not preferred for machining of flat surfaces due to a smaller number of samples, the butting surfaces are machined by milling. Identify two holes that are in line as tooling holes (TH) and locate them on a co-ordinate drilling machine to finish to the size. By taking one of the tooling hole center as origin, move the coordinates to drill, ream, and bore the remaining holes to the required size. This tooling hole concept permits to locate hole centers any number of times either during the inspection or reworks without any deviation.



Figure: 4 Machine part without external flat surfaces

3.2 Ease of verification of part dimensions that are going to be assembled

Usually, the parts that are going to be assembled will have a common hole center distance for screw holes, dowels, punches, inserts, but with various block sizes. If two datum features are used for dimensioning either by manual or computer-aided drafting, the dimensions need to be verified by suitable addition or subtraction. The process of dimensions verification is simplified by the tooling hole concept in the drawings. It is depicted in Figure 5 with two die plates having similar dimensions from tooling hole center for easy verification.

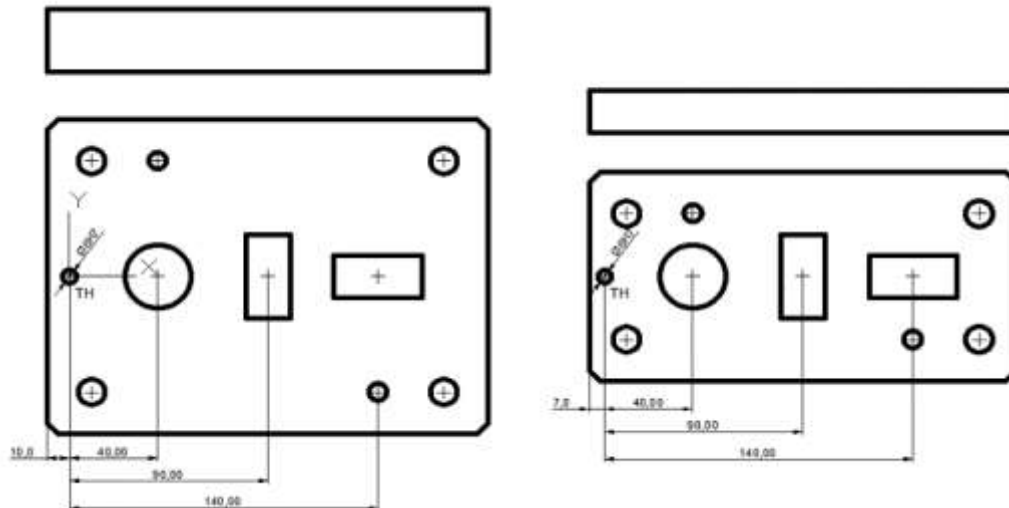


Figure:5 Die plates having similar dimensions for verification

3.3 Rapid location of hole centers utilizing TH for machining or inspection

Parts with one tooling hole will have one reference side machined to be set straight and the tooling hole center to be located by dialing directly or with an inserted plug gauge. The tooling hole center is set as the origin to check the position of other holes or profiles. This practice applies to all conventional machines like co-ordinate drilling, jig boring, or jig grinding machines. On non-conventional machines like EDM or Wire EDM, it is quickly done by setting the reference side straight followed by tooling hole location with an electrode tool. It is easier to set the datum as shown in Figure 3 on co-ordinate measuring machine (CMM) and from one hole center, other hole locations are checked. Figure 6 depicts an example of part drawing with a polar coordinate system, which can be quickly done by the tooling hole concept by taking a $\text{Ø}.875$ hole as a TH.

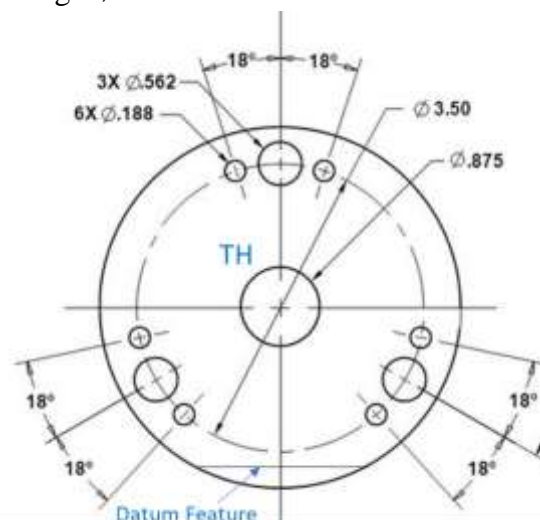


Figure:6 An example of part drawing with a polar coordinate system

3.4 Small capacity machines using TH for operations on lengthier workpieces

Sometimes it is necessary to drill the holes in the workpiece which is more than the travel capacity of the machine. In such cases, it is necessary to make several tooling holes with the known centerdistance, which is less than machine capacity, and in one line. This setup permits the completion of one set of holes by setting the datum straight and moving co-ordinates from the first tooling hole. The left-out holes are machined by resetting the workpiece to move co-ordinates from the second tooling hole. Figure 7 illustrates an example of a die plate with two tooling holes when its length is larger than the machine's capacity.

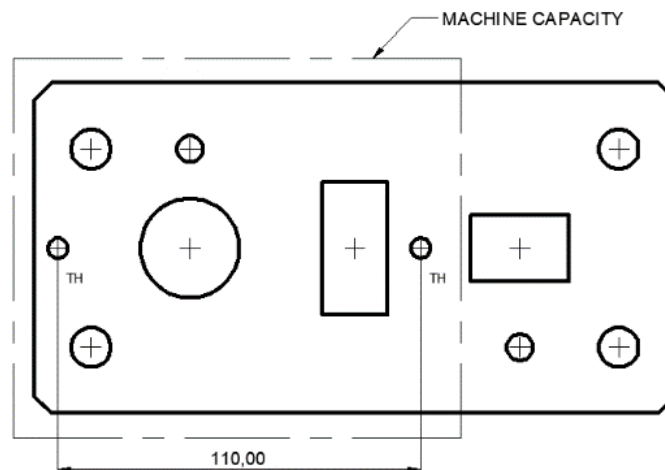


Figure:7 Sample die plate with two TH larger than machine capacity

3.5 Accurate positioning of angular holes using TH

It is the major advantage of tooling hole by accurate positioning for machining of angular holes. It can be either a single or compound angle. This can be done on co-ordinated drilling machine with a sine table attachment. It does not require any complicated CNC part program. Figure 8(a) depicts a part drawing with angular hole requirement in front and top views. Figure 8(b) shows the part setup (i.e., 30°) on sine table and a calculated distance (i.e., 20.00) to be moved from the tooling hole (TH) center to drill the hole $\text{Ø}10$.

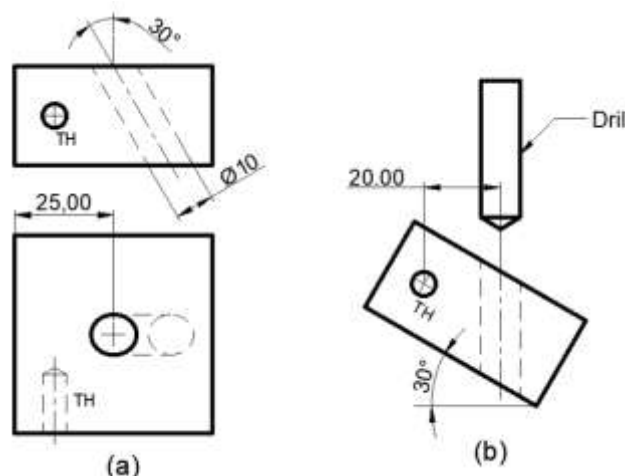


Figure:8 Sample part drawing and its machine setup for angular hole drilling

In this process an additional hole (i.e., tooling hole) is provided to fit a gauge pin. After tilting the workpiece on the sine table, the calculated movement is given to the workpiece to complete the required hole. In the end, the tooling hole needs to be blocked and protected for future reference.

4. Conclusion

The dimensioning of manufacturing part drawing is normally given from two datum features. As the tolerance is given for the machining of two perpendicular datum features, it is difficult to locate the same hole center accurately for repetitive tasks especially in series of machining operations. This is because the machine operator may choose to move x and y coordinate values from any point on datum features. The task of positioning the hole center is simplified by the addition of a tooling hole (TH) and moving the x , and y distances from its center. When two tooling holes are used then a datum can be set to machine or inspect the plates. It further improves the readability of the various part drawings of their similar center distance in their assembly. The machine capacity is enhanced by the addition of two or more tooling holes in line with their center distance being less than the machine's table travel distance. This concept will be best suitable for angular holes with either a single or compound angle that can be accurately positioned.

References

1. "ASME Y14.5-2009 Dimensioning and Tolerancing. American Society of Mechanical Engineers." 2009.
2. Shi, S., Wang, Z., & Li, X. (2012). An Improved Process for Enhancement of Positional Precision in WEDM. *Energy Procedia*, 17, 1339–1344. <https://doi.org/10.1016/j.egypro.2012.02.249>
3. Jiang, G., & Cheraghi, S. H. (2001). Evaluation of 3-D feature relating positional error. *Precision Engineering*, 25(4), 284–292. [https://doi.org/10.1016/S0141-6359\(01\)00080-0](https://doi.org/10.1016/S0141-6359(01)00080-0)
4. Movahedi, M. M., M. Khounsiavash, M. Otadi, and M. Mosleh (2017). "A New Statistical Method for Design and Analyses of Component Tolerance." *Journal of Industrial Engineering International* 13 (1): 59–66. doi:10.1007/s40092-016-0167-5.
5. Jbira, I., Tlija, M., Louhichi, B., & Tahan, A. (2017). CAD/Tolerancing integration: Mechanical assembly with form defects. *Advances in Engineering Software*, 114, 312–324. <https://doi.org/10.1016/j.advengsoft.2017.07.010>
6. Wu, Yuguang. 2018. "The Correlational Design Method of the Dimension Tolerance and Geometric Tolerance for Applying Material Conditions." *The International Journal of Advanced Manufacturing Technology* 97: 1697–1710. doi:10.1007/s00170-018-2052-4.
7. Pandya, G., Lehtihet, E. A., & Cavalier, T. M. (2002). Tolerance design of datum systems. *International Journal of Production Research*, 40(4), 783–807. <https://doi.org/10.1080/0020754011002101901>
8. Jietong, L., & Thimm, G. (2004). Constraint Generation for Alternative Dimensional specifications. *Computer-Aided Design and Applications*, 1(1–4), 675–681. <https://doi.org/10.1080/16864360.2004.10738313>
9. Meifa, H., and Z. Yanru. 2007. "Optimized Sequential Design of Two-dimensional Tolerances." *The International Journal of Advanced Manufacturing Technology* 33 (5–6): 579–593. doi:10.1007/s00170-006-0475-9.
10. Pierre, L., D. Teissandier, and J. P. Nadeau. 2009. "Integration of Thermomechanical Strains into Tolerancing Analysis." *International Journal on Interactive Design and Manufacturing* 3 (4): 247–263. doi:10.1007/s12008-009-0058-8.
11. Korbi, A., M. Tlija, B. Louhichi, and A. BenAmara. 2018. "CAD/tolerancing Integration: A New Approach for Tolerance Analysis of Non-rigid Parts Assemblies." *The International Journal of Advanced Manufacturing Technology* 98 (5–8): 2003–2013. doi:10.1007/s00170-018-2347-5.

Optimization of Composite Quality Attributes in Turning of SS410 Using PSI Method

*M. Sailaja, *Ch. Maheswara Rao, B. Sai Kiran, K. Swamy Tarun, S. Sushant Paul, PNBS Krishna, S. Kumar

*Assistant Professor, Department of Mechanical Engineering, ANITS, Sangivalasa-531162,
Visakhapatnam, A.P., India

B.Tech, Department of Mechanical Engineering, ANITS, Sangivalasa-531162,
Visakhapatnam, A.P., India

Corresponding Author: maheswararao.me@anits.edu.in

Abstract: In the current investigation, two carbide tool inserts—one coated (MT-CVD) and the other un-coated were used to test the machinability of SS410 grade material on a CNC turret lathe. Work materials are frequently used in petrochemical and mineral processing equipment, gate valves, Cutlery, Petroleum Refining and Petrochemical Processing Equipment, Ore Processing, Sugar Processing, Gate Valves, Press Plat etc. because they possess high strength, hardness, and corrosion resistance. The trials were carried out in a dry environment with different feed rates (0.1, 0.15, and 0.2 mm/rev), cutting speeds (1000, 1250, and 1500 RPM), and depths of cut (0.5, 1 and 1.5 mm) by using the $L_{18} (2^1 * 3^3)$ orthogonal array. Preference Selection Index (PSI) method, an MCDM tool, has been used to assess how changing process parameters affect Material Removal Rate (MRR), Roughness Characteristics (R_a and R_t), and Dimensional Deviation (DD) performance. The PSI data are used to determine the ideal process parameters and they found at Tool Type: Coated (level 1), 1250 RPM (level 2), 0.1 mm/rev (level 1), and 0.5 mm (level 1), accordingly, are the speed, feed, and DOC parameters. Finally, Signal-to-Noise ratios and ANOVA were used to analyse the generated composite index values. According to the investigation, Depth of cut significantly influences the various replies. It has been determined how parameters like depth of cut and tool type interacts. The models were created for the composite index, and the goodness of fit was assessed by plotting residual plots. It was determined that the errors follow normality and constant variance, making them the most accurate and adequate models because they are best fitted.

Key words: Orthogonal Array (OA), Preference Selection Index (PSI) method, Material Removal Rate (MRR), Roughness Characteristics (R_a and R_t), Dimensional Deviation (DD), Signal-to-Noise (S/N) ratios and ANOVA

1. Introduction

Turning is a machining process used to create cylindrical objects. It can be defined as the machining of an exterior surface in its most basic form: 1) While the work item is rotating, 2) With a single-point cutting tool, 3) with the cutting tool feeding parallel to the axis of the work piece and at a distance sufficient to remove the work's outer surface. The performance and wear of the mating parts are significantly influenced by the quality of the mating components whenever two machined surfaces come into contact with one another. These surface irregularities on the work item might vary in height, shape, arrangement, and direction depending on a number of variables, including: Depth of cut, Feed rate, Cutting

speed, Material removal rate, Cutting tool wear & other parameters. The term optimization describes the art and science of efficiently allocating limited resources. The Taguchi approach is a well-known technique that offers a way for design and process optimization that is methodical and effective. In order to address material selection MCDM issues, Maniya and Bhatt presented the PSI technique in 2010. The PSI method does not necessitate establishing the relative relevance of the criteria, making it unnecessary to establish criteria weights, in contrast to the majority of Multiple Criteria Decision-Making (MCDM) techniques. In situations when there is a disagreement over the relative relevance of different criteria, the technique is thus especially helpful. Actually, the PSI technique uses an objective methodology to calculate the criteria weights, such as the standard deviation or entropy method, by using the data presented in the decision matrix. There are two well-established vapour processing approaches for coating: Chemical Vapour Deposition (CVD) and Physical Vapour Deposition (PVD) (e.g. evaporation, sputtering and ion plating). In recent years, moderate temperature CVD (MTCVD) has been developed to address the problem of TRS reduction. Because metal-organic compounds such as acetonitrile are used instead of methane or nitrogen, the deposition temperature in MTCVD can be reduced to 700-800 C. At the moment, the most prevalent coatings on the market are TiC, TiN, Ti(C,N), TiAlN, and Al₂O₃, with Ti(C,N) being a desirable coating that offers better hardness and abrasive wear resistance than typical TiN coating and outstanding chemical stability superior to TiC.

Do Duc Trung [1] optimized turning process parameters using (PEG), (PSI), and Collaborative Unbiased Rank List Integration are three MCDM techniques that were employed (CURLI). Using Steel SB410 as a test substance and TiN is used to coat cutting instruments. Determined To obtain the “minimum” surface roughness and “maximum” MRR at the same time, it is necessary to select the cutting velocity, feed rate and depth of cut. **He Le Hoang Anh et. al. [2]** determined the maximum Material Removal Rate and the minimal surface roughness by combining the Taguchi method with the PSI approach on 0A4 steel where the cutting device is a face milling cutter constructed from High Speed Steel (HSS). **Arti Saxena et. al. [3]** used the H-13 (P8) material is turned and drilled with the cutting tools CNMG190616-M5-TM2501 and SD205A-1050-056-12R1-P, respectively. Taguchi L9 array analysis and additional ANOVA analysis are then used to improve the performance of the CNC machine by taking into account the input control factors cutting speed (CS), feed rate (FR), and depth of cut (DOC). **P. Sivaiah and D. Chakradhar [4]** examined the use of TGRA to optimise multiple responses when turning 17-4 Precipitation Hardened Stainless Steel (PH SS) under the jetting of liquid nitrogen. The TGRA result showed that the enhanced turning process could be achieved at cutting velocity of 120.89 m/min, feed rate of 0.048 mm/rev, and depth of cut of 0.4 mm. **Ali Kalyon et. al. [5]** analyzed the amounts of influence that machining parameters had on FR and Ra (ANOVA), to simultaneously minimise FR and Ra, a grey relational grade (GRG) was calculated. According to the ANOVA results based on GRG, the feed rate was followed by the cutting depth, The chrome ratio, cutting speed, feed rate, and cutting depth that produced the best results were 12%, 100 m/min, 0.05 mm/r, and 0.1 mm, respectively. **Muhammad Jamil et.al. [6]** applied the RSM-based GRA to discover the trade-off between four matrices under EMQL. For multi-objective optimisation, the tribological behaviour of cutting speed, feed, depth of cut, and EMQL flow rate on sustainable leading responses (MRR, tool life, surface roughness, and power consumption) was simulated and analysed. **Ponugoti Umamaheswarrao et.al. [7]** optimised the cutting parameters by utilising the Technique for

Order Preference by Similarity to Ideal Solution (TOPSIS) on AISI 52100 steel using polycrystalline cubic boron nitride (PCBN) tools by hard turning machining process. The use of analysis of variance (ANOVA) is used to determine how process parameters affect results. **Umamaheswarrao P et.al. [8]** conducted experiment on AISI 52100 steel by hard turning using multi-objective optimization to produce the best surface quality, machining force. experiments are carried out by Taguchi L9 orthogonal array, using the MINITAB14 software package, a parametric inquiry is conducted to determine the impact of input parameters on the response. **R. Vara Prasad et.al. [9]** focussed on the responses of material removal rate and surface roughness at various combinations of speed and feed depth of cut. Machining is done for AA7075 work parts on the L9 orthogonal array of Taguchi by utilizing the preference selection index approach. **Dr. G. Bhanodaya Reddy et.al. [10]** investigated parametric optimization of turning of 7075 aluminium alloy utilising Taguchi L27 orthogonal array, which was used for both DOE and S/N to examine the effects of the selected parameters. The outcome shows that different cutting parameters have distinct effects on cutting force, surface roughness, and temperature for two samples when comparing the samples. **Maya Radune et.al. [11]** focused on the primary high energy ball milling (HEBM) parameters of milling time (MT), ball to powder weight ratio (BPWR), and milling speed (MS) on the size of the CaCO₃ crystallite were examined using Taguchi's method. To demonstrate the efficiency of the Taguchi optimization method, a confirmation test with a 90% confidence level was conducted. The examination of the signal-to-noise (S/N) ratio was used to establish the best milling parameter combination. **Do Duc Trung et.al. [12]** conducted the experiment on by using a CNC milling machine, a TiAlN cutting tool, SCM400 steel for the experimental material, and Caltex Aquatex 3180 oil as the coolant. The impact of input parameters on output parameters has been identified by Pareto chart analysis of experimental findings. The input parameter values have been determined using the Moora method. **Nguyen Huu Quang et.al. [13]** made an article that presents a multi-objective optimization of the turning process analysis with four input parameters— nose radius, cutting velocity, feed rate, and cutting depth the experimental matrix was designed using the Taguchi method. The multi-objective optimization problem has been solved using Copra's technique. In the end, the ideal values of the minimum surface roughness and the maximum MRR were found. **He Le Hoang Anh et.al. [14]** studied the machinability of vertical milling machine to mill this sort of 060A4 steel using a multi-objective optimization approach. A face milling cutter constructed of High Speed Steel (HSS) is the cutting tool. The best value of three input parameters has been calculated using the Taguchi technique and the PSI method in conjunction to concurrently meet the requirements of the least surface roughness and the maximum Material Removal Rate (MRR). **Nguyen Huu-Phan et.al. [15]** worked on the process parameters of titanium-based PMEDM for machining die steels were optimised using Taguchi PSI. According to the trials and investigations, PSI, TOPSIS, and MOORA outperform GRA in multi objective optimization in PMEDM utilising titanium powder. Because of their relevance in determining spark energy, the electrode material and powder concentration may have a considerable impact on performance measurements. **Fulya Erdemir, Murat Tolga Ozkan [16]** used the Taguchi method to design the experiment set, and 27 experimental sets were created instead of 729 experimental sets, saving time and money. Full factorial analysis was performed in the ANSYS environment for the applied method, and the method used in the analysis is verified and detailed in the article. **S. Ghosh et. al. [17]** The goal of this work

is to use the Taguchi L9(34) Method to straight turn AISI 1018. Here two vegetable-based cutting fluids and a commercial semi-synthetic cutting fluid are employed and values of response variables are studied to determine whether utilising vegetable-based cutting fluids for sustainable machining improves the performance of response machining parameters. **Dipayan Mukherjee et. al. [18]** done this research, Taguchi Grey relational analysis is used to maximise response qualities such as surface roughness and material removal rate. The Taguchi technique was used to undertake 18 experimental runs on an L18 mixed-orthogonal array. A grey relational grade derived from grey relational analysis is used to determine optimum parameters with numerous performance attributes. **Hilmi Pekşen & Ali Kalyon [19]** evaluated the machinability of AISI 430 stainless steel based on the cutting insert coating type, cutting speed, and feed rate. Experiments were conducted out in a moist environment with a constant 1.5 mm depth of cut. By extracting an 801 900 mm³ volume of chip from the working material, VB and Ra were investigated. The Taguchi-based GRA was used to identify the best processing settings. **Dušan Petković et. al. [20]** described the use of a new MCDM method, the PSI method, for tackling discrete machining optimization issues. The detailed computing technique of the PSI method is presented by addressing two case studies dealing with material machinability and the selection of the best cutting fluid for the particular machining application. **Ning Li et. al. [21]** optimised the design of process parameters for turning Ti-6Al-4V under dry conditions including kind of inserts, feed rate, and depth of cut. The depth of cut has the greatest impact, according to the range analysis's findings. **Zahid Hussain [22]** interchanged two phases straight cemented tungsten carbide-cobalt mixed (WC-Co) By Taguchi coupled grey relational analysis, a insert grade (CSTC—K20) tool has been introduced for the best turning parameters in the turning process. It is advised that metal cutting enterprises utilise these optimal ways to decrease material waste and production costs while machining EN31-535A99 SS. **D. Palanisamy et. al. [23]** demonstrated that improved surface finish is obtained by combining greater machining speed with lower feed, and that machining depth has a large impact on surface roughness. Precipitation In the hardened state, 17Cr-4Ni is used as a PH stainless steel. Different machining parameters were taken into consideration as responses, including tangential force, surface roughness, and vibration components in three axes. **M. V. Satish Kumar et. al. [24]** optimised the CNC turning parameters for cutting EN19 alloy steel. Analysis of variance is used to determine how parameters affect MRR and surface roughness (ANOVA). Optimization is done using the desirability technique. **Engin Nas et.al. [25]** addressed an approach based on the Taguchi method with grey relational analysis for enhancing the turning parameters of hardened DIN 1.2344 hot work tool steel (54 HRC) with various performance traits. Cryogenically treated and untreated uncoated carbide cutting tools were used in dry turning testing. **N.M. Vaxevanidisa et.al. [26]** examined the effects of rotating speed, feed rate, and depth of cut on the machinability properties of a high-leaded brass alloy (CuZn39Pb3). It was decided to use an L18 mixed-level Taguchi Orthogonal Array experimental design. **A. Johnson Santhosh et.al. [27]** generated the Face Centred Central Composite Design (CCD) technique is used in the Coded and Actual Empirical model. In order to determine the ideal machining process parameters, this study recommends combining Artificial Neural Network (ANN) with Genetic Algorithm (GA) technique. **Muhammad Ali Khan et.al. [28]** developed the best machining parameter by optimising the formulated multi-objective function. To maximise the efficiency of the machining process, concurrent responses were optimised with the best-suited values of the input parameters.

According to the results of the analysis of variance, the most effective parameter is feed, followed by cutting condition. **Djordje Cica et.al. [29]** presented the results of an experimental investigation and multi-objective optimization of the machining parameters for turning Inconel 718 with coated carbide tools under high pressure jet assistance. The experimental design made use of the Taguchi L27 orthogonal array, and the analytic hierarchy process was used to determine the weights of the responses. **Saran Keeratihattayakorn et.al. [30]** developed a fast tool servo compensation technique to reduce out-of-roundness when milling with a traditional CNC machine. A conventional CNC machine was used to fabricate and instal the fast tool servo with piezoelectric actuator. A representative profile was created after analysis of the profiles of machined femoral heads.

2. Experimental Details

In current experiment are Alloy 410 (UNS S41000) of a 12% Chromium Martensitic stainless steel with a wide range of mechanical qualities that has used. The alloy possesses great strength and hardness as well as outstanding corrosion resistance. When annealed, 410 is ductile and may be produced. It retains its magnetic properties when annealed and heat treated. It has extensive applications in Cutlery, Petroleum Refining and Petrochemical Processing Equipment, Ore Processing, Sugar Processing, Gate Valves, Press Plates. The chemical properties and mechanical features of work material used depicted in table 1&2 respectively. In current work, The experiment were planned by taking Tool Type, Speed ,Feed rate, DOP as variable factors showing in Table 3, a suitable L18 design considered and the experiment were performed as per the chart given in. The CNC Turret Lathe used for the expirement and the finished samples were shown in figure 1& 2 respectively.



Figure 1. CNC Turret Lathe



Figure 2. Machined Components Samples

Material	Composition%	Material	Composition%
Chromium	11.5 min- 13.5 max	Phosphorus	0.04
Nickel	0.75	Sulfur	0.03
Carbon	0.08 min- 0.15 max	Silicon	1.0
Manganese	1.0	Iron	Balance

Table 1:
Chemical
Composition of
SS410

Table 2: Mechanical Properties of SS410

Yield Strength 0.2% Offset		Ultimate Tensile Strength		Elongation in %	Hardness (Max)
Psi	(Mpa)	Psi	(MPa)	34	96 Rb
42,000	290	74,000	510		

Table 3: Process Parameters and their Levels

	Level-1	Level-2	Level-3
Tool type	Non Coated	Coated	
Speed, RPM	1000	1250	1500
Feed, mm/Rev	0.1	0.15	0.2
DoC, mm	0.5	1	1.5

Table 4. Input Parameters & L18 OA

S.No.	Tool Type	Speed, RPM	Feed, mm/rev	DoC, mm
1	Non Coated	1000	0.1	0.5
2	Non Coated	1000	0.15	1
3	Non Coated	1000	0.2	1.5
4	Non Coated	1250	0.1	0.5
5	Non Coated	1250	0.15	1
6	Non Coated	1250	0.2	1.5
7	Non Coated	1500	0.1	1
8	Non Coated	1500	0.15	1.5
9	Non Coated	1500	0.2	0.5
10	Coated	1000	0.1	1.5
11	Coated	1000	0.15	0.5
12	Coated	1000	0.2	1
13	Coated	1250	0.1	1
14	Coated	1250	0.15	1.5
15	Coated	1250	0.2	0.5
16	Coated	1500	0.1	1.5
17	Coated	1500	0.15	0.5
18	Coated	1500	0.2	1

3. Proposed Methodology

Step1: Define the objective, attributes and alternatives.

Step2: Formation of the decision matrix based on the available information.

Step3: Determination of Normalized decision matrix by following equations:

$$N_{ij} = \frac{X_{ij}}{X_{ij}^{\max}}, i = 1, 2 \dots m; \text{ for beneficial criteria}$$

$$N_{ij} = \frac{X_{ij}^{\min}}{X_{ij}}, i = 1, 2 \dots m; \text{ for non – beneficial criteria}$$

Step4: Determine the mean value of the normalized data by using following equation:

$$N = \frac{1}{n} \sum_{i=1}^m N_{ij}$$

Step5: Determine the preference variation value from the mean value by following equation:

$$\varphi_j = \sum_{i=1}^m [N_{ij} - N]^2$$

Step6: Determine the deviation in the preference value.

$$\Omega_j = [1 - \varphi_j]$$

Step7: Determine the criteria weights by following equation:

$$w_j = \frac{\Omega_j}{\sum_{j=1}^n \Omega_j}$$

$$\text{subjected to } \sum_{j=1}^m w_j = 1$$

Step8: Preference selection index is calculated for each alternative by

$$\theta_i = \sum_{j=1}^n N_{ij} w_j$$

Step9: Ranking the alternatives in descending order of preference selection index value of θ_i .

4. Results & Discussion

The output responses of Material removal rate, roughness and dimensional deviation measured were depicted in Table 5. By following the proposed methodology steps the normalized and weighted normalised values calculated and given in the table 6&7 respectively.

Table 5 : Measured Output Responses

S.No.	MRR	Ra	Rt	DD
1	0.0500	0.231	1.973	0.1413
2	0.1500	0.487	3.524	0.0688
3	0.3000	0.635	4.521	0.0675
4	0.0625	0.275	2.276	0.0438
5	0.1875	0.847	5.717	0.0100
6	0.3750	0.614	4.142	0.1238
7	0.1500	0.372	3.928	0.0425
8	0.3375	0.406	3.140	0.0638
9	0.1500	1.266	5.734	0.1600
10	0.1500	0.214	3.463	0.0638
11	0.0750	0.319	2.282	0.0413
12	0.2000	0.651	3.833	0.0613
13	0.1250	0.217	1.635	0.0200
14	0.2813	0.325	2.921	0.1763
15	0.1250	0.412	3.125	0.0025
16	0.2250	0.341	3.836	0.1063
17	0.1125	0.309	2.229	0.0320
18	0.3000	0.668	3.483	0.0750

Table 6: Normalised Values(N_{ij})

S.No.	MRR	Ra	Rt	DD
1	0.133	0.928	0.829	0.018
2	0.400	0.440	0.464	0.036
3	0.800	0.337	0.362	0.037
4	0.167	0.778	0.718	0.057
5	0.500	0.253	0.286	0.250
6	1.000	0.349	0.395	0.020
7	0.400	0.576	0.416	0.059
8	0.900	0.528	0.521	0.039
9	0.400	0.169	0.285	0.016
10	0.400	1.000	0.472	0.039
11	0.200	0.672	0.716	0.061
12	0.533	0.329	0.427	0.041
13	0.333	0.986	1.000	0.125
14	0.750	0.658	0.560	0.014
15	0.333	0.520	0.523	1.000
16	0.600	0.628	0.426	0.024
17	0.300	0.693	0.734	0.078
18	0.800	0.321	0.469	0.033

Table 7 : Weighted Normalized values

S.No.	MRR	Ra	Rt	DD	θ_i	S/N of θ_i
1	-0.0677	-0.2534	1.1454	0.0071	0.8314	-1.6053
2	-0.2036	-0.1200	0.6413	0.0145	0.3322	-9.5725

3	-0.4072	-0.0920	0.4999	0.0148	0.0155	-36.1929
4	-0.0848	-0.2124	0.9929	0.0228	0.7186	-2.8707
5	-0.2545	-0.0689	0.3953	0.0999	0.1718	-15.3011
6	-0.5090	-0.0952	0.5456	0.0081	0.0505	-25.9320
7	-0.2036	-0.1572	0.5753	0.0235	0.2380	-12.4670
8	-0.4581	-0.1440	0.7197	0.0157	0.1333	-17.5056
9	-0.2036	-0.0461	0.3941	0.0062	0.1506	-16.4413
10	-0.2036	-0.2729	0.6526	0.0157	0.1918	-14.3449
11	-0.1018	-0.1834	0.9903	0.0242	0.7294	-2.7410
12	-0.2715	-0.0898	0.5896	0.0163	0.2447	-12.2288
13	-0.1697	-0.2691	1.3822	0.0500	0.9934	-0.0578
14	-0.3818	-0.1797	0.7737	0.0057	0.2179	-13.2349
15	-0.1697	-0.1419	0.7229	0.3997	0.8110	-1.8166
16	-0.3054	-0.1713	0.5891	0.0094	0.1219	-18.2820
17	-0.1527	-0.1890	1.0139	0.0312	0.7034	-3.0561
18	-0.4072	-0.0875	0.6488	0.0133	0.1675	-15.5214

For the weighted Normalised Preference selection values are obtained Taguchi analysis and ANOVA were employed to analyse the ratio's of depicted in Table 8&9 respectively, main effect plot and residual plot drawn also were shown in figures 3&4 respectively. From the result it is noticed that depth of cut has highest influence over the composite index significant interaction effects between Speed* Speed and DOC* Tool type were also well noticed. Residual plots showed that the modals prepared were best fit and accurate.

Table 8: Response Table for Signal to Noise Ratios Larger is better

Level	Tool Type	Speed	Feed	Doc
1	-9.031	-12.781	-8.271	-4.755
2	-15.321	-9.869	-10.235	-10.858
3		-13.879	-18.022	-20.915
Delta	6.289	4.010	9.751	16.160
Rank	3	4	2	1

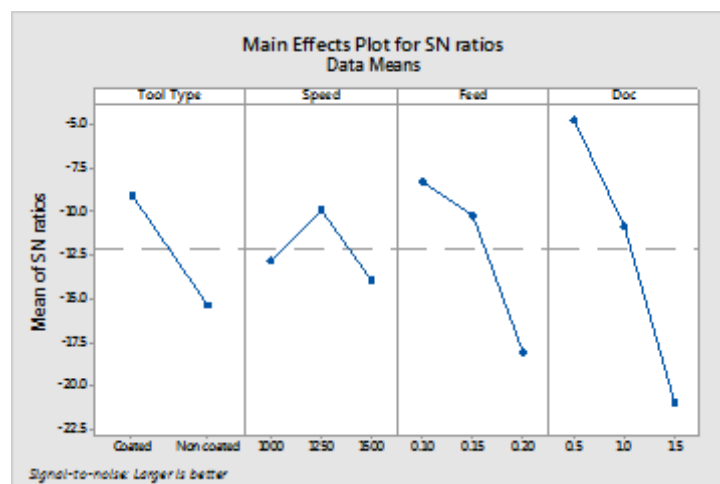


Figure 3. Main Effects plot for S-N ratios of θ_i .

Table 9 : Analysis of Variance for θ_i .

Source	DF	Adj SS	Adj MS	F	P
Model	13	1.57975	0.121520	3.47	0.119
Linear	4	1.10709	0.276774	7.91	0.035

Speed	1	0.03606	0.036063	1.03	0.367
Feed	1	0.26602	0.266024	7.61	0.051
Doc	1	0.50829	0.508292	14.53	0.019
Tool Type	1	0.10410	0.104104	2.98	0.160
Square	3	0.11531	0.038437	1.10	0.447
Speed*Speed	1	0.09981	0.099812	2.85	0.166
Feed*Feed	1	0.01822	0.018225	0.52	0.510
Doc*Doc	1	0.00017	0.000171	0.00	0.948
2-Way Interaction	6	0.17905	0.029842	0.85	0.590
Speed*Feed	1	0.01326	0.013263	0.38	0.571
Speed*Doc	1	0.01011	0.010111	0.29	0.619
Speed*ToolType	1	0.00997	0.009967	0.29	0.622
Feed*Doc	1	0.00363	0.003629	0.10	0.763
Feed*Tool Type	1	0.00368	0.003679	0.11	0.762
Doc*Tool Type	1	0.10425	0.104251	2.98	0.159
Error	4	0.13989	0.034973		
Total	17	1.71964			

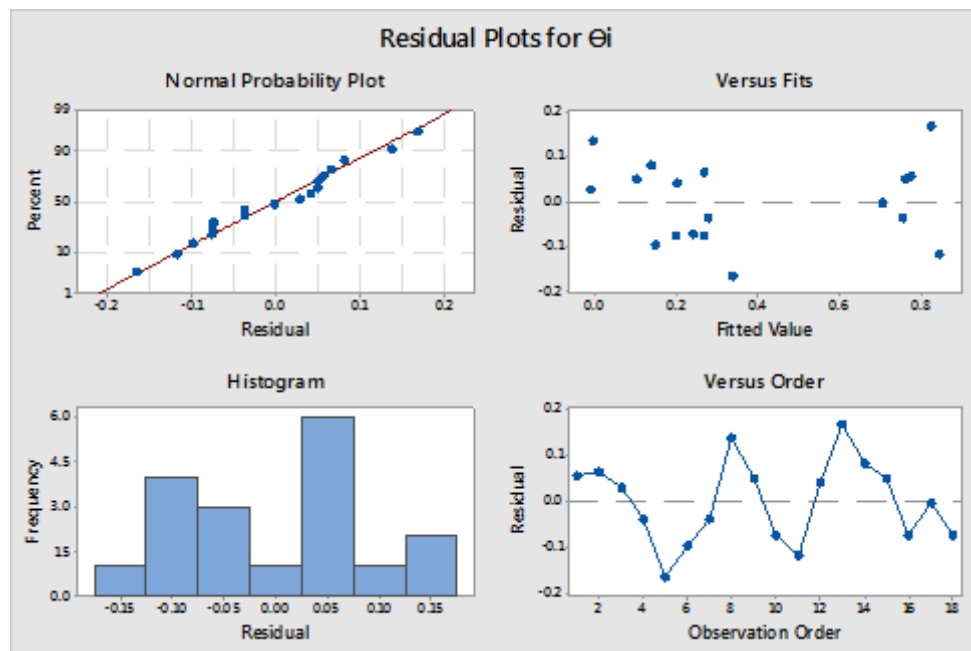


Figure 4. Residual Plots for θ_i .

5. Conclusions

The following conclusions can be drawn from Taguchi and ANOVA analysis.

- 1) DOC is found to be the most significant factor among all parameters.
- 2) Interaction effects of speed* speed and DOC * Tool type are found to be significant.
- 3) Residual plots showed that the models prepared are more significant and accurate as they following normal distributions and constant variance.
- 4) The proposed method of Preference Selection Index proves significant applications in solving many Industrial problems with less efforts and computational simplicity.

References

- 1) Duc Trung, D. (2022) "Multi-criteria decision making of turning operation based on Peg.psi and curli methods," <https://doi.org/10.1051/mfreview/2022007>

- 2) Anh, H.L. et al. (2021) "Optimization of milling process by Taguchi-Psi Method," E3S Web of Conferences, 309, p. 01019. <https://doi.org/10.1051/e3sconf/202130901019>
- 3) Saxena, A. et al. (2021) "Optimization of input machining parameters in SBCNC-60 for turning and drilling on p8 (H-13, HSS) material," The International Journal of Electrical Engineering & Education, 58(2), pp. 640–663. <https://doi.org/10.1177/0020720920988487>
- 4) Sivaiah, P. and Chakradhar, D. (2018) "Multi Performance Characteristics Optimization in cryogenic turning of 17-4 PH stainless steel using Taguchi Coupled Grey Relational Analysis," Advances in Materials and Processing Technologies, 4(3), pp. 431–447. <https://doi.org/10.1080/2374068x.2018.1452132>
- 5) Kalyon, A., Günay, M. and Özyürek, D. (2018) "Application of grey relational analysis based on Taguchi Method for optimizing machining parameters in hard turning of high chrome cast iron," Advances in Manufacturing, <https://doi.org/10.1007/s40436-018-0231-z>
- 6) Jamil, M. et al. (2019) "Multi-response optimisation of machining aluminium - 6061 under eco-friendly electrostatic minimum quantity lubrication environment," International Journal of Machining and Machinability of Materials, 21(5/6), p. 459 <https://doi.org/10.1504/ijmmm.2019.103137>
- 7) Umamaheswarrao, P. et al. (2019) "Optimizing cutting parameters in hard turning of AISI 52100 steel using topsis approach," Journal of Mechanical and Energy Engineering, 3(3), pp. 227–232. <https://doi.org/10.30464/jmee.2019.3.3.227>
- 8) Umamaheswarrao, P. et al. (2018) "Multi objective optimization of process parameters for hard turning of AISI 52100 steel using hybrid GRA-PCA," Procedia Computer Science, 133, pp. 703–710. <https://doi.org/10.1016/j.procs.2018.07.129>
- 9) R. Vara Prasad et. al. (2018) "Application of preference selection index (PSI) method for the optimization of turning process parameters" International Journal of Modern Trends in Engineering & Research, 5(5), <http://dx.doi.org/10.21884/IJMTER.2018.5152.IISGD>
- 10) Reddy, D.G. (2017) "Parametric optimization of lathe turning for Al-7075 alloy using Taguchi: An experimental study," IOSR Journal of Mechanical and Civil Engineering, 14(03), pp. 39–45. <https://doi.org/10.9790/1684-1403063945>
- 11) Radune, M. et al. (2022) "Use of Taguchi method for high energy ball milling of CaCO₃," International Journal of Mechanical and Materials Engineering, 17(1). <https://doi.org/10.1186/s40712-021-00140-8>
- 12) Trung, D.D. et al. (2021) "Combination of taguchi method and Moora method for multi-objective optimization of SCM400 steel milling process," E3S Web of Conferences, 309, p. 01092. <https://doi.org/10.1051/e3sconf/202130901092>
- 13) Trung, D.D. et al. (2021) "Optimization study on turning process by using Taguchi-COPRAS method," <https://doi.org/10.1051/e3sconf/202130901010>.
- 14) He Le Hoang Anh.et.al.(2021), "Optimization of Milling Process by Taguchi-PSI Method", E3S Web of Conferences 309, 01019, <https://doi.org/10.1051/e3sconf/202130901019>
- 15) Huu-Phan, N. et al. (2019) "Multi-criteria decision making using preferential selection index in titanium based die-sinking PMEDM," Journal of the Korean Society for Precision Engineering, 36(9), pp. 793–802. <https://doi.org/10.7736/kspe.2019.36.9.793>
- 16) Erdemir, F. And Özkan, M.T. (2022) "Application of taguchi method for optimization of design parameters in enhancement the robust of 'C' type snap-fits," Journal of Polytechnic [Preprint]. <https://doi.org/10.2339/politeknik.1076061>
- 17) S. Ghosh et al. (2022) "Optimization of cutting parameters of AISI 1018 Low Carbon Mild Steel in turning using green cutting fluid by Taguchi method," Journal of Mechanical Engineering: Prakash, 01(01), pp. 62–67. <https://doi.org/10.56697/jmep.2022.1108>
- 18) Mukherjee, D., Ranjan, R. and Moi, S.C. (2022) "Multi-response optimization of surface roughness and MRR in turning using Taguchi Grey Relational Analysis (TGRA)," International Research Journal of Multidisciplinary Scope, 03(02), pp. 01–07. <https://doi.org/10.47857/irjms.2022.v03i02.068>
- 19) Pekşen, H. and Kalyon, A. (2021) "Optimization and measurement of flank wear and surface roughness via Taguchi based grey relational analysis," Materials and Manufacturing Processes, 36(16), pp. 1865–1874. <https://doi.org/10.1080/10426914.2021.1926497>
- 20) Petković, D. et al. (2017) "Application of the performance selection index method for solving machining MCDM problems," Facta Universitatis, Series: Mechanical Engineering, 15(1), p. 97. <https://doi.org/10.22190/fume151120001p>
- 21) Li, Ning et. al. (2019). Multi-response optimization of Ti-6Al-4V turning operations using Taguchi-based grey relational analysis coupled with kernel principal component analysis. Advances in Manufacturing. doi:10.1007/s40436-019-00251-8
- 22) Hussain, Zahid (2020). Multi performance optimization in machining of EN31-535A99SS with interchangeable straight cemented tungsten carbide-cobalt mixed (WC-Co) insert grade (CSTC—K20) using Taguchi coupled grey relational analysis. SN Applied Sciences, 2(2), 197–. doi:10.1007/s42452-020-2011-1

- 23) Palanisamy, D.; Balasubramanian, K.; Manikandan, N.; Arulkirubakaran, D.; Ramesh, R. (2019). Machinability analysis of high strength materials with Cryo-Treated textured tungsten carbide inserts. *Materials and Manufacturing Processes*, 34(5), 502–510. doi:10.1080/10426914.2019.1566612
- 24) M. V. Satish Kumar et.al. (2020) Optimization of CNC Turning Parameters in Machining EN19 using Face Centered Central Composite Design Based RSM, *International Journal of Recent Technology and Engineering (IJRTE)*. DOI:10.35940/ijrte.B3923.079220
- 25) Nas, Engin; Altan Ozbek, Nursel (2019). Optimization the Machining Parameters in Turning of Hardened Hot Work Tool Steel Using Cryogenically Treated Tools. *Surface Review and Letters*, (), S0218625X19501774–. doi:10.1142/S0218625X19501774
- 26) Vaxevanidis, N.M.; Fountas, N.A.; Koutsomichalis, A.; Kechagias, J.D. (2018). Experimental investigation of machinability parameters in turning of CuZn39Pb3 brass alloy. *Procedia Structural Integrity*, 10(), 333–341. doi:10.1016/j.prostr.2018.09.046
- 27) A. Johnson Santhosh; Amanuel Diriba Tura; Iyasu Tafese Jiregna; Wendimu Fanta Gemechu; N. Ashok; Murugan Ponnusamy; (2021). Optimization of CNC turning parameters using face centred CCD approach in RSM and ANN-genetic algorithm for AISI 4340 alloy steel . *Results in Engineering*, doi:10.1016/j.rineng.2021.100251
- 28) Khan, Muhammad Ali; Jaffery, Syed Husain Imran; Khan, Mushtaq; Younas, Muhammad; Butt, Shahid Ikramullah; Ahmad, Riaz; Warsi, Salman Sagheer (2020). Multi-objective optimization of turning titanium-based alloy Ti-6Al-4V under dry, wet, and cryogenic conditions using gray relational analysis (GRA). *The International Journal of Advanced Manufacturing Technology*, doi:10.1007/s00170-019-04913-6
- 29) Cica, Djordje; Kramar, Davorin (2019). Multi-objective optimization of high-pressure jet-assisted turning of Inconel 718. *The International Journal of Advanced Manufacturing Technology*, doi:10.1007/s00170-019-04513-4 3
- 30) Keeratihattayakorn, Saran; Tangpornprasert, Pairat; Prasongcharoen, Warich; Virulsri, Chanyaphan (2020). Out-of-roundness compensation technique in machining of femoral head prosthesis using conventional CNC machine. *The International Journal of Advanced Manufacturing Technology*, doi:10.1007/s00170-020-05149-5

Evaluation of Suitable Wire EDM Process Parameters Using AHP & TQLFA

*Ch.Maheswara Rao, *K.Venkata Subbaiah, N.Sai, T.Chaithanya, M.Rajesh,
K.Sriharsha, Y.Surendra Kumar

*Assistant Professor, Department of Mechanical Engineering, ANITS, Sangivalasa-531162,
Visakhapatnam, A.P., India

*Senior Professor, Department of Mechanical Engineering, Andhra University,
Visakhapatnam-530003, A.P., India

Corresponding Author email: maheswararao.me@anits.edu.in

Abstract: The aim of the current work is to create an acceptable set of Wire EDM process parameters for cutting AISI1040 steel. The work material offers good heat resistance capabilities as well as resistance to chloride pitting and crevice corrosion cracking. As a result, it mostly fits in with marine engineering, nuclear power plants, boilers, pressure vessels and gas turbines, etc. The controllable parameters during machining have been identified as flushing pressure (FP), pulse-on-time (T_{ON}), pulse-off-time (T_{OFF}), wire tension (WT), wire feed (WF), and servo voltage (SV). The responses obtained from Material Removal Rate (MRR) and Surface Roughness Characteristics (R_a & R_z) were optimized using Analytical Hierarchy Process (AHP) combined with Taguchi's Quality Loss Function Analysis (TQLFA) methods. L18 OA ($2^1 \times 3^5$) was used. Here, the criterion weights are determined using AHP, and the results are produced as consistency ratio (CR) = $0.04 < 0.1$, $\lambda_{max} = 3.039$, $W_{MRR} = 0.637$, $W_{R_a} = 0.258$, and $W_{R_z} = 0.105$ respectively. Pulse-Off-Time (T_{OFF}) is discovered to be the highest influencing factor and Wire Feed (WF) to be the lowest influencing factor for providing the best values of the quality loss function from the Analysis of Means (ANOM) and Signal-to-Noise (S/N) ratio analysis. The ideal process parameter setting was achieved at the following values: Flushing Pressure: 8 kg/cm² (level 2), Pulse-On-Time: 125 μ s (level 3), Pulse-Off-Time: 55 μ s (level 1), Wire Tension: 6 kg-f (level 3), Wire Feed: 4 mm/min (level 3) and Servo Voltage: 20 volts (level 1), respectively.

Keywords: Analytical Hierarchy Process (AHP), Taguchi's Quality Loss Function Analysis (TQLFA), Material Removal Rate (MRR), Surface Roughness Characteristics (R_a & R_z), Analysis of Means (ANOM), Signal-to-Noise (S/N) ratio.

1. Introduction

In order to attain the desired size and form by carefully managing the various parameters, machining is a technique that involves removing extra material from the work piece. A useful unconventional machining (UCM) technique that aids in machining hard materials is wire-cut electrical discharge machining (WEDM). [1-3] It differs from other non-traditional cutting technologies in a number of important ways, including great machining versatility, minimal stress on the workpiece, high flexibility, and modest cutting forces. The WEDM technique allows for the manufacture of items with ± 0.016 accuracy. [4-6] Ashish Goyal [7] (2017) examined the impact of WEDM process parameters on material removal rate (MRR) and surface roughness (R_a) during Inconel 625 machining. In 18 trials, different tool electrodes (zinc coated and cryogenically treated zinc coated) were used. The material

removal rate and surface roughness were found to be significantly influenced by the pulse on time, tool electrode, and current intensity, according to the ANOVA results. Carmita Camposeco-Negrete [8] (2021) used WEDM to conduct studies on AISI O1 tool steel. He investigated the effects of pulse-on time, servo voltage, and voltage over machining time, electric power, overall energy consumption, surface roughness, and rate of material removal, among other things. The pulse-on time was discovered to be the most important factor influencing the responses. A. Pramanik et al. [9] (2019) examined the geometrical mistakes, such as cylindricity, circularity, and diametric errors of a feature (a hole), created through wire electrical discharge machining of Ti6Al4V alloy. R. Prasanna et al. [10] (2019) optimized WCEDM process parameters for machining titanium alloy (Ti-6Al-2Sn-4Zr-2Mo). On material removal rate and surface roughness, the effects of the pulse on time, pulse off time, voltage, and wire feed rate were examined. They deduced from the findings that voltage, out of all the parameters, is the most important one. Raymond Magabe et al. [11] (2019) used WEDM to machine Ni_{55.8}Ti shape memory alloy. On productivity, measured by the metal removal rate (MRR), and surface quality, measured by the mean roughness depth (R_z), the impacts of input parameters including spark gap voltage, pulse on-time, pulse off-time, and wire feed have been examined. For optimizing the various answers, NSGA-II was used. The MRR and R_z values are correctly predicted by the derived empirical models. Ni_{55.8}Ti wire-EDM with NSGA-II-optimized settings produced better surface quality (R_z - 6.20 μm) and process productivity (MRR-0.021 g/min). The NSGA solutions found in this work might be referred for better process performance depending on the requirements. S. Suresh et al. [12] (2019) investigated the effects of WEDM parameters including gap voltage, wire feed, pulse-off time, and pulse-on time on surface roughness (R_a) and MRR (material removal rate) in Al7075 and nano-silicon carbide-based metal matrix nanocomposites (SiC). They discovered that the key parameters for material removal rate and surface roughness are gap voltage and reinforcement weight percentage respectively. Varying the input process parameters in WEDM has the biggest impact on the surface quality performance characteristics. Due to the unsystematic nature of the WEDM process, optimizing the input process variables is an extremely vigorous task for the researchers. Amit Kumar et al. [13] (2018) enhanced the WEDM process parameters during the machining of M2-grade high-speed steel (HSS). For optimizing the response variables material removal rate (MRR), surface roughness, and Kerf width, the regression model of significant factors such as pulse-on time, pulse-off time, peak current, and wire feed is taken into consideration. Ramy Abdallah et al. [14] (2020) studied the effect of operational parameters and cut direction on composites (parallel and perpendicular to fiber orientation). For each cut direction, a Taguchi L18 fractional factorial orthogonal array with four variable parameters-open voltage, ignition current, pulse-on and pulse-off time was conducted. Titus Thankachan et al. [15] (2017) performed an experiment and investigated the impact of pulse discharge on time (Pulse on), pulse discharge off time (Pulse off), wire feed rate (Wire FR), as well as the material characteristics of different Boron Nitride (BN) volume fractions while machining a friction stir processed (FSPed) copper-BN surface composite. Methods such as ANOVA and grey analysis were used to optimize the responses. Yan et al. [16] investigated the machining properties and establishes the ideal wire electrical discharge machining process settings for the SiCp/Al composite. It is noticed that the material removal rate increases with increasing pulse-on time and decreases with increasing pulse-off time, servo voltage, wire feed, and

wire tension. Surface roughness rises with longer pulse-on and pulse-off times, but induced current and wire-feed only have fewer effects.

WEDM technique uses a thin wire as an electrode to convert electrical energy to heat energy. EDM has been successfully utilized to machine tough, very durable, and temperature-resistant materials. Rapid, repeated spark discharges over the space between the electrode and work piece which removes the unwanted material. Amit Kumar et al. [17] (2017) used an Al₂O₃ nanopowder mixed dielectric medium to machine Inconel 825. The experimental examination found that the maximum MRR was 47 mg/min and the minimum SR was 1.487 m, which are 44 and 51% greater than the standard EDM technique, respectively. Nanopowder Mixed Electric Discharge Machining (NPMEDM) was used to significantly increase the surface topography of the machined surface. Rakesh Chaudhari et al. [18] (2021) used MWCNTs combined with dielectric fluid in wire electrical discharge machining (WEDM) to improve the machining performance of Nitinol shape memory alloy (SMA). The effect of WEDM machining variables such as current, pulse-on time (T_{on}), pulse-off time (T_{off}), and change in MWCNT powder concentration on material removal rate (MRR) and surface roughness (SR) is investigated. The best combination of several responses is found using a sophisticated parameter less TLBO algorithm. Himanshu Payal et al. [19] (2019) employed the GRA and PCA methodologies to optimize the die-sinking EDM process parameters when milling Inconel 825 using three different electrode types namely, graphite, copper, and copper-tungsten. With a graphite electrode, they saw good MRR, TWR, and SR outcomes. Therefore, while working with hard materials like composites etc, the EDM process becomes the most essential. Many researchers worked on this area by employing different optimization techniques to study the effect of WEDM process parameters on various multi-responses. K. Anand Babu et al. [20] (2021) use the Taguchi technique coupled with the Entropy-VIKOR approach to examine the optimization of electrical discharge wire-cutting process parameters on AA6082/fly ash/Al₂O₃ hybrid composite. The analysis leads to the conclusion that pulse OFF time, followed by pulse ON time, servo feed, and wire type, is the most highly relevant parameter for process performances, cutting speed, wire wear ratio, kerf width, and over-cut. Gopal P.M. et al. [21] (2016) optimized the surface finish (R_a) and material removal rate (MRR) of a novel Mg/BN/CRT hybrid MMC. Through the Taguchi-based orthogonal array technique, reinforcement weight percentage and size, pulse on time, pulse off time, and wire feed are taken into account as process parameters to build the WEDM trials. The created mathematical models for MRR and R_a are found to have greater predictive power and generate values that are consistent with experimental findings. Meinam Annebushan Singha et al. [22] (2020) focus on the manufacture of silicon carbide utilizing a rapid hot press sintering approach and the subsequent discovery of the relevant parameters that best correspond to a superior machining scenario in wire electric discharge machining. Amresh Kumar et al. [23] (2022) used the WEDM technique to machine an aluminum-based hybrid composite made of (Al/(SiC_p+ Gr_p+ Fe₂O_{3p})). The ideal machining conditions for hybrid composites have been determined using an analytical hierarchy process and a genetic algorithm. V. Kavimani et al. [24] (2017) studied the effect of the Wire Electric Discharge Machining (WEDM) parameter on the material removal rate (MRR) and surface roughness (R_a) of a newly designed magnesium metal matrix composite. In order to investigate their impacts on the required output responses, two material parameters and three machining parameters have been chosen. The Taguchi coupled Grey relation analysis is then used to analyze the output response variables like MRR and R_a . Malik Shadab et al. [25]

(2018) employed Metaheuristic Techniques to optimize the WEDM parameters. The Taguchi L25 orthogonal array is required for the experiments that were done. For the optimization, a TLBO algorithm based on RSM was employed. R. Karthikeyan et al. [26] (2020) enhanced the material removal rate and surface roughness using a feed-forward artificial neural network model and a genetic algorithm by optimizing the network's weighing factors in neural power software. P. Vaidyaa et al. [27] (2021) used a hybrid artificial neural network (ANN) coupled genetic algorithm approach to optimize the multi-objective properties of wire electrical discharge machining (WEDM) in SLM-fabricated AlSi10Mg. The Taguchi experimental design is used to determine the microhardness and surface roughness outcomes while taking into account the three major influencing elements. Ahmed A et al. [28] (2020) used the WEDM technique to machine AISI 1045 steel. The goal of this study is to develop an ANN model that can forecast surface roughness (R_a) and metal removal rate (MRR) values. The Taguchi technique (Design of Experiments), artificial neural network (ANN), and analysis of variances (ANOVA) were utilized in this study as the approach to carry out the research. C. Balasubramaniyan et al. [29] (2021) focus on coated wire electric discharge machining of high-temperature $Ni_{44}Ti_{50}Cu_4Zr_2$ SMA (W-EDM). Surface undulation and material removal were evaluated in terms of machining quality attributes using current (I), servo voltage (SV), pulse on time (T_{on}), angle of cut (AC), and pulse off time (T_{off}). The response surface technique, based on central composite design, has been used in trials to study parametric analysis of machining features (RSM-CCD). Soutrik Bose et al. [30] (2020) experimental research was based on a novel optimization technique known as desirable grey relational analysis (DGRA), in which the desirability function is connected with grey relational analysis for multi-objective optimization. With multi-criteria decision-making approach like the fuzzy methodology for order preference by similarity to ideal solution (FTOPSIS) combined with a fuzzy analytical hierarchy process for criteria weights, the experimental and anticipated results are compared. Daniel Das A et al. [31] (2021) investigate the effect of wire-cut electrical discharge machining on input parameters in Ti alloy. The TOPSIS approach has been used to anticipate the optimization portion.

2. Experimental Details

In the current experiment, a brass electrode of 0.25 mm was used to machine medium carbon steel, AISI1040, utilizing Wire EDM, as illustrated in "Fig. 1." Work material can be used to make gears, axles, bolts, spindles, shafts, studs, and other automotive parts. It is also utilized in technical applications where higher tensile strength is needed. Tables 1 and 2 lists the chemical and mechanical characteristics of AISI1040 steel. Table 3 shows the levels of the selected process parameters. Table 4 contains information of the L18 orthogonal array used for the experiments. SJ 301 tester as shown in "Fig. 2." is used to measure the roughness of the cutting faces at three distinct positions, with the mean value being used as the final result.

Table1. Chemical Composition of AISI 1040

Element	Carbon	Silicon	Manganese	Sulphur	Phosphorus
%	0.36 - 0.44	0.10 - 0.40	0.60 - 1.00	0.05	0.05

Table 2. Mechanical Properties of AISI 1040

UTS (MPa)	YS (MPa)	Elongation (%)	Hardness
550	280	16	201-255

Table 3. Fixed Parameters and Corresponding Levels

Process Parameter	L - 1	L - 2	L - 3
Flushing Pressure (kg/cm ²)	4	8	-
Pulse-on-Time (μs)	115	120	125
Pulse-off-Time (μs)	55	58	61
Wire Tension (kg-f)	2	4	6
Wire Feed (mm/min)	2	3	4
Servo Voltage (volts)	20	25	30

Table 4. L18 OA Design

S.NO	Flushing Pressure	Pulse-On-Time	Pulse-Off-Time	Wire Tension	Wire Feed	Servo Voltage
1	4	115	55	2	2	20
2	4	115	58	4	3	25
3	4	115	61	6	4	30
4	4	120	55	2	3	25
5	4	120	58	4	4	30
6	4	120	61	6	2	20
7	4	125	55	4	2	30
8	4	125	58	6	3	20
9	4	125	61	2	4	25
10	8	115	55	6	4	25
11	8	115	58	2	2	30
12	8	115	61	4	3	20
13	8	120	55	4	4	20
14	8	120	58	6	2	25
15	8	120	61	2	3	30
16	8	125	55	6	3	30
17	8	125	58	2	4	20
18	8	125	61	4	2	25

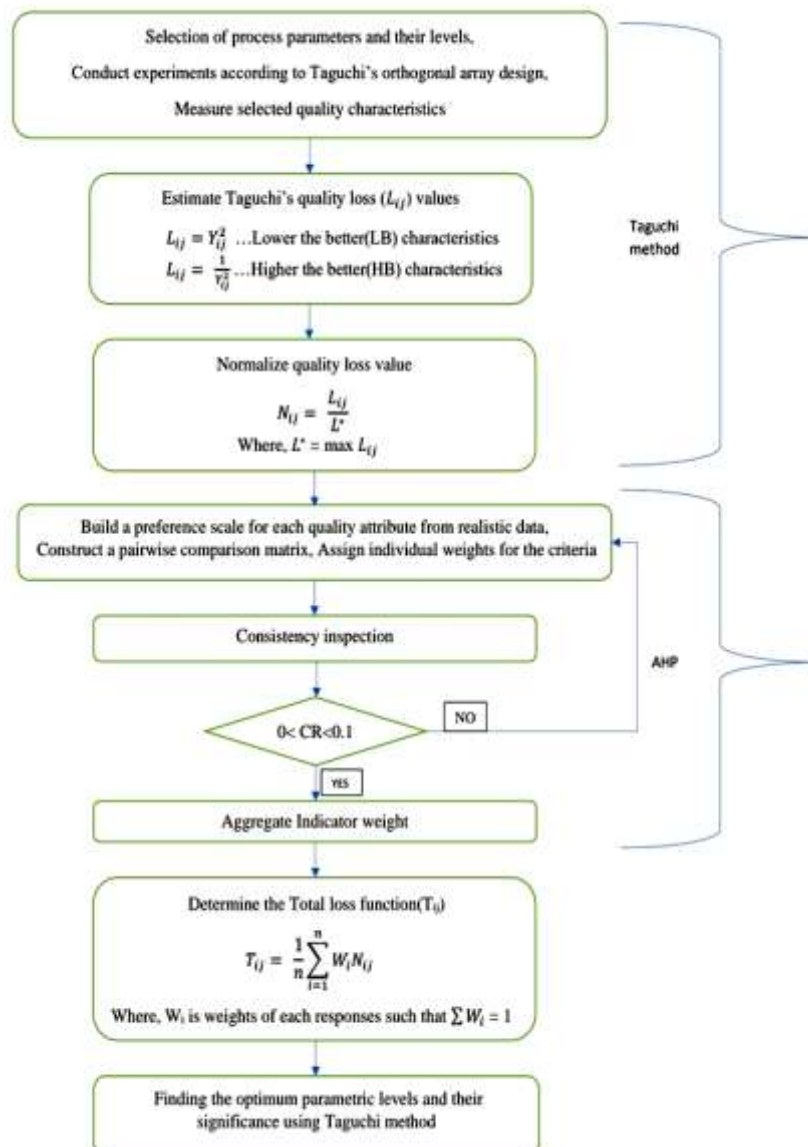


Figure 1. WEDM Experimental Setup



Figure 2. SJ301 Surface Roughness Tester

3. Proposed Methodology: (AHP+TQLFA)



4. Results & Discussion

To determine how the WEDM process settings affect the various performance characteristics, a total of 18 tests were conducted. Table 5 lists features of material removal rate and surface roughness that were measured. The values for Taguchi's quality loss were tabulated in Table 6 and the replies were later normalized, the results are shown in Table 7. The weights of the individual criteria were discovered using AHP. The weights are calculated and discovered to be, $W_{MRR} = 0.632$, $W_{Ra} = 0.258$, and $W_{Rz} = 0.105$ respectively and $CR = 0.04 < 0.1$, $\lambda_{max} = 3.039$. After determining the individual weights for the responses, the weighted normalized values of the responses are determined. The outcomes are listed in Table 8. Using MINITAB-17 Software, the Taguchi method has been used for the analysis. Taguchi analysis was performed on the responses using the Lower-the-Better characteristic. The findings of the Taguchi analysis are shown in Table 9. The main effect plots are shown in Fig. 3 and were produced using the mean values of the process parameters.

Table 5. Output Responses

S.NO	MRR	R _a	R _z
1	8.4204	2.5032	13.9056
2	7.2597	2.6216	15.2776
3	6.9008	2.4008	15.3151
4	7.8915	2.4237	14.1967
5	7.1902	2.4955	15.9591
6	7.3215	2.5658	16.3575
7	7.7430	2.4728	15.8616
8	8.8791	2.6294	16.6926
9	6.9232	2.6065	16.0197
10	8.3181	2.5323	15.3131
11	6.9764	2.5105	15.0291
12	7.7513	2.6403	16.0149
13	9.8805	2.7400	16.9233
14	8.4247	2.9679	16.9644
15	6.6119	2.6071	15.5482
16	9.1397	2.5923	16.6620
17	9.0195	2.7440	16.8876
18	7.4033	2.6909	16.698

Table 6. Quality Loss Function values (L_{ij})

S.NO	MRR	R _a	R _z
1	0.0141	6.2660	193.3657
2	0.0190	6.8728	233.4051
3	0.0210	5.7638	234.5523
4	0.0161	5.8743	201.5463
5	0.0193	6.2275	254.6929
6	0.0187	6.5833	267.5678
7	0.0167	6.1147	251.5904
8	0.0127	6.9137	278.6429
9	0.0209	6.7938	256.6308
10	0.0145	6.4125	234.4910
11	0.0205	6.3026	225.8738
12	0.0166	6.9712	256.4770

13	0.0102	7.5076	286.3981
14	0.0141	7.2787	287.7909
15	0.0229	6.7970	241.7465
16	0.0120	6.7200	277.6222
17	0.0123	705295	285.1910
18	0.0182	7.2409	278.8232

Table 7. Normalized Values (N_{ij})

S.NO	MRR	R_a	R_z
1	0.6159	0.8322	0.6719
2	0.8286	0.9128	0.8110
3	0.9170	0.7655	0.8150
4	0.7012	0.7802	0.7003
5	0.8447	0.8271	0.8850
6	0.8146	0.8743	0.9297
7	0.7284	0.8121	0.8742
8	0.5539	0.9182	0.9682
9	0.9111	0.9023	0.8917
10	0.6311	0.8517	0.8148
11	0.8972	0.8371	0.7849
12	0.7268	0.9258	0.8912
13	0.4473	0.9971	0.9952
14	0.6153	0.9667	1.0000
15	0.9989	0.9027	0.8400
16	0.5228	0.8925	0.9647
17	0.5368	1.0000	0.9910
18	0.7967	0.9617	0.9688

Table 8. Weight Normalized Values of Responses ($W_i N_{ij}$)

S.NO	MRR	R_a	R_z	Total Quality Loss(T_{ij})	SN of T_{ij}
1	0.3923	0.2147	0.0705	0.2259	12.9233
2	0.5278	0.2355	0.0852	0.2828	10.9699
3	0.5841	0.1975	0.0856	0.2891	10.7800
4	0.4467	0.2013	0.0735	0.2405	12.3779
5	0.5380	0.2134	0.0929	0.2815	11.0119
6	0.5189	0.2256	0.0976	0.2807	11.0349
7	0.4640	0.2095	0.0918	0.2551	11.8660
8	0.3528	0.2369	0.1017	0.2305	12.7479
9	0.5804	0.2328	0.0936	0.3023	10.3924
10	0.4020	0.2197	0.0856	0.2358	12.5503
11	0.5715	0.2160	0.0824	0.2900	10.7530
12	0.4630	0.2389	0.0936	0.2651	11.5305
13	0.2849	0.2572	0.1045	0.2156	13.3287
14	0.3919	0.2494	0.1050	0.2488	12.0839
15	0.6363	0.2329	0.0882	0.3191	9.9207
16	0.3330	0.2303	0.1013	0.2215	13.0919
17	0.3419	0.2580	0.1041	0.2347	12.5912
18	0.5075	0.2481	0.1017	0.2858	10.8792

Table 9. Taguchi Analysis: T_{ij} versus FP, T_{ON} , T_{OFF} , WT, WF, SV

Level	Flushing Pressure	Pulse-On-Time	Pulse-Off-Time	Wire Tension	Wire Feed	Servo Voltage
1	0.2654	0.2648	0.2324	0.2687	0.2644	0.2421

2	0.2574	0.2644	0.2614	0.2643	0.2599	0.2660
3	-	0.2550	0.2903	0.2510	0.2598	0.2760
Δ	0.0080	0.0098	0.0580	0.0177	0.0046	0.0340
Rank	5	4	1	3	6	2

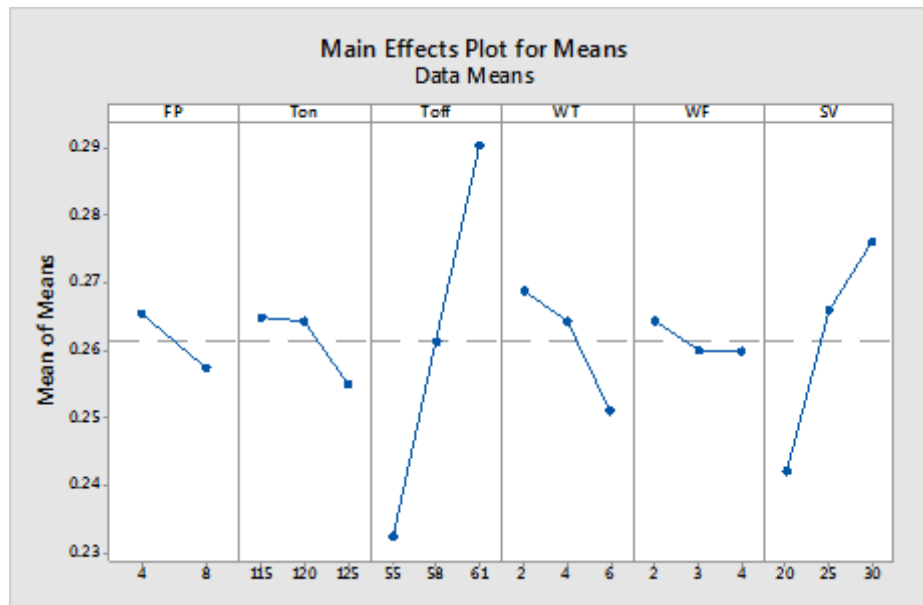


Figure 3. Main Effect Plots for Means of T_{ij}

5. Conclusions

From the experimental results on WEDM machining, the following conclusions can be drawn

- Pulse-off-time is found to be the most influencing control parameter in affecting the multi-responses.
- The optimal setting of process parameters was obtained at FP: Level-2, 8 kg/cm²; T_{ON}: Level-3, 125μs; T_{OFF}: Level-1, 55μs; WT: Level-3, 6 kg-f; WF: Level-3, 4 mm/min; SV: Level-1, 20 volts respectively.
- The proposed methodology can be effective for employing/solving multi-objective optimization problems efficiently with very less effort.

References

1. Natarajan, K. et al. (2022) "Study on optimization of WEDM process parameters on stainless steel," Journal of Nano materials, 2022, pp. 1–7, Available at: <https://doi.org/10.1155/2022/6765721>.
2. Sharma, S., Kumar Vates, U. and Bansal, A. (2021) "Parametric optimization in Wire EDM of D2 tool steel using Taguchi method," Materials Today: Proceedings, 45, pp. 757–763, Available at: <https://doi.org/10.1016/j.matpr.2020.02.802>.
3. Kumar, P., Dewangan, S. and Pandey, C. (2020) "Analysis of surface integrity and Dimensional Accuracy in EDM of P91 steels," Materials Today: Proceedings, 33, pp. 5378–5383, Available at: <https://doi.org/10.1016/j.matpr.2020.03.119>.
4. Bisaria, H. and Shandilya, P. (2018) "The machining characteristics and surface integrity of Ni-rich NITI shape memory alloy using wire electric discharge machining," Proceedings of the Institution of Mechanical Engineers, Part C: Journal of Mechanical Engineering Science, 233(3), pp. 1068–1078, Available at: <https://doi.org/10.1177/0954406218763447>.
5. Gupta, N.K. et al. (2021) "Revealing the WEDM process parameters for the machining of pure and heat-treated titanium (Ti-6Al-4V) alloy," Materials, 14(9), p. 2292, Available at: <https://doi.org/10.3390/ma14092292>.
6. Kumar, J., Soota, T. and Rajput, S.K. (2020) "Experimental evaluation and modelling of wire-EDM process parameter for stainless steel AISI 630," Materials Today: Proceedings, 26, pp. 1151–1158, Available at: <https://doi.org/10.1016/j.matpr.2020.02.231>.

7. Goyal, A. (2017) "Investigation of material removal rate and surface roughness during wire electrical discharge machining (WEDM) of Inconel 625 Super Alloy by cryogenic treated Tool Electrode," *Journal of King Saud University - Science*, 29(4), pp. 528–535. Available at: <https://doi.org/10.1016/j.jksus.2017.06.005>.
8. Camposeco-Negrete, C. (2021) "Analysis and optimization of sustainable machining of AISI O1 Tool Steel by the wire-EDM process," *Advances in Manufacturing*, 9(2), pp. 304–317. Available at: <https://doi.org/10.1007/s40436-021-00353-2>.
9. Pramanik, A. et al. (2019) "Optimizing dimensional accuracy of titanium alloy features produced by wire electrical discharge machining," *Materials and Manufacturing Processes*, 34(10), pp. 1083–1090. Available at: <https://doi.org/10.1080/10426914.2019.1628259>.
10. Prasanna, R. et al. (2019) "Multicriteria optimization of machining parameters in WEDM of titanium alloy 6242," *Lecture Notes in Mechanical Engineering*, pp. 65–75. Available at: https://doi.org/10.1007/978-981-13-6374-0_9.
11. Magabe, R. et al. (2019) "Modeling and optimization of wire-EDM parameters for machining of Ni_{55.8}Ti shape memory alloy using hybrid approach of Taguchi and NSGA-II," *The International Journal of Advanced Manufacturing Technology*, 102(5-8), pp. 1703–1717. Available at: <https://doi.org/10.1007/s00170-019-03287-z>.
12. Suresh, S. and Sudhakara, D. (2019) "Investigations on wire electric discharge machining and mechanical behavior of al 7075/nano-sic composites," *Journal of The Institution of Engineers (India): Series D*, 100(2), pp. 217–227. Available at: <https://doi.org/10.1007/s40033-019-00198-x>.
13. Kumar, A., Soota, T. and Kumar, J. (2018) "Optimisation of wire-cut EDM process parameter by grey-based response surface methodology," *Journal of Industrial Engineering International*, 14(4), pp. 821–829. Available at: <https://doi.org/10.1007/s40092-018-0264-8>.
14. Abdallah, R., Soo, S.L. and Hood, R. (2021) "The influence of cut direction and process parameters in wire electrical discharge machining of carbon fibre–reinforced plastic composites," *The International Journal of Advanced Manufacturing Technology*, 113(5-6), pp. 1699–1716. Available at: <https://doi.org/10.1007/s00170-021-06641-2>.
15. Thankachan, T., Soorya Prakash, K. and Loganathan, M. (2017) "WEDM process parameter optimization of FSPed copper–BN composites," *Materials and Manufacturing Processes*, 33(3), pp. 350–358. Available at: <https://doi.org/10.1080/10426914.2017.1339311>.
16. Yan, H. et al. (2021) "Analysis and optimization of the machining characteristics of high-volume content SiCp/AL composite in wire electrical discharge machining," *Crystals*, 11(11), p. 1342, Available at: <https://doi.org/10.3390/cryst11111342>.
17. Kumar, A. et al. (2017) "Performance evaluation of Al₂O₃ nano powder mixed dielectric for electric discharge machining of Inconel 825," *Materials and Manufacturing Processes*, 33(9), pp. 986–995. Available at: <https://doi.org/10.1080/10426914.2017.1376081>.
18. Chaudhari, R. et al. (2021) "Experimental investigations and optimization of MWCNTS-mixed WEDM process parameters of nitinol shape memory alloy," *Journal of Materials Research and Technology*, 15, pp. 2152–2169. Available at: <https://doi.org/10.1016/j.jmrt.2021.09.038>.
19. Payal, H., Maheshwari, S. and Bharti, P.S. (2019) "Parametric optimization of EDM process for Inconel 825 using GRA and PCA approach," *Journal of Information and Optimization Sciences*, 40(2), pp. 291–307. Available at: <https://doi.org/10.1080/02522667.2019.1578090>.
20. Anand Babu, K. and Jeyapaul, R. (2021) "Process parameters optimization of electrical discharge wire cutting on AA6082/fly ash/al₂o₃ hybrid MMC using Taguchi method coupled with hybrid approach," *Journal of The Institution of Engineers (India): Series C*, 102(1), pp. 183–196. Available at: <https://doi.org/10.1007/s40032-020-00640-0>.
21. P. M., G. and K., S.P. (2018) "Wire electric discharge machining of silica rich e-waste CRT and BN reinforced hybrid magnesium MMC," *Silicon*, 11(3), pp. 1429–1440. Available at: <https://doi.org/10.1007/s12633-018-9951-8>.
22. Singh, M.A. et al. (2020) "Identification of wire electrical discharge machinability of SiC sintered using rapid hot pressing technique," *Ceramics International*, 46(11), pp. 17261–17271. Available at: <https://doi.org/10.1016/j.ceramint.2020.04.013>.
23. Kumar, A. et al. (2021) "Multi-objective optimization of WEDM of aluminum hybrid composites using AHP and genetic algorithm," *Arabian Journal for Science and Engineering*, 47(7), pp. 8031–8043. Available at: <https://doi.org/10.1007/s13369-021-05865-4>.

24. Kavimani, V., Soorya Prakash, K. and Thankachan, T. (2019) “Multi-objective optimization in WEDM process of graphene – sic-magnesium composite through hybrid techniques,” *Measurement*, 145, pp. 335–349. Available at: <https://doi.org/10.1016/j.measurement.2019.04.076>.
 25. Shadab, M., Singh, R. and Rai, R.N. (2018) “Multi-objective optimization of wire electrical discharge machining process parameters for AL5083/7% B4C composite using metaheuristic techniques,” *Arabian Journal for Science and Engineering*, 44(1), pp. 591–601. Available at: <https://doi.org/10.1007/s13369-018-3491-9>.
 26. Karthikeyan, R. et al. (2020) “An integrated ANN - GA approach to maximize the material removal rate and to minimize the surface roughness of wire cut EDM on titanium alloy,” *Advances in Materials and Processing Technologies*, 8(1), pp. 22–32. Available at: <https://doi.org/10.1080/2374068x.2020.1793267>.
 27. Vaidyaa, P. et al. (2021) “Wire EDM parameter optimization of AlSi10Mg Alloy,” *Transactions of the Indian Institute of Metals*, 74(11), pp. 2869–2885. Available at: <https://doi.org/10.1007/s12666-021-02344-0>.
 28. Alduroobi, A.A. et al. (2020) “Wire EDM process optimization for machining AISI 1045 Steel by use of Taguchi Method, artificial neural network and analysis of variances,” *International Journal of System Assurance Engineering and Management*, 11(6), pp. 1314–1338. Available at: <https://doi.org/10.1007/s13198-020-00990-z>.
 29. Balasubramaniyan, C., Rajkumar, K. and S, S. (2021) “Wire-EDM machinability investigation on quaternary ni44ti50cu4zr2 shape memory alloy,” *Materials and Manufacturing Processes*, pp. 1–10. Available at: <https://doi.org/10.1080/10426914.2021.1905833>.
 30. Bose, S. and Nandi, T. (2020) “Experimental investigation of WEDM on titanium hybrid composite reinforced with boron powder: A novel approach,” *The European Physical Journal Plus*, 135(11). Available at: <https://doi.org/10.1140/epjp/s13360-020-00904-9>.
- A, D.D., K, S.K. and R, P. (2021) “Investigating the effect of wire cut EDM of Titanium Alloy 6242 using Topsis,” *Advances in Materials and Processing Technologies*, 8(3), pp. 2824–2836. Available at: <https://doi.org/10.1080/2374068x.2021.1945261>.

Two-body abrasive wear of Alumina and Alumina-graphene composite ceramic material: Effect of Speed and Sliding Distance

Dr. K.I.Vishnu Vandana^{1*}, Dr. M. Rajyalakshmi², Dr. P. Phani Prasanthi³, S. Chandrasekhar⁴, Tirumala Kumar⁵

^{1,2}Assistant Professor, ³Associate Professor, ^{4,5} UG Student
Department of Mechanical Engineering, Prasad V Potluri Siddhartha Institute of Technology,
Vijayawada.

* kodeyvandana@gmail.com

Abstract: The present work studied the wear behaviour of microwave sintered alumina-graphene composite samples. The wear tests of ceramic composite samples were conducted on pin-on-disk apparatus at speed of 0.5 m/sec, 1 m/sec and 1.5 m/sec and with sliding distance of 50,100 & 150 m. The wear rate of ceramic composites influenced by speed and sliding distance was analyzed and compared with wear behaviour of monolithic alumina by conducting tests at a constant load of 10 N. Investigated results shows that alumina composite reinforced with 0.35 wt% of graphene yielded superior wear resistance compared to other alumina-graphene composites and also to monolithic alumina prepared under same conditions. This study revealed the superior wear properties of alumina ceramic composite at 0.35 wt% of graphene reinforcement.

Key words: Alumina, Graphene, wear rate, ceramic composites, pin-on-disk

Introduction

Ceramics have been receiving great attention in manufacturing world due to their superior intrinsic characteristics. Alumina was important representative of ceramic materials. It's various properties like high chemical inertness, relatively low cost, great hardness, high erosion resistance, good temperature resistance made alumina much attractive in several applications like aerospace, biomedical, cutting tool and automobiles especially when working conditions are severe. Hence, Al_2O_3 is the most widely used material in applications requiring high wear resistance. Large variety of commercial alumina grades are available with a percentage variation of alumina ranging between 85% - 99.99%. This grade of materials can also exhibit various densities, grain sizes with different microstructural characteristics. But, Wear of the ceramic materials is a serious concern and a big issue of industrial importance as it leads to reduction of the overall efficiency of ceramic components. Of all wear mechanisms, abrasive wear and adhesion wear are frequently observed in dry sliding ceramics. To improve wear properties and tribological properties of pure alumina further, numerous experimental studies and investigations have been made by adding individual reinforcements to alumina matrix.

Zhao Xingzhong et. al [1] employed Si_3N_4 ceramic material to machine AISI 321 stainless steel and conducted friction and wear tests under dry and water-lubricated conditions on a pin-on-disk tribometer. This experimentation revealed that with the increasing speed and load, the wear rate of Si_3N_4 ceramic material was also increasing in both dry and water lubricated conditions and wear rate was rapid under dry conditions at higher load (235.2 N). The test concluded that even water or water based cutting fluids were not effectively reducing the wear of Si_3N_4 ceramic cutting tools during tests. R.F. Silva, et al. [2] adopted

Dept. of Mech. Engg. PVPSIT 389

Si₃N₄ based ceramic cutting tools to machine tool steel and gray iron and studied the distinct wear behaviour of ceramic tool by using SEM images. The wear mechanism was also investigated by pin-on-disk tests conducted under atmospheric conditions and concluded that selective abrasion and corrosion of ceramic grain boundary of tool are changed according to the change in temperatures at the contact of metal ceramic surfaces.

Z.S. Rak, et al. [3] prepared dense Al₂O₃-TiN (Titanium Nitride) composites with 5-25 vol% TiN and studied the effect of TiN content on the electrical resistivity, mechanical properties, wear resistance and oxidation resistance. Their microscopic study of prepared samples revealed even distribution of TiN particles in the alumina matrix of all prepared composites. They identified that TiN crystals were located either in between the alumina grains or incorporated into the alumina grains basing on the size of TiN particles. They reported formation of a near continuous network of titanium nitride grains in the alumina matrix in the composite with 25 vol% TiN was responsible for achieving highest strength of 567 MPa and the lowest electrical resistivity of $2.5 \times 10^{-3} \Omega \cdot \text{cm}$. M. Parchoviansky, et al. [4] prepared alumina-silicon carbide composites by adding SiC (volume fractions 3, 5, 10, 15, and 20 vol%) and evaluated the effect of size and vol% of SiC particles on dry sliding wear behaviour and mechanical properties of obtained composite. during wear test, they observed no grain pull-out in the matrix even at high volume reinforcement of SiC particles.

Since a decade graphene has been strongly identified as a promising reinforcing material for composite materials. Many research articles informed that the addition of grapheme or CNT as a second phase in ceramics lead to an enhancement of the tribological properties of resulting composite. J.W. An, et al. [5] fabricated alumina-CNT composites with the CNT contents ranging from 0 to 12.5 wt% by hot-pressing and investigated the effect of CNT addition on wear resistance. They reported enhanced wear and mechanical properties of the prepared composites when the CNT content range is 0-4% in the composite. Anton Smirnov, et al. [6] fabricated graphene-reinforced Al₂O₃-SiC_w (silicon carbide whisker) ceramic nano composites and investigated the wear behavior of 0.5 vol% graphene reinforced prepared alumina composite using ball-on-disk wear apparatus at 10 N and 40 N of sliding loads. They reported around higher wear resistance of these nanocomposites than the wear resistance of pure alumina ceramic regardless of the applied load. They stated that graphene present in ceramic matrix was acting as an auto-lubricating layer and improving the wear behaviour of the prepared composite. They also confirmed that graphene was providing enough lubrication in between the sample and alumina ball during wear test by forming tribofilm through Raman and SEM observations. They concluded that this composite is suitable for heavy applications like valves, high temperature valve system, protective coating applications and conveyor system bearing.

It is well known that fabrication method also plays a major role in deciding the fundamental characteristics of obtained composite and also can significantly affect various mechanical properties of the obtained composite [7]. Ceramics are brittle, hard and melt at very high temperatures, hence their manufacturing involves powder pressing and consolidation at high temperature called as sintering [8]. Attaining full density (near to the actual) without affecting the final structure of the composite is a fundamental prerequisite and one of the challenges in the sintering of the ceramic composites [9]. Hence for the present work to choose the appropriate sintering method for preparation of the proposed ceramic composites, a vast survey was done on different sintering methods adopted by several authors to fabricate

ceramic composites and identified that microwave sintering the suitable process for ceramic composites [10,11,12,13].

Hence, the present work mainly concentrated on preparation of alumina ceramic composite material reinforced with different weight proportions of graphene through microwave sintering method. Studies also carried out on the effect of graphene on wear resistance properties of obtained ceramic composite by performing wear tests at varying speeds and sliding distances using Pin-on-disk machine.

Wear Test on Pin-On-Disk Apparatus

Pin on disk apparatus (Shown in Fig. 1) was used to carry out the wear tests on prepared alumina-graphene composite samples. Along with pure alumina samples, ceramic composite samples are prepared using powder metallurgy technique by reinforcing graphene in to alumina at weight fraction ranging i.e from 0.15 - 0.45 wt% maintaining an interval of 0.1 (shown in Fig. 2) and consolidated through microwave sintering [14]. The tests were carried under 10N load and at a speed of 0.5 m/Sec, 1.0 m/sec and 1.5 m/sec at sliding distances of 50 m, 100 m and 150 m on a SiC (Silicon carbide) emery paper of grit size 150 μm . This emery sheet serves as an abrasive medium during wear test.



Fig. 1: Pin-on-Disk Apparatus

Fig. 2: Pin shaped Ceramic Composite Samples

Using an electronic weighing machine, weights of the samples were measured before and after wear test to obtain the weight loss. Wear rate of all samples was calculated by employing the formulae (1). The wear rate of samples at different sliding distances and speeds were calculated and obtained values are noted.

$$\text{Wear rate} = (\Delta W) / \rho * S \dots \dots \dots (1)$$

$$\Delta w = \text{Weight loss in grams} = \Delta w = w_i - w_f$$

$$w_i = \text{Initial weight of sample in grams}$$

$$w_f = \text{Final weight of sample in grams}$$

$$\rho = \text{Density of material in g/cc}$$

$$S = \text{Sliding distance in meters.}$$

Results and Discussions

The obtained wear rate values are depicted in the form of bar graphs and were presented in the Fig. 3. From the Fig. 3, it can be observed that, of all samples tested for wear, samples containing 0.35 & 0.45 wt% of graphene have shown remarkable improvement in the wear rate when compared with pure alumina samples.

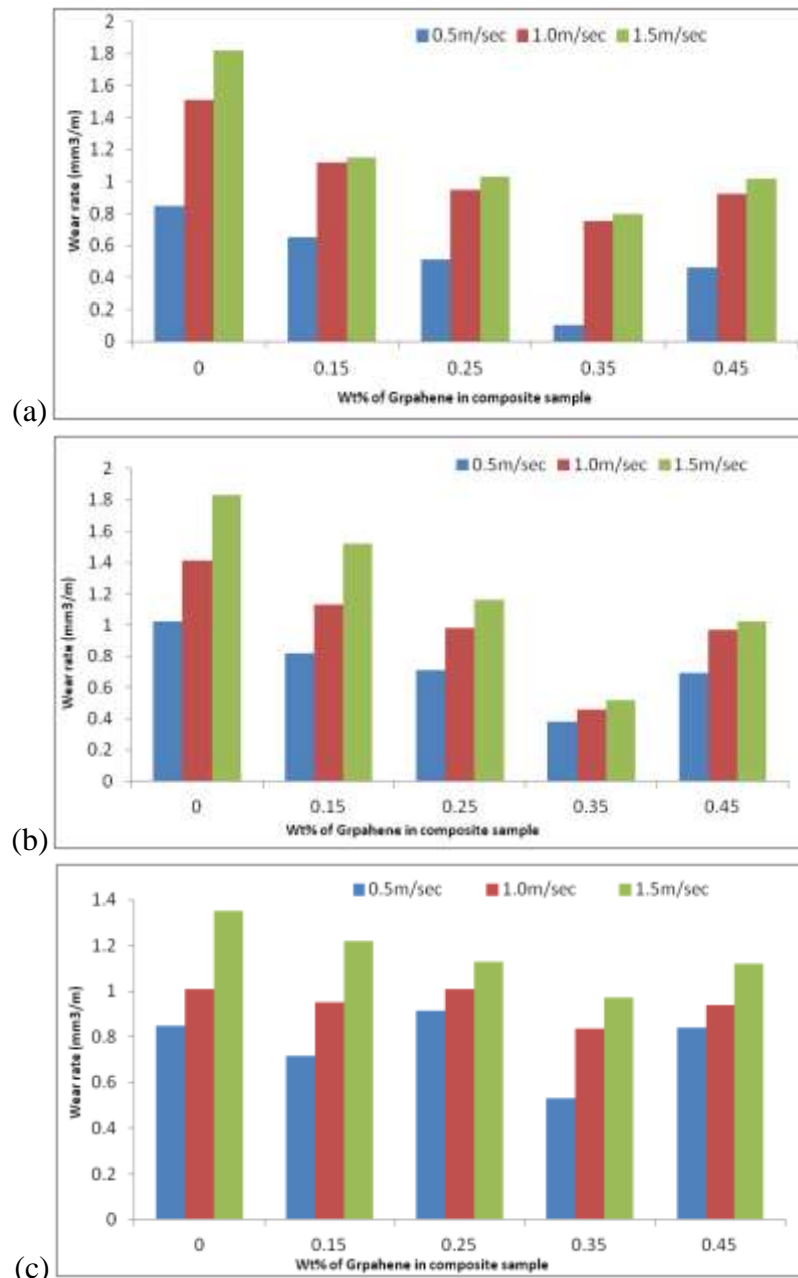


Fig. 3: Wear rate Vs Speed of samples at different sliding distance : (a) 50m; (b) 100m; (c) 150m on 150 μ grit size emery paper

The higher wear rate in other samples can be attributed to low wt % of graphene reinforcement. During reciprocating movement of samples, the graphene particles in the ceramic composite might be exposed from its top surface to the wear track and thereby might aid for formation of lubricating tribofilm. The slippery nature of graphene exhibits lubricating property and might restrict the higher damage in 0.35 and 0.45 wt% of graphene reinforced alumina composite samples.

From the obtained wear rate values it was noted that, the percentage decrease in wear rate at a speed of 0.5 m/sec (with sliding distance of 50 m, 100 m, 150 m respectively) was 88.11%, 62.74%, 37.64% in the composite samples reinforced with 0.35 wt% of graphene and 45.64%, 32.35%, 1.17% in the composite samples reinforced with 0.45 wt% of graphene when compared with wear rate of pure alumina samples. The percentage decrease in wear rate at a speed of 1.5 m/sec (with sliding distance of 50 m, 100 m, 150 m respectively) is 56.04%, 71.58%, 28.14% in the composite samples reinforced with 0.35 wt% of graphene

and 43.95%, 44.26%, 17.03% in the composite samples reinforced with 0.45 wt% of graphene when compared with wear rate of pure alumina samples. It is also observed that the decrease in wear rate of ceramic composite samples at graphene reinforcement of 0.35 wt% & 0.45 wt% was much noticeable at all speeds and sliding distances when compared with wear rate of remaining composite samples also.

Conclusions

The present work studied the wear behaviour of alumina-graphene composite samples on pin-on-disk apparatus at different sliding distances and speeds.

1. Wear rates of alumina-graphene composite samples were calculated and compared with the wear rates of pure alumina
2. In addition to that, effect of different wt% of graphene reinforcement in alumina matrix on wear performance of composite samples also analysed.
3. It is observed that, alumina ceramic composite samples reinforced with 0.35 wt% and 0.45 wt% of graphene showed improved wear performance when compared with pure alumina samples.

References

- [1] Zhao Xingzhong, Liu Jiajun, Zhu Baoliang, Miao Hezhou, Luo Zhenbi, "Wear behavior of Si₃N₄ ceramic cutting tool material against stainless steel in dry and water-lubricated conditions", *Ceramics International*, Vol. 25, 1999, pp. 309-315.
- [2] R.F. Silva, J.M. Gomes, A.S. Miranda, J.M. Vleria, "Resistance of Si₃N₄ ceramic tools to thermal and mechanical loading in cutting of iron alloys" *Wear*, Vol. 148, 1991, pp. 69-89.
- [3] Z.S. Rak, J. Czechowski, "Manufacture and properties of Al₂O₃-TiN particulate composites", *Journal of European Ceramic Society*, Vol. 18, 1998, pp. 373-380.
- [4] Parchovianský. M, Galusek. D, Michálek. M, Ňvanc̣árek. P, Kaňiarová. M, Dusza. J, Hnatko. M, "Effect of the volume fraction of SiC on the microstructure and creep behavior of hot pressed Al₂O₃/SiC composites", *Ceramic International*, Vol. 40, 2014, pp. 1807-1814.
- [5] J.W. An, D.H. You, D.S. Lim, "Tribological properties of hot-pressed alumina/CNT composites", *Wear*, Vol. 255, Issues 1-6, 2003, pp. 677-681.
- [6] Anton Smirnov, Pavel Peretyagin, Nestor Washington Solís Pinargote, Iosif Gershman, Jose F Bartolomé, "Wear Behavior of Graphene-Reinforced Alumina/Silicon Carbide Whisker Nanocomposite", 9(2):151, 2019, doi:10.3390/nano9020151.
- [7] M.N. Rahaman, "Ceramic processing and sintering", Marcel Dekker, New York, USA, 1996.
- [8] C.B. Carter, M.G. Norton, *Ceramic Materials Science and Engineering*, in: *Int. Sci. Colloq. Model. Mater. Process*, Springer, 2007.
- [9] M. A. Occhionero, J. W. Halloran, "The influence of green density upon sintering" Springer US, 1984, pp. 89-102.
- [10] Yu Chenga Yong Zhanga, Taoyu Wan, Zengbin Yina, Jiaao Wang, "Mechanical properties and toughening mechanisms of graphene platelets reinforced Al₂O₃/TiC composite ceramic tool materials by microwave sintering", *Material Science and Engineering*, Vol. 680, 2017, pp. 190-196.
- [11] I. Ahmad, B. Yazdani, Y.Q. Zhu, "Recent advances on carbon nanotubes and graphene reinforced ceramics nanocomposites", *Nanomaterials*, Vol. 5, 2015, pp. 90-114.
- [12] R. Benavente, M.D. Salvador, F.L. Penaranda-Foix, E. Pallone, A. Borrell, "Mechanical properties and microstructural evolution of alumina-zirconia nanocomposites by microwave sintering", *Ceramic International*, Vol. 40, 2014, pp. 11291-11297.
- [13] Z.B. Yin, J.T. Yuan, Y. Cheng, C. Wang, Z.H. Wang, X.Q. Hu, "Microstructure and mechanical properties of Al₂O₃/Ti(C, N) ceramic tool materials by one-step and two-step microwave sintering", *Material Science Engineering A*, Vol. 670, 2016, pp. 159-165.
- [14] K.I.Vishnu Vandana, K.N.S.Suman, "Finite element modelling and experimental investigation on mechanical properties and micro structural studies of alumina-graphene composites", *New Materials, Compounds and Applications* Vol.5, No. 3, 2021, pp. 156-170.

Multi-Response Optimization of Machining factors in Pocket Milling of AA6082 Using Grey Relational Analysis

M. Rajyalakshmi^{1*}, K. I. V. Vandana², S. Naga Kumar³

^{1,2,3} Department of Mechanical Engineering, PVP Siddhartha Institute of Technology,
Andhra Pradesh, India.

Email: mrajyalakshmi@pvpsiddhartha.ac.in

Abstract: Pocket milling is used in the ship building and aerospace industries. Various tool trajectories can be used to cut the required profile of the pocket on the material. Surface quality is one of the parameters to accept products while also reducing production time to reduce production costs. This demonstrates the importance of selecting the best machining parameters to achieve a good surface finish in a short amount of time. Tool trajectories are also important in pocket generation and production time. In the present paper, best combination of process parameters are identified for AA6082 using Taguchi L9 OA and Multi- objective optimization is done using Grey Relational Analysis. Experiments are carried out with the experimental factors Speed (S), Feed (F), and Stepover (SO). Second, an appropriate tool path must be identified in order to enhance surface quality (SR) and Material Removal Rate (MRR). To create pockets, two tool paths are used: follow periphery and zigzag. Grey Relational Grade is calculated for each tool path based on the obtained results. The optimal parameters are identified as the combination of parameters with the highest Grey Relational Grade. Confirmation experiments show that predicted responses are closer to optimal.

Keywords: Multi-Objective Optimization, Pocket Milling, AA6082, Taguchi, GRA

1. Introduction

In the current scenario, the manufacturing industry is being forced to use advanced technologies in order to maintain object quality while reducing production costs and increasing production volume. Pocket milling is one of the basic processes in the manufacture of dies and moulds. The surface roughness of the pocket directly reflects its quality. Characteristic derived from the product's functional properties.

Aluminium (AA) alloys are the most machinable materials where less weight and corrosion resistance are important criteria for machining. Aluminium and its alloys are typically not difficult to machine. AA6082 is one among the most often used alloys in the moulding business, although it is recommended for moulding due to its strength, polishing ability, corrosion resistance, and wear resistance. Productivity depends on production time and material removal rate. Surface roughness and material removal rate are affected by many factors like feed, Speed, Depth of cut, stepover, Number of passes, tool geometry etc., The selection of tool trajectory for pocket milling is very important as it influences the machining time and cost. Firstly, a rough cut of pocketing takes place with the tool trajectory selected for machining. Then final finish cut is performed to get the required surface finish and correctness in the pocket profile. Many researchers worked to identify the best tool path to reduce the machining time. Number of algorithms are available to select required tool path for obtaining minimum surface roughness[1]–[3]. P.E. Romero et al.[4] investigated how pocket

shape and tool movement affect surface quality and cutting forces. According to the findings of the study, each tool route has its own impact on the answers dependent on the pocket shape chosen. H. Perez et al. [5] developed a novel mathematical model to investigate the influence of tool route on surface roughness and cutting force. Martin Held et al.[6] used an algorithm in the POWERApX package to build a spiral tool path in machining at high speeds. Bouard et al.[7] use a constrained-based optimization approach for tool path calculation in pocket milling to investigate the influence on machining time. J Medina et al.[8] used simulation to examine alternative tool motions for determining cutting time. They attempted to investigate the effect of interpolation, distance between points, and toolpath curvature on cutting time in the study. A. Ghani et al. [9] investigated the effect of cutting parameters on surface roughness using Taguchi optimization. Mohamed T. Hayajneh et al.[10] investigate the effect of cutting factors on surface roughness in end milling. They conducted random tests at all feasible factor level combinations. Milon D. Selvam et al. [11] used Taguchi and the Genetic Algorithm to investigate the influence of process factors on surface roughness in Mild Steel face milling. B.Jabbaripour et al.[12] investigated the impact of four cutter directions and speed changes on surface polish and cutting force. Taguchi OA with grey relational analysis was used by A. Noorul Haq et al.[13] to study multi response optimization in drilling Al/SiC metal matrix composite. M Maiyar et al.[14] used Taguchi and grey relational analysis to investigate multi-response milling of Inconel 718 Super Alloy. They demonstrated through experiments that this strategy may enhance machining performance. Taguchi method coupled grey relational analysis is applied by Santha kumar et al.[15] to optimize one direction tool movement in pocketing of Ti-6Al-4V. By doing confirmation experiments, they observed that MRR, radial tool deflection and surface roughness are optimized by this method. Rajyalakshmi and Babu [16] optimized surface roughness in pocket milling of SAE304 using Taguchi analysis. In the experimental study, they have applied two different tool paths and compared the surface roughness in both criteria. Sukumar et al.[17] On Al 6061, Taguchi and Artificial Neural Networks techniques were used to improve cutting parameters in face milling. They discovered that, despite the fact that both procedures produce distinct combinations of parameters, experimental findings indicated that the surface roughness value was practically same. Malvade et al. [18] employed the Taguchi technique to investigate the effect of cutting settings on Material Removal Rate, Surface Integrity, and Parallelism during end milling operations on OHNS steel. They discovered that the depth of cut influences the rate of material removal and the speed influences the surface roughness. Shunyao et al. [19] employed the Taguchi Grey Relational Analysis approach to determine the influence of tool geometry on achieving a satisfactory surface quality when milling Titanium alloy TB17. Etyemez[20] The Grey Taguchi technique was used to investigate the influence of cutting parameter and tool route on milling AA7075. Emel Kuram and Babur Ozcelik[21] performed experimental study to optimise cutting settings for micro milling of AA7075 using the grey-based taguchi approach. Surface roughness, cutting forces, and tool wear are all evaluated to get the best reaction values. M. Nurhaniza et al.[22] investigated the influence of procedure on surface integrity while milling Al-CFRP composites using a Taguchi orthogonal array. Within the specified boundaries, they observed good surface integrity at high speed, low feed, and low DOC. Biswajit Das et al. investigated the influence of procedure on surface integrity while milling Al-CFRP composites using a Taguchi orthogonal array. Within the specified boundaries, they observed good surface integrity at high speed, low feed, and low DOC. Biswajit Das et al.[23] used Grey-based fuzzy logic to adjust the response parameters during milling Al-4.5%Cu-TiC metal matrix composites.

According to the preceding study, It is observed that the majority of the researchers concentrated on single goal optimization. Several studies have been conducted on pocket milling. In pocket

generation, the effect of step over in conjunction with speed and feed is not stated. It is also possible to investigate tool trajectory selection for multi response optimization in pocket milling. For multi-response optimization, the Grey Taguchi approach provides a superior combination. As a result, in the current work, multi-response optimization with Taguchi-based Grey relational analysis is used to determine the best combination of parameters for producing pockets employing two different tool paths.

2. Material and methodology

AA6082 grade Aluminium Alloy workpieces of size 80X80X10mm are selected. The chemical composition of the material by weight percentage is shown in table 1.

Table1: Composition of AA6082

Element	Al	Si	Fe	Cu	Mn	Cr	Mg	Zn	Ti	Others
Composition (Wt. %)	97.506	0.903	0.223	0.002	0.411	0.016	0.852	0.071	0.010	0.05 max

Taguchi OA produce effective and efficient outcomes with fewer experiments and at a lower cost. An appropriate OA is chosen based on the number of variables and the number of levels for each component. For surface roughness, the lower the Signal to Noise ratio, and for MRR, the greater the signal to Noise ratio are considered as better choice.

The machining parameters considered for this investigation are speed, feed, and stepover. The parameter levels are determined by a survey of the literature, machine specs, and material attributes. Table 2 displays various degrees of machining parameters and reactions.

Table 2: Machining parameters and their Levels selected for experimentation

Symbol	Parameters	Units	Level 1	Level 2	Level 3	Responses
S	Speed	RPM	2000	3000	4000	Surface Roughness (SR)(μm) Material Removal Rate (MRR) (gm/sec)
F	Feed	mm/ min	500	1000	1500	
SO	Step Over	%	20	30	40	

Table 3 displays the combinations of experimental runs utilizing the L9 orthogonal array for the supplied parameters and level combinations.

Table 3: Experimental runs in L₉ orthogonal array

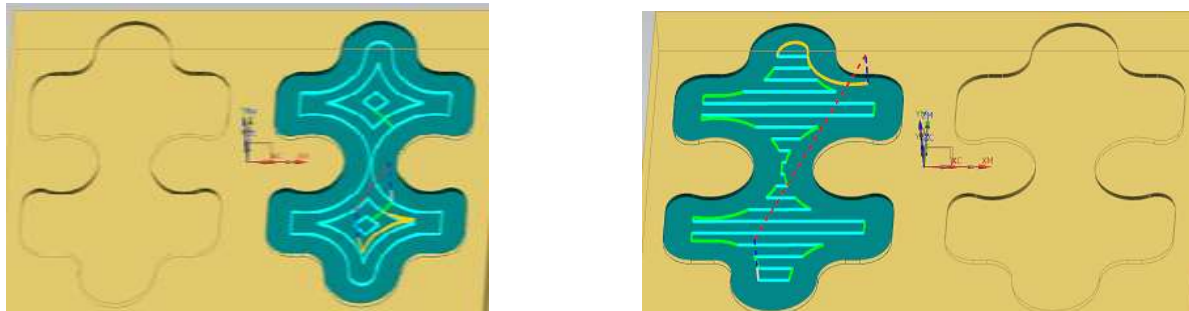
Run No.	Speed (RPM)	Feed (mm/min)	Step Over (%)
1	2000	500	20
2	2000	1000	30
3	2000	1500	40
4	3000	500	30
5	3000	1000	40
6	3000	1500	20
7	4000	500	40
8	4000	1000	20
9	4000	1500	30

A number of studies used Grey Relational Analysis (GRA)[24]–[27] to improve the answers by better combining machining parameters in many industries of production. The experimental data are subsequently analyzed in the current study with the following methods to determine the parameter values for surface roughness and MRR utilizing Grey relational Analysis (GRA). Procedure to calculate Grey Relational Grade is explained by Rajyalakshmi and Babu [28].

3. Simulation and Experimental set up

Siemens NX 11.0 software is used to simulate the shape of the pocket that will be formed on the workpiece. The tool paths, namely follow periphery and zigzag, are simulated independently on the pocket shape, as illustrated in fig. 1. To create the geometry appropriately, the zigzag tool trajectory requires a final cut as well. After simulation, the NC part programme for each tool route was also created.

Pockets are machined using a vertical machining centre with a Fanuc O controller and a 10mm Carbide coated four flutes cutter. Tests were carried out in accordance with the run sequence produced by Minitab 11.0 software, as indicated in table 3. Each experiment was carried out five times. After ten tests, a fresh cutter is employed for each tool route.



a) Follow Periphery

b) Zigzag

Fig.1: selected Tool Trajectories for Pocket Milling

The weight of the work pieces is recorded before and after cutting using a precision balance with a least count of 0.01gm. Throughout the experimentation, the machining time for each trial was recorded. Mitutoyo SJ201P surfest is used to detect surface roughness (SR). MRR is computed using equation (1)

$$MRR = \frac{W_1 - W_2}{t_m} \text{ gm/sec} \text{ --- (1)}$$

Where, W_1, W_2 are the workpiece weights before and after machining respectively and t_m is time taken for generating the pockets in seconds

4. Results and discussion

Experimental tests were carried out in the order described in the preceding section, and the surface roughness of each component was measured. MRR was estimated using Equation 1. As indicated in table4, signal to noise ratios were determined for each response in both tool trajectories.

Table 4: Response values and Signal to Noise Ratio for both the tool paths for AA6082

Expt. Run	Follow periphery				Zigzag			
	SR (µm)	S/N Ratio	MRR (g/s)	S/N Ratio	SR (µm)	S/N Ratio	MRR (g/s)	S/N Ratio
1	1.850	-5.3493	0.0928	-6.6652	1.9536	-5.8167	0.0689	-9.2592
2	2.132	-6.5794	0.1280	-3.8762	1.8276	-5.2376	0.1638	-1.7239
3	2.892	-9.2261	0.1625	-1.8016	2.3222	-7.3759	0.2019	0.0959
4	2.008	-6.0559	0.1618	-1.8375	1.8448	-5.319	0.0970	-6.2834
5	2.756	-8.8152	0.2025	0.1104	1.9416	-5.7632	0.1775	-1.0359
6	2.766	-8.8429	0.1967	-0.1428	2.8416	-9.0713	0.1679	-1.5144
7	2.148	-6.6805	0.2208	0.8611	2.0608	-6.281	0.0958	-6.378
8	2.152	-6.6573	0.3113	3.8486	2.0236	-6.124	0.1320	-3.6087
9	2.310	-7.2799	0.4170	6.3935	2.9508	-9.3988	0.2362	1.4534

After computing the Signal to Noise (S/N) ratios, Taguchi analysis is performed on the experimental data. The improved surface roughness and MRR values for both tool trajectories are determined by calculating the level means. Table 5 shows the level means for both tool paths for surface roughness.

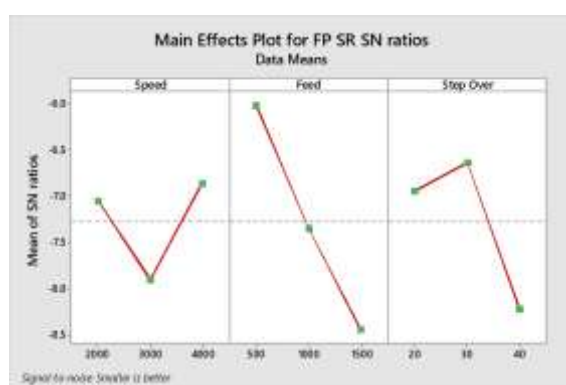
Table 5: Taguchi Method for Surface Roughness for AA6082

Tool Path	Level	Speed (RPM)		Feed (mm/Min)		Stepover (%)	
		Raw Data	S/N Ratio	Raw Data	S/N Ratio	Raw Data	S/N Ratio
FP	1	2.29133	-7.05160	2.0020	-6.028567	2.2560	-6.9498
	2	2.51000	-7.90467	2.3467	-7.35063	2.1500	-6.6384
	3	2.20333	-6.87257	2.6560	-8.44963	2.5987	-8.2406
Delta		0.30667	1.03210	0.6540	2.42107	0.4487	1.6022
Rank		3		1		2	
ZZ	1	3.39078	-6.1434	3.2551	-5.80557	3.78822	-7.0040
	2	3.68222	-6.71783	3.2182	-5.70827	3.67956	-6.6518
	3	3.90844	-7.26793	2.7028	-8.61533	2.10767	-6.4734
Delta		0.51767	1.12453	0.5523	2.90707	1.68056	0.5306
Rank		2		1		3	

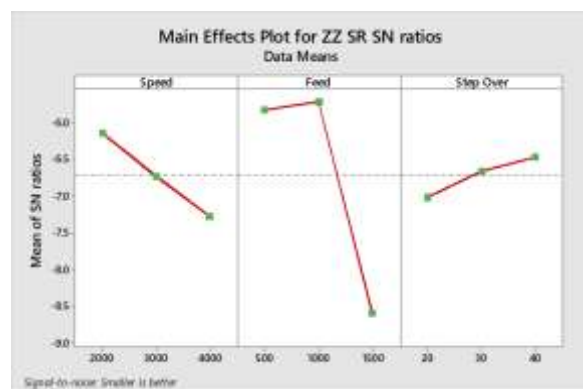
Table 5 shows that in the FP tool path, high speed, low feed, and medium step over produce the lower of surface roughness. In the ZZ tool path, low speed, high feed, and high step over produce the least amount of surface roughness.

Figure 2 (a) and (b) show a means plot for signal to noise ratios for tool routes indicate for FP tool path, high speed, medium feed and medium step over gives low surface roughness value whereas lower speed, medium feed and higher feed generate less surface roughness for ZZ tool path.

In zigzag tool trajectory, surface roughness is affected by speed and feed. Similarly, Taguchi Analysis applied on MRR also indicate that high speed, high feed and medium stepover gives high value of MRR for FP tool path and ZZ tool paths. The detail of the analysis is shown in table 6.



a. Follow Periphery



b. Zigzag

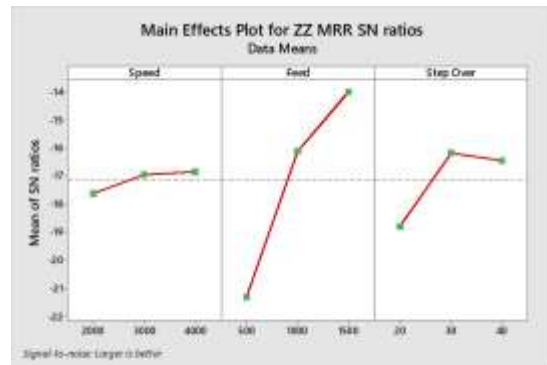
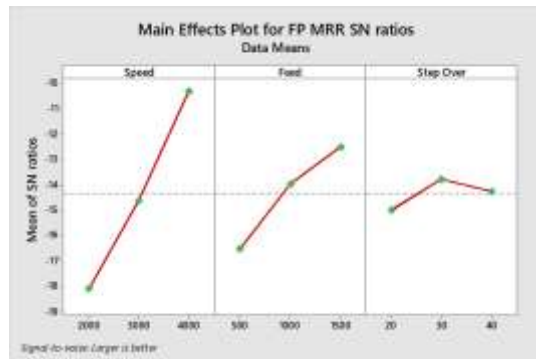
Figure 2: Level Means graph of S/ N Ratios for Surface Roughness for AA6082

Table 6: Taguchi Method for Material Removal Rate for AA6082

Tool Path	Level	Speed (RPM)		Feed (mm/Min)		Stepover (%)	
		Raw Data	S/N Ratio	Raw Data	S/N Ratio	Raw Data	S/N Ratio
FP	1	0.12777	-4.11433	0.158467	-2.5472	0.20027	-0.9865
	2	0.18700	-0.62330	0.213933	0.0276	0.23560	0.2266
	3	0.31637	3.701067	0.258733	1.4830	0.19527	-0.2767
Delta		0.1886	7.8154	0.10027	4.03023	0.040333	1.2131

Rank		1			2	3	
ZZ	1	0.144867	-3.62907	0.08723	-7.30687	0.12293	-4.7941
	2	0.147467	-2.94457	0.15777	-2.12283	0.16567	-2.1846
	3	0.154667	-2.84443	0.20200	0.01163	0.15840	-2.4393
Delta		0.00980	0.78463	0.11477	7.31850	0.04273	2.609467
Rank		3			1	2	

It is also observed that for FP tool path, Speed is the most influencing factor whereas Feed is the significant factor for ZZ tool path.



a. Follow Periphery

b. Zigzag

Figure 3: Level Means graph of S/ N Ratios for Material Removal rate for AA6082

Figure 3 indicates the level means of the factors selected for the study. From the figure it is observed that Higher speed, Higher feed and medium step over for both the tool trajectories generate maximum MRR value.

ANOVA applied on the experimental results of AA6082 for both the responses indicate that Feed is the influencing factor for both tool trajectories for surface roughness. In case of MRR, Speed is the influencing factor for FP tool path and Feed is the most effecting parameter for ZZ tool path.

For both the materials from the Taguchi analysis it is observed that better results are obtained for follow periphery tool trajectory, compared to zigzag tool. This may be because of the chip remained between the cutting tool and the pocket's edge, which helped to scratch the surface, allowing the material to be easily removed.

4.1 Grey Relational Analysis of AA6082

The link between the desired and the actual experimental findings is shown by grey relational coefficients. Grey Relational Grade (GRG) for the experimental results is calculated for the two tool trajectories and tabulated. Table 7 shows the GRG value and the ranks allotted for Follow periphery tool trajectory.

Table 7: Grey Relational values for Follow periphery

Expt. No	SR (μm)	MRR (g/s)	Normalized		Delta		Grey Coefficient		GRG	Rank
			SR (μm)	MRR (g/s)	SR (μm)	MRR (g/s)	SR (μm)	MRR (g/s)		
1	1.85	0.0928	0	1	1	0	0.3333	1	0.6667	2
2	2.132	0.128	0.1086	0.7294	0.8914	0.2706	0.3593	0.6488	0.5041	6
3	2.892	0.1625	0.2150	0	0.7850	1	0.3891	0.3333	0.3612	9
4	2.008	0.1618	0.2128	0.8484	0.7872	0.1516	0.3884	0.7673	0.5779	4
5	2.756	0.2025	0.3384	0.1305	0.6616	0.8695	0.4304	0.3651	0.3978	7
6	2.766	0.1967	0.3205	0.1209	0.6795	0.8791	0.4239	0.3626	0.3933	8
7	2.148	0.2208	0.3948	0.7140	0.6052	0.2860	0.4524	0.6361	0.5443	5
8	2.152	0.3113	0.6740	0.7102	0.3260	0.2898	0.6053	0.633	0.6192	3

9	2.31	0.417	1	0.5585	0	0.4415	1	0.5311	0.7656	1
---	------	-------	---	--------	---	--------	---	--------	--------	---

From Table 7, it is observed that high speed, high feed and medium stepover gives the highest GRG value. This combination gives minimum surface roughness and near to optimum material removal rate. The grey relational grade is 0.7656. From the level means plot shown in figure 4, it is identified that higher speed, low feed and medium stepover is the combination that gives the highest Grey relational Grade.

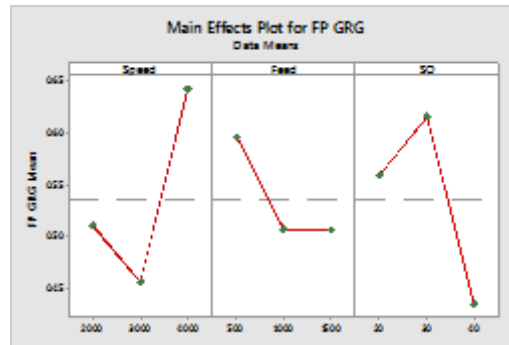


Figure 4: Level Means graph for GRG Value for FP tool path

From the means plot, it is observed that high speed, low feed and medium stepover gives maximum GRG value. The Grey relational Coefficient obtained with 4000RPM speed, 500mm/min feed and 30% stepover is 0.8428. From the confirmation tests, it is observed that surface roughness is $1.98\mu\text{m}$ and MRR value is 0.396 g/s. There is a 10.08% improvement in the GRG Value for the optimal combination of parameters.

Grey Relational Grade is also calculated for zigzag tool trajectory and tabulated. Table 8 shows the gray relational analysis of the zigzag tool path.

Table 8: Grey Relational values for Zigzag

Expt. No	SR (μm)	MRR (g/s)	Normalized		Delta		Grey coefficient		GRG	Rank
			SR (μm)	MRR (g/s)	SR (μm)	MRR (g/s)	SR (μm)	MRR (g/s)		
1	1.9536	0.0689	0	0.8878	1	0.1122	0.3333	0.8168	0.5751	7
2	1.8276	0.1638	0.5672	1	0.4328	0	0.536	1	0.768	1
3	2.3222	0.2019	0.7950	0.5597	0.2050	0.4404	0.7092	0.5317	0.6205	5
4	1.8448	0.097	0.1680	0.9847	0.8320	0.0153	0.3754	0.9703	0.6729	3
5	1.9416	0.1775	0.6491	0.8985	0.3508	0.1015	0.5876	0.8313	0.7095	2
6	2.8416	0.1679	0.5918	0.0972	0.4083	0.9028	0.5505	0.3564	0.4535	9
7	2.0608	0.0958	0.1608	0.7924	0.8392	0.2076	0.3734	0.7066	0.54	8
8	2.0236	0.132	0.3772	0.8255	0.6228	0.1745	0.4453	0.7413	0.5933	6
9	2.9508	0.2362	1	0	0	1	1	0.3333	0.6667	4

The level means plot drawn for grey relational data of zigzag trajectory is shown in figure 5. From the figure also it was evident that lower speed, medium feed and medium stepover gives optimum response values.

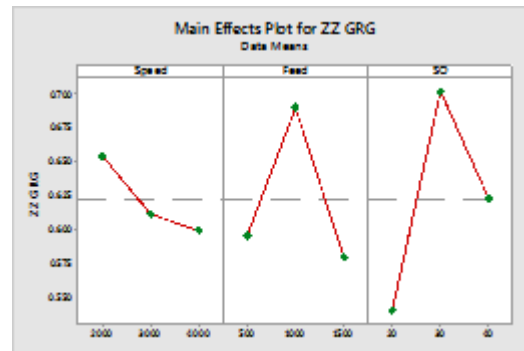


Figure 5: Level Means graph for GRG Value for FP tool path

Level means graph also indicates that 2000 RPM speed, 1000 mm/min feed and 30% stepover gives Optimum surface roughness and MRR values.

Conclusions

Present study is concentrated on multi response optimization of machining parameters using Taguchi and Grey Relational Analysis. One linear and one nonlinear tool trajectories viz, zigzag and follow periphery are used to generate pockets. For each tool trajectory, Experimental results are further processed with Grey relational analysis. Following conclusions can be drawn from the study.

1. For follow periphery tool path, The Grey relational Coefficient obtained with 4000RPM speed, 500mm/min feed and 30% stepover. Confirmation test ensures the result with 10.085% increase in the GRG value.
2. For zigzag tool path, the optimal combination from the mean plot is lower speed, medium feed and medium stepover and experimental GRG value confirms the combination as the best combination for generating surface roughness closer to minimum and MRR closer to maximum values.
3. When coupled with Grey relational analysis, the Taguchi technique produces superior results in finding the best combination of parameters in multi-response optimization. Within the settings chosen, follow periphery produces superior surface roughness and material removal rate than zigzag.
4. According to the ANOVA results, the influencing element for follow periphery feed is speed, whereas speed is the greatest influencing factor for zigzag.

References

- [1] M. B. Bieterman and D. R. Sandstrom, "A curvilinear tool-path method for pocket machining," *J. Manuf. Sci. Eng. Trans. ASME*, vol. 125, no. 4, pp. 709–715, 2003, doi: 10.1115/1.1596579.
- [2] C. K. Toh, "A study of the effects of cutter path strategies and orientations in milling," *J. Mater. Process. Technol.*, vol. 152, no. 3, pp. 346–356, 2004, doi: 10.1016/j.jmatprotec.2004.04.382.
- [3] C. Gologlu and N. Sakarya, "The effects of cutter path strategies on surface roughness of pocket milling of 1.2738 steel based on Taguchi method," *J. Mater. Process. Technol.*, vol. 206, no. 1–3, pp. 7–15, 2008, doi: 10.1016/j.jmatprotec.2007.11.300.
- [4] P. E. Romero, R. Dorado, F. A. Díaz, and E. M. Rubio, "Influence of pocket geometry and tool path strategy in pocket milling of UNS A96063 alloy," *Procedia Eng.*, vol. 63, no. 1998, pp. 523–531, 2013, doi: 10.1016/j.proeng.2013.08.194.
- [5] H. Perez, E. Diez, J. Perez, and A. Vizan, "Analysis of machining strategies for peripheral milling," *Procedia Eng.*, vol. 63, pp. 573–581, 2013, doi: 10.1016/j.proeng.2013.08.193.
- [6] M. Held and C. Spielberger, "A smooth spiral tool path for high speed machining of 2D pockets," *CAD Comput. Aided Des.*, vol. 41, no. 7, pp. 539–550, 2009, doi: 10.1016/j.cad.2009.04.002.
- [7] M. Bouard, V. Pateloup, and P. Armand, "Pocketing toolpath computation using an optimization method," *CAD Comput. Aided Des.*, vol. 43, no. 9, pp. 1099–1109, 2011, doi: 10.1016/j.cad.2011.05.008.
- [8] G. Medina-Sánchez, E. Torres-Jimenez, R. Lopez-Garcia, and R. Dorado-Vicente, "Cutting time in pocket machining for different tool-path approximation segments," *Procedia Manuf.*, vol. 13, pp. 59–66, 2017, doi: 10.1016/j.promfg.2017.09.009.

- [9] J. A. Ghani, I. A. Choudhury, and H. H. Hassan, "Application of Taguchi method in the optimization of end milling parameters," *J. Mater. Process. Technol.*, vol. 145, no. 1, pp. 84–92, 2004, doi: 10.1016/S0924-0136(03)00865-3.
- [10] M. S. T. J. B. Mohammed T. Hayajneh, "A Study of the Effects of Machining Parameters on the Surface Roughness in the End-Milling Process," *Jordan J. Mech. Ind. Eng.*, vol. 1, no. 1, pp. 1–5, 2007.
- [11] M. D. Selvam, G. Karuppusami, and A. K. S. Dawood, "Optimization of Machining Parameters for Face Milling Operation in a Vertical Cnc Milling Machine Using Genetic Algorithm," *An Int. J. (ESTIJ)*, vol. 2, no. 4, pp. 2250–3498, 2012.
- [12] B. Jabbaripour, M. H. Sadeghi, and S. Faridvand, "a Study of the Effects of Cutter Path Strategies and Cutting Speed Variations in Milling of Thin Walled Parts," *7th Jordanian Int. Mech. Eng. Conf.*, no. September, pp. 27–29, 2010.
- [13] A. N. Haq, P. Marimuthu, and R. Jeyapaul, "Multi response optimization of machining parameters of drilling Al/SiC metal matrix composite using grey relational analysis in the Taguchi method," *Int. J. Adv. Manuf. Technol.*, vol. 37, no. 3–4, pp. 250–255, 2008, doi: 10.1007/s00170-007-0981-4.
- [14] L. M. Maiyar, R. Ramanujam, K. Venkatesan, and J. Jerald, "Optimization of machining parameters for end milling of Inconel 718 super alloy using Taguchi based grey relational analysis," *Procedia Eng.*, vol. 64, pp. 1276–1282, 2013, doi: 10.1016/j.proeng.2013.09.208.
- [15] J. Santhakumar, U. M. Iqbal, and M. Prakash, "Optimization of one direction tool path orientation for pocket milling of Ti-6Al-4V using taguchi based grey relational analysis," *IOP Conf. Ser. Mater. Sci. Eng.*, vol. 402, no. 1, 2018, doi: 10.1088/1757-899X/402/1/012166.
- [16] M. Rajyalakshmi and P. S. Babu, "Optimization of Process Parameters in Pocket Milling of SAE304 Based on Tool Path Strategies using Taguchi Method," vol. 8, no. 3, pp. 49–56, 2018.
- [17] M. S. Sukumar, P. Venkata Ramaiah, and A. Nagarjuna, "Optimization and prediction of parameters in face milling of Al-6061 using taguchi and ANN approach," *Procedia Eng.*, vol. 97, pp. 365–371, 2014, doi: 10.1016/j.proeng.2014.12.260.
- [18] N. V. Malvade and S. R. Nipanikar, "Optimization of Cutting Parameters of End," *J. Eng. Res. Stud.*, vol. v, no. ii, pp. 14–17, 2014, [Online]. Available: <http://www.technicaljournalsonline.com>.
- [19] S. Du, M. Chen, L. Xie, Z. Zhu, and X. Wang, "Optimization of process parameters in the high-speed milling of titanium alloy TB17 for surface integrity by the Taguchi-Grey relational analysis method," *Adv. Mech. Eng.*, vol. 8, no. 10, pp. 1–12, 2016, doi: 10.1177/1687814016671442.
- [20] M. Ay and A. Etyemez, "Optimization of effects of cutting parameters and cutting tool path by using grey based taguchi method," *Acta Phys. Pol. A*, vol. 134, no. 1, pp. 125–128, 2018, doi: 10.12693/APhysPolA.134.125.
- [21] E. Kuram and B. Ozcelik, "Multi-objective optimization using Taguchi based grey relational analysis for micro-milling of Al 7075 material with ball nose end mill," *Meas. J. Int. Meas. Confed.*, vol. 46, no. 6, pp. 1849–1864, 2013, doi: 10.1016/j.measurement.2013.02.002.
- [22] M. Nurhaniza, M. K. A. M. Ariffin, F. Mustapha, and B. T. H. T. Baharudin, "Analyzing the Effect of Machining Parameters Setting to the Surface Roughness during End Milling of CFRP-Aluminium Composite Laminates," *Int. J. Manuf. Eng.*, vol. 2016, pp. 1–9, 2016, doi: 10.1155/2016/4680380.
- [23] B. Das, S. Roy, R. N. Rai, and S. C. Saha, "Application of grey fuzzy logic for the optimization of CNC milling parameters for Al-4.5%Cu-TiC MMCs with multi-performance characteristics," *Eng. Sci. Technol. an Int. J.*, vol. 19, no. 2, pp. 857–865, 2016, doi: 10.1016/j.jestch.2015.12.002.
- [24] K. Gajalakshmi, N. Senthilkumar, and B. Prabu, "Multi-response optimization of dry sliding wear parameters of AA6026 using hybrid gray relational analysis coupled with response surface method," *Meas. Control (United Kingdom)*, vol. 52, no. 5–6, pp. 540–553, 2019, doi: 10.1177/0020294019842603.
- [25] G. Kibria, B. Doloi, and B. Bhattacharyya, "Experimental investigation and multi-objective optimization of Nd:YAG laser micro-turning process of alumina ceramic using orthogonal array and grey relational analysis," *Opt. Laser Technol.*, vol. 48, pp. 16–27, 2013, doi: 10.1016/j.optlastec.2012.09.036.
- [26] M. K. Pradhan, "Estimating the effect of process parameters on surface integrity of EDMed AISI D2 tool steel by response surface methodology coupled with grey relational analysis," *Int. J. Adv. Manuf. Technol.*, vol. 67, no. 9–12, pp. 2051–2062, 2013, doi: 10.1007/s00170-012-4630-1.
- [27] M. K. Mallik, C. Srinivasa Rao, V. V. S. Kesava Rao, and S. K. Abdul Munaf, "Effect of heat treatment on corrosion behavior of weld deposited co-cr-mo alloy," *ARNP J. Eng. Appl. Sci.*, vol. 11, no. 20, pp. 12188–12191, 2016.
- [28] M. Rajyalakshmi and P. Suresh Babu, "Influence of cutting parameters and tool path strategies on surface roughness in pocket milling of UNS a96082 alloy," *Int. J. Eng. Adv. Technol.*, vol. 9, no. 1, pp. 6241–6245, 2019, doi: 10.35940/ijeat.A1995.109119.

Development of bio composite materials for construction industries

Haroon Ali Khan¹, K. Ramanaiah^{2*}, Katta Pavani³, Velpula Kasi Kalyani³,
Odugu Nagasree³

¹ Department of Civil Engineering, VR Siddhartha Engineering College, Vijayawada-520 007, India

*² Department of Mechanical Engineering, VR Siddhartha Engineering College, Vijayawada-520 007, India

³ UG Students, Department of Civil Engineering, VR Siddhartha Engineering College, Vijayawada-520 007, India

Corresponding author*: ramanaiah@vrsiddhartha.ac.in

Abstract: In the present work, waste jute mat (gunny bags) and sugar cane bagasse fibers are used as reinforcement in polyester matrix for the development of bio-composites. Hand layup technique was adopted for the preparation of composite samples. Three types of bio composite (Jute mat+ Polyester, Bagasse+ Polyester, Jute mat +Bagasse+ Polyester) were developed. Mechanical properties such as tensile, flexural and impact properties in each case were tested as per standard test methods. Tensile strength of Jute mat +Bagasse+ Polyester composite (Hybrid composite) is 121% greater than that of bagasse composite. Flexural strength of hybrid composite is 4.2 times that of bagasse composite. Hence, Hybrid bio composite materials can be used in place of petroleum-based materials in construction industries.

Key words: Mechanical properties, Bio-composite materials, Jute mat, Bagasse fiber

1. Introduction

Due to growing environmental consciousness and worries about the use of renewable natural resources, there has been a lot of work done to develop eco-friendly and biodegradable materials for the next generation of composite products. The number of natural materials used in composites has increased, which has decreased their carbon footprint and associated greenhouse gas emissions. In addition to the advantages of using green materials, there are also drawbacks, such as the natural fibers relatively high moisture absorption and the poor compatibility of the reinforcing natural fiber and matrix. Petroleum-based materials may be adequately replaced by green composites. The fundamental physical and mechanical characteristics of natural fibers, natural fiber reinforced bio composite materials, as well as their prospective applications, were examined [1]. Natural composites consisting of rice husk powder and sugarcane bagasse fiber were evaluated using the hand layup method. They show a minimum level of ductility and have lower tensile and yield strength. The flexural strength was reduced as a result of a lack of cohesion in the bonding between the reinforcement and matrix [2]. The mechanical properties in banana and Sugarcane Bagasse hybrid composites improved with an increase in Sugarcane Bagasse fiber content from 6%, acting as a positive reinforcement in providing the composite with additional strength and a smooth surface finish, while at the same time the Banana fiber gave the composite elasticity [3]. The JFRP composite system of strengthening showed that the JFRP material has great potential as a structural strengthening material by having the highest deformability index [4]. Hybridization has been found to be usually advantageous in terms of raising the tensile and flexural moduli, decreasing the likelihood of brittle failure, and stopping the decline in tensile modulus caused by moisture absorption [5]. The mechanical qualities of jute reinforced epoxy composite were superior to jute polyester composite [6]. Sansevieria natural fiber in the creation of green composites that are partially biodegradable. Maximum fiber resulted in tensile and

impact strengths that were 2.55 and 4.2 times, respectively, greater than those of pure resin. Sansevieria fiber addition significantly reduced the matrix's heat release rate (HRR) and peak heat release rate (PHRR) by 10.4% and 25.7%, respectively. The thermal conductivity of the composite decreased as the fiber content increased, but the temperature trend showed a completely different pattern [7]. When natural Borassus seed shoot fiber is incorporated into polymers as reinforcement, partially green polymer composites can have a fiber content ranging from 0.116 to 0.305 by volume. It was discovered that the composite produced from Borassus seed shoot fibers had tensile and flexural strengths that were, respectively, 77.1% and 112.6 percent more than those of pure matrix. The impact at the maximum fiber volume percent is found to be 88.54 J/m [8]. Reaction of a hybrid composite made of jute, bagasse, glass, and epoxy under tension and indentation stress. Bagasse-glass/epoxy hybrid composite is less dense than jute-glass/epoxy hybrid composite, but it is more durable than bagasse-glass hybrid composite [9]. Using epoxy resin and sugarcane bagasse powder as a base, their study examined the tensile, hardness, and impact characteristics of the material. With a rise in sugarcane content, the composites can become less ductile [10]. Study on the tensile characteristics of epoxy composites reinforced with sugarcane short fiber and bagasse fiber. Tensile strength rises with a rise in bagasse fiber weight % and falls with a rise in bagasse fiber weight percentage [11]. Natural fibers have a wide range of industrial and commercial applications, including the interior of vehicles, partition and false ceiling panels, partition boards, roof tiles, coir fiber packaging, furniture, low-energy home insulation, geo-textiles for erosion control and soil protection, enhancing barrier properties, composite materials, and more [12]. Tensile and bending strength are negatively impacted by an increase in fiber content. The 10% Bagasse Fiber Composite has the strongest tensile and bending strength when compared to the 20% and 30%. Water is absorbed faster when the fiber content rises. The composite with a 30% bagasse fiber content absorbs the most water [13]. The physical and sound-absorbing qualities of five distinct composite materials produced from used sugarcane bagasse and bamboo charcoal were studied. Because the components are denser, the natural green composite mats demonstrated superior physical and auditory absorption. The outcomes demonstrate that natural fiber composites, which can absorb more than 70% of sound resistance, have the best acoustic absorption capabilities [14]. A thorough analysis was done on jute-based bio and hybrid composites. Hybrid jute-based composites have outstanding mechanical and physical characteristics. Thermophysical characteristics, moisture resistance, and fiber/matrix adhesion are all improved in hybrid jute composites [15].

Waste Jute mat and sugar cane bagasse are renewable and abundantly available. This economical source compared to other natural sources is still underutilized. The overall objective of this work is to prepare fibers and incorporating them into polyester resin matrix to prepare the composite materials. The composites were tested and characterized to evaluate the tensile, flexural and impact properties.

2. Experimental details

2.1. Materials

Polyester resin used as matrix and Jute fiber mat, and Sugar bagasse fibers are used as reinforcement in the preparation of composites.

2.2. Extraction of fiber

Bagasse fibers are extracted from sugarcane rind in two steps: mechanical separation and chemical extraction. The two main types of jute: white jute (*Corchorus capsularis*) & dark jute (*Corchorus Olitorius*). Jute fiber has some unique physical properties like high tenacity, bulkiness, Sound & heat insulation property, low thermal Conductivity, Anti-static Property etc.



Fig 1: Sugar bagasse fibers



Fig 2: Jute fiber mat

Table 1 Physical and mechanical properties of Jute fiber

Material	Properties	Values
Jute fiber	Density	1300 – 1500 kgm ⁻³
	Length	1.5-120 mm
	Elongation %	1.5-1.8
	Tensile strength	393-800 Mpa
	Young's Modulus	10-55 Gpa
	Water Absorption %	12

Table 2 Physical and mechanical properties of Sugarcane Bagasse fiber

Material	Properties	Values
Sugarcane Bagasse	Density	1.2 g/cm ³
	Tensile Strength	20-290 Mpa
	Young's Modulus	19.7-27.1 Gpa
	Elongation Break %	1.1

Table 3 Physical and mechanical properties of Polyester resin

Material	Properties	Values
Unsaturated Polyester Resin	Density	1.2 to 1.5 g/cm ³
	Young's Modulus	2 to 4.5 Gpa
	Tensile Strength	40 to 90 Mpa
	Compressive Strength	90 to 250 Mpa
	Tensile elongation at break %	2
	Cure Shrinkage %	4 to 8
	Water Absorption 24h at 20 ° C	0.1 to 0.3

2.3. Fabrication of composites

In this process resins are impregnated by hand into fibers which are in the form of woven, knitted, stitched or bonded fabrics. Hand lay-up is the simplest and oldest open moulding method for fabricating composites. At first, dry fibers in the form of woven, knitted, stitched, or bond fabrics are manually placed in the mould, and a brush is used to apply the resin matrix on the reinforcing material. Subsequently, hand rollers are used to roll the wet composite to ensure an enhanced interaction between the reinforcement and the matrix, to facilitate a uniform resin distribution, and to obtain the required thickness. Finally, the laminates are left to cure under standard atmospheric conditions. Generally, this process is divided into four steps: mould preparation, gel coating, lay-up, and curing. Curing is the process of hardening the fiber-reinforced resin composite without external heat. A pigmented gel coat is first applied to the mould surface to obtain a high-quality product surface.

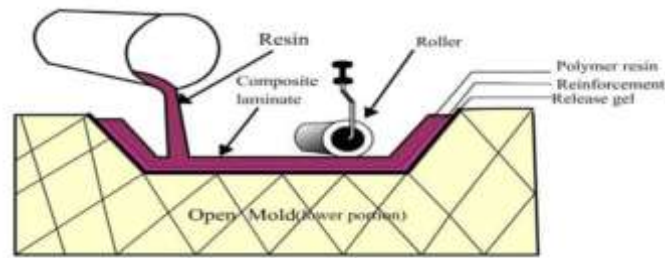


Fig 3: Hand layup method



Fig 4: Cutting of composite into samples according to ASTM standards

2.4. Tensile and Flexural Testing

The tensile properties of the samples of sizes 160 mm long, 12.5 mm wide and 3 mm thick were measured in accordance with ASTM: D638-10. The samples were tested at a cross head speed of 5 mm/min, using an UTM 5000kgf computerized advanced equipment. Three-point bend tests were performed in accordance with ASTM D 790M test method I (procedure A) to measure flexural properties. The specimens were 100 mm long, 25 mm wide and 3 mm thick. In three point bending test, the support distance of 100mm and samples were tested at a strain rate of 10 mm/min.



Fig 5: Tensile test experimental setup

2.5. Impact Testing

Impact strength of notched specimens were tested in accordance with ASTM: D256-10 using plastic impact testing machine (Resolution- 0.0001J), supplied by 3.46 m/s. The specimens were 63.5 mm long, 12.7 mm deep and 10 mm wide.



Fig 6: Impact test experimental setup

3. Results and discussion

3.1. Tensile Properties of composite materials

The experimental values of tensile strength of jute fiber reinforced composite material, sugar cane bagasse fiber reinforced composite material and jute + sugar cane bagasse fiber reinforced hybrid composite materials are presented in Table 4. From the results, It was clearly evident that Tensile strength of jute fiber and hybrid composite is 13.6 % and 68.3 % higher than that of plain matrix respectively. This is due to the fact that the polyester resin transmits and distributes the applied stress to the fibers resulting in higher strength. Therefore, the composite can sustain higher load before failure compared to the unreinforced polyester. Jute mat +Bagasse+ Polyester composite (Hybrid composite) is 121% greater than that of bagasse composite. The tensile strength of hybrid composite considered in this study is far better than that of peach palm fiber reinforced polyester composites [11]. Hence, Hybrid bio composite materials can be used in place of petroleum-based materials as building material for light load structural applications.

Table 4 Tensile properties of Composite materials

Material	Tensile strength (MPa)
Polyester Resin	20.5
Jute fiber composite	23.28
Bagasse fiber composite	15.61
Jute+ Bagasse fiber hybrid composite	34.53

3.2. Flexural Properties of composite materials

The experimental values of Flexural strength of jute fiber reinforced composite material, sugar cane bagasse fiber reinforced composite material and jute + sugar cane bagasse fiber reinforced hybrid composite materials are presented in Table 5. From the results, It was clearly evident that Flexural strength of jute fiber, sugar cane bagasse and hybrid composite is 2.53, 1.35 and 5.16 times that of polyester resin, respectively. This is due to the fact that the polyester resin transmits and distributes the applied stress to the fibers resulting in higher strength. Therefore, the composite can sustain higher load before failure compared to the unreinforced polyester. Among all the materials , Jute mat +Bagasse+ Polyester composite (Hybrid composite) exhibits higher flexural strength compared to other materials. Hence, Hybrid bio composite materials can be used in place of synthetic fiber reinforced composite materials in construction industries.

Table 5 Flexural properties of Composite materials

Material	Flexural strength (MPa)
Polyester Resin	44.6
Jute fiber composite	113.142Mpa
Bagasse fiber composite	59.95 MPa
Jute+ Bagasse fiber hybrid composite	261.6Mpa

3.3. Impact strength of composite materials

The results of pendulum Impact tests of composite materials are shown in table 6. The impact strength of jute fiber is 51.4 % and 35 % higher than that of polyester resin and soft wood. Hence Jute fiber reinforce composite material can be placed in the category of tough engineering materials.

Table 6 Impact strength of Composite materials

Material	Impact strength (J/m)
Polyester Resin	35

Jute fiber composite	52.9
Bagasse fiber composite	26.4
Jute+ Bagasse fiber hybrid composite	37.6

4. Conclusions

Bio composite materials were successfully developed using Hand layup technique. The tensile, flexural and impact properties of the composites with these fibers were found to be higher than that of the matrix conforming the reinforcing action of the fibers. Tensile strength of Jute mat + Bagasse + Polyester composite (Hybrid composite) is 121% greater than that of bagasse composite. Flexural strength of hybrid composite is 4.2 times that of bagasse composite. Hence, Hybrid bio composite materials can be used in place of petroleum-based materials in construction industries.

References

- [1]. Anindita saha, Ruhul A khan and Kazi M karaz, Physio-mechanical properties and applications of natural fiber reinforced biocomposites , GSC Advanced Engineering and Technology, Vol. 03(01), 2022, 001-010.
- [2]. Hemnath A., Anbuhezhiyan G., Nantha Kumar P. and Senthilkumar N., Tensile and flexural behaviour of rice husk and sugarcane bagasse reinforced polyester composites, Materials Today: Proceedings, Vol. 46(9), 2021, 3451-3454.
- [3]. Gopinath V., Abinath R., Babhu Sankar G. and Barathraj S., Evaluation of Mechanical Behavior of Banana and Sugarcane Bagasse Fiber Reinforced Epoxy Hybrid Composite, International Journal of Engineering Science and Computing (IJESC) , Vol. 11(03), 2021, 2321-3361.
- [4]. Archana D.P., Jagannatha Reddy H.N., Jeevan N., Prabhakara R., Aswath M.U. and Basavaraju Paruti., Natural Jute Fiber- Reinforced Polymer Composite System for Posttensioned Beam Strengthening in Flexure, Advances in Materials Science and Engineering, 2021, 1687-8434.
- [5]. Ashok mache, Anindya deb, Sumitesh das and Rokesh laishram, A study on the mechanical behaviors of jute-polyester composite, Procedia Engineering , Vol. 173, 2017, 631-638.
- [6]. Prabhakar kaushik and Kapil mittal, Analysis of mechanical properties of jute fiber strengthened epoxy/polyester composites, Engineering solid mechanics , Vol. 5(2), 2017, 103-112.
- [7]. K. Ramanaiah, A.V. Ratna Prasad , K. Hema Chandra Reddy , Mechanical, thermophysical and fire properties of sansevieria fiber-reinforced polyester composites, Materials & Design, Vol. 49, 2013, 986-991.
- [8]. K. Ramanaiah , A.V. Ratna Prasad , K. Hema Chandra Reddy , Effect of Fiber Loading on Mechanical Properties of Borassus Seed Shoot Fiber Reinforced Polyester Composites, Journal of Materials and Environmental Science, Vol. 3(2), 2012, 374-378.
- [9]. Prashant Tripathi, Vivek Kumar Gupta, Anurag Dixit, Raghvendra Kumar Mishra and Satpal Sharma, Development and characterization of low cost jute, bagasse and glass fiber reinforced advanced hybrid epoxy composites, AIMS Materials Science, Vol. 5(2), 2018, 320-337.
- [10]. Sebastin joyal J., Karthick A., Mahendran K., Palanisamy K. and Ramkumar R., Analysis of composite material formed by sugarcane bagasse and epoxy resin, International Journal of Creative Research Thoughts (IJCRT), Vol. 8, 2020, 2320-2882.
- [11]. Piyush Tiwari and Preetam Kumar Patel, Experimental Study on the Mechanical (Tensile Strength) Performance of Sugarcane Bagasse Fiber Reinforced Epoxy Composite, International Journal of Research in Engineering, Science and Management , Vol. 2(06), 2019, 2581-5792.
- [12]. Madhuputtegowda, Harikrishnan pulikkalparambil and Sanjay mavinkere rangappa, Trends and developments in natural fiber composite, Applied science and engineering progress, Vol. 14(04), 2021, 543-552.
- [13]. Biraj Dhibar, Siddharth Vikram Singh, Shoeb Anwar and Abhineet Singh, Sugarcane Bagasse Reinforced Polyester Composites, International Research Journal of Engineering and Technology (IRJET) , Vol. 5, 2018, 2395-0072.
- [14]. Fasika Abedom , Sakthivel S., Daniel Asfaw, Bahiru Melese, Eshetu Solomon and Senthil Kumar , Development of Natural Fiber Hybrid Composites Using Sugarcane Bagasse and Bamboo Charcoal for Automotive Thermal Insulation Materials, Advances in Materials Science and Engineering, 2021, 001-010.
- [15]. Muhammad Ahsan Ashraf, Mohammed Zwawi, Muhammad Taqi Mehran, Ramesh Kanthasamy and Ali Bahadar, Jute Based Bio and Hybrid Composites and their Applications, National University of Sciences and Technology (NUST), Vol. 07, 2019, 001-077.

Development of B4C Particulate Reinforced AA7075 Composite by Friction Stir Welding: Evaluation of Microstructure and Mechanical Properties

Ch. Kishore Reddy^{1*}, K. Sri Ram Vikas², Dr. M. Srinivasa Reddy³, VSN Venkata Ramana⁴, Rahul⁵

1*, Department of Mechanical Engineering, Prasad V. Potluri Siddhartha Institute of Technology, Vijayawada, Andhra Pradesh, 520007, India. (kishorereddymtech@gmail.com)

2, Department of Metallurgical Engineering, Andhra University, Visakhapatnam, 530003, Andhra Pradesh, India. (sriramvikas@gmail.com)

3. Department of Basic Sciences & Humanities, ANU college of Engineering & Technology, Guntur, Andhra Pradesh, 522510, India. (msreddy2004@gmail.com)

4, Department of Mechanical Engineering, GITAM Institute of Technology, GITAM (Deemed to be University), Visakhapatnam, Andhra Pradesh. 530045, India. (vsivr74@gmail.com)

5, Department of Mechanical Engineering, Chaitanya Bharathi Institute of Technology(A), Gandipet, Hyderabad, 500075, Telangana, India. (luhar6100@gmail.com)

Abstract: Owing to their outstanding strength to specific weight ratio and good mechanical properties, the use of heat treatable aluminium alloys is going on increasing for the last two decades especially for structural and ballistic applications in aerospace, marine, automobile and defence industries. The present investigation aims to develop and evaluate the microstructural behaviour of the surface composite of AA7075-T6 (Al-Zn-Mg-Cu) reinforced with boron carbide (B4C) ceramic particulate by solid-state technique-friction stir welding (FSW). A long groove of 1mm depth and width 1mm were made along the centre of the plate (150×300mm). B4C powder Particulates which were ballmilled for 50 hours were incorporated in the groove, Pinless tool is used for closing the groove. Bead on plate welding is performed at rotational speed 1400rpm with transverse speed 40mm/min, the axial force of 10kN and tilt angle of 2° is maintained. Mechanical Properties such as tensile strength, hardness have improved by the addition of B4C particles. Mechanical and microstructural changes have been studied and correlated using optical microscopy (OM), scanning electron microscopy (SEM).

Keywords: Friction Stir Welding (FSW); AA7075; B4C Particulate, Ball mill, Microstructure

Introduction

In many Industries like automobile, marine, defense, armory, aerodynamic, space etc., the application of AA 7XXX grade aluminium alloys have been emerged in last decade in big way [1-2]. The enhanced high strength to weight ratio property of these AA7XXX series alloys was processed by the process called precipitation hardening. Similar kind of properties may be enhanced by using fabrication techniques like stir casting, powder metallurgy, etc. [3-4]. The enhanced properties of materials in the above techniques are achieved by incorporating high hard particulate in to base material [5-6]. But the main drawback in these techniques is porosity [7]. In order to overcome these problems, a secondary process like extrusion, rolling etc., has to undergo for the prepared material [8]. Friction stir process (FSP) is a derived technique by modifying friction stir welding process in which the properties of the surface will be enhanced according to the requirement [9]. In this novel FSP,

ceramic like high had particulate is filled in the pre-prepared blind holes on the surface of substrate, against which a revolving tool with a probe is plunged with moderate force [10]. In the FSP process the rotating speed and travelling speed are considered as the process variables [11]. This process is a proven technique for the effective modification of both surface and subsurface with enhanced properties [12]. Ceramic particulate like SiC, TiB₂, Al₂O₃, ZrO₂ etc, were used as reinforcement material in many of AA7XXX series alloys using FSP [13-15]. With these reinforcements though higher hardness is achieved, poor impact properties are exhibited due to poor grain refinement [16]. AA7075 is the harder and stronger alloy among all AA 7XXX series which poses better mechanical and thermal properties at normal room temperature [17]. B₄C particulate stances outstanding properties like low density to weight ratio and which can with stand for high temperature environments and have excellent ballistic properties [18-19]. Neutron absorptivity is observed in Al-B₄C FSP composites which causes high strength at high temperatures and better surface properties. [20]. In the present study surface composites were prepared from base substrate AA 7075 by incorporating B₄C particulate for achieving the combined effect of these two which leads to better microstructural and mechanical properties.

Materials and Methods

A 300 mm × 150 mm × 6 mm sized high strength AA7075 aluminum alloy strips were used as the substrate in the present work. Boron carbide powder is used as the filler material, as it is a outstanding capable material for various applications. Due to its nearness to AA7075 in its density, compared to SiC, Alumina etc., B₄C is more suitable as filler material [21]. The chemical composition of the substrate is given in the table 1. The top surface of the plate was drilled with 1 mm and then passed along the length of the work piece. The depth of the groove is 4 mm. Boron carbide powder particles is milled for 50 hours using ball mill. The obtained 60 nm-sized B₄C powder particulate was filled in the groove that made on the plates. Initially the powder-filled groove of the plates was closed with the help of friction stir processing (FSP) tool. After processing with FSP tool, the processed region was then friction stirred with FSW tool. The tool was made to move along the rolled direction of the substrate plates. The schematic representation of plate with groove, tool setup, the tool and the welded plates were shown in figure 1 (a), (b), (c) and (d). Due to interface surface deformation process, heating process and solid-state deformation process the plates were joined together. In order to obtain a defect free joint, the process is undergone through three passes. FSW parameters were tabulated in table 2. The samples were prepared for metallographic analysis. The tensile test specimens were cut using wire EDM, as per ASTM E-8/E8-M-09 standards. The extracted samples from the welded plates were heat treated to T6 condition. Tensile test was conducted on the INSTRON testing machine (± 100 kN load rating) attached with an extensometer. Hardness of the samples were measured using micro-Vickers Hardness Tester (LV700 USA make) with 0.2kgf load applied at 10 sec dwell.

Table 1. Chemical composition (wt. %) of the substrate AA7075 alloy

Element	Si	Fe	Cu	Mn	Mg	Cr	Zn	Ti	Al
Wt. %	0.4	0.5	1.2	0.3	2.1	0.2	5.4	0.3	Bal

Table 2. FSW parameters

Parameter	Load, kN	Tool axial feed, mm/ min.	Depth, mm	Tool down feed, mm/ min.	Spindle speed, RPM
Value	10	40	3	20	550



Figure 1(a) The schematic representation of plate with groove before FSW



Figure 1(b) FSW tool setup



Figure 1(c) FSW tool



Figure 1(d) After welding the plates

Result and Discussion

Hardness:

The micro hardness values of the specimens of base alloy AA7075, friction stir welded AA7075 without filler particulate and FSW AA7075 with B₄C particulate as filler were tabulated in Table 3 and Table 4. The hardness of base AA7075 alloy is 141 HV. The hardness of friction stir welded (FSW) AA7075 at stir zone (SZ) has been increased because of fine refinement of grains. Usefully, in SZ regions, hardness increases because of very fine grain size due to dynamic recrystallization [22]. The hardness in base alloy is less because of large grain size. We can see this in the SEM graph as show in figure 4. The hardness in the thermo mechanical affected zone (TMAZ) region shows slight decrement because of subsequent increase in grain size and partially recrystallized grains. In the heat affected zone (HAZ) hardness is further decreased because of increase in grain size. Moreover, in the HAZ and TMAZ regions, coarsening of MgZn₂-η precipitates causes decrease in hardness. Similar observations were reported by Li J.F. et.al [23]. The hardness for FSW AA7075 with B₄C reinforcement is increased by 73% compared to base alloy. A. Karaaslan et. al. reported that, due to substituted primary GP zones and finer precipitates during post heat treatment hardness of weld zone in AA7075 reinforced with SiC drastically increased [24].

Table 3. Hardness of AA7075, FSW without filler and FSW with B₄C filler

Specimen	Base Alloy AA7075 (BM)	FSW without Filler (FWF)	FSW with B ₄ C Filler (FBF)
Hardness, VHN	141±1	192±3	243±3

Table 4. Hardness of AA7075, FSW without Filler (TMAZ, HAZ), FSW with B₄C Filler (TMAZ, HAZ)

Specimen	Base Alloy AA7075	FSW without Filler			FSW with B ₄ C Filler		
		SZ	TMAZ	HAZ	SZ	TMAZ	HAZ
Hardness, VHN	141±1	192±3	172±1	152±1	243±3	220±1	208±1

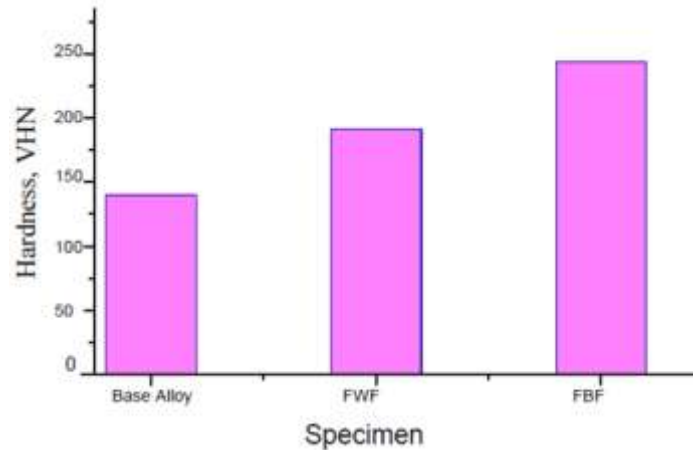


Figure 2 Hardness Graph

Tensile strength:

The tensile strength of base alloy AA7075, FSW AA7075 without filler and FSW AA7075 with B₄C as filler material were tabulated in Table 5. The yield strength (YS) of base alloy AA7075 obviously improved by 20% when FSWed with B₄C nano particulate. Further, the Ultimate Tensile Strength (UTS) of FSWed with B₄C filler material was increased by 12% to that of base alloy and the same was observed with percentage elongation. The percentage elongation of FSWed AA7075 with B₄C specimens is 13.6% greater than that of base alloy AA7075. It is clear that, the strength coupled to elongation property is increased. From the above discussion, it can be clearly observed that the addition of nano B₄C particulate to the weld nugget improved the yield strength, ultimate tensile strength and percentage elongation of the friction stir welds. Again, the tensile strength properties YS and UTS for FSWed with B₄C filler material, were improved by 48% and 42% respectively compared to FSWed AA7075 without any filler material. Higher ballistic and tensile strength were observed when the ordinary B₄C particulate was added justifying the above results [25].

Table 5. Tensile properties of AA7075, FSW with B₄C, post heat treated FSW with B₄C

Specimen	Yield strength, MPa	Ultimate Tensile Strength (UTS), MPa	% Elongation, (%)
Base alloy AA7075	402	457	6.6
FSWed without Filler (FWF)	325	356	4.5
FSWed with B ₄ C Filler (FBF)	482	512	7.5

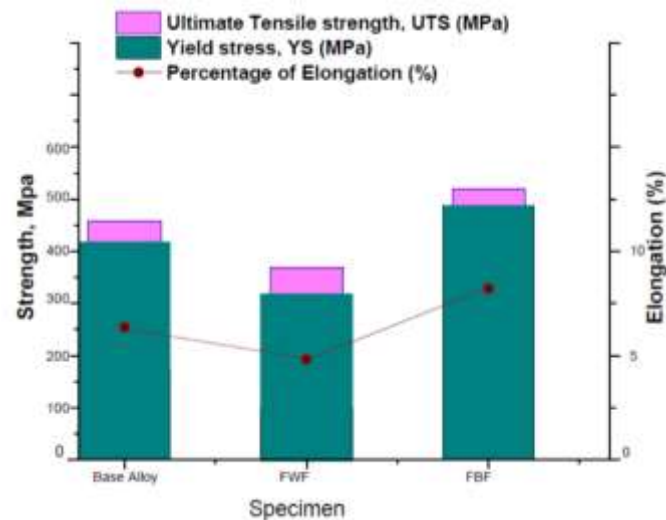


Figure 3 Tensile strength of base AA7075 and FSWed Samples

Microstructure:

Scanning electron micrograph of the base material AA7075 is shown in the figure 4 (a & b). Grain boundaries and grain size are clearly visible in 1000X and 2000X zoom. The eutectics of MgZn₂ that seems like dark spots are observed nearby the grain boundaries. These are the grain boundary precipitates labeled as M-phase [26-27]. The SEM graph in the figure 5 (a & b) shows the micro structure of the stir zone of the friction stir welded (FSWed) AA7075 without filler material. The grain refinement at the zone is clearly seen, which is the evidence for improvement in the hardness. The figure 6 (a & b) and figure 7 (a & b) shows the SEM micro graphs of FSWed AA7075 (HAZ) and FSWed AA7075 (TMAZ) respectively. The grains and boundaries are perfectly visible. The bottom corner of the figure shows the HAZ and moving to right side the zone depletes and TMAZ is visible. The holes in the microstructure are not identified. Moving to the left of microstructure the grain is same as the shape as base metal but in HAZ and TMAZ the grain is pea shape. Grains in HAZ and TMAZ regions are less finer in size as compared with that of the grains in SZ. Again, in the base material AA7075 the size of grain (50-60 μm) were comparatively larger to that of the grains in SZ (10-20 μm) of FSWed AA7075. The grain size in TMAZ region were observed comparatively larger in size (20 -30 μm) when compared with that of grains in SZ. Whereas the average grain size is not much affected in HAZ compared to that of the grains in base material AA7075 alloy.

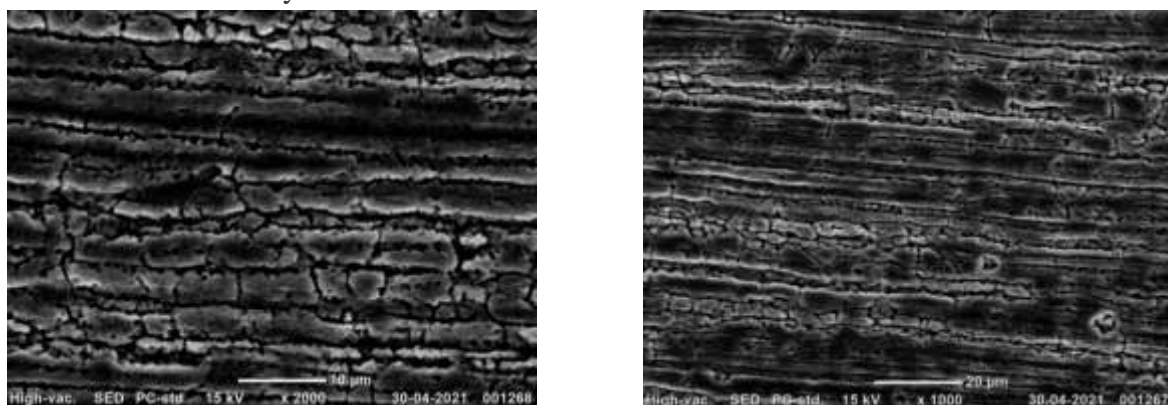


Figure 4. SEM micrographs of Base AA7075 alloy

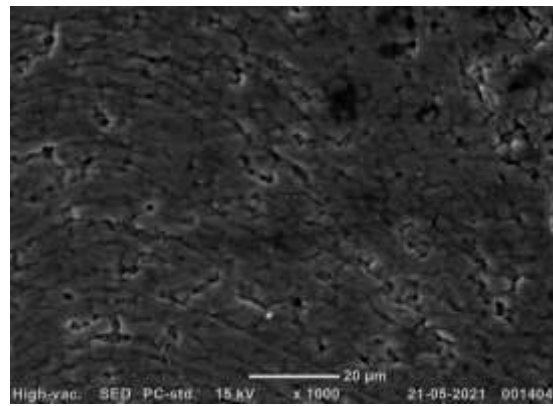
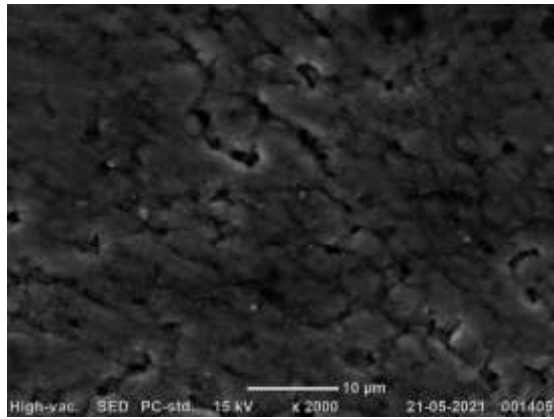


Figure 5. SEM micrographs of FSWedAA7075 without filler material (SZ)

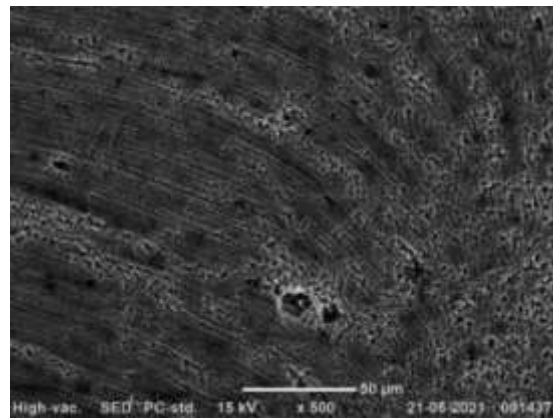
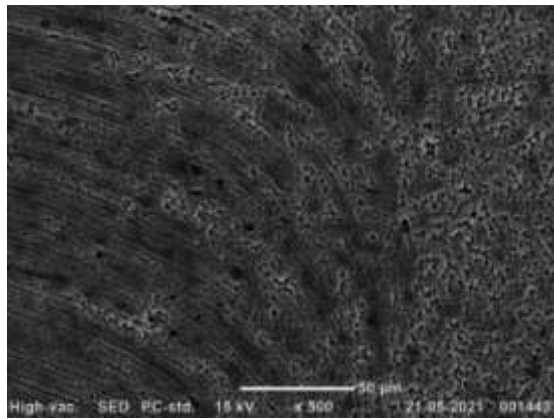


Figure 6. SEM micrographs of FSWedAA7075 without filler material (HAZ)

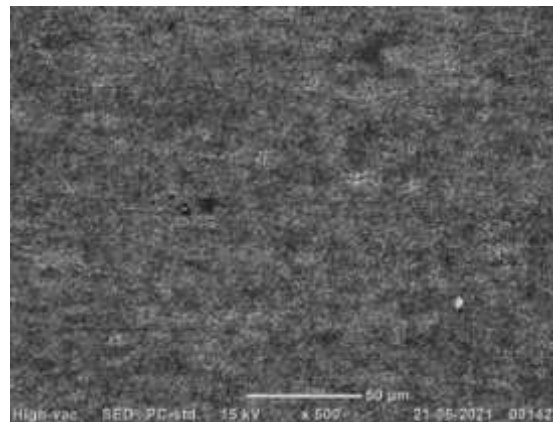
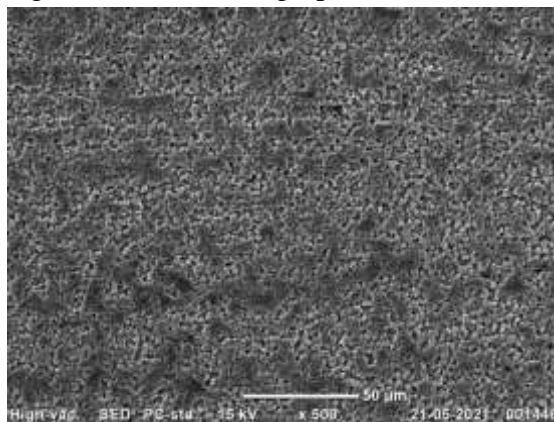


Figure 7. SEM micrographs of FSWedAA7075 without filler material (TMAZ)

Electron micrographs of different zones, viz. weld zone, SZ, HAZ and TMAZ of FSWed AA7075 with B4C as reinforcement were shown from the figure 8 to figure 11 respectively. The figure 8 (a & b) shows the weld zone of FSWed AA7075 with B4C as filler material. Weld path with presence of various zones is clearly visible. There are no holes or porous is observed in the microstructure.

In the figure 9 (a & b), which shows the SZ of FSWed AA7075 with B4C, the B4C particles are clearly visible. Due to tool stirring action and temperature while rotation, in SZ zone finer and equiaxed recrystallized grains were present. The finer grains and grain boundaries are clearly visible. The hole in the microstructure is found due to the irregularities happened during the process of friction stir welding. The size of the grains in the other zone as shown in figure 10 (a & b) and figure 11 are not as finer as in SZ. Onion rings type rings were observed in the SZ as well as in TMAZ. Tool rotational speed affects the microstructure, high rotational speed leads to an increase in a temperature gradient, this widens HAZ, and

also it causes grain coarsening, dissolution, and accumulation of hardening precipitates near grain boundaries [28].

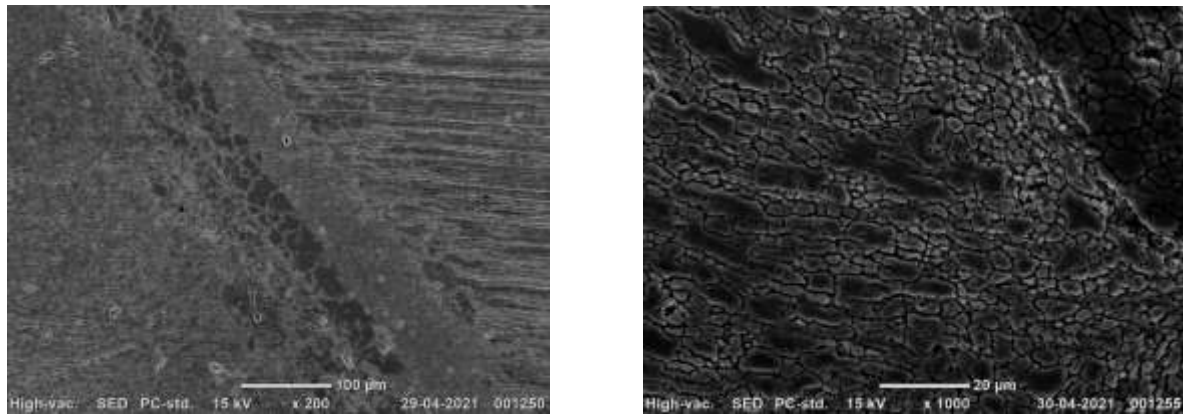


Figure 8. SEM micrographs of FSWedAA7075 with B₄C as filler material

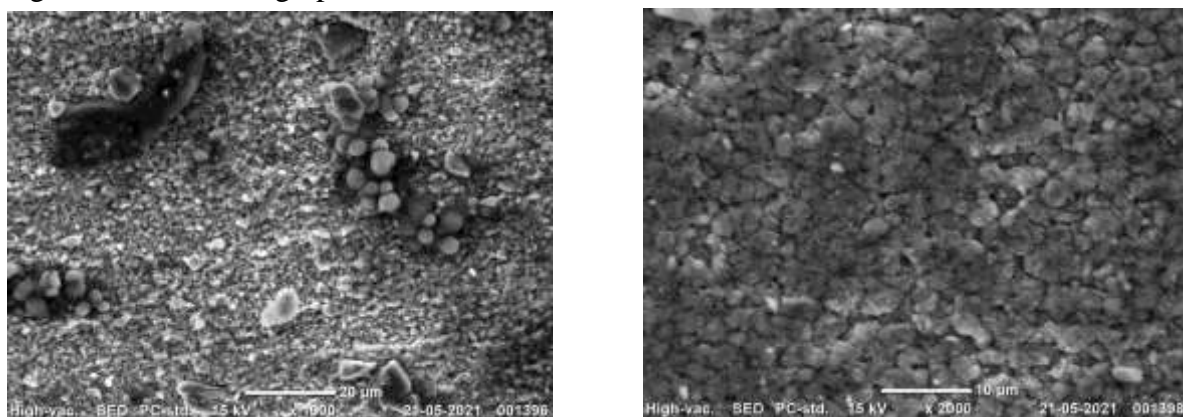


Figure 9. SEM micrographs of FSWedAA7075 with B₄C as filler material (SZ)

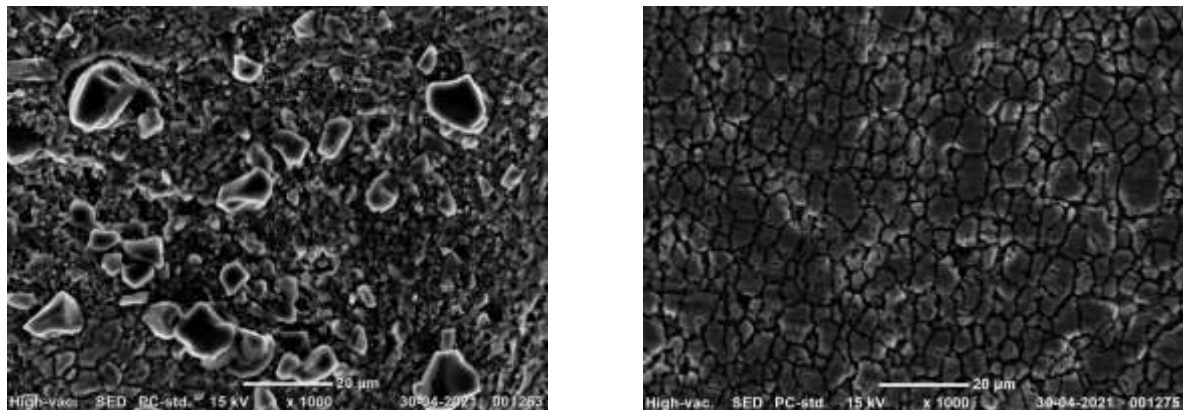


Figure 10. SEM micrographs of FSWedAA7075 with B₄C as filler material (TMAZ)

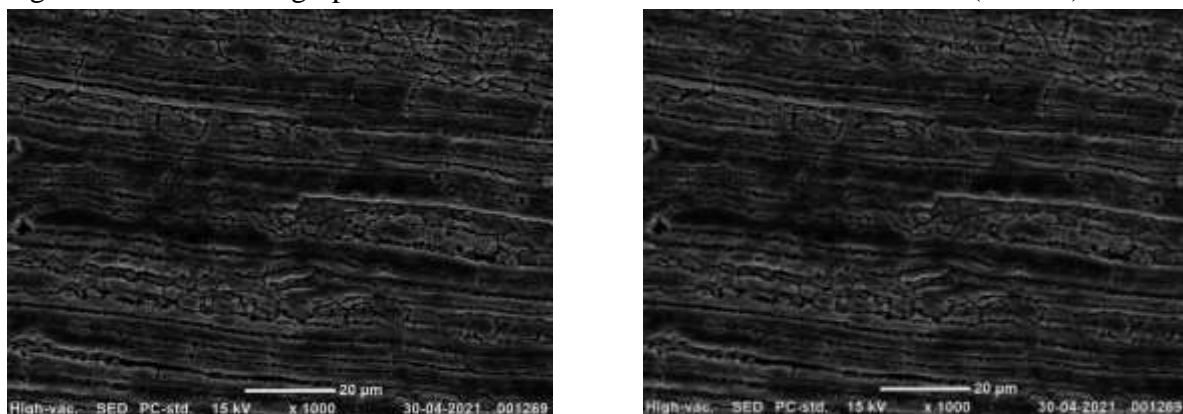


Figure 11. SEM micrographs of FSWedAA7075 with B₄C as filler material (HAZ)

Conclusions

The fabrication of FSW processed AA7075 alloy reinforced with B₄C was done successfully. The micro-Vickers hardness is increased by 73% for FSW specimens with nano B₄C reinforcements compared to base AA7075 alloy. This is manifested by the observation of finer precipitations. The mechanical strength properties viz. YS, UTS and percentage elongation were also significantly increased by 20%, 12% and 13.6% in order. The microstructural evidence is revealed in SEM micrographs.

References

- [1] Morisada Y, Fujii H, Nagaoka T, et al. Effect of friction stir processing with SiC particles on microstructure and hardness of AZ31. *Mater Sci Eng* 2006; 433: 50–54.
- [2] Asadi P, Faraji G and Besharati MK. Producing of AZ91/SiC composite by friction stir processing (FSP). *Int J Adv Manuf Technol* 2010; 51: 247–260.
- [3] Suryanarayana C. Synthesis of nanocomposites by mechanical alloying. *J Alloys Comp* 2011; 509:S229–S234.
- [4] Khodabakhshi F, Yazdabadi HG, Kokabi A, et al. Friction stir welding of a P/M Al– Al₂O₃ nanocomposite: microstructure and mechanical properties. *Mater Sci Eng* 2013; 585: 222–232.
- [5] Sajjadi SA, Ezatpour H and Beygi H. Microstructure and mechanical properties of Al–Al₂O₃ micro and nanocomposites fabricated by stir casting. *Mater Sci Eng* 2011; 528: 8765–8771.
- [6] Lieberthal M and Kaplan WD. Processing and properties of Al₂O₃ nanocomposites reinforced with sub-micron Ni and Ni Al₂O₄. *Mater Sci Eng* 2001; 302: 83–91.
- [7] Khodabakhshi F, Yazdabadi HG, Kokabi A, et al. Friction stir welding of a P/M Al– Al₂O₃ nanocomposite: microstructure and mechanical properties. *Mater Sci Eng* 2013; 585: 222–232.
- [8] Patel VV, Badheka V and Kumar A. Influence of friction stir processed parameters on superplasticity of Al–Zn–Mg–Cu alloy. *Mater Manuf Process* 2016; 31: 1573–1582.
- [9] Mishra RS and Ma Z. Friction stir welding and processing. *Mater Sci Eng* 2005; 50: 1–78.
- [10] Mishra RS, Ma Z and Charit I. Friction stir processing: a novel technique for fabrication of surface composite. *Mater Sci Eng* 2003; 341: 307–310.
- [11] Sharma V, Prakash U, Manoj Kumar BV. Surface composites by friction stir processing: a review. *J Mater Processing Tech* 2015; 224: 117–134.
- [12] Mishra RS, Mahoney MW, McFadden SX, Mara NA, Mukherjee AK. High strain rate superplasticity in a friction stir processed 7075 Al alloy. *Scripta Mater*. 1999; 42: 163–168.
- [13] Mahmoud ER and Al-qozaim AM. Fabrication of in situ Al–Cu intermetallics on aluminum surface by friction stir processing. *Arab J Sci Eng* 2016; 41: 1757–1769.
- [14] Mahmoud E, Takahashi M, Shibayanagi T, et al. Effect of friction stir processing tool probe on fabrication of SiC particle reinforced composite on aluminium surface. *Sci Technol Weld Join* 2009; 14: 413–425.
- [15] Mahmoud E, Ikeuchi K and Takahashi M. Fabrication of SiC particle reinforced composite on aluminium surface by friction stir processing. *Sci Technol Weld Join* 2008; 13: 607–618.
- [16] Shahraki S, Khorasani S, Behnagh RA, et al. Producing of AA5083/ZrO₂ Nanocomposite by Friction Stir Processing (FSP). *Metall Mater Transac B* 2013; 44: 1546–1553.
- [17] McDanel DL. Analysis of stress-strain, fracture, and ductility behavior of aluminum matrix composites containing discontinuous silicon carbide reinforcement. *Metall Transac A* 1985; 16: 1105–1115.
- [18] Madhu V, Bhat BT. Armour protection and affordable protection for futuristic combat vehicles. *Def Sci J* 2011; 61(4): 394–402.
- [19] Sudhakar I, Madhu V, Reddy GM, Srinivasa R. Enhancement of wear and ballistic resistance of armour grade AA7075 aluminium alloy using friction stir processing. *Def Tech* 2014; 20: 1–8.
- [20] Subramanian C, Suri A and Murthy T. Development of boron-based materials for nuclear applications. *BARC News Letter*, March–April, 2010.
- [21] G.S. Frankel, Pitting corrosion of metals; a summary of the critical factors, *J. Electrochem. Soc.* 1998; 145: 2186–2198.
- [22] Fuller CB, Mahoney M.W, Calabrese M, Miconi L, Evolution of microstructure and mechanical properties in naturally aged AA7050 and AA7075 Al friction stir welds. *Mater Sci Eng A* 2010; 527(9): 2233–40.
- [23] Li J.F. et al. Influence of retrogression temperature and time on the mechanical properties and exfoliation corrosion behavior of aluminum alloy AA7150. *Mater Charact*, 2009; 60: 1334–41.
- [24] A. Karaaslan et al. Effect of aging temperature and of retrogression treatment time on the microstructure and mechanical properties of alloy AA7075, *Metal Science and Heat Treatment* 2007; 49: 9–10.
- [25] Madhu V, Bhat BT. Armour protection and affordable protection for futuristic combat vehicles. *Def Sci J* 2011; 61(4): 394–402.
- [26] Isadare, Adeyemi Dayo, et al. "Effect of heat treatment on some mechanical properties of 7075 aluminium alloy." *Materials Research* 16.1 (2013): 190–194.

Two-day International Conference on Recent Advances in Mechanical and Industrial Engineering – 2023
(ICRAMIE-2023)

[27] Lotfi, Amir Hossein, and Salman Nourouzi. "Effect of welding parameters on microstructure, thermal, and mechanical properties of friction-stir welded joints of AA7075-T6 aluminum alloy." *Metallurgical and Materials Transactions A* 45.6 (2014): 2792-2807.

[28] H. Rezaei, M. H. Mirbeik, and H. Bisadi, "Effect of rotational speeds on microstructure and mechanical properties of friction stir-welded 7075-T6 aluminium alloy," *Proc. Inst. Mech. Eng. Part C J. Mech. Eng. Sci.*, vol. 225, no. 8, pp. 1761–1773, 2011.

Experimental Investigation on Multi material Additive manufacturing by using ABS and PLA

M. Sumalatha, Ch. Karthik, K.V.S. Rohith, T.Ganesh, V.Rakesh and S. Mahi Charan

Velagapudi Ramakrishna Siddhartha Engineering College (VRSEC), Vijayawada, India
sumalathame@vrsiddhartha.ac.in

Abstract: Fused Deposition Modeling (FDM) is a popular additive manufacturing technique used to build parts layer by layer. In this study, the mechanical properties of specimens made from the blends of Polylactic Acid (PLA) and Acrylonitrile Butadiene Styrene (ABS) were investigated. The goal was to determine if combining the two materials could enhance the mechanical properties of the resulting parts. Various compositions and parameters were used to produce specimens that were then tested for resistance against different tests such as tensile, flexural. The study was conducted by following the ASTM standards which are internationally recognized guidelines for testing and evaluating materials. The results showed that the addition of PLA with ABS improved the mechanical properties of the parts, indicating that using the combination of these two materials could lead to an increase in strength. Therefore, it can be concluded that using blended PLA and ABS can be a viable alternative to pure ABS for achieving increased strength in FDM parts.

Keywords: 3D Printing; FDM; Flexural Test; ABS; PLA

1. Introduction

Additive manufacturing, also known as 3D printing, is the process of building three-dimensional objects layer by layer. It's similar to how standard desktop printers create images—but 3D printers use materials other than ink, such as polymer composites, metals, ceramics, food, foams, gels, and even living tissue. Chuck Hull invented stereolithography, now known as 3D printing, in the 1980s, which paved the way for additive manufacturing. After becoming frustrated with the long production times of prototyping, he developed a method, in which using UV lasers, 3D models are built up layer by layer.

He was ultimately recognized as the originator of 3D printing after successfully patenting his idea in 1986. This inspired the subsequent wave of manufacturing techniques. Because it enables greater flexibility, quicker manufacturing times, and more complex shapes, this technology has transformed how goods are created and made. Several industries, including aerospace, automotive, healthcare, and consumer goods, can benefit from additive manufacturing.

Fused Deposition Modeling (FDM), one of the most well-liked types of additive manufacturing, constructs things through the use of a material extrusion procedure. Alternative techniques include electron beam melting (EBM), selective laser sintering (SLS), and stereolithography (SLA) process.

Today, complicated parts for the aerospace and automotive industries, prosthetics and medical devices, and consumer goods like jewellery, toys, and home décor are all made using additive manufacturing. Rapid prototyping is another area where it is employed, allowing designers and engineers to test and improve their creations before mass production. Due to its ability to produce only the components that are required, additive manufacturing also helps to reduce waste by eliminating the need for extra raw materials.

1.1 Materials

1.1.1 Acrylonitrile butadiene styrene (ABS):

Acrylonitrile Butadiene Styrene (ABS), which has the chemical formula $(C_8H_8)_x(C_4H_6)_y(C_3H_3N)_z$, is a thermoplastic polymer that is frequently used in a variety of

applications because it has superior mechanical qualities to other popular polymers, including impact resistance, toughness and stiffness. It has a glass transition temperature of about 105 °C (221 °F) but lacks a genuine melting point because it is amorphous. By altering the ratios of its components, ABS can be improved for impact resistance, toughness, and heat resistance.

For instance, improving impact resistance may be achieved by increasing the percentage of polybutadiene to styrene and acrylonitrile but doing so will also have an impact on other qualities. At lower temperatures, the impact resistance does not rapidly diminish and ABS has good load stability with modest loads. Several grades of ABS, including ABS for extrusion and ABS for injection moulding as well as varying levels of impact resistance, including high and medium impact resistance, can be made. -20 to 80 °C (-4 to 176 °F) is a wide range of temperatures in which ABS can be utilized.

1.1.2 Polylactic acid (PLA):

A thermoplastic polymer called polylactic acid (PLA) is created from renewable resources like sugarcane or maize starch. It has gained popularity in many applications because of its environmentally friendly manufacture. Because of its low melting point, strong strength, minimal thermal expansion, good layer adhesion, and great heat resistance when annealed, it is frequently used in 3D printing. However, compared to other typical 3D printing polymers, PLA has one of the lowest heat resistances without annealing. Despite being widely used, PLA still has several technical and physical restrictions that prevent its extensive adoption in other applications. Despite these drawbacks, it continues to be the popular bioplastic worldwide and has the biggest consumption volume among them.

1. 2. Equipment

1.2.1 Fused Deposition Modelling:

Fused filament manufacturing (FFF), also known as fused deposition, is a 3D printing technique that makes use of a continuous thermoplastic filament. A big filament spool is fed into a moving, heated printer extruder head, which is extruded onto the expanding work. To specify the printed shape, the print head is moved by computer. Typically, the print head or work is moved a short amount vertically to start a new layer after the head has deposited one horizontal plane, or layer, at a time as it was moved in two dimensions. To stop and start deposition and create an interrupted plane without stringing or dribbling between portions, the speed of the extruder head can also be adjusted. The Rep Rap project participants came up with the term "fused filament fabrication" to provide an acronym (FFF) that might have been employed without breaking the rules.

By the number of machines, fused filament printing has risen to the top of the list for hobbyist-grade 3D printing. Although more expensive, other methods like photopolymerization and powder sintering might produce superior outcomes. Feedstock material is forced through an extruder in fused filament fabrication to print objects. The feedstock material for the majority of fused filament fabrication 3D printing machines is a filament wrapped onto a spool. The main element in this kind of printing is the 3D printer liquefier. For extruders, there is a cold end and a hot end on these printers. The cold end draws material from the spool using gear- or roller-based torque, while a stepper motor regulates the feed rate. Feedstock is pushed into the hot end by the cold end.

The hot end is made up of a nozzle and a heating chamber. The liquefier, which melts the feedstock to turn it into a liquid, is housed in the heating chamber. It enables the molten material to emerge from the tiny nozzle in the form of a slim, sticky plastic bead that will stick to the surface it is put on. The typical nozzle diameter ranges from 0.3 mm to 1.0 mm. Depending on the material being printed, various nozzle types and heating techniques are employed. Various nozzle types require different replacement procedures. The V6 and MK8 nozzles, which were made popular by E3D, are the most often used nozzles. To prevent plastic leaks, the nozzle must be changed while still hot.

1.3. Experimental Setup

Specimens were created using an FDM printer following the ASTM standards in order to assess the mechanical characteristics of the pieces generated from PLA and ABS. To make sure the outcomes

were trustworthy, for each test, five identical samples were created. To guarantee the accuracy and reproducibility of the results, this is a standard procedure in material testing. Tensile, flexural, and impact qualities were among the mechanical attributes assessed. These characteristics can be used to compare the performance of various materials and are frequently used to assess a material's overall strength and durability. The ASTM standards offer instructions for sample preparation, test settings, and methods for assessing mechanical properties, assuring that the outcomes are comparable among investigations.

1.3.1 Tensile Test:

To ascertain the mechanical characteristics of materials under tension load, tensile tests are frequently utilized as a method. The sample is loaded until it breaks in a tensile direction as part of the test. The quantity throughout the test, the amount of force applied, and the lengthening of the sample is measured. The information gathered is used to determine the material's ultimate tensile strength or the highest stress it can endure before failing.

The qualities of a material are frequently represented in terms of strain (percentage change in length) and stress (force per unit area). Strain is computed by dividing the length change by the sample's original length, while stress is calculated by dividing force measurements by the sample's cross-sectional area. A stress-strain curve, an XY graph, is then used to plot these numbers.

Depending on the substance being tested and the intended use, different testing and measuring techniques may be used. The ASTM standards offer instructions for sample preparation, test conditions, and methods for calculating mechanical properties. The standards also offer guidance on how to compare the effectiveness of various materials and how to interpret the results.

1.3.2 Flexural test:

A mechanical test called the flexural test, commonly referred to as the bend test, gauges a material's resistance to fracture under bending loads. The strength and flexibility of materials including metals, polymers, and ceramics are frequently assessed with this test. Flexural tests are frequently performed to ascertain a material's elastic modulus, yield strength, and ultimate tensile strength.

A sample of the material is supported on two places during a flexural test, and a load is applied at a third point, usually in the middle. The test determines the sample's deflection under load, and using this information, the flexural strength, elastic modulus, and other parameters can be computed.

Depending on the substance being tested and the intended use, different testing and measuring techniques may be used. The ASTM standards offer instructions for sample preparation, test setup, and methods for calculating the flexural characteristics of materials. The standards also offer guidance on how to compare the effectiveness of various materials and how to interpret the results.

2. Literature Review

Mst Faujiya Afrose[1] This paper tells about the fatigue behaviour of the PLA material on FDM by taking the three building orientations. The specimen in dog bone structure. In the above three building orientations. The ultimate tensile stress is highest at the 0° . Orientation while compared to the 90° and 45° orientations. They observed the temperature and surface finish based on the knowledge of fatigue characteristics of FDM Parts.

Tybox Sonsalla[2] They conducted various experiments by varying printer Settings (FDM) which effect on thermal conductivity. 3D printer Settings (i.e. layer height, fill density, nozzle diameter) must be set as on a macro scale. This study uses the macro-scale and micro-scale to characterize the printer Settings. In this study, the highest thermal conductivity part with a height of 0.4 mm and 100% infill density.

Dinesh S.I Arun Prakash[3] They conducted experiments by various (2020) compositions of ABS and PLA used and finds the flexural and tensile of that material combinations. To calculate those Parameters they used the ASTM standards. Finally results are compared to the properties of normal ABS and PLA material. And in this one new filament material is introduced. This gives higher resistance to stresses.

Emila Brancewicz[4] They aims to analyze the available information on elements produced from more than one material with additive manufacturing resulting from printing using PLA. And by combining with other materials several parameters (process temperatures, filling and surface development) are also noted.

Ranvijay kumar [5] In this multi-material printing is happened. The materials are ABS, PLA, and HIPS. The combining of these three materials in a composite form on the FDM. They observed some parameters (thermal test, break load, break strength, break elongation percentage elongation, and Young's Module). This also highlights the process parameters with photomicrographs.

M.Samkaro [6] In this paper there are three parameters are calculated for the material ABS. Parameters tensile strength, fracture strain toughness and taken properties layer height, raster angle, and infill percentage. Mathematical equations has been developed using surface response methodology which can be used to predict the ABS tensile properties numerically and also the optimum parameter for ultimate properties.

Sachin Wickramasingh [7] This paper tells about the defects on FDM based 3D Printing of Polymer and associated Composite. Here the FRC is used as composite combined with the polymer on the FDM. This results some most common defect. The void formation, Surface roughness and poor bonding between materials. An inclusive discussion on the effectiveness of chemical, laser heat and ultrasound treatments to minimize these drawbacks.

Daniyar syrlrbayer [8] In this paper the properties of FDM is tested. It is evident that part qualities are greatly influenced by the various process parameter was carried out infill density, infill Patterns, extrusion temperature, layer thickness, nozzle diameter, raster angle. This study improves the part strength and new research trends such as vacuum assisted FDM.

Liu Zhaobing [9] In this study, the mechanical properties—including tensile and flexural properties—of samples made from polylactic acid (PLA) composites based on wood, ceramic, copper, aluminum, and carbon fiber using FDM with various additives are thoroughly examined. The technical attributes of PLA and its mixture have been assessed while accounting for key printing factors.

Mohammed Algarni[10] Based on information from the literature, this paper analyzes and examines how process parameters affect the mechanical behavior of printed parts. These process parameters influence parts' mechanical properties differ based on the FOM material. It prioritizes (PLA), (ABS), both (PEET) (PETG). The outcome demonstrates that the process parameter most affected by infill percentage is layer thickness.

Dr. Sudhir Kumar[11] In this study, materials on the multi-material components are fused or laminated together into a single standard flexural specimen using the laminated object manufacturing method for sustainable polymer using materials ABS and TPU and tested in accordance with ASTM D790 standards. They found that, when compared to solo materials, the specimen's flexural strength had increased.

Xingshaung Peng[12] The research details the creation of CF/PA6 composite filaments as a feedstock for FDM printing. It also looked into the effects of processing factors on mechanical properties and interlayer adhesion during FDM printing and the tensile properties of CF/PA6 specimens printed using these materials. Three different printing supervisors are evaluated. It is discovered that CF/PA6 printed in the direction of the tensile loading has better tensile properties than the other 2 printing directions.

Gholamhossein Sodelfian[13] In this study, printing was carried out using pure polypropylene (PP), glass fiber (GF), and PP/GF composites containing materials of anhydride polyolefin (POE-g-MA) at three distinct weight percentages. Tensile experiments were carried out to assess the specimens' mechanical qualities. Results reveal suggested higher crystallinity of specimens prepared via the CM method rather than 3D printing

Shilpesh R. Rajpurohit[14] The tensile strength of the FDM printed PLA part is being studied in this article. As part of the ASTM D638 fabrication process, three process parameters—raster angle, layer height, and raster width—have been chosen to investigate their effects on tensile properties. It has

been found that the 0° raster angle produces the highest tensile strength. To investigate their impact on the tensile strength of the FDM-printed PLA part, the layer height, raster width, and raster angle have also been changed.

Lai-Chang Zhang[15] The processing, microstructure, and properties of titanium alloys and the composites made from them by EBM have made recent strides, which are reviewed in this article. The article details important advancements in porous and solid bulk structures in EBM. Ti-24Nb-4Zr-8Sn, a novel biomedical titanium alloy with low modulus and non-toxic elements, has the ability to replace current biomedical implants as the preferred implant material.

Zharyaylkassyn Beibit[16] In this study they looked into factors like nozzle diameter, raster angle, build direction, extrusion temperature, infill density, infill patterns, and layer thickness. They came to the conclusion that by adjusting various factors, the testing's outcomes were optimized.

Sunpreet Singh[17] The fabrication of multi-material 3D Printing using ABS and HIPS is the goal of this study. They experimented with parameters like raster angle, layer height, and fill density to perform tests like flexural, impact, and tensile tests. They came to the conclusion that the material's strength had improved with the inclusion of these two components.

Ajay Batish[18] The sustainable polymer used in these papers, made from materials ABS and TPU, is used to fuse and laminate the multi-material components into a single standard flexural specimen, which is then evaluated in accordance with ASTM D790 standards. They came to the conclusion that, when compared to single materials, the specimen's flexural strength had grown.

3. Experimental Procedure

3.1 Tensile testing:

Tensile testing is a standard method used to determine the mechanical properties of materials, such as their strength, elasticity, and ductility. The following are the steps involved in conducting a tensile test of a D638 specimen:

The first step is to prepare the specimen according to the ASTM D638 standard. The standard specifies the dimensions and shape of the specimen, as well as the type of material to be used. The specimen is mounted in the grips of a tensile testing machine. The grips should be aligned with the long axis of the specimen and tightened securely. Align the specimen such that the longitudinal axis of the specimen is aligned with the axis of the testing machine. This ensures that the load is applied in the correct direction. Before the test begins, it is necessary to set up the testing machine and software to ensure that the test is performed accurately. This includes calibrating the load cell and setting the crosshead speed. Gradually apply a tensile load to the specimen using the tensile testing machine.



Fig: 3.1: Tensile Testing Set Up on UTM Machine

The load should be applied in a smooth and continuous manner until the specimen breaks. During the test, the machine records the force (load) applied to the specimen, as well as the deformation (strain) of the specimen. This data is used to create a stress-strain curve for the material. The results of the test are calculated based on the stress-strain curve. The most common results include ultimate tensile strength, yield strength, elongation at break, and modulus of elasticity. The results of the test can be analyzed to determine the mechanical properties of the material, as well as to assess its suitability for specific applications.

It is important to note that the specific testing procedures and requirements may vary depending on the testing machine, the material being tested, and the specific testing standard being followed. Therefore, it is crucial to follow the appropriate testing standards and guidelines for accurate and reliable results.



Fig No. 3.2 Tensile Specimens before Testing

Fig No. 3.2 shows the specimens prepared by 3D printing for tensile test. The specimens printed with set 1 parameters are shown in the left side of the picture and specimen printed with set 2 parameters are shown in right side of the picture. The tensile test specimens after testing are shown in the Fig No. 3.3.

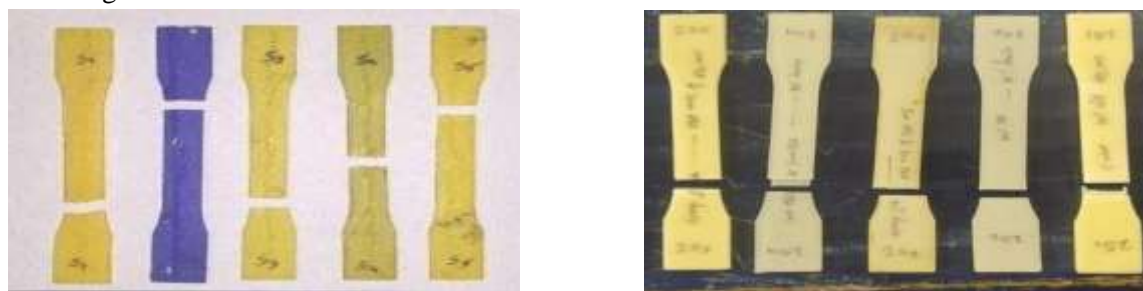


Fig:3.3 Tensile test Specimens After Testing

3.2 Flexural testing:

Flexural testing, also known as the bend test or transverse testing, is a common method used to determine the strength and stiffness of a material when subjected to bending forces. The following are the general steps involved in the flexural testing process

First, prepare the test specimen according to the relevant standards, typically rectangular in shape with specific dimensions. The material should be homogeneous, and any surface imperfections should be removed. Mount the sample onto the testing machine in a way that allows it to be subjected to a bending force. The test apparatus should be set up according to the relevant standards or specifications. Conduct pre-test calibration of the testing machine, including verifying the load cell and displacement transducer readings. Apply a load to the center of the specimen at a constant rate of displacement or strain, and record the resulting load and displacement data.

The load is usually applied until the specimen fractures or reaches a specified deflection. Calculate the flexural strength, modulus of elasticity, and other relevant mechanical properties using the recorded load-displacement data. These values can be used to evaluate the material's performance and compare it with other materials. Document the test results, including the sample preparation, test conditions, and test results, as well as any relevant observations. The results should be reported in accordance with the relevant standards or specifications.



Fig: 3.4 Flexural Test Set Up

Fig No. 3.5 shows the specimens prepared by 3D printing for Flexural test. The specimens printed with set 1 parameters are shown in the left side of the picture and specimen printed with set 2 parameters are shown in right side of the picture. The Flexural test specimens after testing are shown in the Fig No. 3.6.



Fig 3.5 Flexural Test Specimens before testing

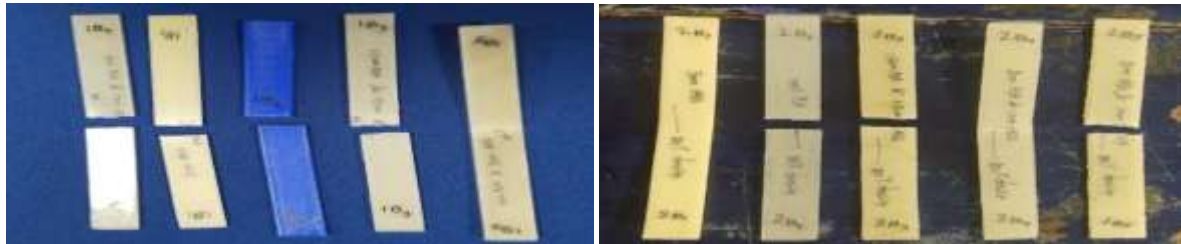


Fig 3.6 Flexural test Specimens after testing

4. Results

4.1 Tensile test:

From tensile test peak load, peak elongation, percentage of elongation, tensile strength and yield strength are found. The results for 10 Specimens are tabulated in Table No. 1.

Table No.1: Tensile Test Results

	SampleNo.	Infill Density(%)	Orientation($^{\circ}$)	PeakLoad(kg)	Peak Elongation(m m)	Young's modulus (MPa)
Set 1 parameters	1S1	100	45	179	6.69	23338.34
	1S2	100	45	251.5	6.15	46676.84
	1S3	100	45	210.5	6.8	31117.87
	1S4	100	45	228	6.6	46676.61
	1S5	100	45	190.5	7.47	46676.39
Set2 parameters	2S1	80	0	105.5	5.52	20227.396
	2S2	80	0	150	4.49	40451.684
	2S3	80	0	122	3.69	40452.852
	2S4	80	0	149.5	4.92	30341.096
	2S5	80	0	117.5	3.58	40453.238

Table No.1 shows the results from the tensile test for 5 different material combinations and two set of varying parameters. Set 1 parameter has 100% fill density, 45° orientation and set 2 parameter has 80% fill density, 0° orientation. From the table, it clearly depicts that set 2 parameters showing less performance than the set 1 parameters.

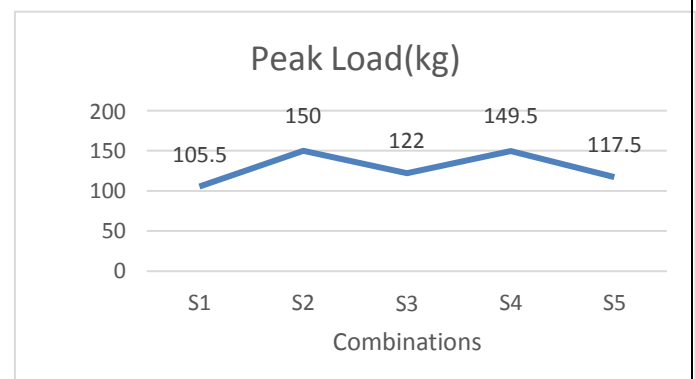
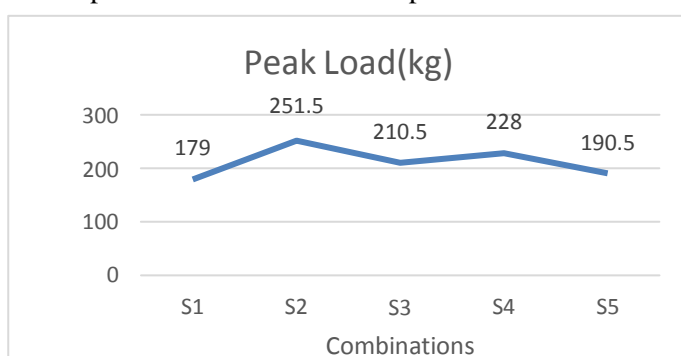


Fig No. 4.1 Peak load Graph for Set 1 parameters

Fig No. 4.2 Peak load Graph for Set 2 parameters

Fig No. 4.1 shows the graph plotted between combinations and peak load for the parameter values 100% fill density and 45° orientation (Set 1). The graph clearly depicts that combination 1S2 i.e. PLA bears more Load 251.5 Kg than remaining combinations. 1S4 has second highest value 228 Kg. 1S1 (ABS) shows low peak load value than others. We can say combination of ABS with PLA shows better peak load value than pure ABS.

Fig No. 4.2 shows the graph between combination and peak load for the parameter values 80% fill density and 0° orientation (Set 2). From the graph the highest peak load is for material 2S2 150 Kg and the lowest value is for material 2S1 105.5 Kg. 2S4 has the second highest peak load value 149.5 Kg, in set2 parameters material 2S2 and 2S4 shows nearly equal peak load.

Fig No. 4.3 shows the graph between combination and peak elongation for the set 1 parameters. From the graph the maximum elongation is 7.47mm for the material combination 1S5 and lowest value 6.15mm for material 1S2. It depicts that 1S5 has more ductile than others.

The graph between combination and Peak elongation for Set 2 parameters is shown in Fig No.4.4, from the graph the maximum elongation is 5.52 mm for material 2S1 and minimum elongation is 3.58 mm for material 2S5. We have observed that the elongation for S5 is reduced for set 2 parameters.

From this test we have observed that there is a great influence of printing parameters on the behaviour in tensile test. Printing with 80% fill density and 0° orientation shows poor behaviour than the set 1 parameters. The combination of ABS with PLA shows better values than a pure ABS.

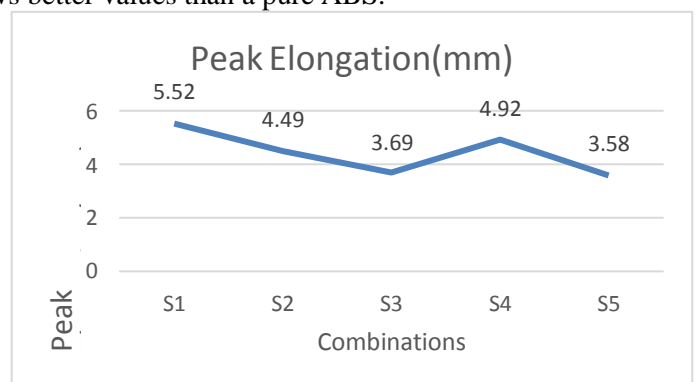
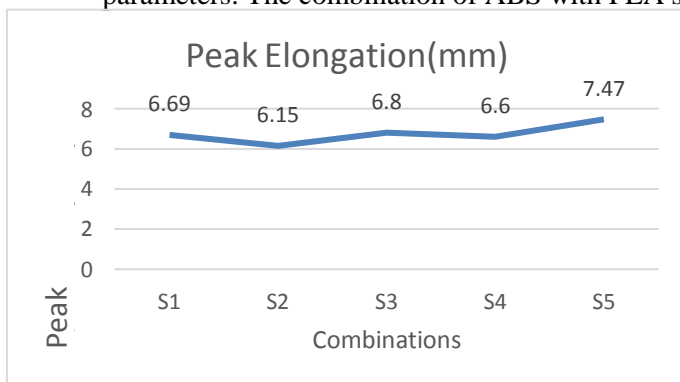


Fig No. 4.3 Peak Elongation Graph for Set 1 parameters

Fig No. 4.4 Peak Elongation Graph for Set 2 parameters

Flexural Test

Table No. 2 Flexural test results

	Specimen	Infill Density(%)	Orientation(°)	Peak Load(kg)	Flexural Strength(Mpa)
Set 1 parameters	1S1	100	45	7	114.45
	1S2	100	45	8	130.2
	1S3	100	45	9.5	155.325
	1S4	100	45	8	130.8
	1S5	100	45	8	130.5
Set 2 parameters	2S1	80	0	5.5	89.925
	2S2	80	0	7	114.45
	2S3	80	0	6	98.1
	2S4	80	0	7	114.5
	2S5	80	0	6	98.1

Five combinations of materials printed with two set of parameters are tested under bending load on UTM machine and their results from the flexural test are tabulated in Table No.2. Table consisting values of peak load and Flexural strength from the test.

The graphs plotted between combination and peak load for two set of parameters respectively are represented in fig no.4.5 and 4.6. From the fig no. 4.5 the maximum peak load is 9.5 Kg for material 1S3 and minimum peak load is 7Kg for material 1S1. Where forset 2 parameters from fig no. 4.6 the maximum peak load is 7Kg for 2S2 and 2S4, the minimum peak load is 5.5 kg for 2S1. Combination 1S3 shows best peak load value than the other combinations, depicts that more bending load capacity. Graph between combinations and flexural strength is also plotted as shown in fig. 4.7 and 4.8. Fig No. 4.7 shows the graph forset 1 parameters, The maximum flexural strength is 155.32 Mpa for 1S3 and minimum value is 114.5 Mpa for 1S1. 1S3 combination shows high flexural strength, the combinations 1S2, 1S4 and 1S5 shows nearly equal flexural strength.

Fig No. 4.8 shows the graph for set 2 parameters, the maximum flexural strength is 114.5Mpa for combinations 2S2 and 2S4 which is equal to the minimum strength of set 1 parameters. Minimum value is 89.5 Mpa for combinations 2S1. 2S3 and 2S5 shows similar values in strength.

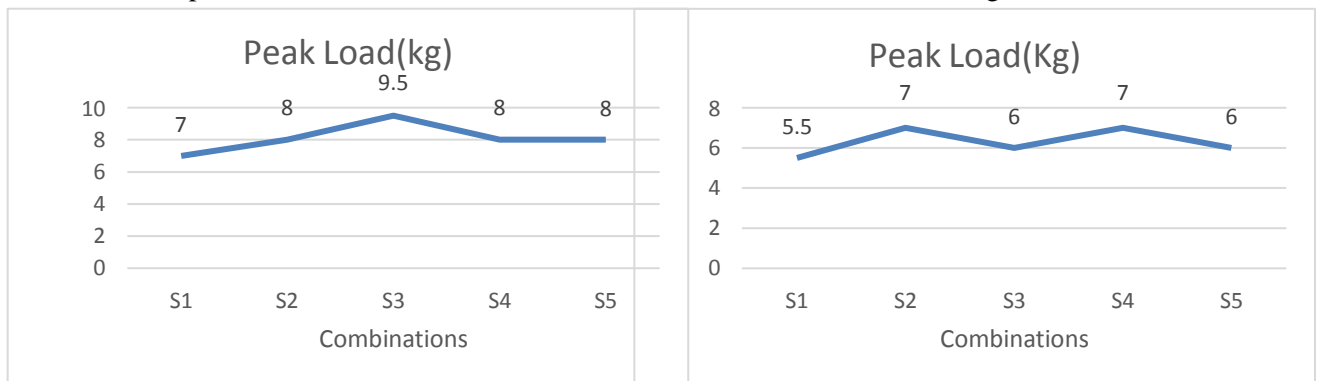


Fig No.4.5 Peak Load graph of flexural test for Set 1 parameters

Fig No.4.6 Peak Load graph of flexural test for Set 2 parameters

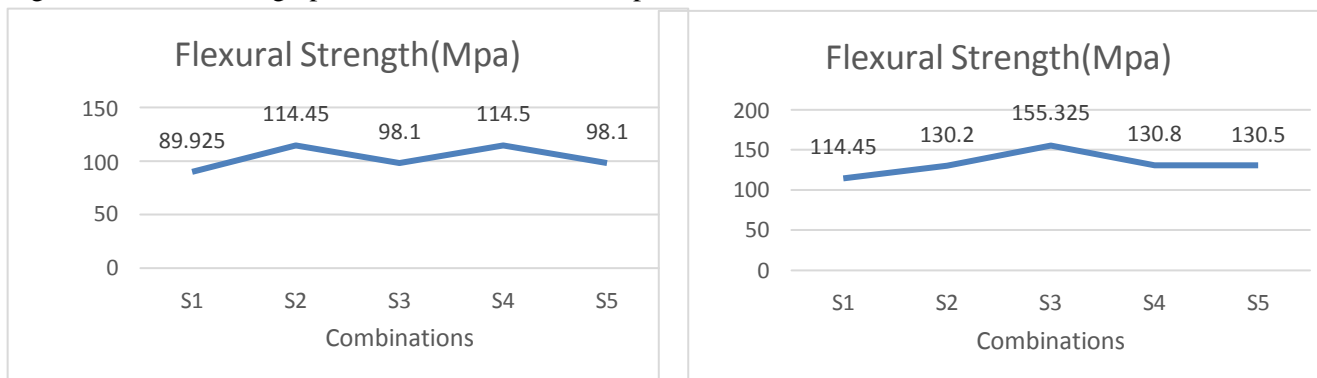


Fig No. 4.7 Flexural Strength Graph for Set 1 parameters

Fig No. 4.8 Flexural Strength Graph for Set 2 parameters

5. Conclusion

5.1 Tensile test:

Based on the results, sample 1S2 i.e 100% PLA infill density of 100%, and orientation of 45° has the highest peak load of 251.5 kg and the highest peak strength of 47.446 MPa among all the samples tested. It also has a relatively high peak elongation of 6.15mm and a percentage elongation of 3.73%. This means that the sample can withstand a higher amount of stress before breaking and has a higher overall strength than the other samples.

Additionally, sample 1S2 has a higher Young's modulus of 46,676.84 MPa compared to the other samples, which indicates that it is stiffer and more resistant to deformation under stress. It also has a higher yield stress of 9.055 N/mm², which means that it can withstand a greater amount of stress before it starts to deform plastically. Overall, sample 1S2 appears to have the best combination of strength and mechanical properties among all the samples tested.

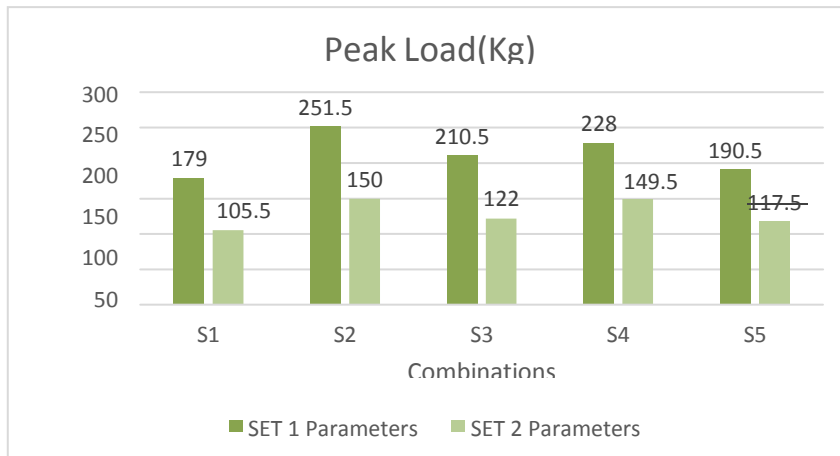


Fig No. 5.1 Peak load Comparison between Set 1 and Set 2 parameters

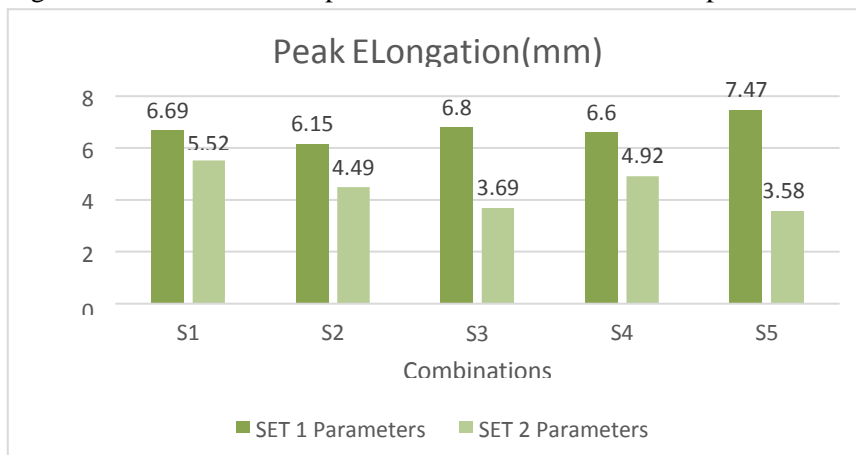


Fig No. 5.2 Peak Elongation Comparison between Set 1 and Set 2 parameters

A comparison is made between the set 1 and set 2 parameters for peak load and peak elongation as shown in Fig No. 5.1 & 5.2. From Fig No. 5.1 The combination has shown better peak load values than the pure ABS(S1). From peak elongation graph Fig No. 5.2 the combination S5 has shown more elongation than other combinations.

5.2 Flexural test:

Based on the results provided, sample S3 i.e 50% ABS and 50% PLA, infill density of 100%, and orientation of 45° have a peak load of 9.5 kg, flexural strength of 155.325 MPa, and a deflection of 7.23 mm. Flexural strength indicates the material's ability to withstand bending stress without breaking. The high flexural strength S3 indicates that it can resist bending stresses better than the other samples tested. Furthermore, the high flexural strength of S3 can be attributed to its high peak load which indicates that it can sustain high loads without breaking.

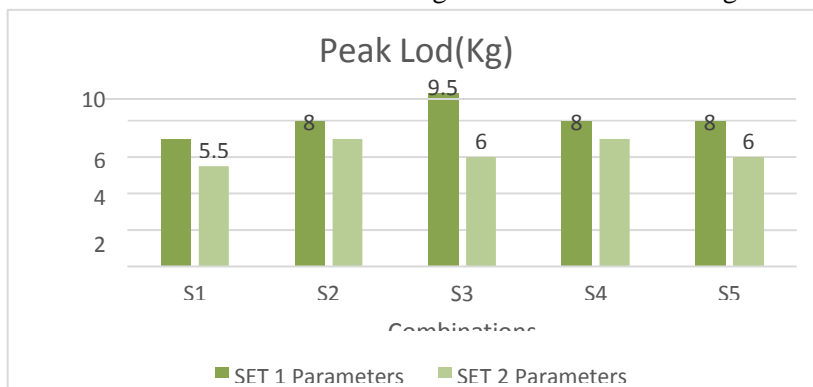


Fig No. 5.3 peak Load Comparison between Set 1 and Set 2 parameters

Fig No. 5.3 shows comparison graph between two parameters for Peak load in Flexural test, S3 shows the maximum peakload. Fig No. 5.4 shows the comparison graph between set 1 and set 2 parameters

for flexural strength. The maximum flexural strength is shown for the set 1 parameters and S3 combination.

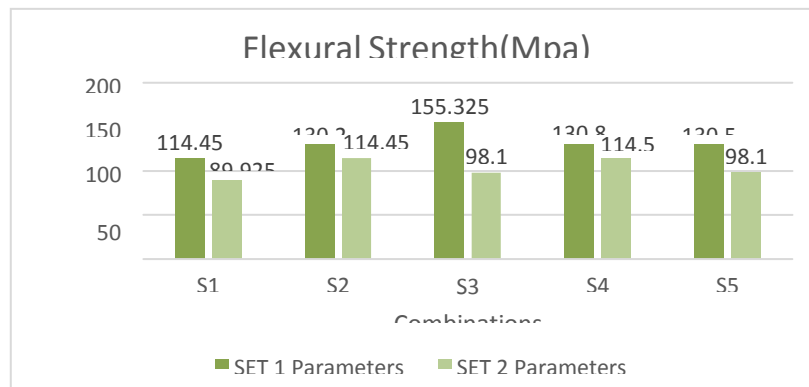


Fig No. 5.4 Flexural Strength Comparison between Set 1 and Set 2 parameters

From this experimental investigation we have found that the combination of PLA with ABS has shown better properties than the Pure ABS. From this we conclude that S3 combination is best in flexural strength. S5 combination with printing parameters 100% fill density and 45° orientation is more ductile than others.

Specimens printed with set 1 parameters shows best results, whereas in both the tests set 2 parameters has low performance. Hence 3D printing with set 1 parameters with combinations gives better results.

References

1. Mst Faujiya Afrose, S.H. Masood, "Effects of part build orientations on fatigue behavior of FDM processed PLA Material", Springer International publishing (2015).
2. T. Sonnsalla, A.L. Moore, W. J. Meng, "3D Printer Settings effects on thermal conductivity of acrylonitrile styrene (ABS)", Polymer testing (2018).
3. Dinesh S K, Arun Prakash S, Senthil Kumar K L, " Study on Flexural and tension Behavior of PLA, ABS, and ABS – PLA materials", Material Today (2020).
4. Emila Brancewicz, Jack Sawicki, " Bonding and Strengthening the PLA Biopolymer in Multi-Material Additive Manufacturing", Materials (2022)
5. Ranvijay Kumar, Rupinder Singh, " On the 3D Printing of recycled ABS, PLA, HIPS thermoplastics for Structural applications, PSU Research Review", Emerald Publishing Limited (2018).
6. M. Samykano, K. Kadirgama, W. K. Ngui, " Mechanical Properties of FDM printed ABS: Influence of Printing Parameters", Springer – Verlag London Ltd (2019).
7. Sachini Wickramasinghe, Truong Do, Phuong Tran, " FDM based 3D printing of Polymer and associated composite", Polymers(2020).
8. Sylrbayev D, Parveen A, "Optimisation of Strength Properties of FDM Printed Parts", Polymers (2021).
9. Zhaobing Liu , Qian Lei , "Mechanical properties of wood , ceramic , metal and carbon based PLA composites fabricated by FDM, Journal of Materials Research and Technology (2019)
10. Mohammed Algarni , Sami Ghazail , " Comparative Study of the Sensitivity of PLA, ABS, PEEK, and PETG's Mechanical Properties to FDM Printing Process Parameters", Crystals(2021).
11. Sudhir Kumar , Rupinder Singh , Mohit Singh, " Multi material 3D printing of PLA-PA6/TiO₂ polymeric matrix: Flexural, wear and morphological properties", Journal of Thermoplastic Composite Materials(2020).
12. Xingshuang Peng , Miaomimo Zhang , "Investigation of processing parameters on tensile performance for FDM-Printed carbon fiber reinforced polyamide", Composites Communication(2020)
13. Gholamhossein Sodeifiana, Saghar Ghaseminejada , Ali Akbar Yousefid, "Preparation of polypropylene/short glass fiber composite as Fused Deposition Modeling (FDM) filament", Results in Physics (2019).
14. Shilpesh R. Rajpurohit and Harshit K. Dave, " Effect of process parameters on tensile strength of FDM printed PLA part", Rapid Prototyping Journal(2018).
15. Lai-Chang Zhang,* Yujing Liu,* Shujun Li, and Yulin Hao, " Additive Manufacturing of Titanium Alloys by Electron Beam Melting": A Review, Advanced Material Sciences (2017).
16. Zharyaykassyn Beibit, "Optimisation of strength properties of 3D printed materials", Materials(2020)
17. Sunpreet Singh, Narinder Singh, Munish Gupta, " Mechanical feasibility of ABS/HIPS Structures primed by low-cost Polymer print", Emerald insight (2018).
18. Ajay Batish, M. P Singh, " 3D Printed Mechanical properties of a matrix reinforced with multi-material", Materials Today(2020)